Detection of abandoned mineshafts in the proximity of railways

Francis H. Drossaert

Doctor of Philosophy

The University of Edinburgh

2008

Declaration

This thesis, the work discussed and results shown were carried out solely by me unless otherwise stated within the text.

Francis H. Drossaert

Edinburgh, February 2008

Abstract

This thesis contains the results of a project funded by Network Rail. The mining industry left a legacy of numerous concealed abandoned mineshafts throughout Britain. Decades later an improperly sealed mineshaft can cause subsidence or even collapse. In order to provide a safe and reliable railway system, Network Rail set itself the target to locate and treat all known mineshafts in the proximity of railways. Several geophysical surveys were commissioned by Network to locate mineshafts, with limited results.

The first goal of the project was a literature survey to assess the performance of geophysical and non-destructive testing techniques to locate buried mineshafts. Some preliminary geophysical surveys were conducted at the University of Edinburgh's full-scale track bed model. These surveys showed that the presence of the railway affects the performance of the survey techniques. The second goal of this project was to investigate further potential techniques to detect mineshafts near railways. Network Rail preferred techniques that do not require possession of the track and therefore the research was focused on the seismic techniques and in particular on the transmission method.

Numerical modelling software was developed in order to gain an understanding of how the presence of the mineshaft affects the seismic data. In order to obtain noise free data, a new absorbing boundary condition was developed. Three formulations of this condition are presented. Numerical tests showed that they perform considerably better than conventional conditions. Then, various 3D models of mineshafts were run to simulate synthetic seismograms. From the seismograms and the snapshots, it was concluded that mineshafts give rise to diffracted waves, which are superimposed on other waves,

which render the seismograms difficult to interpret. The analysis of attributes – the first breaks, the dominant frequencies and the amplitudes – of the traces in the seismograms showed that anomalies in the curves are related to the presence of the mineshaft.

Field experiments were conducted on a farm land that contained two mineshafts: one capped with known location and one completely backfilled with unknown location. The resulting seismograms were complex and difficult to interpret. The attribute curves were erratic, partially due to the variable geology and the variable receiver responses. Nevertheless, the data showed anomalies related to the presence of the mineshafts.

Acknowledgements

This project, described in this thesis, was sponsored by Network Rail and its financial support is greatly acknowledged. Special thanks go out to Brian Bell and John Stothard for initiating this project and also for their contribution and involvement.

I wish to thank Professor Forde and Dr Giannopoulos for their supervision and advice. I also would like to thank my two other supervisor, Professor Dave McCann and Peter Fenning, who provided numerous references and ideas.

Furthermore the efforts of the field crew and especially Ria Diamanti, Craig Warren, Richard Bates and Peter Fenning, are very much appreciated.

It is impossible for me to singular thank all my colleagues and friends who made Edinburgh and Scotland feel like home.

"HEEL VEEL DANK ALLEMAAL"

Table of contents

List of figures

List of tables

List of symbols

C_{ijkl} : stiffness tensor

E : strain rate tensor

E_{var} : variance

F : Fourier transform

f : frequency

f_{ij} : seismic trace with i is the trace number and j the time sample

H : Hilbert transform

i : imaginary number

i,j : location in grid

M : number of traces

N : length of time window

S : stress rate tensor

t : time step

t : travel time of diffracted wave

v : wave velocity

v_p : P-wave velocity

v_s : S-wave velocity

x_d, z_d : location of the projected diffraction point

x_r, z_r : location of the receiver

x_s, z_s : location of the source

α : attenuation coefficient of the complex frequency shifted PML

$\delta(t)$: dirac delta function

Δt : time step

Δx : cell size

ε : stretching function

κ : attenuation coefficient of the complex frequency shifted PML

λ : fluid incompressibility

λ : wavelength

Λ : multiplication factor

μ : shear modulus

ξ : multiplication factor

ρ : density

σ : attenuation coefficient

σ : Poisson's ratio

τ : stress

φ : multiplication factor

Υ^{i} : attribute value at receiver i

Ψ : strain rate sum

ω : angular frequency

Ω : stress rate sum

List of abbreviations

ABC	: absorbing boundary condition
ADEPML	: auxiliary differential equation perfectly matched layer
bf	: back filling
CFS	: complex frequency shifted
CPML	: convolution perfectly matched layer
EM	: electromagnetic
FDM	: finite difference method
FDTD	: finite-difference time-domain
FEM	: finite element method
GPR	: ground penetrating radar
MDS	: multipath diffraction summation
NCC	: normalised cross correlation
OHLE	: overhead line equipment
PML	: perfectly matched layer
ref	: reference
RIPML	: recursive integration perfectly matched layer
Rp	: reflected P-wave
Rs	: reflected S-save
RSG	: rotated staggered grid
SBM	: semblance based migration
Tp	: transmitted P-wave
Ts	: transmitted S-save
2D	: two dimensional
3D	: three dimensional

1. Introduction

1.1. Motivation

It was estimated that there exist about 80.000 mineshafts throughout the United Kingdom. A certain number of these mineshafts are located in the proximity of railways and some of them are concealed and might even be overlain by the railway structure itself. Often mineshafts were not properly capped or were not completely backfilled. Due to decay these mineshafts may collapse eventually. Collapsing of a mineshaft or subsidence due a mineshaft can cause serious problems for the railway operators.

Network Rail owns and operates the railway infrastructure in Britain. In order keep providing safe and efficient railway transportation, Network Rail sets itself the target to treat all mineshafts in the proximity of railways. From historic documents the approximate location of the mineshaft is known, but for treatment the exact location has to be known.

There are various methods to locate the mineshaft. The conventional method is by drilling boreholes. Drilling is a proven method however numerous boreholes can be required to locate the mineshaft conclusively. This can be expensive and very destructive to the railway structure. Other detection methods include geochemical and geophysical methods. These methods are generally non-destructive and can be cost efficient. Network Rail had commissioned several geophysical surveys e.g. microgravity, resistivity and ground penetrating radar. Unfortunately the results of these surveys were very limited.

1.2. Purpose of research

Geophysical and geochemical surveys have proven to be successful in the detection of hidden mineshafts. However, very few of these surveys were carried out near railways. The objectives of this PhD project can be summarized as follows:

- Assess non-destructive testing techniques to delineate mineshafts in the proximity of railways – focusing on both existing commercially available techniques, plus other potential techniques to delineate mineshafts. This assessment is based on available publications and small scale tests conducted at the track bed of the University of Edinburgh.
- Develop new tools – e.g. numerical algorithms – to further examine certain techniques which were selected from the assessment.
- Use the new numerical tools to examine the potential to delineate mineshafts of the selected investigation techniques - for various model cases.
- Establish the limitations, difficulties and the general performance of the selected investigation techniques in the field, by conducting a full-scale trial.

1.3. Outline of thesis

The first part of this thesis contains the literature review regarding mineshaft detection in the proximity of railways conducted by the author for Network Rail. Some general background information about railways and mining is presented in chapter 2. In the same chapter the procedures for locating a mineshaft at a site as recommended by the Department of Environment are discussed. Chapter 3 summarizes the results of the assessment of the studied methods to delineate mineshafts. These methods include visual inspections, geochemical and

geophysical reconnaissance. A shortened version of the assessment can be found in the Appendices A-C.

The second part of thesis deals with the assessment of seismic methods. In chapter 4, the theory of the numerical modelling and the theory of the novel absorbing boundary conditions are explained and discussed. In chapter 5, some examples and the analysis of the novel absorbing boundary conditions are presented. In chapter 6, numerical models of mineshafts are presented along with the resulting synthetic seismograms and snapshots. In chapter 7, the analyses of the synthetic seismogram are presented.

Since there is often a discrepancy between numerical data and field data, field experiments were conducted in order to verify the knowledge obtained from numerical modelling. Furthermore the experiments were used to identify problems in the field. The results of the field experiments are presented in chapter 8.

Chapter 9 contains the discussion and conclusions of the research and also some recommendations for further work are discussed.

2. Mining and Railways

This chapter provides some background information about mining and railways and deals with the issues of mineshafts present in the proximity of railways. Furthermore the general procedures for locating mineshafts as outlined by the Department of Environment are discussed briefly.

2.1. History of Mining

The earth has been worked for its minerals and other materials. Evidence of mining from long before the times of the ancient Egyptians can be found in Swaziland, where the oldest known mine of around 43,000 years old can be found. At this site hematite was mined to produce the pigment ochre. Around the same millennium in Hungary, Neanderthals mined flint for weapons and tools. Also in the United Kingdom evidence of pre-historic flint mining can be found at various locations, but it was not until the Romans invaded Britain that mining was conducted on a larger scale. The Romans mainly mined metals such as gold and lead, but also limestone for their buildings.

The oldest written records of coal mining in the United Kingdom date from the 12th century (*Burke, 1988*). It is reasonable to assume that mining operations prior to these records were not extensive since the market for coal and minerals was small. A century later peat and fuel wood were getting scarce - especially in and around the cities - which resulted in an increase in demand for coal. During the golden age of Elizabeth, the power and influence of Britain grew worldwide. Increased demand for nails, fastenings, shot, canon and canon balls for the ship

building industry resulted in a significant increase in demand for coal and iron. Furthermore the strong population growth caused an increased demand for bricks, salt and glass which all require coal for its manufacturing. During the following centuries the mining industry increased steadily, but it was not until the beginning of the industrial revolution that it really boomed. The coal mining industry grew exponentially to fulfil the demand for coal needed for fuelling steam engines. Due to the surplus of imported cheap coals in the 20th century, the coal mining industry declined and was no longer sustainable. After several turbulent decades of mine closures and violent strikes, the British coal mining industry has withered and nowadays only a few pits remain open in Yorkshire and Nottinghamshire (*BBC, 2004*).

2.1.1. Mineshafts

The early mining operations in the United Kingdom consisted of quarrying the materials from exposed outcrops and from shallow seams (*Burke, 1988*). Often adits were driven from the outcrops into the seam permitting the extraction of the ore or coal. Another common method used in the early days of mining is by means of bell pits. Bell pits were mainly used for flint mining and mining iron stones; although some bell pits have been found in shallow coal fields. A bell pit is a single vertical shaft sunk to the bottom of the seam which is worked to a limited extent around the shaft till there were signs of roof collapsing. Generally, bell pits were no more than 12m deep, although bell pits of up to 30m deep were constructed. The diameter of mined area around the central shaft spanned from 8m to a maximum 20m. Bell pits were used until the 17th century (*Littlejohn, 1979*).

In the 15th century new techniques to extract the seam came into existence. Using partial extraction techniques such as room-and-pillar mining, the extraction of the materials was no longer restricted to the area around shaft and larger areas could be mined. Later total extraction techniques emerged such as shortwall mining in Scotland and longwall mining in Shropshire. In the beginning these mine workings were accessed by one single mineshaft. Although sometimes a connection with another colliery was established allowing air ventilation. During the 17th and 18th centuries it became more common to have two or more mineshafts. The separation between these mineshafts can be merely 3m apart to being opposite of the mine workings. For deeper mine workings it was still common to use one single mineshaft, but due to frequent accidents it became compulsorily in 1852 to have at least two mineshafts per mine working.

The invention of steam-driven pumps in 1712 improved the draining of the mine workings and greater depths could easily be achieved. At the end of the 18th centuries mineshafts of 250m deep were constructed. The trend of increasing maximum depths continued until modern times. Figure 2.1 illustrates the general trend of maximum depths of mineshafts for the last four centuries. The deepest mineshaft in the United Kingdom at present times can be found in Boulby near Middlesbrough. At Boulby, an 1150m deep mineshaft was constructed in order to mine the potash present in seams at 1200m and 1500m depth.

The diameter of the mineshaft in Boulby is about 5.5 metres. Similar to maximum depth of the mineshaft, the width of mineshafts increased over the last centuries. During the 1600s the average diameter of a mineshaft was merely 1m. The average diameter rose to 2m around 1750, although mineshafts with 1m diameter were still constructed. The diameters of mineshafts around the 1900s were between 2.5 and 7.5m. More recently, the National Coal Board, which is now the Coal Authority, has standardized the diameters to a typical value of

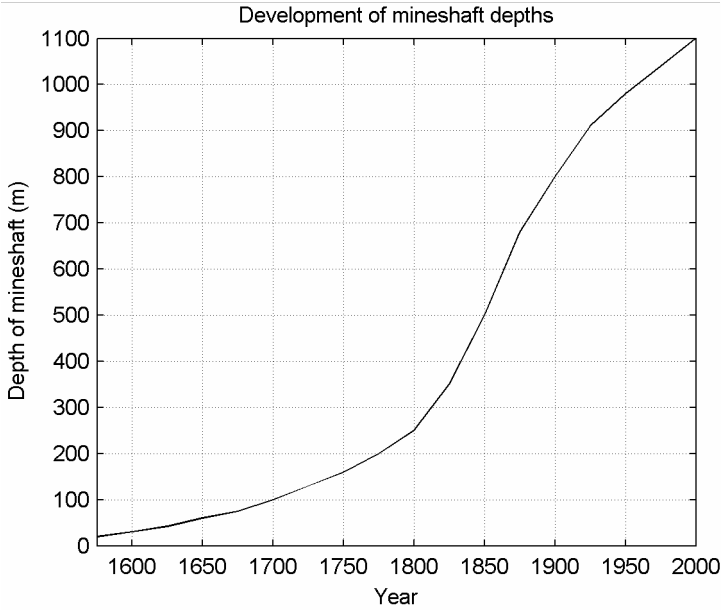

Figure 2.1. An generalisation of the development of maximum depths of coal mineshafts, after (*Department-of-the-Environment, 1976*)

6.1m and 7.3m. It is unlikely that the maximum size of mineshafts increased much after the turn of 20th century. An overview of the development of the diameter of the mineshafts over the last centuries can be found in Figure 2.2.

With increasing mineshaft depths and diameters, it became necessary to support the mineshaft to prevent it from collapsing. Mineshaft linings were used since the 17th century. In the beginning wooden linings were used and two centuries later it became common practice to use bricks for lining. During the sinking of the mineshaft, wooden and sometimes iron frames were to support the mineshaft initially and thereafter brickwork was constructed within the frame. The use of metal linings became common through the 19th and 20th century. At the close of the 20th centuries concrete lining was introduced.

Figure 2.2. The development of the diameter of mineshafts from 1550 to 1900, after (*Department-of-the-Environment, 1976*)

2.1.2. Closure of mines and mineshafts

After the seam was mined, the mine became unprofitable. In most cases the mining site was closed and the operations were continued at a new site. Other reasons for closure could be collapse danger, drainage problems, change of management or the mine becomes unprofitable due to economical changes.

After closure of the mine working, the mineshaft had to be sealed for safety reasons. There were various methods to secure an abandoned mineshaft and today abandoned mineshafts can be encountered in various conditions. The most common conditions are represented in Figure 2.3.

The chosen practice to secure a mineshaft depended mainly on the size of the mineshaft. Deep mineshafts were very unlikely to be completely backfilled and the most common practice was to backfill the abandoned mineshafts partially. This method consisted of building a scaffold just below ground level or near the

bed rock. Sometimes the upper part of the lining was removed and the scaffold was built on the remaining lining. In 1871 the Mines Inspectorate recommended the use of large wooden logs for the scaffolding. These logs were fixed together and laid across the mineshaft. However regardless of the recommendation, it was more common to dump mine tubs, trees or even colliery steam engines into the mineshaft, which formed an obstruction. Hereafter the mineshaft was backfilled till ground level.

The material used for backfilling consisted of almost anything that was available at the site. Generally it consisted of colliery and building waste such as wood, ropes, ashes from the engines, some lining material, and remnants of rock through which the mineshaft was sunk. The backfilling might be mixed with superficial deposits.

Abandoned mineshafts that were not partially or completely backfilled were secured by either fencing the area off or by capping. There was little consistency in the methods of capping.

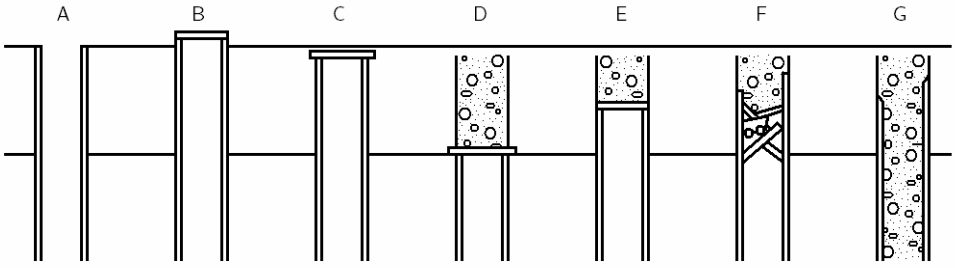

Figure 2.3. The various states of mineshafts encountered at present day: A – completely open, B – capped with the platform above the surface, C – capped with platform on the or just below the surface, D – backfilled with platform on the bedrock head, E – backfilled with platform on the rim of the lining, F – backfilled with material clogging the mineshaft and G – completely backfilled

2.2. History of railways

One of the first railway-like constructions can be found in Greece. Around the 7^{th} century B.C. a rut way was built enabling boats to cross the Isthmus of Corinth safe and quickly. The Diolkos was such a success that it remained in use for thousands of years till the 10^{th} century A.D. The Romans introduced a similar system using horses to haul wagons from and to the quarries along tracks cut in rocks. In the 16^{th} century German miners used a wooden rail to move ore in tubs within a mine. Not long after that, wooden rails were used to transport coal from the mines in Strelley to Wollaton, west of Nottingham. Similar railway systems were introduced in the whole of Britain, mainly to transport coal from the mine to the waterside where the coal was hauled onto boats for further transportation. The first iron railways appeared in the late 18^{th} century. Until the early 19^{th} century railways were primary used to transport heavy loads, but in 1803 the first public railway was opened to transport passengers from Wandsworth to Croydon in south London.

The first steam locomotive was built in 1804, but it was not until 1811 when John Blenkinsop built a practical locomotive which was used to connect Middleton colliery with Leeds. In 1825 and 1830 the Stockton-Darlington railway and the first intercity line between Manchester-Liverpool was constructed. The Manchester-Liverpool line showed that rail transport was viable and the golden age of train transport began. Soon railways appeared all over the United Kingdom and the rest of the world. Even in these modern times with automobiles and jet powered aircrafts, railways play a vital role in the national and international transport system.

2.2.1. Railways

Trains and railways have been around for almost 200 years and many developments have taken place. However, the outline of a railway has been little altered over the decades. Figure 2.4 shows a schematic cross section of a railway (*Coombs, 1971*). The following key elements can be identified:

- Rails are needed to guide the train and consist of two parallel high quality steel beams.
- Sleepers, also known as railroad ties, are laid transversely to the rails on which the rails are supported and fixed. The purpose of the sleepers is to transfer the load due to passing trains into the ballast and the foundation. Sleepers are generally made of wood or concrete.
- Ballast layers are required to disperse the load over a large area such that the safe bearing pressure is not exceeded.
- Blankets are often used to prevent the ballast being driven into soft clays and it usually consists of a layer of sand.
- Foundation is a part of the formation which includes the ballast and the blankets. Originally the foundation layer was built with large stones, but nowadays it is built with soils.
- Embankments are built to prevent strong gradient fluctuations in the railway.
- Cuttings are often needed to lower the ground such that changes in the railway gradients are small.
- Drains are required to transport precipitation away the railway to prevent weakening of soils due to saturation.
- Cable trough is a gutter containing cables for signalling and communication.

- Overhead line equipment (OHLE) consists of a mast and overhead lines which are used to transmit the electrical energy to the trains. Although the majority of the railways in the United Kingdom are electrified, there are various railway sections which do not have overhead line equipment.
- Ditches are constructed to provide better drainage of the railway.
- Fences are often placed for security reasons.

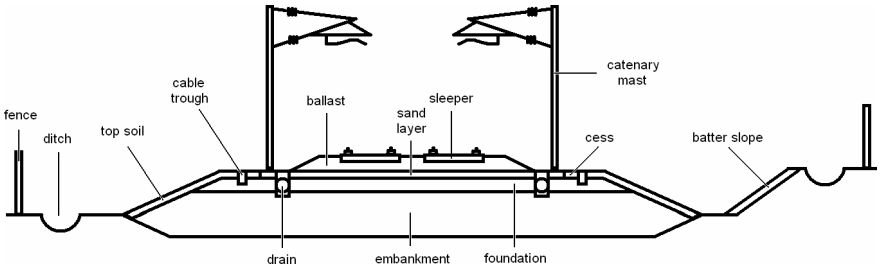

Figure 2.4. Schematic cross-section of a railway (not to scale) with some key elelments noted, modified from (*Coombs, 1971*)

2.3. Mineshafts in proximity of railway infrastructures

From the history of the railways, presented in section 2.2, it is clear that the history of railways and mining are closely entangled. The first railways in the United Kingdom were built to transport materials from inside the mine to the surface and later to transport the mining materials to the waterways or cities. It was not until the 19th century that railways were constructed to transport humans. It is therefore not strange that the density of railways, defined as total length of railway per surface, is much larger near areas that were mined intensively. Furthermore since the mining industry provided employment, large cities sprawled in these areas. Furthermore increased mobility in the 20th century caused an increase railway length and density. Figure 2.5 shows the national rail

network overlain by a map with the mined areas indicated by a grey colour (*Woodland and Statham, 1992*). Note that only the national rail network is presented in the figure and that railways primarily used by industry and unused railways are not represented. In the figure high concentrations of railways can be found in mining areas near Bristol, Doncaster, Leeds, Manchester, Middlesbrough, Newcastle upon Tyne and Sheffield in England. In Scotland railways are concentrated around Edinburgh, Falkirk and Glasgow in Scotland and in Wales north of Cardiff.

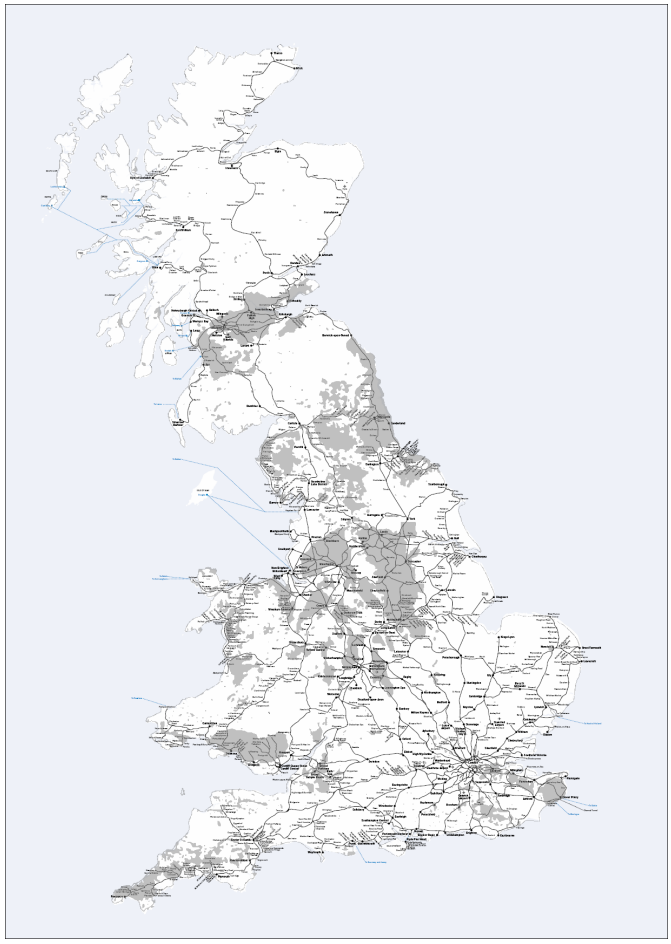

Figure 2.5: Map of Great Britain with the mining areas (*Woodland and Statham, 1992*) and the railway network

2.3.1. Mineshaft collapses

From Figure 2.5 it can be observed that vast areas were mined in the United Kingdom. Numerous mineshafts were sunken into the subsurface in order to access the seam. Additionally, numerous shafts were sunken for air ventilation. It is estimated that about 80.000 old mineshafts are present in the United Kingdom (*Littlejohn, 1979*). After closure of the mine these mineshafts were often hidden from the eye. Decades or even centuries later the site was redeveloped for the construction of railways. Hence, it is not surprising that a certain number of mineshafts are located close to railways and several mineshafts may even be located beneath the railway.

Most of these mineshafts were partially backfilled. When the scaffold that holds the backfill up gives way, the mineshaft can collapse instantly. The collapse of a mineshaft can have severe consequences. For example in 1945 near Wigan, a mineshaft reopened beneath the railway just when a locomotive with wagons loaded with coal passed by (*Shryhane, 2007*). Some wagons fell into the mineshaft and their weight dragged the locomotive with its driver into the hole. In Figure 2.6, a picture of the collapsed mineshaft can be found. The front and the buffer of the locomotive called Dolly can be observed. The wreckage and the body of the driver were never salvaged.

More recently in March 2001, a mineshaft collapsed in Machen in South Wales. A picture of the collapse mineshaft can be found Figure 2.7. The mineshaft was located 2.7m from the Rumney railway which was closed at the end of 1962 (*Crawford, 2001*). The mineshaft was about 20m deep and partially filled with water. The cause of the collapse was the failure of the wooden platform that was located about 4m beneath the surface. The mineshaft appeared to be backfilled from the platform to the surface (*Stothard, 2007*).

Figure 2.6. Photograph of collapse mineshaft with the front of the locomotive visible (*Shryhane, 2007*)

Incidents with fatalities like the one present previously are fortunately a rare occurrence. However, abandoned mineshafts near railways do regularly cause problems due to subsidence or collapsing. Subsidence or a collapse close or beneath the railway, can cause instabilities in the railway embankment. To prevent serious incidents, it is necessary that the railway is closed until the mineshaft is treated such that it does not pose a long term threat to the stability of the railway. In extreme cases the railway needs to be relocated. For example at Dolphinstone, east of Edinburgh, a large area consists of shallow mine workings and multiple mineshafts causing subsidence and hollows at the surface. The overlying east coast line connecting Newcastle upon Tyne with Edinburgh needed to be relocated to prevent instabilities at the railway. The whole rerouting operation was conducted between 1988 and 2001 at a cost of 56 million pounds (*Clarke et al., 2006*).

Figure 2.7. A mineshaft collapse in proximity of the railway near Machen, in South Wales in 2001

2.3.2. Causes of mineshaft collapse

The primary cause of the collapse of a partially backfilled mineshaft is the failure of the platform or obstruction that supports backfill (*Dean, 1967*). There are various reasons why the platform or obstruction may give way:

- In the situation where an obstruction, constructed by dumping discarded tubs, trees, it is obvious that the construction is inherently unstable.
- In the case where there was a proper platform built from wood inside the mineshaft, it is still possible that it will collapse due to disintegration of the wood and the backfilling migrates to the bottom.
- In the situation where the platform was built on the rim of the lining, it is possible that the lining itself gives way. A possible cause is that the wooden frame between soil or rock and the brick lining has disintegrated, leaving the brick lining unsupported.

- The backfilling has a porous nature or consist of fine material. When subjected to water, the backfilling becomes plastic and can be forced down the mineshaft like a paste.
- In the case where the platform is built on the rock head, failure of the rock head can occur due to the load of the platform on the brittle bedrock (*Littlejohn, 1979*).

2.4. Detection of abandoned mineshafts

Travelling by railways is one of the safest ways of transportation. Network Rail owns and operates the fixed infrastructure assets of the British railway e.g. the railways, marshalling yards, stations and etc. Until recently Network Rail did not routinely search for and treat abandoned mineshafts, which might cause subsidence or collapse near railways. Actions were only taken when problems occurred. In order to keep providing a safe and reliable railway system, Network Rail set itself the target to treat all known mineshafts near railways. In order to treat a mineshaft its exact location has to be known.

A suitable procedure to investigate the location of a mineshaft was outlined by the Department of Environment (*McCann et al., 1987*). A summary can be found in Figure 2.8. Basically the investigation procedure consists of three phases. The first phase is a comprehensive desk study to gather all potential information about the site and the mineshaft. The desk study is followed by a field reconnaissance which includes geophysical or geochemical surveys. Culshaw and Waltham suggested that a simple walkover site investigation should be included in the field reconnaissance since visual evidence of the mineshaft may still be present (*Culshaw and Waltham, 1987; Bell, 1975; Culshaw et al., 2004*).

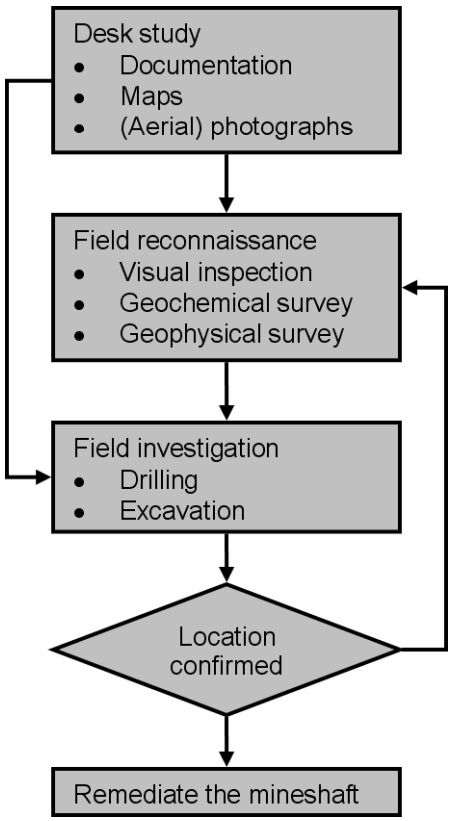

Figure 2.8. Flowchart of the investigations of an abandoned mineshaft

The visual inspection, geochemical and geophysical field reconnaissance are discussed in the next chapter. Other possible field reconnaissance methods do exist. For example subsidence monitoring measures the ground displacement due to subsidence caused by the presence of a mineshaft. Great advances have been made using satellite and air-borne instrumentation to measure subsidence (*Kircher et al., 2003; Weeks, 2004*). These and other subsidence monitoring techniques are passive techniques and therefore they are not considered any further.

All field reconnaissance techniques identify anomalies which might be associated with the presence of the mineshaft. In order to locate the mineshaft conclusively it is necessary conduct field investigations. These field investigations

usually comprises of drilling boreholes at the location of the anomalies identified during the field reconnaissance. In the case that the field investigations do not positively prove the location of mineshaft, it is necessary to conduct further detailed geophysical surveys followed by more drilling.

2.4.1. Desk study

The first phase of a site investigation for a mineshaft is the desk study. It should be pointed out that a comprehensive desk study of the area must be carried out before commencing the second or third phase of the investigation program. In many cases the results of the desk study yields sufficient information to proceed to the field investigation without the need of any geophysical or geochemical surveys. Moreover the desk studies will provide some knowledge about the survey site, such as geological data, as well some knowledge about the properties of the mineshaft itself. Since the geological setting and the properties of the mineshaft determines the success of geophysical or chemical survey, it is important to obtain any a priori information about the geology and the mineshaft (*McCann et al., 1987*).

Although it was not compulsory to produce mine abandonment plans and up-to-date mine working maps until 1872, a great number of documentary records is available about older mines. Available historical data can be obtained from a wide range of sources which are listed below (*McCann et al., 1988; Woodland and Statham, 1992*)

- The Coal Authority
- British Geological Survey
- Corus and other valuers

- Local and regional authorities
- Local and regional mining museums
- Local libraries
- Mining history organisations

Besides documents, photo material and especially aerial photographs can be of value during the desk studies stage. Not only pictures at the time of mining, but also pre-World War II aerial photos might contain visible information about the location of the mineshaft. There are various sources where historic aerial photographs can be found, such as mining museums, private collections and government organisations.

2.4.2. Field reconnaissance

After the first phase in the investigation procedure is completed, it is normal to proceed with the field reconnaissance. However, in some cases the desk study yields enough information about the likely position of the mineshaft that the second phase can be omitted to proceed with the field investigations.

However, in most cases the desk studies do not yield enough information about the exact location of the mineshaft. Especially mineshafts that date from before 1872 little to no information can be found on them. Even when there is information on the location of the mineshaft, it should be processed with caution since its reliability and accuracy are questionable. After 1872, the year when it became compulsory to keep plans of mine workings, the situation improved. However, the accuracy of these mining plans remains dubious for several decades.

The purpose of the field reconnaissance is to identify anomalies which might be related to the presence of the mineshaft. Anomalies that manifest on the

surface can be identified by a visual inspection. Visual inspection is a cheap and fast survey method. Anomalies in the subsurface can be identified by either a geochemical or a geophysical survey. The choice of the geochemical or geophysical survey technique depends on its ability to quantify the anomaly produced by the mineshaft. This anomaly can be produced by the following mineshaft elements or by a combination of the following elements

- Void
- Backfilling
- Lining
- De-stressed rock

Whether the anomaly can be observed in the data obtained by the chosen survey technique depends on the physical dimensions, shape and depth, the physical or chemical properties of the mineshaft and the surrounding material; this is in relation to the penetration depth, resolution and signal-to-noise ratio of the selected technique (*McCann et al., 1987*). Hence knowledge about properties of the mineshaft and surrounding is pivotal in the process of selecting the survey method that most likely will resolve the mineshaft. Various field reconnaissance methods are summarized in chapter 3.

2.4.3. Field investigations

Although the recommended investigation procedures as summarized in Figure 2.8 states that field investigation such as drilling should be carried out after the field reconnaissance, it is very common practice to by-pass the field reconnaissance. An important reason for omitting the field reconnaissance is the lack of positive

results from using geophysical or geochemical survey methods whereas delineation of mineshafts by drilling is a fail-safe method. Therefore the most common method commissioned by Network Rail is by drilling boreholes in the ground.

However, the result of the drilling is only valid for an area equal to the diameter of the shaft around the borehole. This means that numerous boreholes are required to delineate a mineshaft at a site. Theoretically, in order to have a hundred percent probability to detect a circular shaped mineshaft, the distance between boreholes should be less than diameter of the shaft divided by $\sqrt{2}$. For a survey area of 50 by 50 metres this results in almost 1300 boreholes in order to detect a shaft with a 2m diameter. Drilling many boreholes is not very feasible. Geochemical and geophysical surveys do not exhibit this problem. Although the measurements are taken at discrete intervals, it typically accounts for large volumes around the sample point.

Drilling numerous boreholes is not only very expensive, but also destructive to the investigation site. Drilling in the embankment is not desirable since it could weaken the railway structure. Omitting the drilling into the embankment would leave a large investigation area un-sampled.

Another consideration that should be taken into account when drilling boreholes is the safety issues involved of having a heavy drilling rig on a potentially unstable site. Appropriate safety measures have to be taken in order to prevent the rig falling into a reopened mineshaft.

2.4.4. Possession management

One of the important issues involving the field reconnaissance and field investigations is the possession of the track during the survey. Most of the techniques discussed in this thesis require that measurements are taken at the

railway itself. Furthermore in order to guarantee the safety of the surveyors, possession management is required i.e. railway traffic can not take place when access to the railway is required. Possession management impose logistically and financial problems for the railway operators. Alternative transportation has to be arranged for commuters and goods trains have to be detoured. These measures cost money which can even outweigh the total cost of the survey.

2.5. Summary

The history of mining and railways are closely entangled and as a result numerous mineshafts are located in the proximity of the railways. Due to decay backfilled mineshafts may collapse and hence they pose a treat to the railways. To provide safe transportation and continuity, Network Rail set it self the target to locate all known mineshafts near existing railways.

The procedures to delineate mineshafts are outlined by the Department of Environment. These procedures consist of the following steps: desk study, field reconnaissance, field investigations and eventual further detailed investigations. The field reconnaissance can consists of a visual inspection, geochemical survey or a geophysical survey. Network Rail has commissioned several field reconnaissance surveys with limited result and therefore the field reconnaissance is often omitted. However, numerous boreholes are required to detect a mineshaft conclusively. Drilling many boreholes is destructive and also very expensive. It is therefore recommended that field reconnaissance should be carried out to identify anomalies that are related to mineshaft. Field investigations are still required to prove the location of the mineshaft conclusively.

3. Field reconnaissance

The purpose of the field reconnaissance is to identify and localize anomalies that are associated with the presence of the mineshaft. As discussed in section 2.4.2, the field reconnaissance consists of visual inspection, geochemical and geophysical methods. This chapter summarizes the results of the literature review regarding field reconnaissance method. An extended overview of all examined reconnaissance methods can be found in the Appendices A-C.

An unbiased review of all the techniques is difficult since most publications often only show the successes and not the failures. Furthermore some techniques were used by a limited group of people which makes their performance statistically questionable. It should be stressed that no literature was found regarding geophysical surveys to locate mineshafts in the proximity of railways.

As part of the assessment various experiments were conducted at the full scale trackbed at the University of Edinburgh. The experiments included magnetromery, resistivity tomography, self-potential and GPR. The results of the experiments can also be found in the Appendices.

3.1. Visual inspection

Often the mineshaft expresses itself at the surface. The purpose of the field reconnaissance by visual inspection is to identify anomalous features at the surface. The following features can be related to the presence of the mineshaft:

- Subsidence depression and hollows caused by compaction or collapse.
- Surface discoloration caused by difference in soil or drainage.
- Conspicuous lineaments such as lone standing trees, excessively wet areas or vegetation withering.

The visual inspection can be carried out by foot or by air. A simple walk-over site investigation is cheap and fast. Airborne inspections using either photography or multi-spectral scanners were proven to be successful in the delineation of mineshafts (Cooper, 1989; Mooijmans et al., 1998).

There are various examples which suggest that visual inspection can identify surface anomalies which might be related to the presence of mineshafts (*Sladen et al., 1984; Mooijmans et al., 1998*). Several sites were visited for the field experiment presented in chapter 8 and 7 sites out of 11 showed conspicuous features related to the mineshaft – results are presented in Table A.1. However, the railway and its embankment are likely to mask any features that might have been present at the surface. It is therefore concluded that it is unlikely that visual inspection can identify anomalies related to the mineshaft.

3.2. Geochemical reconnaissance

This section summarizes the results of the review regarding the use of geochemical surveys as a field reconnaissance method presented in Appendix B. The examined geochemical techniques consisted of soil gas emanometry and additionally some radiometric techniques were also considered.

Few geochemical surveys, measuring the soil gas chemistry were conducted. These surveys show that measured anomalies in gas concentrations can be related to mine workings (*Sibley and Grainger, 1988; Donelly and Bramford, 1996;*

Bondarenko et al., 1983; Misquitta, 1989). In particular radon gas anomalies seem to correlate well to the location of the mineshaft.

Only a few publications were found regarding the use of geochemical techniques to located mineshafts or mine workings. At this moment it is not clear how gas anomalies are related to the presence of mineshafts and some results in literature are contradictory. Furthermore the prevailing weather conditions seem to affect the measurements. It is not clear how these weather conditions affect the results. However, the dependency on the weather makes the geochemical survey methods impractical.

Gas samples taken from the ballast are unlikely to be representative for subsurface and hence a large area is uncovered by the survey. Additionally the presence of clay could limit the performance of the soil gas emanometry survey. Unfortunately in the United Kingdom most mineshafts are related to coal measures which are more than often overlain by boulder clay.

Geochemical surveys might be a useful tool to delineate mineshafts away from the railway, but considering its characteristics a geochemical survey should not be the sole field reconnaissance method and should be conducted conjointly with other geophysical surveys.

3.3. Geophysical reconnaissance

This section summarizes the study of geophysical survey methods presented in Appendix C. The purpose of geophysical methods is to estimate the physical properties in the subsurface such as density, elasticity, resistivity and temperature. There exist numerous geophysical methods and each method having many varieties. New geophysical techniques and varieties emerge regularly and hence this overview may not be complete. The focus is mainly on existing

techniques that geophysical survey companies can provide. Exotic geophysical methods are only included when they appear to be suitable for mineshaft detection. The geophysical methods that make use of boreholes are discussed separately in section C.7.

3.3.1. Summary

The geophysical methods presented in Appendix C are summarized in Table 3.2. In this table the level of usage indicates the number of surveys conducted to locate mineshafts. This is based on the number of publications found concerning mineshaft detection. Additionally an indication of the cost of a survey is given. In Table 3.1 the values of the usage and costs are described. Note that the costs concern only the costs of the survey and not the costs of possession management. In the table it is also mentioned if possession of the track is required during the survey. “Yes” means that possession of the track is required; whereas a “No” means that the technique does potentially not require possession of the track.

In the last column of Table 3.2, the effectiveness of each technique is noted. The effectiveness is divided in three levels: low, medium and high.

- Low effectiveness means that the probability of a successful survey using the considered method is nil or very slim i.e. using this method only a few out of many surveys will have positive results.
- Medium effectiveness means that the examined method might be successful to delineate mineshaft. However, the success rate depends very much on the properties of the mineshaft and local geology. Furthermore the success rate depends strongly on the quality of the survey data and the competence of the surveyor and interpreter.

- High effectiveness means that the success rate of the method can be high. This does not mean that the every survey will be a success. As with the medium effective methods, the success rate depends very much on the properties of the mineshaft in relation to the local geology and the quality of data and competence of the surveyor/interpreter.

These three effectiveness levels are an interpretation by the author based on the available publications and should be considered as such. The optimal method to delineate a mineshaft at a certain site depends very much on the site conditions. It is possible that a combination of methods is required to delineate a mineshaft. The geophysicist or engineer in charge of the survey should select the optimal method or methods based on the site conditions.

Table 3.1. Explanation of the usage and costs variables presented in Table 3.2; note that the usage concerns the number of surveys conducted to locate mineshafts

Usage levels			Costs		
0	–	Never	£	–	Cheap
1	–	Rarely	££	–	Average
2	–	Sometimes	£££	–	Expensive
3	–	Regularly	££££	–	Very expensive

3.3.2. Geophysical methods

From the geophysical methods summarized in Table 3.2, the most commonly used methods to locate mineshaft are magnetometry, electro-magnetics, resistivity tomography and microgravity. **Magnetometry** is considered as ineffective due to the presence of metal parts at the railway. The results of the experiment at the

full scale track bed presented on page 299 confirm this conclusion. For the same reason **electromagnetics** are also considered as ineffective to delineate mineshafts in the proximity of railways.

Microgravity surveys have been successfully used for detection of air filled mineshafts. A priori information about water levels, geology, size of mineshaft, depth to the top of mineshaft can be useful to assess the probability of detection. For microgravity surveys various accurate corrections on the data are needed. Therefore microgravity surveys can be slow, tedious and very expensive. This makes microgravity unpopular, although its effectiveness is rated high. The same holds for the **vertical gradient** gravity method.

Resistivity tomography is effective in the delineation of water filled mineshafts and to a lesser degree air filled mineshafts. However, in order to image the subsurface beneath the railway, electrodes need to be placed in the ballast. The ballast consists of coarse aggregate with many air voids and the contact resistance can be a serious problem, although the experiment at the full scale track bed presented on page 307 shows that contact improving measures can improve the quality of the data. However, these measures do not improve penetration depth which is limited due to the high resistive ballast. Resistivity tomography surveys should only be conducted where the ballast layer is reasonably thin and the embankment is small. **Resistivity profiling** offers no advantages over resistivity tomography and **induced polarization** and **self potentials** are sensitive to noise; no publications were found regarding these techniques and mineshaft detection.

Ground penetrating radar is a popular tool since it provides quick data, readily interpretable in the field. Several surveys have been conducted using GPR to detect mineshafts with variable success. The track bed experiments presented on page 318 showed that the sleepers affect the data and limit the interpretation.

The biggest disadvantage of ground penetrating radar is its limited penetration depth in high conductive materials, such as clays. Unfortunately most mineshafts are related to coal which is often overlain by clay or boulder clay. Therefore GPR is not suitable for the detection of most of the mineshafts in the United Kingdom.

Thermal imaging techniques have been used to detect mineshafts with reasonable success. The dependency on the prevailing weather conditions is a problem for the practicability in the field. No publications deal with railways, but it is very unlikely that mineshafts beneath the ballast can be located by thermal measurements, because the aggregate dissipates any temperature anomalies.

Most seismic methods have never been used to delineate mineshafts. The main reason is that seismic methods lack enough resolution to resolve small mineshafts. According Figure 2.2 on page 8 large mineshafts, with diameters over 4m, were not built until the end of the eighteenth century and even after the turn of the century the number of large mineshafts constitutes a very small percentage of the total number of mineshafts. According Network Rail most of the mineshafts found near railways are not much larger than 2m in diameter, hence it can be concluded that most mineshafts are unlikely to be detected by **reflection seismics**, **refraction seismics** or **SASW** methods.

The **transmission** method was briefly used in the 1970s and the results are very promising. Despite the fact that only a few surveys were reported which were conducted by the same group of people, the effectiveness of the transmission method is estimated as high. The **diffraction imaging** method was also considered as very promising method. However, data from the numerical models presented in chapter 6 and the data from the experiments presented in chapter 8 demonstrate that the mineshaft does not produce any diffracted body waves which are not superimposed by other stronger waves. The effectiveness of the diffraction imaging method is therefore considered as low.

Cross-borehole and borehole-to-surface geophysical methods extend the mineshaft detection capability beyond the performance limitations of surface methods. Seismic tomography and cross-hole resistivity surveys are used regularly. However, the lack of lateral resolving power requires numerous boreholes to satisfy the probability that the survey space between two boreholes intersects the mineshaft in a large survey area. Drilling numerous boreholes is expensive and destructive. Therefore borehole methods are not considered as a viable non-destructive testing method for the railways environment and they are not considered any further.

Table 3.2. Summary of geophysical reconnaissance methods;

Method	Usage	Costs	Possession	Issues	Effectiveness
Magnetics	3	£	Yes	Susceptible to metal	Low
Microgravity	3	£££	Yes	Sensitive to vibrations, corrections	High
Vertical Gradient	1	££££	Yes	Sensitive to vibrations, corrections	High
Resistivity Profiling	2	£	Yes	Bad coupling, penetration depth at ballast	Medium
Resistivity Tomography	3	££	Yes	Bad coupling, depth penetration	Medium
Induced Polarization	0	£££	Yes	Bad coupling, depth penetration, sensitive	Low
Self Potentials	0	£	Yes	Bad coupling, depth penetration, sensitive	Low
Electromagnetics	3	£	Yes	Susceptible to metal	Low
GPR	2	££	Yes	Limited penetration depth in clay	Medium
Seismic Reflection	0	££££	Yes	Resolution	Low
Seismic Refraction	0	£££	Yes	Resolution	Low
SASW	0	£££	Yes	Resolution	Low
Diffraction imaging	0	£££	No	Mine shafts do not produce body wave diffractions	Low
Resonance	0	££	Yes	Resonance not always observed	Low
Transmission	1	££	No	Unknown	High
Thermal	2	££	Yes/No	Dependent on weather	Low

3.4. Course of action

In this chapter a brief overview was given on the detection of mineshafts and the issues of surveying in the proximity of railways. The following chapters cover an in-depth investigation of some these methods. Network Rail had expressed its preferences for methods that:

- Are simple in use and practical in the field, such that commercial geophysical survey companies can easily use the methods.
- Can survey the whole area including beneath the railway embankment.
- Are non-destructive i.e. do not require boreholes to be drilled.
- Do not require access to the railway embankment and hence possession management of the track is not required.

Only a few methods match the preference of Network Rail. As noted in this chapter electromagnetic methods are inefficient near railways and ground penetrating radar lacks sufficient penetration depth at most mineshaft sites. In agreement with Network Rail, the research focuses on seismic methods to locate mineshafts and in particular the transmission method as discussed in section C.5.6.

Diffraction imaging as discussed in section C.5.4 were also considered. The numerical data of three dimensional models presented in chapter 6 as well as the experimental data presented in chapter 8 did not contain any diffracted body waves. Therefore no in-depth study was carried out regarding the feasibility of diffraction imaging as survey tool for mineshaft detection. Some of the results are presented in Appendix H.

3.4.1. Transmission method

The work conducted by Dresen (*1979*) on the transmission method focuses on certain attributes of the individual traces. These attributes consisted of amplitudes, frequencies and arrival times. By plotting the values of the attributes along the survey line, anomalies related to the position of the mineshaft could be identified. The survey lay out consisted of one receiver and several shots which were positioned equidistant from the source. Figure 3.1 illustrates the survey lay-out as used by Dresen.

Using an equidistant spatial arrangement has the advantage that changes in the attribute values are solely related to the changes in the medium and not related to variations in travel distance. However, this arrangement is not practical in a railway environment since survey lines need to cross the railway i.e. possession of the track is necessary. Furthermore in order to cover a reasonably large area the source and receivers need to be relocated many times and the method becomes very time consuming and expensive.

Therefore the possibility of using a rectangular survey grid was examined in the project. The advantage of a rectangular survey grid is that there is no need for possession management and just by varying the shot positions a large area can quickly be covered. This survey lay-out bares resemblances with broadside refraction shooting (*Telford et al., 1990*), although previous surveys using this technique merely focussed on the first break of refracted waves. The concept of broadside shot gathers in the delineation of mineshafts in the proximity of railways is explained in Figure 3.1.

Since little research has been conducted regarding seismic methods to locate mineshafts, experiments are required. For basic understanding, field experiments are not useful since the geometrical structure and the physical properties of the mineshaft as well the detailed geology of the mineshaft area are often unknown.

Furthermore mineshafts can be found in various conditions and various geological settings. Numerous field experiments would be required to gain an insight of the potential of seismic methods to delineate mineshafts. Therefore numerical experiments are opted for. The following two chapters deal with the basics of numerical modelling and chapter 6 deals with the results of the numerical modelling.

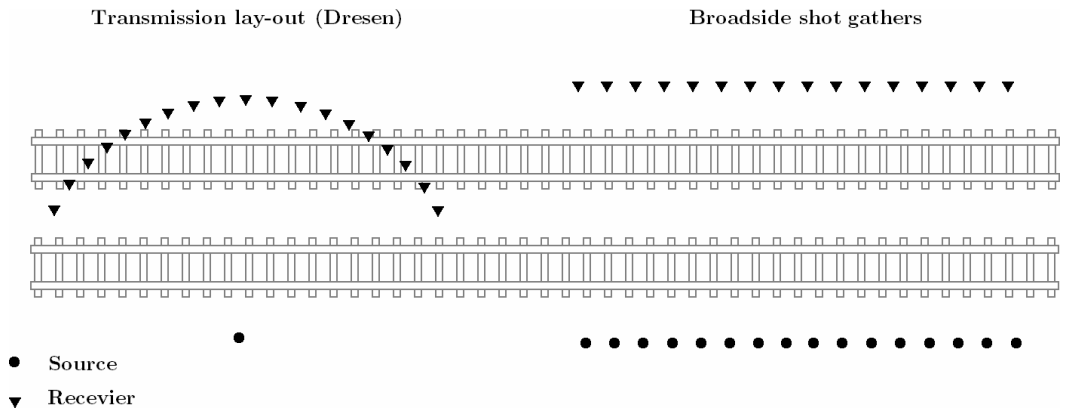

Figure 3.1. Survey concept of the transmission lay-out as used by Dresen (left) and the proposed lay-out using broadside shot gathers (right)

4. Numerical Modelling - Theory

To gain more insight of the seismic behaviour of mineshafts and the possibility of using elastic waves to delineate the mineshaft, there is a need for experimentation. Since field trials are expensive and require ground proofing, a series of experiments were conducted by means of numerical modelling.

This chapter deals with the theory of the numerical modelling. The first part of this chapter discusses the principles of seismic wave propagation and the various numerical modelling techniques and mainly focuses on the finite difference technique based on a rotated staggered grid.

The second part of this chapter deals with the boundary condition problems. In order to improve the performance of the boundary condition, new absorbing boundary conditions are introduced. The computational efficiency – memory requirements and floating point operators – of these conditions is analysed and compared to the conventional methods. Some of the boundary condition theory presented in this chapter is based on the papers published in Geophysics (*Drossaert and Giannopoulos, 2007b*) and Wave Motion (*Drossaert and Giannopoulos, 2007a*), by the author.

4.1. Principles of seismic wave propagation

When a stress is applied to an elastic medium the corresponding strain propagates outward as elastic waves which are also called seismic waves. There are two principal types of elastic waves: body and surface waves.

4.1.1. Body waves

In an elastic medium subject to stress there exist two types of strains which are the normal strains and the shearing strains. As a result all body waves are compressional or shear waves. In the compressional wave the medium particles move along the direction of propagation (Figure 4.1A) and in the shear wave the medium particles motion is perpendicular to the direction of propagation (Figure 4.1B). The shear wave is often abbreviated to S-wave and the compressional waves as P-wave.

The propagation velocities of both body waves are related to the elastic moduli e.g. the resistance to the deformation and the density of the medium. Assuming that the medium is isotropic, the velocity of the P-wave and the S-wave are given by the following equations respectively:

$$v_p = \sqrt{\frac{\lambda + 2\mu}{\rho}} \tag{4.1}$$

$$v_s = \sqrt{\frac{\mu}{\rho}} \tag{4.2}$$

where ρ is the density, λ is the fluid incompressibility and μ is the shear modulus. It follows from equations (4.1) and (4.2) that compressional waves have higher velocities than S-waves since the elastic moduli λ and μ are always positive numbers. Hence, compressional waves arrive first at the receivers and therefore the compressional wave is often referred as the primary wave which is why it is abbreviated to P-waves.

Furthermore from equation (4.2) it follows that velocity of the shear waves becomes zero when μ=0. Therefore S-waves do not propagate through liquid and gas mediums.

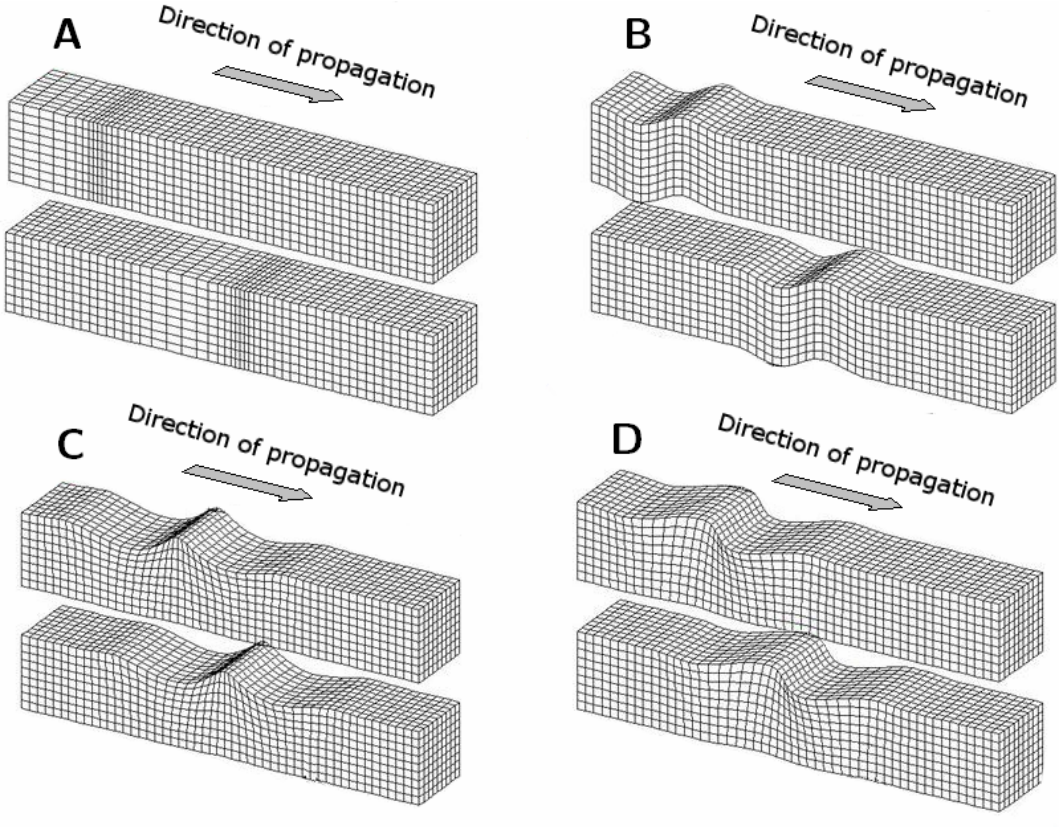

Figure 4.1. Illustration of the various seismic waves: P-wave (A), S-wave (B), Rayleigh wave (C) and Love wave (D); modified from http://www.geo.mtu.edu/UPSeis/waves.html

4.1.2. Surface waves

Lord Rayleigh found that fulfilling the boundary conditions at a free surface leads to the existence of surface waves. These waves are confined to the surface and their amplitudes decreases with increasing depth and hence they are often referred to as evanescent waves. Two types of surface exist: Rayleigh waves and Love waves. The medium particles in a Rayleigh have an elliptical retrograde motion in the vertical plane along the direction of propagation (Figure 4.1C) whereas the particles in the Love waves move perpendicular to the direction of

propagation along the surface (Figure 4.1D). Love waves consist of horizontal polarized S-wave which are only generated using special sources or in complex media and therefore are not considered further in the thesis.

The Rayleigh wave can be considered as a system of coupled P-waves and vertical polarized S-waves. The velocity of Rayleigh waves depends on the elastic moduli and the density near the surface and is generally less than the velocity of S-wave. The velocity of the Rayleigh can be approximated by the following equation (*Viktorov, 1967*):

$$v_r \approx \frac{0.87+1.12\sigma}{1+\sigma} v_s \approx 0.93 v_s \tag{4.3}$$

where σ is the Poisson ratio. Rayleigh waves exhibit dispersion which means that the velocity depends on the frequency components of the wave. Since the wave consists of a bandwidth of frequencies interference of the various frequency components produces constructive and destructive patterns. Constructive wave patterns behave as wave packages.

4.1.3. Reflections, refractions and diffractions

Whenever a wave impinges on the interface separating two media having different elastic properties such as the superficial-deposits and bedrock interface, a part of the energy is reflected back and a part of the energy is transmitted. To fulfil the boundary conditions at the interface any P- or S-wave impinging on the interface will generate a reflected P- and S-wave and also a transmitted P- and S-wave (Figure 4.2A). This phenomenon is referred as partitioning.

The angles of the transmitted waves conform to Snell's law. When the angle of the impinging wave approaches a critical angle, the transmitted waves

propagates parallel to the interface. While travelling along the interface otherwise known as the refractor energies of the transmitted wave are refracted back into the other medium as illustrated in Figure 4.2B. These waves are called refracted waves.

Although reflected and refracted seismic waves conform to Snell's law, this law is not applicable when the wave encounters features smaller than its wavelength such as sharp outcrops and also mineshafts. The laws of diffractions are complex but at greater distances from the diffraction point, the wavefront is essentially given by the Huygens' construction (*Telford et al., 1990*). A diffracted wave is illustrated in Figure 4.2C.

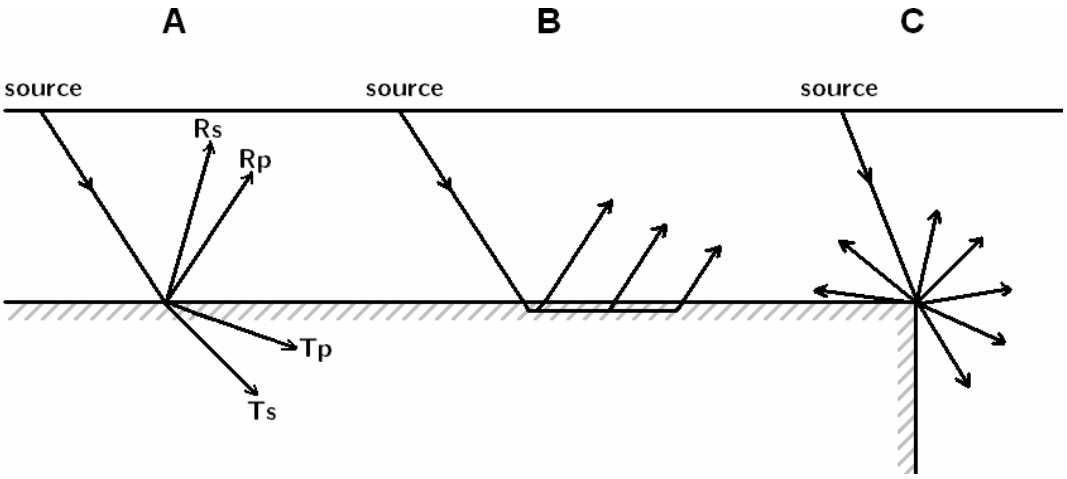

Figure 4.2. Reflections and the partitioning of waves (A), refractions (B) and diffractions of seismic waves (C); Rs denotes the reflected S-wave, Rp denotes the reflected P-wave, Ts denotes the transmitted S-wave and Tp denotes the transmitted P-wave

4.2. Numerical modelling of seismic waves

In order to analyse complex 3D structures such buried mineshafts, from seismic data observations, it is necessary to be able to predict how the seismic wave fields are affected by these structures. Exact analytical expressions can only predict the wave fields of simple structures. Responses from realistic complex structures cannot be obtained by analytical methods and therefore various numerical methods have been developed to take into account these structures. These methods can be divided in three subgroups, namely direct methods, integral equation methods and miscellaneous methods (*Carcione et al., 2002*). These subgroups can be subdivided as follows:

- Direct methods
  - Pseudo-spectral methods (*Gazdag, 1981; Kosloff and Baysal, 1982*)
  - Finite element methods (*Lysmer and Drake, 1972; Schlue, 1979*)
  - Finite difference methods (*Virieux, 1984, 1986*)
- Integral equation methods
  - Domain integral-equation method (*Pao and Varatharajulu, 1976*)
  - Boundary integral-equation method (*Tan, 1976*)
- Miscellaneous
  - Reflectivity methods (*Fuchs and Müller, 1971; Müller, 1985*)
  - Ray-tracing methods (*Cerveny et al., 1977*)

Both integral equations methods are restrictive in their application since for large models the memory requirements become exorbitant. The reflectivity method is effective for a simple layered earth. Although dipping layers can be resolved, the reflectivity method is unsuitable for complex structures. The ray-tracing method

is frequently being used in seismic modelling and imaging. This method is however approximative, since it does not take into account the complete wave-field. Furthermore, ray-tracing methods can only resolve heterogeneities larger than the maximum wavelength. Modelling small mineshafts in bedrock would require unreasonable high wave frequencies of over 1000Hz.

The direct methods are very popular since they provide full-wave solutions. Furthermore these methods can handle heterogeneities and can be very accurate when a sufficiently fine mesh is being used. The pseudo-spectral methods are generally considered to be the most accurate methods for forward modelling of seismic waves. However, these methods become computationally expensive when a dense grid is required for models including strong heterogeneities such as air filled mineshafts.

Finite element method (FEM) and finite difference methods (FDM) provide accurate full-wave solutions on the condition that some stability conditions are fulfilled. The governing wave propagation equations are solved by discretizing the geological model by a numerical mesh. The major advantage of the FEM is that it is very flexible in handling irregular shapes. This can be very useful to model fluctuating surfaces and voids in the subsurface e.g. embankments and buried mineshafts. This makes the FEM particularly useful for modelling mineshafts in a railway environment. On the other hand, the FDM requires a regularly shaped grid consisting of rectangular cells. Non-rectangular shapes such as round mineshafts cannot be modelled straightforwardly and need to be approximated by rectangular cells. However, the FEM solves the wave propagation equations implicitly whereas the FDM solves these explicitly. In other words, the FEM is an approximation to its solution whereas the FDM is an approximation to the differential equations in the wave propagation equations. Although inherently FEM is more accurate than the FDM, in order to obtain the solution using the

FEM large sparse matrices need to be inverted. In the case of large models this leads to an exponential increase in the required computer resources whereas in the FDM the required computer resources scale linearly to the size of the model. FDMs are the most commonly used numerical modelling method in seismics. The primary reason is that FDMs are relatively easy to program when compared to other methods. Secondary, finite difference methods can be efficient in terms of memory requirements and computational duration. For these reasons the FDM was selected for the modelling of the mineshaft.

4.3. Finite Difference methods

Virieux (*1984*) introduced the staggered grid which is nowadays considered the archetype of modelling grids. Compared to non-staggered grids the staggered grid shows an increased stability of finite difference schemes. Inherently staggered grids schemes proved to suffer less from grid dispersion and can handle larger variations of the Poisson's ratio without becoming unstable when compared to the non-staggered grid schemes (*Virieux, 1986*). In this thesis the staggered grid by Virieux will be referred to as the standard staggered grid. In a standard staggered grid scheme, wave propagation equations are written as a coupled velocity-stress system. Other systems have been proposed e.g. coupled displacement-strain system. These systems bare similar characteristics as the standard staggered grid and are not be further discussed.

The derivation of the coupled velocity-stress system of wave propagation equations is presented in the text box on page 47. A more extended derivation is written by Lay and Wallace (*1995*). Using the indicial notation the velocity-stress system can be written in the frequency domain as

$$i\omega\rho\tilde{v}_j = \frac{\partial \tilde{\tau}_{jk}}{\partial x_k}$$
$$i\omega\tilde{\tau}_{jk} = C_{jklm}\frac{\partial \tilde{v}_l}{\partial x_m} \qquad \text{where } j,\ k,\ l,\ m = x,\ y \text{ or } z \tag{4.4}$$

where τ and v are the stress field and the velocity field; the tilde denotes their frequency domain counterpart. C is the elasticity tensor and i and ω is the imaginary unit and the angular frequency. The standard grid scheme solves these equations by discretizing them in space, where the velocity field components are located half a grid cell away from the stress field components. Also these equations are discretized in time, where the velocity field components are updated half a time space after the update of the stress field components.

The elementary cell of the standard staggered 2D grid for isotropic media is represent in Figure 4.3a. The field components are positioned such that the components required for the update are merely a half a cell away. Note that the density and shear modulus are located on the edge of the cell. Consequently it is necessary to interpolate these variables between adjacent cells or take the value at half a grid cell away from the position. This can lead to a mismatch between the wave field components and the model parameters resulting into an anisotropic behaviour of the wave field. Furthermore interpolation of the density can lead to stability problems for inhomogeneous media with high density contrasts.

The anisotropic behaviour and instability problems can be avoided by adopting the rotated staggered grid introduced by Saenger (*2000*) for a displacement-strain equation system. Mineshaft models contain strong density contrasts; therefore the rotated staggered grid is considered to yield better results than the standard staggered grid. However, it should be pointed out that the rotated staggered grid is an experimental grid. This grid will be discussed in the next section.

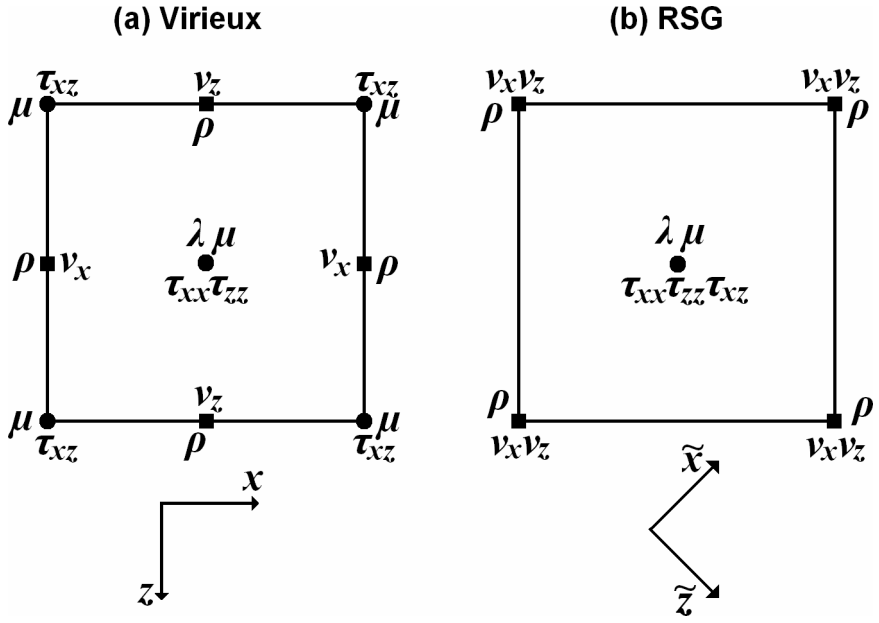

Figure 4.3 The elementary cells of (a) the Virieux grid and (b) the Rotated Staggered Grid for a 2-D isotropic elastic medium

4.3.1. Rotated Staggered Grid

The rotated staggered grid – hereafter called RSG – is an experimental grid introduced in 2000 by Saenger (*2000*). The first RSG was based on a displacement-strain equation system and in 2004 a grid based on velocity-stress system was introduced (*Saenger and Bohlen, 2004*). The main strength of the RSG is that it can deal with strong heterogeneities. Therefore the RSG find its application in the modelling of irregular surfaces, shallow cavities (*Gélis et al., 2005*) and cracks in media (*Saenger et al., 2000; Krüger et al., 2005*). Although a few papers have been published regarding the RSG, this grid remains experimental and should be considered as such.

The elementary cell of the RSG is represented in Figure 4.3b. Note that the shear modulus μ is now located in the middle of the elementary cell and no longer on the edges. Therefore interpolation with adjacent cells is not required and the

grid does not show any anisotropic behaviour. Since the density is located at the edge of the elementary cell it is required to interpolate the density with the three adjacent cells and seven cells in the case of a 3D model.

Numerical experiments showed that the RSG is conditionally stable, even when modelling strong inhomogeneities, such as voids and cracks, where the standard staggered grid becomes unconditionally unstable (*Bohlen, 2003; Saenger and Bohlen, 2004; Krüger et al., 2005*).

One of the conditions to which the RSG should comply for a stable scheme is the Neumann stability condition. The study of the stability of a finite-difference scheme consists of finding the conditions under which the error, defined by the difference between the theoretical and numerical solutions of the finite-difference equation, remains bounded as the number of time iterations tends to infinity (*Pereda et al., 2001*). It is demonstrated that the Neumann stability condition is less restrictive for the RSG than the standard staggered grid i.e. the time step of RSG scheme can be larger given the same model parameters (*Saenger et al., 2000*).

It is also demonstrated that the dispersion relations of the RSG are independent of any value of the Poisson ratio (*Saenger et al., 2000*). Therefore the free surface condition can easily be implemented by setting the Lamé's parameters to zero. By setting these elasticity parameters to zero the stress tensor components at the surface and above remain zero. Furthermore to prevent small grid dispersion caused by the free surface interface, the density of the cells above the free surface should be very high such that inverse of the density is very low; therefore the velocity field remains zero at the interface cells.

Wave propagation equations

Waves propagating in an elastic medium are subjected to two laws which are Newton's second law and Hooke's law. Newton's second law relates the forces acting on a body to its mass and its acceleration. Assuming an infinitesimal small particle in a 3D space is displaced due to a propagating wave, Newton's second law states that

$$\begin{aligned}
\rho \frac{\partial^2 u_x}{\partial t^2} &= \frac{\partial \tau_{xx}}{\partial x} + \frac{\partial \tau_{xy}}{\partial y} + \frac{\partial \tau_{xz}}{\partial z} \\
\rho \frac{\partial^2 u_y}{\partial t^2} &= \frac{\partial \tau_{yx}}{\partial x} + \frac{\partial \tau_{yy}}{\partial y} + \frac{\partial \tau_{yz}}{\partial z} \\
\rho \frac{\partial^2 u_z}{\partial t^2} &= \frac{\partial \tau_{zx}}{\partial x} + \frac{\partial \tau_{zy}}{\partial y} + \frac{\partial \tau_{zz}}{\partial z}
\end{aligned} \tag{4.5}$$

where u_i is the displacement of the particle in the i-direction. The subscript i can be x, y or z in a Cartesian coordinate system. In the thesis the indicial notation is used for convenience. The indicial notation was introduced by Albert Einstein and therefore often referred as the Einstein notation. Using this notation, equations (4.5) can be written simply by

$$\rho \frac{\partial^2 u_i}{\partial t^2} = \frac{\partial \tau_{ij}}{\partial x_j} \tag{4.6}$$

Note that repeated indexes – in this equation j – imply a summation. Hooke's law relates the stresses with the strains in the medium and the strains are related to the displacement. A general form of Hooke's law can be written as

$$\tau_{ij} = C_{ijkl} \frac{\partial u_k}{\partial x_l} \tag{4.7}$$

where C is the elasticity tensor. It should be mentioned that throughout the thesis it is assumed that the modelled medium is isotropic. The elastic tensor in such medium can than be approximated by

$$C_{ijkl} = \lambda \delta_{ij} \delta_{kl} + \mu \left(\delta_{ik} \delta_{jl} + \delta_{il} \delta_{jk} \right) \tag{4.8}$$

where λ and μ are called the Lamé constants. The λ is often referred as the fluid incompressibility and μ is referred as the shear modulus. The coupled displacement-stress equations (4.6) and (4.7) are the governing wave propagation. In order to obtain the coupled velocity-stress system, equation (4.7) is differentiated in time which results into the following equation:

$$\frac{\partial \tau_{ij}}{\partial t} = C_{ijkl} \frac{\partial}{\partial t} \frac{\partial u_k}{\partial x_l} \quad \Leftrightarrow \quad \frac{\partial \tau_{ij}}{\partial t} = C_{ijkl} \frac{\partial}{\partial x_l} \frac{\partial u_k}{\partial t} \tag{4.9}$$

The velocity and the acceleration of the displacement can simple be written as

$$\begin{aligned} \frac{\partial u_i}{\partial t} &= v_i \\ \frac{\partial^2 u_i}{\partial t^2} &= \frac{\partial v_i}{\partial t} \end{aligned} \tag{4.10}$$

Replacing the displacement by the velocity of the displacement using equations (4.10), equations (4.6) and (4.7) are transformed into the coupled system of the velocity and the stress equations used throughout the thesis:

$$\begin{aligned} \rho \frac{\partial v_j}{\partial t} &= \frac{\partial \tau_{jk}}{\partial x_k} \\ \frac{\partial \tau_{jk}}{\partial t} &= C_{jklm} \frac{\partial v_l}{\partial x_m} \end{aligned} \tag{4.11}$$

4.4. Perfectly Matched Layer

In finite difference modelling the energy of the waves needs to be absorbed at artificial boundaries in order to avoid spurious reflections caused by the truncation of the computer model. Therefore, absorbing boundary conditions were developed in order to effectively simulate infinite space. The development of stable and effective absorbing boundary conditions was an important issue in numerical modelling over the last three decades. Numerous techniques were developed e.g. one wave equations (*Clayton and Engquist,* ; *Higdon, 1991; Liao et*

al., 1984), damping zones (*Cerjan et al., 1985; Sochacki et al., 1987*), optimal boundary conditions (*Peng and Töksoz, 1995*). Unfortunately, most absorbing boundary conditions are not very effective for waves impinging on them at all angles of incidence and often exhibit instabilities.

In 1994 Bérenger (*1994*) introduced a new and very effective absorbing boundary layer for electromagnetic wave modelling. This absorbing layer appears to work very well for a wide range of incident angles and frequencies. In a continuous domain Bérenger's boundary condition causes no reflection at the interface between the absorbing layer and the interior; hence the name perfectly matched layer (PML). Although small reflections can arise from the discretization of the equations, the PML is nowadays generally considered to be the optimal available absorbing boundary condition method. Chew and Liu (*1996*) and Hastings (*1996*) independently demonstrated that the PML can also be used effectively for finite difference modelling of elastic waves.

One formulation of the PML for elastic wave modelling is based on the concept of coordinate stretching. The basic principle of this formulation is that computational space in the boundary PML layer is stretched by a complex function. Most current finite-difference time-domain (FDTD) implementations of PMLs require an artificial splitting of the velocity and stress field components in the PML layers.

Implementations of the PML that do not require splitting of the fields were thought to be computationally ineffective since in their implementation they have to take into account a convolution term. However, effective techniques that do not require splitting of the field were developed for electromagnetic wave modelling (*Sacks et al., 1995*) and recently for elastic wave modelling (*Wang and Tang, 2003*). Most of these techniques make use of either the auxiliary differential equation technique (*Gedney, 1998*) or the recursive convolution technique (*Roden*

and Gedney, 2000). In this chapter various non-splitting techniques are presented and their performances are compared with the split field technique.

4.4.1. Perfectly matched layer – Theory

In this section the theory of the perfectly matched layer is explained for a first-order velocity-stress system – equation (4.4) – and the formulation is based on the complex coordinate stretching. The theory can be easily extended for higher order equations and can also be adapted for other equation systems such as displacement-strain. For brevity, the derivations of the formulas are written using the indicial notation.

In order to obtain absorbing properties in the PML layer, the velocity-stress equations are transformed into a stretched coordinate domain by using a complex stretching function (*Chew and Liu, 1996*):

$$\varepsilon_j = 1 + \frac{\sigma_j}{i\omega} \tag{4.12}$$

In this thesis this stretching function is referred to as the classical stretching function. The attenuation coefficient σ_j represent the loss in the PML boundary zone. The spatial derivatives in the stretched PML domain space can be written as:

$$\frac{\partial}{\partial \overline{x}_j} \Rightarrow \frac{1}{\varepsilon_j}\frac{\partial}{\partial x_j} \tag{4.13}$$

Using equations (4.13) the first-order velocity and stress equations in the stretched coordinate space can now be written as the following set of coupled equations

$$\begin{aligned} i\omega\rho\tilde{v}_j &= \frac{1}{\varepsilon_k}\frac{\partial\tilde{\tau}_{jk}}{\partial x_k} \\ i\omega\tilde{\tau}_{jk} &= C_{jklm}\frac{1}{\varepsilon_m}\frac{\partial\tilde{v}_l}{\partial x_m} \end{aligned} \tag{4.14}$$

Various methods can be used to solve these equations which can be divided into two groups: the split-field perfectly matched layer and the non-split perfectly matched layer.

Split-field Perfectly Matched Layer

The conventional method in elastic wave propagation modelling (*Chew and Liu, 1996; Hastings et al., 1996*) is the Split-field Perfectly Matched Layer (SPML) which is a modification of the original formulation for electromagnetic wave propagation modelling by Bérenger (*1994*). The SPML technique consists of splitting the wave propagation equations in separate components. In order to obtain the full wave field solution these components have to be added together:

$$\begin{aligned} i\omega\rho\tilde{v}_{jk} &= \frac{\partial\tilde{\tau}_{jk}}{\partial x_k} \\ \tilde{v}_j &= \sum_j \tilde{v}_{jk} \\ i\omega\tilde{\tau}_{jkm} &= C_{jklm}\frac{\partial\tilde{v}_l}{\partial x_m} \\ \tilde{\tau}_{jk} &= \sum_m \tilde{\tau}_{jkm} \end{aligned} \tag{4.15}$$

Non-split Perfect Matched Layer

Techniques that do not require splitting of the wave field were thought to be ineffective since they involve the calculation of a convolution. However, Gedney (*Gedney, 1998*) showed that using the recursive convolution techniques (*Herrman and Peterson, 1968; Luebbers and Hunsberger, 1992*) these convolutions can be solved effectively for electromagnetic wave modelling. Despite the fact that non-split techniques are well established for electromagnetic wave modelling, there are few papers regarding non-split techniques for FDTD modelling of elastic waves.

- Wang and Tang (*2003*) introduced a non-split PML (NPML) for elastic wave modelling and showed that non-split formulations can be used such that the PML acts as a perturbation to the original wave propagation equations. In their formulation the stretched wave propagation equations are transformed directly in the time domain resulting into equations containing convolution terms. These convolution terms are solved by rewriting the equations into integrals. These integrals are then approximated by the Trapezoidal integration rule.
- The CPML technique, original introduced by Roden and Gedney for electromagnetic wave modelling (*Roden and Gedney, 2000*) solves the convolution terms by approximating them by a recursive convolution technique (*Herrman and Peterson, 1968; Luebbers and Hunsberger, 1992*). In section 4.4.4, the CPML technique for elastic wave modelling is presented.
- A different and simpler non-split approach – recursive integration perfectly matched layer (RIPML) – has been proposed by Drossaert and Giannopoulos (*2007b*) where the coupled stress-velocity wave propagation equations are rewritten as a four coupled system by introducing two auxiliary tensors. In

the time-domain these tensors are simply solved by approximating their integrals by the Trapezoidal integration rule.

- Another technique to solve equation (4.14) is the auxiliary differential equation perfectly matched layer (ADEPML). For the EM modelling, an efficient implementation of this technique has been proposed by Ramadan (*2003*). In section 4.4.5 the ADEPML modified for elastic wave modelling is presented.

4.4.2. Complex frequency shifted perfectly matched layer

An important limitation of current PML implementations, that rarely has been addressed in elastic wave modelling, is that their performance is severely reduced when waves are incident on them at near grazing angle (*Collino and Monk, 1998; Bérenger, 2002b*). This phenomenon has been observed in electromagnetic modelling and in the models presented in chapter 5. Grazing angles of incidence are important when a scatterer or a source is located close to the PML. Also near grazing angles are also common in elongated models. Elongated domains can be useful in earthquake hazard modelling as well as in models including tunnels or mineshafts and many other modelling scenarios. In addition, Bérenger (*2002a*) reported that evanescent waves may be strongly reflected at the interface between the boundary layer and the model interior. Another limitation of current PML implementations is that modelling low frequency waves could lead to spurious reflections at the PML interface (*Gedney, 1998*). The main reason for the deterioration in performance is that the stretching function given by equation (4.12) becomes singular for very low frequencies or for waves with a long-time interaction with the PML interface (*Kuzuoglu and Mittra, 1996; Roden and Gedney, 2000*). To circumvent these problems Kuzuoglu and Mittra (*1996*)

proposed the complex frequency shifted (CFS) stretching function for PMLs which shifts the singularity in the stretching function off the real-axis into the negative imaginary half of the complex plane and hence improves the performance of the PML.

The CFS stretching function as proposed by Kuzuoglu and Mittra (*1996*) can be written as:

$$\varepsilon_j = \kappa_j + \frac{\sigma_j}{\alpha_j + i\omega} \tag{4.16}$$

where κ and α are auxiliary attenuation coefficients. It has been shown that the CFS tensor is both causal and stable assuming that $\alpha \geq 0$, $\kappa \geq 1$ and $\sigma \geq 0$ and that the values are real (*Bécache et al., 2004*). Note that by setting $\alpha = 0$ and $\kappa = 1$ the CFS tensor becomes equivalent to the classical stretching tensor as given by equation (4.12). The attenuation coefficient κ mainly affects waves that impinge the PML interface at near grazing angles, whereas the attenuation coefficient α mainly affects low frequency waves. However, numerical tests presented in chapter 5 show that a combination of both attenuation coefficients can lead to optimum performance. Their optimal scaling and maximum values are problem dependent.

In sections 4.4.3, 4.4.4 and 4.4.5 the theory of the RIPML, CPML and the ADEPML is presented. For completeness the CFS stretching function is used for all three of the PMLs. It is noteworthy that the SPML cannot efficiently incorporate the CFS stretching function. In order to take into account the CFS stretching function a CFS SPML requires considerably more memory compared to the non-split CFS PMLs.

4.4.3. Recursive Integration PML

The recursive integration PML has been introduced as an alternative to the split PML such that the CFS stretching function can be adopted (*Drossaert and Giannopoulos, 2007b*). The basic principle of the RIPML is to rewrite the velocity-stress equations by introducing two new auxiliary tensors: the stress rate tensor S and the strain rate tensor E. Their components are denoted as

$$\begin{aligned} \tilde{S}_{jk} &= \frac{1}{\varepsilon_k}\frac{\partial \tilde{\tau}_{jk}}{\partial x_k} \\ \tilde{E}_{lm} &= \frac{1}{\varepsilon_m}\frac{\partial \tilde{v}_l}{\partial x_m} \end{aligned} \tag{4.17}$$

By introducing the stress rate and strain rate tensors, it is no longer necessary to split the velocity and stress fields in separate components. The wave propagation equations now simply becomes

$$\begin{aligned} i\omega\rho\tilde{v}_j &= \tilde{S}_{jk} \\ i\omega\tilde{\tau}_{jk} &= C_{jklm}\tilde{E}_{lm} \end{aligned} \tag{4.18}$$

Transforming the wave propagation equation (4.18) from the frequency to the time domain results in the following equation

$$\begin{aligned} \frac{\partial v_j}{\partial t} &= \frac{1}{\rho}S_{jk} \\ \frac{\partial \tau_{jk}}{\partial t} &= C_{jklm}E_{lm} \end{aligned} \tag{4.19}$$

Since the structure of the equations (4.19) is not altered by introducing the tensors S and E, the RIPML can readily be implemented for any medium,

anisotropic and heterogeneous, that can be described by the velocity-stress equations. The velocity-stress equations in (4.19) can be solved straightforwardly by first or higher order Taylor expansions when the stress and strain rate tensors are known. In order to solve the tensors S and E, equations (4.17) are rewritten. Inserting the CFS stretching function given by equation (4.16) into the equations (4.17) and rearranging the terms results into the following equations

$$\begin{aligned}
\sigma_j \tilde{S}_{jk} - \alpha_j \frac{\partial \tilde{\tau}_{jk}}{\partial x_k} - \alpha_j \kappa_j \tilde{S}_{jk} &= i\omega \left(\frac{\partial \tilde{\tau}_{jk}}{\partial x_k} - \kappa_j \tilde{S}_{jk} \right) \\
\sigma_m \tilde{E}_{lm} - \alpha_m \frac{\partial \tilde{v}_l}{\partial x_m} - \alpha_m \kappa_m \tilde{S}_{lm} &= i\omega \left(\frac{\partial \tilde{v}_l}{\partial x_m} - \kappa_m \tilde{S}_{lm} \right)
\end{aligned} \tag{4.20}$$

Equation (4.20) can be solved straightforwardly but this requires the time derivative of the spatial derivative of the stresses in the right hand side of the equation. This potentially leads to inaccuracy and even instabilities. A more stable and elegant solution to equation (4.20) can be found be dividing the left and right hand side by $i\omega$

$$\begin{aligned}
\frac{1}{i\omega} \left(\sigma_j \tilde{S}_{jk} - \alpha_j \frac{\partial \tilde{\tau}_{jk}}{\partial x_k} - \alpha_j \kappa_j \tilde{S}_{jk} \right) &= \frac{\partial \tilde{\tau}_{jk}}{\partial x_k} - \kappa_j \tilde{S}_{jk} \\
\frac{1}{i\omega} \left(\sigma_m \tilde{E}_{lm} - \alpha_m \frac{\partial \tilde{v}_l}{\partial x_m} - \alpha_m \kappa_m \tilde{S}_{lm} \right) &= \frac{\partial \tilde{v}_l}{\partial x_m} - \kappa_m \tilde{S}_{lm}
\end{aligned} \tag{4.21}$$

These equations are transformed from the frequency domain into the time domain

$$\begin{aligned}
\int_0^t \left(\sigma_j S_{jk} - \alpha_j \frac{\partial \tau_{jk}}{\partial x_k} - \alpha_j \kappa_j S_{jk} \right) dt &= \frac{\partial \tau_{jk}}{\partial x_k} - \kappa_j S_{jk} \\
\int_0^t \left(\sigma_m E_{lm} - \alpha_m \frac{\partial v_l}{\partial x_m} - \alpha_m \kappa_m E_{lm} \right) dt &= \frac{\partial v_l}{\partial x_m} - \kappa_m S_{lm}
\end{aligned} \tag{4.22}$$

The equations now contain integrals. In the RIPML, these integrals are approximated by the Trapezoidal integration rule. Assuming that velocity field is updated before the stress field, the integral equations (4.22) can be approximated by

$$\begin{aligned}
&\tfrac{1}{2}\Delta t\sigma_j S_{jk}^0 - \tfrac{1}{2}\Delta t\alpha_j \frac{\partial \tau_{jk}^0}{\partial x_k} - \tfrac{1}{2}\Delta t\alpha_j \kappa_j S_{jk}^0 + \Delta t\sum_{t=1}^{n-1}\left[\sigma_j S_{jk}^t - \alpha_j \frac{\partial \tau_{jk}^t}{\partial x_k} - \alpha_j \kappa_j S_{jk}^t\right] \\
&\quad + \tfrac{1}{2}\Delta t\sigma_j S_{jk}^n - \tfrac{1}{2}\Delta t\alpha_j \frac{\partial \tau_{jk}^n}{\partial x_k} - \tfrac{1}{2}\Delta t\alpha_j \kappa_j S_{jk}^n = \frac{\partial \tau_{jk}^n}{\partial x_k} - \kappa_j S_{jk}^n \\
&\tfrac{1}{2}\Delta t\sigma_m E_{lm}^{\frac{1}{2}} - \tfrac{1}{2}\Delta t\alpha_m \frac{\partial v_l^{\frac{1}{2}}}{\partial x_m} - \tfrac{1}{2}\Delta t\alpha_m \kappa_m E_{lm}^{\frac{1}{2}} + \Delta t\sum_{t=1}^{n-1}\left[\sigma_m E_{lm}^{t+\frac{1}{2}} - \alpha_m \frac{\partial v_l^{t+\frac{1}{2}}}{\partial x_m} - \alpha_m \kappa_m E_{lm}^{t+\frac{1}{2}}\right] \\
&\quad + \tfrac{1}{2}\Delta t\sigma_m E_{lm}^{n+\frac{1}{2}} - \tfrac{1}{2}\Delta t\alpha_m \frac{\partial v_l^{n+\frac{1}{2}}}{\partial x_m} - \tfrac{1}{2}\Delta t\alpha_m \kappa_m E_{lm}^{n+\frac{1}{2}} = \frac{\partial v_l^{n+\frac{1}{2}}}{\partial x_m} - \kappa_m E_{lm}^{n+\frac{1}{2}}
\end{aligned} \tag{4.23}$$

The variables in the superscripts denote the time step. Implementing these equations directly in order to solve for the components of tensor E and S at time step n and $n+½$ respectively requires that all the values of the tensors and spatial derivatives of τ and v to be stored in the memory. Not only would the memory requirements become intolerable, also the number of floating point operations increases with every time step which will lead to unacceptable computation times. However given the form of equations (4.23), good efficiency can be realized by using a recursive-integration (RI) technique (*Drossaert and Giannopoulos, 2007b*).

Assuming that the source is not located in the PML layer, the components of the tensors S and E at the first time step are equal to zero. Therefore equations (4.23) can be rewritten as

$$
\begin{aligned}
S_{jk}^{n} &= \xi_k \frac{\partial \tau_{jk}^{n}}{\partial x_k} - \varphi_k \sum_{t=1}^{n-1} \left[\sigma_k S_{jk}^{t} - \alpha_k \frac{\partial \tau_{jk}^{t}}{\partial x_k} - \alpha_k \kappa_k S_{jk}^{t} \right] \\
E_{lm}^{n+\frac{1}{2}} &= \xi_m \frac{\partial v_l^{n+\frac{1}{2}}}{\partial x_m} - \varphi_m \sum_{t=1}^{n-1} \left[\sigma_m E_{lm}^{t+\frac{1}{2}} - \alpha_m \frac{\partial v_l^{t+\frac{1}{2}}}{\partial x_m} - \alpha_m \kappa_m E_{lm}^{t+\frac{1}{2}} \right]
\end{aligned}
\tag{4.24}
$$

where the multiplication factors are defined by

$$
\begin{aligned}
\xi_i &= \frac{1 + \frac{1}{2}\Delta t \alpha_i}{\frac{1}{2}\Delta t \left(\sigma_i + \alpha_i \kappa_i \right) + \kappa_i} \\
\varphi_i &= \frac{\Delta t}{\frac{1}{2}\Delta t \left(\sigma_i + \alpha_i \kappa_i \right) + \kappa_i}
\end{aligned}
\tag{4.25}
$$

In order to solve equation (4.24) by the recursive integration technique, the sums in these equations are replaced by introducing two auxiliary variables resulting in following equations:

$$
\begin{aligned}
S_{jk}^{n} &= \xi_k \frac{\partial \tau_{jk}^{n}}{\partial x_k} - \varphi_k \Omega_{jk}^{n-1} \\
E_{lm}^{n+\frac{1}{2}} &= \xi_m \frac{\partial v_l^{n+\frac{1}{2}}}{\partial x_m} - \varphi_m \Psi_{lm}^{n-\frac{1}{2}}
\end{aligned}
\tag{4.26}
$$

The variables Ω and Ψ are referred as the stress rate sum and the strain rate sum. In this form, these auxiliary variables be solved advancing in time using a simple time-marching procedure

$$
\begin{aligned}
\Omega_{jk}^{n} &= \Omega_{jk}^{n-1} + \Lambda_k S_{jk}^{n} - \alpha_k \frac{\partial \tau_{jk}^{n}}{\partial x_k} \\
\Psi_{lm}^{n+\frac{1}{2}} &= \Psi_{lm}^{n-\frac{1}{2}} + \Lambda_m E_{lm}^{n+\frac{1}{2}} - \alpha_m \frac{\partial v_l^{n+\frac{1}{2}}}{\partial x_m}
\end{aligned}
\tag{4.27}
$$

where the multiplication factor Λ is defined by

$$\Lambda_i = \sigma_i + \alpha_i \kappa_i \tag{4.28}$$

By employing the recursive integration technique, an efficient FDTD implementation of a non-split PML with the CFS stretching function can be derived using formula (4.19) and formulas (4.24) to (4.28)

Note that for updating the stress rate tensor S and the strain rate tensors E, their values at the previous time step are not required and therefore there is no need to allocate extra computer memory for them. The only auxiliary variables that need to be stored in the computer memory to be available for the next time step, are the values of the recursive sums Ψ and Ω.

4.4.4. Convolution PML

In order to solve for the velocity-stress equations (4.14) by the convolution PML, the Roden and Gedney (*2000*) approach for electromagnetic wave modelling is adopted and converted to suit the elastic wave equations. Their adopted approach is based on a recursive-convolution technique which leads to a computationally efficient set of equations. The first step in the deduction is to transform the equations (4.14) back into the time domain making use of the following relation

$$F^{-1}\left(\frac{1}{\varepsilon_k}\frac{\partial}{\partial x_k}\right) = F^{-1}\left(\frac{1}{\left(\kappa_k + \frac{\sigma_k}{\alpha_k + i\omega}\right)}\frac{\partial}{\partial x_k}\right) = \left(\frac{\delta(t)}{\kappa_k} - \frac{\sigma_k}{\kappa_k^2} e^{-\left(\frac{\sigma_k}{\kappa_k} + \alpha_k\right)t}\right) * \frac{\partial}{\partial x_k} \tag{4.29}$$

where F^{-1} is inverse Fourier transform and * denotes a convolution operator. Since the convolution of a function with a Dirac delta function is the function itself, the velocity-stress equations can simply be written in time domain as:

$$\begin{aligned}\rho\frac{\partial v_j}{\partial t} &= \frac{1}{\kappa_k}\frac{\partial \tau_{jk}}{\partial x_k} + \zeta_k * \frac{\partial \tau_{jk}}{\partial x_k} \\ \frac{\partial \tau_{jk}}{\partial t} &= C_{jklm}\left(\frac{1}{\kappa_m}\frac{\partial v_l}{\partial x_m} + \zeta_m * \frac{\partial v_l}{\partial x_m}\right)\end{aligned} \tag{4.30}$$

where

$$\zeta_k = -\frac{\sigma_k}{\kappa_k^2} e^{-\left(\frac{\sigma_k}{\kappa_k}+\alpha_k\right)t} \tag{4.31}$$

Implementing the discrete convolutions straightforwardly would be computationally too expensive in terms of memory and number of floating point operators. To solve the equations (4.30) Wang and Tang (*2003*) rewrote the convolution terms as integrals and approximated these integrals by the Trapezoidal rule. Although their formulation does not include the CFS stretching function it can easily be modified to do so. However, for a more efficient implementation the convolution terms can be approximated by a recursive-convolution technique. Roden and Gedney (*2000*) showed that the form of $\zeta_k(t)$ allows the convolution of it with a spatial derivative to be approximated by a recursive-convolution technique (*Herrman and Peterson, 1968; Luebbers and Hunsberger, 1992*). Using this technique the convolution operators in the equations (4.30) can be approximated in the discretized time domain at time step n as

$$\Omega_{ij}^{n} = \zeta_j(n\Delta t) * \frac{\partial v_i(n\Delta t)}{\partial x_j} \approx b_j \Omega_{ij}^{n-1} + c_j \frac{\partial v_i^n}{\partial x_j}$$
$$\Psi_{ij}^{n+\frac{1}{2}} = \zeta_j(n\Delta t + \tfrac{1}{2}\Delta t) * \frac{\partial \tau_{ij}(n\Delta t + \frac{1}{2}\Delta t)}{\partial x_j} \approx b_j \Psi_{ij}^{n-\frac{1}{2}} + c_j \frac{\partial \tau_{ij}^{n+\frac{1}{2}}}{\partial x_j} \tag{4.32}$$

where the multiplication factors are given by:

$$b_j = e^{-\left(\frac{\sigma_j}{\kappa_j} + \alpha_j\right)}$$
$$c_j = \frac{\sigma_j}{\sigma_j \kappa_j + \kappa_j^2 \alpha_j}\left(e^{-\left(\frac{\sigma_j}{\kappa_j} + \alpha_j\right)} - 1\right) \tag{4.33}$$

The recursive convolution tensors Ψ and Ω are discrete unknowns and need to be calculated before the velocity and stress field update. These tensors are collocated with their associated field in the time domain e.g. Ψ_{xx} is collocated with v_x and Ω_{xz} is collocated with τ_{xz}. Unlike the stress field tensor these auxiliary tensors are not symmetrical. To solve the auxiliary tensors by equations (4.32), their values at the previous time step and the spatial derivatives at the present time step are required. In the NPML formulation by Wang and Tang (*2003*) the calculation of their auxiliary tensors requires in addition the spatial derivatives at the previous time step. This can potentially lead to a more complicated and/or less effective implementation of the PML.

The wave propagation equations in the PML (4.30) can now be simply written as

$$\rho \frac{\partial v_j}{\partial t} = \frac{1}{\kappa_k} \frac{\partial \tau_{jk}}{\partial x_k} + \left[\Psi_{jk}\right]$$
$$\frac{\partial \tau_{jk}}{\partial t} = C_{jklm} \frac{1}{\kappa_m} \frac{\partial v_l}{\partial x_m} + \left[C_{jklm} \Omega_{lm}\right] \tag{4.34}$$

These equations can easily be solved by first or higher order Taylor expansions resulting in an efficient implementation of a non-split PML with the CFS stretching function.

4.4.5. Auxiliary Differential Equation PML

The auxiliary differential equation PML is based on the concept suggested by Ramadan (*2003*). The original concept is formulated for electromagnetic wave modelling. Moreover the original implementation is based on the classical stretching function. In this section the modified formulation of the ADEPML for elastic wave modelling is presented. Unlike Ramadan's formulation for electromagnetic wave modelling, this formulation is based on the CFS stretching function.

To solve equations (4.14) by the ADE technique these equations have to be rewritten. Making use of partial fraction expansion the inverse of the stretching tensor can be written as

$$\frac{1}{\varepsilon_j} = \frac{1}{\kappa_j} - \frac{\sigma_j}{\alpha_j \kappa_j^2 + \kappa_j \sigma_j + \kappa_j^2 i\omega} \tag{4.35}$$

Inserting the stretching function (4.35) in the first-order hyperbolic velocity-stress system (4.14) results in following set of equations

$$\begin{aligned} i\omega \tilde{v}_j &= \frac{1}{\kappa_k} \frac{\partial \tilde{\tau}_{jk}}{\partial x_k} - \tilde{\Omega}_{jk} \\ i\omega \tilde{\tau}_{jk} &= C_{jklm} \left(\frac{1}{\kappa_m} \frac{\partial \tilde{v}_l}{\partial x_m} - \tilde{\Psi}_{lm} \right) \end{aligned} \tag{4.36}$$

where the auxiliary tensors Ω and Ψ are given by:

$$\tilde{\Omega}_{jk} = \frac{\sigma_k}{\alpha_k \kappa_k^2 + \kappa_k \sigma_k + \kappa_k^2 i\omega} \frac{\partial \tilde{\tau}_{jk}}{\partial x_k} \quad \text{and} \quad \tilde{\Psi}_{lm} = \frac{\sigma_m}{\alpha_m \kappa_m^2 + \kappa_m \sigma_m + \kappa_m^2 i\omega} \frac{\partial \tilde{v}_l}{\partial x_m} \tag{4.37}$$

The tensors Ω and Ψ can be regarded as a correction to the velocity-stress system to account for the loss in the PML zones.

In FDTD modelling the wave propagation equations are discretized in time and space. The time derivatives are approximated by central differences. In this implementation the stress field is updated ½ time step after the update of the velocity field. The velocity-stress equations (4.36) can be written after transforming back into the time-domain in discretized time as:

$$\begin{aligned} v_j^{n+\frac{1}{2}} &= v_j^{n-\frac{1}{2}} + \frac{\Delta t}{\rho}\left(\frac{1}{\kappa_k} \frac{\partial \tau_{jk}^n}{\partial x_k} - \frac{\Omega_{jk}^{n+\frac{1}{2}} + \Omega_{jk}^{n-\frac{1}{2}}}{2} \right) \\ \tau_{jk}^{n+1} &= \tau_{jk}^n + \Delta t C_{jklm} \left(\frac{1}{\kappa_m} \frac{\partial v_l^{n+\frac{1}{2}}}{\partial x_m} - \frac{\Psi_{lm}^{n+1} + \Psi_{lm}^n}{2} \right) \end{aligned} \tag{4.38}$$

In order to update the velocity and stress field the tensors Ω and Ψ have to be pre-calculated. To do so, equations (4.37) are rewritten:

$$\begin{aligned} i\omega \tilde{\Omega}_{jk} &= \frac{\sigma_k}{\kappa_k^2} \frac{\partial \tilde{\tau}_{jk}}{\partial x_k} - \left(\alpha_k + \frac{\sigma_k}{\kappa_k} \right) \tilde{\Omega}_{jk} \\ i\omega \tilde{\Psi}_{lm} &= \frac{\sigma_m}{\kappa_m^2} \frac{\partial \tilde{v}_l}{\partial x_m} - \left(\alpha_m + \frac{\sigma_m}{\kappa_m} \right) \tilde{\Psi}_{lm} \end{aligned} \tag{4.39}$$

After transforming the equation back into the time domain these equations can written as:

$$\begin{aligned}
\frac{\Omega_{jk}^{n+\frac{1}{2}} - \Omega_{jk}^{n-\frac{1}{2}}}{\Delta t} &= \frac{\sigma_k}{\kappa_k^2} \frac{\partial \tau_{jk}^n}{\partial x_k} - \left(\alpha_k + \frac{\sigma_k}{\kappa_k} \right) \frac{\Omega_{jk}^{n+\frac{1}{2}} + \Omega_{jk}^{n-\frac{1}{2}}}{2} \\
\frac{\Psi_{lm}^{n+1} - \Psi_{lm}^{n}}{\Delta t} &= \frac{\sigma_m}{\kappa_m^2} \frac{\partial v_l^n}{\partial x_m} - \left(\alpha_m + \frac{\sigma_m}{\kappa_m} \right) \frac{\Psi_{jk}^{n+1} + \Psi_{jk}^{n}}{2}
\end{aligned} \tag{4.40}$$

After rearranging the terms in equation (4.40), the auxiliary tensors Ω and Ψ can simply be calculated as follows:

$$\Omega_{ij}^{n+\frac{1}{2}} = a_j \Omega_{ij}^{n-\frac{1}{2}} + b_j \frac{\partial \tau_{ij}^n}{\partial x_j} \qquad \text{and} \qquad \Psi_{lm}^{n+1} = a_m \Psi_{lm}^{n} + b_m \frac{\partial v_l^{n+\frac{1}{2}}}{\partial x_m} \tag{4.41}$$

where the multiplication a and b factors are defined as:

$$\begin{aligned}
a_j &= \frac{\frac{1}{\Delta t} - \frac{1}{2}\left(\alpha_j + \frac{\sigma_j}{\kappa_j} \right)}{\frac{1}{\Delta t} + \frac{1}{2}\left(\alpha_j + \frac{\sigma_j}{\kappa_j} \right)} \\
b_j &= \frac{\sigma_j}{\kappa_j^2 \left(\frac{1}{\Delta t} + \frac{1}{2}\left(\alpha_j + \frac{\sigma_j}{\kappa_j} \right) \right)}
\end{aligned} \tag{4.42}$$

It should be mentioned that the multiplication factors (4.42) are constant in time. In an efficient implementation these multiplication factors are pre-calculated before the time updates. Note that, since the spatial derivatives are not discretized in above equations, the formulations of the CFS ADEPML are derived independently of the grid definition and hence it is suitable for standard staggered grids (*Virieux, 1986; Randall, 1989*) as well as rotated staggered grids (*Saenger and Bohlen, 2004*).

4.4.6. PMLs as perturbations

In the source code implementations, it can beneficial to formulate PMLs as a perturbation to the original wave propagation equation in order to take into account the effect of the boundary layer.

The RIPML can easily be written as a perturbation to the original wave propagation equation by rewriting equation (4.14) into

$$\begin{aligned} \rho i\omega\tilde{v}_j &= \frac{\partial\tilde{\tau}_{jk}}{\partial x_k} + \left[\frac{1-\varepsilon_j}{\varepsilon_j}\frac{\partial\tilde{\tau}_{jk}}{\partial x_k}\right] \\ i\omega\tilde{\tau}_{jk} &= C_{jklm}\frac{\partial\tilde{v}_l}{\partial x_m} + \left[C_{jklm}\frac{1-\varepsilon_j}{\varepsilon_j}\frac{\partial\tilde{v}_l}{\partial x_m}\right] \end{aligned} \tag{4.43}$$

The terms between the square brackets acts as the perturbation. In order to solve for these equations, two auxiliary variables are introduced:

$$\begin{aligned} \tilde{S}_{jk} &= \frac{1-\varepsilon_j}{\varepsilon_j}\frac{\partial\tilde{\tau}_{jk}}{\partial x_k} \\ \tilde{E}_{jk} &= C_{jklm}\frac{1-\varepsilon_j}{\varepsilon_j}\frac{\partial\tilde{v}_l}{\partial x_m} \end{aligned} \tag{4.44}$$

These auxiliary variables can be solved similar to the recursive integration technique as proposed in section 4.4.3.

The equations for the CPML (4.34) and the ADEPML (4.36) can be regarded as perturbation equations. This requires that the original wave propagation equations include the inverse of the attenuation coefficient κ. This leads to an unnecessary increase in the run times. However, this disadvantage can easily be circumvented by rewriting equations (4.34) and (4.36). The wave propagation equations in the CPML can be written as:

$$\begin{aligned}\rho\frac{\partial v_j}{\partial t} &= \frac{\partial \tau_{jk}}{\partial x_k} + \left[\frac{1-\kappa_k}{\kappa_k}\frac{\partial \tau_{jk}}{\partial x_k} + \Psi_{jk}\right] \\ \frac{\partial \tau_{jk}}{\partial t} &= C_{jklm}\frac{\partial v_l}{\partial x_m} + C_{jklm}\left[\frac{1-\kappa_m}{\kappa_m}\frac{\partial v_l}{\partial x_m} + \Omega_{lm}\right]\end{aligned} \tag{4.45}$$

and in the ADEPML the wave propagation equations become

$$\begin{aligned}\frac{\partial v_i}{\partial t} &= \frac{1}{\rho}\frac{\partial \tau_{ij}}{\partial x_j} - \frac{1}{\rho}\left[\frac{1-\kappa_j}{\kappa_j}\Omega_{ij}\right] \\ \frac{\partial \tau_{ij}}{\partial t} &= C_{ijkl}\frac{\partial v_k}{\partial x_l} - C_{ijkl}\left[\frac{1-\kappa_l}{\kappa_l}\Psi_{kl}\right]\end{aligned} \tag{4.46}$$

The terms between the square brackets act as perturbations to the original wave propagation equations. Unlike the CPML formulation by Roden and Gedney (*2000*), this formulation does not involve the attenuation coefficient κ in the original equations. The implementation of this formulation in a computer code becomes more refined and easier. Furthermore for large models where the interior domain is substantially larger than the boundary layers this can lead to a reduction in the total number of floating point operators and thus computation time.

4.5. Attenuation coefficients

The attenuation coefficients provide the loss of the elastic wave energies in the perfectly matched layer. The choice of values for the coefficients is pivotal for the performance of the boundary condition. This section deals briefly with the attenuation coefficients.

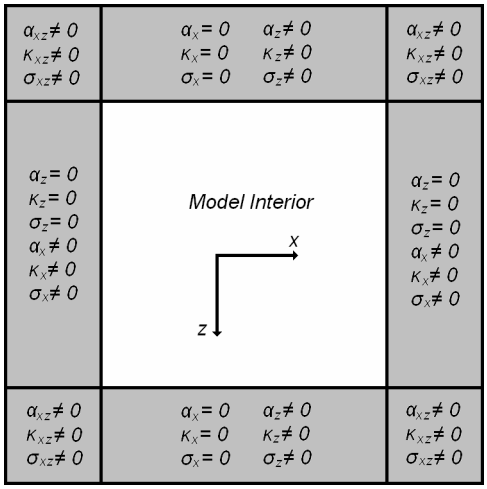

Figure 4.4. Assignment of the attenuation coefficients in the perfect matched layer which is represented by the grey area

In order to obtain PML absorbing properties in the RIPML formulation the values of the CFS attenuation coefficient α, κ and σ have to be chosen such that only its orthogonal components are non-zero, whereas the parallel components are set to zero. Figure 4.4 illustrates a general 2D case where the model is truncated by the perfectly matched layer on all sides.

In a continuous domain the interface between the PML boundary layer and the model interior is perfectly matched i.e. no reflection will arise due to the presence of the interface regardless of the physical properties at each side of the interface. However, in finite difference modelling spurious reflections can arise due to the discretization of the space domain. In order to avoid the numerical reflections from the interface between the PML and the computational domain, the attenuation coefficients have to increase gradually. A commonly used polynomial scaling function for the attenuation coefficient σ is given by (*Collino and Tsogka, 2001*):

$$\sigma_i(l) = \sigma_i^{\max}\left(\frac{l}{d}\right)^m \qquad \text{when} \qquad 0 \le l \le d \tag{4.47}$$

where the interface between the PML and the interior is assumed to be located at $l = 0$, d is the thickness of the PML and m is the scaling order. Other scaling functions have been proposed such as the logarithmic scaling (*Gedney, 1998*). The optimum value for $\sigma^{\max}$ can be calculated by the following empirical formula used by various authors (*Collino and Tsogka, 2001*):

$$\sigma_i^{\max} = \frac{3v_p}{2d}\log\left(\frac{1}{R}\right) \tag{4.48}$$

where R is the theoretical reflection coefficient after discretization and v_p is the P-wave velocity. Note that the scaling and optimum value of the attenuation coefficient is derived for the classical stretching function and not the CFS stretching function. A detailed study of scaling functions is beyond the scope of this thesis and therefore only the polynomial scaling function (4.47) is considered. The other scaling functions perform similarly as the polynomial scaling function. Numerical tests indicated that optimum polynomial scaling (4.47) and that the optimum maximum value of the attenuation coefficient κ (4.48) is similar for CFS PMLs.

The CFS stretching function has recently been introduced in elastic wave modelling (*Drossaert and Giannopoulos, 2007b*). Therefore little is known about the optimum values of the attenuation coefficients other than the σ which is similar as in the classical stretching function. The optimum values and scaling of the attenuation coefficients α and κ depends strongly on the model e.g. media parameters, PML thickness d and also the values are related to the value of the other attenuation coefficients. Furthermore numerical results presented in chapter

5 show that the optimum values, and very likely the scaling of the attenuation coefficients, depend on the shape of the model domain and location of the source and the observation point in relation to each other and the location of the PML. The sheer number of variables involved makes it almost impossible to determine the optimum value and scaling.

Since elastic wave modelling has similarities with electromagnetic modelling, the theory behind the attenuation coefficients is similar. Therefore similar scaling functions are used as in the electromagnetic wave modelling. Similar to the attenuation coefficient σ, the attenuation coefficients α and κ have be scaled by a smooth function such that minimal reflection will occur at the interface between the PML and the model interior due to discretization of the space domain.

Similar to the attenuation coefficient σ, the coefficient κ is scaled by a polynomial function for the models presented in chapter 5 and chapter 6. However, the value of κ has to be equal or larger than one. Hence, for the attenuation coefficient κ the following polynomial scaling function is adopted for the models presented in this thesis:

$$\kappa_i(l) = 1 + \left(\kappa_i^{\max} - 1\right)\left(\frac{l}{d}\right)^m \quad \text{when} \quad 0 \le l \le d \tag{4.49}$$

The attenuation coefficient α has to be large at the interface in order to prevent singularity problems of the CFS stretching function for low frequency waves (*Gedney, 1998*). However, including a large value for the coefficient α reduces the efficiency of the PML to absorb the impinging waves. Therefore inside the boundary layer, the value of α should be reduced such that the PML can attenuate the elastic waves appropriately. To this end, the following polynomial scaling function has been adopted:

$$\alpha_i(l) = \alpha_i^{\max}\left(\frac{d-l}{d}\right)^m \qquad \text{when} \qquad 0 \le l \le d \tag{4.50}$$

where the interface between the PML and the interior domain is assumed to be located at $l = 0$, m is scaling order, and d is the thickness of the PML.

As mentioned before in this section, the optimum values of the attenuation coefficients α and κ depend strongly on the model parameters, source and observation point locations and also on each others value and scaling, it is difficult to determine the optimum value. No attempts have been undertaken to find empirical relationships between various variables. The values chosen for $\alpha^{\max}$ and $\kappa^{\max}$ for models in chapter 5 are determined by trial and error.

4.6. Computer resources

The PML is generally considered as the optimal absorbing boundary condition available nowadays. However, the PML requires more memory compared to some other absorbing boundary conditions. Although for large models the memory requirements of the PML become negligible compared to the memory required for the interior. This section compares the memory requirements and the floating point operations required for the various PMLs.

4.6.1. Memory

The total amount of memory needed to implement the RIPML, CPML, ADEPML or SPML depends on how efficient the PML is implemented in the source code. The RIPML, CPML and the ADEPML all require the same amount

of memory. In a 2D model, the absorbing boundary zones can be divided in corners and edges in order to save memory space. For a 3D model additional faces are required. It is then possible to make use of the fact that some attenuation coefficients are zero in certain PML zones. Consequently, some of the stress rate and strain rate sums as defined by the equations in (4.27) and the auxiliary tensors (4.32) and (4.41), remain zero and hence there is no need to take these sums into account.

In Table 4.1 the minimum amount of variables require to be stored in the memory by the RIPML is compared with the one required by the SPML. In this table the fact that only the split field components for the SPML needs to be stored and not the field components themselves is taken into account. This leads to considerable memory savings, but this also leads to an increase of floating point operators. If the field components are calculated in the boundary layers, the number of variables to be stored in the memory increases with 5 variables in each cell for the 2D SPML and with 9 variables for the 3D SPML. This implementation of the SPML will be referred as the Total SPML. In this case the non-split PML is much more effective than the conventional SPML in terms of memory requirement. Since in most cases, the corner areas are small compared to the size of the edges and faces, the implementation of the RIPML requires less memory than the SPML.

Table 4.1: Minimum number of variables required to store in memory per PML cell for different zones and for different PML models

Model	2D SPML	Total 2D SPML	2D RIPML	3D SPML	Total 3D SPML	3D RIPML
Faces	-	-	-	17	26	15
Edges	10	15	9	24	33	21
Corners	10	15	13	24	33	27

Figure 4.5 shows the ratio between the total memory required for RIPML and the SPML. The models used for the figure are a square 2-D model and a 3-D cube model with varying model length. The models edges are truncated by the RIPML or SPML on all sides. The ratio is defined as:

$$Ratio = \frac{Total\ memory\ required\ \ for\ RIPML}{Total\ memory\ required\ \ for\ SPML} \tag{4.51}$$

From the Figure 4.5a and Figure 4.5b it can be observed that the total memory required for the RIPML is generally less than the total memory required for the SPML. Only for really small 2D square models of less than 50 by 50 cells with thick boundary layer of 10 cells, the RIPML requires more memory than the SPML. With increasing size of the model, the ratio decreases and converges to the value of 0.9 for the 2D model and to the value of 0.88 for the 3D model. For large 2D models implementing the RIPML and also the CPML or ADEPML can save 10% of the total required memory when compared to the SPML and for a large 3D model with RIPML the amount of memory saved can be up to 13.3%. These savings percentages do not change and remain the same for different shapes of the model.

Furthermore, another advantage of the RIPML over the SPML is that the velocity and stress fields are calculated inside the PML zone, greatly simplifying the interaction between the PML zone and the interior of the model. The Total SPML implementation does not adhere to the problem of the boundary interaction. However, in the case of the Total SPML implementation the memory requirement increases significantly and adopting the RIPML instead of the Total SPML could save up to 66% for 2D models and 73% for 3D models.

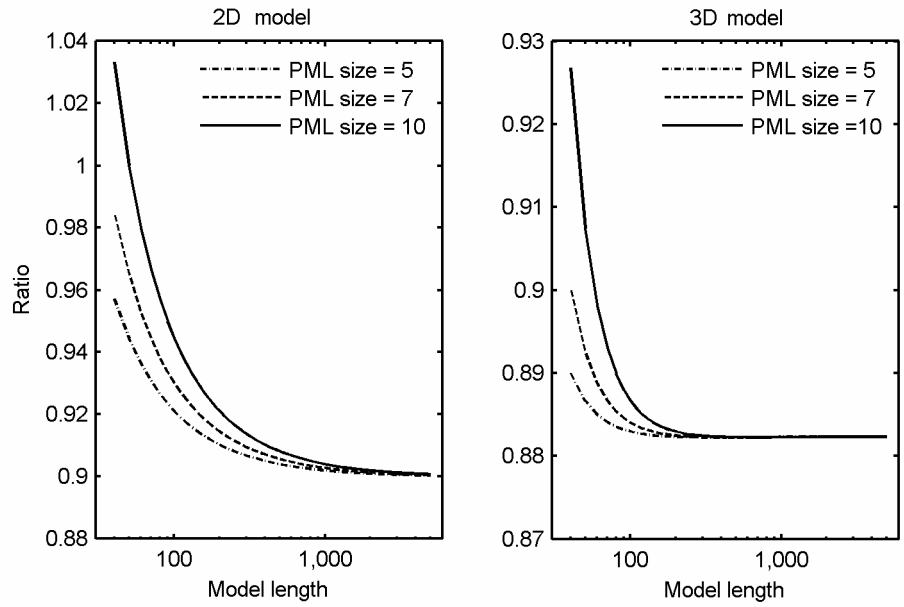

Figure 4.5. The ratio between the required memory of the SPML and of the RIPML for 2D square model and 3D cube model with varying PML thickness

4.6.2. Floating Point Operations

Perfectly matched layers are considered to be most efficient method to absorb wave energies at the model edges. This does not mean that the PML is efficient in terms of memory requirements or computer run time. The memory requirements of the various PMLs are discussed in section 4.6.1. The run times depend on the model parameters: the number of cells, the PML size and the number of time steps and it also depends on the time required to update a cell. The time required to update all the cell components in one cell depends on the number of floating point operators. Small numbers of floating point operators per cell lead to shorter calculation time, whereas a large number of operators lead to longer calculation time.

In order to calculate the floating point operators MATLAB v5.3 and the FLOP script was used. The number of floating point operators of the PMLs were calculated for various 2D scenarios:

- PMLs based on the classical stretching function.
- PMLs based on the complex frequency shifted stretching function.
- PMLs based on the complex frequency shifted stretching function and written as perturbations which is presented in section 4.4.6.

PMLs with classical stretching function

In Table 4.2 the results of floating point operators per interior cell and boundary cell are presented. The cell components in the boundary layer are calculated separately from the interior cells i.e. the PML is not treated as a perturbation. The non-split PMLs are based on the classical stretching function in order to make a comparison with the SPML. Since the equations for the update of the interior cells are unaffected by the type of PML, the number of floating point operators in the interior cells are independent of the PML. The floating point operators for the boundary cells are dependent on the choice of PML. The CPML requires the least number of floating point operators followed by the Total SPML, RIPML, ADEPML and the SPML. It should be mentioned that the Total SPML requires considerably more memory than the other PML implementations.

Although the number of floating point operators for boundary cells is higher than for interior cells, the increase is not significant. In most model cases the number of interior cells outnumbers the boundary cells and therefore the run times should be similar for the different PMLs, although a slight increase in run times can be achieved by adopting the CPML.

Table 4.2. Number of floating point operators per cell for a 2D model with PMLs based on the classical stretching function

	Interior cell	Boundary cell
RIPML	106	146
ADEPML	106	154
CPML	106	132
Total SPML	106	138
SPML	106	166

PMLs with CFS stretching function

In Table 4.3 the number of floating point operators required for the update of the interior cells and boundary cells are presented. The PMLs are based on the CFS stretching function. As the SPML cannot incorporate this stretching function it is not included in the comparison. Although the number of floating point operators for boundary cells is larger for the CFS RIPML when compared to the other two non-split PMLs, it is clear from the results that the numbers of floating point operators required for interior cells of the models truncated by the CFS ADEPML and the CFS CPML are larger than the number for the CFS RIPML. Since the interior domain is significantly larger than boundary layers in most model cases, deploying the CFS RIPML can lead to a considerable reduction in the total floating point operators and hence a considerable reduction in the model times.

Table 4.3. Number of floating point operators per interior cell and the number of floating point operators required to update the boundary cell

	Interior cell	Boundary cell
CFS RIPML	106	162
CFS ADEPML	116	150
CFS CPML	116	130

CFS PML as perturbation

In order to prevent the increase of floating point operators in the interior, the cell update equations can be modified such that the attenuation coefficient κ does not appear in the update of the interior cells in the CFS CPML and CFS ADEPML. This modification has been presented in section 4.4.6. The results can be found in Table 4.4. The number of floating operators for the CFS RIPML model remains the same as in Table 4.1. However, the number of floating point operators required for the interior cells of the CFS ADEPML and CFS CPML has decreased from 116 to 106. Although, the decrease is coupled with the increase in floating point operators for boundary cells, the total number of floating point operators will increase for common models where the interior domain is significantly larger than the boundary layer. The CFS CPML is slightly more efficient in terms of floating point operators when compared to the other two non-split PMLs.

Table 4.4. Number of floating point operators required for each cell and number of floating point operators required to update boundary cells

	All cells	Boundary cell
CFS RIPML	106	162
CFS ADEPML	106	170
CFS CPML	106	150

4.7. Conclusions

In this chapter theoretical aspects of the numerical aspects are presented, which are briefly summarized below.

- Various numerical modelling methods are discussed of which the finite difference methods are considered the most suitable to model abandoned mineshafts.
- The experimental rotated staggered grid by Saenger is preferred over the standard staggered grid by Virieux, since it provides various advantages:
  - The rotated staggered grid can handle strong heterogeneities, whereas the standard grid becomes unstable.
  - The Von Neumann stability condition is less restrictive for the rotated staggered grid than the standard staggered grid i.e. the time step can be larger given the same model parameters.
- Three new perfectly matched layer boundary conditions are introduced.
  - Recursive Integration Perfectly Matched Layer (RIPML)
  - Convolution Perfectly Matched Layer (CPML)
  - Auxiliary Differential Equation Perfectly Matched Layer (ADEPML)
- These new boundary conditions are non-split PMLs which provide advantages over the conventional SPML:

  - The Complex Frequency Shifted stretching function can easily be incorporated which is more versatile and can enhance the performance of the absorbing boundary layer.
  - The non-split PMLs can be rewritten such that they act as perturbations to the original wave equation.
  - Memory requirements can be less.
  - Communication between boundary cells and interior cells is straight forward, whereas SPML can be cumbersome.
  - Number of floating point operators is less unless Total SPML is used which requires considerably more memory.
- All three non-split PMLs require the same amount of memory.
- The floating point operators required to update a cell differs per PML and implementation: CPML is the most efficient for PMLs based on the classical stretching function. However, the CFS RIPML is the most efficient unless the PML is considered as a perturbation to the original wave propagation equations.

5. PML – Numerical Experiments

In the previous chapter three new formulations of the perfectly matched layer were presented. In this chapter the performance of these PMLs are compared to each other and to the conventional SPML using various models:

- A simple square 2D model to compare the ADEPML, RIPML, CPML with the SPML – all based on the classical stretching function.
- A model with an elongated domain to analyse the complex frequency shifted stretching function for the new PML.
- A model with predominant surface waves to further investigate the performance of the complex frequency shifted stretching function.

For the simulations, the formulas are implemented in MATLAB v7.04. The script of the RIPML can be found in Appendix D. Besides the performance, some numerical analysis of the complex frequency attenuation coefficients α and κ is presented in this chapter. These models are based on the examples presented in Geophysics (*Drossaert and Giannopoulos, 2007b*) and in Wave Motion (*Drossaert and Giannopoulos, 2007a*).

5.1. Simple square model

The first model presented in this chapter consists of a simple homogeneous domain truncated by the absorbing boundary conditions on all sides. The purpose of this model is to compare the performance of the three PMLs introduced in chapter 4 and also compare their performance with the conventional SPML.

5.1.1. The model

A representation of the simple 2D model with its parameters can be found in Figure 5.1. The medium is homogeneous and the measures indicated in the figure are the number of elements. The source is located in the middle of the model domain. The source consists of a vertical force F_z superposed on the vertical stresses τ_{zz} at the source location according the following formula:

$$\frac{\partial \tau_{zz}}{\partial t} = (\lambda + 2\mu)\frac{\partial v_z}{\partial x_z} + \mu \frac{\partial v_x}{\partial x_x} + F_z \tag{5.1}$$

The force has a Ricker shaped signature with a centre frequency of 35 Hz. The force is distributed over several nodes according to a Gaussian distribution function in order to prevent grid dispersion. Unless otherwise stated, the thickness of the PML N = 10.

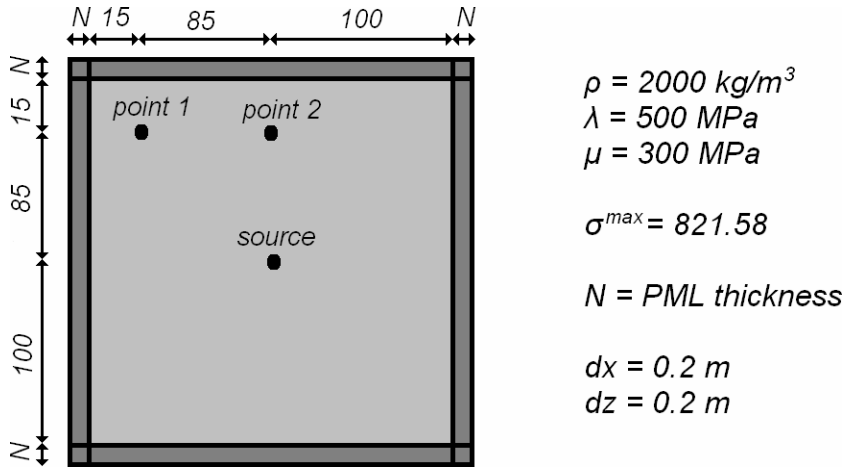

Figure 5.1. Representation of the simple square model

5.1.2. Numerical results

Synthetic seismograms of the vertical velocity are computed for 0.25 seconds at the two locations indicated in Figure 5.1. Reference seismograms were computed using a model sufficiently large such that boundary reflections arrived outside of the required time window. The computed seismograms for the models with various PML implementations and the reference model can be found in Figure 5.2.

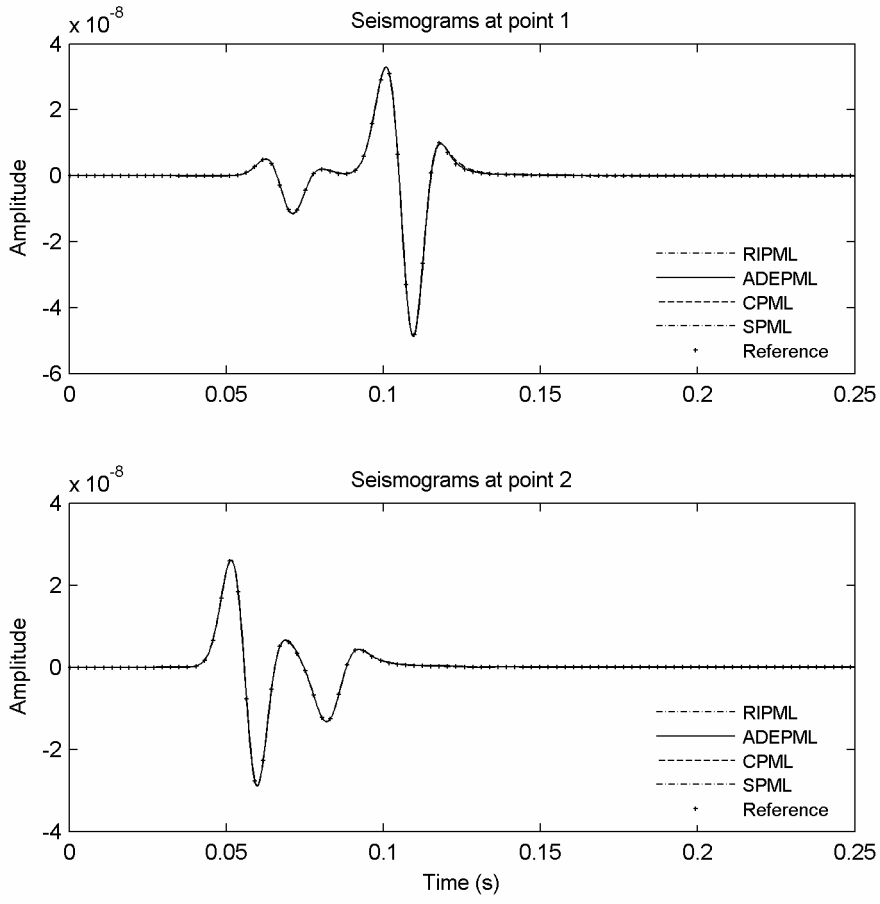

Figure 5.2. Synthetic seismograms calculated for the simple model truncated by the RIPML, ADPML and the CPML boundary condition. Reference seismogram is computed using a sufficient large model.

From this figure it can be observed that seismograms of all the PML models approximate the reference seismogram very closely. Therefore it can be concluded that all the PMLs perform very well for this simple model. The error as defined by the difference between the reference seismograms and the seismograms computed for the PMLs was calculated and can be found in Figure 5.3 for observation point 1 and in Figure 5.4 for point 2.

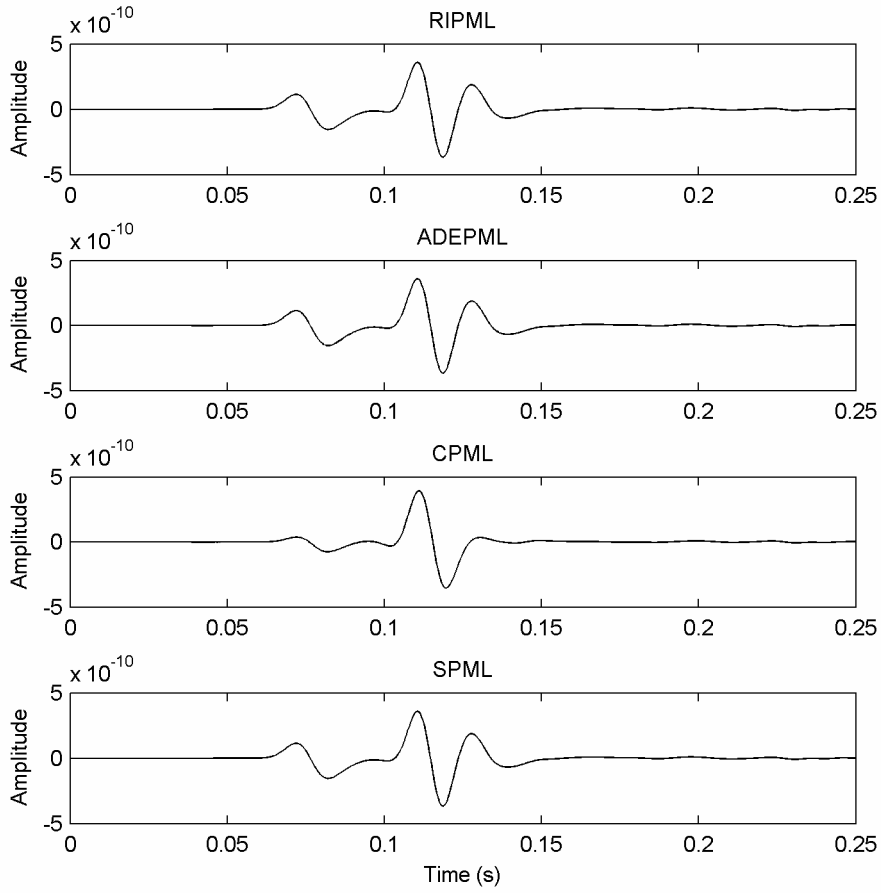

Figure 5.3. Error between the reference seismogram at point 1 and the seismogram computed for the models with the RIPML, ADEPML, CPML and the SPML

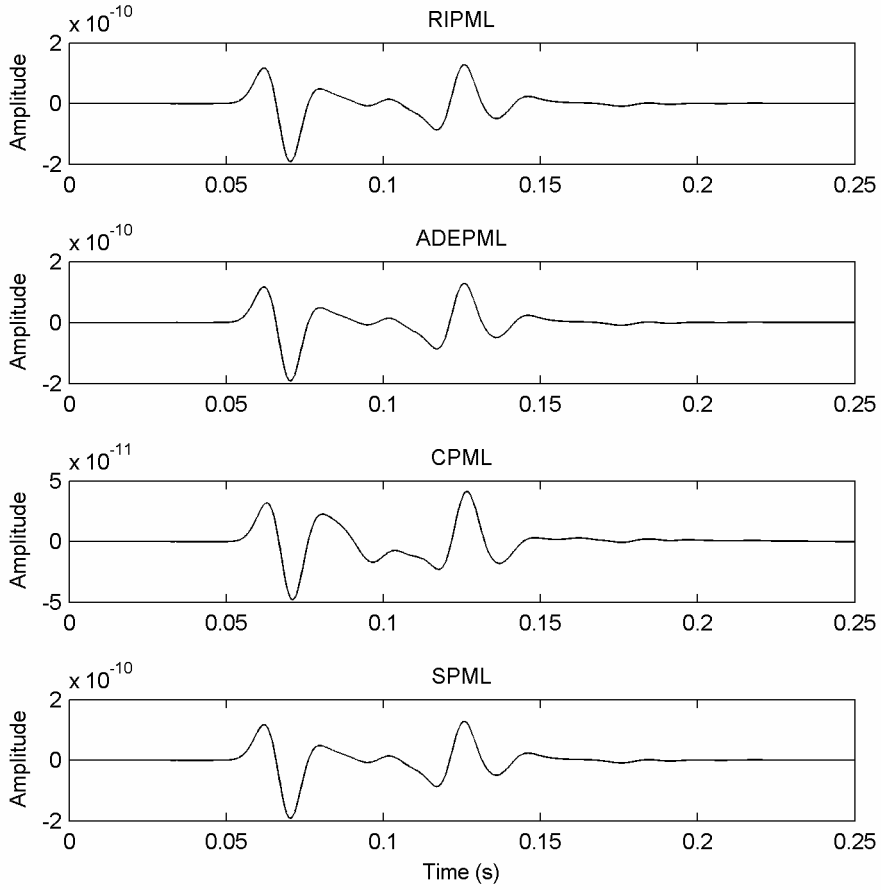

Figure 5.4. Error between the reference seismogram at point 1 and the seismogram computed for the models with the RIPML, ADEPML, CPML and the SPML

From Figure 5.3 it can be observed that the seismograms of the models with RIPML, ADEPML and the SPML show the identical error behaviour. The differences between these three PMLs are down to numerical noise levels. This behaviour can easily be explained due to the fact that all the PMLs are solving the same wave propagation equations (4.14). Although each PML solves these equations differently, the end result should be the same provided the mathematical operators are of the same order.

The error of the seismogram of the model with the CPML is slightly higher than the other PMLs, although the difference is minimal. In Figure 5.4 the error

for the models with various PMLs is presented. Similar to Figure 5.3 the seismograms of the model with RIPML, ADEPML and SPML are identical. However unlike in Figure 5.3 the error of the seismogram of the model with the CPML is smaller than the error of the other three seismograms. At point 2 the CPML performs better than the RIPML, ADEPML and the SPML.

This improved performance of the CPML is contradictory to the theory. The convolution terms are computed by a piece-wise constant approximation. This mathematical operation has lower order accuracy than the operators used in the RIPML, ADEPML and the SPML. Consequently, the CPML should perform less well. In EM modelling it has been shown that the ADEPML performs better than the CPML (*Ramadan, 2003*). A possible explanation why the CPML performed better than the other PMLs is that the results of the simulations were obtained using a script based on an experimental grid that is rotated unlike the grids used in EM. The PML stretches only the derivative components perpendicular to the PML zone. However, in the discretized space the spatial derivatives are computed using the components along the diagonal axes of cell. This potentially leads to small errors. The CPML absorbs the impinging waves less well and therefore this error might be smaller. In order to verify this explanation scripts based on the standard staggered grid with the RIPML and CPML ABC need to written. However, this is beyond the scope of the thesis.

5.1.3. Error analysis

From Figure 5.3 and Figure 5.4 it is obvious that the error of the RIPML, ADEPML and SPML differs from the error of the CPML. In order to understand the behaviour of the various PMLs as a function of the position in the grid, the local error between the seismograms of the models with the various PMLs and

seismograms of the reference model was calculated for every grid point using the following formula:

$$Local\ Error(i,j) = \sqrt{\sum_t \left(v^t_{zi,j} - v^t_{zi,j\,ref} \right)^2} \tag{5.2}$$

where t is the time step, v_z the vertical velocity and i,j denotes the position in the interior of the model domain. The results of the calculations, using the same parameters for the model and the PML, are presented in Figure 5.5.

As expected from the error seismograms in Figure 5.3 and Figure 5.4, the local errors of the RIPML, ADEPML and the SPML are identical for every grid point in the model domain and the differences between them are down to numerical noise levels. From Figure 5.5 it becomes clear that the CPML overall performs better than the other ones with the exception for the corners, where the RIPML, ADEPML and the SPML absorbs the elastic waves slightly better than the CPML.

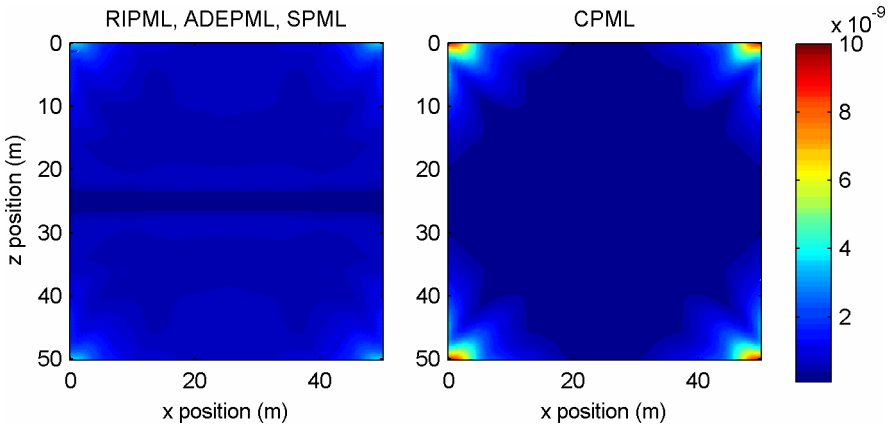

Figure 5.5. Local error calculated for every grid point of the model domain

PML thickness

With the object to comprehend the effect of the PML thickness on the performance of the PML, the local error was calculated for point 1 and point 2 using equation (5.2) for various PML sizes. Since the ADEPML, RIPML and the SPML perform identically, only the RIPML was considered. The size of interior domain does not change and the observation points are located at the same position relative to the source. The results of the calculations can be found in Figure 5.6.

As could be expected the performance of the absorbing boundary layer increases with increasing PML sizes. One of the reasons for the increase of performance is that the scaling of the attenuation coefficient σ becomes smoother with increasing PML size. Therefore reflection due to discretization of the space domain becomes smaller. The second reason is that due to the increased size, the elastic waves are attenuated over a greater distance before reflecting at the model edges. Although in this simple model the PMLs perform well with a thickness of just 3 cells, it is clear from the figure that excellent performances can be achieved with a PML size of 5 cells and higher. Little to no improvement in the error is attained by increasing the PML size over 10 cells and the error becomes stable for PML size of 15 cells and higher.

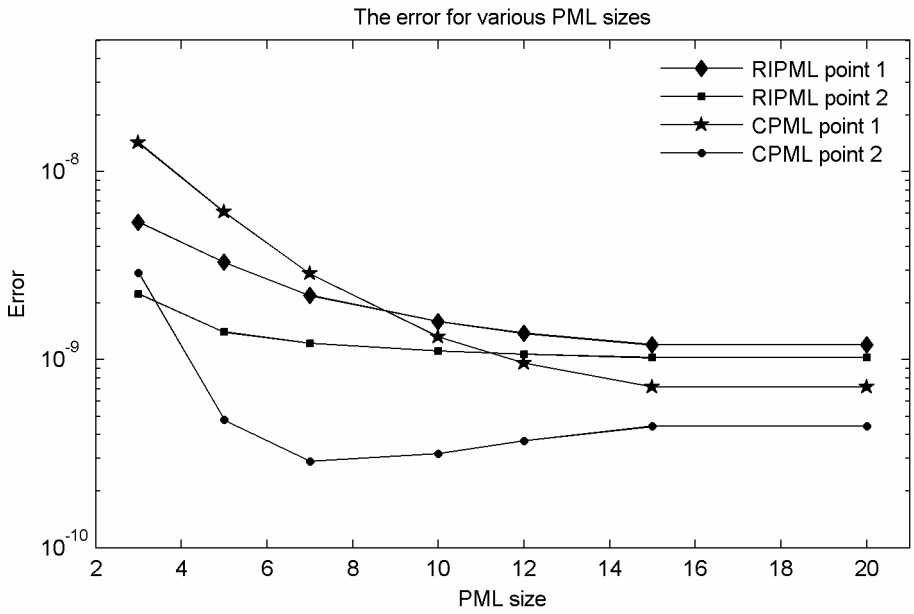

Figure 5.6. Local error as function of the PML size N defined by the number of cells - for the RIPML and the CPML

From Figure 5.6 it can be observed that the RIPML performs better than the CPML for thin boundary layers. However, with increasing thickness the local error of the CPML model decreases quicker than the RIPML and for PML thickness of 10 cells the local error of CPML is smaller than the RIPML at both points. For point 1 the local error of the CPML increases slightly for PML sizes between 7 and 15 cells. A possible explanation for this behaviour is that the errors become close to the smallest floating-point number the computer can handle, which might result in the depletion of the accuracy which can be regarded as random noise. Since random noise is not attenuated by the PML, it can lead to an increase in the error.

Comparison with Higdon absorbing boundary condition

For completeness, a comparison between the CPML and the classical 3rd order Higdon absorbing boundary condition is presented in this section. The model used for the Higdon absorbing boundary condition is based on the Virieux grid as briefly discussed in section 4.3 on page 43, because the Higdon ABC can not readily be implemented in RSG scheme. Reference seismograms were calculated for both grid schemes to avoid errors due to grid scheme differences.

The errors between the reference seismogram and the seismograms obtained by using the Virieux model truncated by the Higdon boundary condition for point 1 and point 2 is presented in Figure 5.7a) and c). Similarly, the errors for the model based on the RSG grid truncated by the CPML are presented in Figure 5.7b) and d). From this figure it is clear that for point 1 in the corner of the simple domain model, the error of the Higdon and CPML seismogram are comparable. However, the error of the CPML seismogram is much smaller for point 2 when compared to the Higdon one.

As noted in chapter 4, the PML performs generally better than most other absorbing boundary conditions. The strength of the PML is not just the good performance, but also the PML has proven that it is unconditionally stable and that it absorbs elastic waves with a wide range of frequencies and incident angles.

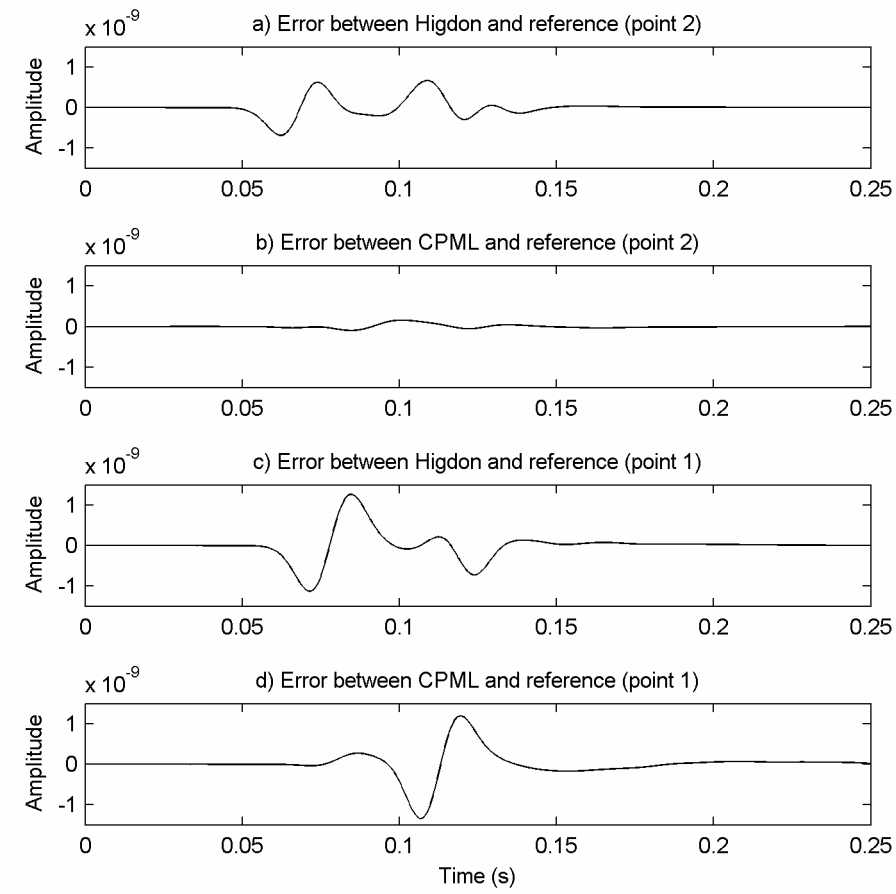

Figure 5.7. The error between the reference seismograms and a) the Higdon and b) the CPML model for point 2, and c) the Higdon and d) the CPML for point 1

5.2. Elongated domain

In this section a model with an elongated domain is presented. Models with elongated domains are prone to cause problems due to the fact that waves impinging the boundary layer at near grazing angles can come into existence. These low angle waves can cause strong reflections at the boundary and in the case of non-PML boundary conditions, such as the Higdon or Liao absorbing boundary conditions these waves can cause the boundary condition to become

unstable. In this example the PMLs with the CFS stretching function are compared to the ones based on the classical stretching function.

5.2.1. The model

The model used in this section is represented in Figure 5.8 – along with some of its model parameters. The model is truncated on all sides by either the ADEPML or the CPML. Numerical tests showed that the results of the RIPML and SPML are similar to the ADEPML and therefore these are not included. The cell thickness of the PML is set to N = 10. The attenuation coefficient σ is polynomial scaled with the order of 2.

The source used is similar to the source used in the simple domain example in section 5.1 except that the centre frequency of the Ricker pulse is now 25 Hz. For comparison reasons, two observation points are assigned with their locations indicated in Figure 5.8 and reference seismograms have been computed using a sufficiently large model such that reflections arrive outside the time frame.

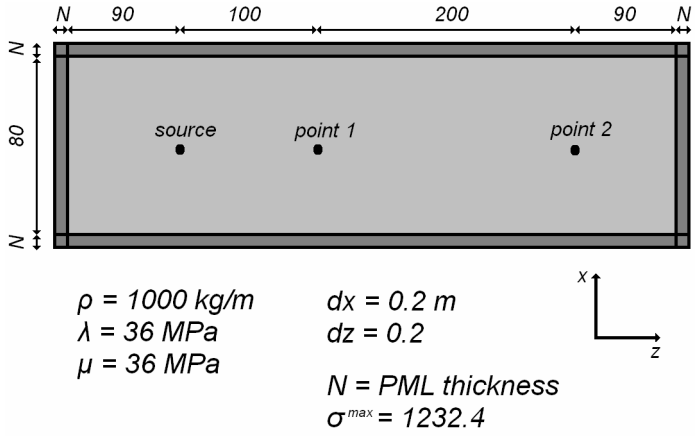

Figure 5.8. Overview of the model with the elongated domain (not to scale) with some model parameters and the size is measured in number of cells

5.2.2. Numerical results

The results of the simulations can be found in Figure 5.9. In the same figure the errors are presented. The errors are calculated as the difference between the reference seismogram and the seismograms obtained from the models truncated by the ADEPML and CPML based on the classical stretching function as well as the CFS stretching function.

The synthetic seismogram of the model with PML with the classical stretching function at point 2 is presented in Figure 5.9b and shows strong fluctuations compared with the reference seismogram. The error of these seismograms can be found in Figure 5.9d. This figure reveals strong errors, whereas the error between the seismograms and the reference seismogram at point 1 presented in Figure 5.9c is considerably smaller. The reason for this is that the further away from the source the angle of incidence becomes smaller – near grazing – and spurious reflections at the boundary interface increases.

In Figure 5.9e) and f) the results of simulations using the models truncated by the CFS PMLs are presented. The attenuation coefficients κ and α are scaled by polynomials using formula (4.49) and (4.50). The following values $\alpha^{\max} = 5$ and $\kappa^{\max} = 15$ are used for the maxima and with $m = 2$ for the scaling factor. Compared to Figure 5.9b, the seismogram in Figure 5.9f approximated the reference seismogram better and a considerable improvement can be observed in the error between the seismogram in Figure 5.9h when compared to the error in Figure 5.9d. However, when comparing the error of the seismograms at point 1, Figure 5.9c) and g), it can be observed that the error slightly increases for the models with the CFS PMLs.

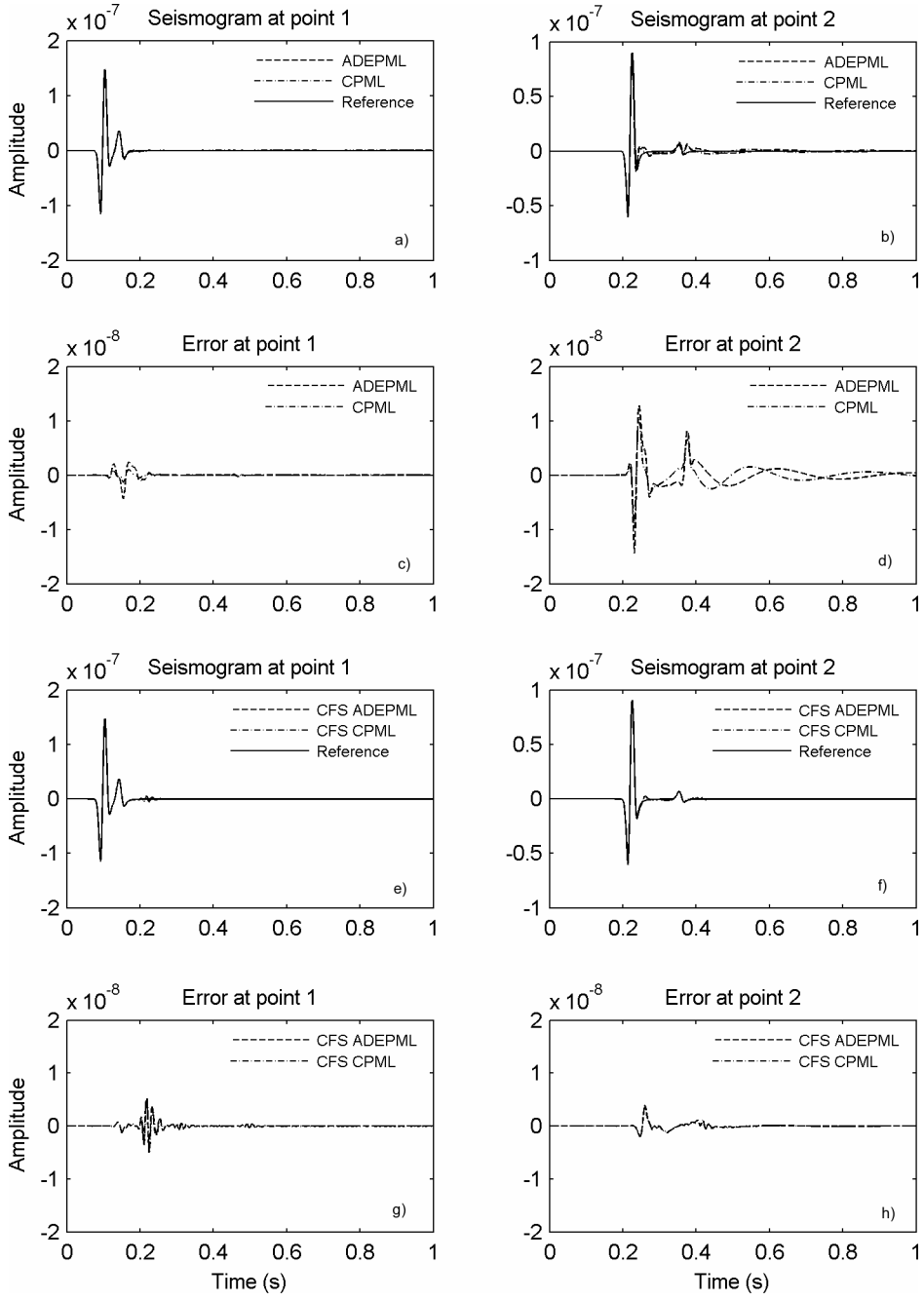

Figure 5.9. Synthetic seismograms of the reference model and the models with ADEPML and CPML (a and b) and their errors (c and d) and the seismogram of models with CFS ADEPML and CFS CPML where $\alpha = 5$ and $\kappa = 15$ (e and f) and their errors (g and h)

5.2.3. Error analysis

With the object of understanding the behaviour of the error as a function of the grid position, the error between the seismogram at every grid point in the interior domain and the reference seismogram for that point has been calculated using the following formula:

$$Local\ Error(i,j) = 20 \cdot \log_{10}\left(\sqrt{\sum_t \left(v^t_{zi,j} - v^t_{zi,j\,ref}\right)^2}\right) \tag{5.3}$$

For the error calculations, the model parameters and PML parameters are identical to the parameters used in the computation of the seismograms in section 5.2.2. The results of the simulations can be found in Figure 5.10. Figure 5.10a) and b) contain the results of the model with the PML based on the classical stretching function. From these figures it is clear that the CPML performs better than the ADEPML. However, it is also clear that the error of both PMLs become very large for grid points further away the source. At these points the waves impinge the interface at a lower angle of incidence, which causes strong spurious reflections.

Figure 5.10c) and d) show the results of the calculations of the local error for models with the ADEPML or CPML based on the CFS stretching function. From these figures it is clear that the performances of the CFS ADEPML and the CFS CPML are comparable. The error at grid points further away has become significantly smaller for both absorbing boundary conditions. The PMLs with the attenuation coefficients α and κ absorb the low incidence waves considerably better than PMLs based solely on the classical stretching function. However, the improved performance comes with a small price. Nearer the source location, where little to no low incidence waves have come into existence, the error

increases slightly. Nevertheless regarding the error in the whole computational domain, the CFS PMLs outperform the PMLs based on the classical stretching function.

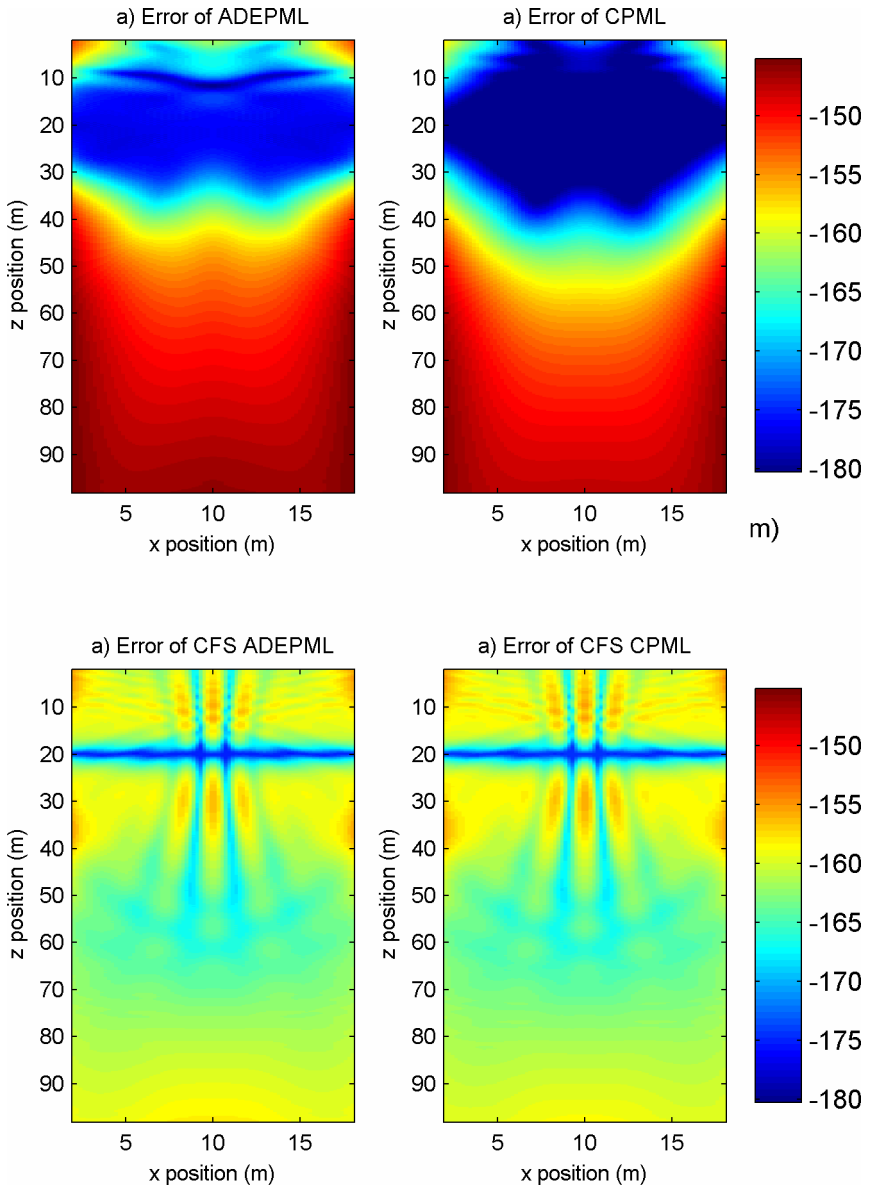

Figure 5.10. Error plots for grid point in the interior domain for different ADEPML and CPML with and without the CFS stretching function with $\alpha = 5$ and $\kappa = 15$ (these figures are not to scale)

In order to gain more insight into the CFS attenuation coefficients α and κ, the local error has been calculated for point 1 and point 2 for a range of values of the attenuation coefficients. For convenience the scaling functions remain the same and also the attenuation coefficient σ remains unaltered. The results of the calculations are presented in Figure 5.11. Note that the error for the PMLs with the classical stretching function can be found by considering $\alpha^{\max} = 0$ and $\kappa^{\max} = 1$ of the CFS stretching function. From the figures it can be concluded that both PML behave almost identically with in respect to the attenuation coefficients. However, in general the CPML performs slightly better than the RIPML. Furthermore it is clear from the plots that for this model problem the error is more sensitive to the attenuation coefficient κ than the attenuation coefficient α. In other words, the choice of the $\alpha^{\max}$ does not improve the error much. Nonetheless, for point 2 a slight improvement can be achieved by selecting the correct value for the $\alpha^{\max}$. Considerable improvement can be achieved by selecting the correct value for the $\kappa^{\max}$.

Regarding point 1, the optimum values for the $\alpha^{\max}$ and $\kappa^{\max}$ are about 10 and 9 respectively for the given scaling functions. Even though little to no near-grazing waves will arrive at point 1, it can be beneficial for the performance of the PML to include the CFS stretching function. Considering the error plots at point 2, Figure 5.11c) and d), it can be observed that the minimum error occurs for $\alpha^{\max} = 75$ and $\kappa^{\max} = 17$. When comparing these values with the optimum values for point 1, it becomes clear that the optimum value for the attenuation coefficients $\alpha^{\max}$ and $\kappa^{\max}$ are shifting from low values to higher values when the observation point is located further away from the source. At greater distances form the source, the angle of incidence becomes smaller and reflections at the interface become larger. In order to attenuate these low angle elastic waves

further away from the source, the higher the values for $\alpha^{\max}$ and $\kappa^{\max}$ have to be in order to prevent spurious reflections at the boundary interface. In other words, the optimum values for $\alpha^{\max}$ and $\kappa^{\max}$ are strongly dependent on the location of the observation point.

It can be concluded that there is no optimum value for the $\alpha^{\max}$ and $\kappa^{\max}$ that would reduce the error to their minimum value for all the grid points. Consequently compromises have to be taken in order to obtain the best results. Gradual variation of the values for $\alpha^{\max}$ and $\kappa^{\max}$ along the boundary layer might be optional. However, this might lead potentially to reflection inside the PML and might even lead to instabilities.

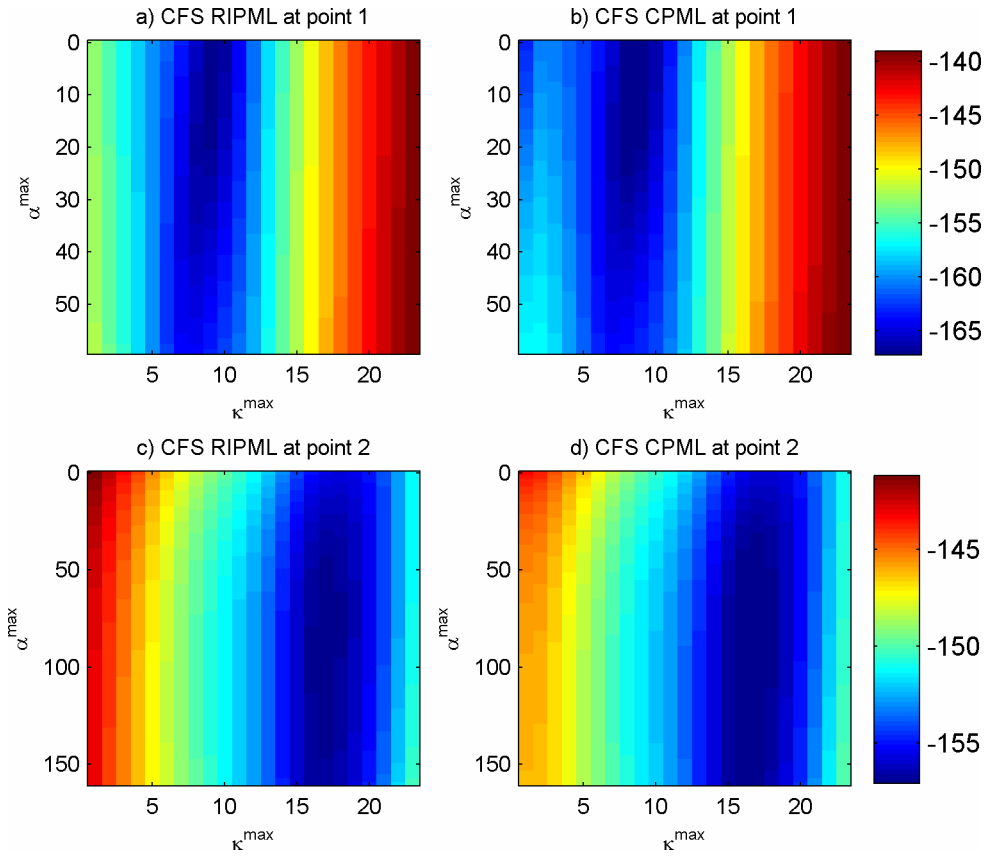

Figure 5.11. Plots of the error at point 1 and point 2 as function of the attenuation coefficients for the CFS RIPML and CFS CPML

5.3. Evanescent waves

This example addresses the problems of absorbing boundary conditions to mitigate evanescent waves such as surface waves. In a continuous space domain the PML should absorb these waves perfectly. However, it has been demonstrated in electromagnetic wave modelling that strong evanescent waves can cause spurious reflections in the discretized space domain (*Bérenger, 2002a*). Bérenger showed that these electromagnetic waves can successfully be mitigated by adopting the CFS stretching function in the PML equations. Analogue to the electromagnetic wave modelling, strong evanescent waves in the elastic wave modelling cause spurious reflections at the boundary interface.

In this section, it is shown that evanescent waves can be mitigated by the PML with the CFS stretching function. To this end, a model representing a half space has been designed such that strong evanescent waves come into existence.

5.3.1. The model

An overview of this model with some model parameters can be found in Figure 5.12. Models like this one can be used for earthquake hazard modelling, where large regions have to be modelled in order to assess the potential risks of earthquakes. It should be pointed out that the purpose of this example is merely to demonstrate the performance the PML with CFS stretching function. To decrease the size of the model and hence the required memory space and calculation time we can opt for a thin slab model. However, strong evanescent waves travelling parallel to the boundary layer interface can cause very large reflections. Similar effects are observed in electromagnetic wave modelling. In order to demonstrate the performance of the CFS PMLs the model contains only homogeneous material such that waves measured at the geophones are purely

direct and surface waves and are not contaminated with refracted, reflected and diffracted waves

The excitation source used in the model is a Ricker shaped pulse with a centre frequency of 1.5 Hz acting on the stress component τ_{zz}. The air is modelled by setting both the Lamé constants to zero and the density to a very low value of $1 \cdot 10^{-6}$ kg/m^3.

The attenuation coefficients are polynomial scaled with the order of m = 2. The size of the PML is selected to be $N = 5$ and additionally some results are presented where $N = 10$. Several synthetic seismograms have been computed for point 1; the model which is truncated by the RIPML or CPML based on the classical stretching function or the CFS stretching function. The classical stretching function is simply obtained by setting $\alpha^{\max} = 0$ and $\kappa^{\max} = 1$.

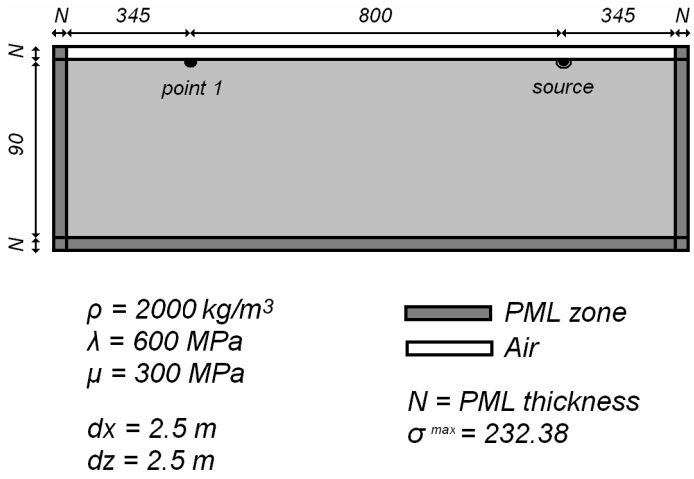

Figure 5.12. Overview of the evanescent model (not to scale) with its parameters

5.3.2. Numerical results

The results of the simulations are presented in the Figure 5.13. For comparison reasons a reference model was calculated using a model sufficiently large enough that evanescent waves do not constitute a problem.

In Figure 5.13a) the reference seismogram is presented. In Figure 5.13b) and c) the errors between this seismogram and the seismograms for the model with 5-cell RIPML and CPML based on the classical stretching function are presented. In Figure 5.13d) and e) the error of the 5-cell CFS RIPML and CFS CPML is presented. For the CFS attenuation coefficients the following values $\alpha^{\max} = 6$ and $\kappa^{\max} = 64$ have been selected. Comparing the results of the models truncated by a 5-cell CFS PML with the 5-cell PML without the CFS stretching function, shows the error of the CFS PMLs is about a factor 10 smaller than the error of the non-CFS PML, which is a considerable reduction. Furthermore the evanescent waves impinging the RIPML and CPML cause the emanation of low frequency waves which undulates with reasonable high amplitudes.

Although the CFS PMLs perform considerable better, reasonably strong reflections at 11 seconds can be observed in Figure 5.13d) and e). The cause of these reflections can be seen in Figure 5.14d) and e) which shows the snapshots of the models taken at 5.6 seconds. Strong reflections caused by the surface waves reflecting on the right boundary can be observed at around 3 km. Since these reflections do not occur in the snapshot of the reference model, Figure 5.14a) and the snapshots of the models with the PMLs based on the classical stretching functions, Figure 5.14b) and c), it is clear that they are associated with the CFS stretching function. For the given model settings, the CFS PMLs absorbs the evanescent waves travelling parallel with the boundary layer considerably better than the PMLs with the classical stretching function. However, by adopting the

CFS stretching function, surface waves impinging the boundary layer at perpendicular angles are less attenuated.

In order to mitigate these waves sufficiently, an increased size of the PML can be opted for. Larger PML size will attenuate the surface waves for a larger duration and hence it will neutralize the negative effect of the CFS attenuation coefficients α and κ for the surface wave impinging the boundary layer at right angles. Figure 5.13f) and g) shows the results of the simulation of the models with a 10-cell CFS PML where $\alpha^{\max} = 4$ and $\kappa^{\max} = 17$. Compared to the 5-cell CFS PML, there is a slight decrease in the error. However, the amplitudes of the strong reflections which could be observed at 11 seconds have diminished. In Figure 5.15 the snapshots of the models with 10-cell CFS PMLs taken at 5.6 seconds can be found. Comparing these snapshots with the snapshots in Figure 5.14 shows that the 10-cell CFS PML has successfully absorbed the spurious reflections emanating from the right boundary layer. Moreover they mitigated the evanescent waves travelling parallel to the boundary layer.

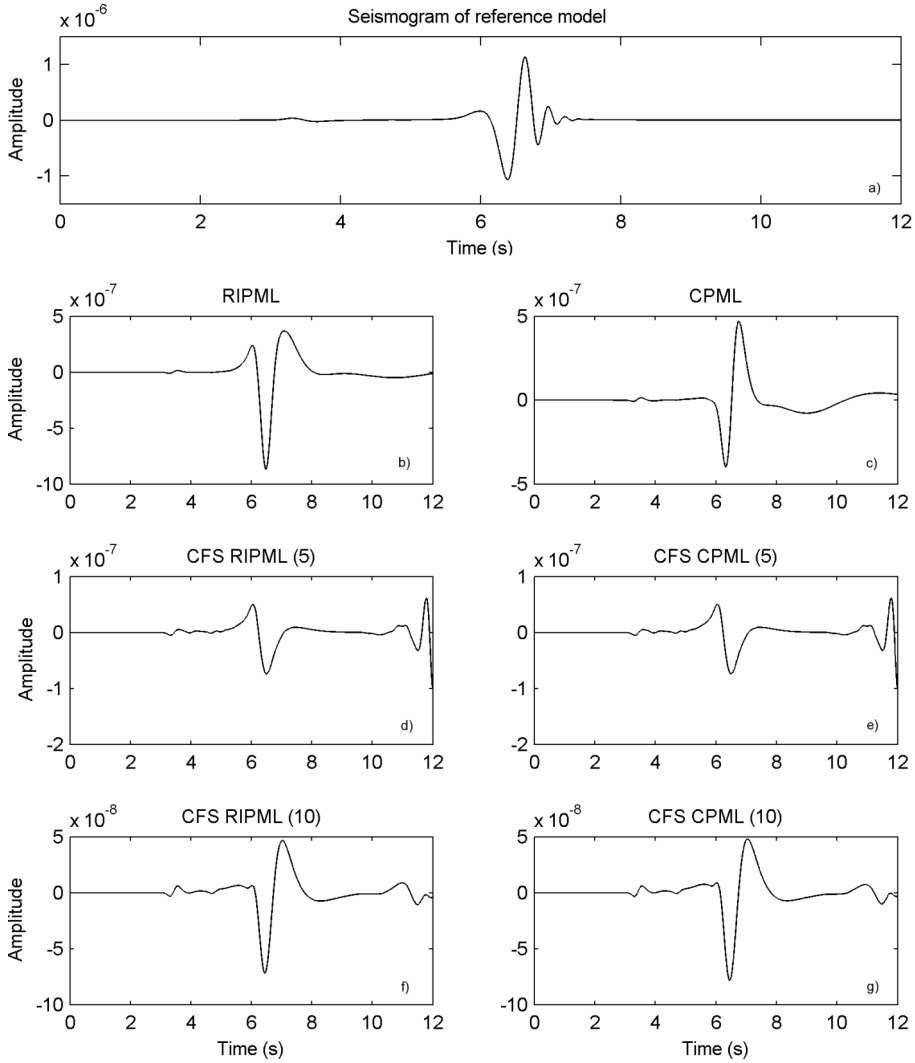

Figure 5.13. The seismogram of the reference model and the error between reference seismogram and the seismograms of the model with b) RIPML c) CPML d) 5 cells CFS RIPML e) 5 cells CFS CPML f) 10 cell CFS RIPML and g) 10 cell CFS CPML

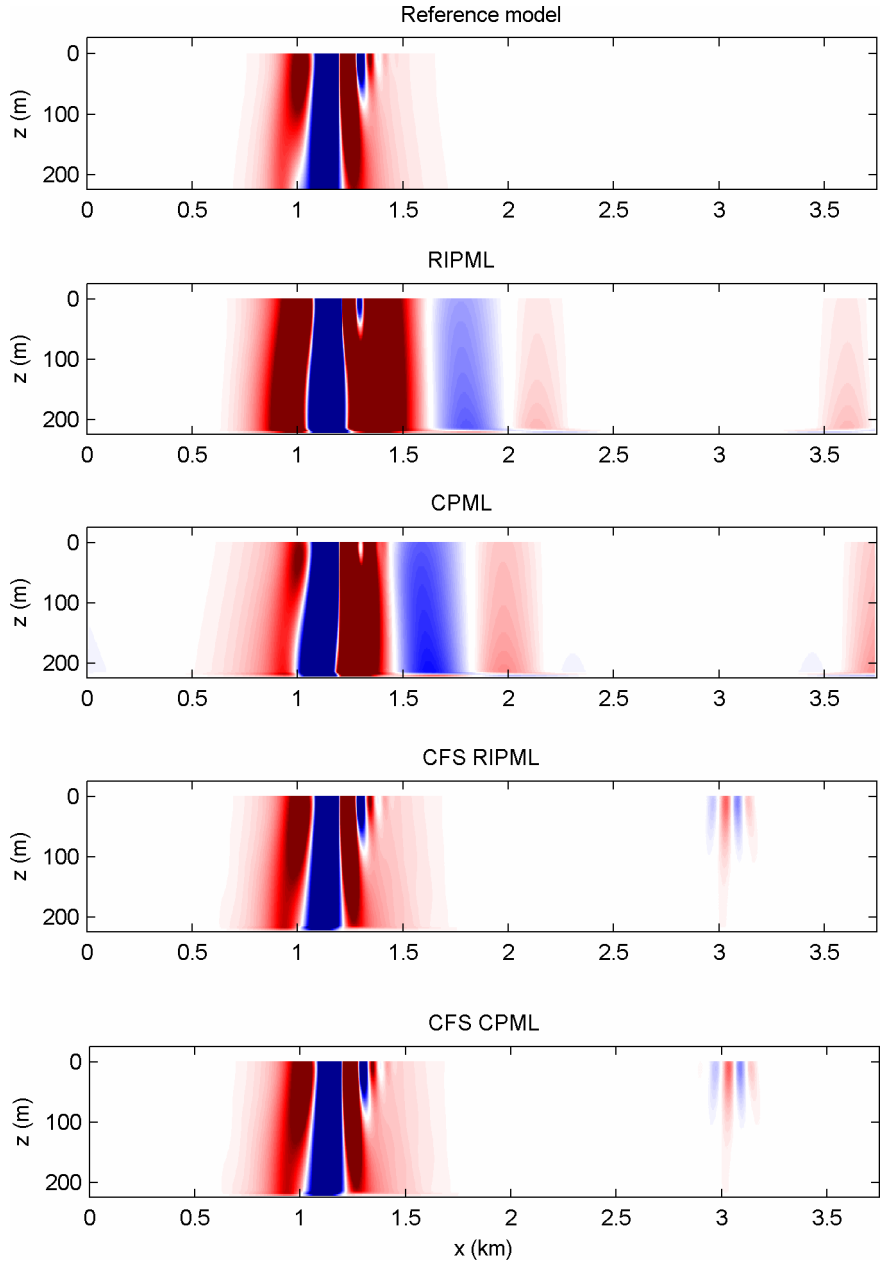

Figure 5.14. Snapshots of the models with 5-cell PML at 5.6 seconds

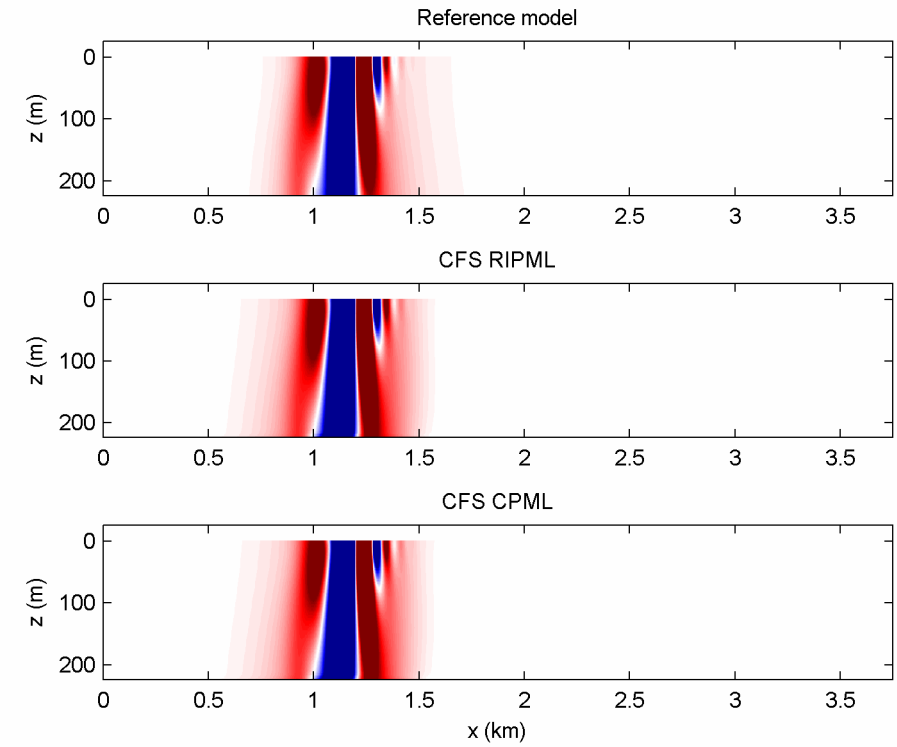

Figure 5.15. Snapshots of various models with 10-cell thick PML at 5.6 seconds

5.3.3. Error analysis

In order to investigate the effect of the CFS attenuation coefficients α and κ on the performance of the PML, the global error of models with varying $\alpha^{\max}$ and $\kappa^{\max}$ is calculated using the following formula:

$$Global\ Error\left(\alpha^{\max},\kappa^{\max}\right)=20\cdot\log_{10}\left(\sqrt{\sum_{i}\sum_{j}\sum_{t}\left(v^{t}_{zi,j}-v^{t}_{zi,j\,ref}\right)^{2}}\right) \tag{5.4}$$

The scaling functions of the attenuation coefficients remain the same as presented in section 5.3.2. The results of the calculations can be found in Figure 5.16. From this figure it is clear that the CFS ADEPML and CFS CPML perform similarly

and that the differences are very small, although the CFS CPML performs slightly better than the CFS RIPML. Both the attenuation coefficients α and κ play an important role in the attenuation of the evanescent waves. Unlike in the case of the long domain model, presented in section 5.2, the attenuation coefficient α has a great influence on the performance of boundary condition. As a matter of fact when $\alpha^{\max}$ is zero, the global error will remain largely independent of the value of the $\kappa^{\max}$.

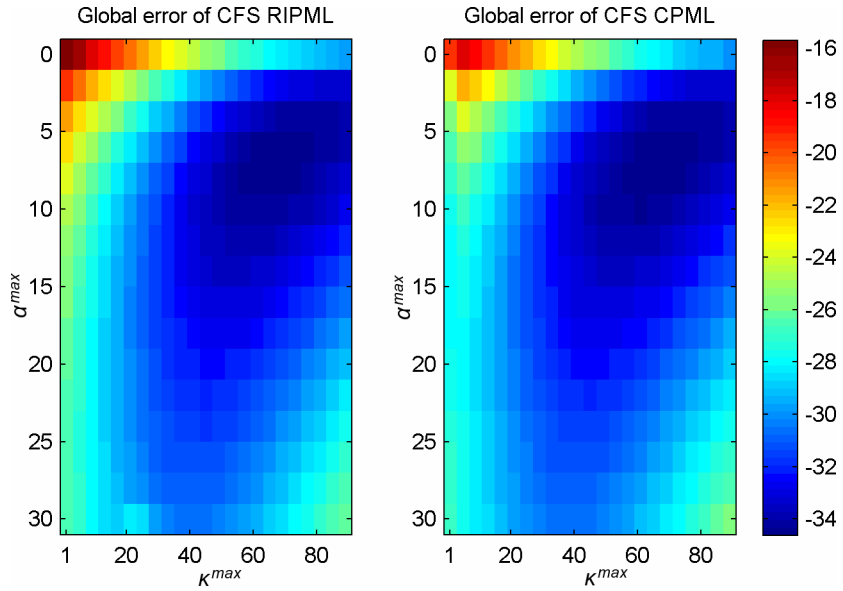

Figure 5.16. Contour plots of the global error for a) CFS RIPML and b) CFS CPML

PML size

In order to examine the influence of the size of the PML zone on the performance, the local error was calculated using equation (5.3) for the models truncated by the PML with variable thickness. Only the observation points with *j=80+N* and *i=15* to *1485* are considered. The size of the interior remains constant. The boundary conditions used are the CFS RIPML and the CFS CPML. The results of the calculations can be found in Figure 5.17. The results of

the RIPML and CPML were calculated by setting the attenuation coefficients $\alpha^{\max}$ and $\kappa^{\max}$ to 0 and 1 respectively. For the CFS PMLs the following values $\alpha^{\max} = 6$ and $\kappa^{\max} = 64$ for the attenuation coefficients have been adopted.

In Figure 5.17a) and b) the results of the PMLs based on classical stretching functions can be found. These PMLs perform very well for grid points close to the source around grid position 1100. However, the local error quickly increases for grid positions further away from the source. At positions further away from the source, evanescent becomes a more dominant presence in the PML zone. These evanescent waves are not mitigated properly by the boundary condition and hence the local error increases. Although by increasing the PML size the local error decreases for grid positions around the source, it is interesting to observe that using thicker PMLs does not enhance the local error at grid points where evanescent waves are predominant.

In Figure 5.17c) and d) the results of the simulations for the CFS PMLs can be found. For the given values for $\alpha^{\max}$ and $\kappa^{\max}$ the local errors for grid positions around the source location are larger for the CFS PMLs than the PML based on the classical stretching function. However, further away from the source where the evanescent waves become dominantly present, the local errors of the CFS PMLs do not increase as dramatically as the PMLs based on the classical stretching function. Furthermore increasing the thickness of the boundary layer does increase the performance of the boundary condition. For the PML sizes larger than 5 cells, the local error remains below an acceptable level of -100 for all the grid positions. The CFS PMLs with a 10-cell boundary layer perform excellently over the whole model.

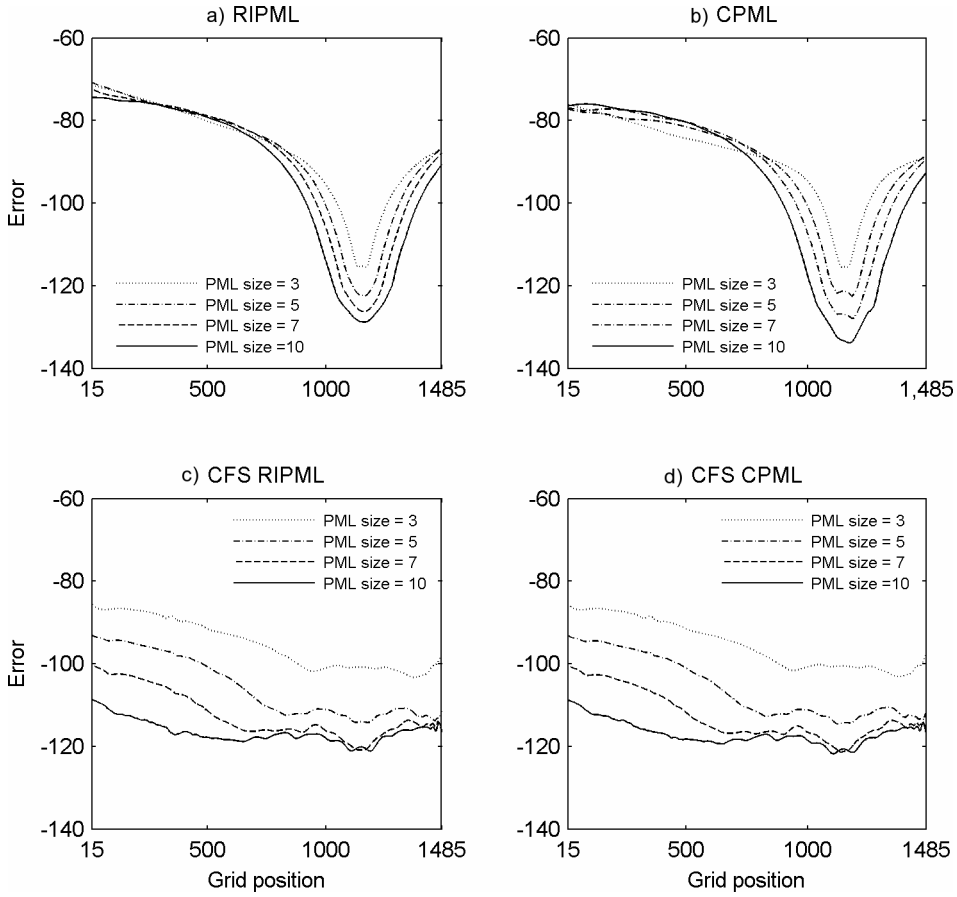

Figure 5.17. Local error calculated for various PML sizes for a) RIPML, b) CPML, c) CFS RIPML and d) CFS CPML where $\alpha^{\max} = 6$ and $\kappa^{\max} = 64$

It should be mentioned that the values for $\alpha^{\max}$ and $\kappa^{\max}$ are kept constant for all the boundary layer sizes. The selected values for $\alpha^{\max}$ and $\kappa^{\max}$ are optimal for the 5-cell thick boundary layers. However, these optimum values for $\alpha^{\max}$ and $\kappa^{\max}$ will vary with the different PML sizes. A complete analysis of the behaviour of the CFS attenuation coefficient is beyond the scope of this thesis. The general trend is that the optimum values for these coefficients are inversely to the size of the boundary layer e.g. the optimum values of $\alpha^{\max}$ and $\kappa^{\max}$ are smaller for bigger PMLs. Furthermore it should be mentioned that the error for PML sizes of 15 and 20 cells increased slightly when compared to global error of the 10-cell

PML. A possible explanation of this behaviour is that the accuracy is depleted and the numerical noise in the PML becomes a source itself.

5.4. Conclusions

In this chapter three different models were presented in order to examine the performance of the three non-split PMLs introduced in chapter 4. Some numerical analysis of the attenuation coefficient and the PML thickness were presented in this chapter. The following observations can be made:

- The RIPML, ADEPML and the conventional SPML perform identically when based on the classical stretching function. Using the RSG, the CPML performs generally better than the other three PMLs except for thin PMLs and in the corners of the model.
- Adopting CFS stretching functions can improve the performance of the PML in the cases when waves impinge the boundary zone at near grazing angles and when evanescent waves are present in the boundary zone, whereas the classical stretching function performs poorly even with increasing PML sizes. The CFS stretching function can be useful in various model scenarios, such as earthquake hazard modelling, modelling of seismic waves for the exploration of oil, gas and minerals and the modelling of impact echo and ultrasonic responses in non-destructive testing.
- The choice of the attenuation coefficients $\alpha^{\max}$ and $\kappa^{\max}$ is pivotal to the performance of the CFS PML. Unfortunately the optimum values depend strongly on the geometry of the model, source and receiver location and hence compromises have to be made.
- Strong reflections can occur at the CFS PML-surface boundary, although increasing the size of the PML will mitigate these reflections better.

6. Numerical models

Very few studies have been conducted on the subject of seismic behaviour of voids. No information can be found regarding voids shaped like mineshafts. In order to understand the dynamic elastic behaviour of mineshafts in relation with its surrounding a computer algorithm was designed in order to simulate synthetic seismograms. These seismograms were used to assess the potential of seismic survey techniques and in particular the transmission method to delineate mineshafts.

The Matlab scripts used in the previous chapter were adapted and rewritten into Fortran source code. This enables the simulations of large 3D models. The final program consists of the main program, twelve subroutines and four data modules adding to a total of 1851 source code lines.

This chapter deals with the descriptions of the models and the results of the simulations. The results of the models are represented as snapshots and the seismograms. The synthetic data was further analysed and the results of the analysis are presented in chapter 7.

6.1. Introduction – 3D models

Modelling of 3D spaces requires substantial computer resources such as large memories and long computational durations. Since computer resources are scarce at the Institute only a limited number of 3D simulations were run.

A standard model was designed which was based on mineshaft D in Figure 2.3. This model represents a space of 40m by 40m and 18.75m deep. A

representation of the plan view and the cross section of the standard model can be found in Figure 6.1. The mineshaft is represented by a box-shaped void which is filled with air and backfilling. The backfilling begins at a 1m depth from the surface and extends to bedrock. The backfilling was not modelled to the surface since it is likely that due to weathering and redevelopment of the land, the backfilling has mixed with the superficial deposits. The superficial deposits-bedrock interface was located at 5m depth from the surface. The lining and the platform were not modelled in order to simplify the models and furthermore their presence would have a negligible effect on the seismic waves.

The position of the shot point and the survey lines with each 20 observation points i.e. receivers are shown. Five survey lines were designed. Although survey line L4 and L5 were of more interest in the mineshaft detection in the proximity of railways using the broadside shot gathers as explained in section 3.4.1, survey line L1, L2 and L3 were included to provide additional insight and understanding of seismic behaviour of the mineshaft. The results of all the survey lines are shown for the standard model in this chapter. The results of the survey lines L1, L2 and L3 of the other models can be found in Appendix E.

The model parameters used in the standard model are summarized in Table 6.1. Given the shape of the model and locations of the source, a PML based on the classical stretching function proved to be sufficient to absorb the seismic waves. Therefore the CFS attenuation coefficients α and κ were set to 0 and 1 respectively.

The medium parameters were chosen such that the simulations could be run on the 2GB memory Pentium IV Linux platforms and such that run times were not exceeding more than 2 days. Given these requirements, high velocity bedrock could not modelled since in order to fulfil the Neumann stability condition (*Saenger, 2000*) this leads to a considerable increase in the run times.

Furthermore, lower shear-wave velocities could not be modelled since at least 30 cells are required to model the shortest wave length to avoid grid dispersion. Modelling slower media requires smaller cells which lead to an increased number of cells and number of iterations. Although the limited computer resources available at the Institute do not allow one to simulate models containing very high velocity variations i.e. higher velocity bedrock and lower velocity superficial deposits, in the same model - the selected velocities for the materials are nevertheless values representative for values in the field. The selected values for the weathered bedrock and superficial deposits are a generalization of velocity values found in the literature e.g. (*Telford et al., 1990; Sharma, 1997; Parasnis, 2000*). Note that no publications were found regarding the wave velocities in the backfilling. However, one can assume that the backfilling is not compacted and consists of loose material. Hence the shear wave velocity and the compressional wave velocity can be assumed to be considerably lower than the surrounding superficial deposits.

In addition to the standard model, 19 other model scenarios were simulated which differ from the standard model in

- Bedrock thickness – presented in section 6.3
- Mineshaft size – presented in section 6.4
- Mineshaft shape – presented in section 6.5
- Source frequencies – presented in section 6.6
- Filling material – presented in sections 6.7 and 6.9
- Embankment – presented in section 6.8
- Source location – presented in section 6.10
- Mineshaft location – presented in section 6.10

The models and their descriptions are summarized in Table 6.2. Additionally, some models without the mineshaft were simulated in order provide reference data used in the analysis.

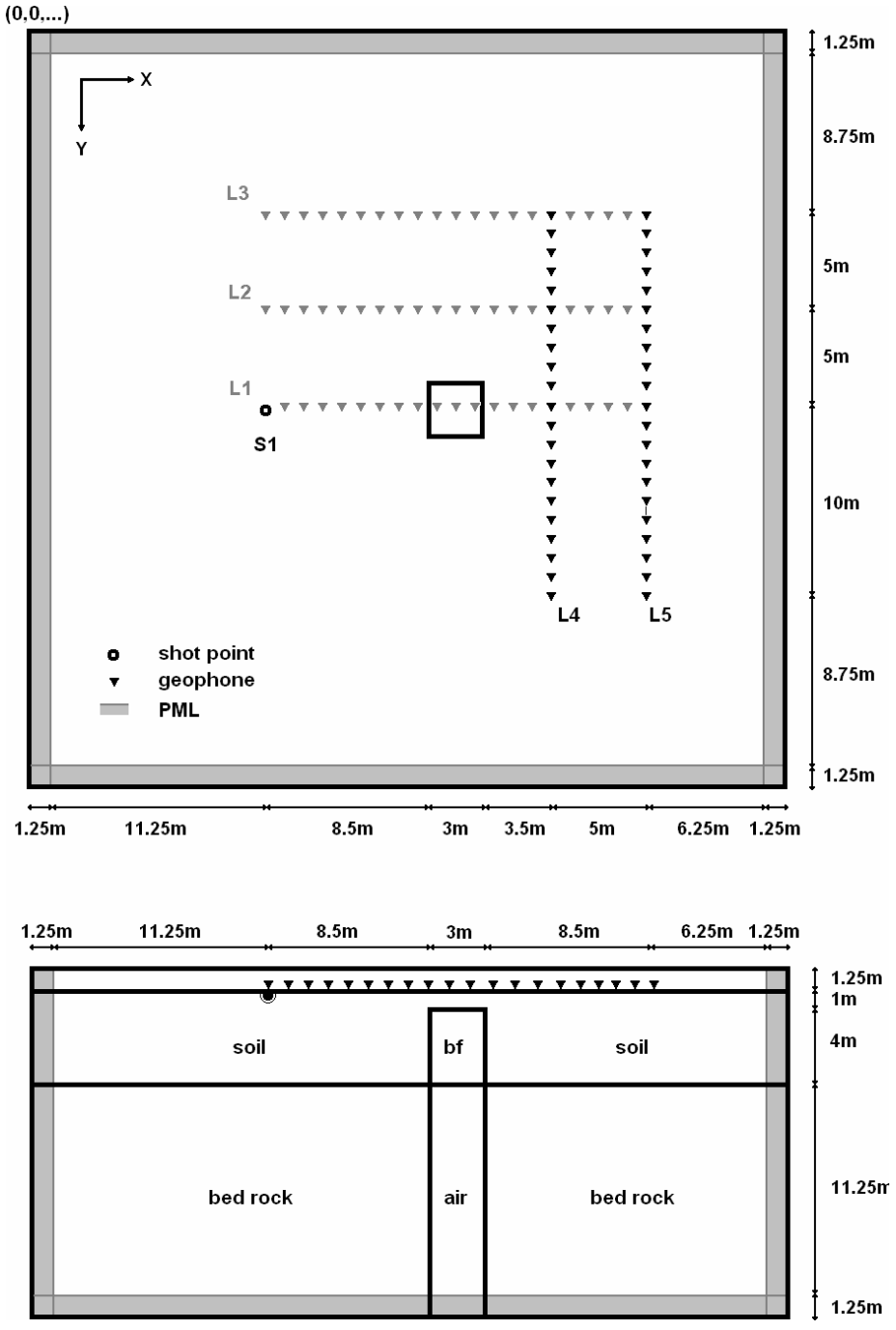

Figure 6.1. Plan view (top) and the cross section along survey line L1 (bottom) of the 3D standard model with the measures and the shot point and survey lines, the mineshaft is outlined by the black box; bf denotes the backfilling

Table 6.1. The model parameters of the standard model

Model parameter	Quantity/description
Actual size of model	40 × 40 × 18.75m
Number of cells	320 × 320 × 150
Size of cells	0.125 × 0.125 × 0.125 m
Simulation time	0.3 s
Source location (centre)	S1 at (12,5m,20m,12.5m)
Source applied on node	τ_{zz}
Source size	7 nodes
Source distribution	Gaussian
Source shape	Ricker
Source frequency	25Hz
Centre of mineshaft location	(180,160,...)
Mineshaft size	3 m (24 cells)
Absorbing boundary condition	Recursive Integration PML
PML thickness	1.25 m (10 cells)

Attenuation coefficients	α	κ	σ
	0	1	2000

Medium	ρ (kg/ m^3)	λ (N/m^2)	μ (N/m^2)	v_p (m/s)	v_s (m/s)
Superficial deposit	2000	$2.50 \cdot 10^8$	$1.25 \cdot 10^8$	500	250
Bedrock (weathered)	2500	$2.35 \cdot 10^9$	$6.25 \cdot 10^8$	1200	500
Backfilling	1800	$2.07 \cdot 10^8$	$4.07 \cdot 10^7$	400	150
Air	$1.0 \cdot 10^{-6}$	0	0	0	0
Water	1000	$2.25 \cdot 10^8$	0	1500	0

Table 6.2. Short summary of the models and the difference in bold

Model	Bedrock depth	Mineshaft	Source frequency	Backfilling	Source location	Mineshaft location	Miscellaneous
1	**5m**	**3m square**	**25Hz**	**Top Backfilled**	**12.5m 20m**	**22.5m 20m**	**Standard model**
2	**10m**	3m square	25Hz	Top backfilled	12.5m 20m	22.5m 20m	-
3	**1.5m**	3m square	25Hz	Top backfilled	12.5m 20m	22.5m 20m	-
4	5m	**2m square**	25Hz	Top backfilled	12.5m 20m	22.5m 20m	-
5	5m	**4m square**	25Hz	Top backfilled	12.5m 20m	22.5m 20m	-
6	5m	**1m square**	25Hz	Top backfilled	12.5m 20m	22.5m 20m	-
7	5m	**3.4m circular**	25Hz	Top backfilled	12.5m 20m	22.5m 20m	-
8	5m	3m square	**20Hz**	Top backfilled	12.5m 20m	22.5m 20m	-
9	5m	3m square	**30Hz**	Top backfilled	12.5m 20m	22.5m 20m	-
10	5m	3m square	25Hz	**Completely backfilled**	12.5m 20m	22.5m 20m	-
11	5m	3m square	25Hz	**Water in void**	12.5m 20m	22.5m 20m	-
12	5m	3m square	25Hz	Top backfilled	12.5m 20m	22.5m 20m	**Embankment**
13	5m	3m square	25Hz	**Void to 2.5m**	12.5m 20m	22.5m 20m	-
14	5m	3m square	25Hz	**Water void (2.5m)**	12.5m 20m	22.5m 20m	-
15	5m	3m square	25Hz	Top backfilled	**12.5m 22.5m**	22.5m 20m	-
16	5m	3m square	25Hz	Top backfilled	**12.5m 25m**	22.5m 20m	-
17	5m	3m square	25Hz	Top backfilled	12.5m 20m	**22.5m 25m**	-
18	5m	3m square	25Hz	Top backfilled	12.5m 20m	**22.5m 30m**	-
19	5m	3m square	25Hz	Top backfilled	12.5m 20m	**17.5m 20m**	-
20	5m	3m square	25Hz	Top backfilled	12.5m 20m	**27.5m 20m**	-

6.2. Model 1 – standard model

The first 3D model presented in this chapter is the standard model. The other models were based on this model and their numerical results were compared to the results of this model. A representation of the model can be found in Figure 6.1 and its model parameters can be found in Table 6.1.

The results of the simulations are presented in the snapshots at various time steps in Figure 6.2 and in the synthetic seismograms in Figure 6.3 and Figure 6.4. The snapshots and seismograms consisted of the recorded vertical velocity v_z at each observation point. The snapshots are taken from observation points at the surface.

6.2.1. Snapshots

The snapshots are presented in Figure 6.3.

- The mineshaft caused diffraction of the surface waves. These waves were superimposed on other waves which can be observed as circles of anomalous amplitudes around the mineshaft. These anomalous amplitudes were caused by constructive and deconstructive interference. Other diffracted waves were too weak or overwhelmed to be observed in the snapshots.
- The snapshots at 93ms, 113ms and 134ms show that the surface waves behind the mineshaft were slowed down. This can be observed considering the wave front of the surface waves which is not perfectly circular. The zone with this delay was not limited to the locations directly behind the mineshafts inline with the source and it spreads out starting from the mineshaft.
- From the snapshots at 93 ms to 155 ms it can observed that the amplitudes of the surface waves directly behind the mineshafts i.e. in the shadow zone of

the mineshaft are stronger than the other amplitudes. The reverse occurred at the observation points away from the shadow zone of the mineshaft. The amplitude of the surface waves were decreased when compared to the amplitudes of surface waves unaffected by the mineshaft. A detailed explanation of this phenomenon is given in the text box on page 121.

6.2.2. Seismograms

In Figure 6.3 the synthetic seismograms computed for the survey lines L1 are presented. In this figure the synthetic seismograms of the reference model without a mineshaft are also shown. Differences between the seismograms of the standard model and its reference model are caused by the presence of the mineshaft, since that is the only variable. The interpretations of each seismic event are shown in the figures on the right hand side. This interpretation was based on calculations of the travel time of each wave.

- The seismogram of the reference model shows that many different seismic waves can be observed at the receivers along survey line L1 before the dominant surface waves arrived. From the interpretation seismogram it is clear that most events were interfering with each other. In practice it could be difficult to interpret seismograms since the subsurface is unknown. After the arrival of the surface waves no waves can be observed other than the surface waves. It should be mentioned that although the events were represented by a single line the actual time length of the wave is much longer.
- When comparing the seismograms of the standard model and the reference model various deviation scan be observed which were related to the presence of the mineshaft:

- A seismic event was superimposed on the S-waves (event g). Very likely this was a Rayleigh wave converted into a refracted S-wave (RcS wave) and/or possibly into a diffracted P-wave (RcP waves).
- Diffracted surface waves consisting of energies related to the first surface waves were superimposed on later arriving surface waves (event h). This leads to anomalous amplitudes observed at the receivers at 0m-8m.
- The later arriving surface waves were diffracted at the mineshaft. These events are denoted by the letter "i" in Figure 6.3.

In Figure 6.4 the numerical results from the other survey lines are presented. On the right hand side the reference seismogram of this model is presented for comparison reasons.

- Diffracted surface wave events are less distinguishable than in Figure 6.3, although at survey line L2 and L3 some diffracted surface wave energies can be observed. At the same survey lines anomalous surface wave amplitudes can be observed which were caused by the superposition with diffracted surface waves.
- At survey line L4 and L5 no diffracted waves can be observed. Due to superposition with diffracted surface waves, the later arriving surface waves show anomalous amplitudes. This is particular clear at survey line L4. It should be mentioned that it appears that the S-waves have smaller amplitudes at geophone 7m-12m however this is caused by scaling of the strong surface waves.
- The delay of the surface waves observed in the snapshots can also be observed in the seismogram of survey line L4 (letter "j").

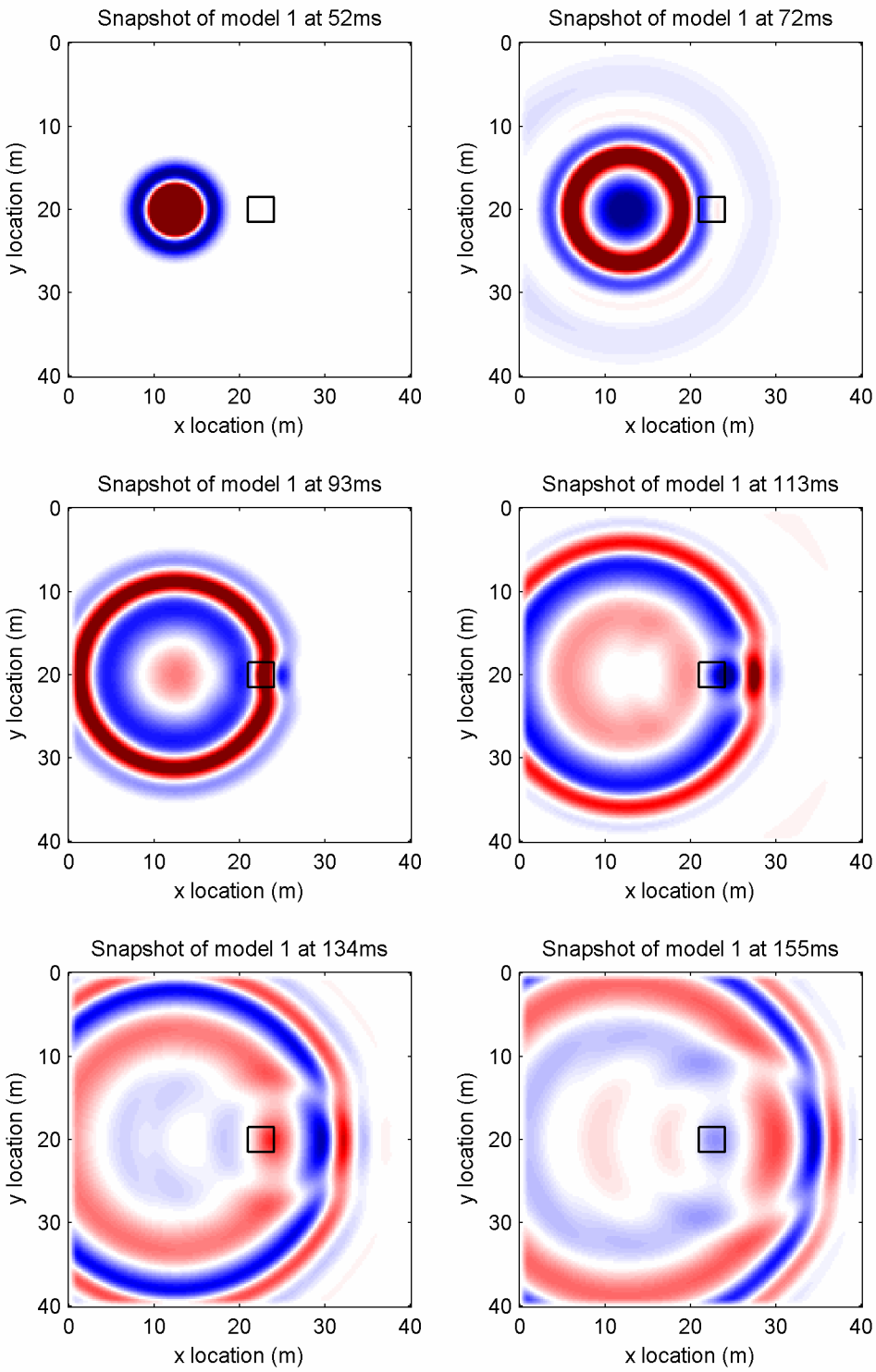

Figure 6.2. Snapshot of model 1 at various times - amplitudes of the vertical velocity are multiplied by a scaling factor of 25

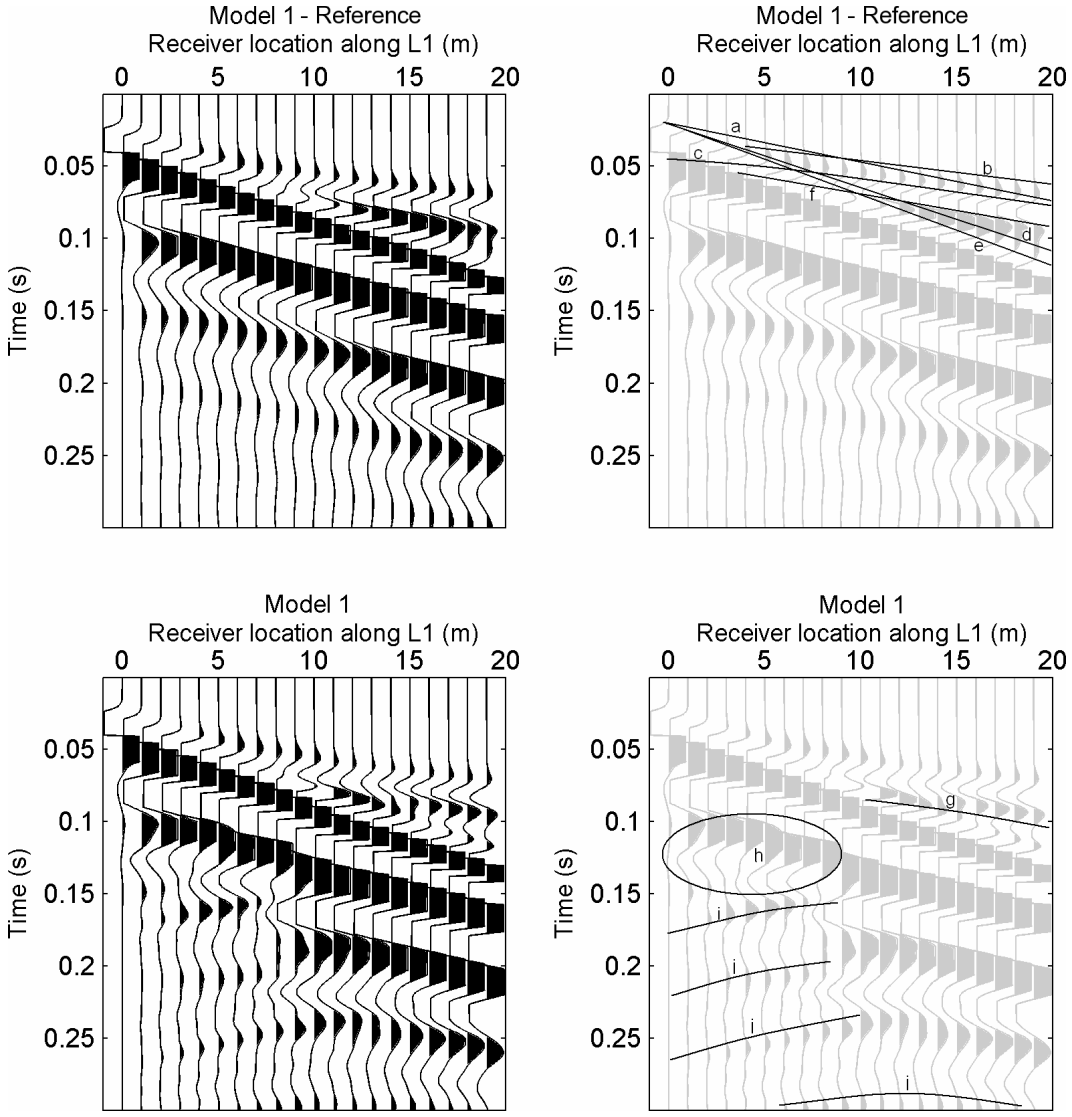

Figure 6.3. Synthetic seismograms computed for model 1 (bottom) and reference model (top) with no mineshaft at survey line L1 (left) and the analysis (right); the traces are individually scaled and multiplied by a factor 5; interpretation of events: a – direct P-wave; b – refracted P-wave; c – reflected P-wave; d – direct S-wave; e – Rayleigh wave; f – refracted S-wave; g – diffracted RcP or RcS wave; h – interference of diffracted surface waves with surface waves; i – diffracted surface waves

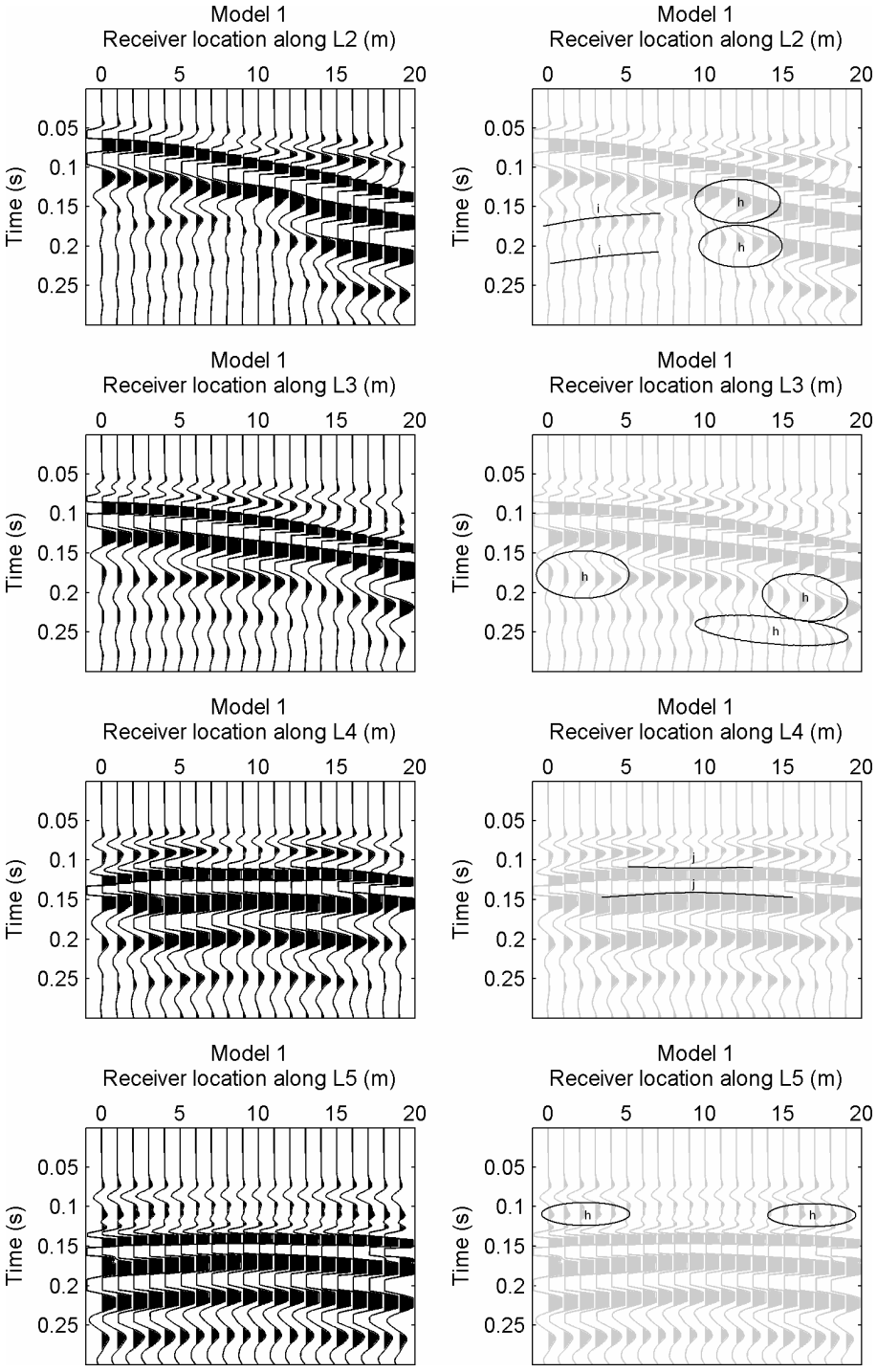

Figure 6.4. Synthetic seismograms of model 1 (left) and its analysis (right) computed at observation points along L2, L3, L4 and L5; explanation of events: h – anomalous amplitudes; i – diffracted surface waves; j – delayed surface waves

Explanation of the amplitude variation

The seismic energy measured at an observation point away from the source is not made up from energy travelling along a single ray but made up of energy coming from a large area. This area is known as the Fresnel zone which denotes the space where the ray paths between source and receivers differs less than a half wave length, such that the energies interfere more or less constructively (*Sheriff and Geldart, 1995*). For the sake of simplicity, it is assumed that the raypaths are straight and that the Fresnel zone is diamond shaped. Figure 6.5 shows a simple plan view of the Fresnel zone, where R is the maximum aperture of the zone. For constructive interference the travel distance along h_1 should not differ more than $\lambda/4$ from h_0. Considering the travel times this can be formulated as:

$$t_{h_1} - t_{h_0} = \frac{\lambda}{4v_1} \tag{6.1}$$

where v_1 is the velocity along h_1 and t_{h0} and t_{h1} are the travel times along h_0 and h_1. The maximum aperture R can be calculated as follows:

$$R = \sqrt{h_1^2 - h_0^2} = \sqrt{\left(t_{h_1} v_1\right)^2 - \left(t_{h_0} v_0\right)^2} = \sqrt{\left(\frac{\lambda}{4} + t_{h_0} v_1\right)^2 - \left(t_{h_0} v_0\right)^2} \tag{6.2}$$

Generally, it can be assumed that the $h_0 \gg \lambda$ and that $h_1 \gg \lambda$ such that the Fresnel aperture R can be approximated by:

$$R \approx \sqrt{\frac{\lambda t_{h_0} v_1}{2} + t_{h_0}^2 v_1^2 - t_{h_0}^2 v_0^2} \tag{6.3}$$

Note that when v_1 and v_0 equation (6.3) becomes the normal equation for the Fresnel zone. From equation (6.3) a few important observations can be made.

- When there is a mineshaft located somewhere along h_0 the effective velocity decreases i.e. v_0 is smaller than v_1 which results according equation (6.3) in an increase of the radius R. In other words the mineshaft causes an increase of the size of the Fresnel zone and more energy is interfering constructively at the observation points behind the mineshaft.

- At observation points away from the shadow zone the mineshaft location shift for example towards h_1. The velocity v_1 along h_1 becomes smaller than v_0 which according equation (6.3) results in a decrease of the size of the Fresnel aperture and less energy will interfere constructively at the observation point.

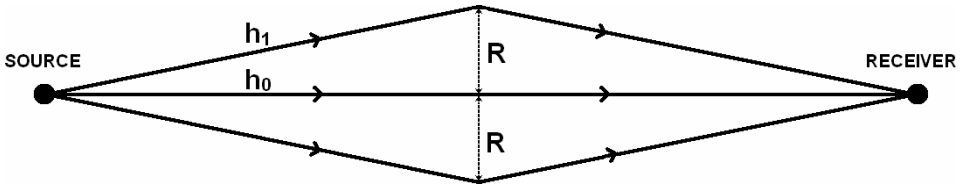

Figure 6.5. Plan view of the Fresnel zone between the source and receiver; R is the maximum aperture of the Fresnel zone, h_0 is the distance from the source to the centre of the Fresnel zone and h_1 is the distance from the source to the point furthest away from the centre

6.3. Models 2 and 3 – bedrock depth

In this section models 2 and 3 are presented. These models differ from the standard model in the modelled bedrock depths. Model 2 consisted of a superficial deposit layer with a thickness of 10m. Model 3 consisted of a superficial deposit layer with a thickness of 1.5m. The mineshaft in model 3 did not have any backfilling and it was completely open. All other model parameters were identical to the standard model. It should be mentioned that model 3 bares resemblances with the capped mineshaft of the field trials which are presented in chapter 8. The capping of the mineshaft will not affect the results of the numerical modelling. A cross section of model 2 and 3 can be found in Figure 6.6.

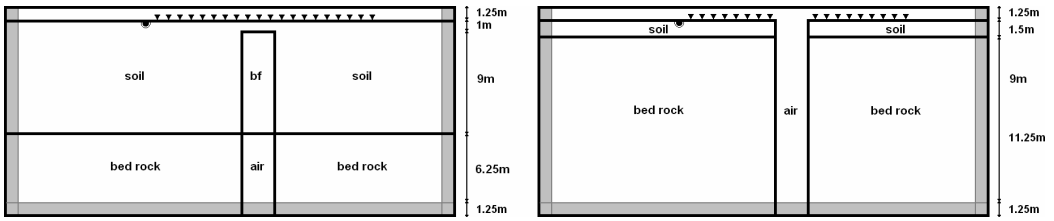

Figure 6.6. Side view of model 2 (left) and model 3 (right); bf is the backfilling

The snapshots of model 2 and 3 are presented in Figure 6.7. The shallow bedrock in model 3 caused reverberation of the surface wave energies and long wave packages consisting of surface waves came into existence. The amplitudes of these waves were considerably smaller than the surface waves in model 2 and the standard model. As a result of the shallow bedrock in model 3, more surface wave energy was present in the faster weathered bedrock and the surface waves travelled faster compared with surface waves in model 2 and the standard model.

In Figure 6.8, the synthetic seismograms computed at the survey lines L4 and L5 are presented. The seismograms of survey line L1-L3 can be found in Appendix E. Similar to the snapshots presented in Figure 6.7, the seismograms of model 3 show strong reverberated surface waves. These diffracted surface waves are superimposed on later arriving surface waves, which can be observed in the seismogram as patches of anomalous low amplitudes. Furthermore, at survey line L4 the geophones at 9-10m show stronger amplitudes.

Diffracted wave events can be observed in model 2 at the edges of survey line L4 and L5. No diffracted waves can be observed in model 3.

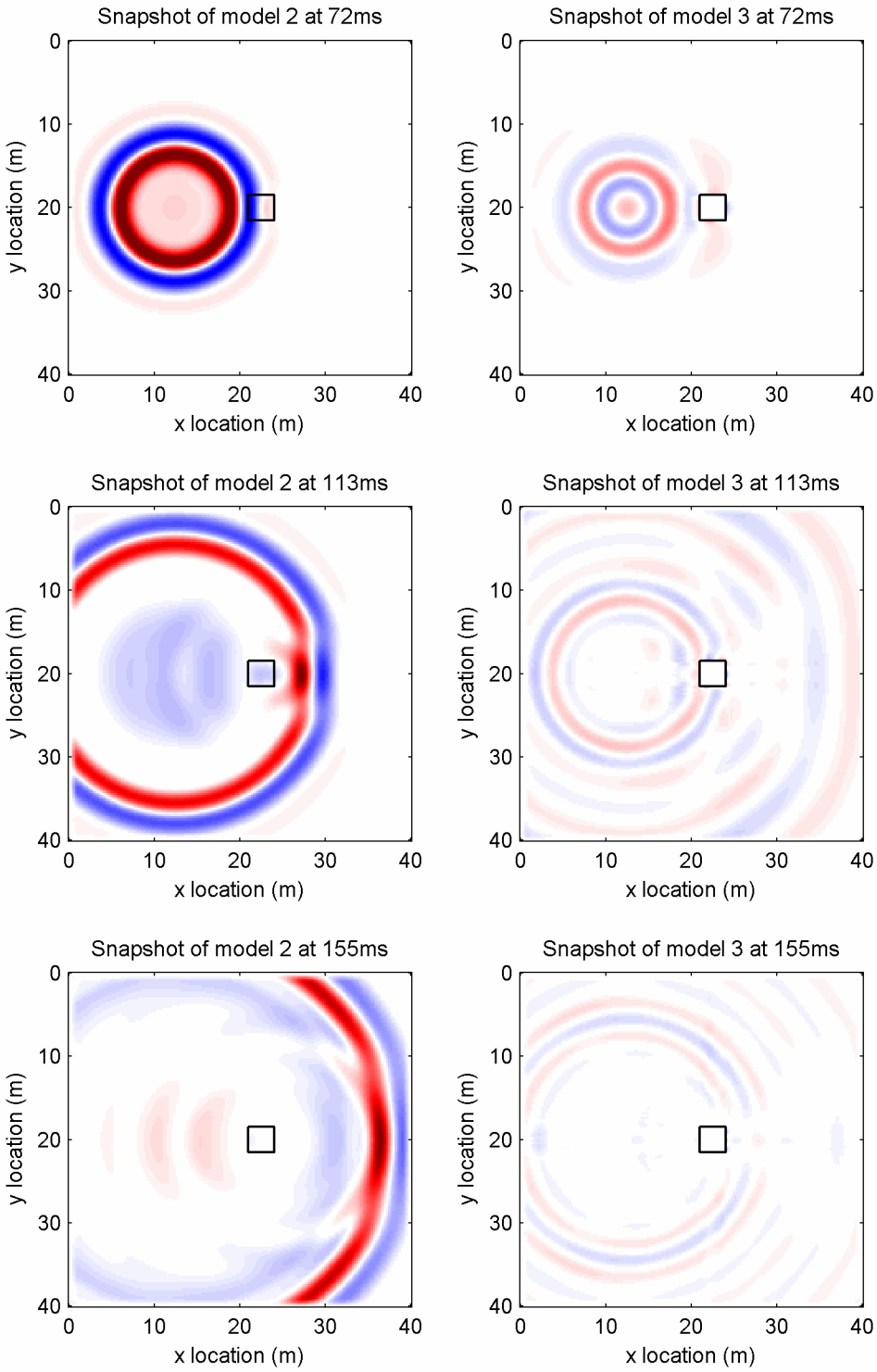

Figure 6.7. Snapshot of model 2 and model 3 at various times; amplitudes are scaled by the maximum amplitudes of model 1 and multiplied by a factor of 25

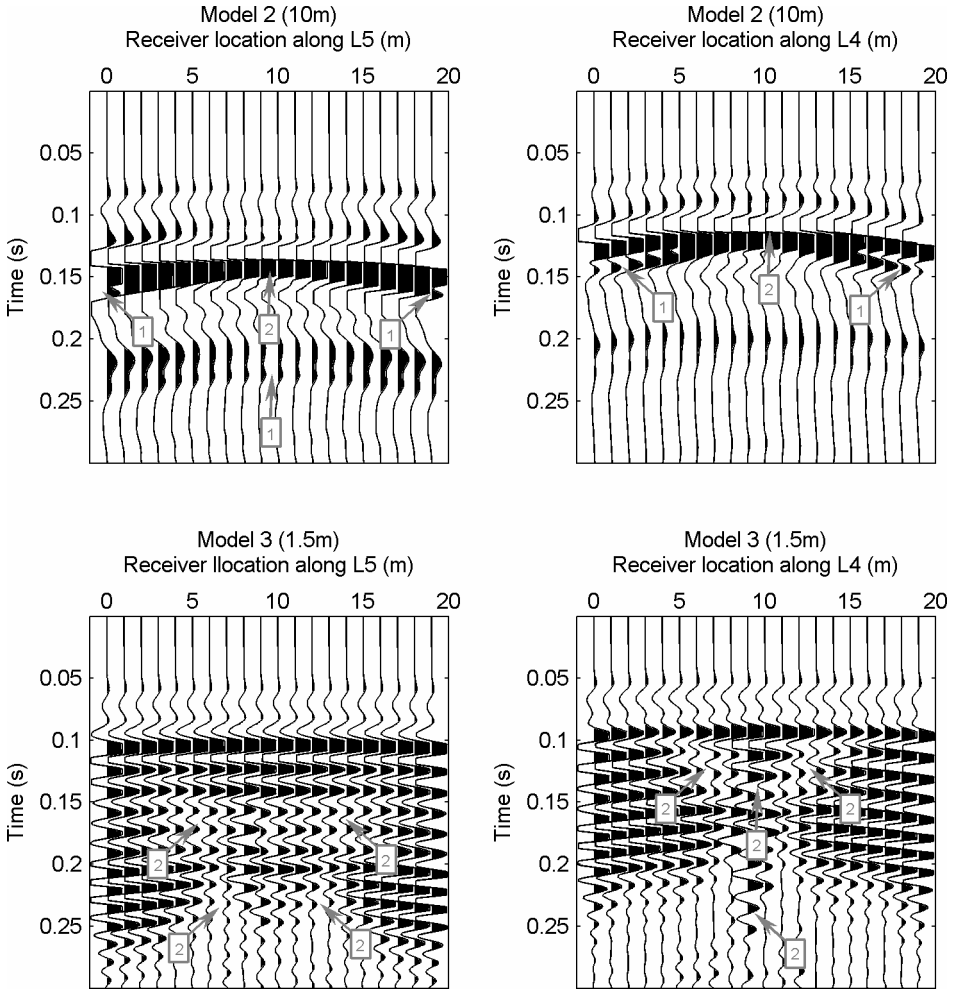

Figure 6.8. Synthetic seismograms computed for model 2: bedrock depth is 10m and model 3: bedrock depth is 1.5m at survey lines L5 and L4; traces are individually scaled and multiplied by a factor 10 and 2 respectively; interpretation of the events: 1 – diffraction, 2 – anomalous amplitudes

6.4. Models 4 to 6 – mineshaft size

Mineshafts were built in various sizes and shapes. From Figure 2.2 it can be concluded that most of the mineshafts built around 1850 had diameters between 1m to 4m. In order to assess the influence of the size of the mineshaft on recorded seismic data, three models based on the standard model but with different mineshaft diameters were simulated:

- Model 6: mineshaft has 1m diameter
- Model 4: mineshaft has 2m diameter
- Model 5: mineshaft has 4m diameter

The centre location and shape of the mineshaft were unaltered. The results of the simulations can be found in Figure 6.9 and Figure 6.10. For comparison reasons the snapshots of the standard model with a mineshaft diameter of 3m are included in the figure.

The snapshots and seismograms show that larger mineshafts created stronger anomalies e.g. delayed surface waves and anomalous amplitudes The mineshaft with a diameter of 1m did not affect the seismic data in an obvious manner and the 2m mineshaft only affected the data by a small amount. More analysis of the numerical data is presented in section 7.3.

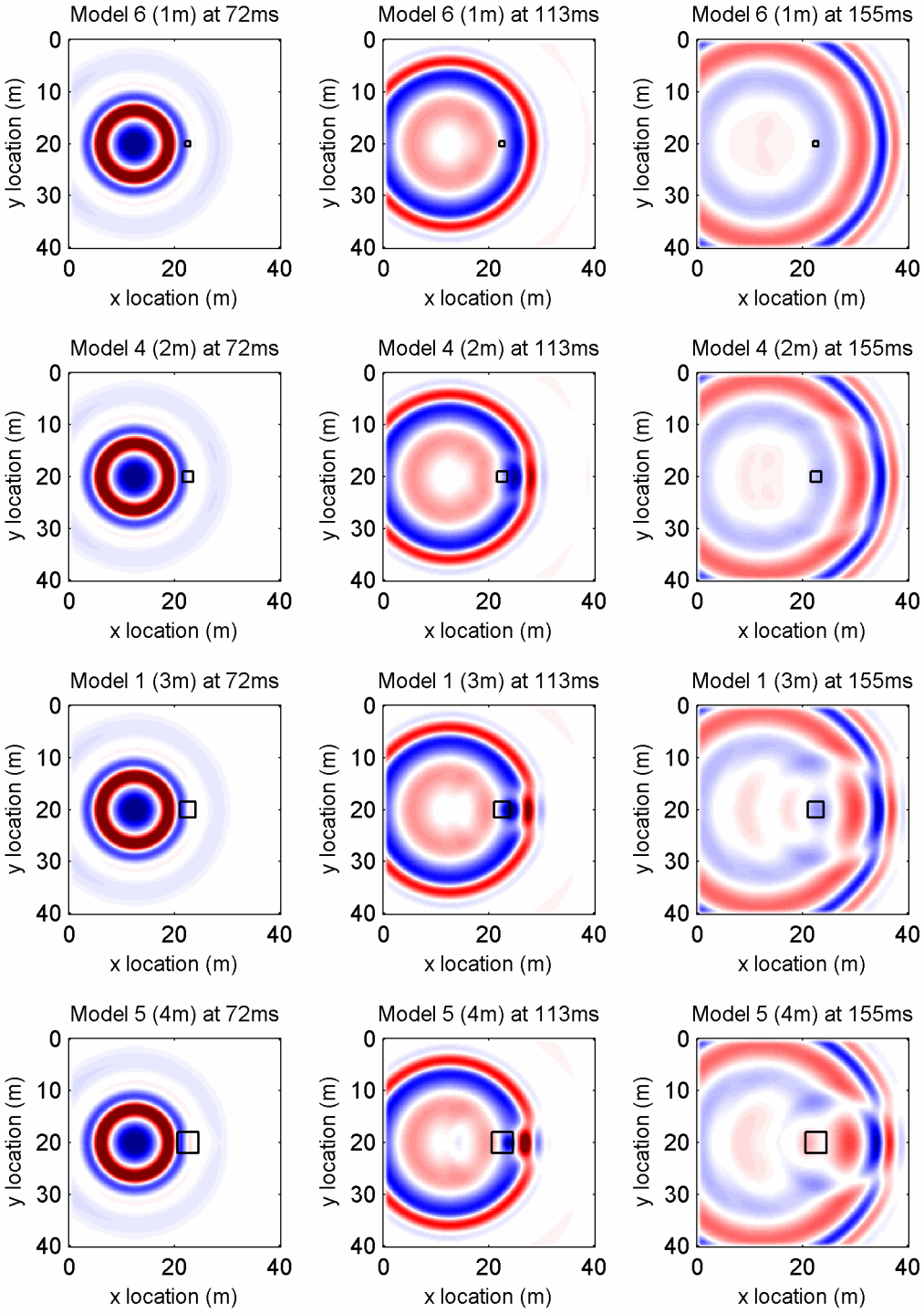

Figure 6.9. Snapshots at various times of model 6 (top): mineshaft is 1m, model 4 (second row): mineshaft is 2m, model 1 (third row): mineshaft is 3m and model 5 (bottom): mineshaft is 4m

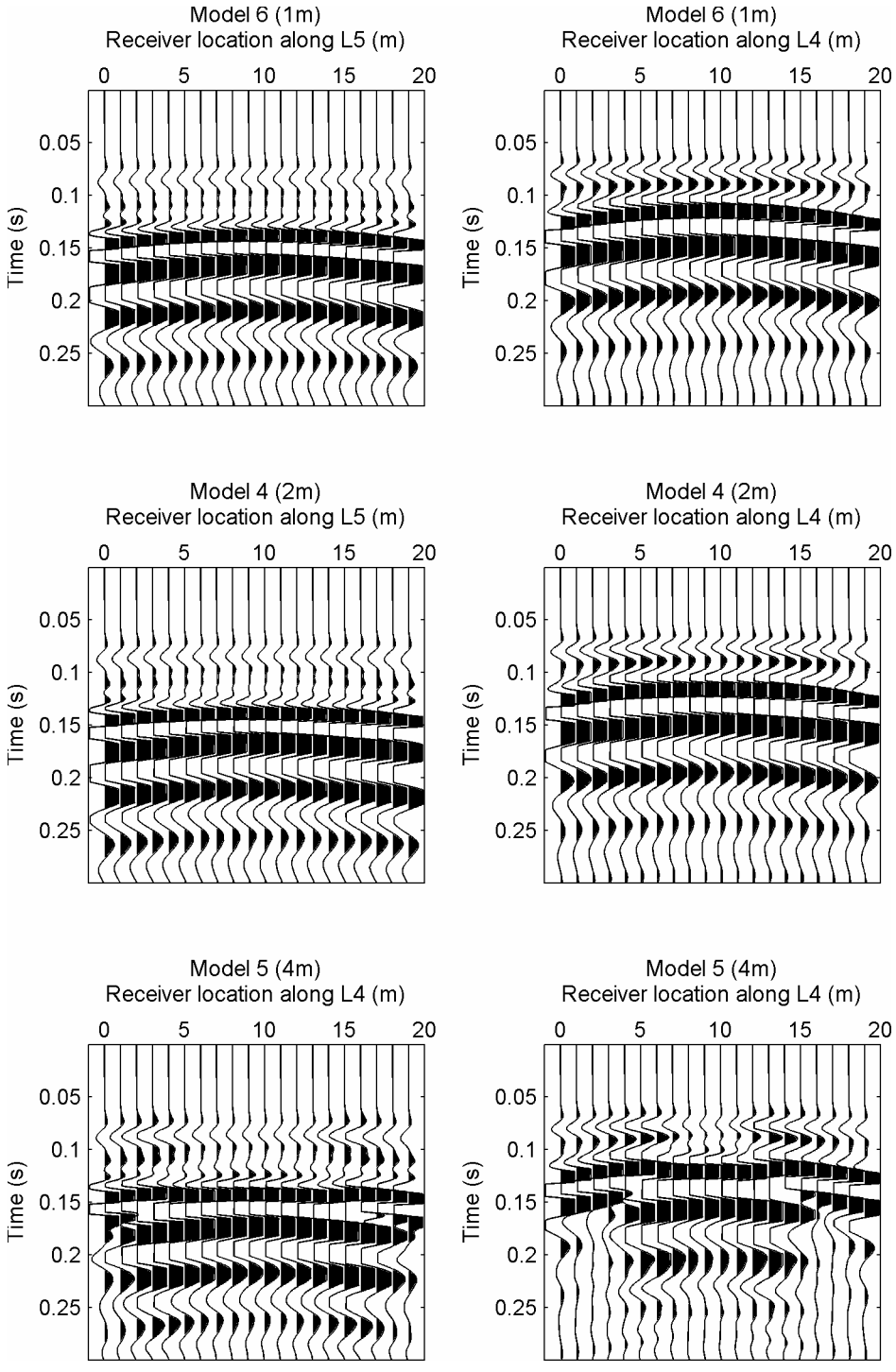

Figure 6.10. Synthetic seismograms computed for model 6 (top): mineshaft is 1m, model 4 (middle): mineshaft is 2m and model 5 (bottom): mineshaft is 4m

6.5. Model 7 – mineshaft shape

Mineshafts can be found in various shapes. Although most abandoned mineshafts were built square or rectangular shaped, circular or elliptical shaped ones were built. In order to verify the effect of variations in the shape, a model with a circular shaped mineshaft was simulated.

The circular mineshaft had a radius of 1.69m such that the volume of the circular mineshaft was similar to the volume of the mineshaft in model 1.

In Figure 6.11 the seismograms of survey line L4 and L5 are presented. The differences in the seismograms of model 7 and the standard model are too small to distinguish. More results of the simulations can be found in Figure 6.12, where the snapshots at various times of model 1 (left) and model 7 (right) are presented. The snapshots of the circular mineshaft model and box-shaped mineshaft are almost identical.

From the results it can be concluded that the shape of the mineshaft did not have much influence on the recorded data. More detailed analysis can be found in section 7.4.

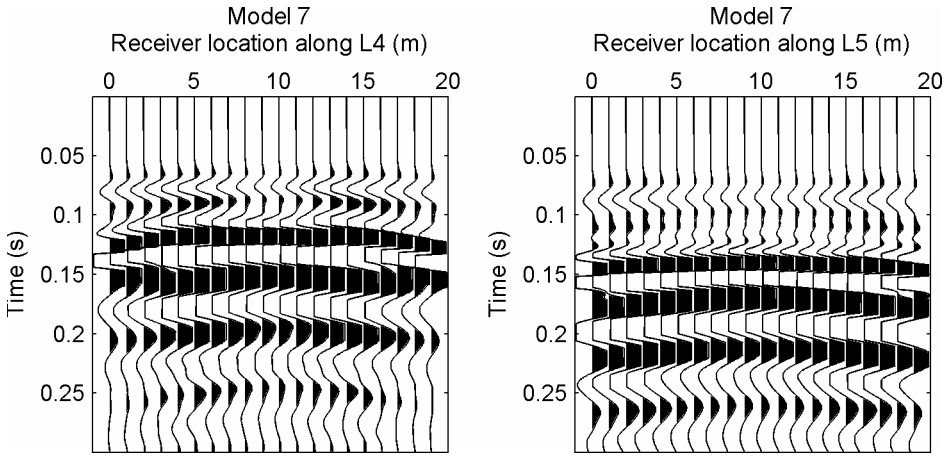

Figure 6.11. Synthetic seismograms computed for model 7 along survey line L4 and L5

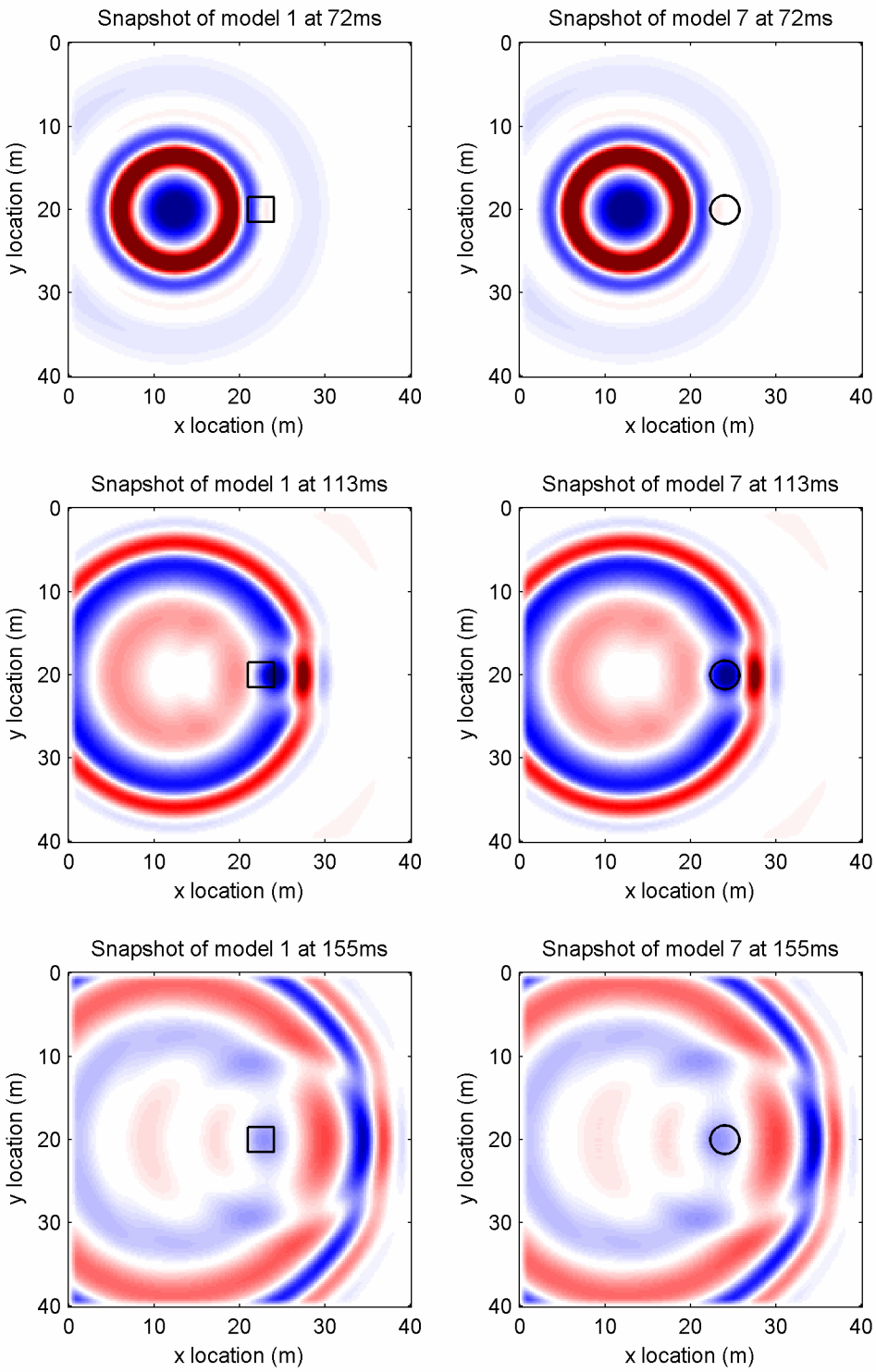

Figure 6.12. Snapshots at various times of model 1: square mineshaft and model 7: cylindrical mineshaft

6.6. Model 8 and 9 – source frequency

In all the previous models, the centre source frequency of the source was set to 25Hz. In practice there is often little control on the source frequency which mainly depends on the type of source and the superficial deposits. For example impact sources placed on loose sand generally generate more low frequencies than when placed on stiff clay.

In order to assess the effect of different source frequencies on the recorded data, two models based on the standard model were simulated:

- Model 8: source frequency is 20Hz
- Model 9: source frequency is 30Hz

The resulting frequency spectrums of model 1, 8 and 9 are presented in Figure 6.13. The frequency spectrums were calculated using the receiver at 10m along survey line L5. The distance between the source and receiver approximated 20m. Reference models were used for the determination of the frequency spectrum such that the mineshaft does not affect the data.

In Figure 6.13 also the frequency spectrum of an experimental trace is plotted. This trace is obtained during the field experiment which is presented in chapter 8. The trace was taken from source-receiver combination - shot gather L6 S24 and receiver at 46m - furthest away of the mineshaft such that the mineshaft did not affect the frequency spectrum.

Note that higher centre source frequencies could not be modelled due to the limitations in the computer resources. In order to prevent dispersion of the high frequency waves caused by discretization of the grid, smaller cells are required. This leads to a significant increase in number of cells and an increase in the run times of the simulations. However, Figure 6.13 shows that the centre frequency of

25Hz used in most models results in a frequency range which is representative of values observed in the field.

The results of the simulations of model 8 and 9 can be found in Figure 6.14 and Figure 6.15. For comparison reasons the snapshots of the standard model is also shown. Note that due to differences in the source signal, the snapshots were taken at different times for comparison reasons.

From the snapshots and seismograms it can be observed that the models with the higher source frequencies exhibit stronger anomalies such as travel time delays, amplitudes and diffractions. This can be explained by considering the Fresnel zone presented in the text box on page 121. Since the wavelength is related to the frequencies by $\lambda = v/f$, high frequency waves have shorter wavelengths. According to equation (6.3) shorter wavelengths have smaller Fresnel apertures and less energy of waves travelling around the mineshaft interferes constructively with waves travelling through the mineshaft. Therefore high frequency waves are more affected by the presence of the mineshaft.

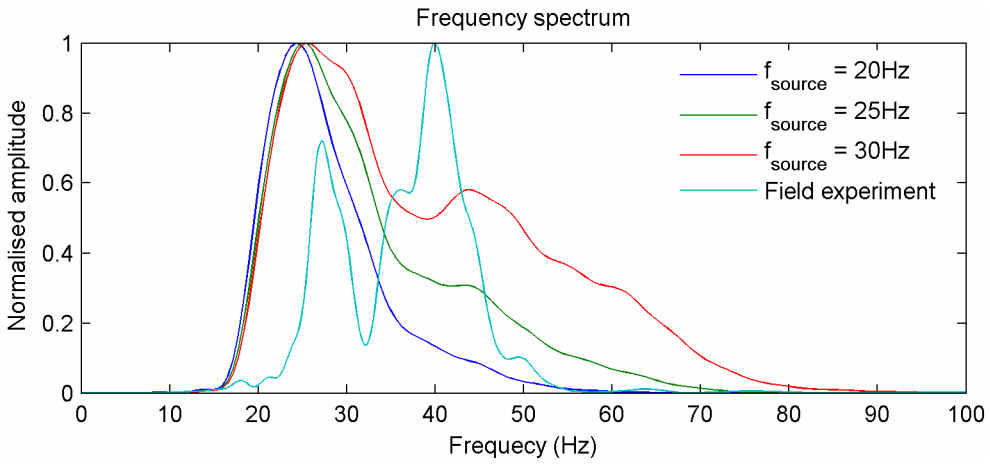

Figure 6.13. The frequency spectrum of the various sources and of the experimental data; source-receiver distance is about 20m for all traces

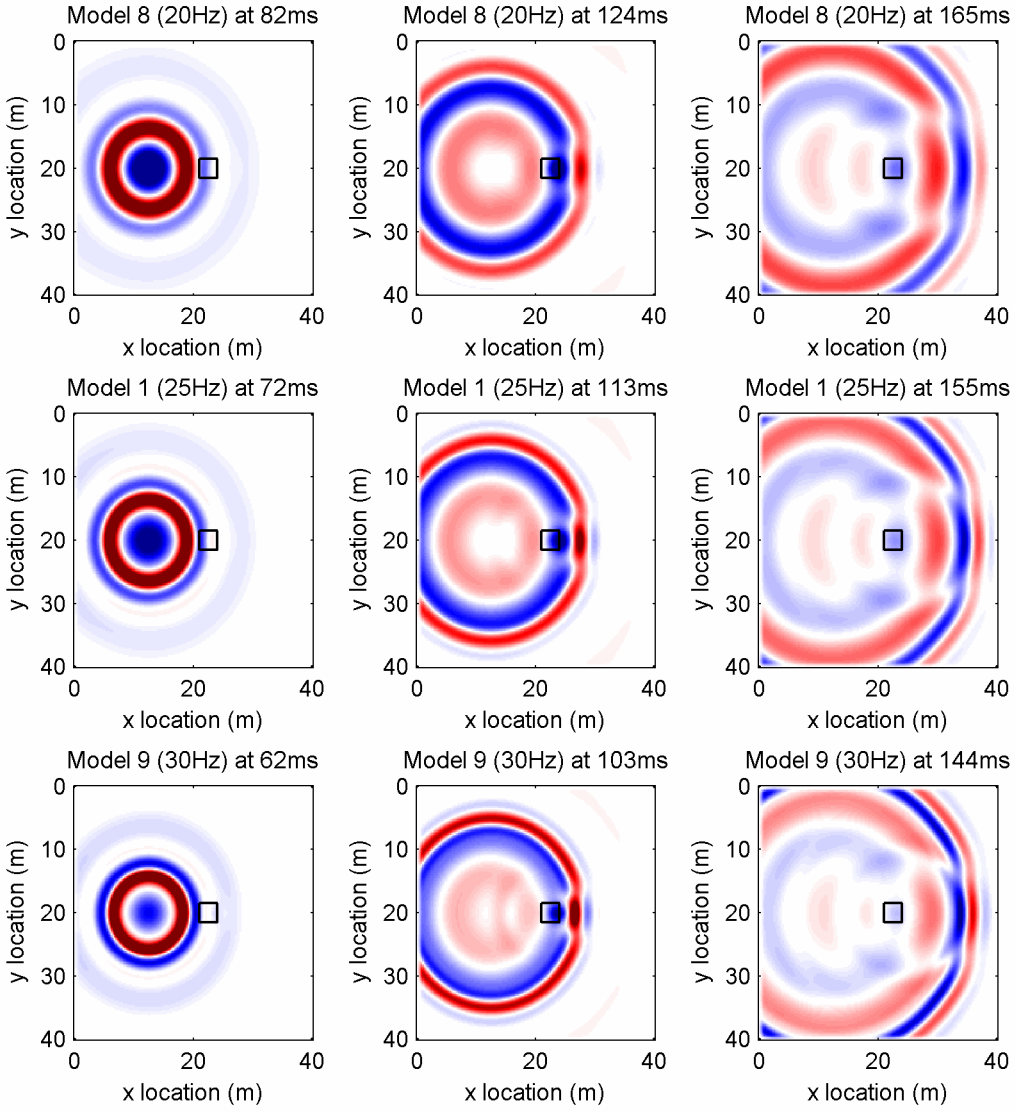

Figure 6.14. Snapshot at various times of model 8: source frequency = 20Hz and model 1: source frequency = 25Hz and model 9: source frequency = 30Hz

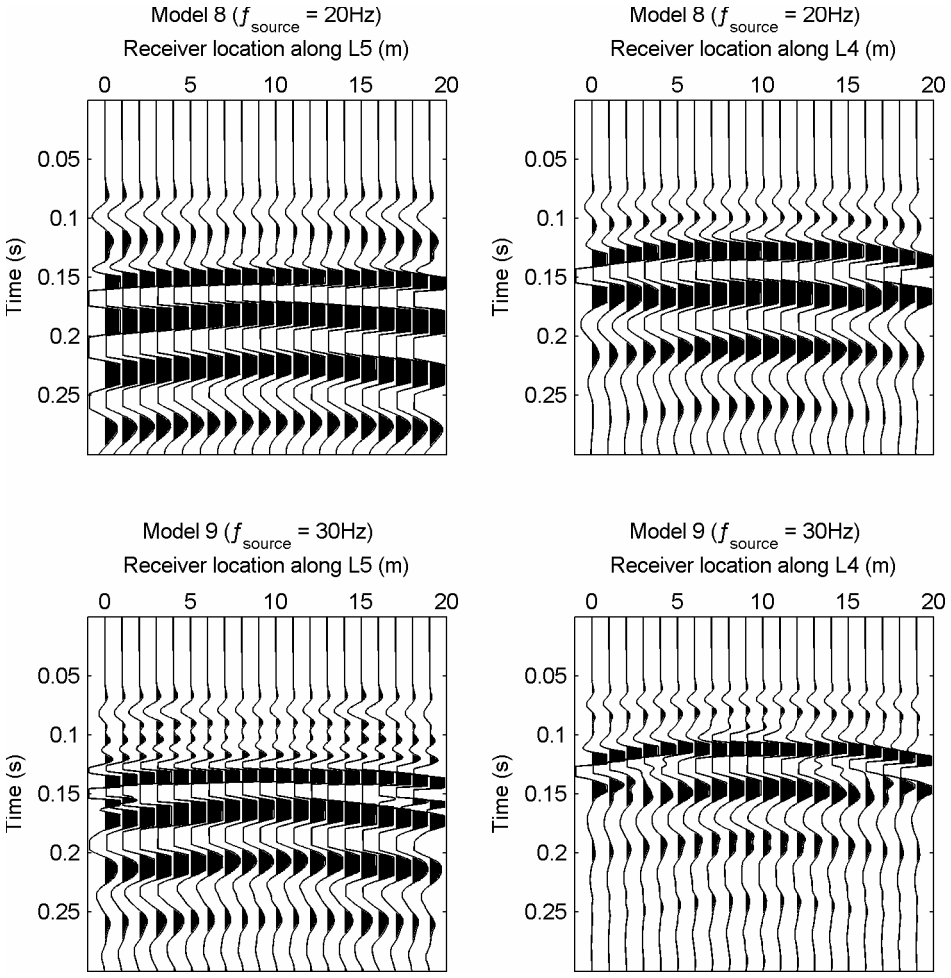

Figure 6.15. Seismograms of model 8: f_{source} =20Hz and model 9: f_{source} = 30Hz

6.7. Model 10 and 11 – filling

The voids of mineshafts can be encountered in various conditions which in most cases are unknown. Although in many cases the voided mineshaft consists of air it might be possible that the void of a targeted mineshaft is water filled or that mineshaft is completely backfilled.

In this section the results of model 10 and model 11 are presented. Both models were based on the standard model. In model 10 the mineshaft was modelled completely backfilled and in model 11 the modelled void was replaced by water.

The results of simulations can be found in Figure 6.16 and Figure 6.17. From these figures and the seismograms presented in appendix E it can be concluded that the filling of the mineshaft void had little influence on the surface waves and the differences were negligible for the given model parameters.

Note that the model 11 differs from model 1 and 10 due to the difference in the time step the snapshots are taken at a different time. More analysis can be found in 7.6 on page 167.

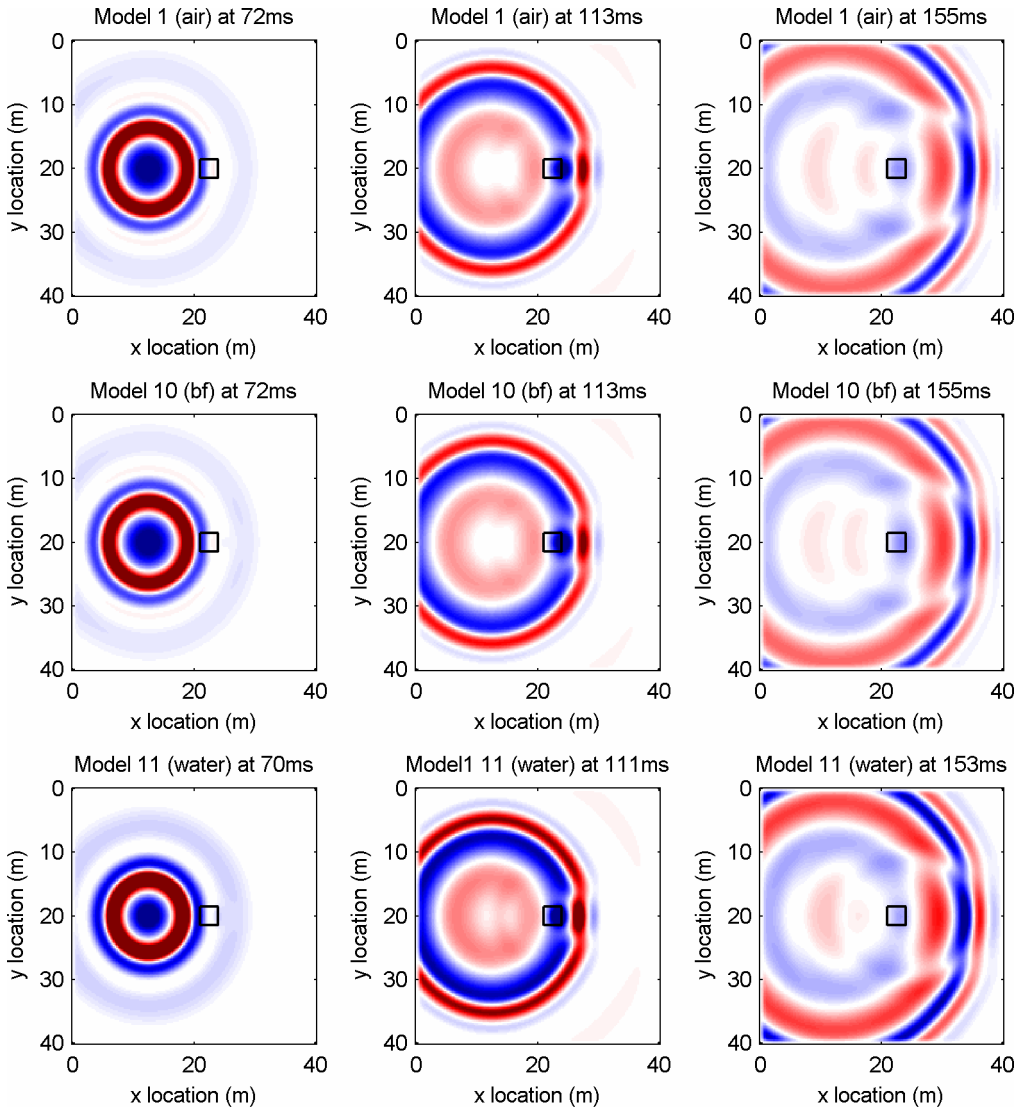

Figure 6.16. Snapshot at various times of model 1: air filled mineshaft, model 10: completely backfilled mineshaft and model 11: water filled mineshaft

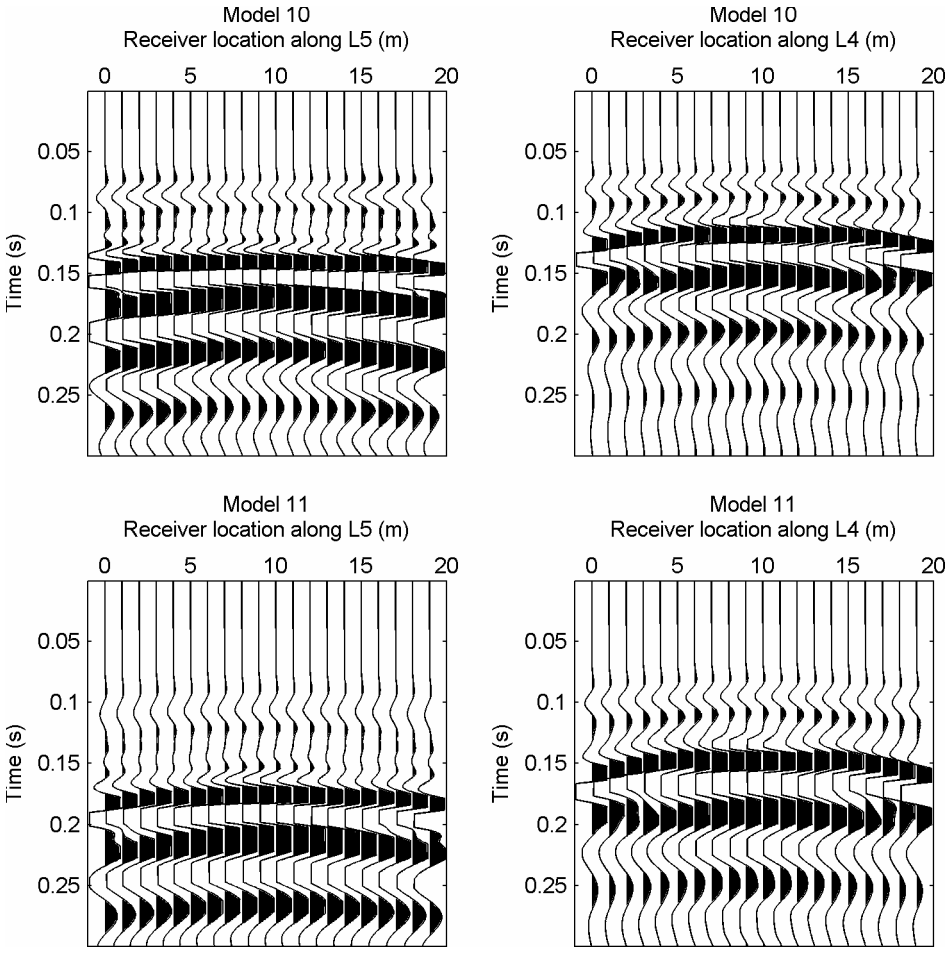

Figure 6.17. Seismograms of model 10 (top) and model 11 (bottom)

6.8. Model 12 – embankment

Railways are often placed on embankments. These embankments can be merely a couple of centimetres high up to a couple of metres. In order to investigate the effect of the embankment on the data, a model with an embankment was simulated. A cross section of model 12 can be found in Figure 6.18. The source and the receiver locations along survey line L5 and L4 had the same distances to the bedrock and mineshaft as in the standard model, such that a direct comparison could be made.

The results of the simulations can be found in Figure 6.19 and Figure 6.20. The snapshots show the amplitudes of the vertical velocities v_z at the depth of 1m and sliced the embankment at 1m depth.

The presence of the embankment causes strong reflections of the surface waves. The surface waves hitting the mineshaft have less amplitude due to the energies loss caused by the reflections at the embankment. The presence of the mineshaft is difficult to distinguish, although in the snapshots at 93ms and 113ms the mineshaft can be identified due to the increased amplitude of the surface waves at the location of the mineshaft.

Regarding the seismograms in Figure 6.20, the embankments appear to have little effect on the direct waves and refracted waves and also the first surface wave events.

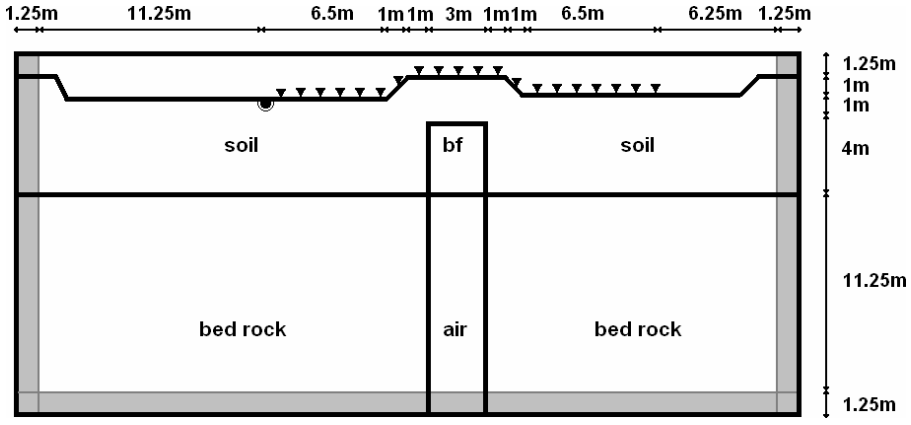

Figure 6.18. Cross section of model 12 with embankment; bf is the backfilling

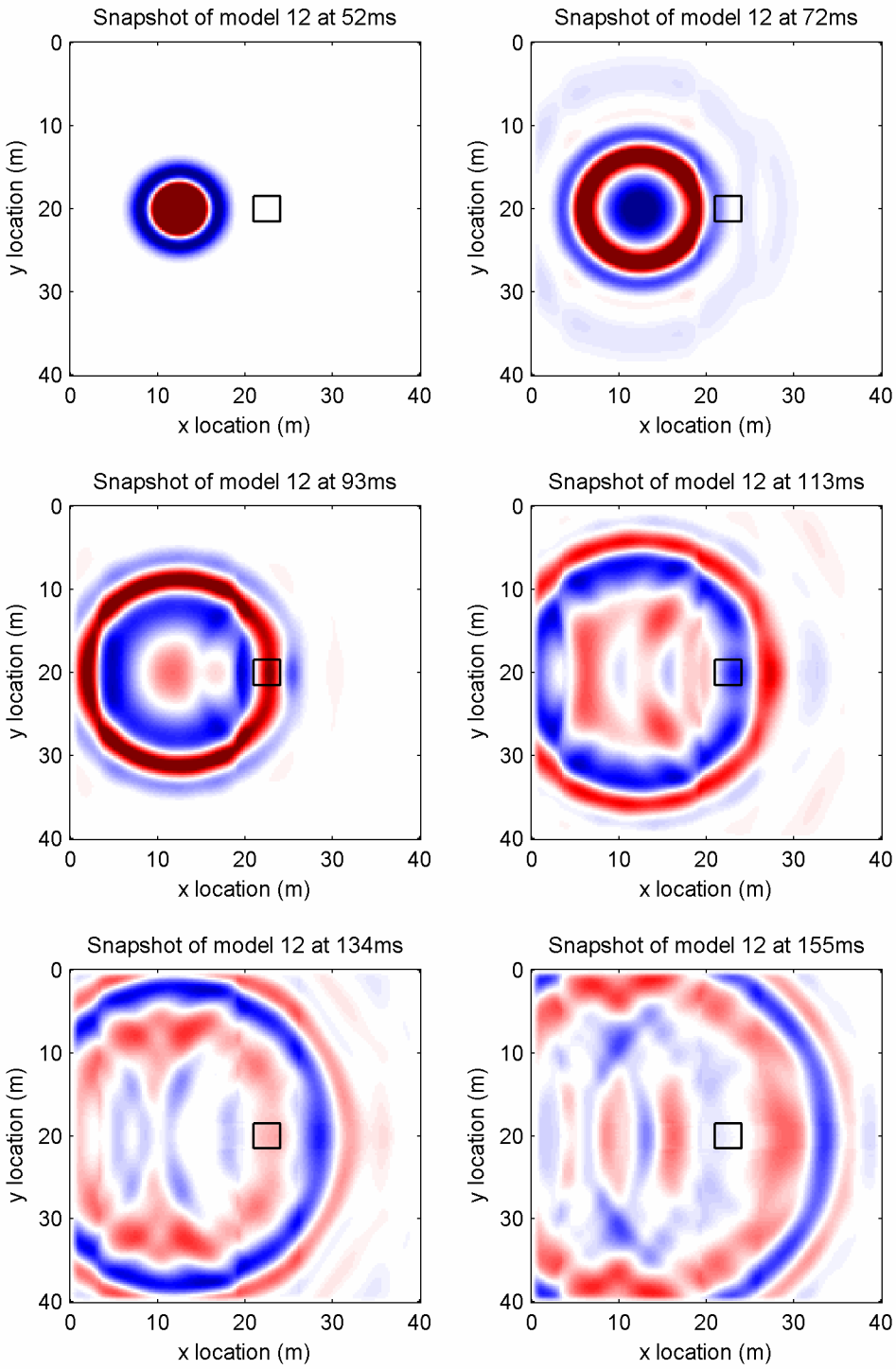

Figure 6.19. Snapshots of model 12 with embankments at various times

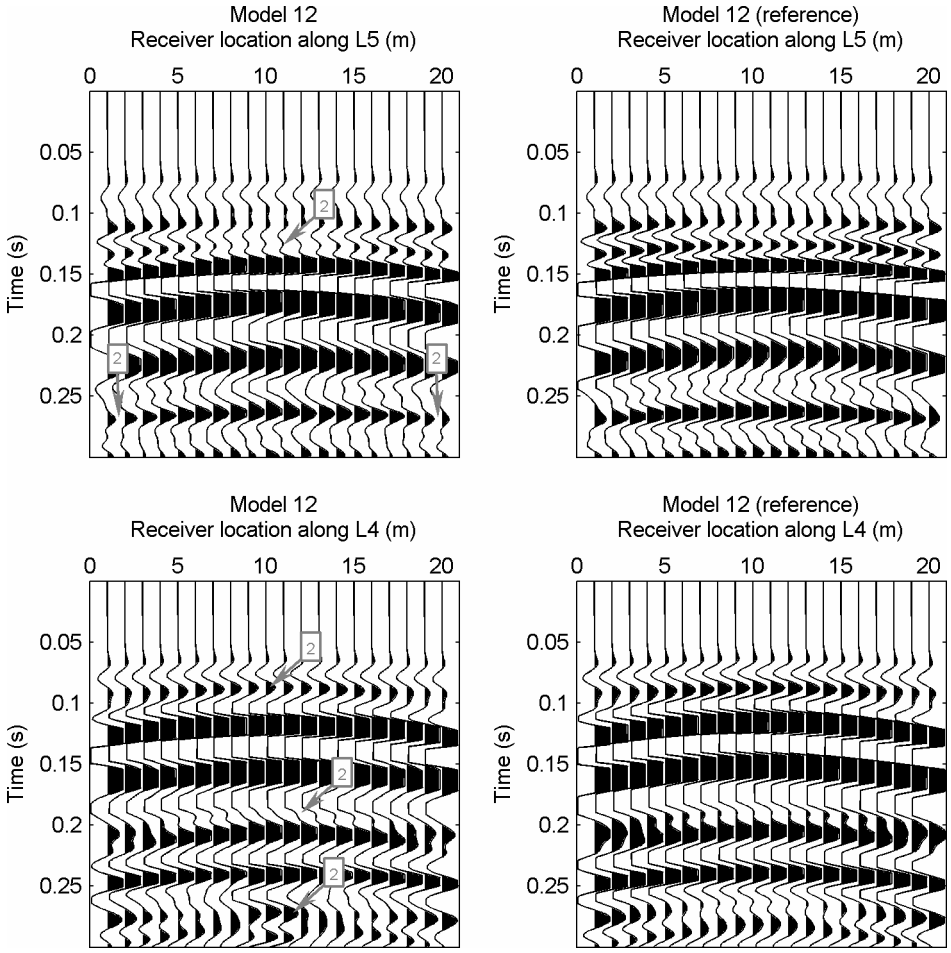

Figure 6.20. Seismograms of model 12 (left) and its reference model without a mineshaft (right); explanation of events: 2 – anomalous amplitudes

6.9. Model 13 and 14 – void

Although most of the partially backfilled mineshafts were backfilled till a platform that was usually placed on the bedrock, some mineshafts can be found where a platform was built in the superficial deposit. Two models were designed to investigate the effect when the void extends into the superficial deposit. In model 13 the void was filled with air and in model 14 the void was filled with water. The top of the void was located at 2.5m depth.

The results of the simulations of model 13 and 14 are presented in Figure 6.21 and Figure 6.22. Note that the amplitudes of water filled void differ in the snapshots from the air filled void due to the difference in the time step and number of iterations. The seismograms show that the shallow air void causes strong diffractions of the surface waves. Furthermore anomalous amplitudes and delayed waves can be observed in model 13. The seismograms of model 14 show also anomalous amplitudes and the surface waves appeared to be delayed. More detailed analysis of the results of model 13 and 14 can be found in 7.8 on page 173.

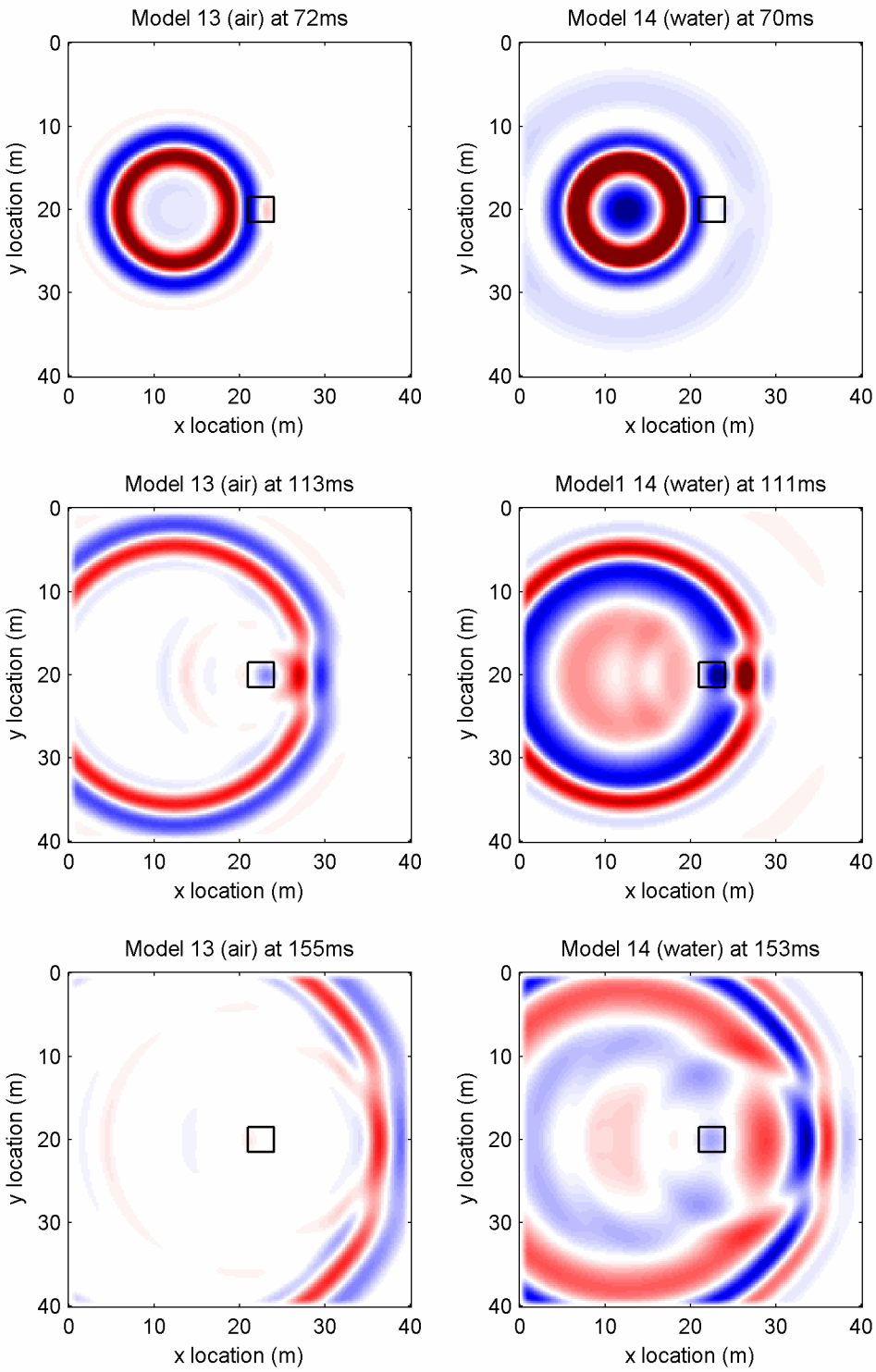

Figure 6.21. Snapshots of model 13 (left): air filled mineshaft and model 14 (right): water filled mineshaft; note that scaling and time steps and time steps

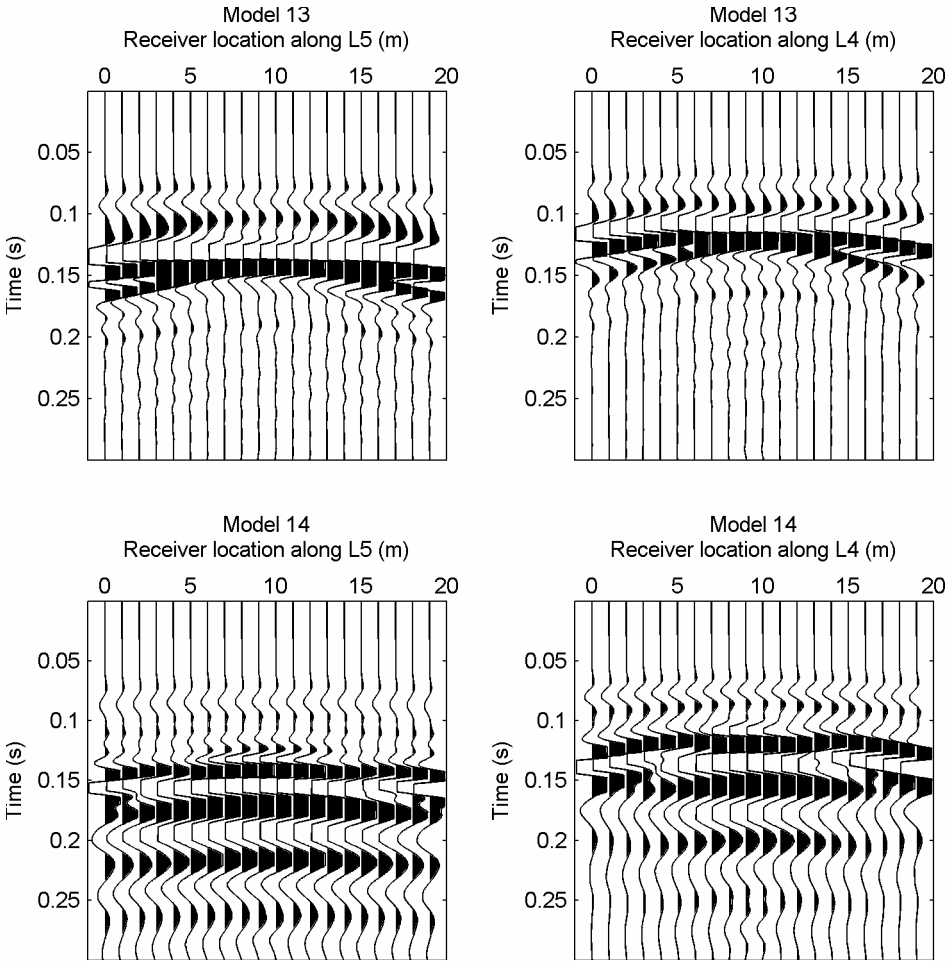

Figure 6.22. Seismograms of model 13 (top) and model 14 (bottom) along survey line L5 (left) and survey line L5 (right)

6.10. Model 15-20 – Source and mineshaft location

In practice the location of mineshaft is unknown and therefore the source locations need to be varied such that the mineshaft is located between the source and the receivers. In order to investigate the effect of the source location on the synthetic data, two models were simulated. In model 15 the source location is shifted by +2.5m in the y-direction and in model 16 the source is shifted by +5m in the y-direction.

Furthermore in the models presented in the previous sections the mineshaft was always located in the middle between the source and the centre of the survey lines. In practice this is rarely the case, although by varying the location of the source there will be a survey lay out such the mineshaft is located directly between survey line and the source. In order to investigate the effect of the mineshaft location on the seismic data, four models were simulated. In model 16 and model 17 the centre of the mineshaft was shifted by +5m and +10m respectively. In model 18 the centre of the mineshaft was shifted by -5m in the x-direction and in model 19 by +5m.

Figure 6.23 shows a representation of the plan view of models 15 to 20.

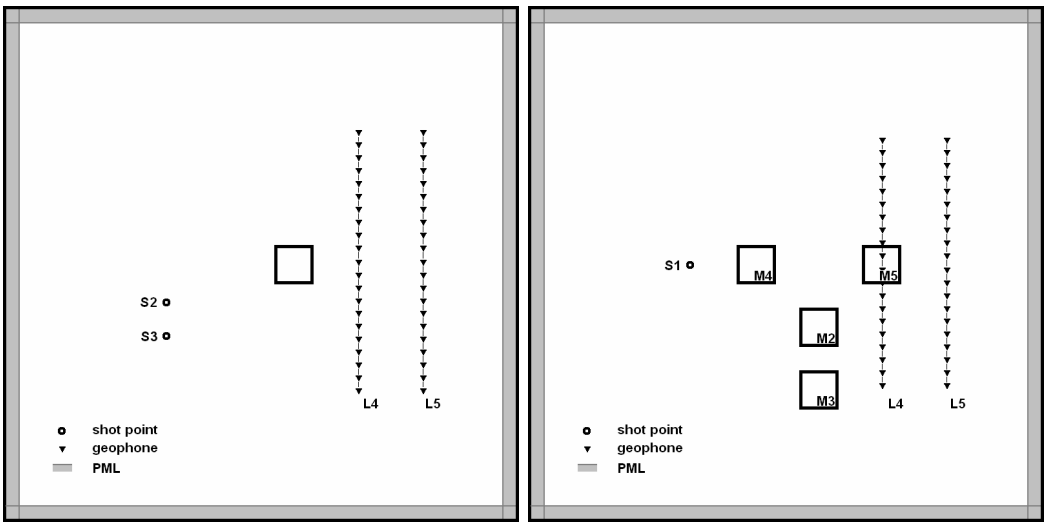

Figure 6.23. Left hand side: plan view of model 15 (source located at S2) and model 16 (source located at S3); right hand side: plan view of model 17 (mineshaft located at M2), 18 (mineshaft located at M3), model 19 (mineshaft located at M4) and model 20 (mineshaft located at M5)

6.10.1. Numerical results of model 15-18

The resulting snapshots of the simulations of model 15 to 18 are presented in Figure 6.24. The snapshots show that the location of the source had little influence on the appearance of the snapshot. The anomalous amplitudes related to the mineshaft rotate at the same angle as the source location rotates with the mineshaft as rotation point. In other words the maximum amplitude observed in the shadow zone of the mineshaft is always in line with the source and mineshaft. The anomalous low amplitudes always appear in all the models at a certain angle from the source-mineshaft line.

In Figure 6.25 the synthetic seismograms of model 15 and 16 and the synthetic seismograms of model 17 and 18 are presented. All the seismograms show anomalous amplitudes caused by superposition of the diffracted surface

waves with the later arriving surface waves. The positions of these anomalies are not solely related to the position of the mineshaft in relation with the receivers and shot point, but very much depends on the travel time and the phase of the diffracted surface waves and the phase and travel time of the later direct surface waves.

6.10.2. Numerical results of models 19 and 20

In Figure 6.26 the resulting snapshots of the simulations of model 19 and model 20 can be found along with the snapshots of model 1. From the snapshots it can be concluded that when the source was positioned near the mineshaft, the zone shaped by the anomalous amplitudes appeared much broader. When the source was located far away from the mineshaft this zone appeared narrower i.e. more focussed.

In Figure 6.27 the seismograms of model 19 and model 20 are presented. The seismograms of model 19 do not exhibit distinguishable anomalies which are related to the presence of the mineshaft. Considering the snapshots in Figure 6.26 it is likely that anomalies would have been observed when the survey line was extended.

The seismograms of the model 20 show very strong anomalies. Some receivers at survey line L4 were directly located above the mineshaft. High amplitude body waves can be observed at L4 at these receivers. The slow backfilling causes an increase in the amplitude. Anomalous amplitudes due to superposition can be observed at both seismograms at survey lines L5 and L4 in model 20. In model 20, delayed arrival times of the surface waves can be observed at both survey lines.

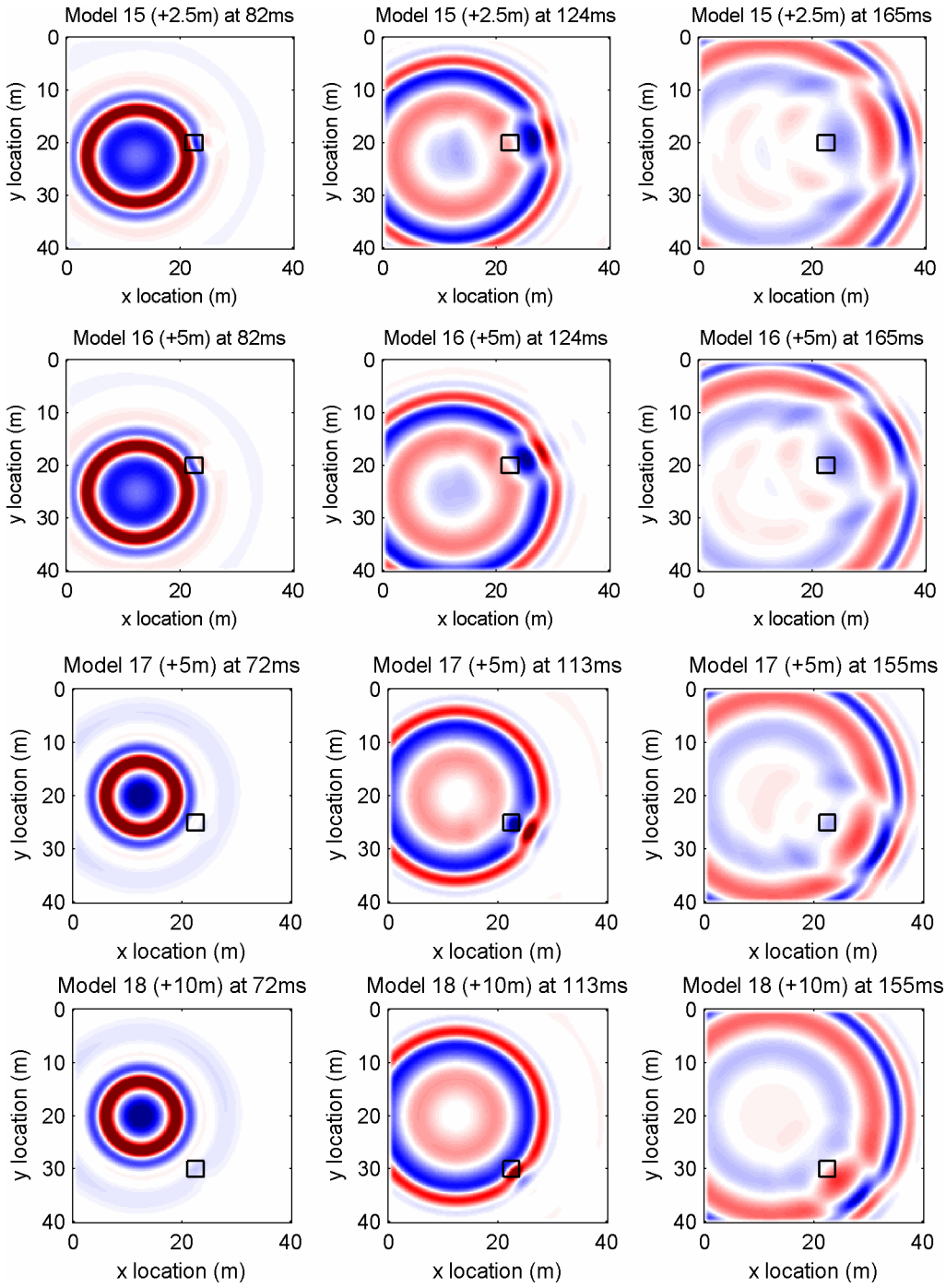

Figure 6.24. Snapshots of model 15 (source at S2 and mineshaft at M1); model 16 (source at S3 and mineshaft at M1); model 17 (source at S1 and mineshaft at M2) and model 18 (source at S1 and mineshaft at M3)

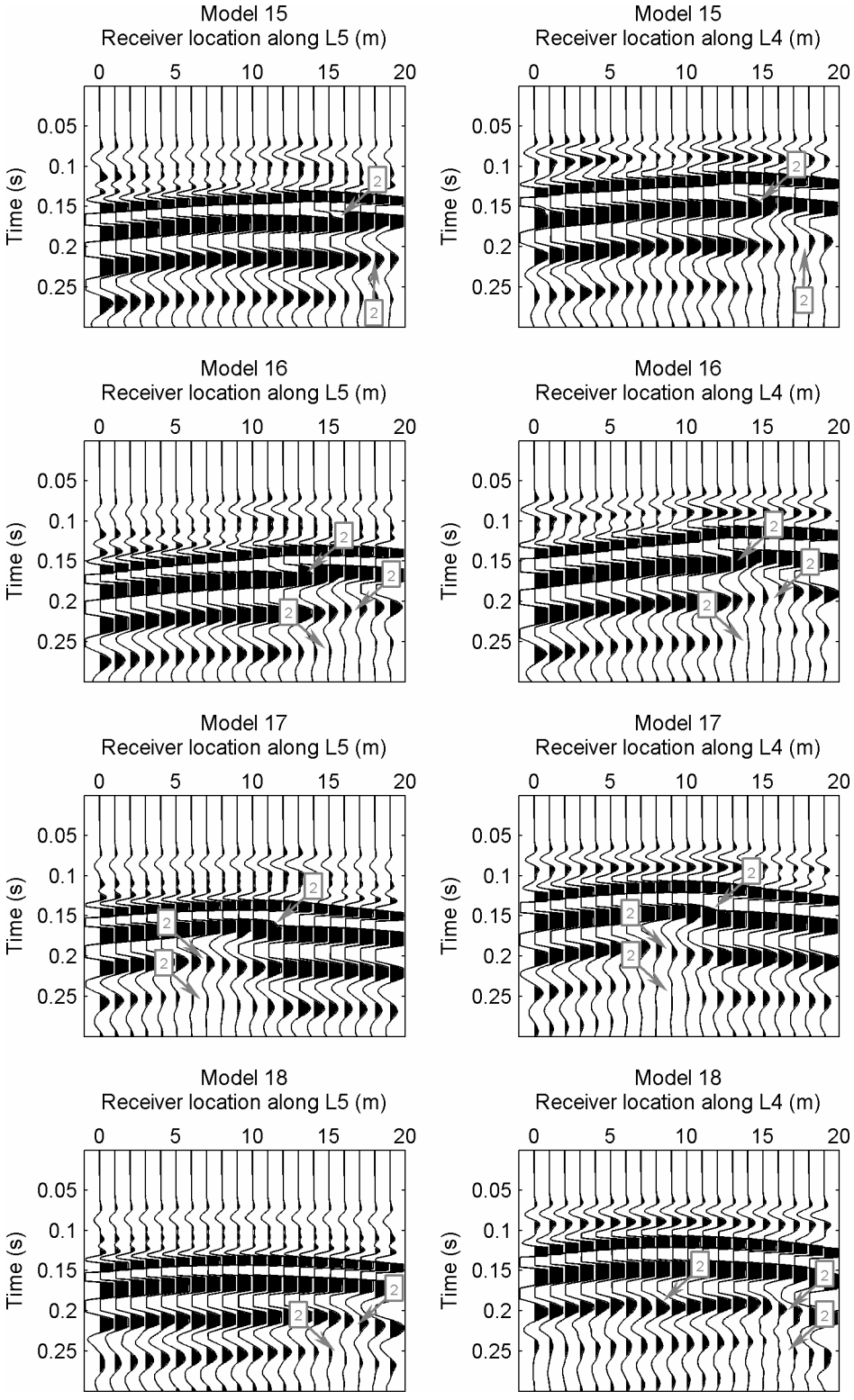

Figure 6.25. The synthetic seismograms of model 15-20 at survey line L4 and L5; explanation of events: 2- anomalous amplitudes

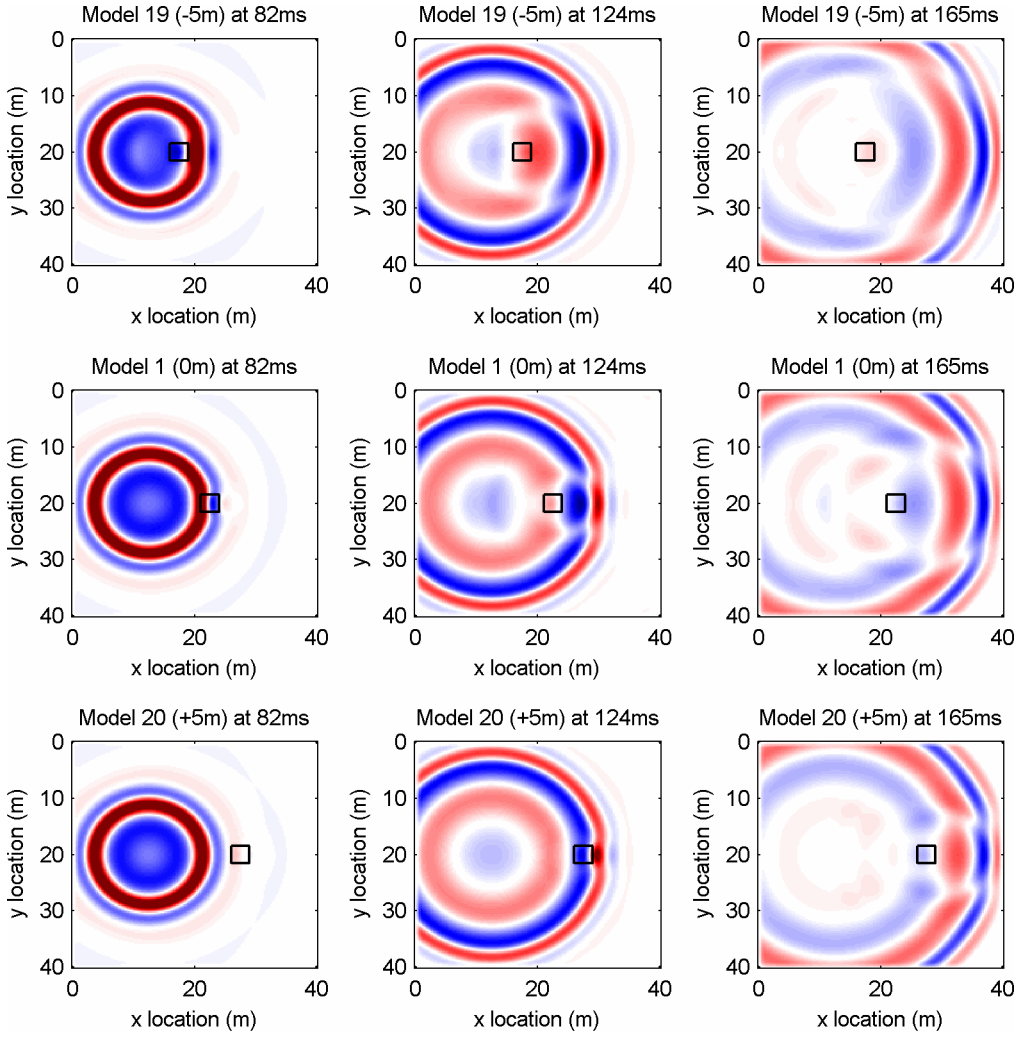

Figure 6.26. Snapshots of model 19 (source at S1 and mineshaft at M3); model 1 (source at S1 and mineshaft at M1); model 20 (source at S1 and mineshaft at M4)

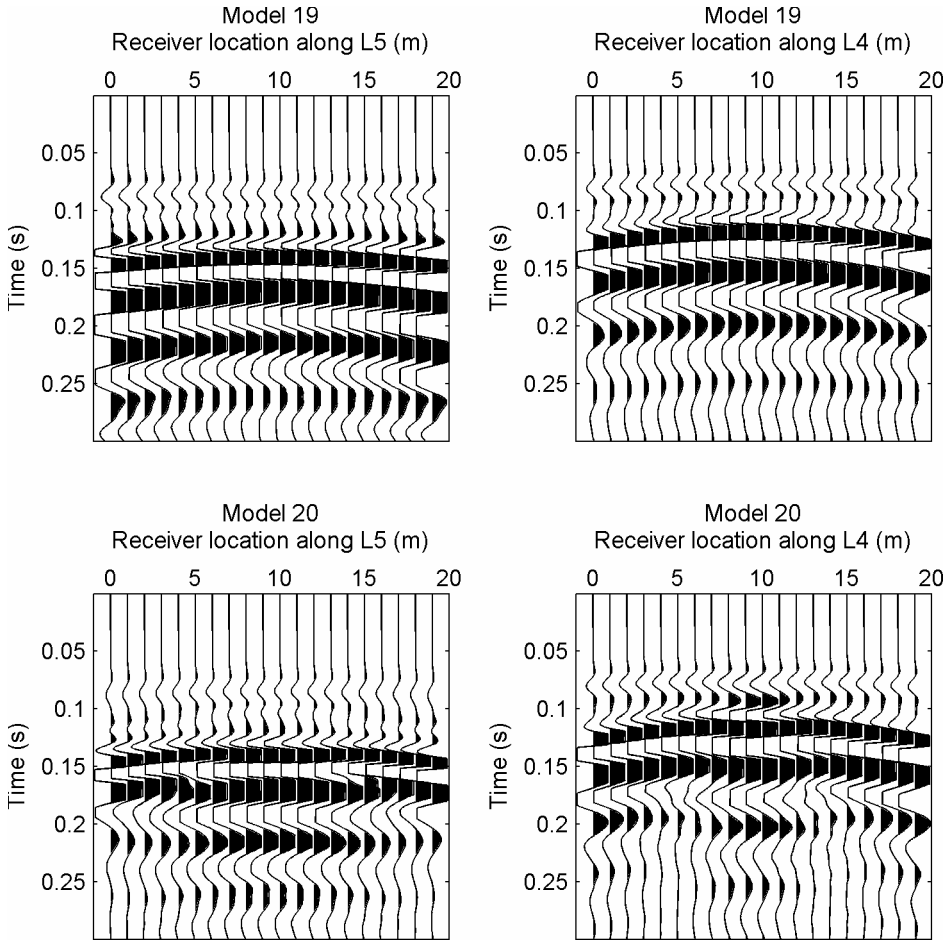

Figure 6.27. Synthetic seismograms of model 19 and model 20

6.11. Conclusion

In this chapter, various models and the results of their simulations are presented. It should be stressed that numerical models never can simulate reality and that the models are merely used for understanding the dynamic elastic behaviour of mineshafts. Conclusions derived from the modelling results should reflect this statement.

Although numerous models were simulated, numerous questions are left unanswered such as the effect of random noise and variable geology. One of the

important unanswered questions is what the influence of the medium parameters is. Due to limited computer resources and time, materials with different medium parameters were not simulated. The medium parameters were selected such that the models could run on computers with 2GB of memory and that the simulations ran within two days. Nevertheless the values used in the models were realistic.

The following observations can be made from the numerical models:

- The synthetic seismograms and snapshots appear to be free from reflections from the model edges. Therefore it can be concluded that the novel RIPML absorbing boundary condition performs adequately, although no actual experiments were carried out to test the performance.
- The source was located relatively close to the receivers this means that the seismic waves were superimposed on each other. Even though the events in the seismogram appear as a single event, this does not mean that the event consisted of one single seismic wave. This makes it hard to interpret the seismograms in practice.
- The location of the mineshaft is difficult to deduce directly from observations of the synthetic seismograms unless the survey lines is located directly above the mineshaft. These survey lines show unmistakable diffractions of the surface waves. However, in practice in order to have survey line above the mineshaft numerous lines are required and also possession of the track is required.
- Although diffractions of surface waves can be observed at other survey lines, these were often partially superimposed by other surface waves. However, in model 5 with the mineshaft with 4m diameter the diffractions are quiet obvious at survey line L5 and L4. The apex of these diffracted surface waves can be used to locate the diffraction point i.e. the mineshaft.

- Diffracted body waves were difficult to observe due to the fact that they contained little energy and furthermore these diffracted body waves were likely superimposed by other waves. Hence diffraction imaging methods such as used by Shtivelman (*2005*) and Heincke (*2006*) are deemed as ineffective.
- From the seismograms it can be concluded that it is beneficial to:
  - Have the survey lines close to the mineshaft. Anomalies appeared more focussed in the seismograms at survey line L4 than in survey line L5 and the location of the mineshaft can easily be determined.
  - Use high frequency sources. Waves containing high frequencies were more affected by the presence of the mineshaft, than low frequency waves. Generating high frequency waves can be achieved by selecting different excitation sources or by using high-pass filters preferably before the analogue-digital conversion. As a rule of thumb a dominant frequency should be achieved such that the diameter of the mineshaft is not be smaller than a quarter of the wavelength (Dmineshaft $> \frac{1}{4}\lambda$)..
- Variations of the surface, such as railways embankments cause a lot of diffraction and reflections of the surface waves. This will complicate the potential of using direct observations near railways. However, the location of the mineshaft could be derived by further analysing the seismograms. The analysis is presented in section 7.7.

7. Analysis of the models

The results of the analysis of the attributes are presented in this chapter.
In this chapter the results of the analysis of the synthetic seismograms presented in Chapter 6 are presented. The synthetic seismograms were analyzed using the transmission method as outlined by Dresen (*1979*).

It should be stressed that this paper is the only publication found dealing with the use of seismic waves in the delineation of mineshafts that does not make use of boreholes. This paper reports the results of only one successful survey, however the geometry of abandoned mineshafts vary and mineshafts can be found in diverse geological settings. This chapter extends the work pioneered by Dresen by ascertaining the feasibility of the transmission method for other mineshafts cases. This method was applied to the synthetic seismograms of the simulations presented in the previous chapter. Although these seismograms were obtained from fairly simple models the results could provide some basic understanding of the limitations of the transmission technique, which could not be obtained in the field without extensive ground proofing.

Furthermore, in section 3.4.1, it is mentioned that the survey layout used by Dresen (*1979*) is impractical at railway sites and the use of broadside shot gathers was proposed. This chapter provides insight on how the different survey layouts affect the transmission method.

7.1. Attributes

The transmission method focuses on certain attributes of the individual traces. By determining and plotting the values of these attributes along the survey lines, anomalies related to the position of the mineshaft could be identified. The following trace attributes are examined:

- The arrival times of the first event
- The dominant frequencies
- The amplitudes of the Rayleigh wave
- The amplitude of the first event

7.1.1. Arrival times of first event

Dresen showed that the mineshaft causes a delay in the arrival times of the Rayleigh, refracted P-wave, converted SP-wave and the reflected P-wave. Since the travel distances between the source and receivers in the models were not constant, using arrival times can lead to errors. With changing travel distances, interference of the wave under consideration with other waves can lead to misinterpretation of the data.

Therefore in this chapter only the travel times of the first event were examined. The first event consisted of refracted waves superimposed with the direct waves depending on the model and the source-receiver distances.

The first arrival time of the individual traces in the seismograms was estimated automatically by determining the time where the amplitude value exceeded the threshold value of $2 \cdot 10^{-9}$.

7.1.2. Dominant frequencies

It was shown by Dresen that the frequencies of the waves can be used to locate mineshafts. Some seismic waves showed a distinctive W-shape in their dominant frequency curves. In this chapter the dominant frequencies of the whole trace were examined. Since the Rayleigh waves were the dominant waves, the dominant frequencies were shaped by these waves.

The individual traces were transformed into the frequency domain by a fast Fourier transformation using the *fft* Matlab script. The traces were padded with zeros to provide better resolution. The power spectrum was calculated from the frequency spectrum. The dominant frequency was determined by locating the frequency with the largest amplitude.

7.1.3. Amplitudes

Similar to the dominant frequencies the amplitudes of the various seismic events were affected by the mineshaft. In this chapter the amplitudes of the Rayleigh wave were determined and also the amplitudes of the first event were determined. The maximum amplitudes were determined by locating the maximum of the Hilbert envelope of each trace calculated according the following formula:

$$Maximum\ Amplitude\ (i) = max\left|H\left(f_{ij}\right)\right| \tag{7.1}$$

The amplitude of the first event was automatically determined by finding the position the first negative derivative. The location of the first negative derivative was associated with the maximum amplitude of the first event.

7.2. Bedrock depth

The first atrribute analyses presented were taken from the numerical data of model 1, 2 and model 3. The bedrock depths in these models were at 5m, 10m and 1.5m respectively. In Figure 7.1 the results of the analysis of the first arrival times and the dominant frequencies were presented. Reference data was calculated using the reference models without the mineshafts.

First break

The first arriving events in model 2 at survey line L4 and L5 were direct P–waves, whereas the first arriving events in model 3 at survey line L4 and L5 were refracted waves. In model 1, the first event consists of the direct wave superimposed by the refracted waves. At survey line L4, the direct waves arrived slightly earlier than the refracted waves and vice versa at L5.

- At survey line L5 the maximum delays caused by the mineshaft were 1.34ms for model 1, 0.72ms for model 2 and 1.44ms for model 3.
- At survey line L4 the maximum delays caused by the mineshaft were 1.34ms for model 1, 0.93ms for model 2 and 1.96ms for model 3.
- The time delay graphs at L4 are characterised by a sharp increase in the travel time at the location of the mineshaft, whereas at L5 the time delay is very broad. In other words the observed delay was not limited to receivers located in the shadow zone of the mineshaft.

Dominant frequencies

In Figure 7.1, the dominant frequencies calculated for each trace along survey line L4 and L5 can be found.

- Although the centre frequency of the source was set to 25Hz, wide variations of dominant frequencies can be observed depending on the model and survey line. Dominant frequencies of model 3 with the shallow bedrock are over 50Hz at L5 and over 70Hz at L4.
- The survey line L5 of model 2 shows increased dominant frequencies at the receivers in the shadow zone of the mineshaft and decreased frequencies away from the shadow zone when compared to the reference models. Model 1 does not exhibit any obvious anomalies, whereas model 3 exhibits strong variations along survey line L5 which can not be correlated to the location of the mineshaft.
- At survey line L4, model 3 shows a strong decrease in the dominant frequencies for receiver location between 7m and 13m, where models 1 and 2 show no anomalies. However, model 2 shows anomalous low dominant frequencies at 2 to 4m and 15 to 17m which increases at both the edges of the survey line. The later feature can also be observed in model 1.

Amplitudes

In Figure 7.1 the results of the analysis of the maximum amplitude and the amplitude of the first arrival are presented.

- The depth of the bedrocks affected the amplitudes of the surface waves considerably. At survey line L4, the maximum amplitudes of the model 1 and model 2 are comparable. However, at L5 the maximum amplitudes of model 2 were larger than of model 1. The maximum amplitudes of model 3 were considerably lower.
- The receivers in the shadow zone of the mineshaft exhibited an increase in the maximum amplitude at the receivers located in the shadow zone of the

mineshaft, i.e. at receivers opposite of the mineshaft. The strongest amplitude can be observed at the receiver directly opposite of the mineshaft.

- The receivers away from the shadow zone showed a decrease in the maximum amplitude compared to the models with a mineshaft. Further away from the mineshaft the maximum amplitudes seem to converge to the maximum amplitudes of the models without the mineshaft.
- The amplitudes of the first arrivals were affected by the presence of the mineshaft. Remarkably the mineshaft affected the amplitudes of all the receivers and it was not confined to the receivers in the shadow zone of the mineshaft.
- At survey line L5 the amplitudes curves of the first arrival are featureless, i.e. the location of the mineshaft is difficult to ascertain just from this figure. At survey line L4 these amplitudes showed a distinctive minimum at the receivers located opposite of the mineshaft.

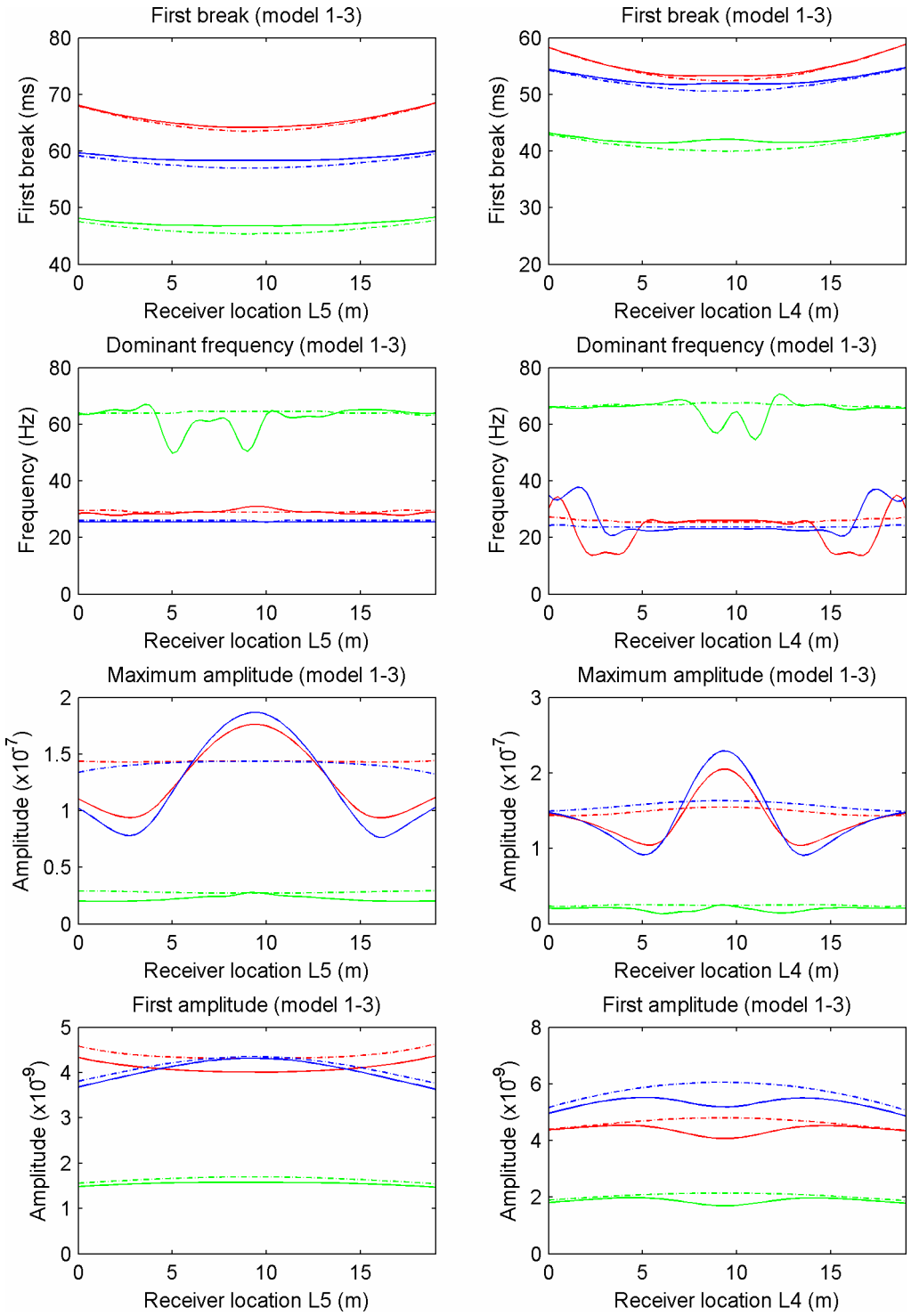

Figure 7.1. Attribute curves at L4 and L5 of model 1 (blue), model 2 (red) and model 3 (green); dash lines are the reference models with no mineshafts

7.3. Mineshaft size

The results of the attribute analysis of the model 4, 5 and 6 are presented in Figure 7.2. The mineshaft diameter varied from 1m to 4m with its centre located at the same spot.

First break

- The maximum time delay caused by the mineshaft at survey line L5 was merely 0.31ms for model 6 and 0.72ms for model 4. For model 1 and model 5 this time delay increased from 1.34ms to 2.06ms respectively.
- The maximum time delay caused by the mineshaft at L4 were identical as at survey line L4, except for model 5 where the maximum time delay is 1.96ms.

Dominant frequencies

In the same Figure 7.2 the estimated dominant frequencies determined at survey lines L5 and L4 are presented.

- Model 5 at the edges of both the survey lines and the standard model at edges of survey line L4 show a distinctive and significant increase of dominant frequencies of over 10Hz.
- Model 5 with the mineshaft diameter of 4m, the zone between the receivers with the anomalous dominant frequencies is much more confined when compared to the standard model.
- Although the models with mineshaft diameters of 1m and 2m show some variations in the dominant frequencies, these variations are very small.

Amplitudes

The maximum amplitude and the amplitude of the first arrival of model 4 to 6 were determined similar to the models presented in section 7.2. The results of the analysis are presented in Figure 7.2.

- Similar as in section 7.2 the presence of the mineshaft caused an increase of the maximum amplitudes at the receivers in the shadow zone and a decrease of the maximum amplitudes at the receivers away from the shadow zone.
- The difference between the maximum amplitudes of model 6 – diameter of mineshaft is 1m – and the model without the mineshaft is very small at survey line L5 as well as survey line L4.
- With increasing mineshaft diameter, the maximum amplitude increased at receivers in the shadow zone of the mineshaft and the maximum amplitude decreased at the receivers away from the shadow zone.
- The amplitudes of the first arrival appear featureless at survey line L5. At survey line L4 the amplitude at the receivers opposite of the mineshaft decreases considerably with increasing mineshaft diameter.

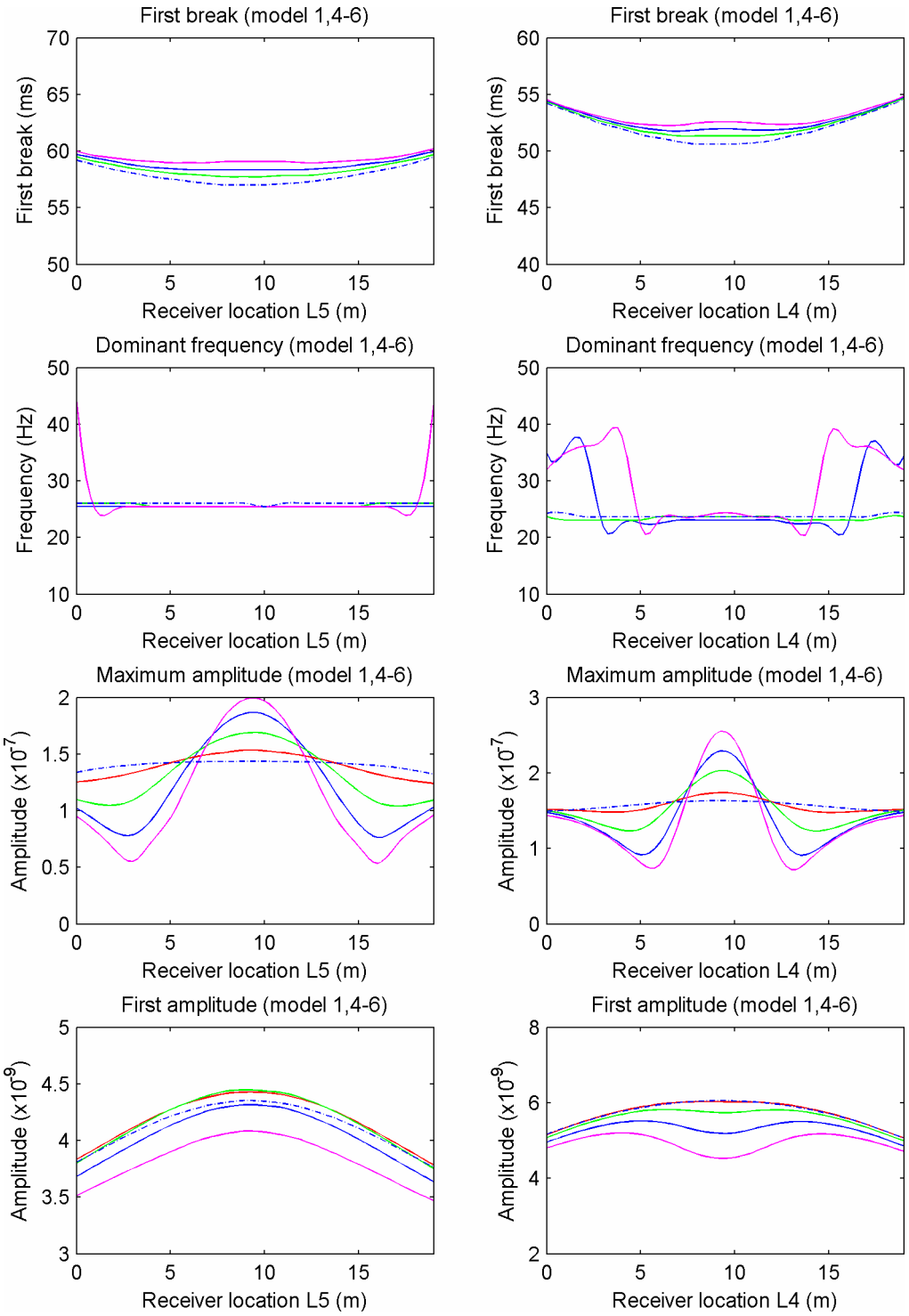

Figure 7.2. Attribute curves at L4 and L5 of model 6 (red): mineshaft is 1m, model 4 (green): mineshaft is 2m, model 1 (blue): mineshaft is 3m and model 5 (magenta): mineshaft is 4m; dash lines are the reference model

7.4. Shape of mineshaft

In section 6.5 it is clear from the snapshots that the shape of the mineshaft had little influence on the outcome of the simulations. In this section a more detailed analysis of the results of the simulations is presented. The analysis of the trace attributes are presented in Figure 7.3.

Figure 7.3 shows a negligible difference between models 1 and model 7. Small differences might be caused by the fact that the discritized volumes of the mineshafts are not perfectly equal and furthermore the cylindrical mineshaft was wider compared to the boxed shaped mineshaft. The latter reason could be the cause of the 1m shift of the anomalous frequencies in Figure 7.3.

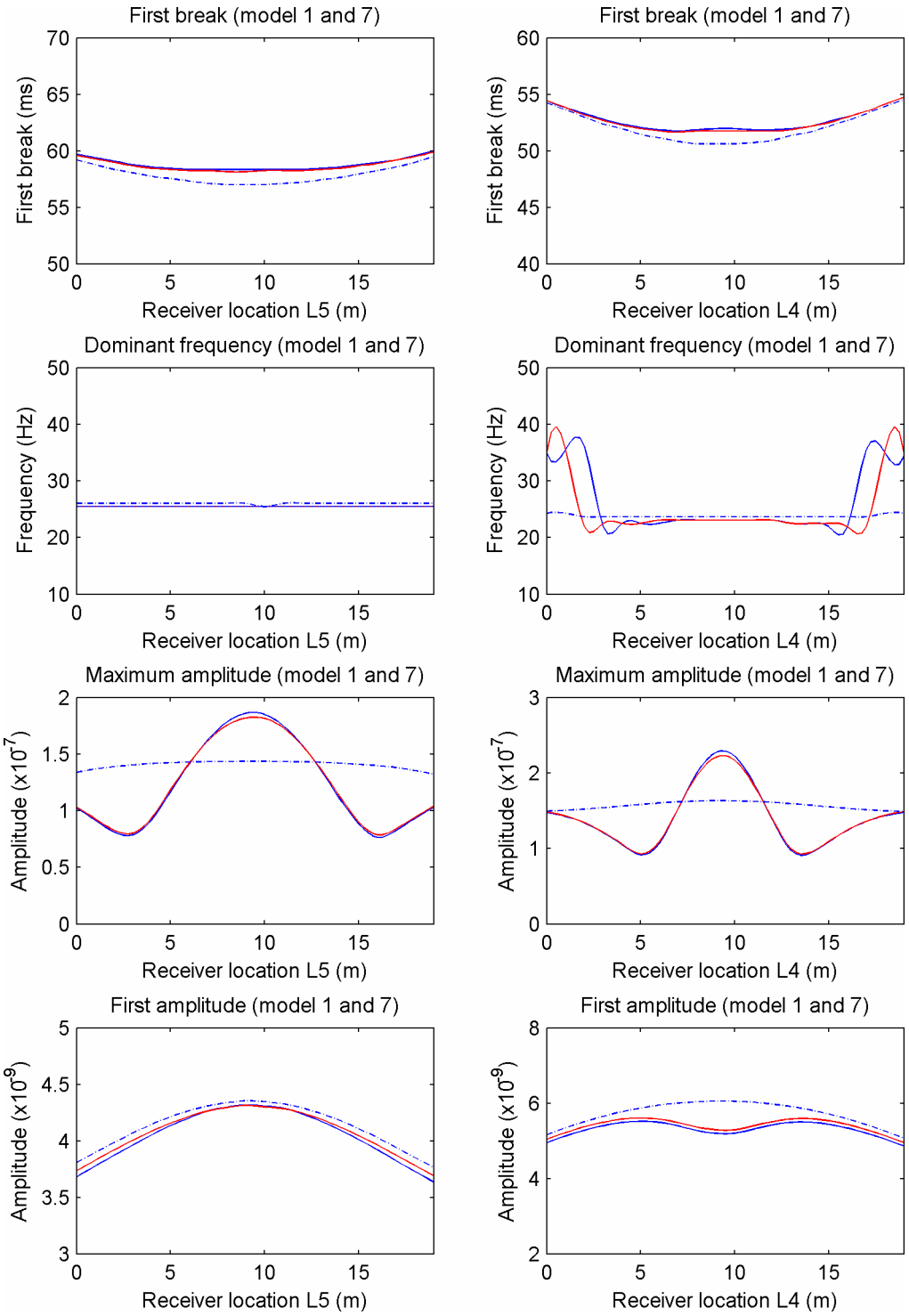

Figure 7.3. Attribute curves at survey lines L5 and L4 of model 1: square mineshaft (blue) and model 7: cylindrical mineshaft (red); model with no mineshaft (dash)

7.5. Source frequency

The models in the analysis in the previous section all had sources with a centre frequency of 25Hz. In practice, there is little control over the frequency of the source. In order to assess the effect of the source frequency on the data, models 8 model 9 were designed with source frequencies of 20Hz and 30Hz respectively. The analysis of the attributes can be found in Figure 7.4. Due to the differences in the shape of the source function, the picked first break i.e. first arrival times, will be different.

First breaks

- The first arrival times at survey line L5 and L4 do not differ much from each other except from the time shift due to different shape of the source function.

Dominant frequencies

- Despite the different source frequencies the dominant frequencies measured at survey line L5 are around 25Hz. Model 9 shows a small increase in the dominant frequencies at receivers

Amplitudes

- With increasing frequencies the maximum amplitudes curve show stronger anomalies. In practice it would be beneficial to use sources which generate high frequency waves.
- The amplitude of the first event curve does not vary much between the models. Strong anomalies can only be observed at survey line L4 whereas the anomalies along survey line L5 appear broad and featureless.

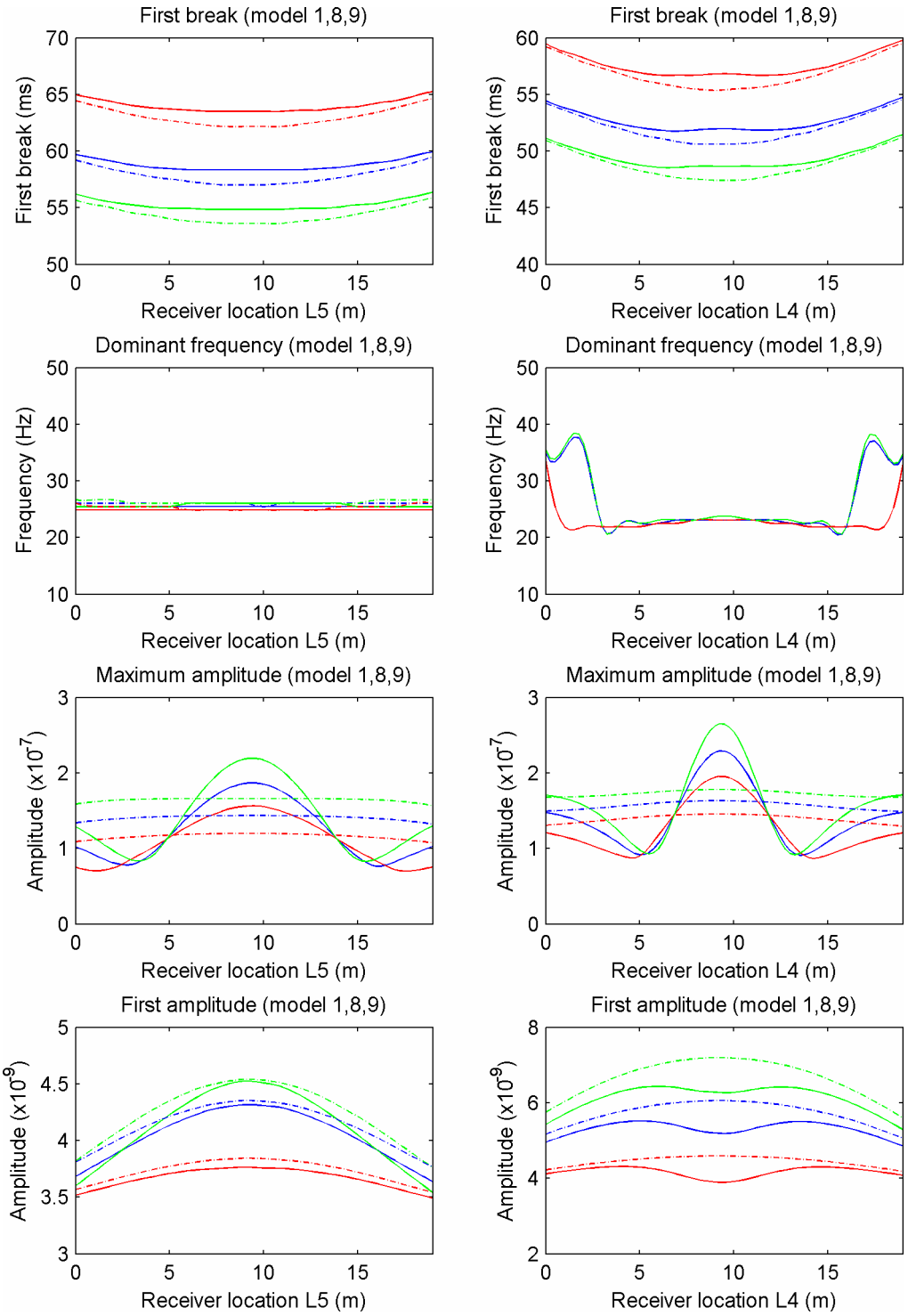

Figure 7.4. Attribute curve at L4 and L5 of model 8 (red): source frequency was 20Hz, model 1 (blue): source frequency was 25Hz and model 9 (green): source frequency was 30Hz, reference models (dash lines): no mineshaft

7.6. Filling of the mineshaft

In this section the analysis of the model 10 and model 11 are presented. In model 10 the mineshaft was completely backfilled and in model 11 the void was filled with water.

Due to the difference in time step size, model 11 required more time steps and more energy was introduced the simulation which resulted in stronger recorded amplitudes. In order to make a comparison between the models a reference model without the mineshaft was modelled using the same step. The results of the determination of the first arrival times and the dominant frequencies can be found in Figure 7.5.

First breaks

- The first arrival times of model 11 seemed to be less affected by the mineshaft compared to model 10. The reason for this is that the velocity difference between the water and surrounding bedrock was merely 300m/s –compare the velocities in Table 6.1.
- Despite the increase in velocity in the water filled mineshaft the first arrivals seemed to arrive later than in the reference model. This is caused by the fact that some energy was converted in diffracted waves and hence the amplitudes at L4 were smaller and the first break was estimated at a different time.
- The difference in the first time arrival between the air void and the completely backfilled mineshaft was small.

Dominant frequencies

- Similar to the dominant frequencies in section 7.5, little variation in the frequencies can be observed along survey line L5. However, along survey line

L4 the frequencies increased significantly by 15Hz at both sides of the survey lines. The zone between the frequency anomalies was smaller for air filled mineshaft model than the completely back filled mineshaft and the water filled mineshaft.

Amplitudes

In Figure 7.5 the analysis of the amplitudes are also presented.

- The maximum amplitude curves of the standard model and model 10 and 11 are similar and the differences are almost negligible. It can be concluded that the filling of the void had little influence on the surface waves. Most of the surface wave energy was likely to be confined in the top 5m and little surface wave energy was presented beneath the bedrock.
- The amplitudes of the first arrivals at survey line L5 as well as survey line L4 were affected by the filling of the void. At survey line L5 the curve of model 10 shows higher amplitudes whereas the model with air void shows smaller amplitudes. The amplitude curve of the water filled mineshaft appears slightly flatter. This might be a result of different scaling.
- At L4, the amplitudes of both models are smaller than the reference model ones. Furthermore at L4 a distinctive amplitude anomaly can be observed in all the mineshaft models at the receivers in the shadow zone of the mineshaft.

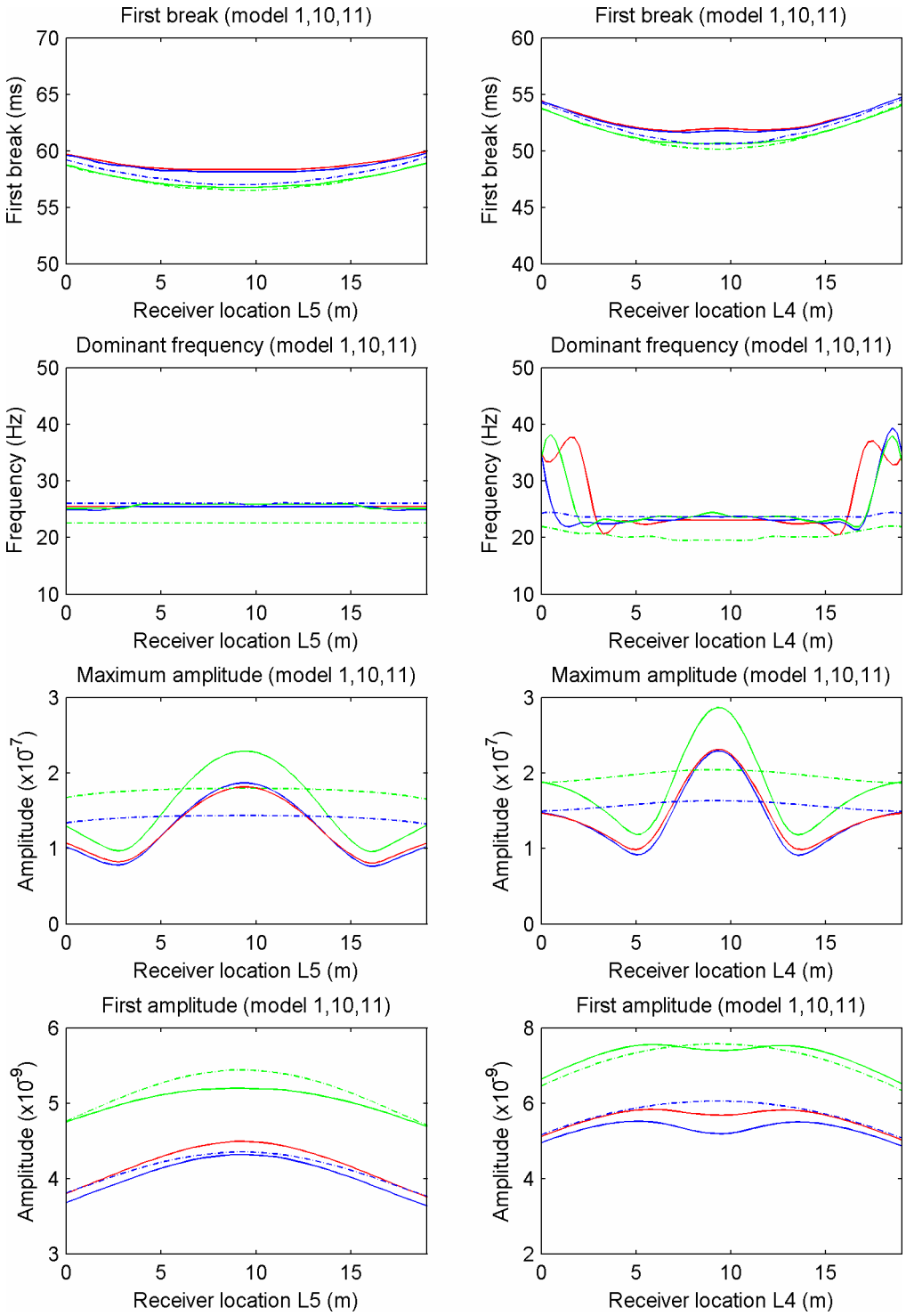

Figure 7.5. Attribute curves at L4 and L5 of model 10 (red): mineshaft is completely backfilled, model 1 (blue): mineshaft void is air filled and model 11 (green): mineshaft void is water filled; dash line is the reference model

7.7. Embankment

In this section the analysis of model 12 is presented. The results of the analysis of the first arrival times and the dominant frequency are presented in Figure 7.6.

First breaks

- The first arrivals show very little variation between model 12 and model 1 along L5 and L4. This could be expected since the refracted waves were unaffected by the presence of the embankment and the direct waves were slightly changed by the presence of the embankment, which is likely to be the cause of the small differences in travel time.

Dominant frequencies

- Similar to the previous sections, the dominant frequencies at survey line L5 show little variation. However, the anomalous increase in the dominant frequencies observed in the standard model, is not presented in model 12 along L4.

Amplitudes

- Due to the reflections at the embankment, the surface waves contained less energy at survey line L5 and L4. This resulted in smaller maximum amplitudes observed in Figure 7.6.
- The mineshaft caused an increase in the maximum amplitude, with the largest maximum amplitude directly opposite the mineshaft. Unlike the maximum amplitudes of model 1, there is no zone where the amplitudes are smaller than the reference model.

- The amplitudes of the first arrivals at L5 of the embankment model were much larger than the ones of the reference model. A possible explanation for this behaviour was that direct waves are diffracted on the edge of the embankment. These diffracted waves were superimposed on the direct waves.

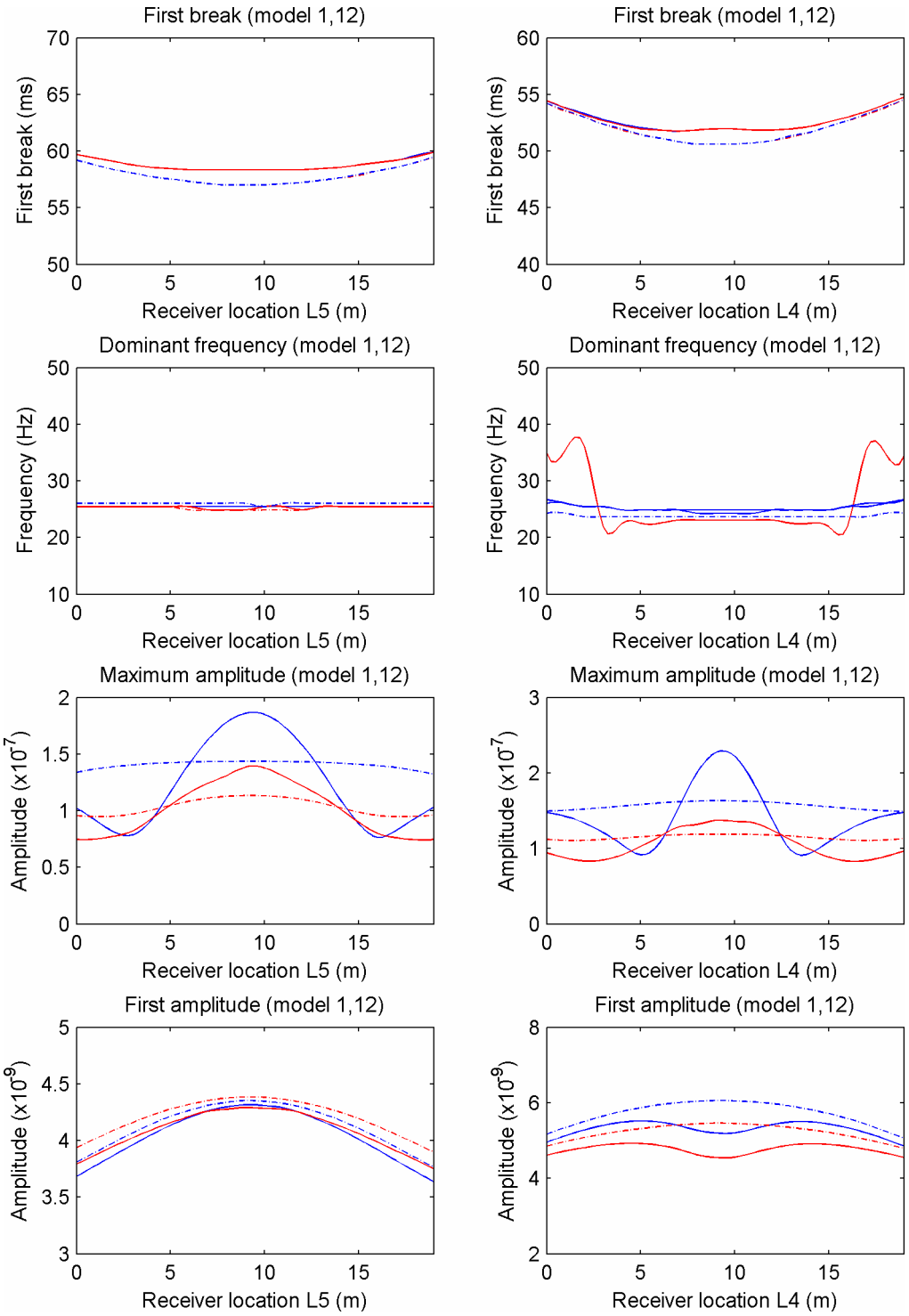

Figure 7.6. Attribute curves at survey lines L5 and L4 of model 12: embankment model (red) and model 1: without embankment (blue); models with no mineshaft (dash)

7.8. Void

In this section the analysis of the model 13 and model 14 are presented. The results of the attribute analysis can be found in Figure 7.7.

First breaks

- The first arrival time delay at survey line L5 of model 13 was considerable. At the survey line L4 this time delay was less. However, the first break curves along survey line L5 does not exhibit any anomalies, whereas along survey line L4 a distinctive time delay can be observed at the receivers directly opposite to the mineshaft.
- Due to the scaling of the amplitudes it is difficult to relate the first arrival times of model 14 with the other models. However, similar to model 13, the survey line L5 does not exhibit a distinctive time delay, whereas survey line L4 does.

Dominant frequencies

- The dominant frequencies of model 13 showed a very strong anomaly at survey line L4. High frequencies were observed at the receivers in the middle and the edges of the survey line. Furthermore the high frequencies can be observed at the edges of the survey line L5.

Amplitudes

- The maximum amplitudes curves of model 13 and model 14 exhibit the increased amplitude for the receivers in shadow zone and decreased values at the adjacent receivers, similar to the models presented in the previous sections.

- The amplitudes of the first events at survey line L5 were affected by the different mineshaft fillings. However, no anomalies were observed along the curves and hence it is difficult to locate the mineshaft by observing the amplitudes of the first arriving events. At survey line L4 a distinctive anomaly can be observed for all the mineshaft models.

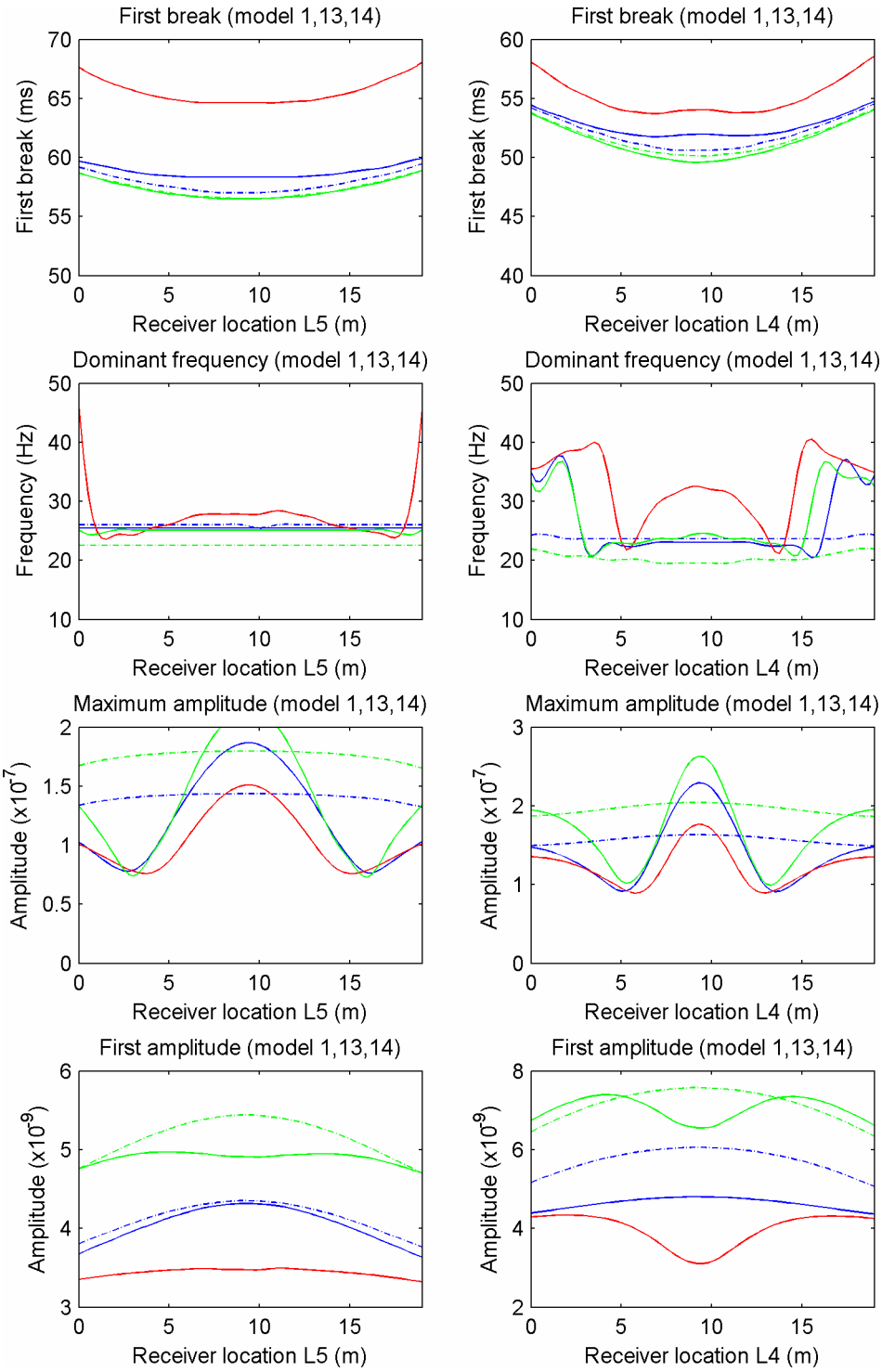

Figure 7.7. Attribute curves at survey lines L5 and L4 of model 13: air void at 2.5m (red), model 1: void at 5m (blue) and model 14: water void till 2.5m (blue); model with no mineshaft (dash)

7.9. Source and mineshaft location

In this section the results of the analysis of model 15 to 20 are presented. In these models the locations of the source of the centre mineshaft were the variable

7.9.1. Model 15 and 16

In model 15 and model 16 the source location was shifted by +2.5m and +5m in the y-direction such that the source locations are opposite of the geophones around +12.5m and +15m.

First breaks

- The apexes of the first arrival times shift in the same direction and with the same distance as the source locations. The apexes also shift in time i.e. the first seismic events arrive faster at the geophones opposite the source location. This is caused by the mineshaft. The first arrival times at L4 are little affected by the presence of the mineshaft and distinguishable anomalies can be found at L5.

Dominant frequencies

- The curves of the dominant frequencies shift in the opposite direction of the source location shift. The high frequency anomalies appear to be related to position of the positive side-lobes of the maximum amplitude curve.

Amplitudes

- The curves of the maximum amplitudes shift in the opposite direction to the source location. The absolute maximum of the maximum amplitude curve is in all the models directly opposite to the source with the mineshaft as centre

point. This makes the maximum amplitude curves particular suitable for triangulating the exact location of the mineshaft.

- The amplitude of the first event shows unexpected behaviour. Very likely the strong variation in the curves is caused by the fact that the amplitude of the first event does not consist of one singular seismic wave, but consists of energies of direct waves, refracted waves and possibly reflected waves. With alternating distances the different waves might become more dominant whereas other ones might become a separate event and do not contribute to the amplitude at all. This effect can make the use of the amplitude of the first event difficult for the delineation of mineshafts.

7.9.2. Model 17 and 18

The analyses of model 17 and model 18 are also presented in Figure 7.9. In model 17 the centre of the mineshaft was shifted by +5m in y-direction of the model and in model 18 by +10m in the same direction.

First breaks

- The apexes of all three first arrival time curves are located near 10m where the source-receiver distance is the shortest. The first arrival times are affected by the location of the mineshaft. These anomalous arrival times can be observed at the receivers opposite of the mineshaft and appear at a broad range of receivers. Therefore first arrival times are not suitable for pinpointing the exact location of the mineshaft. In model 18, the mineshaft is located at the edges of the survey area and the arrival time curves are little affected by the mineshaft.

Dominant frequencies

- The dominant frequencies are affected by the position of the mineshaft. Similar as in Figure 7.8 the anomalous high frequencies appear to be related to the position of the positive side-lobes in the maximum amplitude curves. In practice it might be difficult to pinpoint the exact location of the mineshaft due to the broad nature of the dominant frequencies curves.

Amplitudes

- Similar as in model 15 and 16, the largest maximum amplitudes appear at receivers opposite of the mineshaft. In model 18, the mineshaft is located at the edges of the survey area and its maximum amplitude curves are little affected by the mineshaft.
- The amplitude of the first event curve shows broad anomalies caused by the mineshaft. At survey line L5 the curves have no distinguishable features which can be related to the position of the mineshaft. At survey line L4, the anomalous amplitude values appear at the geophone closest to the position of the mineshaft.

7.9.3. Model 19 and 20

In Figure 7.10 the attribute curves of model 19 and model 20 are presented. In model 19 the centre mineshaft was located -5m in the x-direction and in model 20 the centre of the mineshaft was shifted by +5m in the x-direction.

First breaks

- The first arrival curves show that the position of the mineshaft has a minor effect on the delay of the first event. The anomaly appears very broad when

the mineshaft is located close to the source and when the mineshaft is located close to the receivers the anomaly appears more focused at the receivers closest to the mineshaft.

Dominant frequencies

- The dominant frequencies are affected by the location of the mineshaft. Again, it can be observed that the high frequency anomalies are related to the positive side-lobes of the maximum amplitude curve. When the mineshaft is located close to the source, no high frequency anomalies are observed.

Amplitudes

- The lobes of the maximum amplitude curves become wider when the mineshaft is located close to the source and becomes narrower when the mineshaft is located close to the receivers. In all the models the largest maximum amplitude is always located opposite to the source location.
- In model 19, the amplitudes of the first event are decreased compared to the amplitudes of the standard model. Although the decrease is related to the presence of the mineshaft, the curve is featureless and the exact location of the mineshaft cannot be derived from this curve. In model 20, the mineshaft is located beneath the survey line L4. The amplitude curves show a distinctive anomaly related to the location of the mineshaft at survey line L4.

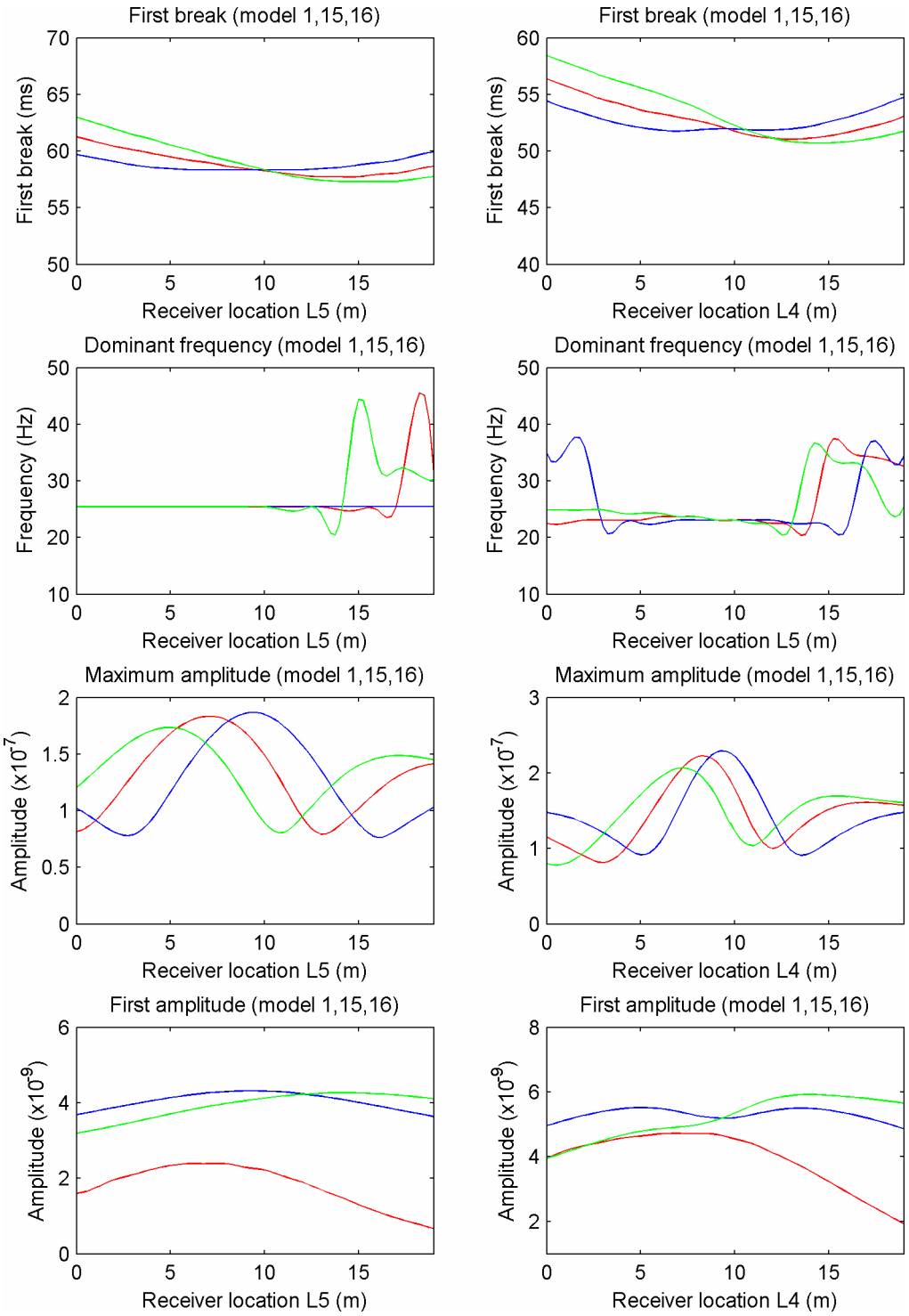

Figure 7.8. The attribute curves of model 15 (red), model 16 (green) and the standard model 1 (blue)

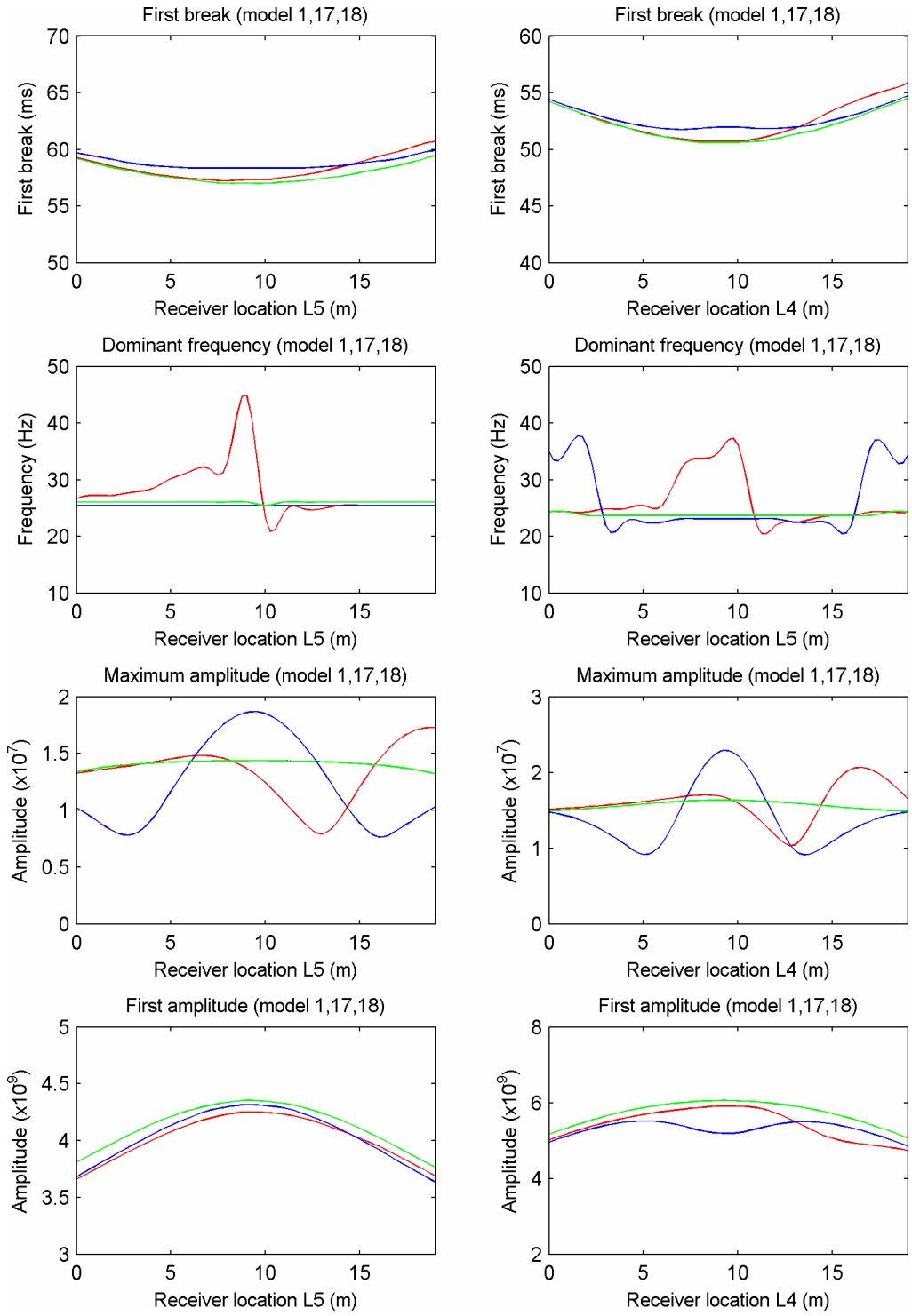

Figure 7.9. The attribute curves of model 17 (red), model 18 (green) and the standard model 1 (blue) and its reference model (dashed blue)

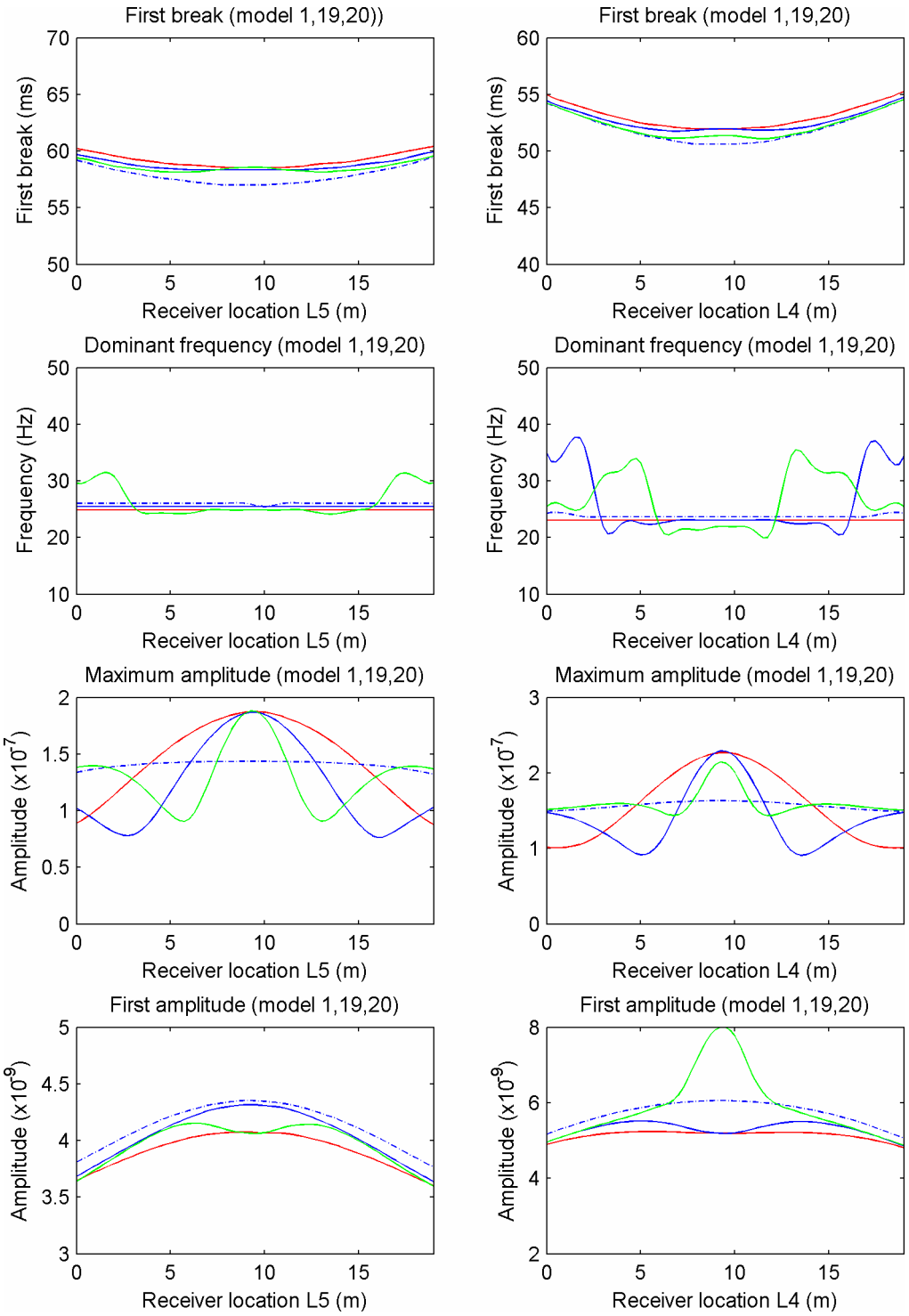

Figure 7.10. The attribute curves of model 19 (red), model 20 (green) and the standard model 1 (blue) and its reference model (dashed blue)

7.10. Discussion

In this chapter the analyses of the synthetic seismograms are presented. Various trace attributes were examined: amplitudes, frequencies and travel times.

It should be stressed that for the detection of mineshafts the value of the anomaly is not as important as the shape of the anomaly! Since the reference curve is unknown in practice, the actual quantitative value of the anomaly caused by the mineshaft with unknown location cannot be derived from the field data. Anomalies in the field can only be identified when these values differ from the expected values i.e. when the attribute curve shows anomalous shapes.

In order to assess the potential of the various attributes to delineate mineshafts, a measure of the variance in shape of each attribute curve was introduced. This measure is an indication of how much the curve differs in shape from the reference curve from the model without the mineshaft. The variance of each curve was calculated using the following equation:

$$\left\| E_{\text{var}} \right\| = \sqrt{\frac{1}{n-1}\sum_{i=1}^{n}\left(\frac{\partial\left(\frac{\Upsilon^{i}}{\Upsilon^{average}}\right)}{\partial x} - \frac{\partial\left(\frac{\Upsilon^{i}_{reff}}{\Upsilon^{average}_{reff}}\right)}{\partial x} \right)^{2}} \qquad (7.2)$$

where E_{var} is the variance quantity, n is the number of points along the attribute curve and Υ^{i} is the value of the attribute at point i along the curve. The attribute curves were scaled by the average value of the curve such that the variance is unaffected by the attribute value and the variances of various attributes can be compared directly to each other. Equation (7.2) can be approximated in discretized space by:

$$\left\|E_{\text{var}}\right\| \approx \sqrt{\frac{1}{n-1}\sum_{i=1}^{n-1}\left(\frac{\Upsilon^{i+1}-\Upsilon^{i+1}}{\Delta x\frac{1}{n}\sum_{i=1}^{n}\Upsilon^{i}} - \frac{\Upsilon^{i+1}_{reff}-\Upsilon^{i+1}_{reff}}{\Delta x\frac{1}{n}\sum_{i=1}^{n}\Upsilon^{i}_{reff}}\right)^2} \tag{7.3}$$

where Δx is the distance between each point on the curve. The results of the variance calculations for attribute curves of the first break, dominant frequencies and the amplitudes of model 1 to 14 are presented in Table 7.2. The maximum value of the delayed firs arrival can also be found in this table. Note that variance of the dominant frequency curves were not determined, since anomalies were located outside the survey line in models. Including the variance of the dominant frequency could lead to erroneous conclusions.

A colour coding is used in Table 7.2 in order to highlight the values of the variance and the maximum delay. The explanation of the colour code is presented in Table 7.1. In this table the probability to delineate the mineshaft can be found as though the data were obtained in an actual field experiment. It should be stressed that the probability to delineate the mineshaft is merely an interpretation by the author to aid the discussion. Numerous field experiments would be required in order to assess the actual probability of being able to delineate a mineshaft using the various attributes.

Table 7.1. Explanation of the colour coding used in Table 7.2

Colour	Max. delay	Variance value	Probability to detect mineshaft
	> 2ms	>20	High
	1-2ms	20-5	Medium
	< 1ms	<5	Low

Table 7.2. The variance of each attribute curve of model 1-14

Model	Description	Maximum delay		First arrival variance ($x10^3$)		Maximum amplitude variance ($x10^3$)		First amplitude variance ($x10^3$)	
		L5	L4	L5	L4	L5	L4	L5	L4
1	Standard model	1.34	1.34	3.13	4.63	152	197	4.34	22.7
2	Bedrock depth: 10m	0.72	0.92	2.11	3.63	114	151	2.82	30.3
3	Bedrock depth: 1.5m	2.06	2.68	4.05	8.62	61	154	4.70	40.1
4	Mineshaft size: 2m	0.72	0.72	2.05	2.86	79.3	104	4.06	9.48
5	Mineshaft size: 4m	2.06	1.96	4.45	6.54	216	270	3.78	39.0
6	Mineshaft size: 1m	0.31	0.31	1.61	2.09	24.7	29.6	2.22	2.42
7	Circular shaft: 3.4m	1.23	1.13	2.89	4.40	146	188	1.89	22.5
8	Source frequency: 20Hz	1.34	1.44	2.89	4.65	111	162	1.5	27.5
9	Source frequency: 30Hz	1.24	1.24	3.36	4.67	181	227	8.96	15.6
10	Completely backfilled	1.13	1.13	2.81	4.11	141	180	5.41	13.3
11	Water in the void	0.25	0.50	1.71	2.67	151	190	6.97	11.9
12	Embankment	1.34	1.34	3.5	4.63	68.2	82.9	3.34	26.4
13	Void to 2.5m deep	8.56	4.02	3.58	7.01	139	162	17.2	69.1
14	Water void to 2.5m	0	-0.01	1.60	2.17	194	209	17.1	35.8

7.10.1. First arrival time

From the results of the first arrival time presented in this chapter, it is clear that the presence of the mineshaft results in a delay in the first break. It is also clear that the delay is not confined to the receivers in the shadow zone but can be noticed in a wide area behind the mineshaft. Tomographic imaging software such as GeoTOM and Rayfract can image the subsurface by refracted waves. However, due to the nature of the first arrival time curves these tomographic software packages will not render the subsurface image well.

For the detection of mineshaft it is required that the observed delay is larger than the picking error, but also it is distinguishable.

- In the third and fourth column of Table 7.2 the maximum delay is shown. The delays in most models are between 0.4ms and 2ms. These values are relatively low. In general the picking error is in the order of 1ms depending on the background noise level, signal strength and the competence of the interpreter. Delay values beneath this value are unlikely to be identified. Values of 2ms and larger can normally be identified easily. The models with the mineshaft diameters of 2m and smaller, the models where the bedrock is located at greater depth and the models where the voids were filled with water all showed very low delays values. Whereas the models were the void extends to or close to the surface and models with large mineshafts showed delays larger than 2ms.
- A large delay, alone is not sufficient to delineate mineshafts in practice. The first break curves should show anomalous shapes i.e. high variance values in order to locate the mineshaft. From the variance values in column 5 and 6 of Table 7.2 it can be concluded that the shape of the first arrival time curves does not exhibit strong anomalies. Although at survey line L4 some of the models show a slight increase in the variance. In practice it might be difficult

to delineate mineshafts using the first arrival times even when the amount of the delay is sufficiently to distinguish from the background noise.

7.10.2. Dominant frequencies

The analyses of the dominant frequencies presented in this chapter showed that high frequency anomalies were associated with the location of the mineshaft. However, these high frequency anomalies appeared at the receivers away from the mineshaft. The dominant frequency curves of models 15 to 18, presented in Figure 7.8 and Figure 7.9, showed that the high frequency anomalies are associated with the location of the side-lobes of the maximum amplitude curves. The broad nature of the dominant frequency curves makes it difficult to use them to pinpoint the exact location of the mineshaft, although they might be a useful tool in addition to other methods.

The experiments conducted by Dresen (*1979*) showed that the dominant frequencies of the Rayleigh waves are little influenced by the mineshaft and the dominant frequency curve showed only a minor increase in frequency at the receivers behind the mineshaft. The reason for this behaviour is that the frequency spectrum of the Rayleigh waves is very much affected by the superposition of the diffracted Rayleigh waves. However, in the Dresen experiment the distance from the receivers to the mineshaft did not alter and hence the traces are more or less equally affected resulting in little variation along the survey line.

In the experiment conducted by Dresen the dominant frequency of waves other than the Rayleigh were also examined. These waves included refracted P-waves, converted SP-wave and reflected P-wave. The dominant frequency curve of these showed a characteristic W-shape. Since the wavelets of these waves are

larger than the differences in arrival time, these waves and other waves are interfering with each other. Therefore it is impossible to single out events. Sliding windows can be used to overcome this problem but the technique is not entirely free of problems. The method is explained in the text box on page 189.

7.10.3. Maximum amplitudes

The maximum amplitude is associated with the amplitude of the dominant surface waves. Most of the results show a very strong increase in the amplitude for the receivers opposite the mine shift and a reasonably strong decrease at the receivers just outside of the shadow zone. Table 7.2 shows that the variance of maximum amplitude curves is very high. Even the models with the embankment and the shallow bedrock show a strong increase in amplitude with its maximum exactly opposite of the mineshaft. The strong amplitude anomalies are caused by the superposition of the direct surface waves and the diffracted surface waves.

The maximum amplitude appears a valuable tool to delineate mineshafts. The variance values for the model with a mineshaft of 1m are considerably smaller than the values of the other models. Additionally, the shallow bedrock in model 3 has a very strong effect on the amplitudes; the variation in the maximum amplitude observed at L5 – is considerably lower than the most other models. The detection of small mineshafts by using the maximum amplitudes might be difficult when the bedrock is shallow.

It should be mentioned that the main cause of this amplitude increase is the velocity difference between the backfilling and the superficial deposit. In a case where the difference is smaller it might be possible that mapping maximum amplitudes will not resolve the mineshaft.

Sliding windows spectrograms

It is impossible to single out seismic events from the traces in order to determine the dominant frequency of that event. However, the traces can be tapered using a window with a certain time length which shows only a part of the trace. The masked trace is then transformed into frequency domain and its dominant frequency is determined in a similar way as the Rayleigh wave discussed in section 7.10.1. The window does not discriminate superposed waves since their amplitudes cannot be separated from the amplitudes of the examined seismic event and hence the frequency spectrum includes will include energies of other seismic waves. Short windows discriminates more of the unrelated events, but leads to lost in resolution in frequency domain since resolution is inversely related to the length of the trace. Furthermore low frequencies are also discriminated since their wavelet is longer than the length of the window. Using long windows will include more energies thus the dominant frequency might not reflected the dominant frequency of examined event.

A quick experiment was carried out to investigate the possibility of using windows. The data consisted of the standard model and its reference model. The results of this experiment can be found in the spectrograms presented in Figure 7.11. A Hann window with a time window of 0.053s was used to taper the traces. The window slides over the traces and the dominant frequency is calculated at every time step. The dominant frequency is plotted against the receiver position and the time which is determined by the centre of the window.

Figure 7.11 shows that the dominant frequency varies with the time of the trace. When comparing the spectrograms of model 1 and the spectrograms of its reference model at both survey lines it is clear that the presence of the mineshaft has a considerable influence on the dominant frequencies. Not only the Rayleigh waves vary strong with time and receiver location, the body waves preceding the

surface waves also show variations. Errors caused by using a window can also be observed as the sharp increase in figure Figure 7.11b) and the ringing observed in all four spectrogram which known the Gibbs effect. A detailed study of using the sliding window spectrograms was beyond the scope this thesis.

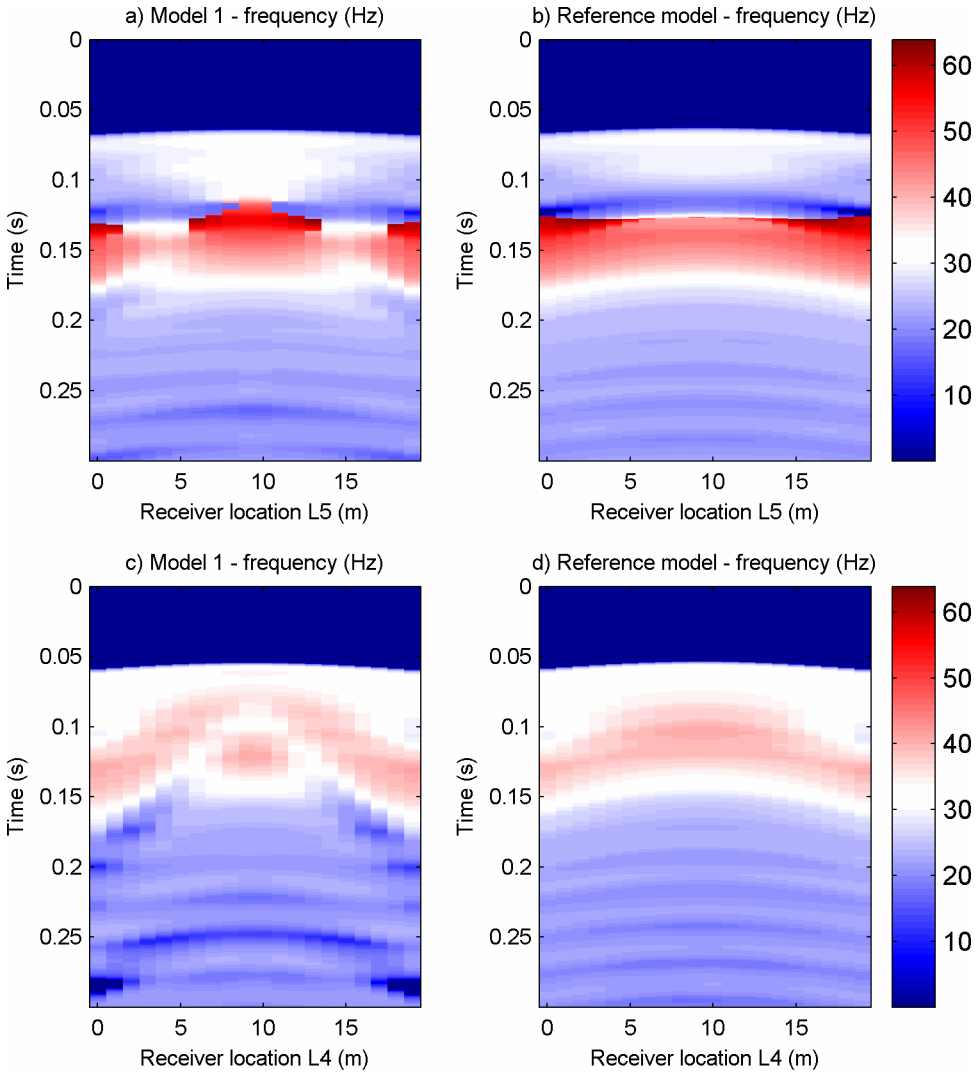

Figure 7.11. The spectrograms of the dominant frequencies determined at each time step using a sliding window of the seismograms of a) survey line L5 in model 1, b) survey line L5 in the reference model, c) survey line L4 in model 1 and d) survey line L4 in the reference model

7.10.4. Amplitudes of first event

From the results it is clear that the mineshaft affects the amplitudes of the first event. However from Table 7.2 it is clear that at survey line L5 the amplitude variance is small and it might be difficult to detect mineshafts by determining the amplitudes of the first event. At survey line L4 the amplitudes show more variance.

The embankment of model 12 does not influence the first arrivals and their amplitude and hence these attributes are unaffected by the presence of the embankment. This might be useful when a large embankment is present.

The amplitudes of the first event can be used for detection of mineshafts. However, the strong anomaly was only observed at the receivers close to the mineshaft. In practice, the location of the mineshaft would be unknown and therefore in order to provide full coverage of the survey area numerous survey lines are required. This could seriously limit the potential of this technique.

7.10.5. Attribute analysis of other seismic events

The transmission method can be applied for any elastic wave that travels through the mineshaft. In this thesis the following attribute analyses are presented:

- The arrival times of the first event
- The dominant frequencies
- The amplitudes of the Rayleigh wave
- The amplitude of the first event

It should be stressed that the transmission method does not have to be limited to these attribute analyses. For example, Dresen (*1979*) showed that amplitude and

dominant frequency of reflected shear waves can be used to delineate mineshafts. However, when using broadside shot gathers rather than semi-circular gathers it becomes more difficult to distinguish the investigated event due to interference with other events arriving at various times.

In order to analyse events other than ones mentioned in the previous points, the investigated events need to be discriminated. There are various post-processing methods available to achieve this. One of the methods which can be used to analyse the dominant frequencies is the sliding window spectrograms as presented in the box text on page 186. Another method to distinguish single events is wave separation. Although wave separation is rarely used in single-component near-surface seismics, wave separation is regularly used in multi-component seismology and in the oil and gas exploration. Wave separation might prove to be difficult in near-surface seismics where typically multiple waves are interfering with each other. A full investigation of the wave discrimination methods is beyond the scope of this thesis.

7.10.6. Miscellaneous analysis methods

This chapter mainly focuses on the transmission methods as pioneered by Dresen (*1979*), but other methods to analyze data do exist. These methods include for example first arrival tomography and the inversion of the frequency-velocity dispersion curve of surface waves. However these methods were never used on data obtained from broadside shot gathers.

Imaging the subsurface by inversion of the dispersion curve of the surface waves is a well established method in the near-surface geophysics (section C.6.3). The technique mainly focuses on determining a vertical profile (1D) of the shear-wave velocity. Although the inversion can be extended to incorporate lateral

variations (2D) and can possibly be extended to 3D, this is less frequently done. The same holds for 3D first arrival tomography. 3D seismic tomography in the near-surface geophysics is typically done with the aid of boreholes (*Polymenakos and Papamarinopoulos, 2007*) or the studied object allows surface measurements, e.g. a protruding hill (*Schicht et al., 2007*).

Both the tomography and the inversion of the dispersion curve are typically ill-posed inversion problems. In other words, numerous inversion models provide the same solution to the measured data. This is especially true for 3D cases. To prevent ill-posed inversions often a smoothness factor is introduced. However, in reality there is a strong physical contrast between the mineshaft and the surrounding material such that smoothness constraints will not provide a realistic image of the subsurface.

Nevertheless, the techniques mentioned above do have some potential to image the subsurface beneath the railway. A full assessment of these techniques is beyond the scope of this thesis.

7.11. Conclusions

In this chapter the attribute analysis of the traces of the simulated seismograms are presented. These attributes include the first breaks, the dominant frequencies and the amplitudes of the first arriving event and the Rayleigh waves. Comparing the results of the mineshaft models with the reference models without the mineshafts showed that the attributes of the traces were affect by the presence of the mineshaft.

In particular the maximum amplitudes were strongly affected by the mineshaft and the anomalies could be easily associated with the location of the mineshaft. Although the mineshaft affected the amplitude of the first arriving

event, it might be difficult to ascertain the position of the mineshaft from this data. The dominant frequencies showed high frequency anomalies at both sides of the survey lines. The position of the mineshaft might be difficult to derive from the dominant frequency curves alone however the technique could be complementary to other techniques. The mineshaft caused anomalies in the first breaks. The values of these anomalies were in order of 1ms depending on the model. These values were small and in practice it would be difficult to differentiate these anomalies due to the picking error of the first breaks.

From the analysis it is clear that large mineshafts affect the attribute curves stronger than small mineshafts. In addition it is clear from the maximum amplitude curves and the dominant frequency curves of model 8 and model 9 that the strength of the anomalies are related to the wavelength. As rule of thumb the diameter of the mineshaft should be larger than the wavelength of the dominant frequency ($D_{mineshaft} > ¼\lambda$). Small mineshafts might be resolved when using high frequencies, however due to the limited computer resources this was not tested. Unless the void of the mineshaft extended close to surface (<5m) the filling of the void had little influence on the amplitudes, although the first breaks were affected. When comparing the results of the embankment model with the results of the standard models showed that the first breaks and the variances of the first break and the amplitude of the first arriving event were little affected by the presence of the mineshaft.

8. Field experiments

In the previous chapters numerical models showed that the presence of the mineshaft affects seismic waves. By observing the seismograms and analysing the signal attributes, the position of the mineshaft can be derived. In reality there is often a discrepancy between synthetic data and field data. Therefore field experiments were conducted with the following objectives:

- Identify problems regarding seismic surveys in the field
- Correlate field observations with the numerical observations
- Assess seismic methods to delineate mineshafts

In this chapter the results of the seismic field experiments are presented and discussed. The experiments were conducted on 18-20 September 2006. There was only a short period available for access to the farmland to prevent damage to the growing crops. For the survey a crew of at least 4 persons was required. The weather during the survey was characterised by strong winds and rain spells on the last day.

The experiment consisted of two surveys. One survey was conducted near a capped mineshaft with its exact location known. The second survey was conducted near a mineshaft that was backfilled completely and its exact location was unknown. The presented data was analysed similarly to the numerical experiments presented in chapter 7.

8.1. Introduction

This experiment was conducted near Huntlaw Farm in Pencaitland located, in East Lothian. The Huntlaw colliery was a small coal mine active in 1840 (*Spence, 1984*). At this site three mineshafts were present. Mineshaft 1 was capped by a concrete slab positioned on brick lining. Since this mineshaft protrudes above the surface, the exact location of the mineshaft was known. The mineshaft was rectangular shaped with dimensions of about 2.5m by 3.5m. The depth of the mineshaft was unknown. However borehole data from the exact same location suggest that the data was taken from the mineshaft. The borehole log records a depth of 52m. It can be expected that the depth of the mineshaft was at least this deep.

The status of mineshaft 2 was unknown but it was very likely that the mineshaft was completely backfilled which was confirmed by local informants. The exact location of the mineshaft was unknown. Evidence of mining could easily be found at this site, such as pieces of brick, roof tiles and ashes. The diameter of the mineshaft was unknown as well its depth. Data from nearby boreholes showed a layer of foul coal exists at a depth of 19.7m. The mineshaft was probably sunk at least till this depth.

The locations of mineshaft 1 and 2 and borehole 1 and 2 were plotted on the map presented in Figure 8.1. At Huntlaw Farm there was another mineshaft present. No survey was conducted at this mineshaft due to the lack of time.

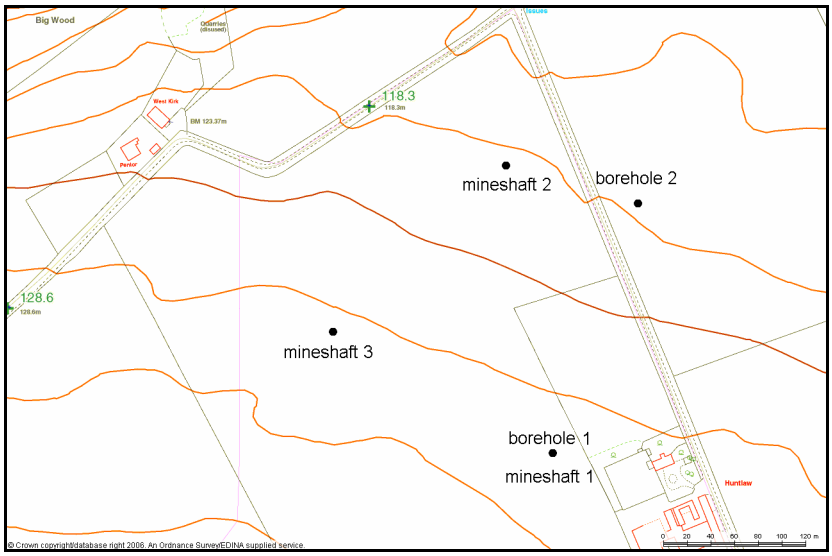

Figure 8.1. Map of the Huntlaw farm with the locations of the mineshafts and the location of the boreholes

8.2. Geology

8.2.1. Geological setting

The geological history of the Lothians is long and complex. In Figure 8.2 a geological map of the East Lothians can be found. The field trial site is situated in the geological measure group called the Clackmannan.

The Clackmannan group was formed in the Carboniferous around 320 million years ago. Within this group four divisions can be made. These divisions comprised of cycles of marine or quasi-marine beds, alternating with fluvial-deltaic sediments (*Clarkson and Upton, 2006*). These divisions are overlain by the Passage Group Formations which were dominantly fluvial in origin, although some layers with marine sediments shows the occasional influx of the sea.

The East Lothians were located most of the time in the Carboniferous in a large delta. In this dynamic environment, a sequence of richly fossiliferous

calcareous shale, micaceous shale, thin sandstone, massive sandstone and some thin coal layers were formed.

In Appendix F, detailed data from two nearby boreholes can be found. These boreholes were obtained from the British Geological Survey. Both borehole logs show similar patterns. The superficial deposits consist of mainly clay. The thickness of the clay layer at borehole 1 is merely 0.8 metres, whereas the thickness of this layer is about 2.85 metres at borehole 2. The clay layer is underlain by the bedrock which consists of mainly cycles of sandstones and blaes. Blaes is spent oil shales (*Winter, 2001*). The sandstone and blaes layers are interrupted by thin coal layers.

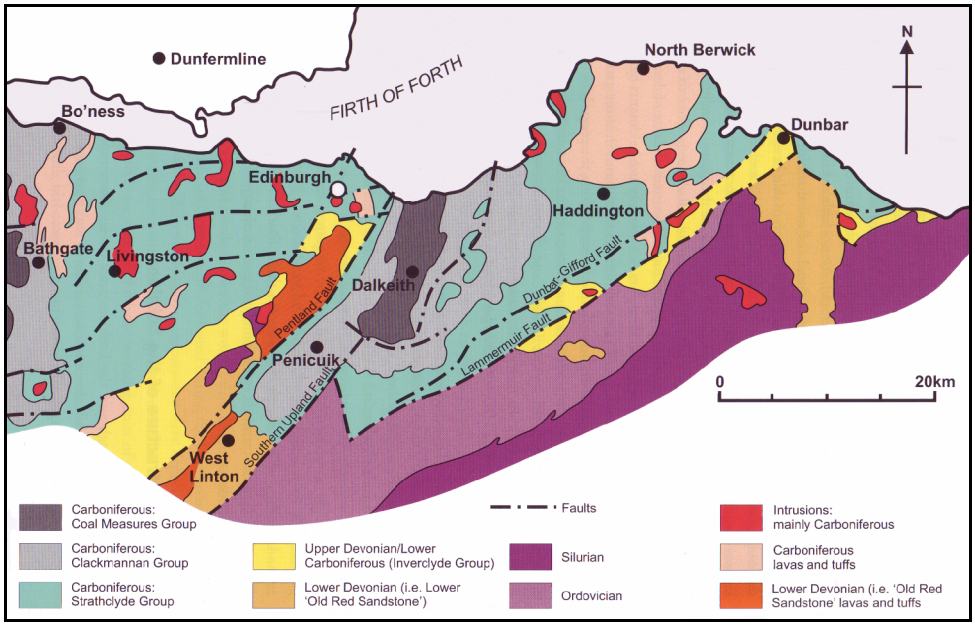

Figure 8.2. Geological map of the Lothians (*Clarkson and Upton, 2006*)

8.2.2. Refraction survey

At both mineshafts a quick refraction survey was conducted in order to estimate the wave velocities in the top soil and the refractor and also the depth to the refractor and the dipping angles were determined. The refraction surveys were conducted at survey line L1 and L6 (section 8.3.2).

Note that there was no refraction survey carried out across the survey lines. The calculations of the velocities and depths did not take into account the cross dip and hence may contain errors. The results of the refraction surveys are summarized in Table 8.1. The cross dip of refractor was estimated by considering the depth of the refractor at L1 and L6. The actual value is an approximate estimation and should only be regarded as such. From the table it can be observed that the geology at mineshaft 1 is strongly variable and that the bedrock is very close to the surface. The refractor at mineshaft 2 is smoother with little dip and cross dip in relation to the surface. The velocities at mineshaft 2 are much higher than the velocities at mineshaft 1.

Table 8.1. Estimated values of the velocities, dips and cross dips for both mineshafts

	Mineshaft 1	Mineshaft 2
v_p of the superficial deposits	370 m/s	520 m/s
v_p of the refractor	950 m/s	1400 m/s
Depth to refractor at L1	1.1 – 1.8m	4.0m
Depth to refractor at L6	2.3m	4.5m
Dip refractor	2°	0.2°
Cross dip refractor	6°	1.5°

8.3. Data acquisition

8.3.1. Equipment

The seismic equipment used in the experiment was rented from ABEM France. The sledge hammer and the trigger plate came from the University of Edinburgh as well as the survey equipment, which was used to obtain the topographic data. The complete list of equipment used at the field trial is given below:

- Seismic equipment
  - DAQlink II - seismic recorder
  - CF27 - field laptop
  - 26 x 4.5Hz vertical geophones
  - 2 x cable for 12 geophones
  - Geometrics trigger
  - 50m extension cable for trigger
  - Metal trigger plate
  - 14 lbs sledge hammer
  - 3 x car batteries
- Survey equipment
  - Several measuring tapes of 25 and 50 metres
  - Level
  - Tripod
  - Level staff
  - Optical square

8.3.2. Survey grids

The positioning of shot points and receivers used for the seismic experiment at both mineshaft sites were selected such that a large amount of data was obtained. The selected survey outline bares resemblance to the survey grid used by Shtivelman and Keydar (*2005*) for a diffraction imaging experiment. However, for this survey a shot and receiver spacing of 2m and a shot line spacing of 4m were selected. The outline and the values were chosen such that the results of the data could be used for the diffraction imaging experiment – presented in Appendix H – as well as the transmission experiment presented in this chapter.

Figure 8.3 shows a schematic overview of the survey grid used at mineshaft 1. The capped mineshaft was located in the middle of the survey. Only one receiver line was active i.e. measurements were taken using receiver line L1 and all the measurements were repeated after relocating the receivers at line L6. Line L1 and L6 were also shot point locations. For the attribute analysis only the following shot gathers were used: shot points at L5S1-S24, L6S1-S24 with the receivers located at survey line L1 and shot points L1S1-S24, L2S1-S24 with the receivers located at survey line L2. The remaining shot gathers were used for the diffraction imaging presented in Appendix H.

Figure 8.4 shows the survey grid used for the mineshaft 2. The survey grid was centred on the suspected mineshaft area. The survey grid spacing was similar to the survey grid spacing used for the capped mineshaft. An additional shot point line (L7) was added to the grid in order to increase the surveyed area and hence to enhance the probability of including the mineshaft for the diffraction imaging experiment presented in Appendix H. Similar to the survey at mineshaft 1, only the following shot gathers are used for the attribute analysis: shot points L5S1-S24, L6S1-S24 with the receivers located at survey line L1 and shot points L1S1-S24, L2S1-S24 with the receivers located at survey line L2.

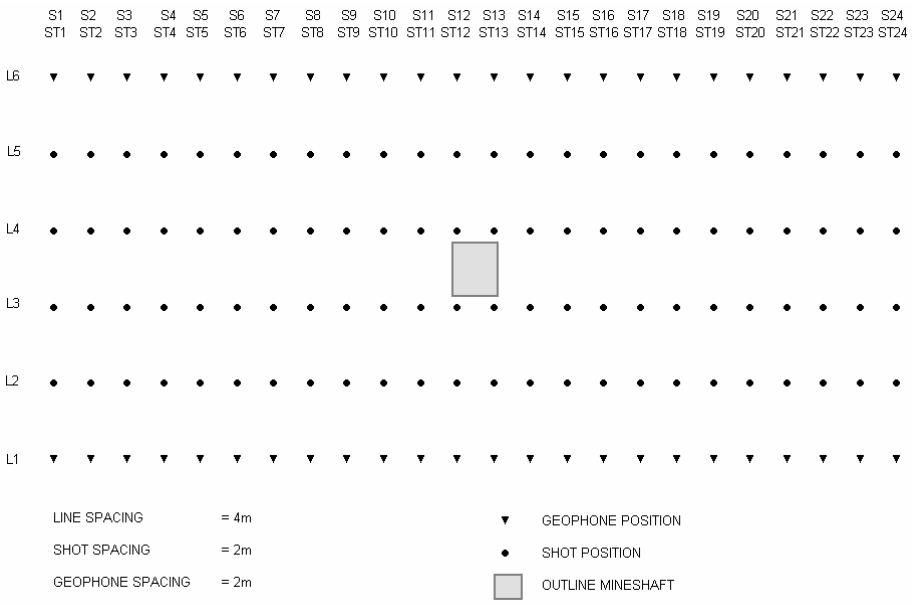

Figure 8.3. Survey grid at mineshaft 1 – capped mineshaft

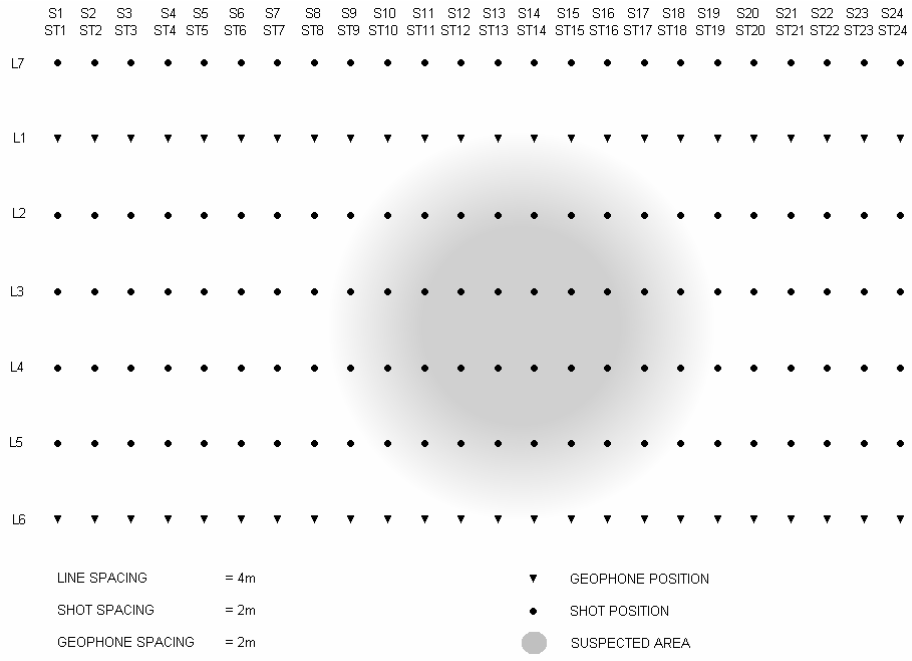

Figure 8.4. Survey grid at mineshaft 2 – completely backfilled mineshaft

8.3.3. Software

The software used to record the seismic data in the field was the software package VScope version 2.3.32 which came with the hired equipment. The same software was used to export the seismic data from the format used by VScope into the standard SEG-Y format.

In order to interpret and present the seismic data, MATLAB was used. MATLAB scripts for the processing, the analysis and the representation of the seismic data written by the Consortium for Research in Elastic Wave Exploration Seismology (CREWES) were downloaded from http://www.crewes.org/. Most of these scripts were modified in order to improve the representation of the experimental data. Furthermore some additional MATLAB scripts were written which were used for the analysis and their representation of the shot gathers.

8.4. Mineshaft 1 - capped mineshaft

The first seismic survey was conducted at the capped mineshaft with known location. Numerous shot gathers were examined. For the sake of conciseness only a few representative shot gathers are presented in this section. Most shot gathers are presented in Appendix G.

In section 8.4.1 the resulting seismograms of some of the selected shot gathers are presented. In Figure 8.5 the selected shot points are represented. Three shot points were selected at the very beginning of each shot line and three shot points were selected closer to the mineshaft with the mineshaft between shot points and the receivers. In all the shot gathers presented in the section 8.4.1, the geophones were located along survey line L1.

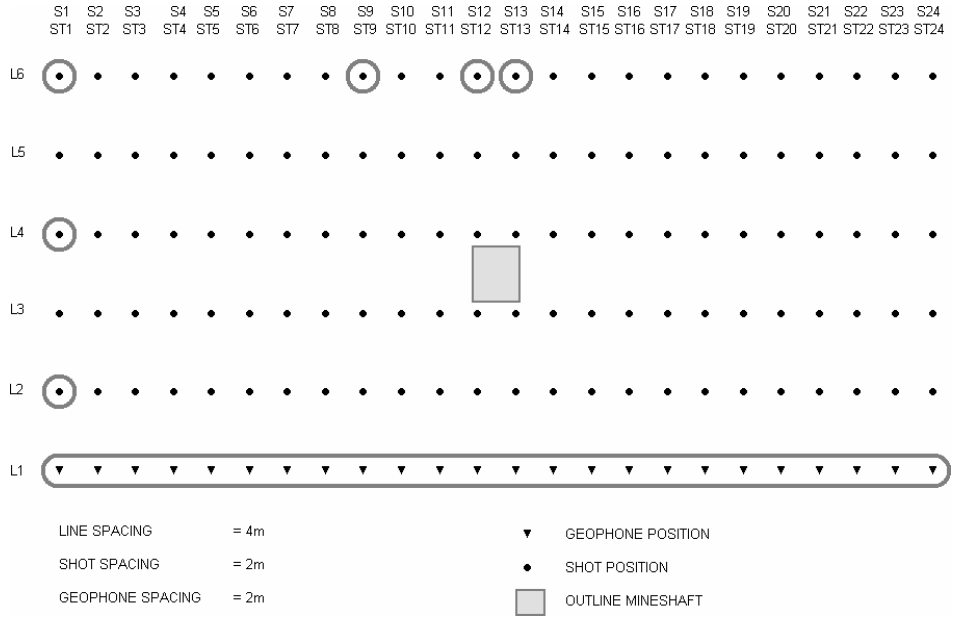

Figure 8.5. Survey grid at mineshaft 1; the selected shot points and the selected receivers are encircled

8.4.1. The shot gathers

In Figure 8.1 the seismograms of shot gather L2S1, L4S1 and L6S1 are presented. The traces were individually scaled and scaled by a factor of 2. The seismograms are presented on the left side and the interpretations of the anomalies in the seismograms are presented on the right side.

- All the three seismograms show dominant surface waves which consists of long wave packages. Similar surface waves are observed in model 3, presented in Figure 6.8 and Figure E-1. This is a result of the fact that the weathered bedrock is shallow.
- Anomalous amplitudes can be observed in all three of the seismograms. The anomalous amplitudes were caused by interference of diffracted surface waves with the later arriving surface waves. The areas with anomalous amplitudes are denoted with the event letter “a”. Although, not all of these areas can be

correlated directly to the location of the mineshaft, it is clear that most areas are associated with the receivers between 20m and 30m.

- High amplitudes were present at the receivers at 22m and 24m between 0.4s and 0.5s in shot gather L4S1 and L6S1. These high amplitudes bare a resemblance with the high amplitudes observed at survey line L2 and L3 of model 3 presented in Figure E-1.
- Interference of diffracted surface waves caused patches in the seismogram of shot gather L6S1 where an area with high surface wave amplitudes is enclosed by an area with low surface wave amplitudes. The patches can be observed around 0.3s. Similar patches were observed at survey line L4 and L5 of model 3 in Figure 6.8.
- Diffraction events can be observed in shot gathers L2S1 and L4S1. The diffraction event in L2S1 appeared to be surface waves. The diffraction event in L4S1 was likely to be a diffracted refracted P-wave. The apexes of both diffraction events were related to the receivers located closest to the mineshaft.

In Figure 8.7 an enlargement of sections of the seismograms is presented.

- In each seismogram diffracted events can be observed. In all three of the enlarged seismograms the diffracted event consisted of diffracted refracted P-wave. In shot gather L6S1 an additional diffracted event can be observed. This diffracted event possibly originates from the SP-wave i.e. a shear wave converted on the deposits-bedrock interface to a refracted P-wave. The apexes of all the diffracted events correlated to the position of the mineshaft.

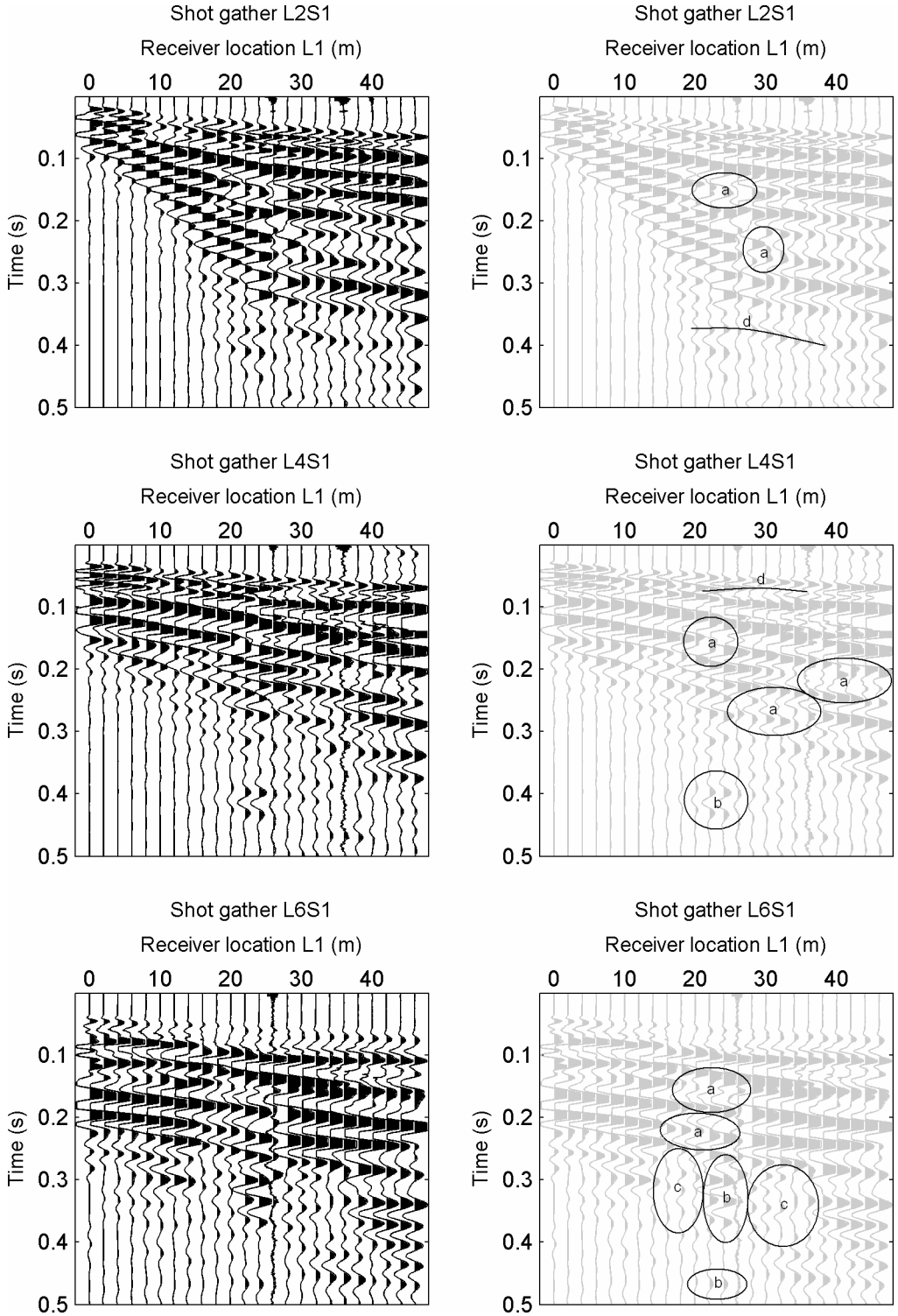

Figure 8.6. Seismogram of shot point L2S1, L4S1 and L6S1 and the interpretation: a – anomalous amplitudes due to interference, b – anomalous high amplitudes, c – anomalous low amplitudes, d – diffraction event

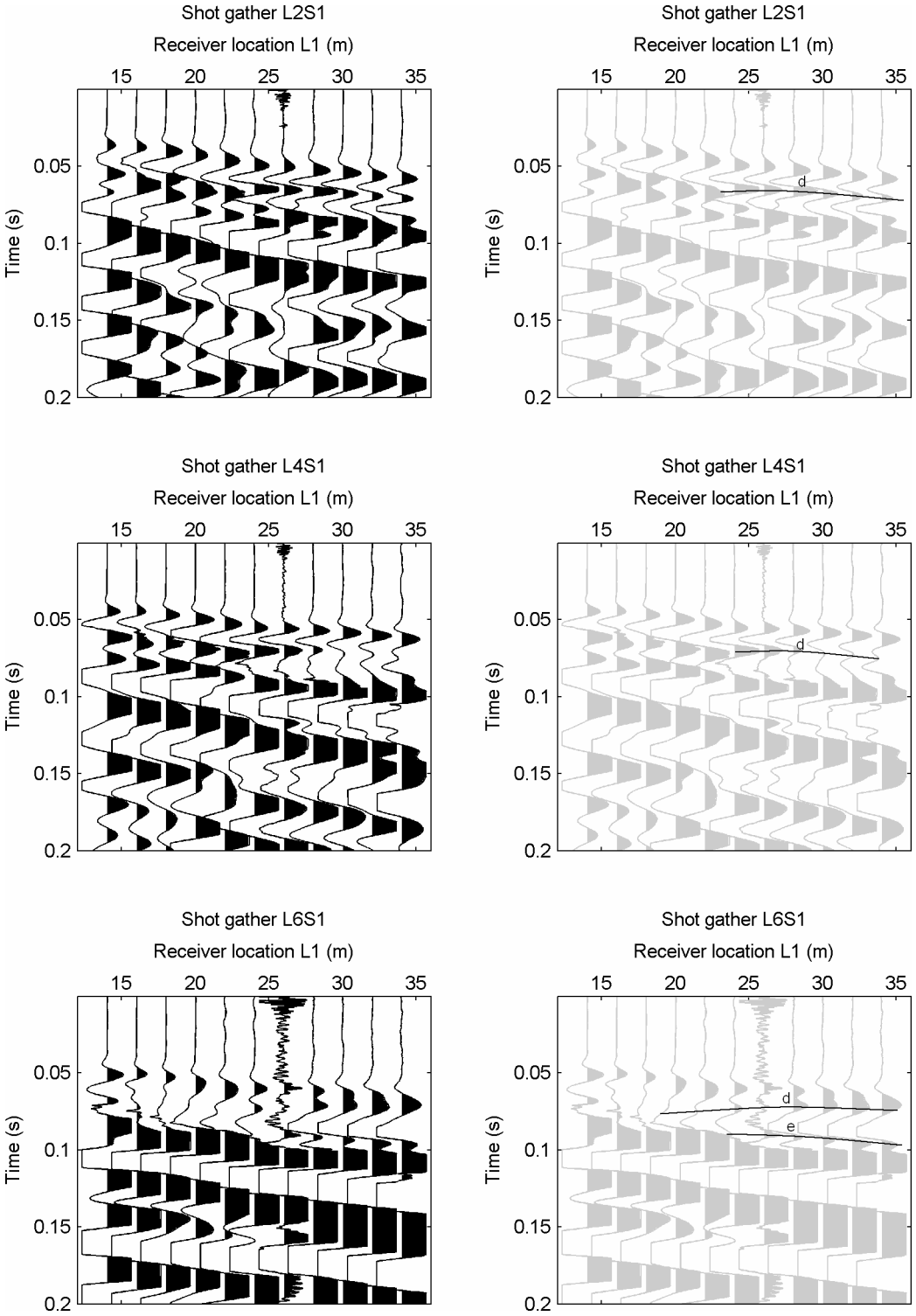

Figure 8.7. Details of the shot gathers; d – diffraction of refracted P-wave, e – diffracted SP-wave

In Figure 8.8, the seismograms of the shot gathers L1 S9, L1 S12 and L1 S13 are presented. The traces are individually scaled by a factor of 2.

- Similarly to the shot gathers presented previously and the shot gathers of model 3, the seismograms are dominated by surface waves.
- Anomalous amplitudes can be observed at the receivers located closest to the mineshaft between 16m and 28m. These amplitudes were caused by interference of diffracted surface waves.
- The amplitudes of the surface waves were strongly affected by the presence of the mineshaft. This renders the seismograms very complex and erratic. The interference was particularly strong in the shot gathers L6S12 and L6S13. In these shot gathers the sources were located close to the mineshaft.
- Observing the positive amplitude, the surface waves appeared to be delayed. The delay is observed at the receivers opposite to the mineshaft at 22m to 28m in shot gather L6S12 and L6S13 and was marked by the letter “h”.
- In shot gather L6S13 a phase jump of the surface waves can be observed at the receivers at 8m and 40m. Both distances are around 16m from the centre of the mineshaft. It is very likely that these phase jumps were related to the presence of the mineshaft. Although these phase jumps were not observed in the numerical model 3, but can be observed in for example model 5 in Figure 6.10 and Figure E-2 and model 14 in Figure 6.22.
- In the figure the estimated first breaks are also shown. It is clear that the first breaks at the receivers opposite of the mineshaft 22m to 26m were delayed by approximately 2ms. Note that in shot gather L6S12 and L6S13 the shot points were located closest to these receivers. Nevertheless an apparent delay was observed. In section 8.5 on page 210 more analysis regarding the first break can be found.

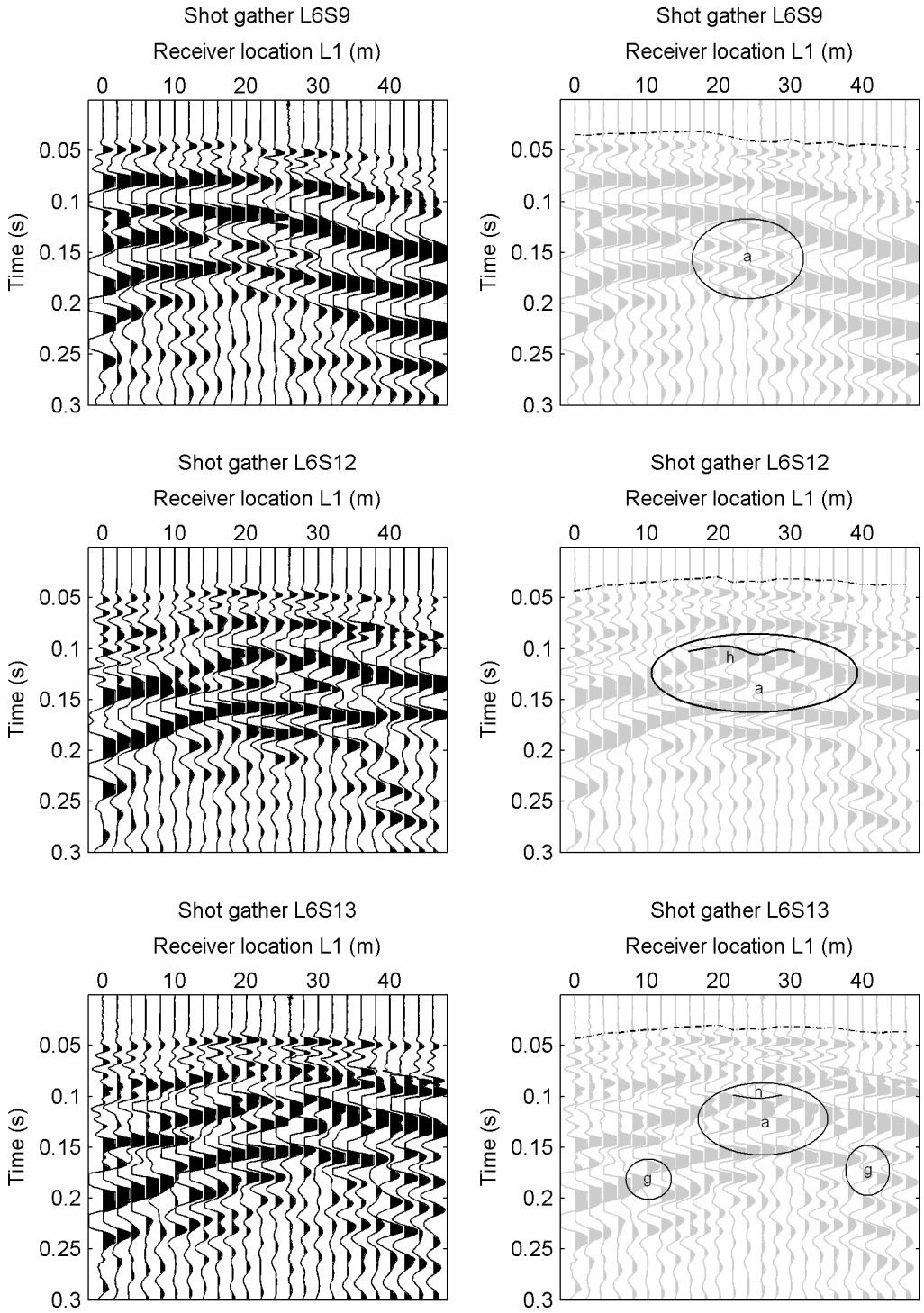

Figure 8.8. Seismogram of L6S9, L6S12 and L6S13; marker: a – anomalous amplitudes, e – Rayleigh wave, f – diffracted Rayleigh wave, g – phase jump, h – delayed Rayleigh wave, dash line – estimated first break

8.5. Analysis

In this section the analysis of the seismograms of field experiment at mineshaft 1 is presented. Similar to the analysis of the synthetic seismograms presented in chapter 7, the first breaks, the dominant frequencies, the maximum amplitudes and the amplitude of the first event were determined and analysed. Only the seismograms of broadside shot gathers were examined. The data consisted of four sets of data:

- Shot points located at L6 and receivers located at L1
- Shot points located at L5 and receivers located at L1
- Shot points located at L1 and receivers located at L6
- Shot points located at L2 and receivers located at L6

8.5.1. First break

The first breaks were hand picked and hence they are subjected to human interpretation and errors. Additionally the geophones were vulnerable to the strong winds creating noise. The low signal-to-noise ratio makes it difficult to pick the first breaks. The receiver at 26m was characterized by constant noise.

The results of the determination of the first breaks of the shot points at L6 and L5 can be found in Figure 8.9 and at L1 and L2 in Figure 8.10. For convenience the location of the shot point was marked with a dotted line. The centre of the mineshaft was located around 23m. It should be mentioned that the file with shot gather L2 S9 is corrupt and hence missing from the figures.

- From both figures it is clear that the travel time curves were not smooth. This was partially caused by the error in picking the first breaks due to the presence of noise and partially due to subjective nature of the human eye.

- In Figure 8.9 it can be observed that the first break at shot point S1 at 0m was slower than at the other side of the survey area at shot point S24 at 46m. This was caused by the dip in refractor layer.
- The minimum travel time at each shot point is normally located opposite the shot point where the travel distance from shot point to the geophone is the shortest, although the geological variations can cause some deviations. In most of the figures this can be observed, however in the L5 curve of shot point S13 (24m), S14 (26m) and to a lesser degree in the curve of shot point S12 (22m) a delay can be observed at the geophones opposite the shot point. These geophones were approximately located in the shadow zone of the mineshaft. The delays were in the order of 2-4ms and larger than the delays observed in the numerical models. The difference might be explained by the fact that the mineshaft causes de-stressing in the bedrock. The velocities in de-stressed rocks are lower and the models do not include de-stressed rocks.
- The first breaks of shot gathers L6S12-S14 (22m-26m) showed also a small delay, albeit the delay is a bit smaller and less noticeable than the shot points at L5.
- The first break curves of L1 and L2 in Figure 8.10 do not exhibit any obvious delays. The seismograms corresponding to these curves are characterized by strong noise caused by the prevailing wind. However, at shot points S10 (18m) and S11 (20m) the travel time curves appear very straight without the typical curvature. It is unclear if this was caused by the presence of the mineshaft or due to picking error. Furthermore at shot point S14 (26m) there was noticeable delay recorded at the geophones at 12-20m. These geophones were located in the shadow zone of the mineshaft.

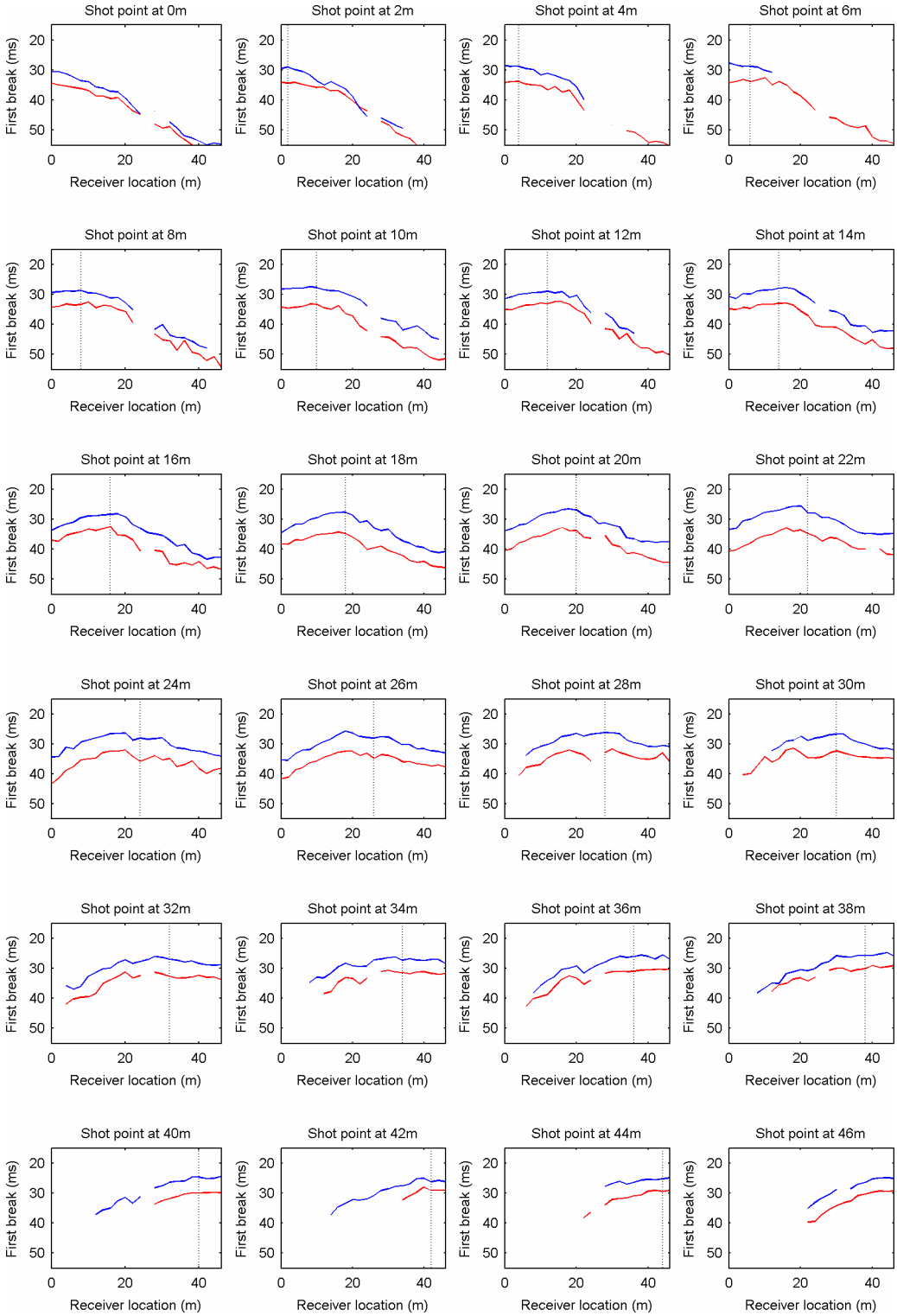

Figure 8.9. The estimated first break of the shot points at L5 (blue) and L6 (red) with the receivers at L1

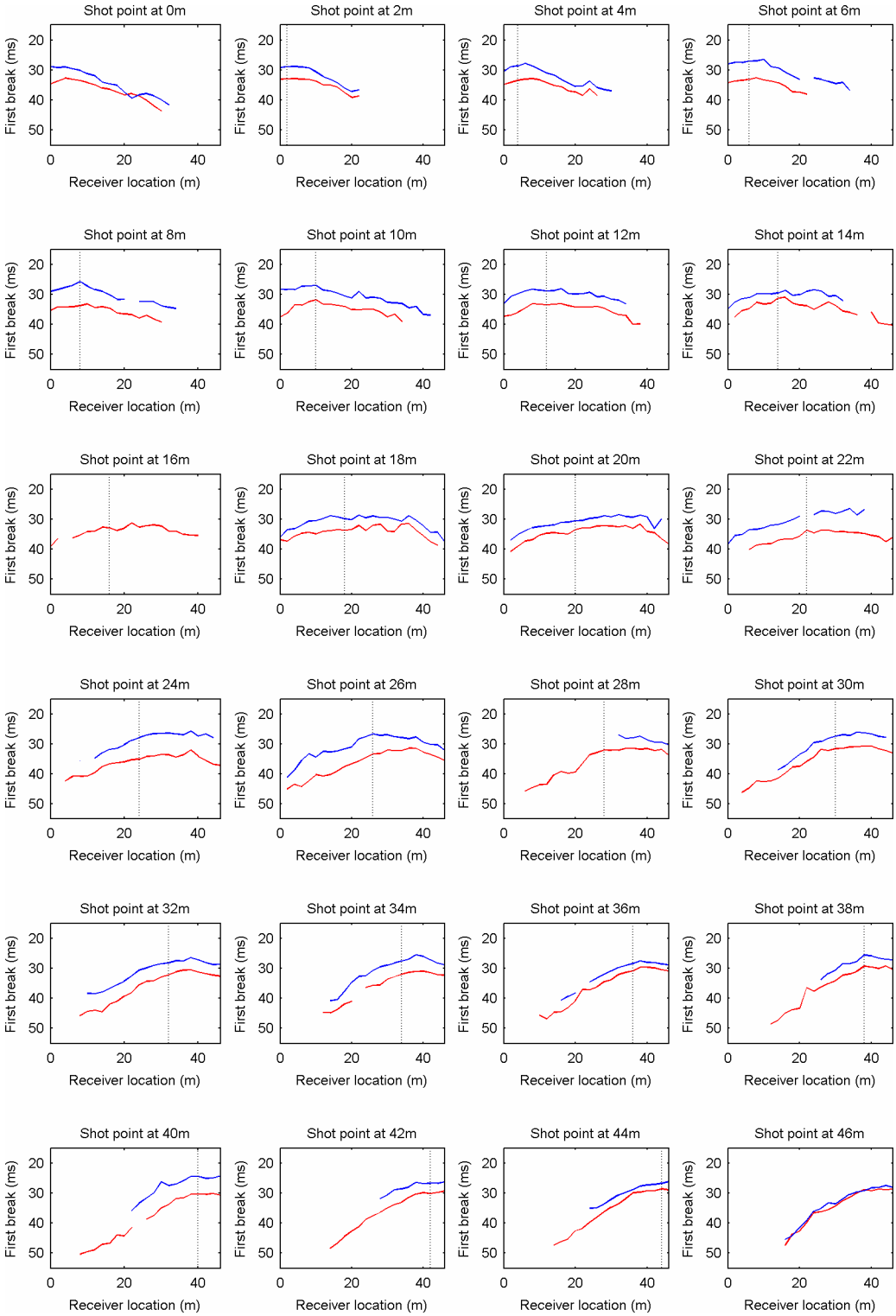

Figure 8.10. The estimated first break of the shot points at L2 (blue) and L1 (red) with the receivers at L6

8.5.2. Dominant frequencies

The dominant frequencies of each spectrum were determined using the MATLAB scripts as in section 7.1.2 and the results of the shot gathers with the shot points at L5 and L6 are presented in Figure 8.11. Figure 8.12 contains the results of the shot points at L1 and L2. The results of the numerical modelling showed that high frequencies can be expected at both sides of the shadow zone. However, model 3 showed erratic behaviour and frequency anomalies were difficult to correlate to the position of the mineshaft.

- The curves of the dominant frequencies were erratic for most shot gathers. It is unclear whether this was caused by the presence of the mineshaft or caused by variations in the receiver response, or in the ground coupling, or in the geology or the strong noise content.
- The erratic behaviour was particularly striking at the shot points at L5, where the dominant frequency curves vary strongly at the shot points between 18m and 34m. Furthermore, at these shot points the dominant frequencies increased to maximum values of 45Hz. At the same shot point locations, but at survey line L6, the dominant frequencies increased from about 30Hz average to maximum frequencies of 40Hz.
- The dominant frequencies increased for shot points at 40m and further at survey line L5 and L6. This was likely to be caused by the fact that the bedrock becomes shallower at the greater distances.
- The dominant curves of survey line L1 and L2 show little to no obvious anomalies that can be related to the presence of the mineshaft. This might be caused by increased back ground noise.

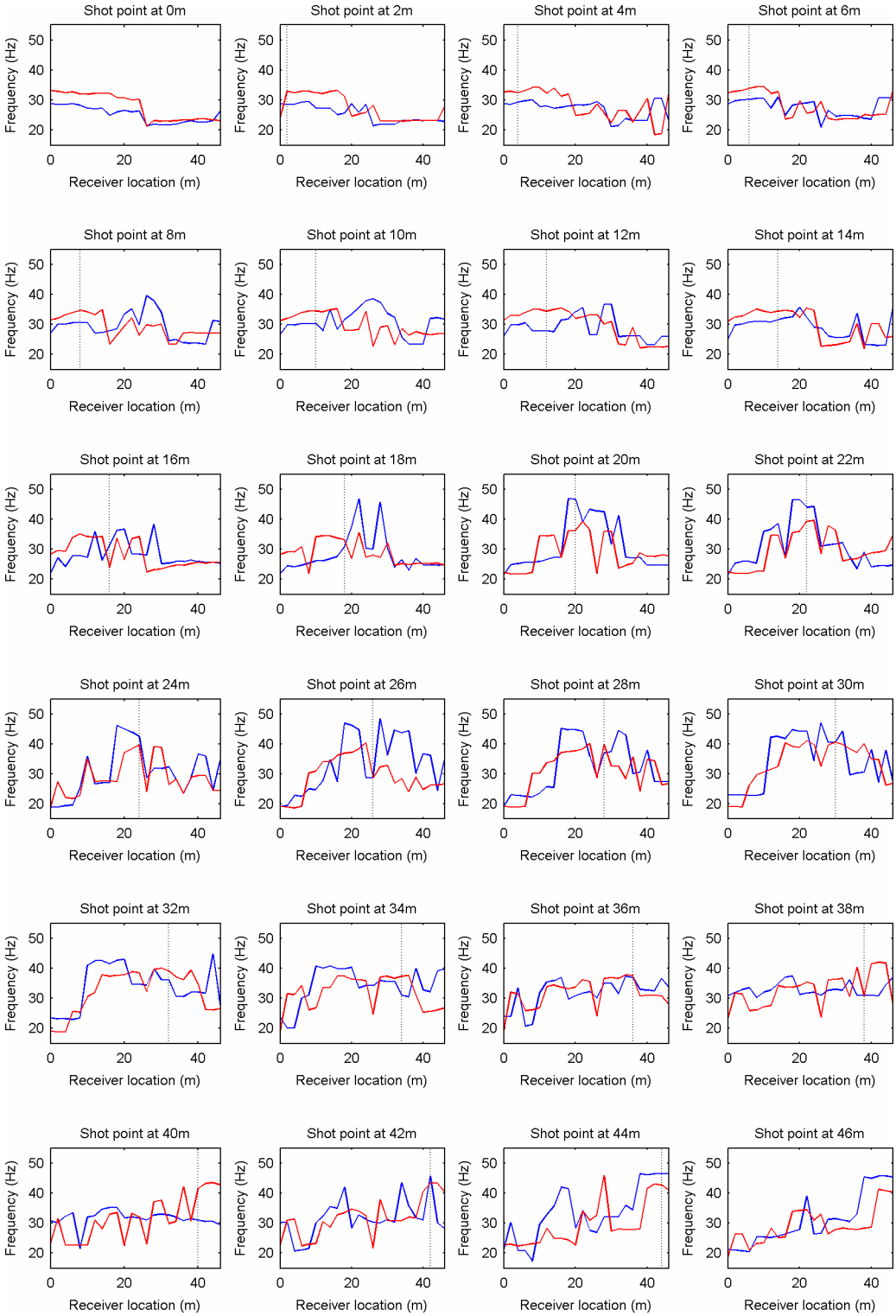

Figure 8.11. The calculated dominant frequencies of the shot points at L5 (blue) and L6 (red) with the receivers at L1

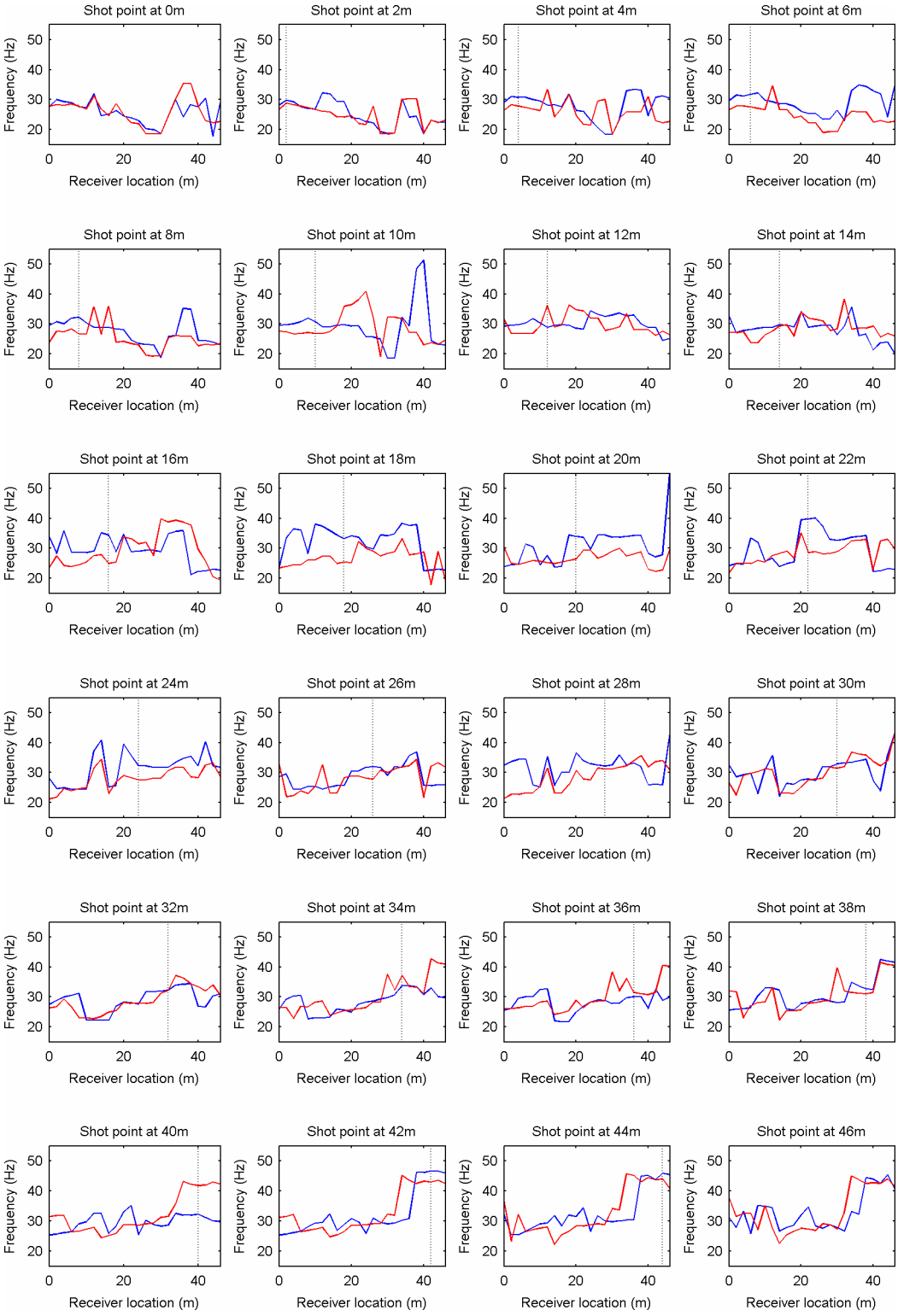

Figure 8.12. The calculated dominant frequencies of the shot points at L2 (blue) and L1 (red) with the receivers at L6

8.5.3. Maximum amplitude

The maximum amplitude of each trace was determined by using a MATLAB script. According to the numerical models, the amplitudes at the receivers in the shadow zone of the mineshaft increased, whereas a decrease in amplitudes could be observed at the receivers adjacent to this shadow zone. The results of the determination of the maximum amplitudes can be found in Figure 8.13 and Figure 8.14.

- Receivers located directly opposite of the shot points should normally exhibit the strongest amplitudes although local geological variations can affect the results slightly. Considering both figures, it can be observed that some geophones exhibit anomalous high amplitudes – for example the geophone at 6m and 22m in line L5 and L6. In line L1 and L2 the geophone at 20m exhibits anomalous amplitudes. A possible reason for this behaviour is that the receivers were not calibrated which results in a different output signal. Furthermore differences in local geology and the quality of the ground-geophone coupling can cause variations in the amplitude.
- Besides the strong anomalous maximum amplitudes observed at various geophones, the maximum amplitudes behave rather erratically. This can be particularly observed at the longer distances.
- It was difficult to interpret the data due to the anomalous strong amplitudes and the erratic behaviour of them.

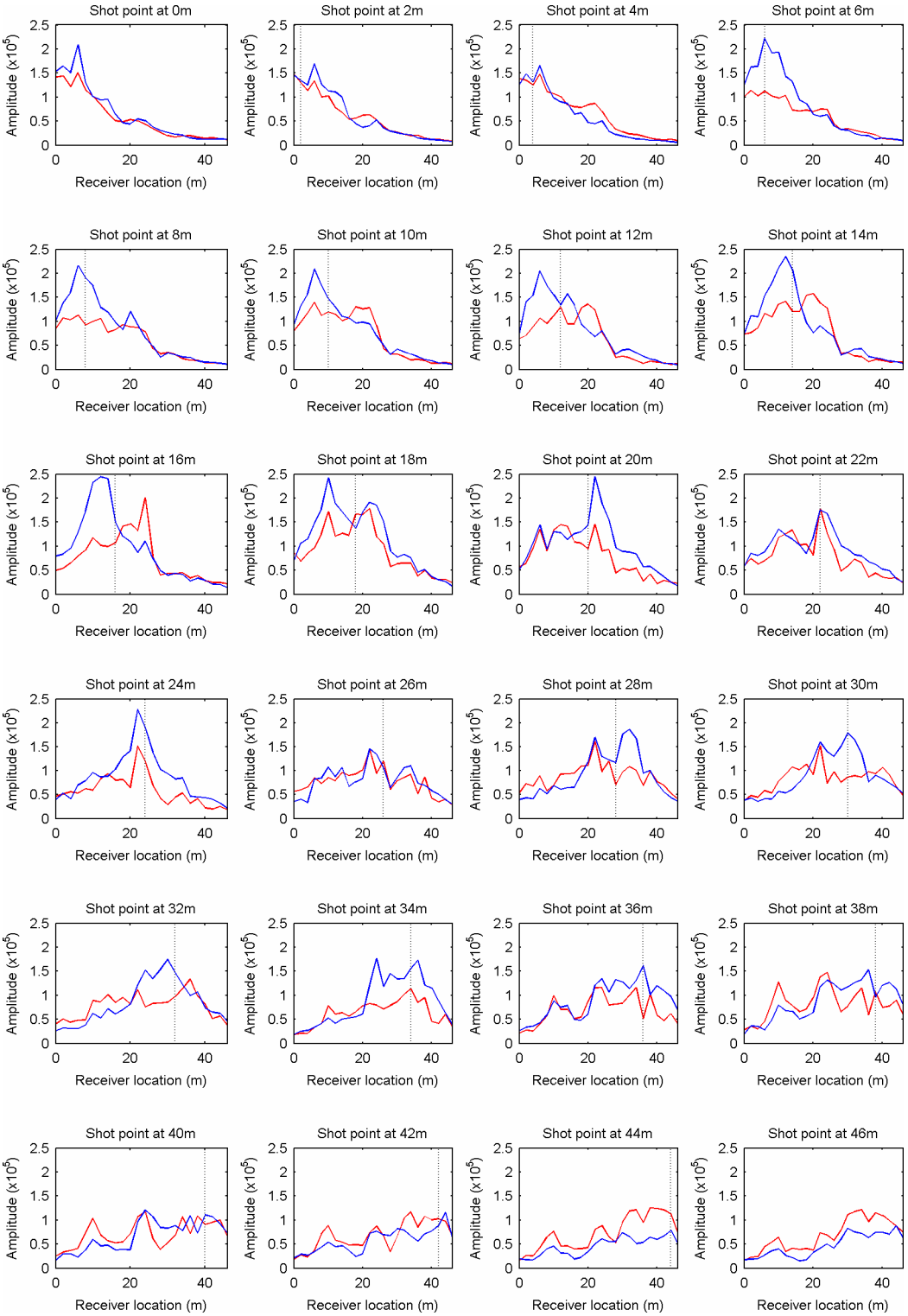

Figure 8.13. The maximum amplitudes of each trace of the shot points at L5 (blue) and L6 (red) with the receivers at L1

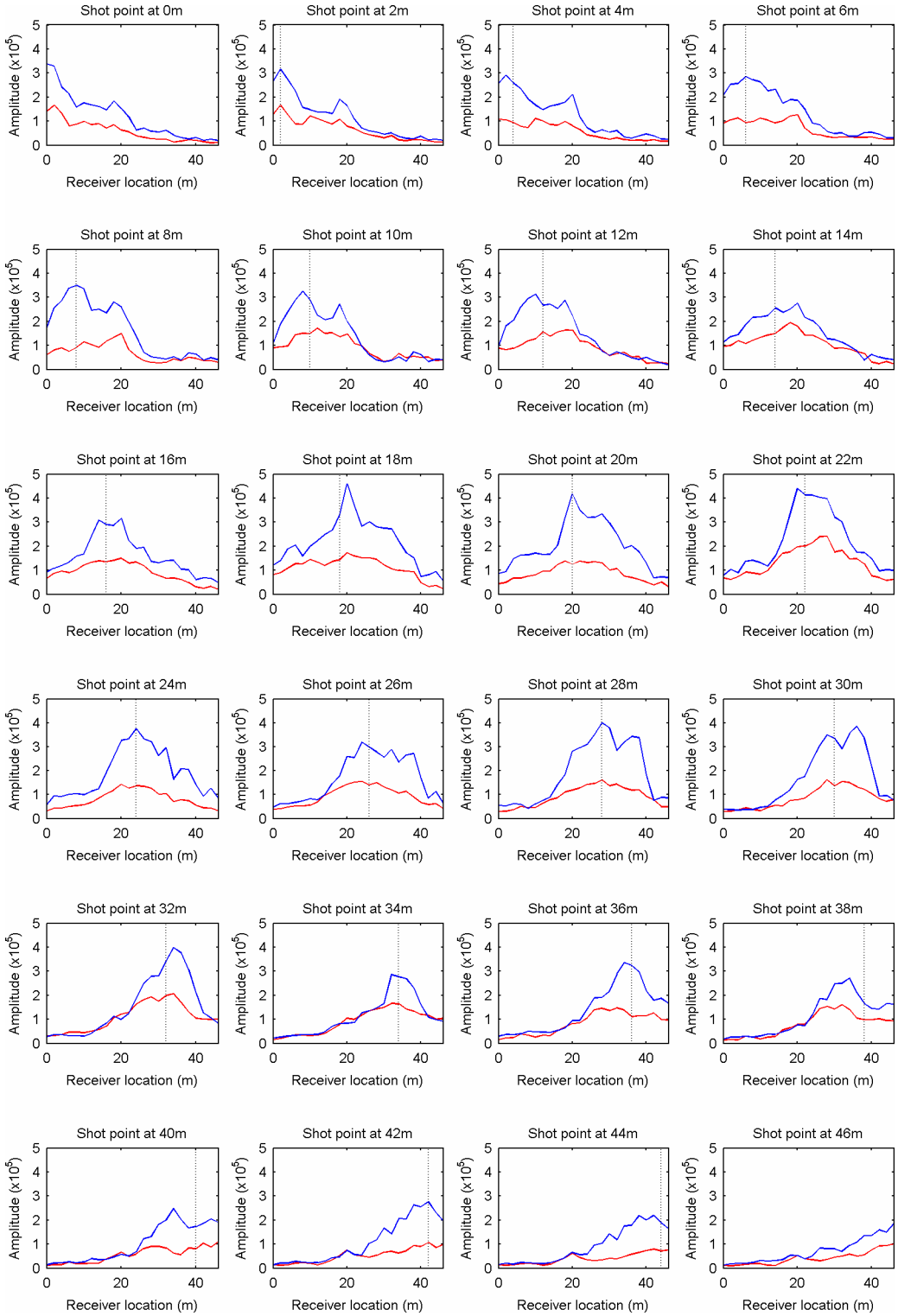

Figure 8.14. The maximum amplitudes of each trace of the shot points at L2 (blue) and L1 (red) with the receivers at L6

8.5.4. Amplitude of first arrival

In this section the results of the determination of the amplitudes of the first arriving events are presented. MATLAB scripts were written which determine the local maximum or minimum around a point which is hand picked by the user. The results can be found in Figure 8.15 and Figure 8.16.

- Similar to the maximum of amplitudes presented in Figure 8.13 and Figure 8.14, some of the receivers showed anomalous responses to the seismic waves compared to others. This involved in particular the receivers at 6m and 20m.
- The figures with the shot points at 22m to 30m at L5 and L6 show a distinctive W-shape anomaly with the source location approximately in the middle of this shape. The receivers directly opposite the source, e.g. the closest to the source, show smaller amplitudes of the first event than the adjacent receivers. This can be also observed at the shot point at 22m, although due to the erroneous behaviour of the geophone at 20m, it was difficult to reassert this statement.
- The amplitudes of the first arrival curve at shot point lines L1 and L2 in Figure 8.16 show less distinctive features compared to lines L5 and L6 in Figure 8.15. Overall the amplitudes of the first events were smaller. The differences were likely to be caused by changes in the source e.g. the person hammering the trigger plate. Furthermore the strong prevailing winds caused errors.

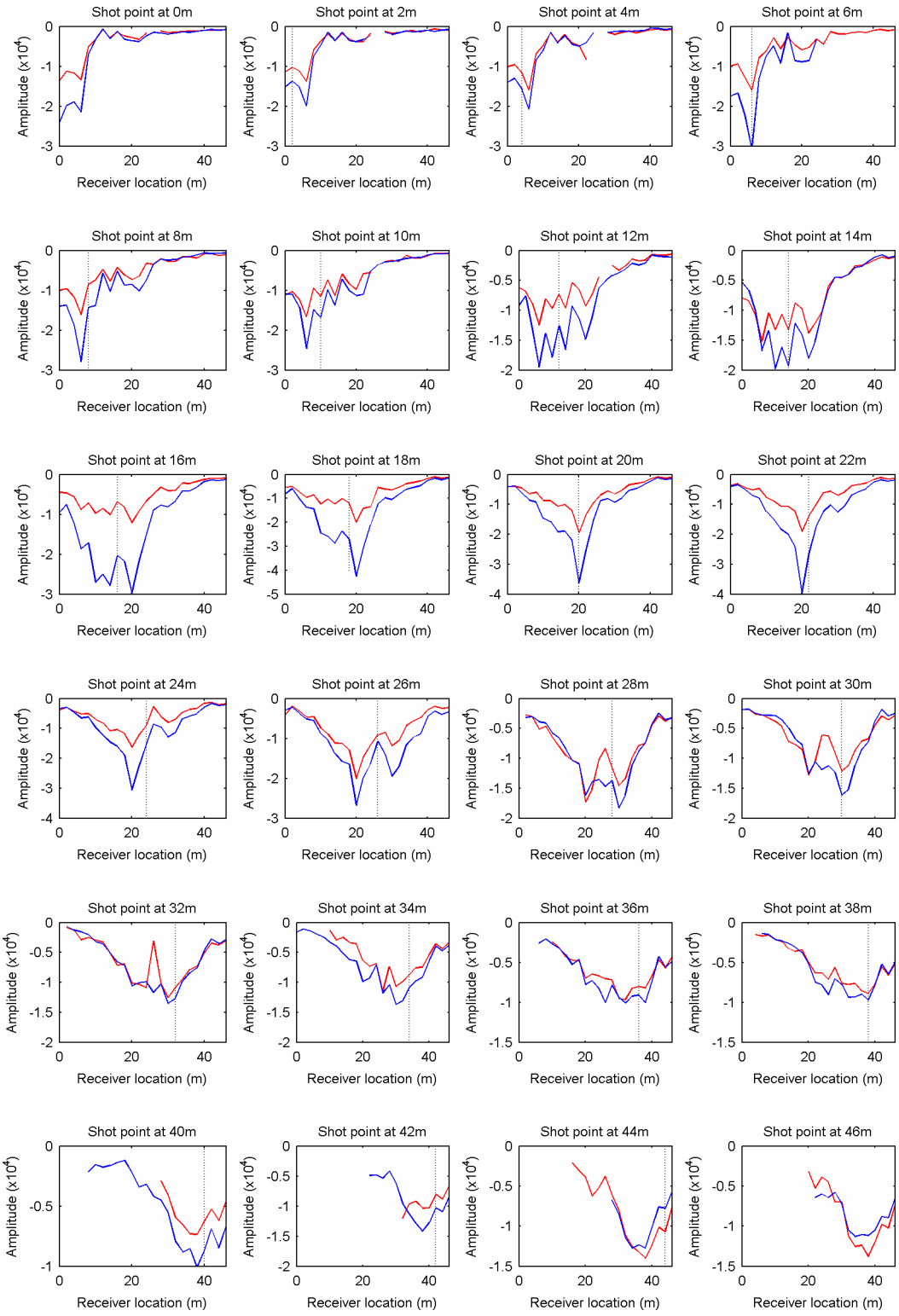

Figure 8.15. The amplitudes of the first arriving event of the shot points at L5 (blue) and L6 (red) with the receivers at L1

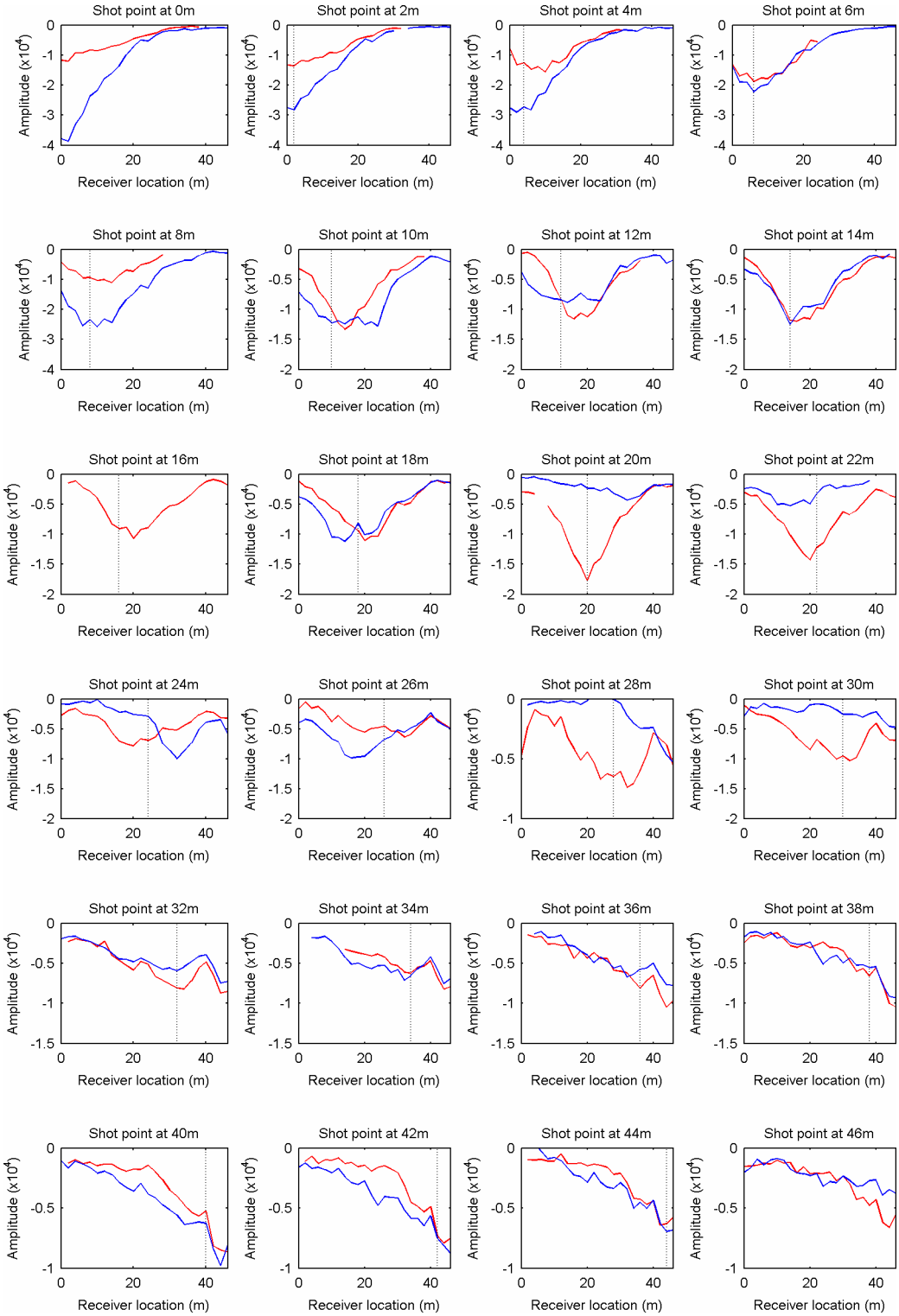

Figure 8.16. The amplitudes of the first arriving event of the shot points at L2 (blue) and L1 (red) with the receivers at L6

8.5.5. Mineshaft location

This section discusses the location of the capped mineshaft as if its location was unknown. The location of the mineshaft was estimated based on the anomalies observed in the seismograms and the attribute curves.

Figure 8.21 shows the interpretation of the experimental data by the author. The dark grey areas indicate high probability of the mineshaft location, whereas the light grey areas indicate medium probability. No colour indicates very low probability of the mineshaft location. Note that the shapes of the probability areas are not related to the outline of the mineshaft, but are merely an indication of the position of the mineshaft.

The probability figure was based on the following observations.

- Regarding the seismograms presented in Figure 8.6 and Figure 8.8.
  - Anomalous amplitudes were observed at the receivers between 20m and 30m. Additionally, anomalous high amplitudes were observed in shot gather L4S1 and L6S1 at the receivers at 24m and 26m.
  - Diffracted waves were observed in shot gather L2S1, L4S1 and L6S1. Their apexes were located around 25m.
  - Delays of the surface waves were observed in shot gather L6S12 and L6S13. In shot gather L6S12 the receivers at 24m and 26m exhibited the delay and in shot gather L6S13 the delay can be observed at 22m to 26m.
- Regarding the attribute curves presented in Figure 8.9 to Figure 8.16.
  - Anomalous first breaks were observed in the shot gathers with the shot points at 24m and 26m at L5 and L6 and the receivers located at L1. Furthermore a delay can be observed at the receivers between 16m and 20m at L2 in the shot gather with shot point at 26m.

- Strong erratic behaviour of the dominant frequencies was observed in the shot gathers with shot points between 18m and 34m and receivers along L5 and L6.
- The values of the amplitudes of the first arriving event showed a distinctive W-shape anomaly in the shot gathers with the shot points between 22m and 30m along L5 and L6.

The anomalies observed in the seismograms and the attribute curves, as mentioned in the previous bullet points, can be used to construct a map with the probability distribution of the mineshaft location. Unlike the synthetic data, the experimental data contains a significant amount of noise and the exact location of the mineshaft is difficult to ascertain from just one of the anomalies. However, gathering all the observations increases the density of observed anomalies within a part of the survey area and increases the confidence that an anomaly is present in that area.

For example, the first break anomalies observed in shot gather L5S13, L5S14 and L2S15 as shown in Figure 8.17 can be used when constructing the probability map. From the first break curve of the reference models presented in Chapter 7, it can be concluded that when there is no mineshaft present the first break curves are smooth parabolic shaped. Using this knowledge, first break anomalies can be identified easily as shown in Figure 8.17. Obviously the cause of these anomalies has to be located between the source and receiver. By marking the receivers for various shot points on the survey map the anomaly can be approximated as shown in Figure 8.18.

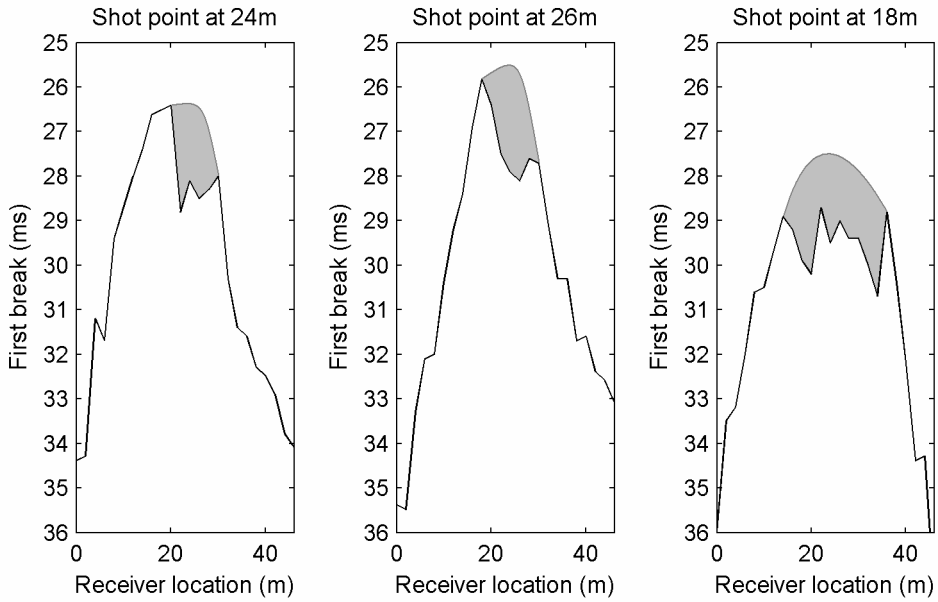

Figure 8.17. The first breaks of shot gather L5S13, L5S14 and L2S15; the grey area marks the difference between a smooth reference curve which would be observed when there is no mineshaft and the observed curve

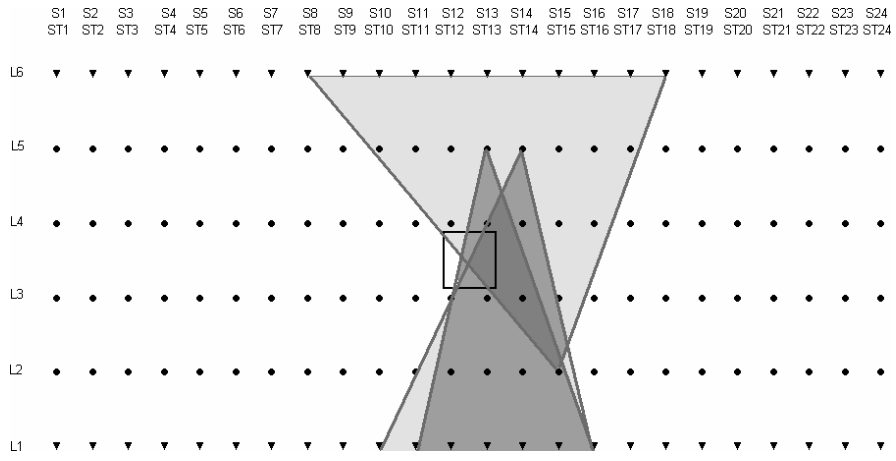

Figure 8.18. Outline of the anomalous first breaks observed in shot gather L5S13, L5S14 and L2S15

Similarly to the first breaks, the anomalous amplitudes observed in shot gather L6S14, L6S15 and L6S16 can be used to outline anomalies in the survey area (Figure 8.19). According to the amplitude curves of the numerical models, for example Figure 7.1, the peak is associated with the location of the mineshaft. According to Dresen (*1979*) the troughs are related to the sides of the mineshaft. By plotting the receivers associated with the peaks and troughs on a survey map, the anomaly causing the unusual amplitude values can be outlined as shown in Figure 8.20.

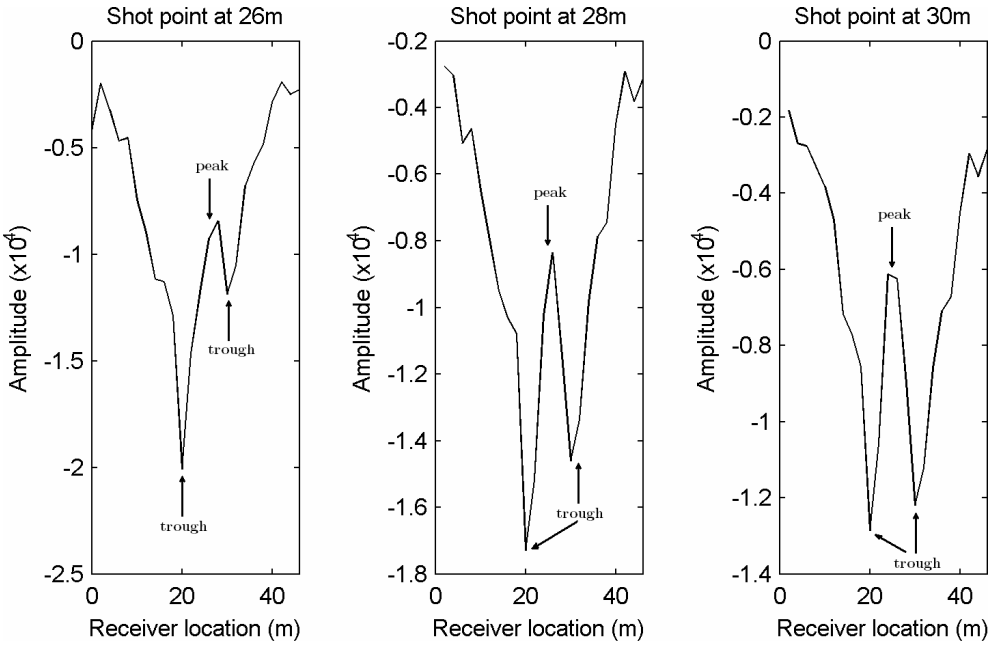

Figure 8.19. The amplitude of the first event of shot gather L6S14, L6S15 and L6S16 with the anomalous amplitude peak and trough values marked

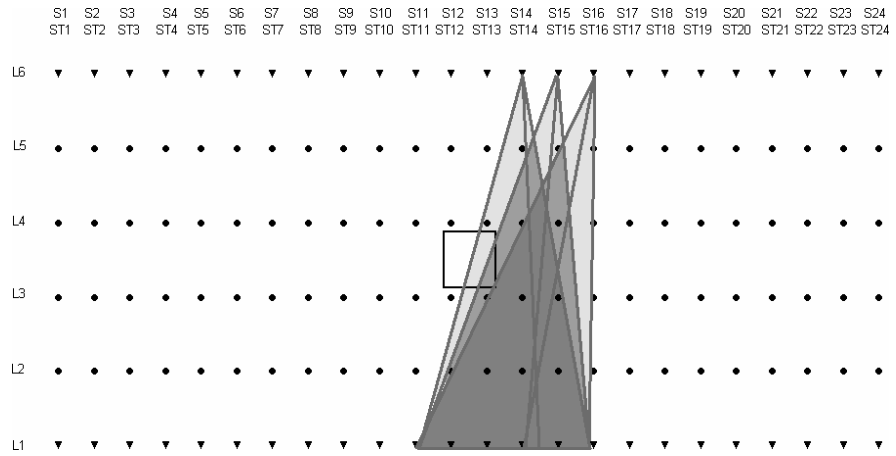

Figure 8.20. Outline of the anomalous amplitudes of the first events in L6S14, L6S15 and L6S16

Due to the fact that no anomalous amplitudes were observed when reversing the survey e.g. receivers at survey line L6 and shot points along L1 and L2, the anomaly is less clear compared to Figure 8.18.

However, when combining Figure 8.20, Figure 8.18 and the observations in seismograms a map with the probability of a mineshaft can be generated (Figure 8.21). Although the map shows the probability of the location of the mineshaft and not the exact location of the mineshaft, this map can be used as a guide for the drilling program to determine the location of the mineshaft conclusively.

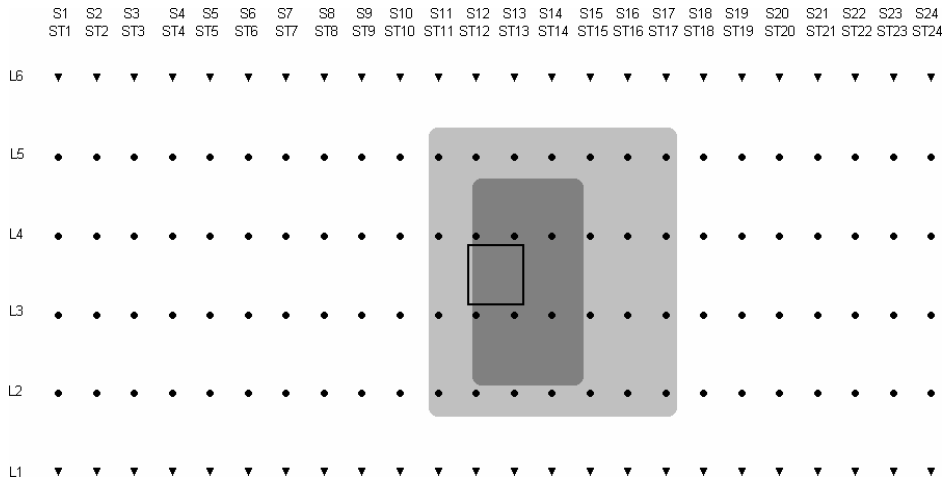

Figure 8.21. The probability of the mineshaft location: high probability (dark grey) and medium probability (light grey); mineshaft contour is outline by the black line

8.6. Mineshaft 2 - backfilled mineshaft

The second survey was conducted at the back filled mineshaft. This mineshaft had no surface expression and hence its exact location was unknown. Although all shot gathers were examined, it is impossible to show all the results of the survey. Therefore a selection of shot gathers was selected. Appendix G shows all the broadside shot gathers at mineshaft 2.

Similar to the capped mineshaft presented in section 8.6.1 six shot gathers are presented and analysed. The shot points were selected such they encircle the suspected area. The selected shot points are presented in Figure 8.22.

In section 8.7 the analysis of attributes of the broadside shot gathers with the shot points at L5, L6, L1 and L2 are presented.

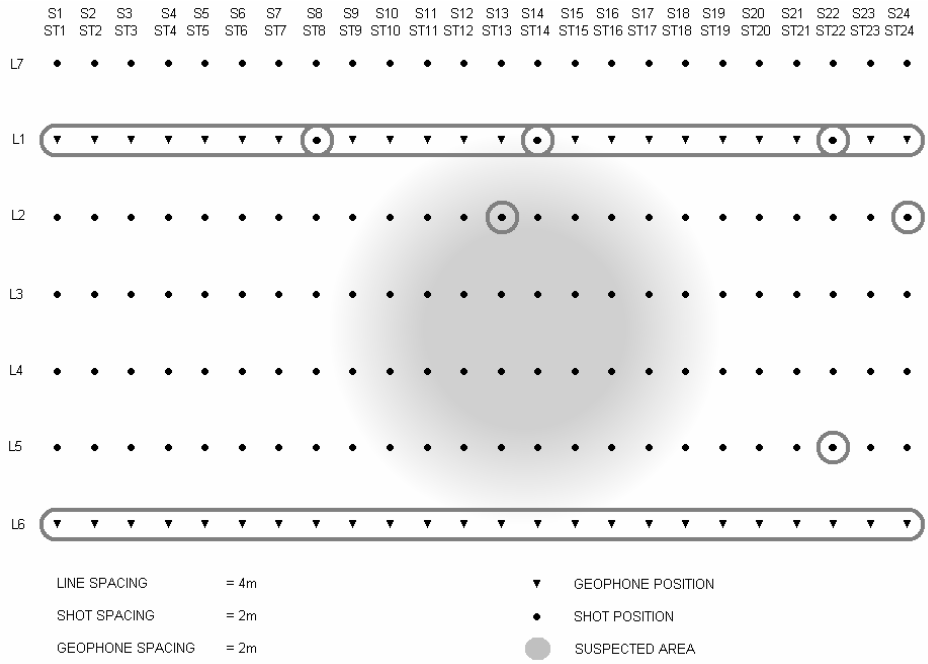

Figure 8.22. Survey grid at mineshaft 2; the selected shot points and the selected receivers are encircled

8.6.1. Shot gathers

The seismograms of shot gathers L1S8, L1S14 and L1S22 are presented in Figure 8.23 and seismograms of shot gathers L2S13, L2S24 and L5S22 are presented in Figure 8.24. The traces were individually scaled and amplified by a factor of 2. In Figure 8.23 various features can be identified:

- Anomalous amplitudes can be observed in all three the shot gather. These anomalies were associated with the receivers around 30m. These anomalous amplitudes were likely to be caused by superimposition with diffracted surface waves.
- In shot gather L1S14, anomalous low amplitudes can be easily observed at all the receivers. These low amplitudes were caused by superposition of surface waves with diffracted surface waves with an opposite phase. An interpretation

of the travel time curve of the diffracted surface wave was outlined by the marker d in the interpretation of the shot gather L1S14.

- In shot gather L1S14 the positive amplitude of the surface wave seems to be delayed by approximately 2ms.
- In shot gather L1S22 the surface waves seem to decrease in velocity at the receivers between 24m and 30m. Similar behaviour of surface waves over cavities have been observed by Grandjean and Leparoux (*2004*). They interpreted this behaviour as phase jumps caused by the void. However, in this case the apparent velocity change was actually caused by phase changes due to interference with the diffracted surface waves and the velocity does not actually change in reality. Similar behaviour can also be observed in the seismograms of model 15 to 18 in Figure 6.24.

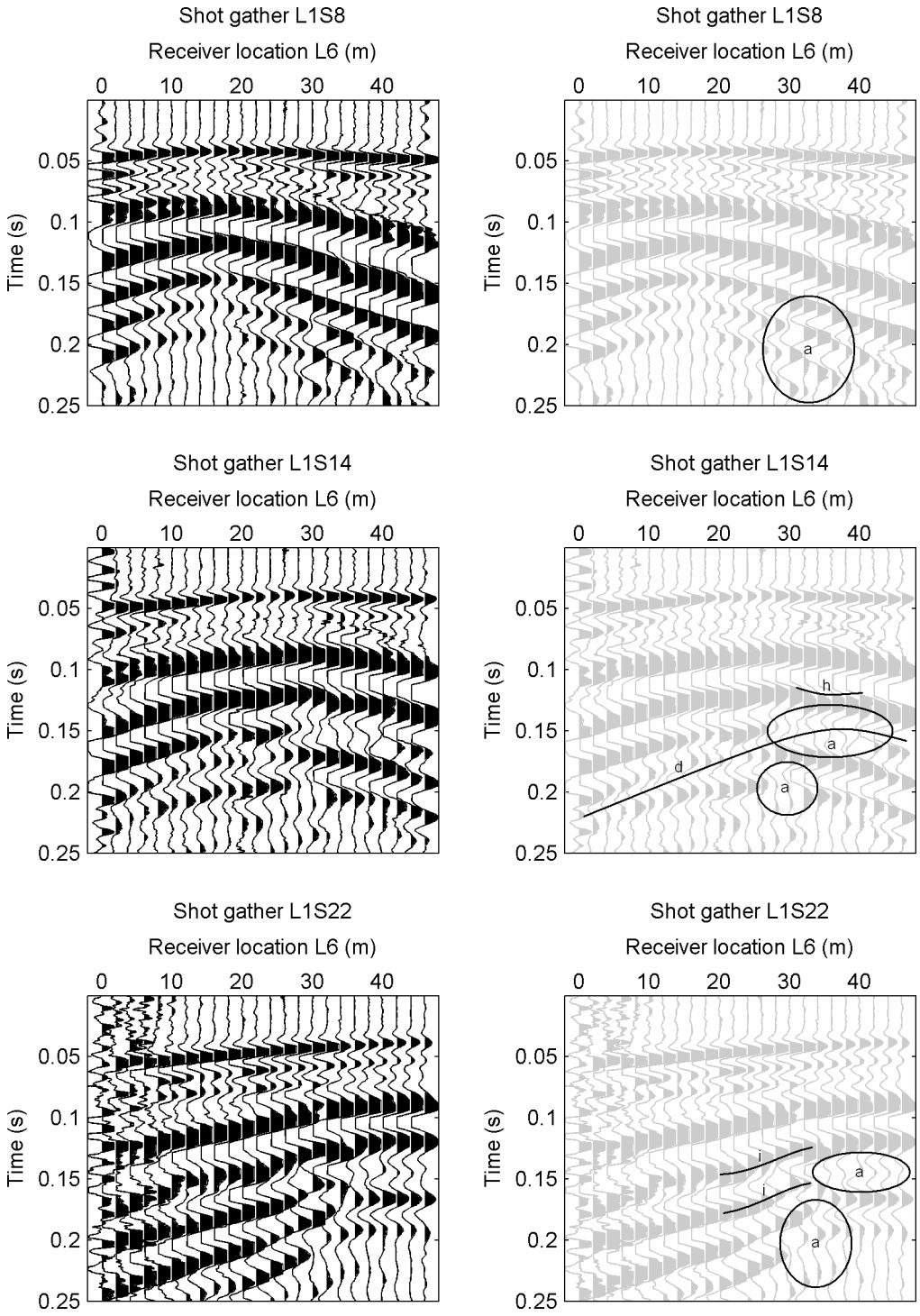

Figure 8.23. Seismogram of L1S8, L1S14 and L1S22; marker: a – anomalous amplitudes, d – diffracted wave, h – delayed surface waves, i – apparent velocity changes

In Figure 8.24 the seismograms of shot gathers L2S13, L2S24 and L5S7 are presented. These seismograms showed similar features identified in Figure 8.23:

- Anomalous amplitudes can be identified in shot gather L2S13 and L2S24. Similar to the anomalous amplitudes in Figure 8.23 these anomalies were located at the receivers around 30m.
- Similar to shot gather L1S14, anomalous low amplitudes can be observed. In shot gather L2S13 an interpretation of the travel time curve of the diffracted surface wave causing these anomalous low amplitudes was shown.
- An apparent velocity change caused by phase changes can be identified in shot gather L2S24.
- In shot gather L5S22 no obvious anomalies could be identified. This is symptomatic for most shot gathers with shot points at L6 and L5. A possible explanation is that the shot point was located close to the mineshaft.

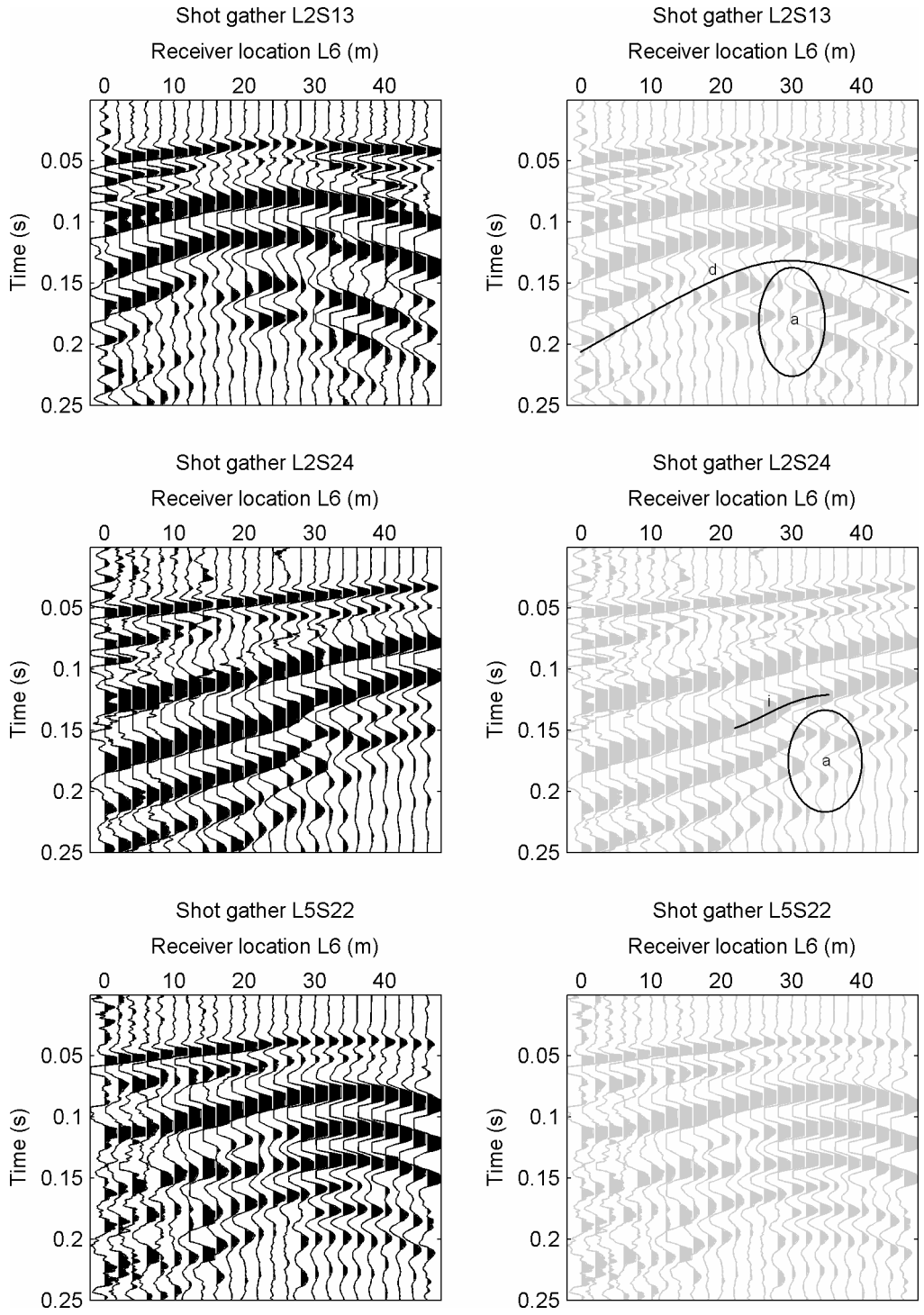

Figure 8.24. Seismogram of L2S13, L2S24 and L5S22; marker: a – anomalous amplitudes, d – diffracted wave, h – delayed surface waves, i – apparent velocity changes

8.7. Analysis

In this section the results of the analysis of the broadside shot gathers are presented. Similar to section 8.5 the data consisted of the following data sets:

- Shot points located at L6 and L5 with the receivers located at L1
- Shot points located at L1 and L2 with the receivers located at L6

8.7.1. First break

The results of the picked first break can be found in Figure 8.25 and Figure 8.26.

- Due to the low signal-to-noise ratio it was difficult to estimate the first break at the large source-receiver locations.
- The first break curves of shot gather S16 (30m) and shot gather S17 (32m) in Figure 8.25 showed that the travel times from the source at L5 were almost the same as the travel times from the source at L6. Furthermore the receivers located closest to the shot points exhibited a small delay of about 2ms when compared to the adjacent shot gathers. This delay decreased the further away the receivers were located. The delay might be caused by the lower velocity backfilling. The broad size of the delay suggested that the mineshaft was located close to the sources.
- Due to the reciprocity of the first breaks, the delays observed in Figure 8.25, should be able to be observed in Figure 8.26. Indeed shot gather S17 and the geophone at 32m exhibited a small delay when compared to shot gather S18 and the geophone at 34m. However, the delay is not observed at shot gather S16.

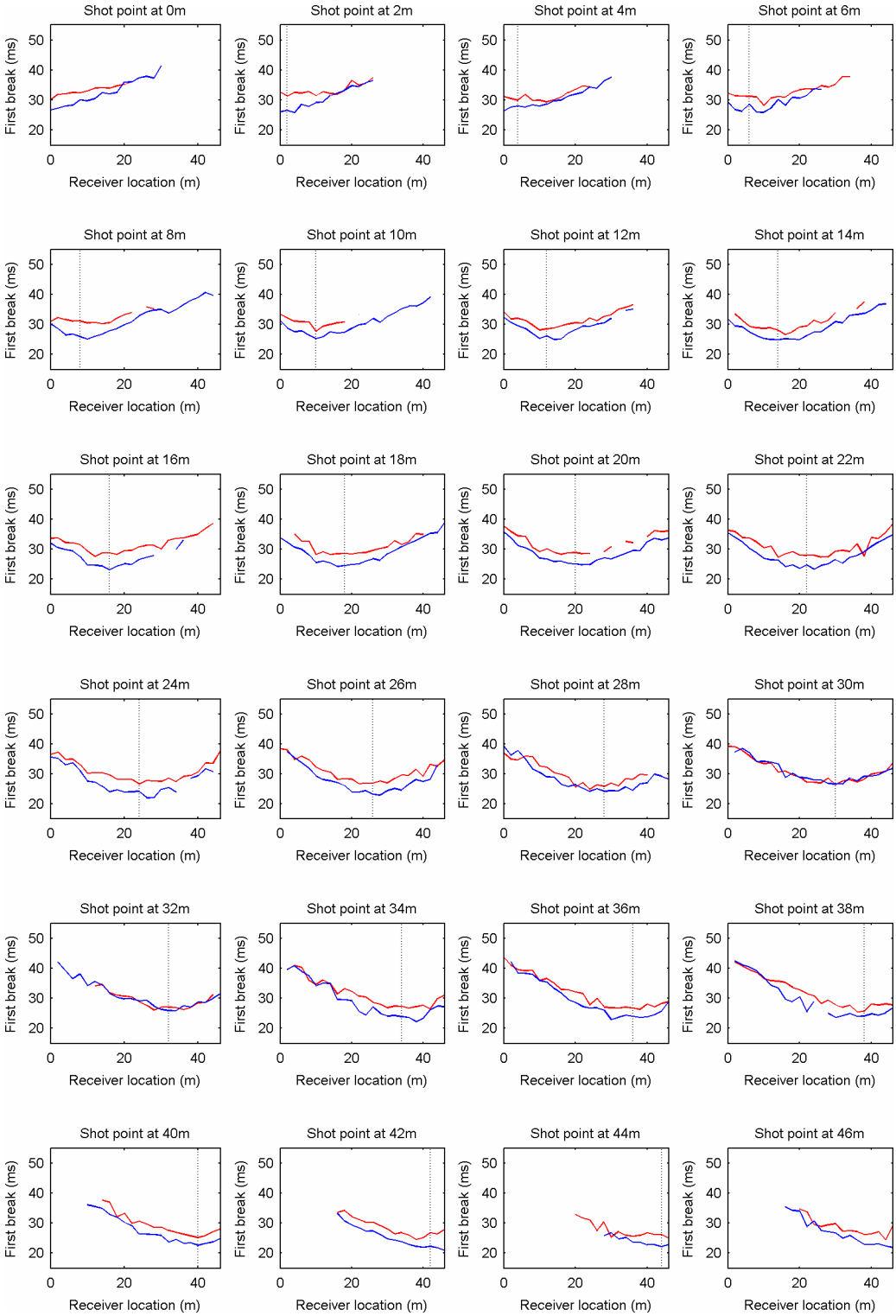

Figure 8.25. The estimated first break of the shot points at L5 (blue) and L6 (red) with the receivers at L1

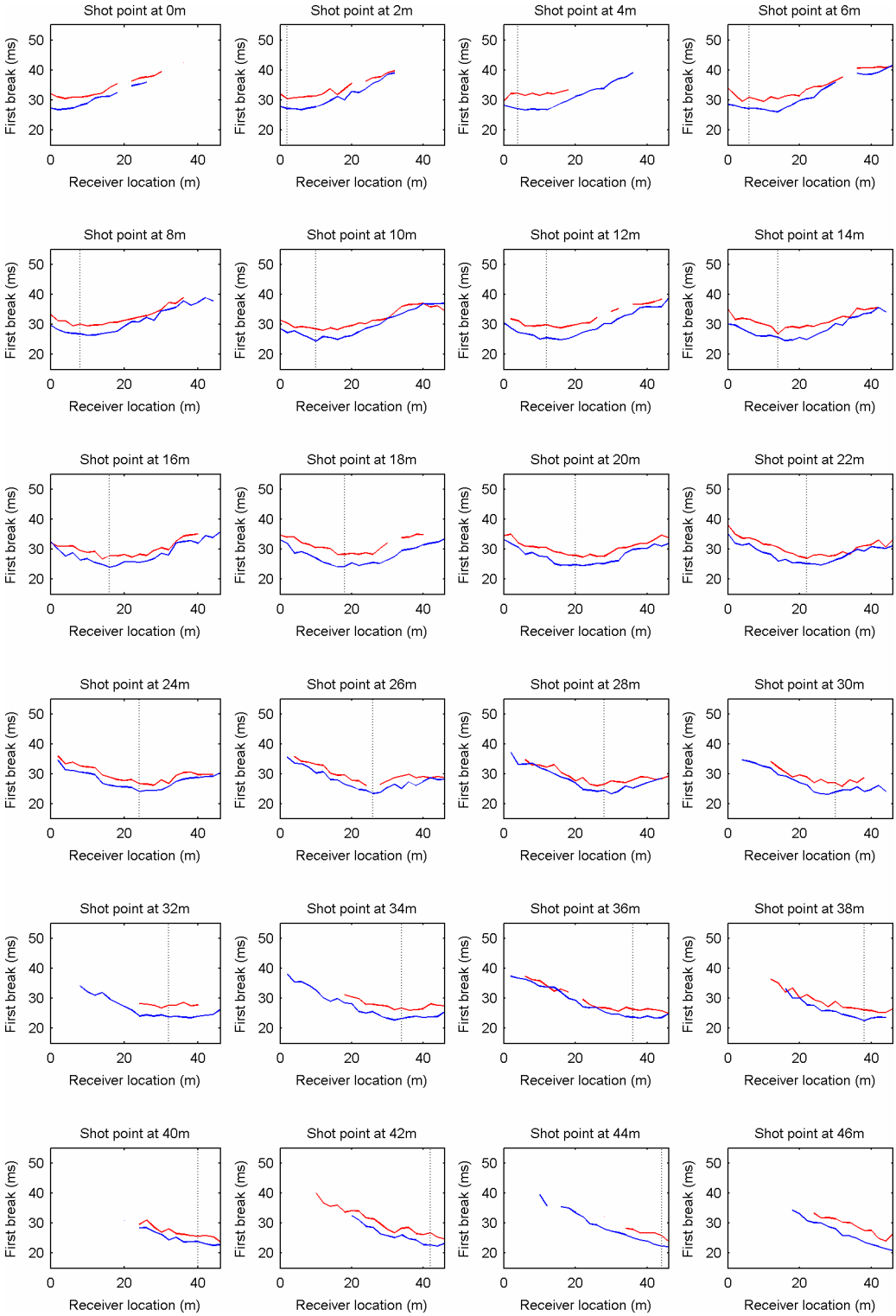

Figure 8.26. The estimated first break of the shot points at L2 (blue) and L1 (red) with the receivers at L6

8.7.2. Dominant frequencies

In this section the results of the calculations of the dominant frequencies at the backfilled mineshaft are presented. The results of the shot gathers with the shot points at L5 and L6 are presented in Figure 8.27, and in Figure 8.28 the results of the shot gathers with the shot point at L1 and L2 are presented.

- Very high frequencies can be observed at the edges of the survey lines. This is likely to be a result of the slow surface waves which are abruptly cut off in the seismograms. This only happens where the source is located far from the receivers.
- In Figure 8.27, a low frequency anomaly can be observed in shot point L6S1 (0m) to L6S6 (12m). This anomaly was located at the receivers between 10m and 14m. Since the anomaly did not move along with the source or in the opposite direction, it is likely that the cause of the anomaly was located directly below the receivers.
- Anomalous high frequencies can be observed in the figure of shot gather L5S15 and L6S16 (28m) and shot gather L5S16 (30m). The dominant frequencies at these shot gathers reached top values of 45Hz.
- The frequencies of the shot points at line L1 and L2 were more erratic compared to the ones at line L5 and L6. This is particularly the case at L5. Potential frequency anomalies related to the mineshaft were difficult to distinguish.

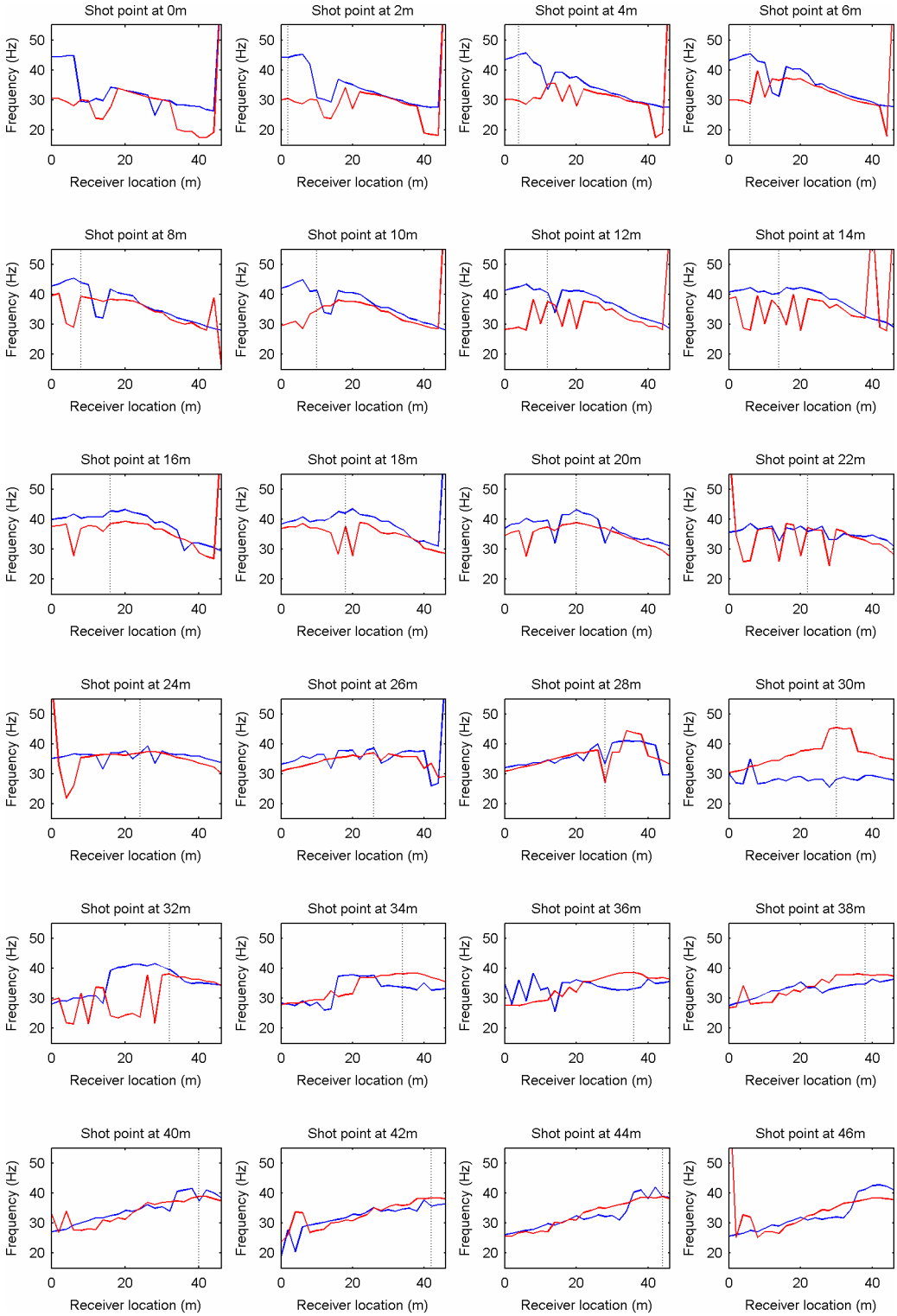

Figure 8.27. Dominant frequencies of the traces in the shot gathers L5 (red) and L6 (blue) with receivers at L1

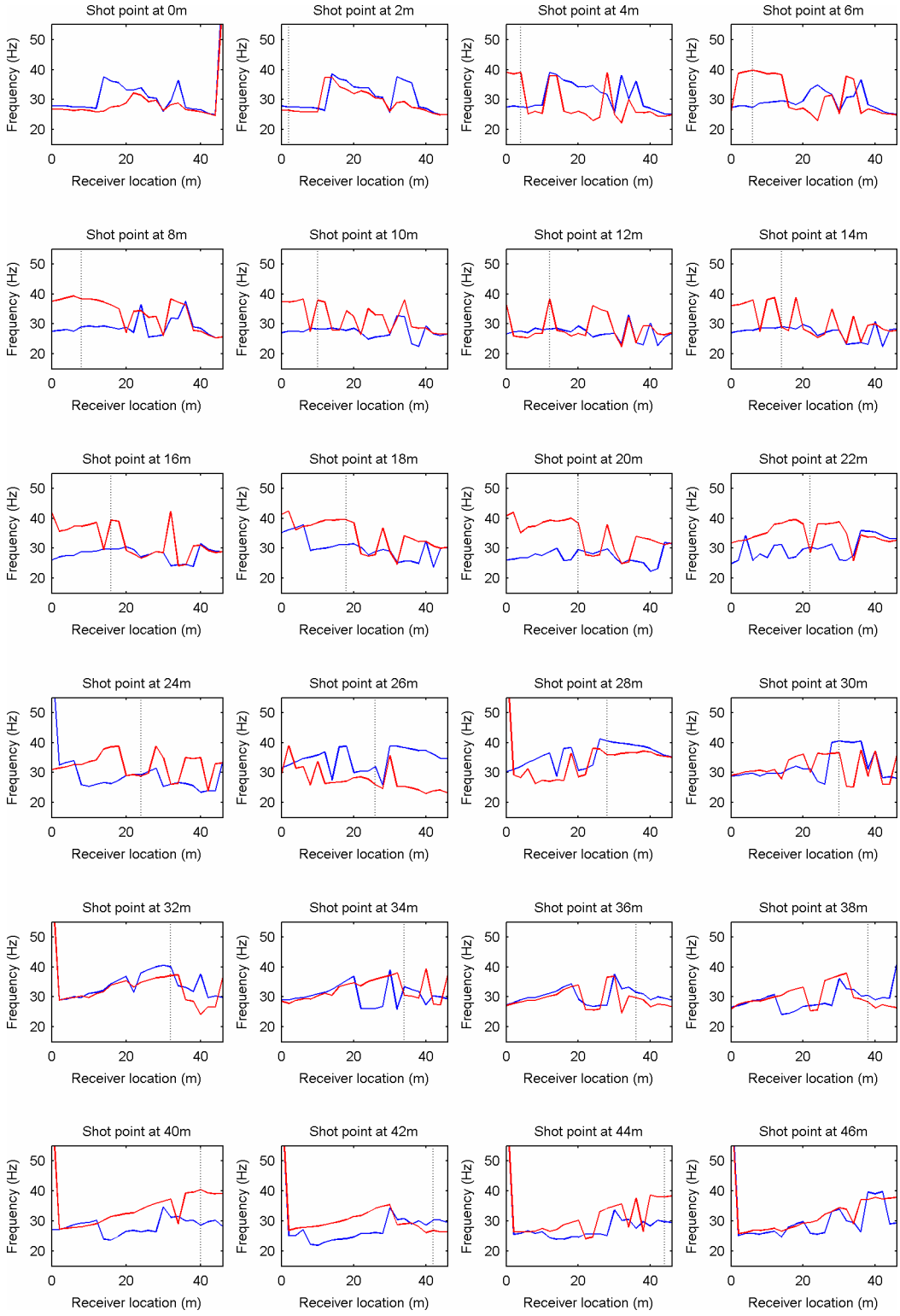

Figure 8.28. Dominant frequencies of the traces in the shot gathers L2 (red) and L1 (blue) with receivers at L6

8.7.3. Maximum amplitudes

In this section the results of the determination of the maximum amplitudes at the backfilled mineshaft are presented. In Figure 8.29 the results of the shot points at L5 and L6 with the receivers at L1 can be found and in Figure 8.30 the results of the shot points at L1 and L2 with the receivers at L6 can be found.

- Similar to the results of the maximum amplitudes at the mineshaft 1, some geophones exhibited stronger response to the signals. This was particularly obvious for the geophone at 14m.
- Regarding the shot points at line L5, the shot points S15-S17 (28-32m) exhibit anomalous low maximum amplitudes at receivers located at 28m to 34m. Similar low maximum amplitude values could be observed in shot points located at survey line L1 and L2.
- The amplitudes of shot gathers L6S17 (32m) and L6S18 (34m) appeared smaller than of the other shot gather. Although this might be related to the presence of the mineshaft near the shot point, it might be related also to the source.
- Regarding the shot point at line L1 and L2, anomalous low amplitudes could be observed at shot point S15-S17.

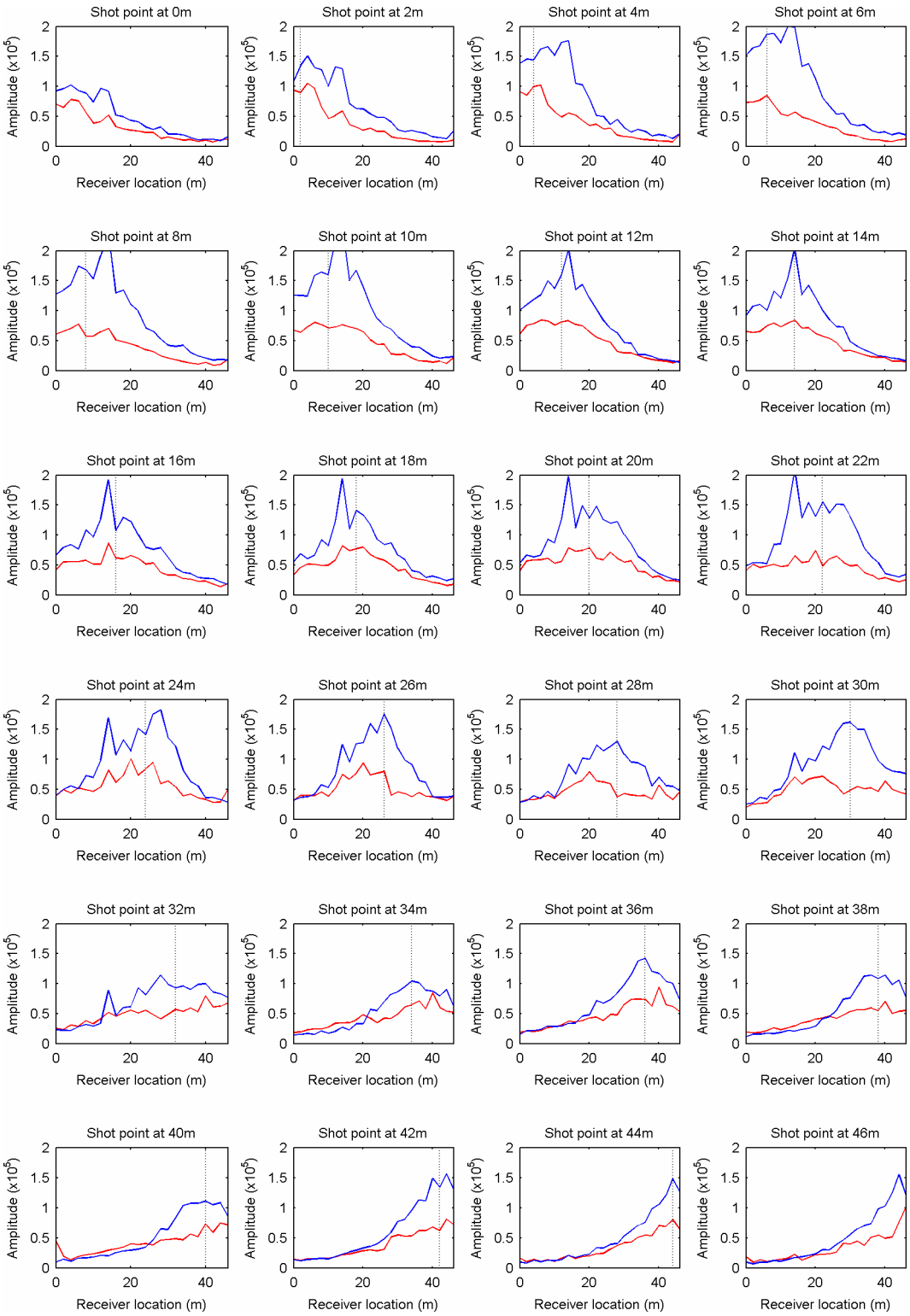

Figure 8.29. Maximum amplitudes of the shot gathers at L5 (red) and L6 (blue) with receivers at L1

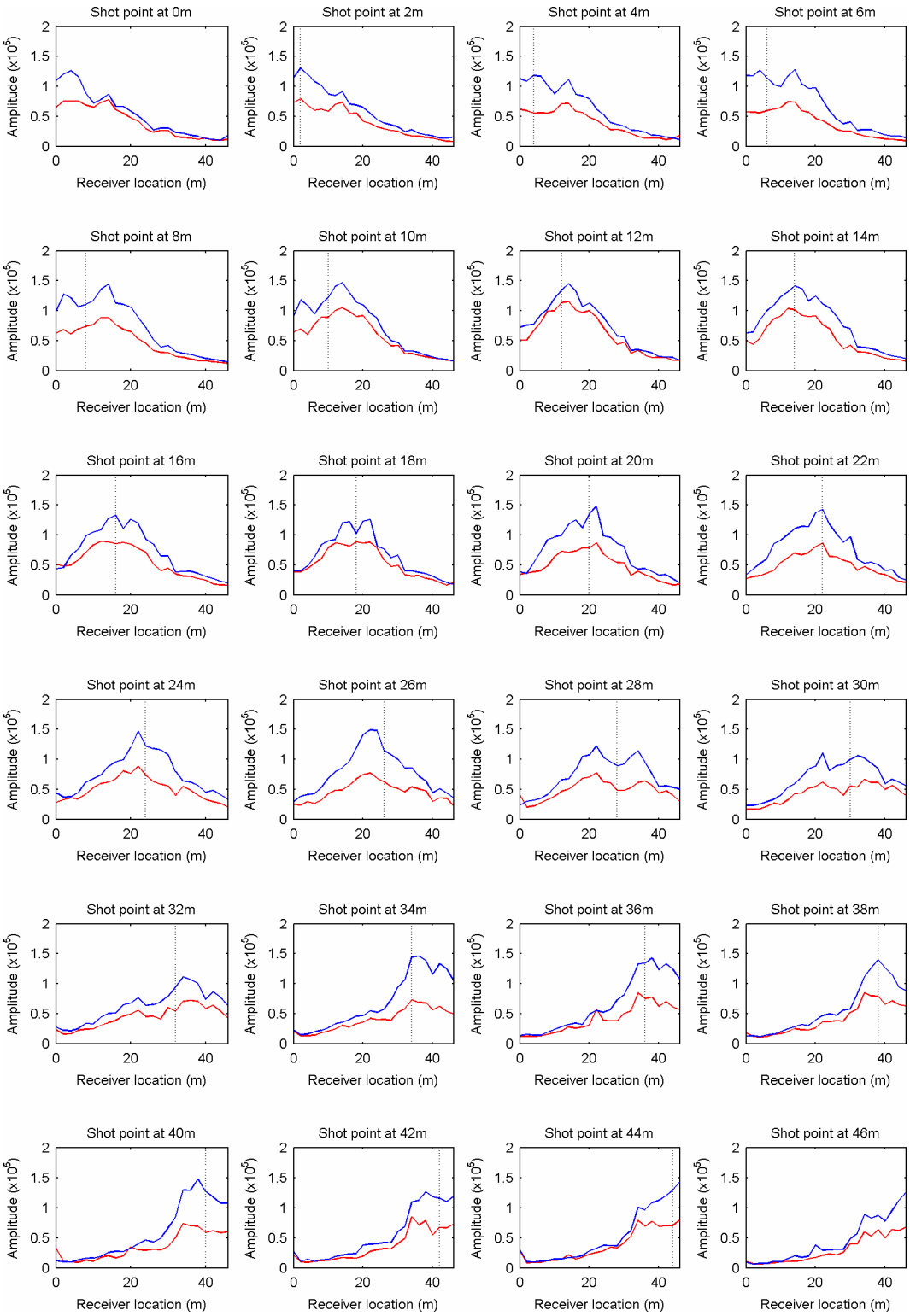

Figure 8.30. Maximum amplitudes of shot gathers at L2 (red) and L1 (blue) with receivers at L6

8.7.4. Amplitude of the first arrival

The final analysis presented in this chapter is the analysis of the amplitudes of the first arriving event. The results are presented in Figure 8.31 and Figure 8.32.

- Both figures exhibit strong erratic behaviour of the amplitudes. The strong prevailing winds caused low signal-to-noise ratio.
- Due to the erratic behaviour of the curves, no anomalies were identified which might be related to the presence of the backfilled mineshaft.

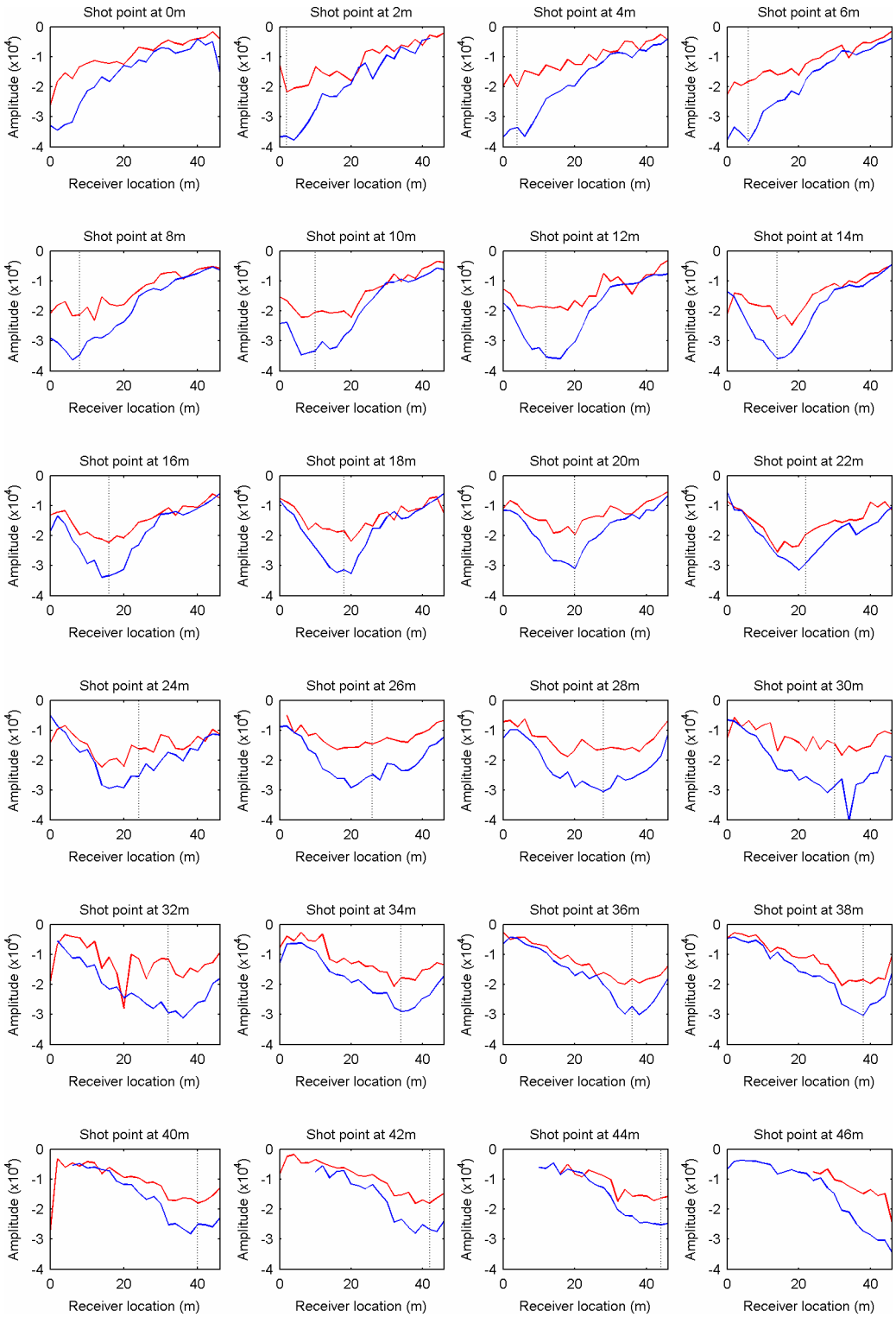

Figure 8.31. Amplitudes of the first arriving event of shot gathers at L5 (red) and L6 (blue) with receivers at L1

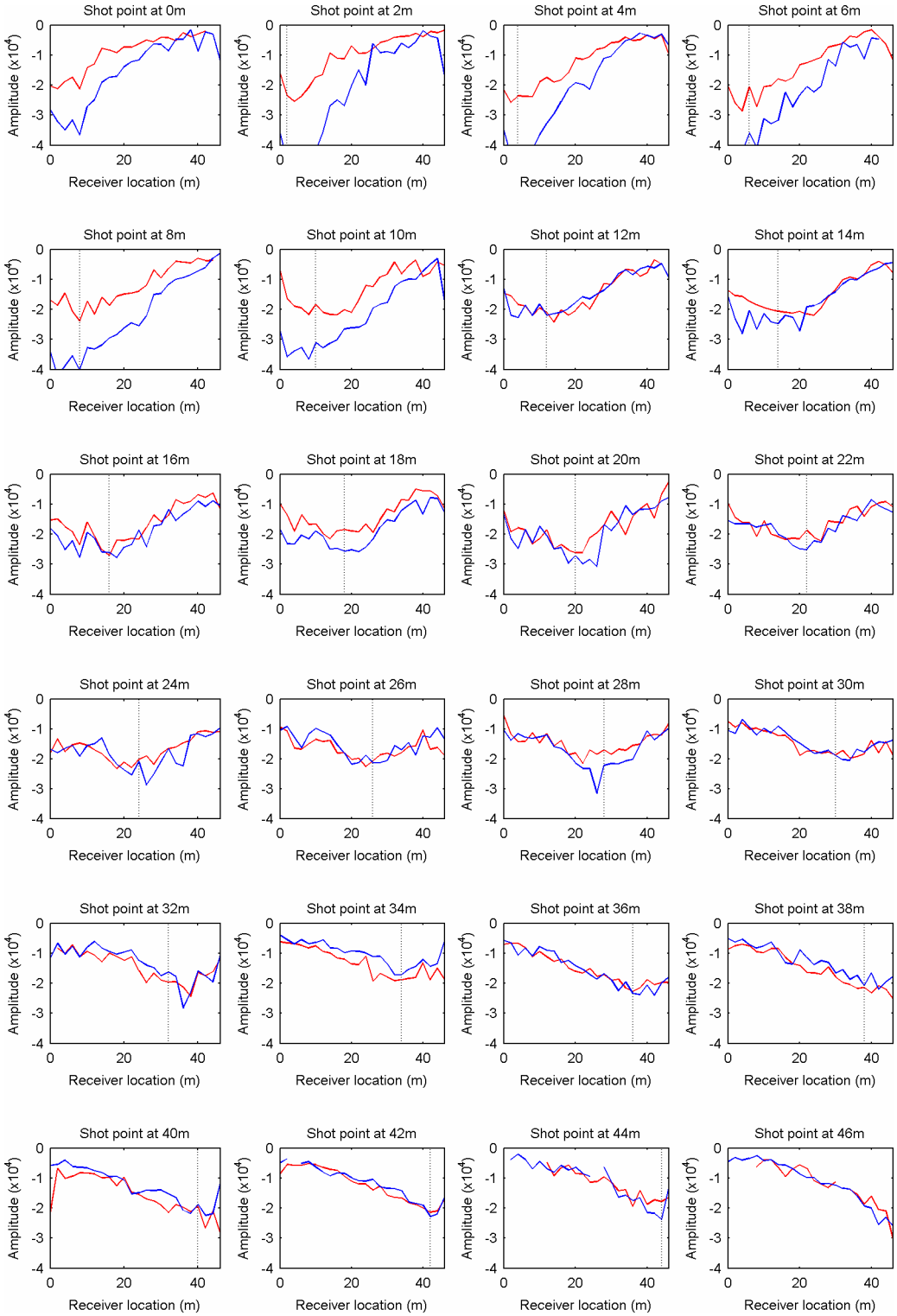

Figure 8.32. Amplitudes of the first arriving event of shot gathers at L2 (red) and L1 (blue) with receivers at L6

8.7.5. Additional geophysical survey

In order to determine the location of the mineshaft 2 more conclusively, an electromagnetic survey with the EM31 was conducted. The results of the survey can be found in Figure 8.33. The zero point in the figure corresponds to the L1S1 station point and the x-axis is along the survey line L1.

Mineshafts appear as a local bi-pole anomaly in the data (*Dresen et al., 1975; McCann et al., 1987*). No local bi-pole anomalies were observed in Figure 8.33. The conductivity variations in Figure 8.33 were likely to be caused by local variations in the soil material and the variations in the thickness of the soil. The large-sized anomaly produced between x-position 0 to 10m and between y-location 30 to 50m might be related to the presence of foundations of the buildings located near the mineshaft.

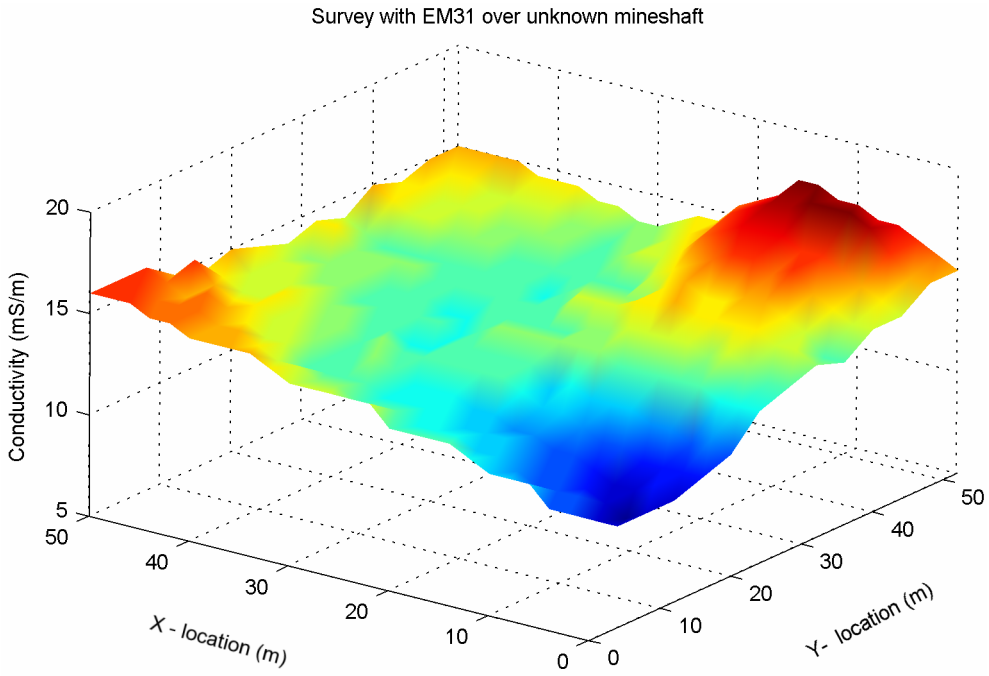

Figure 8.33 The results of the electromagnetic survey with the EM31 at the test site with the unknown mineshaft

8.7.6. Mineshaft location

Field trials were conducted at the backfilled mineshaft with unknown location. This section discusses the location of the mineshaft 2 as if field investigations were conducted after the field reconnaissance. The purpose of the field reconnaissance is after all to guide the field investigations by delineating anomalies that can be related to the location of the mineshaft. The additional EM survey did not exhibit any anomalies related to the mineshaft location. Ground proofing by drilling or other methods was not and will not be conducted because it would cause damage to the growing crops.

Figure 8.34 shows an overview of the probability of the mineshaft position as interpreted from the data. The darker grey indicates high probability of the mineshaft location, whereas the light grey area indicates medium probability. In a real case, a drilling program could be based on Figure 8.34 with the first boreholes located at the dark grey area.

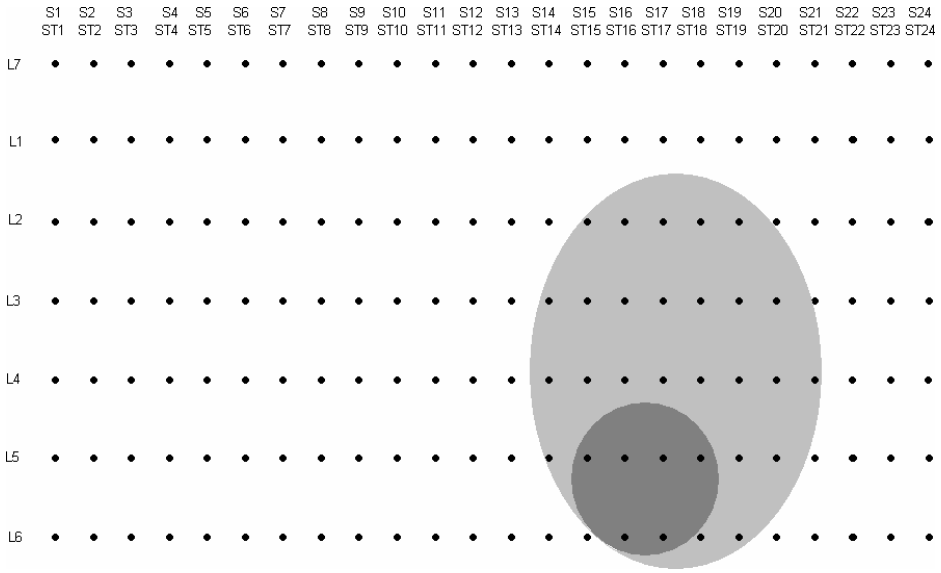

Figure 8.34. Probability of mineshaft location: high (dark grey) and medium (light grey)

The outline of probability location of the mineshaft in Figure 8.34 was based on the following anomalies observed in the seismograms and attribute curves.

- Regarding the seismograms presented Figure 8.23 and Figure 8.24.
  - From the seismograms, it is clear that the observed anomalous amplitudes were related to the receivers around 30m.
  - Furthermore in shot gather L1S14 and L2S13, anomalous amplitudes could be observed away from these receivers. It is likely that these were caused by superposition of a diffracted surface wave. The travel time of this wave was outlined and it appeared that the apex of the curve was located around 30m.
  - In shot gather L1S14 a conspicuous delay of the surface waves could be found at the receivers at 32m-38m. Similar delays can be observed in shot gathers L1S15-S16 in Appendix G.
  - An apparent decrease in the velocity could be observed in shot gather L1S22 and L2S24. Similar behaviour was found in a controlled experiment by Grandjean and Leparoux (*2004*) and in Figure 6.25. The apparent decrease in velocity was caused by phase changes related to superposition of surface waves and was observed at receivers behind the diffractor.
  - Shot gather L5S22 did not show any obvious anomalies. A possible explanation is that the source was located close to the mineshaft and the presence of the mineshaft affected all traces equally.
- Attributes curves presented in Figure 8.25 to Figure 8.32.
  - The first breaks in of shot gather L5S16 (30m) and L5S17 (32m) in Figure 8.25 showed anomalous low values compared to L6S16 (30m) and L6S17 (32m). Mirroring the survey out-lay shows that low first break values could be found in shot gather L1S16 (30m) and L1S17 (32m) in Figure 8.26 at the receivers around 30-32m.

- Despite the variable receiver responses, anomalous maximum amplitudes were observed at the receivers located at 28-32m at shot gathers L5S15-L17.

8.8. Discussion

In this chapter the discussion of the field trials are presented and analysed. The purposes of these field trials were threefold.

- Identify problems regarding seismic surveys in the field
- Correlate field observations with the numerical observations
- Assess seismic methods to delineate mineshafts

8.8.1. Survey problems

There were various problems encountered during the surveys.

- One of the problems was the prevailing weather conditions. The strong wind caused a considerable amount of noise, which makes it difficult to estimate the first break and also caused errors in the determination of the amplitude of the first event.
- Another problem was that some of the geophones were prone to background noise, which was likely caused by the connectors since replacing the geophone did not improve the signal. Some geophones showed a different signal response compared to the other geophones resulting in stronger amplitudes. This limited the interpretation of the maximum amplitudes and the amplitudes of the first arrivals.

- The hammer as a source appears in this case not the best option since the signal-to-noise ratio was considerably low. The first breaks and the amplitudes of the first events were difficult to determine and in several causes they could not be determined at all. For example a heavy drop-weight source would have been a better choice.

8.8.2. Correlation of numerical and field experiments

It is difficult to correlate the results of the numerical experiments directly with the field experiments. The reality is much more complex than the numerical models presented in chapter 6. For example, at Huntlaw Farm the bedrock is dipping and undulates; the surface is not flat, but undulates and dips; the source signatures were different and the physical properties of the media are fluctuating etc. Furthermore due to the difference in geophone response, the recorded amplitudes were difficult to analyse.

The characteristics of Model 3 presented in chapter 6 had similar features to the capped mineshaft i.e. shallow bedrock and a mineshaft without any backfilling or filling. The results of the field trials were compared with the results of the simulations.

- Regarding the seismograms
  - The seismograms of numerical modelling and the field trials show both very strong dominant surface waves which consisted of long wave packages.
  - The striking anomalous amplitudes at 0.27s in the centre of shot gathers L4S1 and L6S1 in Figure 8.6 and in several seismograms presented in Figure G-5 to Figure G-8, bares resemblance with the anomalous

amplitudes observed in Figure 6.8 on page 125 and Figure E-1 on page 345.

- Superposition of diffracted surface waves with later arriving surface waves can be observed in Figure 8.6 and Figure 8.8. The shot gathers of L4 and L5 in Figure E-1 show similar superposition of diffracted surface waves, albeit it is much less distinguishable.

- Regarding the attribute curves. A comparison of the attribute curves of the experimental data and the model 3 are presented in Figure 8.35. For the curves of the experimental data, shot gather L5S12 and L6S12 were taken. Note that the shot positions and receiver positions were not the same in relation to the position of the mineshaft and also that the scaling of the figures might differ.
  - The first breaks of the experimental data showed an obvious delay at both shot gathers. A similar delay could be observed at survey line L4 of the numerical data, but not at survey line L5. The observed anomaly was much larger in the experimental data than the numerical data. An explanation for this was that the wave velocities at the test site were lower. Furthermore, it is possible that the distressed rocks around the mineshaft caused an additional delay which was not taken into account in the numerical models.
  - The curves of dominant frequencies of model 3 cannot be correlated to the curves of the experimental data, although all curves are erratic.
  - All the maximum amplitudes curves in Figure 8.35 show a sharp increase at the receiver opposite to the shot point. However, the distinctive W-shape observed at survey line L4 in model 3 and most other models was not observed in the field experiment data, although the maximum amplitudes curves showed a small decrease in the amplitude value beside

the sharp peak. This is particularly clear when considering the maximum amplitude of the shot gather L6S12 in Figure 8.35. A possible explanation for the lack of resemblance between the model 3 and the experimental data is that the undulation of shallow bedrock and the surface causes focussing and defocusing of the surface wave energies which interfere with surface waves diffracted from the mineshaft.

- The amplitudes of first arriving event in model 3 showed a decrease in value at the receivers in the shadow zone of the mineshaft along survey line L4. The experimental data showed a similar decrease at the receiver direct opposite of shot point with the mineshaft in middle. It might be possible that this was caused by the difference in receiver responses.

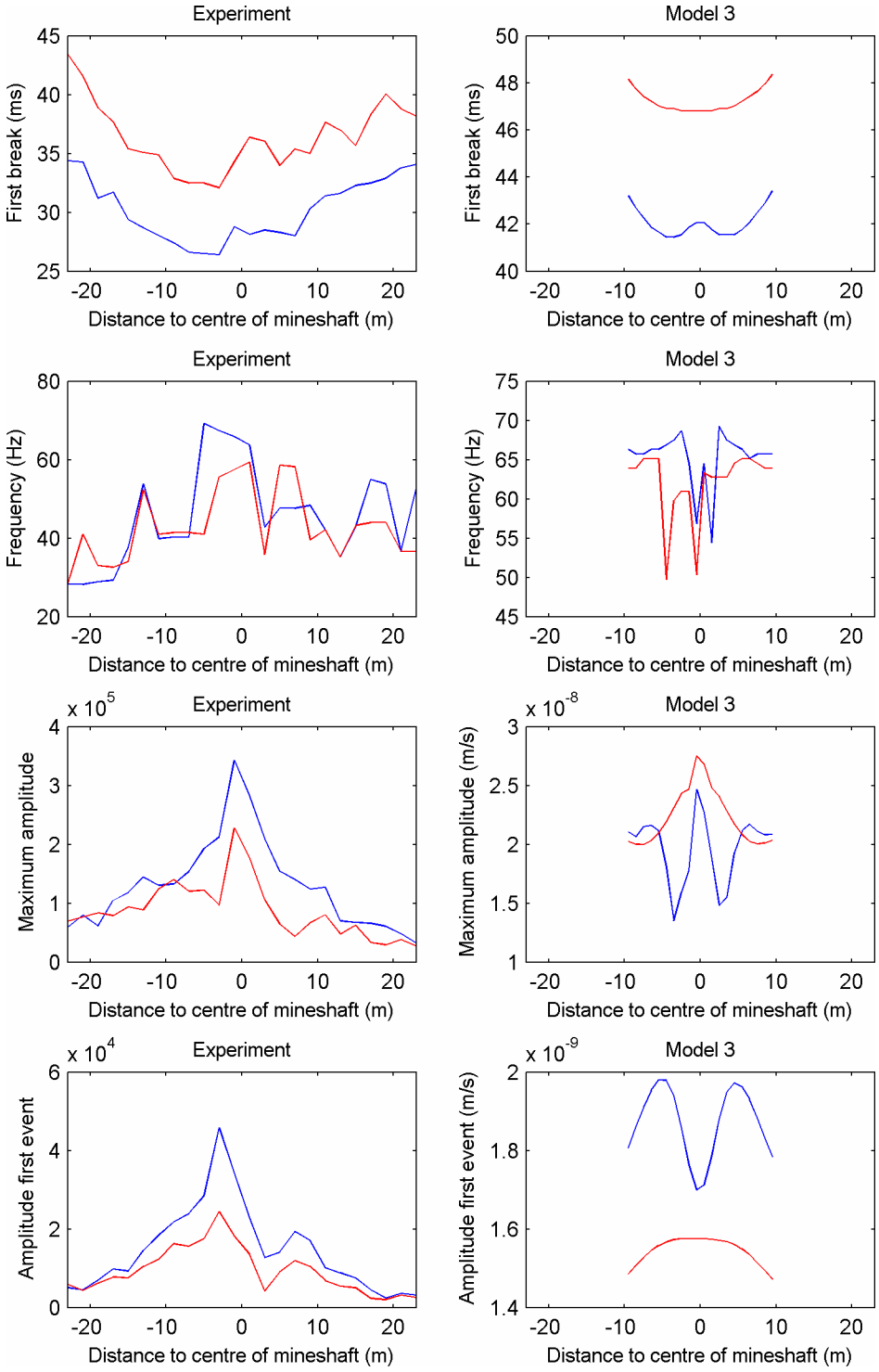

Figure 8.35. Comparison of the attribute curves of the field experiment (left; blue – L5S12, red – L6S12) with the attribute curves of the model 3 (right; blue – L4, red – L5)

8.8.3. Mineshafts detection by seismic methods

The most important question whether seismic methods can be used to delineate mineshaft. Unfortunately there is not a simple “YES” or “NO” answer to this question. From both the numerical and the field experiments it can be concluded that the mineshaft does produce anomalies.

From the numerical results it was concluded that it was difficult to ascertain the location of the mineshaft from direct observations of the seismograms. However, from the results of the field trials it can be concluded that the seismograms do contain obvious anomalies related to the presence of the capped mineshaft. Anomalous amplitudes caused by superposition of diffracted surface waves with direct surface waves are observed as well as some diffracted refracted waves in some of the shot gathers. The feasibility of using seismograms to delineate mineshafts depends strongly on the ability and experience of the interpreter.

The analysis of the transmitted waves is more straight forward and less esoteric than the interpretation of the seismograms, although the interpretation of the data still requires some expertise. The anomalies produced by the mineshaft were less distinguishable than in the numerical models. Partially, the differences were caused by the back ground noise, data acquisition, the human interpretation and largely caused by the stochastic nature of the mediums where the seismic waves travel through.

Anomalous first break curves were observed at the capped mineshaft. The observed delays were in the order of 2-3ms. In general the picking error of first breaks was considered to be about 1ms depending on the quality of the data. Although the observed delays were larger than the picking error, conclusions should be made with caution.

The dominant frequencies at the capped mineshaft showed erratic behaviour. Although anomalous high frequencies are observed it was difficult to relate these anomalies to the location of the mineshaft. The observation did not agree with the results of the numerical experiments and did not agree with the findings by Dresen (*1977*). From model 3 in chapter 8 it was clear that shallow bedrock causes strong variations in the dominant frequency curve. It was possible that when the bedrock was at greater depth the dominant frequency curves would show anomalies related to the mineshaft.

The maximum amplitudes were difficult to interpret due to the fact that some geophones had different responses to the seismic waves, resulting in an erratic maximum amplitude curve. It was difficult to ascertain whether maximum amplitudes can be used to delineate mineshafts. Clearly, accurately calibrated geophones were necessary for a successful survey. Furthermore from the results of numerical model 3 in section 7.2 it was concluded that shallow bedrock limits the use of the maximum amplitude. Perhaps, using the maximum amplitude can resolve mineshafts at locations where the depth to the bedrock was greater than 5m.

Similar problems to the maximum amplitudes exist with the amplitudes of the first event. Due to different geophone responses the amplitude curves were erratic and conclusions are difficult to ascertain.

8.8.4. Recommendation for future surveys

One of the objectives of the field trials was to identify problems regarding seismic surveys in the field. From the observations in the field and the results of analysis of the numerical modelling presented in chapter 7, the following recommendations were made regarding future surveys.

- Receivers: High frequency geophones (vertical) with a natural frequency of 40Hz or higher. To analyse the amplitudes and the power spectrum correctly, the geophones should have identical responses to the displacement due to the passing elastic waves. Therefore the geophones should be calibrated prior to the survey and old geophones (>5 years) should not be used.
- Sources: High impact sources, such as drop weight (10kg or higher) or accelerated hammers to generate a broad range of frequencies with high amplitudes. A surface sparker or auger sparker sources might be optional too.
- Layout: As a result of the experiments the following survey parameters are suggested to investigate an area of 40× 20m.
    - 48 geophones with a spacing of 1m located at one side of the survey area
    - 24 shot points with a spacing of 2m located at the other side of the survey area
    - Spacing between source line and receiver is between 16m and 24m; 20m is recommended.

Due to limited time and resource no further field experiments were possible. Furthermore an extensive field parameter study is beyond the scope of the project.

8.9. Summary

In this chapter the results of two field surveys were presented. The data from the two surveys were examined in two ways. One way was by direct observations from the seismograms and the second way was by analysis of the first breaks, frequencies and amplitudes as discussed in chapter 7.

The seismograms show various features related to the mineshaft.

- Diffractions of refracted waves were observed in various shot gathers.
- Superposition of diffracted surface waves which caused anomalous amplitudes at geophones located close to the mineshaft.

These observations can be used to delineate the mineshaft; however it was argued that some expertise was required to interpret the seismograms.

The analysis presented in this chapter included the study of the first breaks, dominant frequencies and the amplitudes of the recorded data.

- Various receivers exhibited different responses and some receivers were very sensitive to noise. The strong winds caused background noise and the selected source was weak such that the overall signal-to-noise ratio was low. These factors affected the potential for a successful survey.
- Delays in the first breaks were observed at geophones opposite the mineshaft. The delays were of the order of 2-3ms, which was slightly larger than the picking error of about 1ms.
- The undulating shallow bedrock caused strong variations in the dominant frequencies. Its erratic behaviour was difficult to relate to frequency anomalies due to the presence of the mineshaft. It can be argued that in cases where the bedrock is not shallow, the dominant frequencies might contain information regarding the location of the mineshaft.
- Due to the variations in the response of the geophones, the analysis of the maximum amplitudes and the amplitudes of the first events did not resolve the location of the mineshaft. Although the amplitudes of the first events showed some distinctive W-shape. This is in accordance with the results of the transmission method by Dresen.

The experiments were repeated at the backfilled mineshaft with unknown location. Since no ground proofing could be undertaken any discussion or conclusion should be treated circumspectly.

- Anomalous amplitudes were observed in the seismograms. These anomalies were more pronounced at the geophones around 30m.
- At the same geophone location, anomalous first breaks, dominant frequencies and maximum amplitudes were observed. However, the dominant frequencies also showed an anomaly around 12m.

9. Conclusions

In this chapter the conclusions of this thesis are presented. The thesis and therefore the conclusions can be subdivided in three sections:

- Assessment of methods of detection of abandoned mineshafts.
- Numerical modelling of elastic wave propagation in buried mineshaft models.
- Field experiments conducted at two mineshafts near Huntlaw farm.

This chapter is concluded by a section regarding further work and some recommendations.

9.1. The assessment

As a part of this industrially funded PhD, the sponsor Network Rail requested a comprehensive literature review which assessed all reconnaissance techniques that might be able to delineate mineshafts in the proximity of railways. The assessment was subdivided into three sections: visual inspection, geochemical reconnaissance and geophysical reconnaissance and the following conclusions were drawn:

- Visual inspection: Anomalies at the surface e.g. surface depressions, vegetation withering, etc. can be a result of the presence of a mineshaft. These anomalies can be used to delineate the mineshaft. However, it is very unlikely that mineshafts located beneath the railway embankment can be detected since the potential surface expression is masked.
- Geochemical reconnaissance methods: Anomalous soil gas concentrations can be related to the presence of mineshafts. However, very few gas emanometry

surveys, including surveys using the radio-active Radon, are conducted in order to detect mine workings and mineshafts. Gas emanometry surveys are affected by prevailing weather conditions. Furthermore samples taken at the ballast level are unreliable, leaving a large survey area un-sampled.

- Geophysical reconnaissance: The physical properties of the mineshafts cause anomalies which can be measured at the surface. Geophysical methods have successfully detected mineshafts however the presence of the railway limits the performance of most geophysical techniques. The geophysicist responsible for the survey should be aware of the limitations of each technique. In Table 3.2 the major limitations and the estimated effectiveness of the reviewed geophysical techniques were summarized.
    - Resistivity profiling and resistivity tomography were considered to have a medium effectiveness. The bad coupling with the ballast and the limited depth penetration could be a problem. To prevent problems due to the bad coupling countermeasures are recommended. Resistivity surveys should be carried out only at thin ballast layers and small embankments. The GPR method was also considered to be medium effective however GPR surveys should not be conducted at high conductive media such as clays and shales.
    - Gravimetric methods were considered to be very effective. For a successful survey accurate corrections to the measured data are required. Since the instruments are sensitive to strong vibration possession management of the track is required during the whole survey. The transmission method was also considered to be effective. Since only a few transmission surveys were conducted ever, the limitations of this technique were unknown.
    - Other geophysical techniques, not mentioned in previous points were all deemed to be ineffective in the detection of abondaned mineshafts.

- The transmission method and the diffraction imaging method were considered as the only methods that do not require the possession of the track during the survey. From the results of the numerical experiments and the field experiment it was clear that mineshafts do not produce distinguishable diffracted wave and therefore the diffraction imaging methods were deemed to be ineffective.

9.2. Numerical modelling

Very few seismic surveys have been undertaken to delineate mineshafts, therefore numerical experiments were conducted to further assess the potential of seismic techniques and in particular the transmission method. A forward modelling program was designed to simulate various mineshaft models. The modelled space used in the algorithm was meshed using a grid based on the Rotated Staggered Grid. This experimental grid enables one to model strong heterogeneities such as air voids, whereas the standard grids may show instabilities.

9.2.1. Perfectly matched layer

In finite-difference time-domain modelling, absorbing boundary conditions are required to simulate mineshafts in half-spaces. In this thesis three new perfectly matched layer implementations are presented.

- Recursive Integration PML
- Convolution PML
- Auxiliary Differential Equation PML

All three of the PMLs do not require splitting of the wave propagation equations, which is required in the conventional Split PML. These non-split PMLs have various advantages:

- Better performance compared to conventional boundary conditions as demonstrated with 3rd order Higdon.
- Potentially more efficient use of memory compared to conventional PMLs.
- More efficient implementation: less floating point operators required
- More elegant implementation: boundary condition equations can be written as correction to the original wave propagation equations
- The Complex Frequency Shifted stretching function can be adopted

In the thesis it is demonstrated that the CFS stretched can enhance the performance of the ABC considerably when simulating models with elongated domains and when simulating models where surface waves are present in the boundary zone. The CFS stretching function can be useful in various model scenarios, such as earthquake hazard modelling, modelling of seismic waves for the exploration of oil, gas and minerals and the modelling of impact echo and ultrasonic responses in non-destructive testing.

9.2.2. Numerical experiments

Models with various mineshafts and various settings were simulated. From the results of the numerical experiments the following conclusions can be made:

Direct observations of the seismograms

- Mineshafts caused diffraction of seismic waves. These waves were superimposed on other waves which caused anomalous amplitudes or phase jumps.

- Furthermore delays in arriving times of the surface waves were observed. These seismograms can be used for delineation of mineshafts however the interpretation requires some expertise.

Analysis of the attributes of the traces

- The analysis of the first break, the dominant frequencies, the amplitudes of the first event and especially the maximum amplitudes showed that anomalies were related to the presence and location of the mineshaft. However, the potential of using the first break or the amplitude of first arriving event to delineate mineshaft might be limited since their attribute curve showed no distinguishable features related to the presence of the mineshaft. The maximum amplitudes curves showed strong anomalies which could be correlated easily to the location of the mineshaft. The dominant frequencies curve showed high frequency anomalies caused by the mineshaft. Due to the broad nature of the anomalies, the use of the dominant frequencies is limited.

9.3. Field experiment

Two surveys were conducted in order to assess seismic methods to delineate mineshafts: one survey at a capped mineshaft and one survey at a backfilled mineshaft with unknown location. Since no ground proofing was done at the second mineshaft, no hard conclusions can be made from its result.

Direct observations of the seismograms

- Diffractions of refracted waves as well as some diffracted surface waves were observed in various seismograms. The apexes of these diffraction waves agree approximately with the location of the mineshaft.
- Anomalous amplitudes were observed. Generally these anomalies were strongest at the receiver located closest to the mineshaft.

Analysis of the attributes of the traces

- The first breaks showed anomalous delays which could be correlated with the location of the mineshaft. The anomalies were much stronger than predicted from the models. An explanation is that in the models the low velocity due to the de-stressed bedrock around the mineshaft was not taken into account.
- The values of the amplitudes were difficult to correlate to the location of the mineshaft. This was partially caused by the low signal-to-noise ratio and the erratic responses of various receivers.
- The dominant frequencies showed erratic behaviour which could not be correlated directly with the location of the mineshaft.

9.4. Further work and recommendation

9.4.1. Numerical modelling

In this thesis various implementations of non-split PMLs are presented. These PMLs can incorporate the CFS stretching function. Incorporating the complex attenuation coefficients in the stretching function can be beneficial for many model scenarios.

- Although some analysis of the attenuation coefficients is included in the thesis, there is still a lot of research to be done regarding the application of CFS PMLs and the attenuation coefficients. However, this could be a difficult task since the optimum selection not only depends on the model parameters but also on the observation and source locations.
- The results of the PMLs showed that the CPML performs better than the other non-split PMLs. The mathematical operators of the latter PMLs are more accurate than the convolution operator in the CPML. It is mentioned that the RSG might cause small errors since the spatial derivatives are calculated diagonally to the PML interface rather than perpendicular or parallel, such as in the conventional numerical grids. To verify this assumption it is necessary that the PMLs are implemented in non-rotated grids.
- The models presented in this thesis were kept simple such that the models could be compared to each other. Although computer resources might be a limiting factor, more realistic models could be used to simulate synthetic seismograms used in the analysis. However, the physical parameters of the backfilling and of the de-stressed bedrock around the mineshaft are unknown. For realistic modelling it is required that approximative values of these parameters are known.

9.4.2. Mineshaft detection

In this thesis the use of broadside shot gathers to delineate mineshafts in the proximity of railways was explored. The seismic data were analysed using the transmission method pioneered by Dresen (*1979*). The work carried out by Dresen was extended by means of numerical modelling. The numerical results

established that the transmission method can be used in the context of broadside shot gathers.

The transmission method in this thesis was limited to the analyses of four different trace attributes. It should be stressed that the transmission method does not have to be limited to these four attributes. Thus, the transmission method is very flexible. The selection of the optimum attribute depends on the site conditions and therefore should be selected in the field. However, due to the variable travel distances, the analysis of other attributes can become difficult. It was suggested in section 7.10.5 that wave separation and sliding window methods can be used to discriminate waves such that they can be analysed using the transmission method. Although these methods might be difficult to apply on one-component data as typically used in near-surface seismics, they could be useful in the delineation of mineshafts.

The seismic data of the broadside shot gathers were analysed using the transmission method. It is possible to analyse this data using other techniques. In Appendix H, the results of the diffraction imaging method are presented. Due to the fact that mineshafts did not produce diffracted body waves useable for imaging, the diffraction imaging method cannot resolve mineshafts. In section 7.10.6, two other analysis methods were mentioned: first arrival tomography and dispersion analysis. These methods can provide 3D images of the subsurface and the interpretation of anomalies associated with mineshafts becomes straightforward. Although most available algorithms are not readily suitable for delineation of mineshafts, it is possible to use first arrival tomography and dispersion techniques to analyse the data and to provide a 3D image of the subsurface.

In order to assess the potential of using the transmission method in combination with the broadside shot gathers, field experiments were conducted. The results of the field experiment are influenced by differences in the responses of the geophones obtained from the rental company. Furthermore the size of mineshaft is merely 2.5m in the direction along the survey lines. The numerical models show that mineshafts of 2m and smaller produce small anomalies which might be difficult to distinguish. Also the simulations showed that the shallow bedrock limits the potential of detection.

As with all geophysical techniques, the success of a seismic survey strongly depends on the geological setting. From the numerical model 3 it was clear that the shallow bedrock affected the measured data considerably. In order to verify the potential of using the seismic techniques where the bedrock is not shallow more controlled field experiments are required. The results of the experiments should be verified by ground proofing.

The following recommendations regarding any potential future surveys using the broadside shot gathers can be made:

- **Source**: It is clear from the experiment that the signal-to-noise ratio was low. Partially this was caused by the strong prevailing winds and partially by the weak source – in this case a sledge hammer and plate. In order to improve the signal-to-noise ratio heavy impact sources should be used such as a heavy drop weight source or accelerated hammer. From the numerical models it was clear that high frequencies were more affected by the mineshaft. There are various ways to obtain more high frequencies at the survey site. High impact sources generate a broader range of frequencies; analogue band pass filters placed between the receivers and the recorder can remove the undesired low frequencies

- **Receivers**: The receivers used in the field experiment showed erratic responses. The variations in the responses were partially caused by difference in the coupling with the superficial deposits, but largely to the variable responses to the seismic waves. The use of calibrated geophones is strongly recommended to avoid variations between the geophone responses. Furthermore the use of high-frequency geophones (>40Hz) in combination with the recommended sources mentioned in the previous point can also enhance the anomalies related to the mineshaft.
- **Survey lay-out**: A receiver spacing of approximately 1m is strongly recommended, especially when surveying for mineshafts of less than 2m. The same size of survey area is covered when using 48 receivers instead of 24.

References

Ager, C.A., and J.O Liard (1982). Vertical gravity gradient surveys: field results and interpretation in British Columbia, Canada. *Geophysics*, 47, pp 919-925.

Annan, P.A. (2005). Ground-penetrating radar in *Near-surface geophysics* edited by D. K. Butler: SEG, pp 357-438.

Arrowsmith, D. J., and P. R. Rankilor (1981). Dalton by-pass: site investigation in an area of abandoned haematite mine workings. *Quarterly journal of engineering geology*, 14, pp 207-218.

BBC (2007). *Watching the pits disappear* [Last accessed on 10 April 2007]. Available from http://news.bbc.co.uk/1/hi/uk/3514549.stm.

Bécache, E., P. G. Petropoulos, and S. D. Gedney (2004). On the long-time behavior of unsplit perfectly matched layers. *IEEE Transactions on Antennas and Propagation*, 52, pp 1335-1342.

Bérenger, J. P. (1994). A perfectly matched layer for absorption of electromagnetic waves. *Journal of Computational Physics*, 114, pp 185-200.

Bérenger, J. P. (2002a). Application of the CFS PML to the absorption of evanescent waves in waveguides. *IEEE Microwave and Wireless Components Letters*, 12, pp 218-220.

Bérenger, J. P. (2002b). Numerical reflection from FDTD-PMLs: a comparison of the split PML with the unsplit and CFS PMLs. *IEEE Transactions on Antennas and Propagation*, 50, pp 258-265.

Bing, Z., and S. A. Greenhalgh (2000). Cross-hole resistivity tomography using different electrode configurations. *Geophysical Prospecting*, 48, pp 887-912.

Bohlen, T. (2003). *Analysis of seismic waves in the presence of small-scale strong material discontinuities*. PhD Thesis, Christian Albrechts Universität, Kiel.

Bondarenko, V. M., G. G Victorov, N. V. Demin, B. N. Kulkov, E. E. Lumpov, and V. A. Christich (1983). *New methods in engineering geophysics*. Moscow: Press Nedra.

Branham, K. L., and D. W. Steeples (1988). Cavity detection using high-resolution seismic reflection methods. *Mining engineering*, 40, pp 115-119.

Brouwer, J., and V. Nijhof (1994). The use of geophysical techniques for the detection of - partially collapsed - mineshaft. *Symposium on the Application Geophysics Engineering Environmental Problems (SAGEEP)*, in Boston (Massachusetts), pp 645-654.

Burke, T (1988). The significance of mining method to site investigations in areas of old abandoned mine workings. *Construction in Areas of Abandoned Mineworkings*, in Edinburgh (United Kingdom), pp 33-52.

Burton, A. N., and P. I. Maton (1975). Geophysical methods in site investigations in areas of mining subsidence in *Site investigations in areas of mining subsidence* edited by F. G. Bell. London: Newness - Butterworths, pp 75-102.

Butler, D. K. (1980). *Microgravimetric techniques for geotechnical applications*, report number: GL-80-13, U.S. army engineer waterways experimental station, pp 129.

Butler, D. K. (1984). Microgravitmetric and gravity gradient techniques for detection of subsurface cavities. *Geophysics*, 49, pp 1084-1096.

Carcione, J. M., G. C. Herman, and A. P. E. ten Kroode (2002). Seismic modeling. *Geophysics*, 67, pp 1304-1325.

Cerjan, C., D. Kosloff, R. Kosloff, and M. Reshef (1985). A non-reflecting boundary condition for discrete acoustic and elastic wave equation. *Geophysics*, 50, pp 705-708.

Cerveny, V., I. A. Molotkov, and I. Psencik (1977). *Ray methods in seismology*. Prague: University of Karlova Press.

Chew, W. C., and Q. H. Liu (1996). Perfectly matched layers for elastodynamics: A new absorbing boundary condition. *Journal of Computational Acoustics*, 4, pp 341-359.

Clark, M. (2001). *Non-destructive and geotechnical testing of railway track bed ballast*. PhD, University of Edinburgh, Edinburgh.

Clarke, B.G., M. Welford, and D.B. Hughes (2006). The threat of abandoned mines on the stability of urban areas. *IAEG2006*, in Nottingham (United Kingdom), pp 9.

Clarkson, E., and B. Upton (2006). *Edinburgh rock - the geology of lothian*. Edinburgh: Dunedin Academic press Ltd.

Colley, G. C. (1963). The detection of caves by gravity measurements. *Geophysical Prospecting*, 11, pp 1-10.

Collino, F., and P. Monk (1998). Optimizing the perfectly matched layer. *Computer Methods in Applied Mechanics and Engineering*, 164, pp 157-171.

Collino, F., and C. Tsogka (2001). Application of the perfectly matched absorbing layer model to the linear elastadynamic problem in anisotropic heterogeneous media. *Geophysics*, 68, pp 294-307.

Cook, J.C. (1975). Radar transparencies of mine and tunnel rocks. *Geophysics*, 40, pp 865-885.

Coombs, D.H. (1971). *British railway track - design, construction and maintenance*. 4 ed. Nottingham (United Kingdom): The Permanent Way Institution.

Cooper, A.H. (1989). Airborne multispectral scanning of subsidence caused by Permian gypsum dissolution at Ripon. *Quarterly journal of engineering geology*, 22, pp 219-229.

Corwin, R. F. (1990). The self-potential method for environmental and engineering applications in *Geotechnical and Environmental Geophysics* edited by S. H. Ward, pp 127-145.

Crawford, E. *Rumney railway* [Last accessed on 13 April 2007. Available from http://www.railscot.co.uk/Rumney_Railway/frame.htm.

Culshaw, M. G., D. M. McCann, and F. G. Bell (2004). Modern reconnaissance methods for geohazard detection and monitoring in site investigation. *Advances in Geotechnical Engineering: the Skempton Conference*, in London (United Kingdom), pp 1255-1268.

Culshaw, M. G., and A. C. Waltham (1987). Natural and artificial cavities as ground engineering hazards. *Quarterly journal of engineering geology*, 20, pp 139-150.

Darracot, B. W., and M. I. Lake (1981). An initial appraisal of ground probing radar for site investigation in Britain. *Ground Engineering*, 4, pp 14-18.

Dean, J.W. (1967). Old mine shafts and their hazards. *Mining engineering*, 126, pp 368-377.

Debeglia, N., and F. Dupont (2002). Some critical factors for engineering and environmental microgravity investigations. *Journal of Applied Geophysics*, 50, pp 435-454.

Denis, A., A. Marache, T. Obellianne, and D. Breysse (2002). Electrical resistivity borehole measurements: application to an urban tunnel site. *Journal of Applied Geophysics*, 50, pp 319-331.

Department-of-the-Environment (1976). *Reclamation of derelict land - procedures for locating abandoned mineshafts*, report number: DGR482/13, Ove Arup and partners, pp.

Dobecki, T. L. (1988). A rapid seismic technique for detecting subsurface voids and unmapped mine workings. *Symposium on the Application Geophysics Engineering Environmental Problems (SAGEEP)*, in Golden (Colorado), pp 666-690.

Donelly, L. J., and L. V. Bramford (1996). *Exploration for abandoned mine shafts using radon gas soil gas geochemistry*, report number: WN/96/38, Britisch Geological Survey, pp.

Donelly, L. J., and D. M. McCann (2000). The location of abandoned mine workings using thermal techniques. *Engineering Geology*, 57, pp 39-52.

Doyle, R., S. Thomson, M. Neil, W. Price, and J. Young (1992). Investigations into the effectiveness of water infusion using the radio imaging method (RIM). *The Australian Coal Journal*, 36, pp 19-25.

Dresen, L. (1977). Locating and mapping of cavities at shallow depths by the seismic transmission method. *Conference on Dynamical Methods in Soil and Rock Mechanics*, in Karlsruhe (Germany), pp 149-171.

Dresen, L., H. Baule, F. Schluckebier, U. Bleil, U. Casten, G. Gommlich, and G. Ulrich (1975). Ortung eines verdeckten Schachtes mit geophyikalischen Methoden. *Glückauf-forschungshefte*, 36, pp 209-215.

Dresen, L., and C. H. Hsieh (1979). Ortung verlassener Schächte mit Hilfe von Rayleigh-Wellen. *Glückauf-forschungshefte*, 40, pp 190-198.

Drossaert, F. H., M. C. Forde, A. Giannopoulos, D. M. McCann, and P. J. Fenning (2004). Numerical experiments to develop guidelines for selecting geophysical methods for identifying abandoned mineshafts. *Railway Engineering*, in London (United Kingdom), pp 21.

Drossaert, F. H., and A. Giannopoulos (2007a). Complex frequency shifted convolution PML for FDTD modelling of elastic waves. *Wave motion*, 44, pp 593-604.

Drossaert, F. H., and A. Giannopoulos (2007b). A Non-split Complex Frequency Shifted PML based on recursive integration for FDTD modeling of elastic waves. *Geophysics*, 72, pp T9-T17.

Fajklewicz, Z. J. (1976). Gravity vertical gradient measurements for the detection of small geological and anthropogenic forms. *Geophysics*, 41, pp 1016-1030.

Forde, M. C., and H. W. Whittington (1984). Resistivity surveying of mineshafts. *Construction in Areas of Abandoned Mineworkings*, in Edinburgh (United Kingdom), pp 196-220.

Foti, S., L. Sambuelli, V. L. Socco, and C. Strobbia (2003). Experiments of joint acquisition of seismic refraction and surface wave data. *Near surface geophysics*, 3, pp 119-129.

Fuchs, K., and G. Müller (1971). Computation of synthetic seismograms with the reflectivity method and comparison with observations. *Geophysical Journal of the Royal Astronomical Society*, 23, pp 417-433.

Gazdag, J. (1981). Modeling the acoustic wave equation with transforms methods. *Geophysics*, 54, pp 195-206.

Gedney, S. D. (1998). The perfectly matched layer absorbing medium in *Advances in Computational Electrodynamics: the Finite-Difference Time-Domian Method* edited by A. Taflove. Norwood: Artech House, pp.

Gélis, C., D. Leparoux, J. Virieux, A. Bitri, S. Operto, and G Grandjean (2005). Numerical modelling of surface waves over shallow cavities. *Journal of Environmental and Engineering Geophysics*, 10, pp 111-121.

Ghatge, S. L. (1993). Microgravity method for detection of abandoned shafts of the Schuyler copper mine in northeastern New Jersey. *Symposium on the Application Geophysics Engineering Environmental Problems (SAGEEP)*, in San Diego (California), pp 195-207.

Godson, R. H., and J. S. Watkins (1968). Seismic resonace investigation of a near-surface cavity in Anchor reservoir. *Bulletin of the Association of Engineering Geologists*, 5, pp 27-36.

Grandjean, G, and D. Leparoux (2004). The potential of seismic methods for detecting cavities and buried objects: experimentation at a test site. *Journal of applied geophysics*, 56, pp 93-106.

Gritto, R., and E. L. Majer (2000). Seismic mapping of subsurface cavities. *Symposium on the Application Geophysics Engineering Environmental Problems (SAGEEP)*, in Arlington (Virginia), pp 1215-1244.

Gunn, D. A., G. J. Ager, S. H. Marsh, M. G. Raines, C. N. Waters, K. B. McManus, A. Forster, P. D. Jackson, and D. J. Lowe (2002). *The development of thermal imaging techniques to detect mineshafts*, report number: IR/01/24, Britisch Geological Survey, pp 40.

Haeni, F. P., L. Halleux, C. D. Johnson, and J. W. Lane (2002). Detection and mapping of fractures and cavities using borehole radar. *Conference on Fractured rock*, in Denver (Colorado), pp 4.

Hastings, F. D., J. B. Schneider, and S. L. Broschat (1996). Application of the perfectly matched layer (PML) absorbing boundary condition to elastic wave propagation. *Journal of the Acoustical Society of America*, 100, pp 3061-3069.

Hauser, K., J. Jackson, J. Lane, and R. Hodges (1995). Deep tunnel detection using crosshole radar tomography. *Symposium on the Application Geophysics Engineering Environmental Problems (SAGEEP)*, in Orlando (Florida), pp 853-857.

Heincke, B., A. G. Green, J. Van der Kruk, and H. Willenberg (2006). Semblance-base topographic migration (SBTM): a method for identifying fracture zones in 3D georadar data. *Near surface geophysics*, 4, pp 79-88.

Herrman, L. R., and E. F. Peterson (1968). A numerical procedure for visco-elastic stress analysis. *7th meeting of ICRPG Mechanical Behavior Working Group*, in Orlando (Florida).

Jackson, P. D., D. A. Gunn, R. C. Flint, D.M McCann, M. Bent, and D. Howes (2001). Cross-hole seismic measurements for detection of disturbed ground beneath existing structures. *NDT&E international*, 34, pp 155-162.

Keydar, S. (2004). Homeomorphic imaging using path integrals. *66th EAGE Meeting*, in Paris (France), P078-78.

Kilty, K. T., and A. L. Lange (1990). Acoustic tomography in shallow geophysical exploration using transform reconstruction in *Geotechnical and Environmental Geophysics* edited by S. H. Ward: SEG, pp 23-36.

Kircher, M., A. Roth, N. Adam, B. Kampes, and H.J. Neugebauer (2003). Remote sensing observation of mining induced subsidence by means of differential SAR-inteferometry. *International Geoscience and Remote Sensing Symposium*, in Toulouse (France), pp 209-211.

Knapp, R. W., and D. W. Steeples (1986). High resolution common depth seismic reflection profiling: instrumentation. *Geophysics*, 51, pp 276-282.

Kosloff, D., and E. Baysal (1982). Forward modeling by a Fourier method. *Geophysics*, 47, pp 1402-1412.

Krajewsk, C., L. Dresen, C. Gelbke, and H. Rüter (1989). Iterative tomographic methods to locate seismic low-velocity anomalies: a model study. *Geophysical Prospecting*, 37, pp 717-751.

Krüger, O. S., E. H. Saenger, and S. A. Shapiro (2005). Scattering and diffraction by a single crack: an accuracy analysis of the rotated staggered grid. *Geophysical Journal International*, 162, pp 25-31.

Kuzuoglu, M., and R. Mittra (1996). Frequency dependence of the constitutive parameters of causal perfectly matched anisotropic absorbers. *IEEE Microwave and Guided Wave Letters*, 6, pp 447-449.

Lay, T., and T. C. Wallace (1995). *Modern global seismology*. San Diego: Academic press.

Littlejohn, G.S. (1979). Surface stability in areas underlain by old coal workings. *Ground Engineering*, 12, pp 22-30.

Luebbers, R. J., and F. Hunsberger (1992). FDTD for Nth-order dispersive media. *IEEE Transactions on Antennas and Propagation*, 40, pp 1297-1301.

Lysmer, J., and L. A. Drake (1972). A finite element method for seismology in *Methods in Computational Physics II: Seismology* edited by B. Alder, S. Fernbach and B. A. Bolt: Academic Press, pp 181-216.

Maillol, J. M., M. K. Seguin, O. P. Gupta, H. M. Akhauri, and N. Sen (1999). Electrical resisitivity tomography survey for delineating uncharted mine galleries in West Bengal, India. *Geophysical Prospecting*, 47, pp 103-116.

McCann, D. M., M. G. Culshaw, F. G. Bell, and J. C. Cripps (1988). Reconnaissance methods for the location of abandoned mineshafts and adits. *Construction in Areas of Abandoned Mineworkings*, in Edinburgh (United Kingdom), pp 53-60.

McCann, D. M., P. D. Jackson, and M. G. Culshaw (1987). The use of geophysical surveying methods in the detection of natural cavities and mineshafts. *Quarterly journal of engineering geology*, 20, pp 59-73.

Miller, R.D., and D. W. Steeples (1991). Detecting voids in a 0.6-m coal seam, 7 m deep, using seismic reflection. *Geoexploration*, 28, pp 109-119.

Misquitta, N. J. (1989). *Enhanced 222Rn levels over an abandoned underground coal mine*. MSc, University of Akron, Akron.

Mooijmans, O. P. M., J. Van der Kruk, and J. P. A. Roest (1998). The detection of abandoned mine shafts in the Netherlands. *Environmental & Engineering Geoscience*, 4, pp 307-316.

Moscicki, W. J. (1987). Temperature anomalies over underground cavities. *Geophysical Prospecting*, 27, pp 435-448.

Müller, C. (2000). *On the nature of scattering from isolated pertubations in elastic media and consequences for processing of seismic data*. PhD Thesis,

Mathematisch-Naturwissenshaftlichen Fakultät, Christian Albrechts Universität, Kiel (Germany).

Müller, G. (1985). The reflectivity method: a tutorial. *Journal of Geophysics*, 58, pp 153-174.

National-Research-Council (2002). *Coal waste impoundments*. Washington D.C.: National academy press.

Neidell, N. S., and M. T. Taner (1971). Semblance and other coherency measures for multichannel data. *Geophysics*, 36, pp 482-497.

Nielson, D.L., C. Linpei, and S. H. Ward (1990). Gamma-ray spectometry and radon emanometry in environmenta geophysics in *Geotechnical and Environmental Geophysics* edited by S. H. Ward: SEG, pp 219-250.

Onions, K. R., K. Whitworth, and P. D. Jackson (1996). Applications of geophysical methods to site investigations at contaminated old collieries. *Quarterly journal of engineering geology*, 29, pp 219-231.

Owen, T. E. (1983). Detection and mapping of tunnels and caves in *Developments in Geophysical Exploration Methods*. London: Applied Science Publishers, pp 161-258.

Owen, T. E., and S. A. Suhler (1980). Sub-surface void detection using surface resistivity and borehole electromagnetic techniques. *Society of Exploration Geophysicists 50th Annual International Meeting and Exhibition*, Session E-7.

Palmer, L. S., and J. M. Hough (1953). Geoelectrical resistance measurements. *The mining magazine*, 88, pp 16-22.

Pao, Y. H., and V. Varatharajulu (1976). Huygen′s principle, radiation conditions, and integral formulas for the scattering of elastic waves. *Journal of the Acoustical Society of America*, 59, pp 1361-1371.

Parasnis, D. S. (2000). *Principles of applied geophysics*. 5th ed. London: Chapman and Hill.

Park, C. B., R. D. Miller, and J. Xia (1998). Detection of near-surface voids using surface wave. *Symposium on the Application Geophysics Engineering Environmental Problems (SAGEEP)*, in Chicago (Illonios), pp 281-286.

Peng, C. B., and M. N. Töksoz (1995). An optimal absorbing boundary condition for elastic wave modeling. *Geophysics*, 60, pp 296-301.

Pereda, J. A., L. A. Vielva, A. Vegas, and A. Prieto (2001). Analyzing the stability of the FDTD Technique by combining the von Neumann Method with the Routh–Hurwitz criterion. *IEEE Transactions on Microwave Theory and Techniques*, 49, pp 377-381.

Peters, W. R., and R. G. Burdick (1983). Use of an automatic earth resistivity system for detection of abandoned mine workings. *Mining engineering*, 1, pp 55-59.

Phillips, C., G. Cascante, and D. J. Hutchinson (2002). The innovative use of surface waves for void detection and material characterisation. *Symposium on the Application Geophysics Engineering Environmental Problems (SAGEEP)*, in Las Vegas, pp 10.

Polymenakos, L., and St. P. Papamarinopoulos (2007). Using seismic traveltime tomography in geoarchaeological exploration: an application at the site of Chatby cemeteries in Alexandria, Egypt. *Near surface geophysics*, 5, pp 209-219.

Ramadan, O (2003). Auxiliary differential equation formulation: an efficient implementation of the perfectly matched layer. *IEEE Microwave and Wireless Components Letters*, 13, pp 69-71.

Randall, C. J. (1989). Absorbing boundary condition for the elastic wave equation: velocity-stress formulation. *Geophysics*, 54, pp 1141-1152.

Roden, J. A., and S. D. Gedney (2000). Convolutional PML (CPML): An efficient FDTD implementation of the CFS-PML for arbitrary media. *Microwave and optical technology letters*, 27, pp 334-339.

Sacks, Z. S., D. M. Kingsland, R. Lee, and J. F. Lee (1995). A perfectly matched anisotropic absorber for use as an absorbing boundary condition. *IEEE Transactions on Antennas and Propagation*, 43, pp 1460-1463.

Saenger, E. H. (2000). *Wave propagation in fractured media: theory and application of the rotated staggered finite-difference grid*. PhD thesis, Faculty of Physics, University of Karlsruhe, Karlsruhe.

Saenger, E. H., and T. Bohlen (2004). Finite-difference modeling of viscoelastic and anisotropic wave propagation using the rotated staggered grid. *Geophysics*, 69, pp 583-591.

Saenger, E. H., N. Gold, and S. A. Shapiro (2000). Modeling the propagation of elastic waves using a modified finite-difference grid. *Wave motion*, 31, pp 77-92.

Schicht, Th., U. Linder, J. Heckner, G. Strobel, and I. Rappsilber (2007). Seismic tomography on the castle hill in Quedlinburg. *Near Surface Geophysics*, 5, pp 339-343.

Schlue, J. W. (1979). Finite element matrices for seismic surface waves in three-dimensional structures. *Bulletin of the Seismological Society of America*, 69, pp 1425-1438.

Schwarz, S. D. (1990). Interpretation of shallow refraction seismic data by reflection/refraction tomography in *Geotechnical and Environmental Geophysics* edited by S. H. Ward: SEG, pp 281-288.

Sharma, P.V. (1997). *Environmental and engineering geophysics*: Cambridge university press.

Sheriff, R.E., and L.P. Geldart (1995). *Exploration seismology*. 2nd ed. Cambridge: Cambridge University Press.

Shryhane, G. (2007). *For love of Dolly* [Last accessed on 12 April 2007]. Available from http://www.wiganworld.co.uk/stuff/past1.php?opt=past.

Shtivelman, V., and S. Keydar (2005). Imaging shallow subsurface inhomogeneities by 3D multipath diffraction summation. *First Break*, 23, pp 39-42.

Sibley, R. D., and P. Grainger (1988). Soil gas geochemistry: a potential method for detecting old mine workings. *Construction in Areas of Abandoned Mineworkings*, in Edinburgh (United Kingdom), pp 61-68.

Sladen, J.A., C.S. Bodimeade, and V.R. Jobling (1984). Site investigations and urban development guidelines with respect to mining subsidence harzards - two example from Alberta, Canada. *Construction in Areas of Abandoned Mineworkings*, in Edinburgh (United Kingdom), pp 196-220.

Sochacki, J., R. Kubichek, J. George, W. R. Fletcher, and S. Smithson (1987). Absorbing boundary conditions and surface waves. *Geophysics*, 52, pp 60-71.

Sogade, J., Y. Vichabian, and F. D. Morgan (1999). Induced polarization in the detection of cave systems. *Symposium on the Application Geophysics Engineering Environmental Problems (SAGEEP)*, in Oakland (California), pp 317-322.

Spence, D. (1984). Documents illustrative of the long history of coal mining in east Lothian. *Transactions of the east Lothian antiquarian & field naturalist's society*, 18, pp 1-3.

Stolarczyk, L.G. (1990). Radio imaging method in seam waveguide in *Geotechnical and Environmental Geophysics* edited by S. H. Ward: SEG, pp 187-210.

Stothard, J. (2007). Personal communication by E-mail: *Shaft collapses near transport lines*, 12 April 2007.

Tan, T. H. (1976). Diffraction of time-harmonic elastic waves by a cylindrical obstacle. *Applied Scientific Research*, 32, pp 97-144.

Telford, W.M., L.P. Geldart, and R.E. Sheriff (1990). *Applied geophysics*. 2 ed: Cambridge university press.

Titman, D. J. (1992). Aerial thermal imaging of land fill sites. *Construction on Polluted + Marginal Land*, in London, pp 59-62.

Valle, S., and L. Zanzi (1996). Radar tomography for cavities detection. *Symposium on the Application Geophysics Engineering Environmental Problems (SAGEEP)*, in Keystone (Colorado), pp 555–563.

Viktorov, I.A. (1967). *Rayleigh and Lamb Waves: physical theory and applications*. New York: Penum Press.

Virieux, J. (1984). SH-wave propagation in heterogeneous media: Velocity-stress finite-difference method. *Geophysics*, 49, pp 1933-1957.

Virieux, J. (1986). P-SV wave propagation in heterogeneous media: Velocity-stress finite-difference method. *Geophysics*, 51, pp 889-901.

Wang, T., and X. Tang (2003). Finite-difference modelling of elastic wave propagation: A nonsplitting perfectly matched layer approach. *Geophysics*, 68, pp 1749-1755.

Weeks, R.E. (2004). Application of synthetic aperture radar interfermetry (InSAR) in defining mine-related ground deformation and subsidence hazards. *5th biennial Workshop - Interstate Technical Group on Abandaned Underground Mines*, in Tucson (Arizona), pp 11.

Weltham, A. (1987). Assessing ground conditions of small sites by aerial infrared photography. *Quarterly journal of engineering geology*, 20, pp 114-115.

Whiteley, R. J. (2003). Reducing tunnelling risks with seismic imaging. *Underground Construction*, in London (United Kingdom), pp 585-594.

Winter, M. G. (2001). Spent oil shale use in earthwork construction. *Engineering Geology*, 60, pp 285-294.

Woodland, A. R., and I. Statham (1992). Mine of informations - a national review of mines and instability. *Construction on Polluted + Marginal Land*, in London (United Kingdom), pp 234-244.

Xia, J., J. E. Nyquist, Y. Xu, M. J. S. Roth, and R. D. Miller (2007). Feasibility of detecting near-surface feature with Rayleigh-wave diffraction. *Journal of Applied Geophysics*, 62, pp 244-253.

Appendix A - Visual inspection

The purpose of the field reconnaissance is to identify and localize anomalies that are associated with the presence of the mineshaft. As discussed in section 2.4.2, the field reconnaissance consists of visual inspection, geochemical and geophysical methods. This appendix deals with the field reconnaissance by visual inspection. In this appendix two different ways to conduct a visual inspection are discussed - walkover by a simple site inspection by foot and flyover using airborne instrumentation.

A.1. Site inspection – walkover

Objective: Detect surface expressions of the mineshaft by a site inspection.

Availability: Requires some expertise.

Possession of the track: No.

Cost of survey: Very cheap.

Description: More than often, mineshafts buried in the subsurface express themselves at the surface. These expressions can be identified and used to locate the mineshaft. There are various features that can indicate the presence of the mineshaft (*Sladen et al., 1984; Mooijmans et al., 1998*):

- Subsidence hollows: these hollows are caused by the collapse or the partial collapse of the mineshaft.
- Surface depression: due to compaction of the backfilling depression can come into existence at the surface.
- Surface discoloration: the soil at the mineshaft can differ in colour. The source of the discolorization can have different origins:

- The backfilling consists of different material. Often the backfill contains colliery ashes and it tends to be darker when compared to the natural soil.
- Discoloration can also be caused by differences in moisture content due to differences in drainage patterns.
- Other clues for the location of the shafts include conspicuous lineaments:
- Lone-standing trees: sometimes trees have been planted on top of the backfilled mineshaft.
- Excessively wet areas: wet areas can be associated with subsidence hollows and surface depression.
- Vegetation withering: withering can be caused by local reduction in soil moisture content due to better drainage, and trees were sometimes planted above the backfilled shaft.

Issues: Discoloration of the soil can be caused by the backfilling however the discoloration might also be associated with the location of the steam engines. This could lead to misinterpretation of the anomalies.

It is very unlikely that the mineshaft has any expressions at the embankment of the railway and mineshaft located directly beneath the railway cannot be detected. Furthermore the presence of the vegetation and especially dense bushes can mask the surface expression of the mineshaft.

Effectiveness: Site investigation by a simple walk-over is very cheap and considering the result of the site investigation experiment presented on page 284, this method can be effective. However, it is unlikely that mineshafts beneath the railway can be located and therefore a site investigation should always be combined with other field reconnaissance techniques.

Site investigation experiment

In 2006, a survey was conducted in order assess the suitability of mineshaft sites for further geophysical experimentation which are presented in chapter 8. Seventeen sites in Mid- and East Lothian were visited during the survey. The locations of the mineshafts were identified using Ordnance Survey Explorer maps. The results of the survey are presented in Table A.1.

From the 17 sites visited, 11 were easy accessible. The others sites were used for redevelopment or vegetation/crops prevented access for closer inspection. In the case of arable land, the site cannot be accessed without destruction of the crops. These sites might be accessed after the harvest. However, variations in vegetation growth might be an indication of the location of the mineshaft. Therefore for railway sites in the proximity of arable land, it is recommended that the visual inspection survey is conducted before and after the harvest. From the eleven accessible mineshaft sites, eight of them had a surface expression which might be related to the location of the mineshaft.

Examples of these expressions are presented in Figure A-1. At the Edmonstone Mains site there are two surface expressions which are related to mining: a lone-standing tree on an artificial hill and a surface depression with overgrown dense vegetation that differs from the vegetation away from the depression. It is very likely the artificial hill consists of tipped material from the mine and the surface depression is the actual location of the mineshaft.

Another example of surface expression related to the location of a mineshaft can be found in Figure A-2. A surface depression can clearly be observed. The location of the depression matches the location of the mineshaft on the OS Explorer map.

Since no ground proofing could be carried out, it is impossible to ascertain the actual success rate of the site investigation by a simple walk-over.

Table A.1. Overview of the site inspection conducted in Mid- and East Lothian

Location	Grid reference	Mineshaft expression
Edmonstone Mains	NT 302 696	Artificial hill with lone-standing tree Surface depression
Danderhall/Drumbank	NT 300 694	Small depression
Gilmerton depot	NT 302 679	Surface depression
Gilmerton depot	NT 301 680	No surface expression
Gilmerton depot	NT 300 680	Possible expression, dry patch
Campbell Park	NT 338 651	Dense vegetation in the middle not exactly in coordinated with map
Campbell Park	NT 337 651	Possible expression, dry patch
Lingerwood Farm	NT 341 638	Inaccessible (crops)
Lingerwood Farm	NT 342 638	Inaccessible (crops)
Huntlaw Farm	NT 435 677	Capped mineshaft (visible)
Huntlaw Farm	NT 433 678	No surface expression
Huntlaw Farm	NT 435 679	No surface expression
Orminston	NT 418 695	Redeveloped for grain store
Orminston	NT 403 695	Inaccessible (dense vegetation)
Orminston	NT 401 694	Inaccessible (dense vegetation)
Cousland	NT 376 680	Inaccessible (crops on land)
Fuffet wood	NT 362 658	Small hill corresponds with location

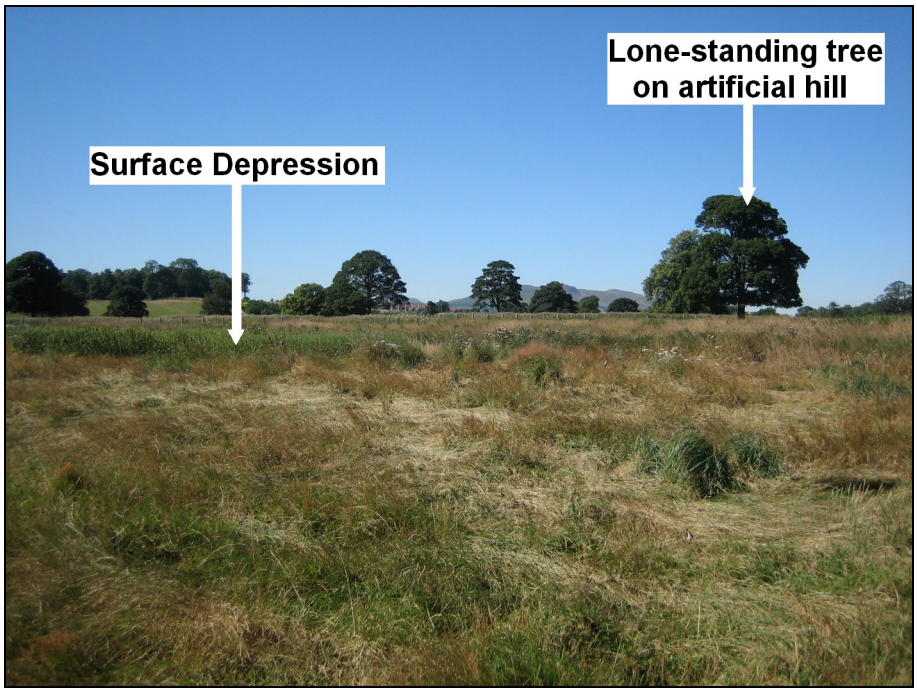

Figure A-1. Surface features at Edmontone Mains site that are related to mining

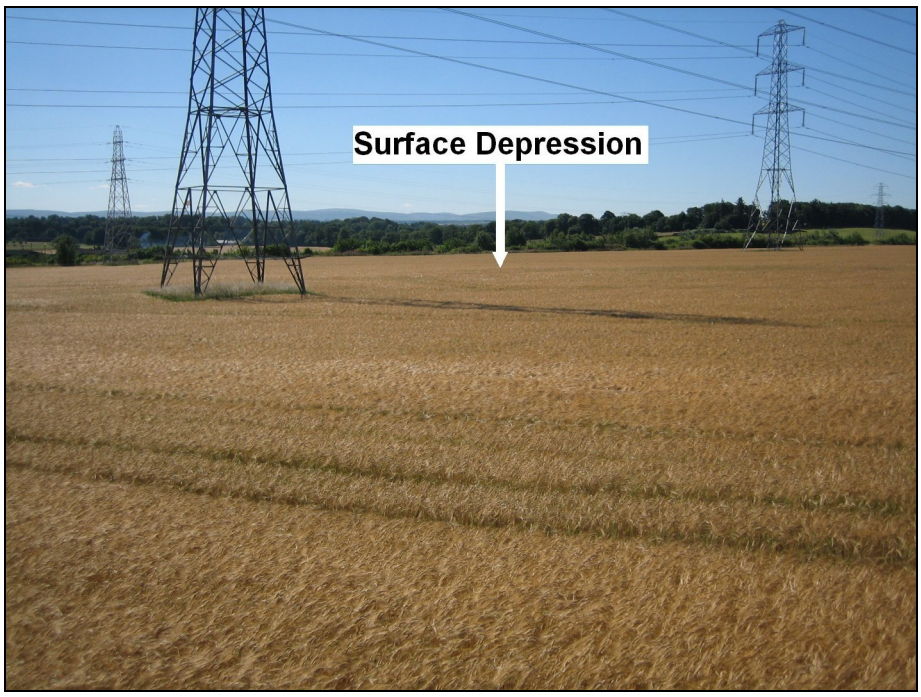

Figure A-2. Surface expression related to mineshaft at the Gilmerton depot

A.2. Airborne inspection

Objective: Detect surface anomalies from greater height.

Availability: Some companies provide airborne scanning and photography.

Possession of the track: No.

Cost of survey: Expensive.

Description: Surface features associated with the presence of mineshafts might not be easy to identify from observation points close to the surface and often it can be easier to identify them from a larger distance. Surface features which could be indicators were discussed in section A.1.

The use of aerial photographs as a tool to identify possible locations of mineshafts is widely known but the technique remains little employed. A reason for this is that people assume that the costs of airborne techniques are fairly high and that the probability of success is reasonable small. However, very little post-processing and interpretation has to be done and also possession of the tracks is not required. The costs could be reduced by using radio controlled airplanes instead of manned airplanes (*Weltham, 1987*). The use of high-resolution satellites might also be an option.

Various governmental and commercial institutes keep large archives containing various aerial photographs of the whole of Great Britain, which might eliminate the need to take the pictures by themselves. Historical photos can also be used as an extra aid in the interpretation. Using present aerial photographs and historical photographs, Mooijmans et al. (*1998*) was able to identify four out of five known mineshafts in the south of the Netherlands. This result can be considered as a good success ratio. Subtle subsidence hollows can be identified using stereographic photographs (Cooper, 1989; Mooijmans et al., 1998).

It was suggested that airborne multi-spectral scanning could pick up the soil discolorations and vegetation changes (*Cooper, 1989*). Both features can be

associated with the presence of a mineshaft. The difference between photography and multi-spectral scanning is the difference in bandwidths. Photos use the whole visual bandwidth, whereas a multi-spectral scanner images various different bandwidths, which can be individually processed and interpreted. Different bandwidths are sensitive for different surface features. It turned out that colour changes caused by soil and moisture content variations can be best observed using near natural colours, whereas bandwidths from red to infrared are considered to be very suitable to identify vegetation variations.

A multi-spectral scanning survey was carried out to define quickly the extent, the cause and the nature of subsidence due to gypsum dissolution around Rippon. Figure A-3 shows an example of the images obtained by the multi-spectral scanner.

The left image uses infrared bandwidths, which were given false colours in order to make the image visual to the human eye. In this image the subsidence hollows can be identified easily as the red dots. Some vegetation variation can also be identified. The right image uses various different bandwidths. The vegetation variations associated with subsidence can be easily identified. The aerial sensing survey revealed more information than the initial ground survey.

Issues: The presence of buildings, infrastructure and dense vegetation could mask the surface expression of the mineshaft. It is very unlikely that aerial photography or multi-spectral scanning would be able to delineate hidden mineshafts which are directly located below the railways. Also it should be stressed that these techniques are only suitable for delineation of mineshafts which have surface expressions, which may not always be the case or sufficiently distinctive.

Effectiveness: Airborne imaging seems to be an effective method however it is unlikely that mineshafts beneath embankments can be resolved. This leaves a large area uncovered and therefore airborne imaging techniques are considered as ineffective.

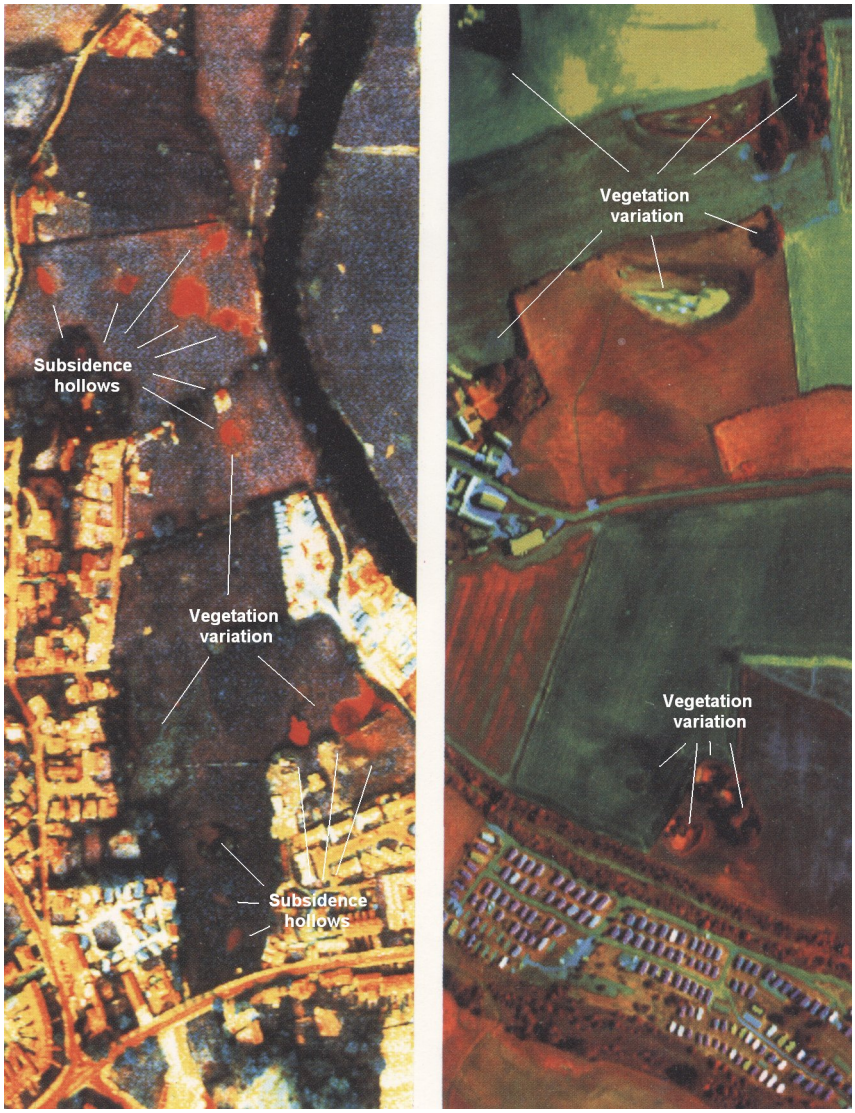

Figure A-3. Two multi-spectral scanner images of subsidence hollows (*Cooper, 1989*)

Appendix B - Geochemical reconnaissance

This appendix discusses the use of geochemical survey techniques as a part of the field reconnaissance. Geochemical survey techniques consist of measuring the concentration of certain chemicals in the soil. Gas concentration anomalies can be related to the presence of the mineshaft. Additionally some radiometric techniques are discussed. The radioactive gas Radon is discussed in the radiometric section.

B.1. Gas emission methods

Objective: Detect gas concentration anomalies in the soil.

Availability: Some survey companies provide this service.

Possession of the track: Yes.

Cost of survey: Average.

Description: The emission of gases from abandoned mines has been recognised as a potential hazard and to a lesser degree as a survey tool. After closure, the cessation of ventilation allows accumulation of the gasses. The accumulations of gasses give rise to variations in gas concentrations in the soil. These variations could indicate the presence of a mineshaft at a site. The most commonly measured gases are methane and carbon dioxide; other gasses include nitrogen, helium and hydrogen sulphide. Gas concentration anomalies are not purely confined to coal mine workings, but were found also in clay, tin and gypsum mines (*Woodland and Statham, 1992*).

The potential and the limitations of gas emission surveys were never researched fully. However various investigations at mining sites indicated that gas concentration fluctuations in the soil can be related to the presence of mine

workings (*Sibley and Grainger, 1988*). Figure B-1 shows an example of surveys using various gas types above a mineshaft. In this case the carbon dioxide and helium gasses were the clearest indicators of the location of the mineshaft. It is recommended when conducting a survey to measure multiple different gasses to increase the probability of detection.

Issues: The performance of gas emission surveys can be influenced by the presence of clay-rich soils. Clay is impermeable to soil gas movement and therefore the actual gas concentrations are difficult to measure by probes. The values measured at clay-rich sites are erratic and difficult to correlate to the presence of mineshafts or workings (*Sibley and Grainger, 1988*).

Meteorological conditions and seasonal variations all affect the gas concentrations and therefore will change the patterns observed above the mineshaft. It was shown that the change in barometric pressure was most pronounced in the upper layers of the soil. It is therefore recommended to take gas samples from at least 50cm depth and/or executing the survey during periods of little barometric changes. According to Donnelly and Bramford (*Donelly and Bramford, 1996*) the most suitable meteorological condition for data acquisition is after a drop in the barometric pressure of between 4 and 8mb in 3 hours, which allows emission of the mine gas that has accumulated in the mine.

Some gasses are soluble in groundwater. It is likely that anomalies measured at the surface are not directly related to the location of the mineshaft due to the mobility of ground water. The interpreter has to bear this in mind. In areas where the water table is close to the surface the gas emission surveys are likely to fail, because the gas concentrations cannot be determined. Also the mobility of water can affect the performance by solution and degassing. Rainfall will reduce the porosity of the surface layers and therefore depress the flux of gasses.

It is unlikely that measurements taken from the ballast layer are reliable due to the large porosity of the aggregate. Wind and barometric pressure changes have free play at the ballast and therefore the gas concentrations may not be representative of the subsurface.

Effectiveness: Measurements taken at the ballast are unreliable and therefore soil gas emission methods are only suitable for mineshaft detection beside the railways. This leaves a large area uncovered. Moreover, the presence of clay in the subsurface could limit the performance. Coal measures are often overlain by clayey soils and most mineshafts in the UK are unlikely to be detected by soil gas emission methods.

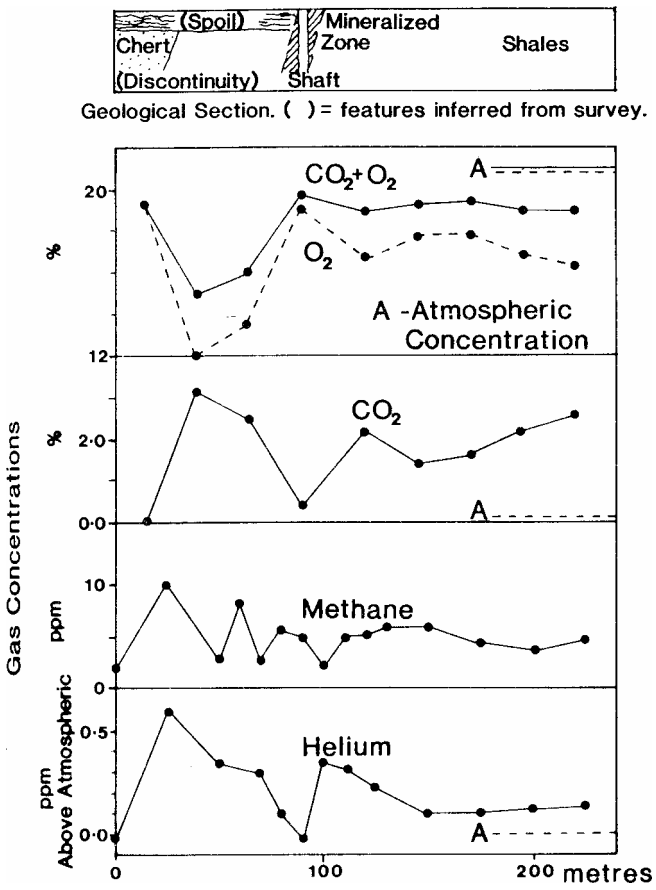

Figure B-1. Gas concentrations over a mineshaft (*Sibley and Grainger, 1988*)

B.2. Radiometric methods

Gamma-ray spectrometry and radon emanometry were regularly used for the detection and mapping of radio nuclides. In the environmental surveys these techniques are used to delineate nuclear waste and mapping of faults, landslides and other geologic structures. Both techniques are often used conjointly.

B.2.1. Gamma-ray spectrometry

Objective: Measuring anomalies in radioactivity.

Availability: Some survey companies provide this service.

Possession of the track: Yes.

Cost of the survey: Cheap.

Description: Radioactivity is a statistical process in which the number of atoms of the natural elements in the earth material decays to produce other nuclides. These transformations involve emissions of alpha particles, beta particles and gamma ray. The absorption range of alpha and beta particles in rocks is practically zero and therefore are not suitable for exploration surveys. The emission of gamma ray occurs due to the decay of uranium, thorium and potassium elements. The concentrations of uranium, thorium and potassium vary between the various geological materials (*Nielson et al., 1990*).

The gamma-ray spectrometry is useful in delineation of radioactive waste and in mapping lithologies, but the technical literature is sparse regarding detection of voids, mine workings and mineshafts. An air-filled or water-filled mineshaft contains no material which produces natural gamma ray. The gamma ray emission above the concealed mineshaft can be expected to be lower than further away from the shaft. Gamma-ray spectrometry might be particularly effective

where the mineshafts have been sunken into material rich in uranium, thorium or potassium.

Issues: There are no papers or reports regarding the use of gamma-ray spectrometry to delineate mineshafts or cavities. In low radioactive environments, the statistical error might be large and erroneous conclusions can be made. Furthermore radioactivity can be produced by other sources of human or astral origin.

Effectiveness: At this moment very little is known about the potential of this technique and therefore this technique is deemed ineffective.

B.2.2. Radon emanometry

Objective: Detect anomalous radioactive gas concentration in the soil.

Availability: Some survey companies can provide this service.

Possession of the track: Yes.

Cost of survey: Average.

Description: Radon is a noble gas and it is formed from decay of the uranium and thorium. All the isotopes of radon gas are radioactive and unstable and will decay into polonium after several days. The radon isotope ^{222}Rn is by far the most abundant present in the natural environment and widely used as a survey tool.

By plotting the concentration of radon as a function of location, a radon concentration map can be made. A radon concentration anomaly could indicate the presence of a mineshaft. Literature is sparse regarding radon surveys and contradictive; Bondarenko et al. (*1983*) showed that negative Radon concentrations are associated with mine workings, whereas Misquitta (*1989*) demonstrated that positive Radon concentrations can be related to mine

workings. Both surveys did not include mineshafts. It was believed that the positive anomaly is produced by radon concentrating in the voids left by mining and then released to the surface by way of fractures or faults resulted from mining activities (*National-Research-Council, 2002*).

Issues: Similar to gas emission methods discussed in section B.1, radon emanometry bares the same meteorological dependencies. Changes in barometric pressure, precipitation and the wind can all affect the performance of the survey.

Radon surveys over mineshafts show that the radon gas anomalies often extend beyond the mineshaft for several metres. This is caused by the tensile deformation in the walls of the shaft and the dilation of the rock mass fissures (*Donelly and Bramford, 1996*). Radon emission methods are therefore not suitable for pinpointing the location of the shaft. Furthermore, since samples taken from the ballast are unreliable a large area is left un-sampled and therefore radon surveys are only suitable to locate anomalies away from the railway.

Effective: It is proven that radon gas anomalies can be associated with mine workings. Measurements taken at the ballast are unreliable which leaves a large and very important area uncovered. Radon gas emanometry might be successful in the delineation of mineshafts away from the embankment.

Appendix C - Geophysical reconnaissance

This appendix discusses field reconnaissance by geophysical survey methods. The purpose of geophysical methods is to estimate the physical properties in the subsurface such as density, elasticity and temperature. There exist numerous geophysical methods and each method having many varieties. New geophysical techniques and varieties emerge regularly and hence this overview is by no means complete. The focus is mainly on existing techniques that geophysical survey companies can provide. Exotic geophysical methods are only included when they appear to be suitable for mineshaft detection. The geophysical methods that make use of boreholes are discussed separately in section C.8.

As a part of the assessment of the geophysical methods, several small scale surveys were conducted at a full scale track bed model. The results were used in the assessment of the geophysical technique and therefore they are included in this appendix.

C.1. Experiments at the full scale track bed

Very little unbiased information is available regarding geophysical surveys at railway sites. Therefore as a part of the assessment several geophysical experiments were conducted at the full scale track bed at the University of Edinburgh. The purpose of these experiments was to provide additional information about the feasibility of some of the geophysical techniques to delineate mineshafts and to identify any problems that are associated with the presence of the railways. The following geophysical survey techniques were tested at the track bed:

- Magnetometry
- Resistivity tomography
- Self-potential
- Ground penetrating radar

In Figure C-1 a schematic overview of the full scale track bed can be found. The track bed consists of a 10.7m long embankment which includes the foundation which is made up of a clay layer and a ballast layer. The ballast layer consists of an aggregate in three different conditions: clean, spent and mixed. The sleepers consist of 4 wooden at both ends and 13 reinforced concrete ones. The sleepers are separated by approximately 65cm.

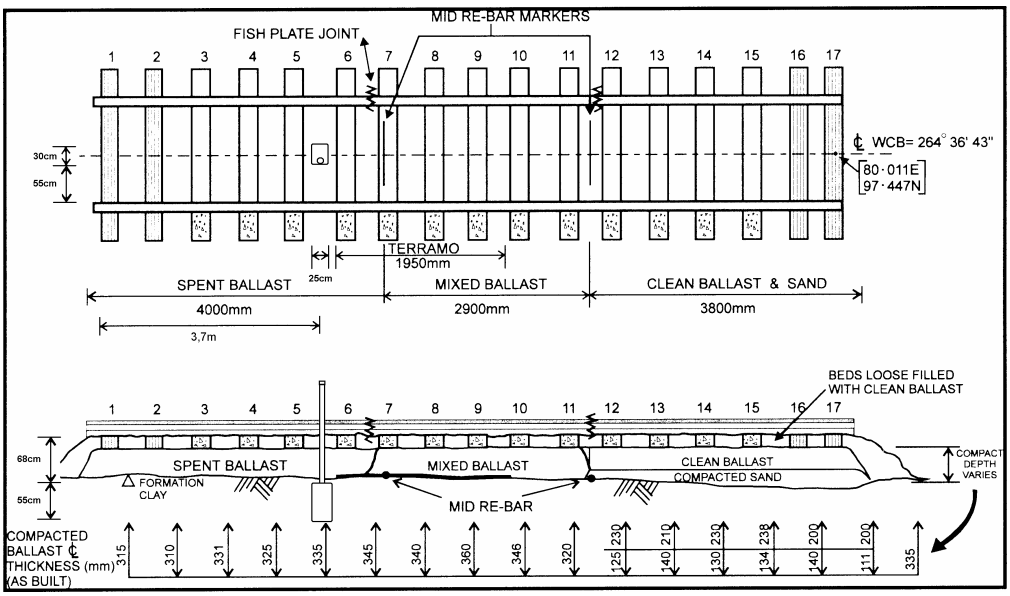

Figure C-1. Schematic overview of the full scale track bed with the canister representing the water of air filled void – modified from (*Clark, 2001*)

In order to assess the potential of the geophysical surveys to detect targets beneath the railway, a small void was inserted in the clay layer just below the ballast. The void consists of a plastic canister of 30 x 25 x 55cm size. The top of the canister is located at 68cm from the surface. The canister is connected with the surface by a plastic pipe such that the canister can be filled with air or water in order to simulate the air or water voids. Some photos of the canister during the insertion and the railway trackbed can be found in Figure C-2.

Figure C-2. Photo of the canister (left) and of the trackbed after the insertion (right)

C.2. Magnetometry

Objective: Measuring the variations in the earth's magnetic field.

Availability: Service widely provided by geophysical survey companies.

Possession of the track: Yes

Costs of survey: Very cheap

Description: The purpose of a magnetic survey is to measure the variations in the earth's magnetic field. Most materials have different magnetic properties. Variations of material in the subsurface could lead to variation in the magnetic field on the surface. By plotting the magnetic values on a grid, anomalies in the subsurface can be outlined. Magnetic surveys are widely used for the detection of mineshafts and caves. The delineation of brick-lined mineshafts and mineshafts backfilled with highly magnetic material were particularly successful (*McCann et al., 1987; Gallagher et al., 1978; Dearman et al., 1977*). Dresen showed the concrete capping of a mineshaft can also be resolved by magnetic surveys (*Dresen et al., 1975*).

Issues: In the case of unlined shafts or when the magnetic susceptibility of the backfilling differs little from the surrounding material, a magnetic method might be unsuccessful in delineating the mineshaft. Furthermore, the magnetic field is strongly attenuated by metal objects, which are present in abundance at railway sites: rails, overhead line equipment, signal cables etc. Also the aggregate in the ballast is composes a magnetic material. Variation in the thickness of the ballast layer can lead to spurious anomalies or even masking of the anomaly caused by mineshafts.

Effectiveness: At railways sites the magnetometric surveys are deemed ineffective due to the presence of metals.

Magnetometry experiment

In order to verify the assumption that the magnetic surveys are inefficient near railways due the metal present, an experiment was conducted at the railway track bed. Results of the magnetic survey at the railway track bed before, and after the insertion of the void, can be found in Figure C-3. The equipment used was a Geometrics G856 proton magnetometer. The data was plotted using

Matlab. The void is water filled and is located at 3.7m. Figure C-3 shows a very erratic behaviour of the magnetic field for both surveys. As could be expected the magnetic survey did not resolve the location of the void due to the presence of metal. The results affirm the conclusion that the effectiveness of magnetometry is very low.

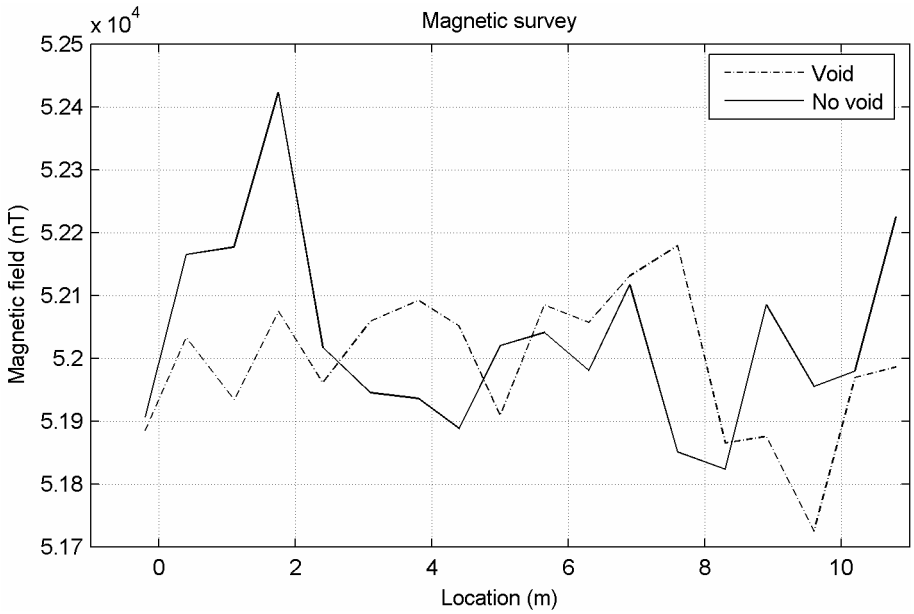

Figure C-3. Results from the magnetic survey at the full-scale track bed

C.3. Gravimetry

C.3.1. Microgravity

Objective: Measuring the gravitational variations along the surface.

Availability: Service provided by most geophysical survey companies.

Possession of the track: Yes.

Costs of survey: Expensive – slow and accurate corrections required.

Description: A microgravity survey consists of measuring the variation in the gravitational acceleration at the surface at equidistant survey points. The variations in the gravitation field reflect the density contrasts in the subsurface. These contrasts can have a geological origin such as caves and outcrops, or man-made such as mineshafts (Colley, 1963; Ghatge, 1993). Due to lower densities, the mineshaft produces a negative gravity anomaly.

Issues: Gravity anomalies caused by density inhomogeneities are relatively small compared to the earth's gravity field. Therefore microgravity surveys require very accurate measurements (*Sharma, 1997*). More than other geophysical methods, additional corrections to the measured gravity data have to be applied. Corrections for the instrument drift, tidal drift and topographic variations all have to be included. The drift in the instruments and the tidal drift can easily be compensated by using a base station, which measures the variation in the gravitational field at one location (*Debeglia and Dupont, 2002*). Topographic corrections which include free-air, Bouguer and terrain corrections, require accurate measurements of the elevation and an elaborate topographic survey is required (*Butler, 1980*).

A serious problem of microgravity surveys is the ambiguity in the interpretation of the data. For example a shallow deposit lens can produce the same anomaly as a mineshaft. Thus a negative anomaly does not always have to be produced by the presence of a mineshaft. Verification by field investigations is absolutely essential.

The duration of an accurate gravity measurement can take several minutes. Large survey sites require many measuring points. Therefore microgravity surveys are expensive and time consuming.

The gravimeters are very sensitive and strong vibrations might cause inconsistency in the data, hence possession of the track is required for the whole duration of the survey.

Effectiveness: Microgravity is regularly used to delineate mineshafts and it has proven to be successful (*Ghatge, 1993; Onions et al., 1996*). A failure of a microgravity survey is more likely to be caused by human errors than errors in the measurements and corrections. Particularly large air filled mineshafts shafts have great potential to be delineated, whereas completely filled shafts and small water filled shafts have limited potential (*Drossaert et al., 2004*).

C.3.2. Vertical gradient

Objective: Measuring the variations of the vertical derivative of the gravity field.

Availability: Not a standard service but can be provided by survey companies.

Possession of the track: Yes.

Costs of survey: Very expensive – more measurements required than microgravity.

Description: The method consists of measuring the gravity on the ground surface and one or more measurements at a different height at the same location. The vertical gradient of gravity field is approximated by taking the difference between the measurements divided by the height. A 3m high mobile tower has been used to measure the gravity gradient to locate a mineshaft (*Fajklewicz, 1976*). Towers of smaller than 1m high were also used (*Ager and Liard, 1982*), which is more convenient at railways sites; certainly when there are overhead lines. The vertical gradient surveys can obtain better results than microgravity

due to the selectivity of the depth penetration which is typically up to 10 to 15 metres (*Butler, 1984*).

Issues: The use of a tower is not practical in the field; especially when there is a lot of relief variation, such as ditches and embankments.

Small errors in the measurements can strongly propagate in the vertical gradient method. Most of the corrections discussed in the section are also necessary in the vertical gradient method. Deploying a vertical gradient survey instead of a normal microgravity survey doubles the number of measurements and also doubles the survey time and costs. For this reason the vertical gradient method has seldom been used.

Effectiveness: Although few vertical gradient surveys were carried out, there is little doubt that this technique can be effective in the delineation of mineshafts. However, the use of a tower might not be practical near railways.

C.4. Resistivity

Resistivity surveys to detect cavities were conducted since the nineteen-fifties (*Palmer and Hough, 1953*). There used to be two types of resistivity methods; sounding and profiling. The first type measures the vertical resistivity profile. Since mineshafts are vertical features the sounding method will not resolve any mineshafts and therefore this method will not be discussed further. The latter type of the resistivity methods focuses on lateral resistivity variations. This method will be discussed briefly in section C.4.1. The development of automatic resistivity equipment and computers in the early eighties increased the popularity of resistivity surveys. Peters and Burdick (*1983*) reported a first successful detection of abandoned mine workings using multi-channel equipment. The multi-

channel method will be referred as resistivity tomography and is discussed in section C.4.2.

Additionally, the feasibility of the self-potential technique and the induced polarization technique to locate mineshafts near railways are discussed in section C.6.3 and C.6.4 respectively.

C.4.1. Resistivity profiling

Objective: Measuring the apparent resistivity in the subsurface.

Availability: Not standard service, but can be provided by survey company.

Possession of the track: Yes.

Costs of survey: Cheap.

Description: The resistivity profiling method is commonly used in the geo-archaeology where this method is referred to as the resistivity mapping method. The technique basically consists of inserting a current into the ground at two electrode locations. The voltage is measured at two different potential electrodes and the resistivity of the subsurface can be calculated. The current electrodes and the potential electrodes are located at fixed distances. By relocating the electrodes configuration, a resistivity profile of the subsurface can be created.

Issues: Typical electrode configurations used in geo-archaeology are not useful for the delineation of mineshafts because it has typical penetration depths of less than 1m. However, it might be possible to detect the difference in electrical resistance of the backfill and surrounding soils. Forde and Whittington (*1984*) suggested the use of large separations between the current and potential electrodes in order to increase the penetration depth. Burton and Maton (*1975*) showed that using a dipole-dipole and a pole-dipole electrode configuration, a penetration depth of 3m and 10m respectively were achieved. The results of the

survey showed that low resistivity anomalies are associated with the location of two known mineshafts.

The ballast and the thickness of the ballast is made up of large aggregate with large air holes hence the resistivity of the ballast is very high which can limit the penetration depth considerably. Furthermore the coupling between electrodes and aggregate is bad and it is difficult to insert a sufficient strong current into the ground. It is very unlikely that it is possible to delineate mineshaft beneath the railway.

Effectiveness: Resistivity profiling can be used to delineate mineshafts, but might be difficult to locate mineshafts beneath the railway. Furthermore it offers little advantage over resistivity tomography.

C.4.2. Resistivity tomography

Objective: Measuring apparent resistivity values using multiple electrode configurations and create image of the subsurface using inversion algorithms.

Availability: Standard service provided by geophysical survey companies.

Possession of the track: Yes.

Costs of survey: Average.

Description: The apparent resistivity is measured at the surface using multiple electrodes at varying distances. Using inversion software the measured apparent resistivity data is used to reconstruct the resistivity image of the subsurface. Unlike the resistivity profiling method, this image provides information about the depth and hence interpretation is less ambiguous.

Since the resistivity tomography gives a complete image of subsurface, interpretation is relatively easy. For this reason alone, resistivity tomography has become one of the most popular near-surface techniques. Numerous examples can

be found in the literature on the subject of void detection (*Hammack, 2004; Hutchinson and Barta, 2004; Morris et al., 1997; Smith, 1986*) and some literature on the subject of mineshaft detection (*Owen and Suhler, 1980*).

Issues: Numerical studies showed that despite the large resistivity contrasts, air filled mineshafts are difficult to detect when the depth to the top of the mineshaft void is equal to or larger than twice the diameter (*Drossaert et al., 2004*). The limited depth resolvability can be explained by the fact that electric currents flow around the air-filled mineshaft, which leaves the mineshaft itself badly sampled. Field experiments showed similar characteristics of resistivity tomography (*Maillol et al., 1999*).

The railway ballast consists of large aggregate. The contact area of the electrode and the aggregate is very small. Hence the contact resistance is very high and also it is difficult to insert a sufficient strong current into the ground resulting into errors. The contact resistance can be address by using countermeasures such as using sponges saturated with an electrolyte solution as used in the resistivity experiment presented on page 307. Since the aggregate itself is high resistive, the penetration depth of the current is very low. Very strong currents are required to assure sufficient penetration depths. Usage of strong currents can be dangerous and can even be fatal. Moreover under no circumstances the electrical current may have any effect on the signal cables which is undesirable. There is no information about the effect of strong currents on the signal cables.

Effectiveness: Electrical resistivity tomography is a popular survey technique and can be efficient in the delineation of mineshafts away from the ballast. However, to detect mineshafts located beneath the ballast might be difficult since the electrodes need to be located in the high resistive ballast.

Resistivity experiment

Several resistivity surveys were conducted at the railway track bed. One survey was carried out with the canister filled with water and one survey with the canister filled with air. The equipment consisted of the Syscal Junior Switch multimode resistivity imaging system. Eighteen electrodes were used for the survey. These electrodes were hammered into the ballast in the middle between the sleepers and at each end of the trackbed. The left photo in Figure C-4 shows the electrode set up. The inversion software Res2Dinv was used to construct the resistivity image of the subsurface.

The results of both surveys can be found in Figure C-6. Noteworthy, the Root Mean Square error of both figures is larger than the 50%. This error is unacceptably large for interpretation and any conclusions made should reflect this. Both resistivity tomographs show a high resistive layer underlain by a low resistive layer. The high resistivity areas can be related to the ballast layer, although the real resistivity would be much higher than the tomographs suggest. Furthermore the thickness of this layer is overestimated by 0.4m. The low resistivity layer can be related to the boulder clay beneath the ballast layer. In the figure a low resistivity area can be observed around 3.7m. This approximates the location of the water filled canister. In the figure of the survey over the air filled canister, a low resistivity area can be observed at the location of the canister. This is contradictive to the fact that air voids have an infinite high electrical resistance.

One of the causes of the large error in the resistivity tomographs is that the contact resistance is too large to get sufficient current into the subsurface to obtain reliable resistivity tomographs. In order to address the contact resistivity, it is possible to use countermeasures.

Figure C-4. Photographs of the electrode lay out (left) and the electrodes with the sponges saturated with an electrolyte solution to address the high contact resistance (right)

One of the countermeasures is the usage of sponges saturated with an electrolyte solution e.g. table salt, in order to increase the contact area between the electrode and the aggregate. Figure C-4 shows a photograph of the electrode and the sponges saturated with an electrolyte solution.

The results of a survey conducted at the track bed using the countermeasures can be found in Figure C-5. The survey was conducted prior the insertion of the void. The RMS error is substantially smaller than the errors in Figure C-6. The depth of the ballast layer is considerably better estimated. However, an anomaly has been modelled around 7.8m which can not be related to any features in the track bed. This anomaly is located in the clean ballast side of the track bed, which has a higher resistivity than spent or mixed ballast. A possible explanation of the phenomenon is that errors are caused by the high resistivity of the ballast. Furthermore it should be pointed out that the usage only improves the contact resistance and not the problems involved in the lack of penetration depth due to high resistive aggregate. Unfortunately no surveys were conducted on the railway with a void using the electrolyte saturated sponges.

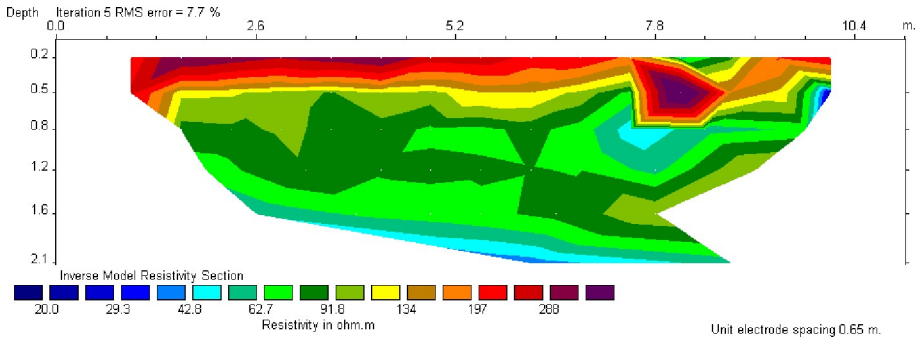

Figure C-5. Resistivity tomograph - railway track bed with no void

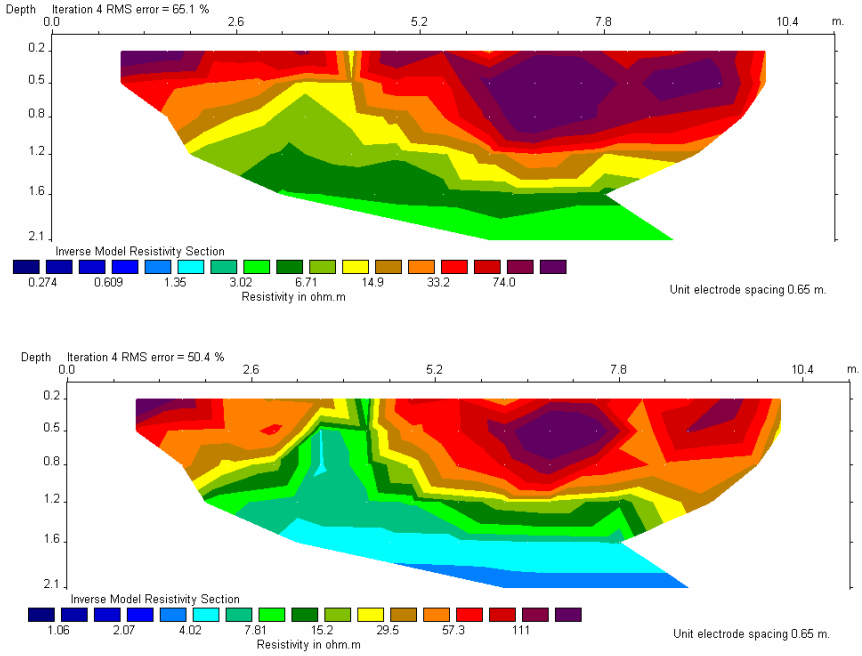

Figure C-6. Resistivity tomograph - track bed with water filled (top) and air filled void (bottom) at 3.4m

C.4.3. Self-potential

Objective: Measuring the natural voltage potentials in the subsurface.

Availability: Not a standard technique, but can be provided.

Possession of the track: Yes.

Costs of survey: Cheap.

Description: Natural voltage potentials can be generated by electrochemical actions between minerals and subsurface fluids or by electrokinetic processes involving the flow of ionic fluids. Potential anomalies produced by the presence of the mineshaft are often related to the flow of fluids, local temperature gradients, variations in electrolytes concentrations (*Sharma, 1997*). Self-Potential surveys in the field are simple and inexpensive; only a pair of non-polarizing electrodes connected to a voltmeter are required, although it may be necessary to remove regional effects from the Self-Potentials profile to enhance the shapes of anomalies (*Telford et al., 1990*).

Issues: Noise can be caused by changing soil conditions, elevation, saturation levels, resistivity variations and telluric current variations. In built up areas grounded electrical machinery, power lines, reinforced concrete, debris, etc. can cause stray potentials. It is important that the noise potentials are discerned to avoid misinterpretation (*Corwin, 1990*).

The presence of low resistance material such as clays in the topsoil diminishes the probability to delineate a mineshaft, whereas higher resistivity material such as sand has little effect on the performance. Moreover recent rain fall and the effects of rainwater percolation can induce spurious SP anomalies in the near-surface. An SP survey should be carried out preferably under dry circumstances (*Corwin, 1990*). A good electrode-to-surface contact is necessary to obtain the most consistent readings. It may be required to place electrodes deep in the

ground up to 50 cm to minimize surface temperature effects and to obtain reliable Self-Potential measurements.

Effectiveness: There is little evidence to support the assumption that the self potential method can delineate mineshafts. Furthermore this method is more susceptible to background noise than methods using active sources such as resistivity tomography. The coupling between the electrode and the aggregate in the ballast layer is a serious problem.

Self-potential experiment

In Figure C-8 the results of the fixed-based Self-Potential survey conducted at the track bed are presented. The equipment used consisted of non-polarizing electrodes, copper wires and a digital high-input-impedance voltmeter (ABEM Terrameter 300). Porous pots suspended in copper sulphate were used as non-polarizing electrodes. In Figure C-7 two photographs of the electrodes and the voltmeter as used in the experiment are presented.

Two surveys were conducted: in one survey the electrodes were placed on the ballast and in one survey the electrodes were placed on the sleepers.

The Self-Potential measurements taken from the ballast show a very erratic behaviour. This might be caused by strong contact resistance due to the aggregate in the ballast. The measurements taken from the sleepers show less erratic behaviour. A weak anomaly can be observed close to the location to the void. However, more anomalies can be found between 5 and 7 metres. These anomalies were not related to any features in track bed. Hence, the SP survey did not resolve the void conclusively.

Figure C-7. Photographs of the porous pots (left) and the ABEM Terrameter 300 digital high-input-impedance voltmeter (right)

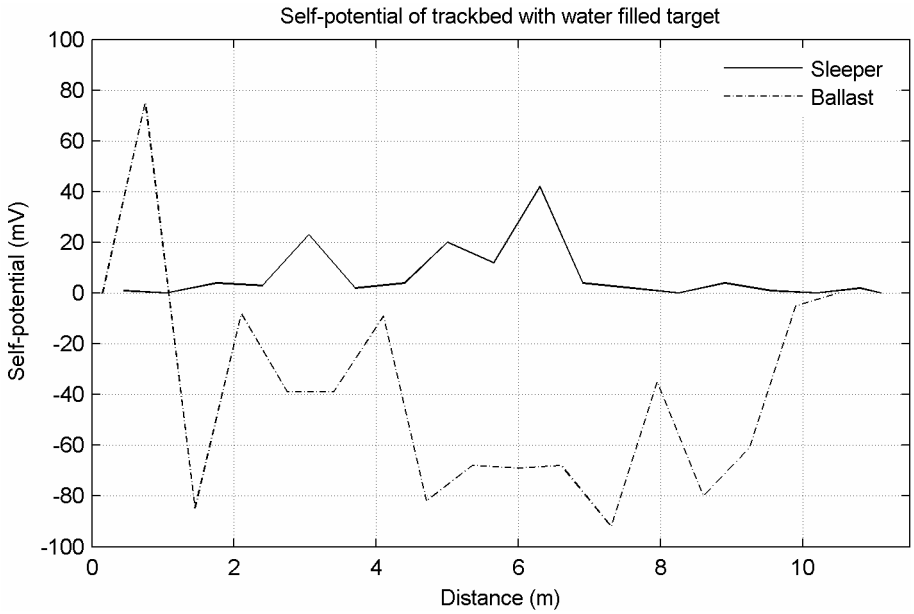

Figure C-8. Results of the self-potential survey at the track bed - void is located at 3.7m

C.4.4. Induced polarization

Objective: Measuring the induced polarization by recording the voltage dissipation after current cut off.

Availability: Service provided by some survey companies.

Possession of the track: Yes.

Costs of survey: Expensive – slower than resistivity.

Description: Induced polarization (IP) is a current-stimulated electrical phenomenon observed as a delayed voltage response i.e. after the switch off of the current the electrical voltage is dissipated, but does not drop to zero instantaneously. There are two processes that induce this phenomenon: electrode polarization and membrane polarization (*Corwin, 1990*). Since these processes are chemical processes, IP surveys are regularly applied in mineral exploration and groundwater contaminations investigations.

There are two different IP parameters depending on whether the measurements make use of a time-domain or frequency-domain waveform. In the time-domain IP surveys the measured parameter is called the chargeability, which is the integrated voltage decay over a certain time normalised with the primary voltage. The frequency-domain survey measures the percent frequency effect and the phase lag.

The data acquisition of an IP survey is similar to the resistivity methods, including tomography. Hence, the IP survey is often employed in conjunction with resistivity surveys.

Issues: The measurements of the IP data are more time consuming. IP data reflects other properties of the subsurface than the resistivity and thus it might be possible that an IP survey succeeds where a resistivity survey fails. This could be the case at water-filled mineshafts and low resistivity conductors, such as clay and marls.

Resistivity surveys are regularly used to detect voids however there has been minimal work done in using IP measurement for cavity detection (*Sogade et al., 1999*) and no literature can be found regarding mineshaft detection. The reason for little use is that the IP measurements have no or little advantages over

resistivity. The IP surveys are more susceptible to electrical noise and also take more time to complete the survey.

Similar to other electrical methods the electrode coupling at the ballast is a problem. The bad coupling can lead to errors in the data and it also limits the penetration depth.

Effectiveness: There is little evidence to suggest that IP methods can delineate mineshafts. Although IP survey measures different medium properties than the resistivity tomography method, there is little advantage to gain since the IP is more susceptible to noise which could be a problem when surveying at the ballast close to the OHLE.

C.4.5. Electromagnetic methods

Objective: Detect anomalies in the conductivity of the subsurface or anomalies in the electromagnetic field components using electromagnetic sources.

Availability: Standard service provided by most geophysical survey companies.

Possession of the track: Yes.

Costs of survey: Cheap.

Description: There exist a wide variety of electromagnetic (EM) survey methods. Each method measures an electric or magnetic field component induced in the subsurface by a primary field produced from a natural or an artificial source. The primary EM field induces eddy currents in the subsurface. These currents give rise to a secondary EM field. By measuring the secondary field the magnetic or electrical properties of the subsurface can be determined.

The most commonly used EM method in geotechnical engineering is the ground conductivity meter. Ground conductivity meters are portable system and measure directly the conductivity at shallow depth. Two different systems are

presently available. One system has transmitter and receiver built in one device. The other system consists of two EM devices; one transmits the primary EM field, whereas the second one receives. The spacing between the transmitter and receiver determines the penetration depth. Limited penetration depth can be achieved with the first system. Typically penetration depth values are 5 to 8 metres, whereas the second system penetration depths can be achieved of 30 metres (*McCann et al., 1987; Sharma, 1997*). EM methods are mainly used in exploration of metallic ores, pipes and cables, although other applications of EM can be found in faults and groundwater studies. The detection of voids and mineshafts is a less frequent application, but there are various successful surveys employed (*McCann et al., 1987; Liao et al., 1984; Witten et al., 1997; Sogade et al., 1999*).

Electromagnetic methods are popular, because they require no contact with the ground and the surveys can be carried out quickly and cost-effectively.

Issues: The primary electromagnetic field is strongly attenuated by metal objects, which are abundantly present at railway sites, e.g. rails, overhead line equipment, signal cables etc. Moreover the electromagnetic waves emanating from the overhead lines will interfere with the measurements. These EM waves can propagate long distances and their inference can be noticed at hundreds of metres away from the railways.

Effectiveness: Due to the susceptibility to metals, electromagnetic survey at and close to the railway are deemed to be ineffective in all cases.

C.5. Ground penetrating radar

Objective: Detect anomalies by measuring the response of a high frequency electromagnetic pulse.

Availability: Standard service provided by most geophysical survey companies.

Possession of the track: Yes.

Costs of survey: Average.

Description: The ground penetrating radar (GPR) has become a popular method in geotechnical engineering surveys and also in the delineation of caves and mineshafts (*Reppert et al., 1999; Darracot and Lake, 1981; Leggo and Leech, 1983; Mooijmans et al., 1998*). The GPR measures the EM response of the subsurface due a short high frequency EM pulse.

The transmission antenna and receiving antenna are usually collocated. By moving the radar along the survey line, an image of the subsurface can be created. Selecting the optimum acquisition parameters is extremely important for the success of a GPR survey, but it is not straight forward. Annan has written an extensive summary of selecting the acquisition parameters based on practical experiences (*Annan, 2005*). These parameters include operating frequency, time window, sampling interval, station spacing, survey grid and the antenna orientation. The parameters depend on the desired depth, resolution and the properties of the subsurface.

Issues: The biggest disadvantage of GPR is its limited penetration depth. There are many factors affecting the radar penetration depth in the subsurface, but the conductivity of the subsurface material and the operation frequency are the most important factors. Figure C-9 shows the penetration depth of various antennas as a function of the conductivity of the subsurface. It is recommended to employ GPR only in areas with a conductivity value of 10 mS/m or lower. This value not only excludes sites with clays and shales, but also some sands and alluviums.

The radar transmits an EM pulse not only into the ground, but in all directions. Strong reflections of high conductivity material, such as rails, overhead line masts etc. will occur. The use of shielded antennas can diminish the influence of these reflections on the GPR data, but can not eliminate these spurious

reflections completely. The interpreter has to bear this in mind. During the site investigations it is necessary to record the location and nature of features that could produce false reflections.

The material in the subsurface between the tracks consists of alternating sleepers and ballast. The conductivity of the sleepers differs substantially from the ballast. The GPR experiment presented on page 318 shows that radargrams taken from the ballast reflect this variation and interpretation is compromised.

Effectiveness: The GPR is a popular tool in geotechnical engineering since it provides quickly a continuous high resolution image of the subsurface readily available in the field. Various surveys demonstrate that the georadar can be used as a mineshaft detector provided the survey is carried out at low conductive sites. However, other surveys demonstrate that mineshaft detection by GPR can fail even when measuring in reasonably low conductive material (*Darracot and Lake, 1981; Brouwer and Nijhof, 1994*).

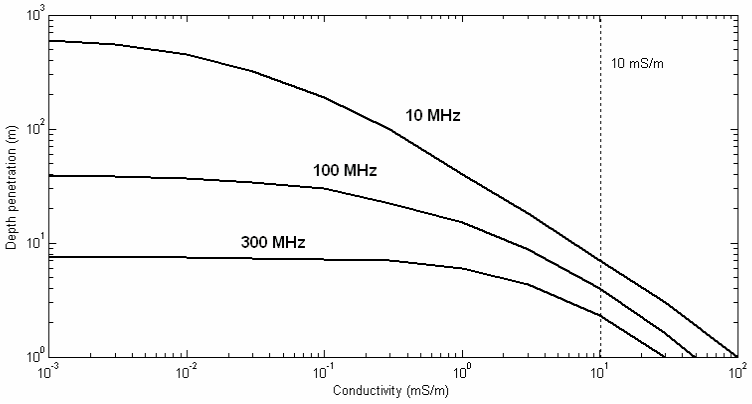

Figure C-9. The penetration depth as function of conductivity - after Cook (*Cook, 1975*)

Ground penetrating radar experiment

As a part of the assessment of the ground penetrating radar as a mineshaft detection tool, several GPR surveys were conducted at the University of Edinburgh railway track bed test site. The results of two survey lines can be found in Figure C-10. In this figure the data obtained by the PulseEKKO 900MHz and GSSI 900MHz is presented. Clearly the presence of the sleepers had a significant effect on the radar signals. Reflections from the ballast-clay interface only happened when the antennas were located between the sleepers. The reflections are easy to identify at the right-hand-side of the data set, but on the left-hand-side the reflections are less well-defined. The logical explanation for this behaviour is that the right-hand-side and the middle part consisted of contaminated, i.e. spent, aggregate which affects the performance of the GPR.

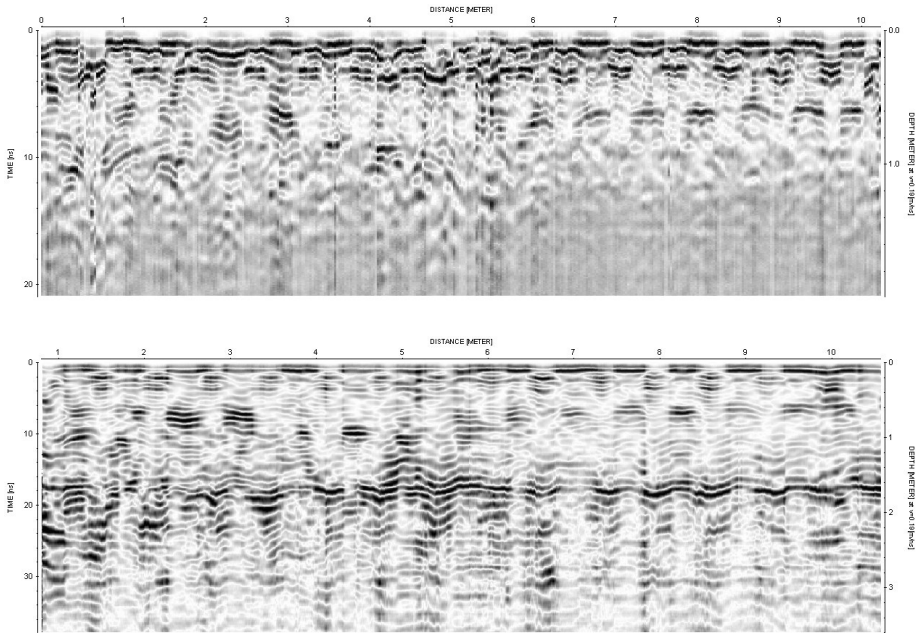

Figure C-10. Raw GPR data of the PulseEKKO system using a 900MHz antenna (top) and of the GSSI system using a 900MHz antenna (bottom); void is located at 3.7m

In Figure C-11 the results of the 450 MHz antenna can be found. The sleepers have even more negative influence on the GPR data than for the 900 MHz antenna. The sleepers cause diffraction and/or refraction of the emitted electromagnetic (EM) pulse, which results in an odd constructive and destructive wave pattern in the ballast layer. The ballast-clay interface can not easily be identified. At the right hand side of the track, where the clean ballast exists, the amplitude of the EM signal decreases significantly after ±13ns. This decrease in amplitude could be related to the ballast-clay interface. Although a small event that appears as a diffraction can be identified at the location of the void, there is no clear indication of the presence of the canister.

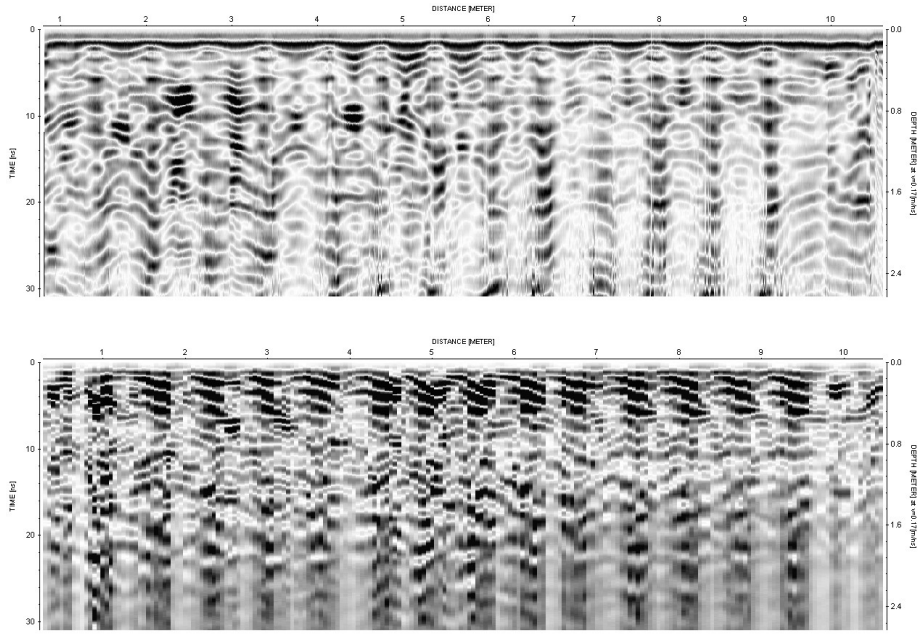

Figure C-11. Raw GPR data obtained with the PulseEKKO 450 MHz antenna (top) and with the GSSI 500 MHz antenna (bottom); void is located at 3.7m

C.6. Seismic methods

C.6.1. Reflection seismics

Objective: Provide images of the subsurface by measuring and processing the reflected elastic waves induced by a seismic source.

Availability: Not a standard service normally provided; very few geophysical survey companies can provide this service.

Possession of the track: Yes.

Costs of survey: Very expensive – large crew required.

Description: Reflection surveys consist of measuring seismic waves that are reflected at an interface – often the soil bedrock interface. The purpose of reflection survey in the delineation of mineshafts is to detect discontinuities in the reflectors. Often the presence of a voids or mineshaft does not produce a discontinuity, but an area of uncorrelated events. These anomalous events can also be used as an indication of the presence of a mineshaft (*National-Research-Council, 2002*). Near-surface reflection is difficult, however several reflection seismic surveys been carried out to delineate cavities and mine work tunnels with variable success (Branham and Steeples, 1988; Dobecki, 1988; Miller and Steeples, 1991).

Issues: More than other geophysical methods, the choice of survey parameters can be crucial to the performance of the seismic reflection survey (*Knapp and Steeples, 1986*). One important consideration in the selection of parameters is the operating frequency. Shallow reflection surveys require high frequencies (*Drossaert et al., 2004*). The generation of high-frequency waves can be difficult at some sites. The amount of energy emanating from a source decreases with increasing frequency. It often can be impossible to generate seismic waves with sufficient energy above a frequency of 200Hz. Moreover high frequency waves are

attenuated more than low frequency and the energy dissipates over a short distance.

The quality of high frequency measurement depends on the quality of the geophone-ground coupling. Poorly coupled geophones fail to record high frequencies adequately. Poor coupling could happen at the aggregate in the ballast layer.

Since seismic surveys measure displacement of ground movement, the method is susceptible to vibration noise. Vibration noise can be generated by various sources, such as moving vehicles or persons, industrial activities, rain and wind. Therefore it is not recommended to conduct a reflection survey close to busy roads and built up areas.

A serious problem in reflection seismics is the presence of the dominant surface waves which often will overwhelm the reflected energies. Depending on the geological setting the travel time of reflected events often approximates the travel time of surface waves, which renders the method ineffective.

Effectiveness: The only reported seismic survey to delineate a mineshaft failed due to the masking of reflection events by surface waves (*Brouwer and Nijhof, 1994*). It might be very difficult to gather reflected energies without interference with surface waves. Even when surface waves are not a problem, there are still various issues to overcome such as the generation and the measuring of sufficient high frequencies. Although in few cases reflection seismics might be successful, in many cases it will not. Therefore reflection seismics is deemed to be ineffective.

C.6.2. Refraction seismics

Objective: Detect anomalies in the travel time of refracted waves; advanced inversion software can reconstruct the velocity profile using these travel times.

Availability: Not a standard service, few survey companies are able to provide this service.

Possession of the track: Yes.

Costs of survey: Expensive.

Description: Refraction seismics measure the travel time of seismic waves that are refracted at an interface. When refracted waves propagate through a mineshaft the travel time of the waves will be lagging behind since the wave has to travel around the shaft or through slow velocity backfilling. The low velocity around the mineshaft caused by de-stressed rocks will cause an additional delay.

Basically a refraction survey consists of placing the geophones equidistantly along the survey line and the source in line with the geophones. The optimum geophone spacing depends on the size of target, the number geophones available and desired penetration depth.

Refraction methods are widely used in geotechnical engineering but mainly in surface to bedrock mapping. Little work has been undertaken in the delineation of cavities and mineshafts. Schwarz (*Schwarz, 1990*) detected successfully an underground mine working by using refraction survey. McCann and others (*McCann et al., 1987*) used the refraction method to locate a disused railway tunnel.

Normally the measured travel time is plotted against the location of the geophone and after that the data is processed to obtain velocity profiles or depth profiles. Recently, tomographic imaging has been introduced in refraction surveying, which enhances the interpretation and the popularity of refraction

seismics (*Zhang and Kim, 2003; Zhang et al., 2003; Carpenter et al., 2003; Ditmar et al., 1999*).

Issues: Refraction surveys do not require the same high frequency waves as the reflection method, however when measuring at the ballast layer it might be required to improve the coupling by stabilizing the geophones by putting sand bags above them.

Refraction methods require a subsurface interface which refracts the seismic energy. Not all survey sites have a good refractor. Moreover in steep dipping geology or highly variable geology the refraction method is likely to fail. Refraction methods work best in areas where the geology is reasonable simple.

Vibration noise induced by industrial activities and traffic can interfere with the recorded data. Strong noise can lead to errors in the travel time picking and potentially lead to erroneous interpretation. Areas where there is much vibration noise should be avoided.

Local near-surface irregularities can produce spurious velocity anomalies. When surveying at the ballast layer, ballast thickness variations can give rise to travel time anomalies that might be misinterpreted as a mineshaft.

Refraction tomography inversion software uses the travel times of refracted waves to create a velocity profile of the subsurface. This software uses Fresnel zones to project travel times into the velocity space. Since these Fresnel zones are larger than the size of most mineshafts, it is very unlikely that tomographic software can resolve mineshafts. Furthermore since the velocity contrast between the void and the bedrock is very large, diffraction will occur. The actual travel paths of some of the waves are no longer solely determined by the velocities and the velocity reconstruction can fail (*Kilty and Lange, 1990*).

Effectiveness: Although the refraction method has some potential, refraction surveys are little employed in order to delineate mineshafts. Refraction methods

are very suitable for determining the depth to bedrock however the method itself a bit insensitive to vertical features such as mineshafts. Tomographic software lacks the ability to take into account diffracted waves and also mineshafts are smaller than the approximate resolution. Therefore refraction methods are not considered to be suitable for mineshaft detection.

C.6.3. Surface wave methods

Objective: Determines the dispersion curve of surface waves and converts it into a shear wave velocity profile using inversion software.

Availability: Not available as standard, few survey companies are able to provide this service.

Possession of the track: Yes.

Costs of survey: Expensive.

Description: The spectral analysis of surface waves (SASW) method is a non-destructive testing method that uses the dispersive nature of seismic Rayleigh waves. The technique is fairly new and received recently much attention in geotechnical engineering. There exist two different measuring methods. One uses two geophones, whereas the other method uses multiple geophones. The first method measures the change in phase of Rayleigh waves between two geophones. The latter one is often referred as Multichannel Analysis of Surface Waves (MASW) and measures the frequency-wave number of a shot gather.

The results are used to calculate a dispersion curve, which is the phase velocity versus the frequency of the wave. The dispersion curve is used to reconstruct the shear wave velocity profile of the subsurface. A low velocity anomaly can indicate the presence of a mineshaft. The conventional SASW method is not capable of solving lateral velocity variations in the subsurface, but

recent advancements were made which are able to measure lateral velocity variations (*Phillips et al., 2002*).

The biggest advantage of using surface waves is that surface waves are the dominant presence in the seismograms. Therefore there will be little interference by other seismic events and noise. Also the penetration depth depends on the wavelength and thus the frequency. Low frequency waves are required to gain a substantial penetration depth. Low frequency waves are not attenuated and also bad ground-geophone coupling does not affect the data.

The survey acquisition of the MASW method is similar to the refraction or reflection method, hence the method can be used in conjunction with refraction or reflection method (*Foti et al., 2003*).

Issues: Lateral variations in the near-surface material could seriously affect the performance of surface waves i.e. the dispersion curve does not represent the material between the geophones and erroneous velocity profiles are obtained. Furthermore the solution to the dispersion curve is not unique; this means that various velocity profiles can exist which equally fit the dispersion curve. A priori information e.g. by drilling is necessary for the correct inversion of the dispersion curve and interpretation of the velocity profiles.

Both SASW and the MASW method require several metres of survey line to obtain the vertical velocity profile at one point. There methods have a limited resolution and especially in the horizontal direction (*Park et al., 1998*). Vertical features are difficult to delineate by spectral analysis of surface wave methods.

Effectiveness: The lack of resolution and especially the horizontal resolution limits the use of SASW and MASW methods to delineate mineshafts. Therefore these methods are considered inefficient.

C.6.4. Diffraction imaging

Objective: Image diffraction point i.e. mineshafts by stacking diffraction events.

Availability: Method is not available at commercial survey companies.

Possession of the track: No.

Costs of survey: Expensive.

Description: Diffraction waves are waves that are scattered in the subsurface due to discontinuities of a limited size in the subsurface. Various surveys demonstrate that small voids can be located using these waves. It is possible that a mineshaft will create similar diffracted waves. Although, no literature can be found regarding the delineation of mineshafts using diffracted waves.

For a long time, diffraction waves were considered as noise in the seismic data. Most data processing techniques are actually designed to suppress this type of noise. However, recently it is being acknowledged that diffracted waves can contain essential information about the subsurface. Diffracted waves can be used to determine the velocity and also the geometrical structure of the scatter.

One of the major problems of diffraction imaging is that the diffracted energies are relatively small compared to the other seismic energies. Therefore most diffraction imaging techniques are designed to amplify diffracted energies and discriminate non-diffracted waves. Various methods are proposed:

- Diffraction stacking (*Müller, 2000*): stacks seismograms of different shot points together. These seismograms are shifted in time according the difference in travel time from source to diffraction point.
- Phase correlation techniques (*Landa and Keydar, 1998; Landa et al., 1987; Müller, 2000; Heincke et al., 2006; Shtivelman and Keydar, 2005*): migrates recorded seismic data from time-location domain into depth-location domain by summing energies along diffraction curves. These

diffraction curves are calculated assuming every point in the survey space is a potential diffractor.

- Diffraction polarization techniques (*Müller, 2000*): images diffraction points utilizing the directional behaviour of particles motion relative to the travelled path.
- Cross correlation techniques (*Gritto and Majer, 2000*): calculates the correlation between the recorded traces and synthetic traces that are calculated assuming every point in the survey space is a potential diffractor.

The above mentioned techniques all make use of body waves. Additionally some techniques utilize surface waves:

- Decomposition of surface waves (*Campman et al., 2004; Herman et al., 2000; Xia et al., 2007*): the surface wave techniques uses decomposition to separate scattered surface waves from the seismograms to located the source of scattering.
- Direct observations of seismograms (*Xia et al., 2007*): seismograms can reveal voids in the subsurface. Frequency-wave number filters can be used to weaken the direct surface waves and enhance scattered surface waves.

Surface waves are predominantly present in the seismograms and therefore no stacking or migration is required.

Issues: Diffraction stacking stacks seismograms that are shifted in time according the difference in travel time from the source to the receivers (*Müller, 2000*). However, for the calculation of the time-shift the location of scatterer e.g. the mineshaft needs to be known. Müller suggest using an optimization algorithm, but this was never proven to work.

The phase correlation techniques and the cross correlation, both require some knowledge about the velocities in the subsurface. However, Shtivelman and

Keydar showed that a range of velocities can be used to locate the diffraction point (*Shtivelman and Keydar, 2005*).

Surface waves travel along the surface and are therefore susceptible to variations present at the surface. Railway sites often consist of embankments and troughs –Figure 2.4 on 12 – which can be sources of scattering which could lead to misinterpretation of the data.

Effectiveness: No publications were found regarding the detection of mineshafts using diffracted waves. At this moment it is neither clear whether mineshafts produce diffractions and nor if these diffracted waves are useful in the delineation of mineshafts.

C.6.5. Resonance methods

Objective: Record ringing caused by resonance induced by oscillation of the mineshaft.

Availability: Method not available as standard.

Possession of the track: Yes.

Costs of survey: Average.

Description: The seismic resonance method for locating cavities was first tested by Godson and Watkins (*Godson and Watkins, 1968*). It is believed that the resonance or ringing is induced by oscillations of the boundaries of the cavity. The oscillation vibrates with the resonant frequency of the cavity. The resonance of cavities is often observed when conducting a seismic survey over a cavity, but the actual delineation of the cavity still appears to be difficult (*McCann et al., 1987*). The survey lay-out is similar to the reflection seismics. At least one

geophone has to be located close to the centre of the mineshaft in order to measure the largest resonance amplitude.

Issues: Several resonance experiments did not produce any satisfactory results. The reason for failure could be that the resonant frequency was not in the frequency range of the source. Surface waves have a large energy and are considered the most effective for the delineation of cavities. Unfortunately surface waves have a limited depth penetration and most of the surface wave energy propagates close to the surface. Moreover the resonant amplitude of deep backfilled mineshafts is likely to be reduced significantly and it could be difficult to distinguish them from other seismic events.

Effectiveness: Experiments using the resonance method were carried out to delineate mine workings; the results were variable and in most cases the presence of mine workings was not detected (*Arrowsmith and Rankilor, 1981*). It can be concluded that resonance is poorly understood and that the outcome of the resonance method are unreliable. Therefore resonance methods are deemed ineffective.

C.6.6. Transmission methods

Objective: Measuring the attributes of seismic waves transmitted through the mineshaft.

Availability: Method not available as standard.

Possession of the track: No – railway can be situated between source and receivers.

Costs of survey: Average.

Description: The transmission method measures the amplitudes of the individual seismic events. Differences in amplitudes could indicate the presence of

a cavity or mineshaft. Cook (*Cook, 1975*) was one of the first to use differences in amplitudes of reflection events to delineate cavities, but it was not until the 1970s that the transmission method became a regularly used method to identify mineshafts in West Germany (*Dresen et al., 1975; Dresen, 1977*). The first transmission method used direct waves (P-waves) propagating between a geophone located at 16 metre depth in a borehole and sources which were located in a semi-circular pattern at a distance of 13.5 and 15 metres. The measured amplitudes were mapped as a function of the angle between the sources and geophone. The amplitudes showed a characteristic W-shape with the middle corresponding to the source-geophone line.

In later studies other seismic events were studied such as reflected waves, reflected converted waves as well as refracted waves and surface waves (*Dresen and Hsieh, 1979*). This method does not require any boreholes. The survey acquisition layout can be found in Figure C-12. The transmission method using surface wave events has been particularly successful in delineating near surface cavities (*Owen, 1983*).

Issues: The surface at railway sites is variable. This could limit the use of the surface wave transmission method, since surface waves are diffracted at embankments and troughs.

It is very likely that near surface irregularities, such as depressions, can focus or defocus seismic waves. This could lead to amplitude variations of the seismic waves measured at the surface and this could lead to erroneous interpretation of the transmission data.

Effectiveness: Although only a few transmission surveys are reported by the same people, the transmission method could be an efficient method to delineate mineshafts. Irregular surfaces e.g. embankment and bedrock interface might limit the use of this method.

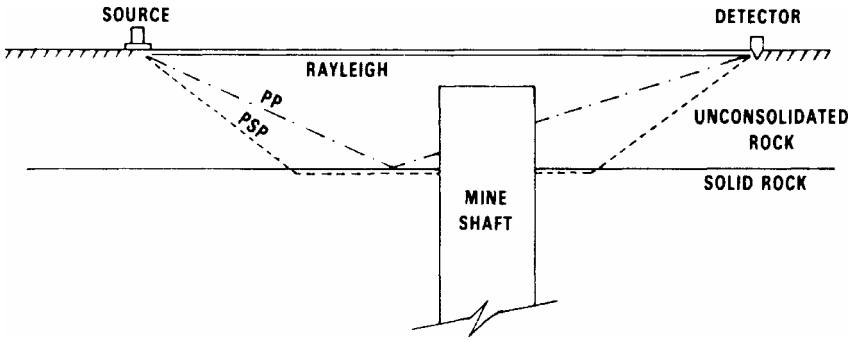

Figure C-12. Transmission method, non-borehole method (*Owen, 1983*)

C.7. Thermal methods

Objective: Measuring the temperature of the soil.

Availability: Most non-destructive testing companies provide inspection services by infrared cameras; few will have soil thermometers or precision radiation thermometers.

Possession of the track: Yes (direct measures) and No (IR measures).

Costs of survey: Average, airborne IR can be cheap when scanning for multiple mineshafts.

Description: The presence of mineshafts causes temperature differences in the soil. There exist three different methods to measure temperature anomalies at the surface. One method is the direct measurements which measures the temperature of the soil typically about 20 cm below the surface by probing a thermometer into the ground. The direct temperature measurement has been successful in the detection of cavities and mineshafts (*Moscicki, 1987*).

A different method is the precision radiation thermometer, which measures the amount of energy emitting from the target. The precision radiation thermometer is portable, requires no contact and the temperature measurement is

immediately available. This thermometer is a rapid survey tool, suitable for quick reconnaissance.

The third method is the infra-red camera. The IR camera has regularly been used in the geotechnical engineering. The IR camera has been successfully used to detect abandoned detect mineshafts (*Dresen et al., 1975; Gunn et al., 2002*). The IR camera can be handheld, mounted on a crane or aircraft; for instantaneously sampling of a large area the IR scanner has to be positioned high above the survey area depending on the lens of the camera.

Issues: Weather conditions influence the measurements strongly and have to be taken into account. This holds especially for non-contact measurements, such as the precision radiation thermometer and the IR camera. As weather conditions changes over time, the slow precision radiation thermometer is not likely to be suitable for surveying sizeable sites. Although the temperature measurement by probes is less influenced by diurnal variations, field experiments showed that certain weather conditions are not favourable for the survey (*Moscicki, 1987*).

The most suitable conditions for an IR survey are dry days with no wind. Snow, rain and wind can alter the surface temperature distribution. Moreover rain absorbs infra-red passing through it. Most important, the sun must not be shining on the ground surface, which can obscure the mineshaft and produce localised heating. The best time is pre-dawn or at first light before the sun heats the earth; this allows any solar heating from the previous day to have dissipated overnight. According to Titmann (*Titman, 1992*) there is approximately one hour of surveying time available before the sun is high enough to shine on the surface. Donelly and McCann (*Donelly and McCann, 2000*) concluded that the best time to observe temperature anomalies is after a barometric pressure drop of between 4 and 8 mbar within 3 hours.

Surveying during the winter is preferable, because the temperature contrast is likely to be large, but good results were achieved during the autumn and spring. The summer is considered to be the worst time of year for IR surveying (*Donelly and McCann, 2000*).

Since the ballast layer consists of lose aggregate it is very unlikely that the temperature in the aggregate correlates to the temperature in the subsurface; the air temperature and the wind influence the temperature in the aggregate strongly. Also probing into the ballast layer is difficult. Therefore mineshafts located below the ballast layer are unlikely to be detected by the thermal imaging.

The presence of trees, bushes and other vegetation could mask the mineshaft when conducting an IR survey (*Gunn et al., 2002*). During the winter the effect of vegetation is less and the survey could be more successful. In forest areas or areas with many bushes it is not recommended to use infra red scanning.

Effectiveness: Good results were obtained during an airborne IR to locate mineshafts (*Culshaw and Waltham, 1987; Culshaw et al., 2004*). The dependency on the prevailing weather makes thermal methods difficult to use in the field. Furthermore it is highly unlikely that measurements at the ballast are reliable, which leaves an important survey area uncovered. Because of the latter reason alone, thermal methods are not considered as effective.

C.8. Borehole geophysics

Objective: Determining anomalies using sources and/or receivers in boreholes.

Availability: Few survey companies provide resistivity tomography and radar tomography services. Other services are usually not available as standard.

Possession of the track: No.

Costs of survey: Very expensive.

Description: Borehole-to-borehole and borehole-to-surface geophysical methods offer the advantages of greatly improving the efficiency of the drilling programme by locating the mineshaft more accurately via underground access and extending the mineshaft detection capability beyond the performance limitations of surface methods.

A big advantage of borehole-to-borehole and borehole-to-surface methods is that these are capable of measuring the subsurface below the railway embankment without the need for possession management or conducting the survey during the night. Borehole-to-borehole methods can be useful to delineate mineshafts below large embankments. There exist various borehole-to-borehole and borehole-to-surface methods which are briefly described below:

- Resistivity: downhole electric measurements greatly extend the anomaly detection capability beyond the performance limits of surface electric surveying and are particularly suitable for surveys in built-up areas (*Bing and Greenhalgh, 2000*). Maillol showed good correlation of borehole-to-borehole resistivity data and the location of mining galleries in coal layers (*Maillol et al., 1999*). Borehole-to-surface resistivity surveys were used during geotechnical pre-investigation at a tunnelling site (*Denis et al., 2002*). Some configurations have a singularity problem in the data acquisition; this could lead to low potential readings, which could easily be obscured by background noise (*Bing and Greenhalgh, 2000*). The use of these configurations should be avoided.
- Electromagnetics: The radio imaging method (RIM) is a borehole-to-borehole electromagnetic method. One transmitter is placed in one hole and the receiver in the other borehole. The transmitter sends radio signals in the frequency range of 100 kHz and 5 MHz which propagate through the rock medium. Anomalies that intersect the travel path may cause

measurable changes in the attenuation factor and phase of the propagating EM wave. The radio imaging method has been used to detect faults in coal layers, mineralization and water intrusion monitoring and never been used to delineate mineshafts or similar (*Stolarczyk, 1990; Doyle et al., 1992*).

- Ground penetrating radar: there exits two modes.
- Reflection mode: In the reflection mode the radar transmitter and receiver antennas are lowered in the same borehole with a fixed, but small spacing between them. A radar pulse is transmitted into the bedrock and moves away from the antenna until reflection occurs due to fracture zone, outcrops, voids or mineshafts. The reflected energy is recorded by the receiver. A radar reflection profile can be created by measuring the radar response at different positions in the borehole (*Haeni et al., 2002*)
- Tomographic mode: The tomographic mode uses crosshole radar measurements with the transmitter in one borehole and the receiver in the other borehole. For each transmitter and receiver combination the travel time and amplitude is measured as the EM pulse travels from the transmitter to the receiving antenna. These data are used to reconstruct the tomography of the radar propagation velocity or the attenuation properties of the material between both boreholes. Anomalous velocity or attenuation values can be interpreted as a mineshaft or other features. The radar tomography has been applied for various targets. In Belgium the method has been used to assess the karstified and fractured limestone below the proposed TGV railway (*Corwin, 1990; Hauser et al., 1995*). Radar tomography to detect a tunnel and also cavities were detected by tomography (*Valle and Zanzi, 1996*).

- Seismic tomography: this tomography method measures the travel time of seismic waves from the source located in one hole to the receivers in the other borehole. A finite element algorithm is then used to reconstruct the velocity profile between both boreholes. Deviations in the travel time are corrected by introducing velocity anomalies in the reconstructed velocity tomograph. Low velocity anomalies can be associated with the presence of a mineshaft. The tomography is particularly successful in the delineation of features with high velocity contrasts (*Krajewsk et al., 1989*). High velocity contrasts between an air-filled and water-filled mineshaft exist in most cases.

Issues: Conducting only borehole-to-borehole surveys at a site requires numerous boreholes. Borehole-borehole methods measure only the properties of material between both boreholes which leaves a large area un-sampled. Similar to the surface method the surveyed section has to cross the mineshaft in order to be detected. The actual number of boreholes required depends on the spacing between the boreholes, the size of the survey site and the diameter of the mineshaft. A large number of boreholes is not feasible and totally undesired, because it is destructive, time consuming and extremely expensive. For example in a 3D cross-hole seismic survey beneath an existing structure, 7 boreholes were used to cover an area of merely 250m^2 (*Jackson et al., 2001*). Large survey sites require over 30 boreholes, which is not only destructive for the subsurface but also extremely expensive. The number of boreholes required could be reduced by using additional borehole to surface seismic data (*Whiteley, 2003*).

In anisotropic material the tomography method can produce spurious anomalies which might be misinterpreted. The anisotropy of material has to be compensated for in order to obtain a true velocity profile of the subsurface. As with all seismic methods, seismic tomography is susceptible to vibration noise.

Effectiveness: Usually borehole data contains less noise than their surface equivalent. Therefore boreholes methods are particularly suitable for mineshaft detection. However, numerous boreholes are required to provide full coverage of the area. This can be very expensive and it is also very obtrusive.

Appendix D - Matlab scripts

Below the Matlab code for the finite difference program used in the thesis can be found. The grid scheme is based on the Rotated Staggered Grid and the boundaries are truncated by the RIPML.

```
% ------------------------------------------------------------------------
% Finite difference program based on the RSG and RIPML
% ------------------------------------------------------------------------

% ------------------------------------------------------------------------
% Initialisation
% ------------------------------------------------------------------------

clear all;

% ------------------------------------------------------------------------
% Read the model parameters and populate the stress and velocity matrices
% ------------------------------------------------------------------------

[nx, nz, dz, dx, R, L, M, endtime] = readmodel;

U = zeros (nx,nz);
W = zeros (nx,nz);

Txx = zeros (nx,nz);
Tzz = zeros (nx,nz);
Txz = zeros (nx,nz);

% ------------------------------------------------------------------------
% Calculate the average buoyancy out of the densities
% ------------------------------------------------------------------------

B = avebuoyancy (R,nx,nz);

clear R

% ------------------------------------------------------------------------
% Calculate the maximum values of the vp, vs and vr
% Note that vr is calculated according Viktorov approximation
% And is only valid for homogeneous half-space
% ------------------------------------------------------------------------

[vp, vs, vr] = maxv (nx,nz,B,L,M);

% ------------------------------------------------------------------------
% Calculate the maximum dt to fulfill the stabilisation criterium and
% calculate the number of iterations required
% ------------------------------------------------------------------------

dt = (dx/vp)*0.99;
iterations=round(endtime/dt)
```

```
% --------------------------------------------------------------------
% Read the source parameters
% --------------------------------------------------------------------

[sourcex, sourcez, sourcesize, src] = readsource(dt,iterations);

% --------------------------------------------------------------------
% Read the absorbing boundary condition parameters
% --------------------------------------------------------------------

[pmlsize, alphamax, kappamax, sigmamax] = abc(vp,dz);

pmlnumber = 4;

pml_vmat = [pmlsize+1, nx-pmlsize, pmlsize+1, nz-pmlsize;
        2, pmlsize, 2, nz-1;
        nx-pmlsize+1, nx-1, 2, nz-1;
        pmlsize+1, nx-pmlsize, 2, pmlsize;
        pmlsize+1, nx-pmlsize, nz-pmlsize+1, nz-1];

pml_smat = [pmlsize+1, nx-pmlsize-1, pmlsize+1, nz-pmlsize-1;
        1, pmlsize, 1, nz-1;
        nx-pmlsize, nx-1, 1, nz-1;
        pmlsize+1, nx-pmlsize-1, 1, pmlsize;
        pmlsize+1, nx-pmlsize-1, nz-pmlsize, nz-1];

% --------------------------------------------------------------------
% Define the paramters and populate matrices required for the ABC
% --------------------------------------------------------------------

Elxx = zeros(nx,nz);
Elxz = zeros(nx,nz);
Elzx = zeros(nx,nz);
Elzz = zeros(nx,nz);

Slxx = zeros(nx,nz);
Slxz = zeros(nx,nz);
Slzx = zeros(nx,nz);
Slzz = zeros(nx,nz);

axv = zeros(nx,1);
axs = zeros(nx,1);
azv = zeros(nz,1);
azs = zeros(nz,1);

fxv1 = ones(nx,1);
fxs1 = ones(nx,1);
fzv1 = ones(nz,1);
fzs1 = ones(nz,1);

fxv2 = ones(nx,1)*dt;
fxs2 = ones(nx,1)*dt;
fzv2 = ones(nz,1)*dt;
fzs2 = ones(nz,1)*dt;

fxv3 = zeros(nx,1);
fxs3 = zeros(nx,1);
fzv3 = zeros(nz,1);
fzs3 = zeros(nz,1);
```

```
for t1 = 1:pmlsize
   axv(pmlsize+1-t1) = alphamax * ((pmlsize+1-t1)^2/(pmlsize)^2);
   azv(pmlsize+1-t1) = alphamax * ((pmlsize+1-t1)^2/(pmlsize)^2);
end

for t1=1:pmlsize
   axv(nx-pmlsize-1+t1) = alphamax * ((pmlsize-t1+1)^2/(pmlsize)^2);
   azv(nz-pmlsize-1+t1) = alphamax * ((pmlsize-t1+1)^2/(pmlsize)^2);
end

for t1=1:pmlsize
   axs(pmlsize+1-t1) = alphamax * ((pmlsize-t1+0.5)^2/(pmlsize)^2);
   azs(pmlsize+1-t1) = alphamax * ((pmlsize-t1+0.5)^2/(pmlsize)^2);
end

for t1=1:pmlsize
   axs(nx-pmlsize-1+t1) = alphamax * ((pmlsize-t1+0.5)^2/(pmlsize)^2);
   azs(nz-pmlsize-1+t1) = alphamax * ((pmlsize-t1+0.5)^2/(pmlsize)^2);
end



for t1 = 1:pmlsize
   kxv = 1 + (kappamax-1) * ((pmlsize+1-t1)^2/(pmlsize)^2);
   kzv = 1 + (kappamax-1) * ((pmlsize+1-t1)^2/(pmlsize)^2);
   sxv = sigmamax * ((pmlsize-t1+1)^2/(pmlsize)^2);
   szv = sigmamax * ((pmlsize-t1+1)^2/(pmlsize)^2);


   fxv1(t1) = (1+0.5*dt*axv(t1))/(0.5*dt*(sxv+axv(t1)*kxv)+kxv);
   fzv1(t1) = (1+0.5*dt*azv(t1))/(0.5*dt*(szv+azv(t1)*kzv)+kzv);
   fxv2(t1) = dt/(0.5*dt*(sxv+axv(t1)*kxv)+kxv);
   fzv2(t1) = dt/(0.5*dt*(szv+azv(t1)*kzv)+kzv);
   fxv3(t1) = sxv+axv(t1)*kxv;
   fzv3(t1) = szv+azv(t1)*kzv;
end

for t1=1:pmlsize
   kxv = 1 + (kappamax-1) * ((pmlsize-t1+1)^2/(pmlsize)^2);
   kzv = 1 + (kappamax-1) * ((pmlsize-t1+1)^2/(pmlsize)^2);
   sxv = sigmamax * ((pmlsize-t1+1)^2/(pmlsize)^2);
   szv = sigmamax * ((pmlsize-t1+1)^2/(pmlsize)^2);

   fxv1(nx-t1+1) = (1+0.5*dt*axv(nx-t1+1))/(0.5*dt*(sxv+axv(nx-t1+1)*kxv)+kxv);
   fzv1(nz-t1+1) = (1+0.5*dt*azv(nz-t1+1))/(0.5*dt*(szv+azv(nz-t1+1)*kzv)+kzv);
   fxv2(nx-t1+1) = dt/(0.5*dt*(sxv+axv(nx-t1+1)*kxv)+kxv);
   fzv2(nz-t1+1) = dt/(0.5*dt*(szv+azv(nz-t1+1)*kzv)+kzv);
   fxv3(nx-t1+1) = sxv+axv(nx-t1+1)*kxv;
   fzv3(nz-t1+1) = szv+azv(nz-t1+1)*kzv;
end

for t1=1:pmlsize
   kxs = 1 + (kappamax-1) * ((pmlsize-t1+0.5)^2/(pmlsize)^2);
   kzs = 1 + (kappamax-1) * ((pmlsize-t1+0.5)^2/(pmlsize)^2);
   sxs = sigmamax * ((pmlsize-t1+0.5)^2/(pmlsize)^2);
   szs = sigmamax * ((pmlsize-t1+0.5)^2/(pmlsize)^2);

   fxs1(t1) = (1+0.5*dt*axs(t1))/(0.5*dt*(sxs+axs(t1)*kxs)+kxs);
```

```
   fzs1(t1) = (1+0.5*dt*azs(t1))/(0.5*dt*(szs+azs(t1)*kzs)+kzs);
   fxs2(t1) = dt/(0.5*dt*(sxs+axs(t1)*kxs)+kxs);
   fzs2(t1) = dt/(0.5*dt*(szs+azs(t1)*kzs)+kzs);
   fxs3(t1) = sxs+axs(t1)*kxs;
   fzs3(t1) = szs+azs(t1)*kzs;
end

for t1=1:pmlsize
   kxs = 1 + (kappamax-1) * ((pmlsize-t1+0.5)^2/(pmlsize)^2);
   kzs = 1 + (kappamax-1) * ((pmlsize-t1+0.5)^2/(pmlsize)^2);
   sxs = sigmamax * ((pmlsize-t1+0.5)^2/(pmlsize)^2);
   szs = sigmamax * ((pmlsize-t1+0.5)^2/(pmlsize)^2);

   fxs1(nx-t1) = (1+0.5*dt*axs(nx-t1))/(0.5*dt*(sxs+axs(nx-t1)*kxs)+kxs);
   fzs1(nz-t1) = (1+0.5*dt*azs(nz-t1))/(0.5*dt*(szs+azs(nz-t1)*kzs)+kzs);
   fxs2(nx-t1) = dt/(0.5*dt*(sxs+axs(nx-t1)*kxs)+kxs);
   fzs2(nz-t1) = dt/(0.5*dt*(szs+azs(nz-t1)*kzs)+kzs);
   fxs3(nx-t1) = sxs+axs(nx-t1)*kxs;
   fzs3(nz-t1) = szs+azs(nz-t1)*kzs;
end

% ---------------------------------------------------------------------
% Set time to zero and the counter for the movie file
% ---------------------------------------------------------------------

t2 = 0;

% ---------------------------------------------------------------------
% Do loop over the number of iterations
% ---------------------------------------------------------------------

for t1 = 1:iterations

   % ---------------------------------------------------------------------
   % Gausian distribute of the source to prevent checker bord pattern
   % ---------------------------------------------------------------------

   for tx = sourcex-sourcesize:sourcex+sourcesize
      for tz = sourcez-sourcesize:sourcez+sourcesize
         distance_x = abs(sourcex - tx) * dx;
         distance_z = abs(sourcez - tz) * dz;
         distance = sqrt(distance_z^2 + distance_x^2);
         Tzz(tx,tz) = Tzz(tx,tz) + src(t1) * exp(-0.5*(distance/dx)^2);
      end
   end

   % ---------------------------------------------------------------------
   % Calculate U and W at (k+1/2)dt from the stresses at (k-1/2)dt
   % ---------------------------------------------------------------------

   for tx = pml_vmat(1,1):pml_vmat(1,2)
      for tz = pml_vmat(1,3):pml_vmat(1,4)
         dxTxx = (1/(2*dx)) * (Txx(tx,tz) - Txx(tx-1,tz-1) + Txx(tx,tz-1) - Txx(tx-1,tz));
         dzTxz = (1/(2*dz)) * (Txz(tx,tz) - Txz(tx-1,tz-1) - Txz(tx,tz-1) + Txz(tx-1,tz));
         dxTxz = (1/(2*dx)) * (Txz(tx,tz) - Txz(tx-1,tz-1) + Txz(tx,tz-1) - Txz(tx-1,tz));
         dzTzz = (1/(2*dz)) * (Tzz(tx,tz) - Tzz(tx-1,tz-1) - Tzz(tx,tz-1) + Tzz(tx-1,tz));

         U(tx,tz) = U(tx,tz)  + dt*B(tx,tz) * (dxTxx + dzTxz);
         W(tx,tz) = W(tx,tz)  + dt*B(tx,tz) * (dxTxz + dzTzz);
      end
```

```
end

% ---------------------------------------------------------------------
% Calculate the velocity in PML zones
% ---------------------------------------------------------------------

for pml = 2:pmlnumber+1

   for tx = (pml_vmat(pml,1)):(pml_vmat(pml,2))
      for tz = (pml_vmat(pml,3)):(pml_vmat(pml,4))

         dxTxx = (1/(2*dx)) * (Txx(tx,tz) - Txx(tx-1,tz-1) + Txx(tx,tz-1) - Txx(tx-1,tz));
         dzTxz = (1/(2*dz)) * (Txz(tx,tz) - Txz(tx-1,tz-1) - Txz(tx,tz-1) + Txz(tx-1,tz));
         dxTxz = (1/(2*dx)) * (Txz(tx,tz) - Txz(tx-1,tz-1) + Txz(tx,tz-1) - Txz(tx-1,tz));
         dzTzz = (1/(2*dz)) * (Tzz(tx,tz) - Tzz(tx-1,tz-1) - Tzz(tx,tz-1) + Tzz(tx-1,tz));

         Sxx = fxv1(tx)*dxTxx - fxv2(tx)*SIxx(tx,tz);
         Sxz = fzv1(tz)*dzTxz - fzv2(tz)*SIxz(tx,tz);
         Szx = fxv1(tx)*dxTxz - fxv2(tx)*SIzx(tx,tz);
         Szz = fzv1(tz)*dzTzz - fzv2(tz)*SIzz(tx,tz);

         U(tx,tz) = U(tx,tz) + dt * B(tx,tz) * (Sxx + Sxz);
         W(tx,tz) = W(tx,tz) + dt * B(tx,tz) * (Szz + Szx);

         SIxx(tx,tz) = SIxx(tx,tz) + fxv3(tx)*Sxx - axv(tx)*dxTxx;
         SIxz(tx,tz) = SIxz(tx,tz) + fzv3(tz)*Sxz - azv(tz)*dzTxz;
         SIzx(tx,tz) = SIzx(tx,tz) + fxv3(tx)*Szx - axv(tx)*dxTxz;
         SIzz(tx,tz) = SIzz(tx,tz) + fzv3(tz)*Szz - azv(tz)*dzTzz;

      end
   end

end

% ---------------------------------------------------------------------
% Update the numerical stresses (k+1/2)dt
% ---------------------------------------------------------------------

for tx = pml_smat(1,1):pml_smat(1,2)
   for tz = pml_smat(1,3):pml_smat(1,4)
      dzU = 1/(2*dz) * (U(tx+1,tz+1) - U(tx,tz) - U(tx+1,tz) + U(tx,tz+1));
      dxU = 1/(2*dx) * (U(tx+1,tz+1) - U(tx,tz) + U(tx+1,tz) - U(tx,tz+1));
      dzW = 1/(2*dz) * (W(tx+1,tz+1) - W(tx,tz) - W(tx+1,tz) + W(tx,tz+1));
      dxW = 1/(2*dx) * (W(tx+1,tz+1) - W(tx,tz) + W(tx+1,tz) - W(tx,tz+1));

      Txx(tx,tz) = Txx(tx,tz) + dt * ((L(tx,tz)+2*M(tx,tz))*dxU + L(tx,tz)*dzW);
      Txz(tx,tz) = Txz(tx,tz) + dt * M(tx,tz) * (dxW+dzU);
      Tzz(tx,tz) = Tzz(tx,tz) + dt * ((L(tx,tz)+2*M(tx,tz))*dzW + L(tx,tz) * dxU);
   end
end

% ---------------------------------------------------------------------
% Update the stress field in the pml zones
% ---------------------------------------------------------------------

for pml = 2:pmlnumber+1

   for tx = (pml_smat(pml,1)):(pml_smat(pml,2))
      for tz = (pml_smat(pml,3)):(pml_smat(pml,4))
```

```
            dzU = 1/(2*dz) * (U(tx+1,tz+1) - U(tx,tz) - U(tx+1,tz) + U(tx,tz+1));
            dxU = 1/(2*dx) * (U(tx+1,tz+1) - U(tx,tz) + U(tx+1,tz) - U(tx,tz+1));
            dzW = 1/(2*dz) * (W(tx+1,tz+1) - W(tx,tz) - W(tx+1,tz) + W(tx,tz+1));
            dxW = 1/(2*dx) * (W(tx+1,tz+1) - W(tx,tz) + W(tx+1,tz) - W(tx,tz+1));

            Exx = fxs1(tx)*dxU - fxs2(tx)*Ixx(tx,tz);
            Exz = fzs1(tz)*dzU - fzs2(tz)*Ixz(tx,tz);
            Ezx = fxs1(tx)*dxW - fxs2(tx)*Izx(tx,tz);
            Ezz = fzs1(tz)*dzW - fzs2(tz)*Izz(tx,tz);

            Txx(tx,tz) = Txx(tx,tz) + dt * ((L(tx,tz)+2*M(tx,tz))*Exx + L(tx,tz) * Ezz);
            Txz(tx,tz) = Txz(tx,tz) + dt * M(tx,tz) * (Ezx + Exz);
            Tzz(tx,tz) = Tzz(tx,tz) + dt * ((L(tx,tz)+2*M(tx,tz)) * Ezz + L(tx,tz) * Exx);

            Ixx(tx,tz) = Ixx(tx,tz) + fxs3(tx)*Exx - axs(tx)*dxU;
            Ixz(tx,tz) = Ixz(tx,tz) + fzs3(tz)*Exz - azs(tz)*dzU;
            Izx(tx,tz) = Izx(tx,tz) + fxs3(tx)*Ezx - axs(tx)*dxW;
            Izz(tx,tz) = Izz(tx,tz) + fzs3(tz)*Ezz - azs(tz)*dzW;
        end
    end

end

% ------------------------------------------------------------------------
% Generate movie files and output matrices
% ------------------------------------------------------------------------

if mod(t1,5) == 0
    t2 = t2 + 1;
    movR(t2,:,:)=W(sourcex-39:sourcex+40,sourcez-89:sourcez+400);
end

traceR1(t1) = W(sourcex,sourcez+100);
traceR2(t1) = W(sourcex,sourcez+300);

% ------------------------------------------------------------------------
% Check if solutions has not become unstable
% ------------------------------------------------------------------------

if max(max(W)) > 1
    disp('Solution has become unstable')
    break
end

end

% ------------------------------------------------------------------------
% Save the output - traces and movie - to output.mat
% ------------------------------------------------------------------------

save('output.mat','traceR1','traceR2','movR')
```

Appendix E - Synthetic seismograms

In this appendix the seismograms that were not presented in chapter 6 are presented. The following synthetic seismograms can be found in this appendix:

- Model 2: survey line L1, L2 and L3 in Figure E-1
- Model 3: survey line L1, L2 and L3 in Figure E-1
- Model 4: survey line L1, L2 and L3 in Figure E-2
- Model 5: survey line L1, L2 and L3 in Figure E-2
- Model 6: survey line L1, L2 and L3 in Figure E-2
- Model 7: survey line L1, L2 and L3 in Figure E-3
- Model 8: survey line L1, L2 and L3 in Figure E-4
- Model 9: survey line L1, L2 and L3 in Figure E-4
- Model 10: survey line L1, L2 and L3 in Figure E-5
- Model 11: survey line L1, L2 and L3 in Figure E-5
- Model 12: survey line L1, L2 and L3 in Figure E-6
- Model 13: survey line L1, L2 and L3 in Figure E-7
- Model 14: survey line L1, L2 and L3 in Figure E-7
- Model 15: survey line L1, L2 and L3 in Figure E-8
- Model 16: survey line L1, L2 and L3 in Figure E-8
- Model 17: survey line L1, L2 and L3 in Figure E-9
- Model 18: survey line L1, L2 and L3 in Figure E-9
- Model 19: survey line L1, L2 and L3 in Figure E-10
- Model 20: survey line L1, L2 and L3 in Figure E-10

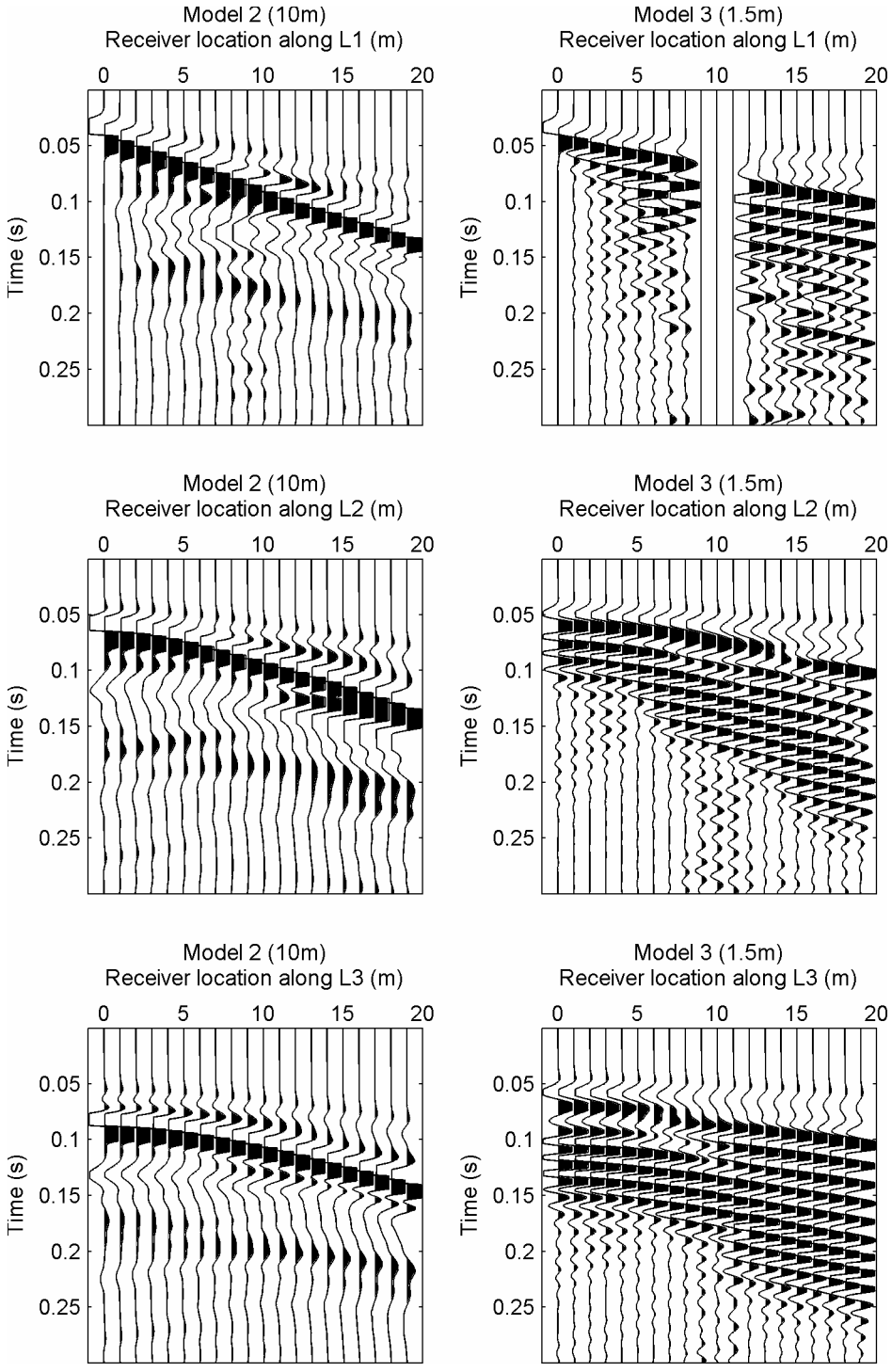

Figure E-1. Seismograms of survey line L1, L2 and L3 of model 2 and 3

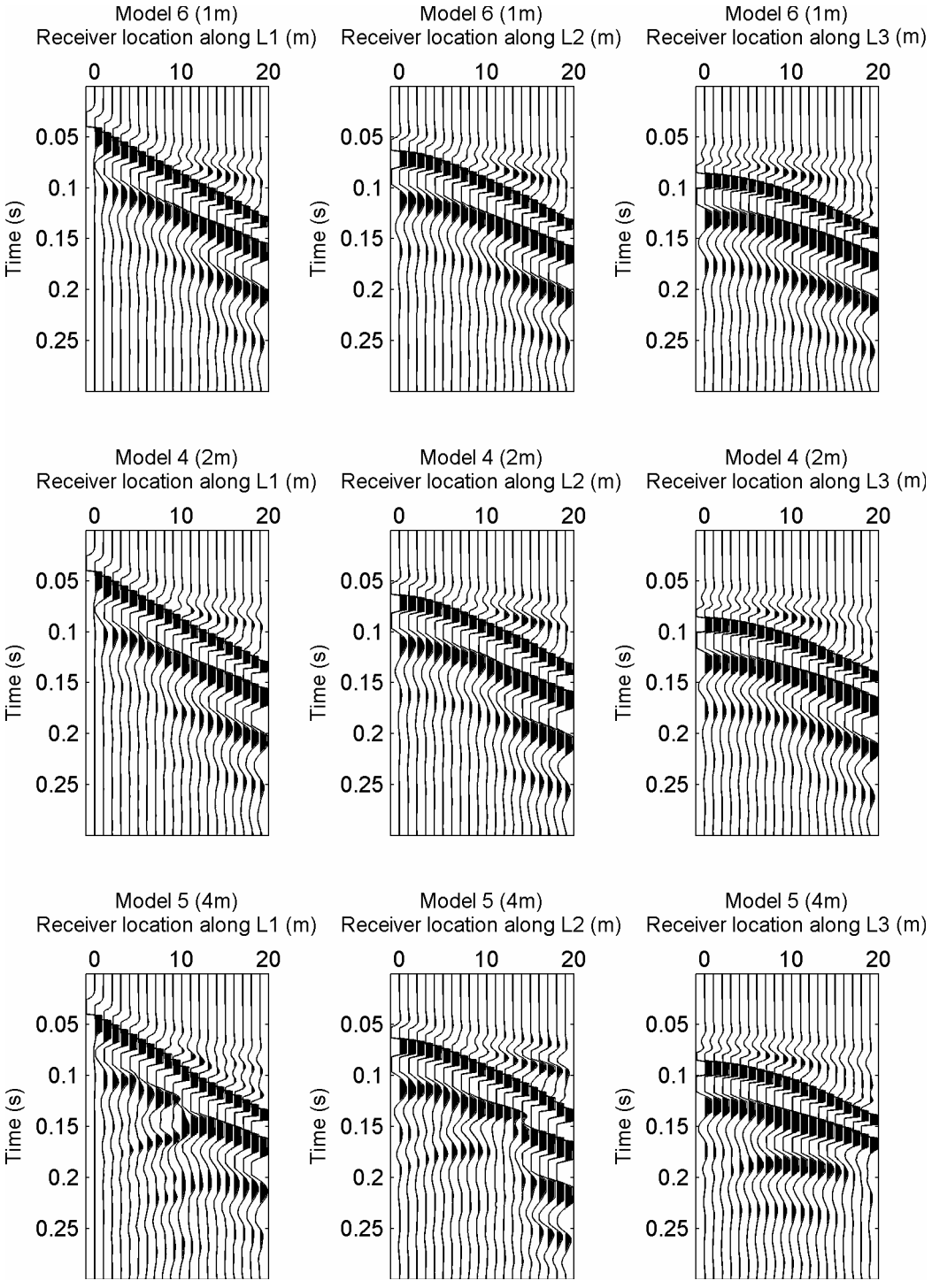

Figure E-2. Seismograms of survey line L1, L2 and L3 of model 6, 5 and 4

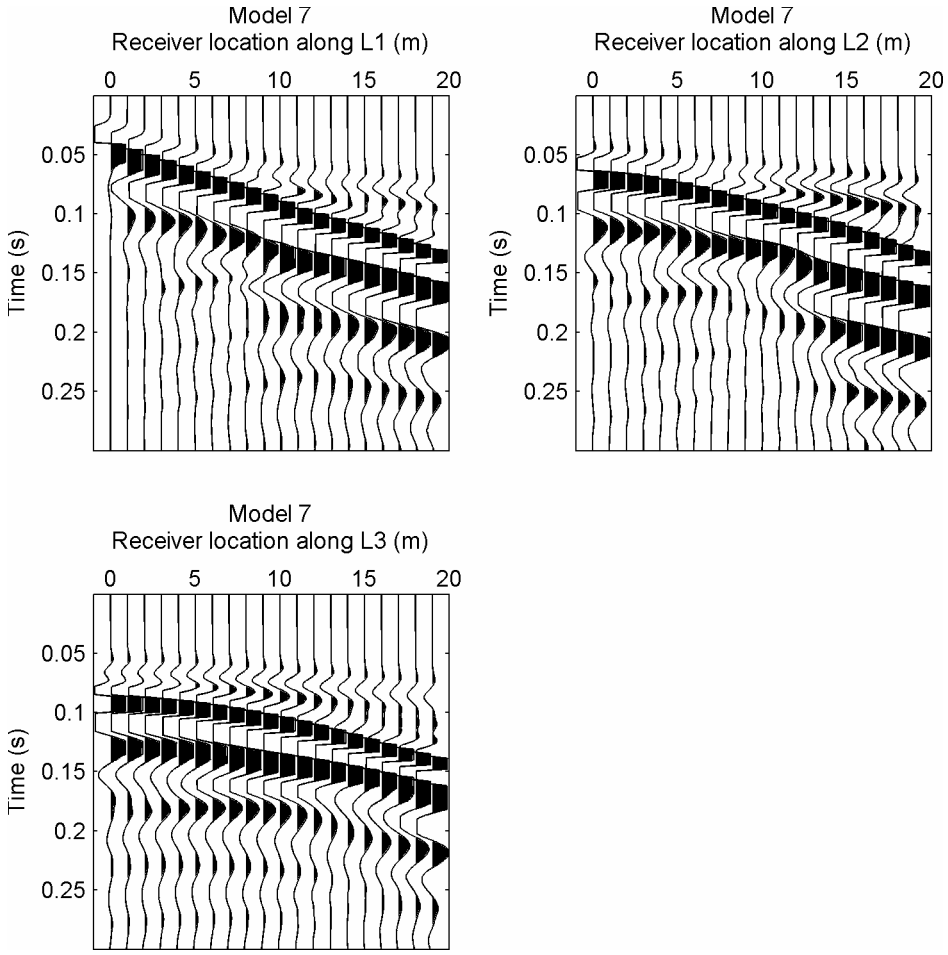

Figure E-3. Seismograms of survey line L1-L5 of model 7

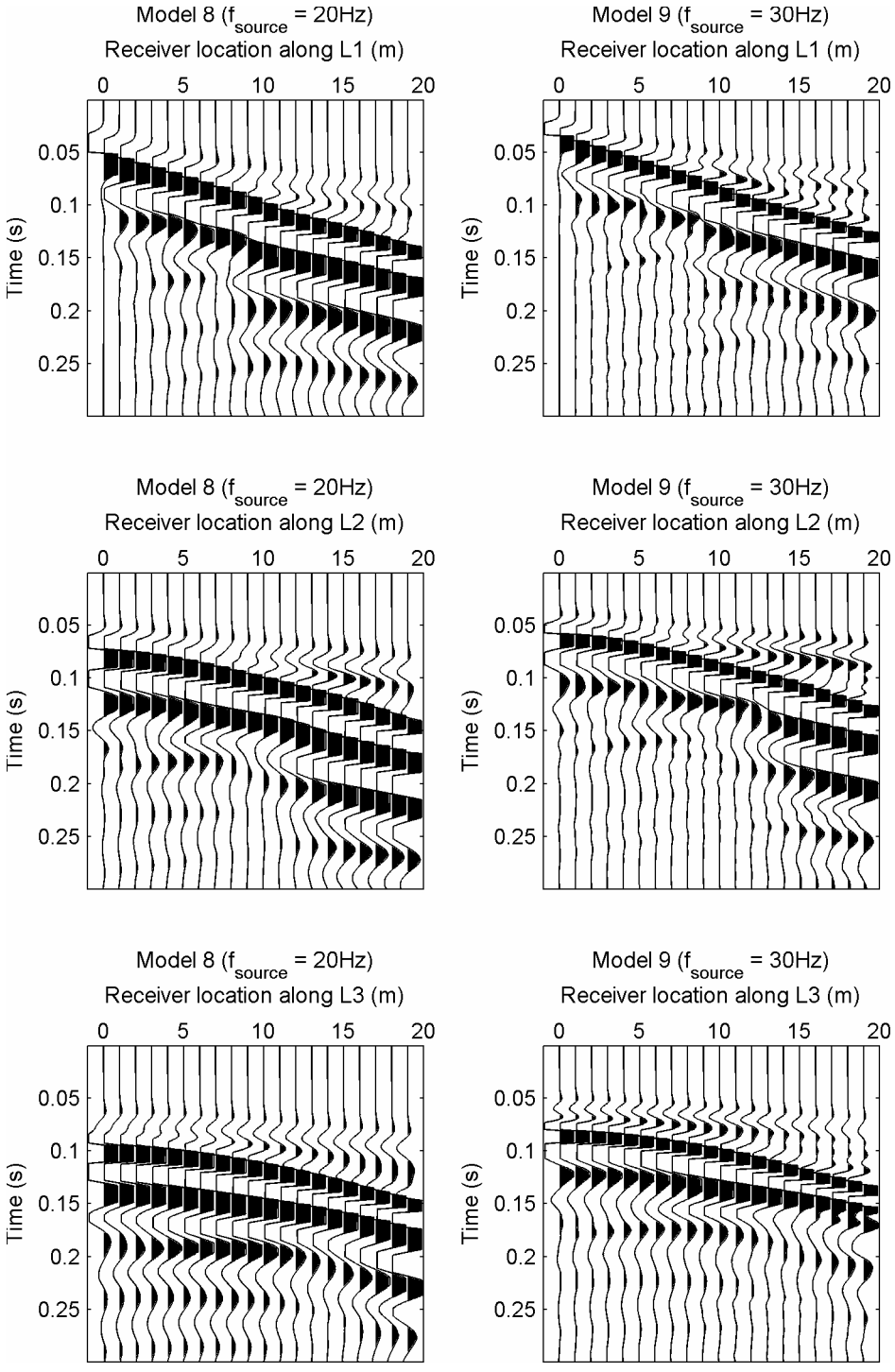

Figure E-4. Seismograms of survey line L1, L2 and L3 of model 8 and 9

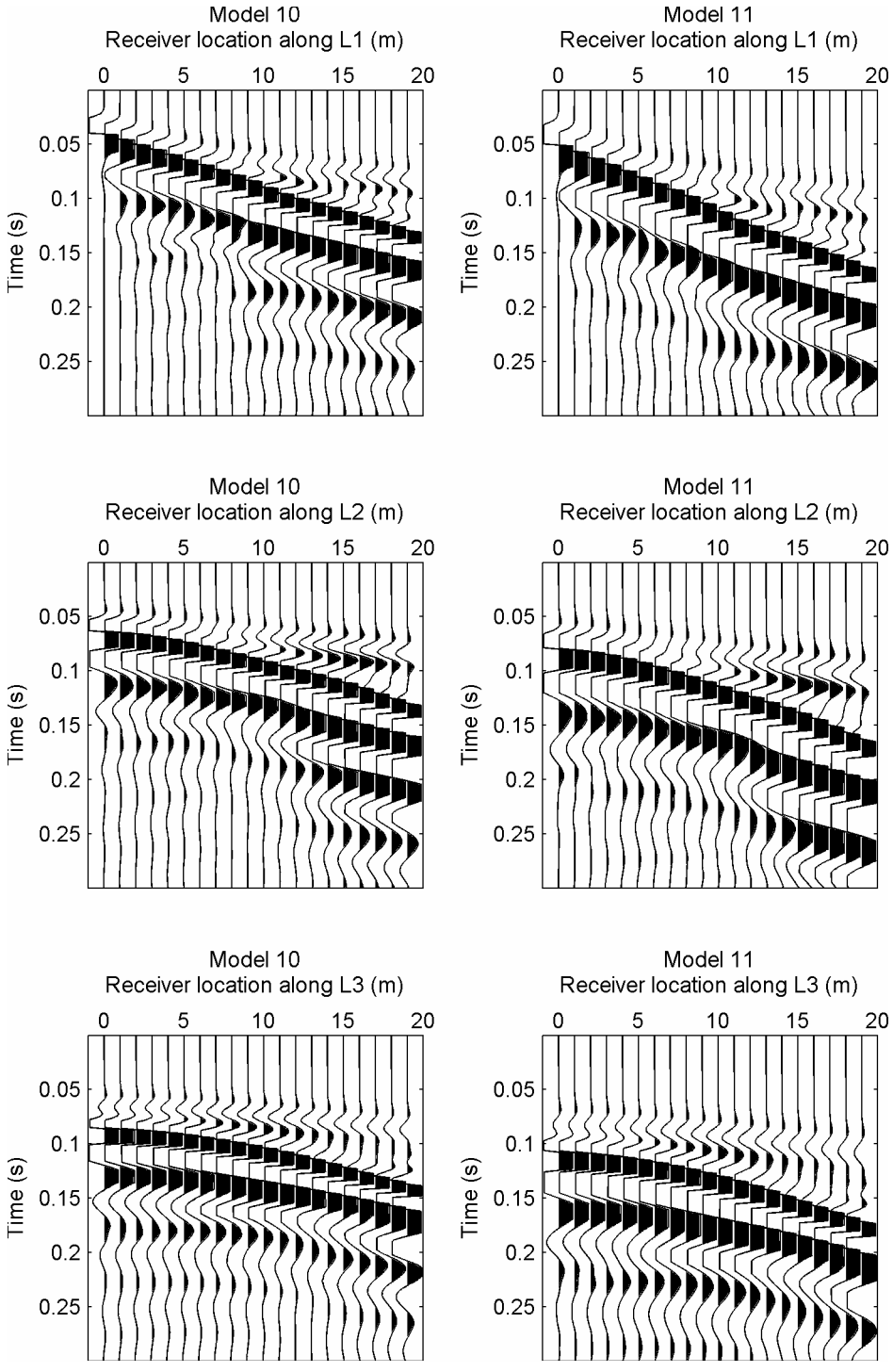

Figure E-5. Seismograms of survey line L1, L2 and L3 of model 10 and 11

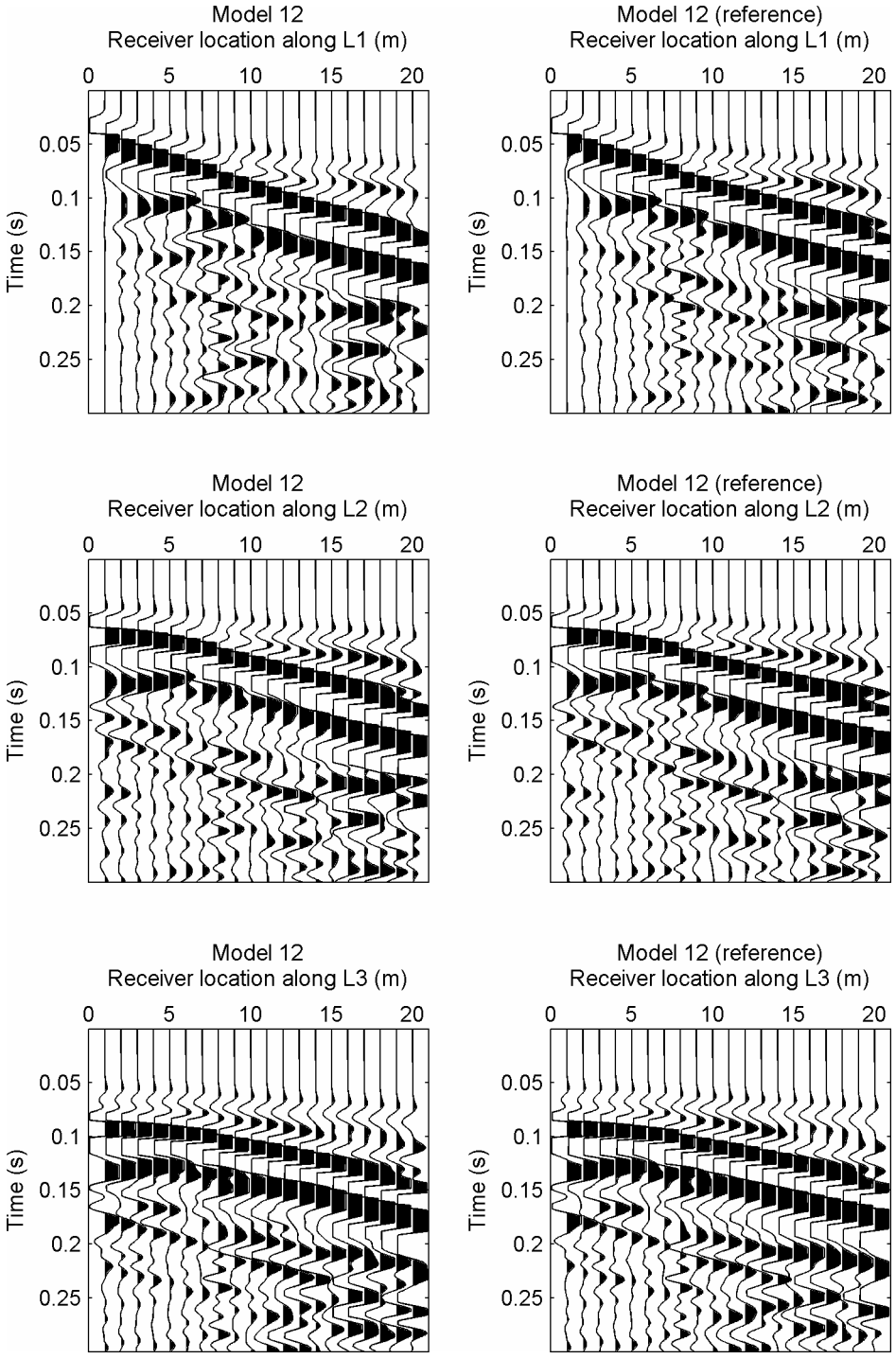

Figure E-6. Seismograms of survey line L1, L2 and L3 of model 12 and its reference model without a mineshaft

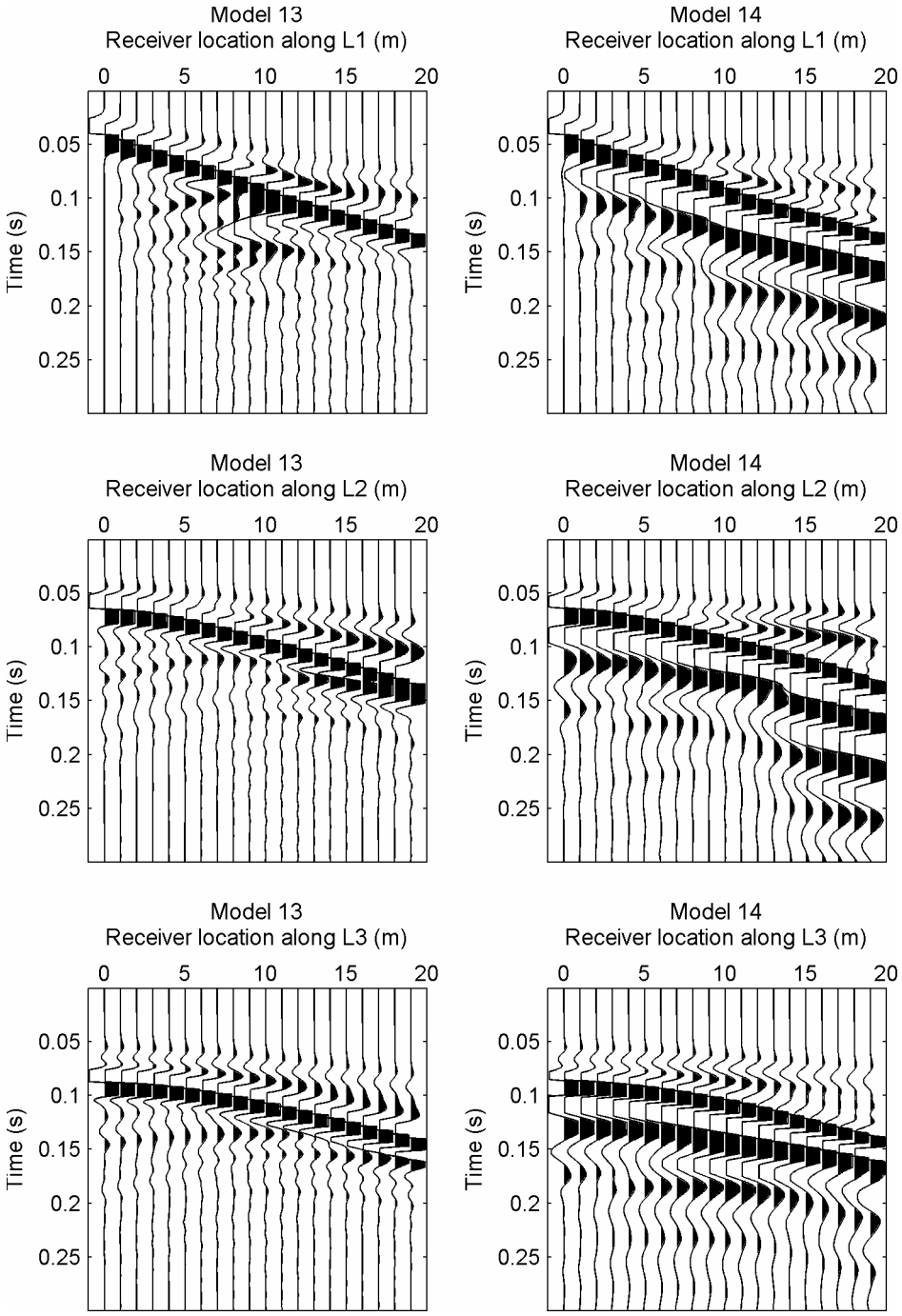

Figure E-7. Seismograms of survey line L1, L2 and L3 of model 13 and 14

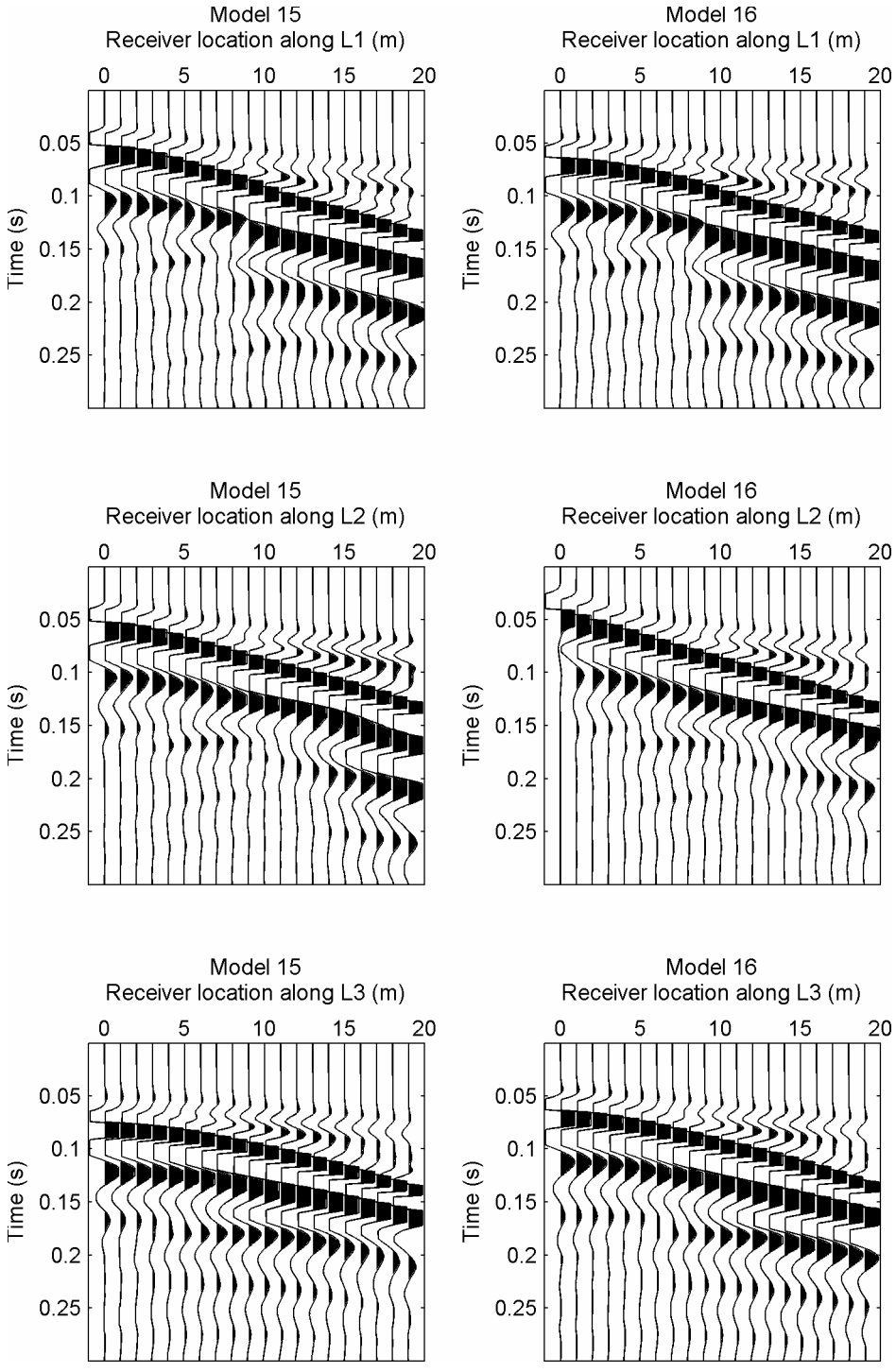

Figure E-8. Seismograms of survey line L1, L2 and L3 of model 15 and 16

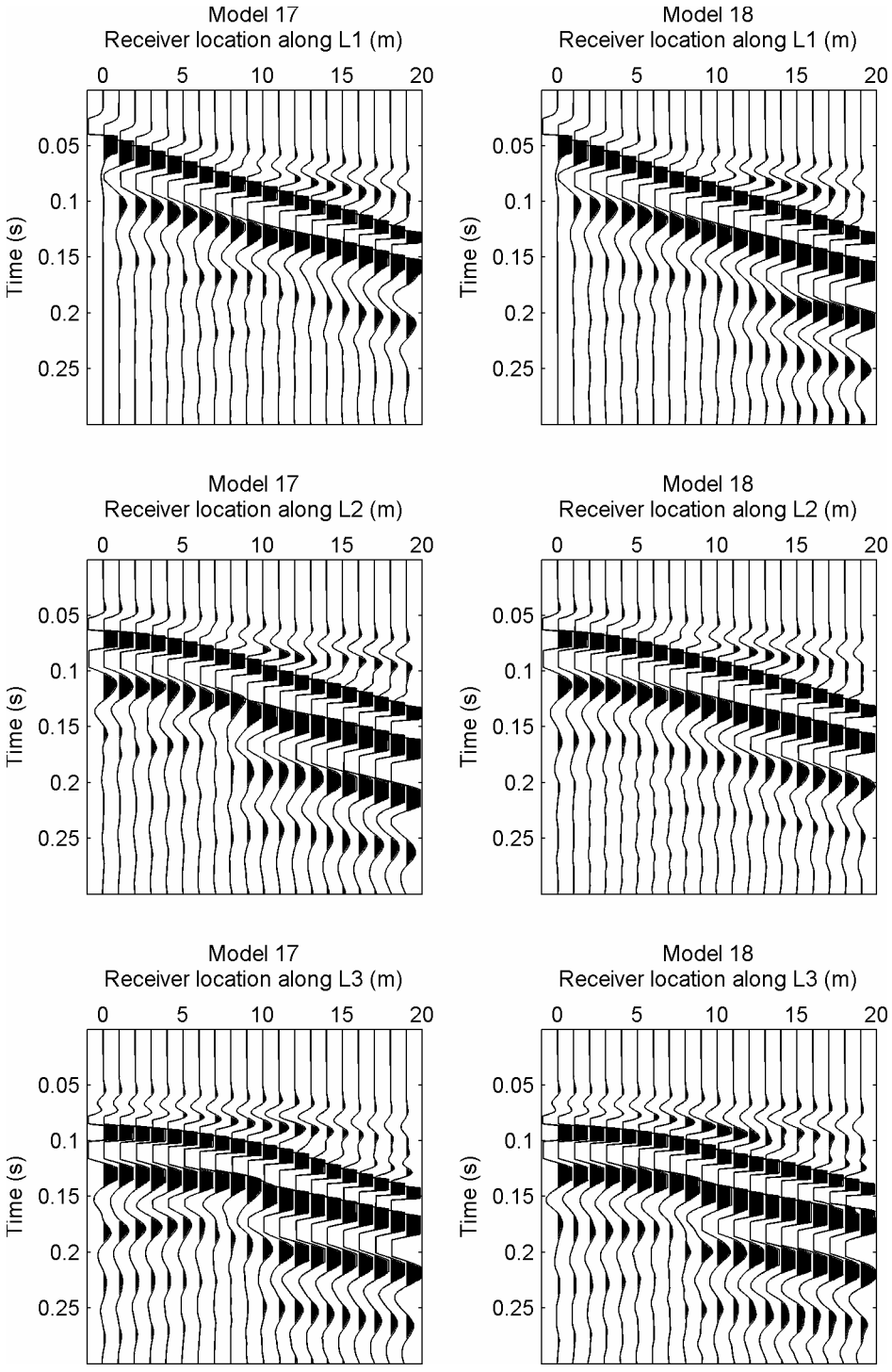

Figure E-9. Seismograms of survey line L1, L2 and L3 of model 17 and 18

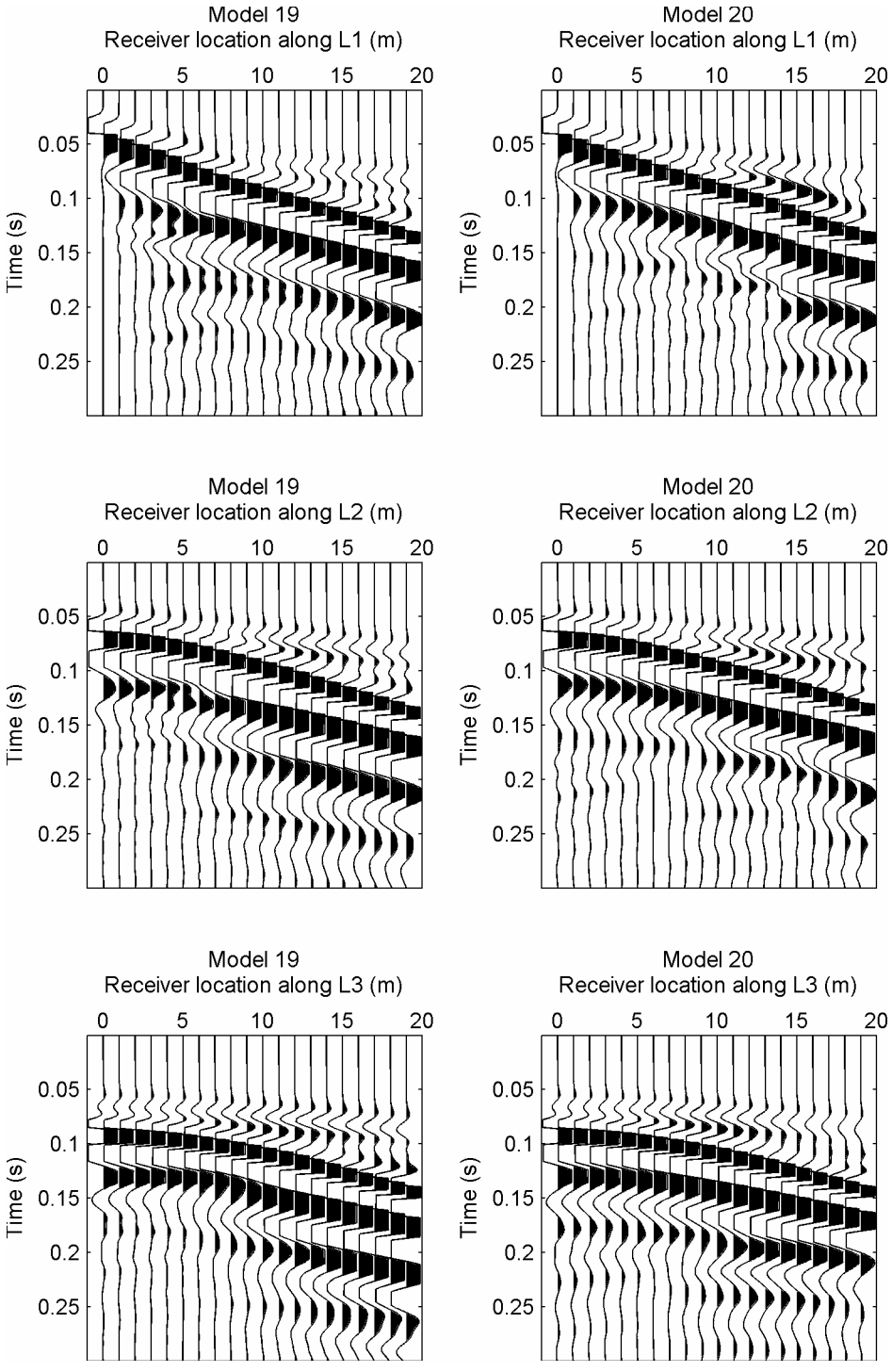

Figure E-10. Seismograms of survey line L1, L2 and L3 of model 19 and 20

Appendix F - Borehole logs

(88/2712) Wt. 12760/47 5000 12/56 M. & Sc., Ltd. G 88.

½ NT46NW/24

SECTION OF No 1 Bore, Huntlaw Colliery
250 yards E. 3 N. of Fountainhall

Surface Level _____ O.D.

Communicated _____ by _____

Date of boring or sinking _____ Borer _____

One-inch Map 33 Six-inch Map (County and Half-Quarter Sheet) Haddington 14 NE. W.

	Thickness. Fathoms.	feet.	ins.	Depth from Surface. Fathoms.	feet.	ins.
Surface		2	6		2	6
Yellow Sandstone		8	2	1	4	8
Parting "		5	9		16	5
Hard parting			2		16	7
" "		15	6		32	1
[illegible]		13	3		45	4
foul COAL			8		46	
Blackbloes			11		46	11
Gray Sandstone		2	1		49	
Black bloes		3	7½		52	4½
" "			11½		55	4
Gray Sandstone		2	10		56	2
Bloes + Sandstone		3	7		59	9
COAL		1	8		61	5
Gray sandstone pavement		2	4		63	9
Dk "		7	2½		70	11½
Dk and white Sandstone			6		71	4½
Gray and white Sandstone		3	1½		74	6
Dk. Sandstone + bloes		2	4½		76	10½
Bloes + Sandstone		1	4½		78	3
Hard ply			3		78	6
Black bloes		1	8		80	2
COAL		1	2		81	4
Ribs of gray Sst.		1	1½		82	5½
COAL			8		83	1½
bloes - pavement			3		83	4½
" + white Sand.		1	6		84	10½

Figure F-1. Borehole log at mineshaft 1

(65/2713) Wt. 12760/47 5000 12/56 M. & St., Ltd. G 65.

NT46NW/122

SECTION OF No 6 Bore, Huntlow
3200 feet E.N.E. of Fountainhall

Surface Level _____ O.D.

Communicated _____ by _____

Date of boring or sinking _____ Borer _____

One-inch Map 33 Six-inch Map (County and Half-Quarter Sheet) Haddington 14 N.E.

	Thickness. Fathoms.	feet.	ins.	Depth from Surface. Fathoms.	feet.	ins.
Clay		9	3½		9	3½
Blue blaes + white Sandstone		5	6½		14	10
Dark white Sandstone, blackstone		5	2		20	
Blue blaes			5		20	5
Dark white Sandstone		8	5½		28	10½
blue blaes		3			31	10½
Light grey Sandstone		2	9½		34	8
Light white + yellow Sandst.		4	10½		39	6½
Light Sandstone		1	5		40	11½
"		7	9½		48	9
White + yellow Sandstone		7	1½		55	10½
" "		2	9		58	7½
Soft grey Sandstone		2	7½		61	3
Rather hard "		2	7		63	10
Foul COAL			7		64	5
Blue blaes		2	4		66	9
Ironstone			3		67	
blue blaes			6		67	6
blue blaes + little coal			5½		67	11½
Grey Sandstone			11		68	10½
Light "		4	10		73	8½
" " + yellow		1	4		75	½
White Sandstone		2	9½		77	11
Dark "		1	5½		79	4½
blue blaes		1	5		80	9½
dark grey Sandstone		1	7		82	4½
Hard grey ply			2½		82	6

Figure F-2. Borehole log at mineshaft 2

Appendix G - Seismograms of experiment

In this appendix the shot gathers used for the attribute analyse of the seismograms of the field experiment presented in chapter 8 are presented:

- Receivers located at L6 at mineshaft 1
  - Shot gather L1S1-S12 in Figure G-1
  - Shot gather L1S13-S24 in Figure G-2
  - Shot gather L2S1-S12 in Figure G-3
  - Shot gather L2s13-S24 in Figure G-4
- Receivers located at L1 at mineshaft 1
  - Shot gather L5S1-S12 in Figure G-5
  - Shot gather L4S13-S24 in Figure G-6
  - Shot gather L6S1-S12 in Figure G-7
  - Shot gather L6s13-S24 in Figure G-8
- Receivers located at L6 at mineshaft 2
  - Shot gather L1S1-S12 in Figure G-9
  - Shot gather L1S13-S24 in Figure G-10
  - Shot gather L2S1-S12 in Figure G-11
  - Shot gather L2s13-S24 in Figure G-12
- Receivers located at L1 at mineshaft 2
  - Shot gather L1S1-S12 in Figure G-13
  - Shot gather L1S13-S24 in Figure G-14
  - Shot gather L2S1-S12 in Figure G-15
  - Shot gather L2s13-S24 in Figure G-16

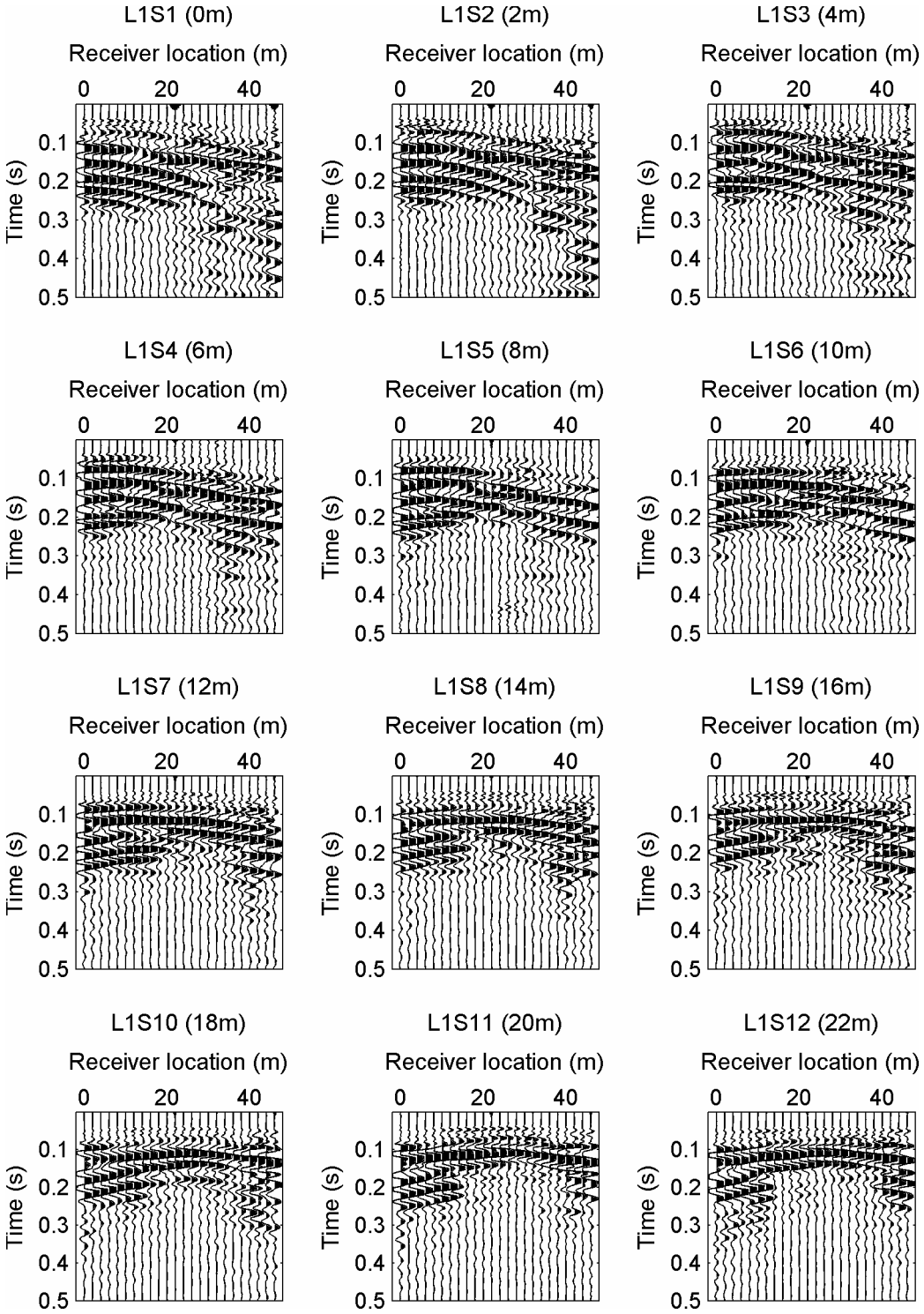

Figure G-1. Shot gather L1S1-S12, receiver located at L6

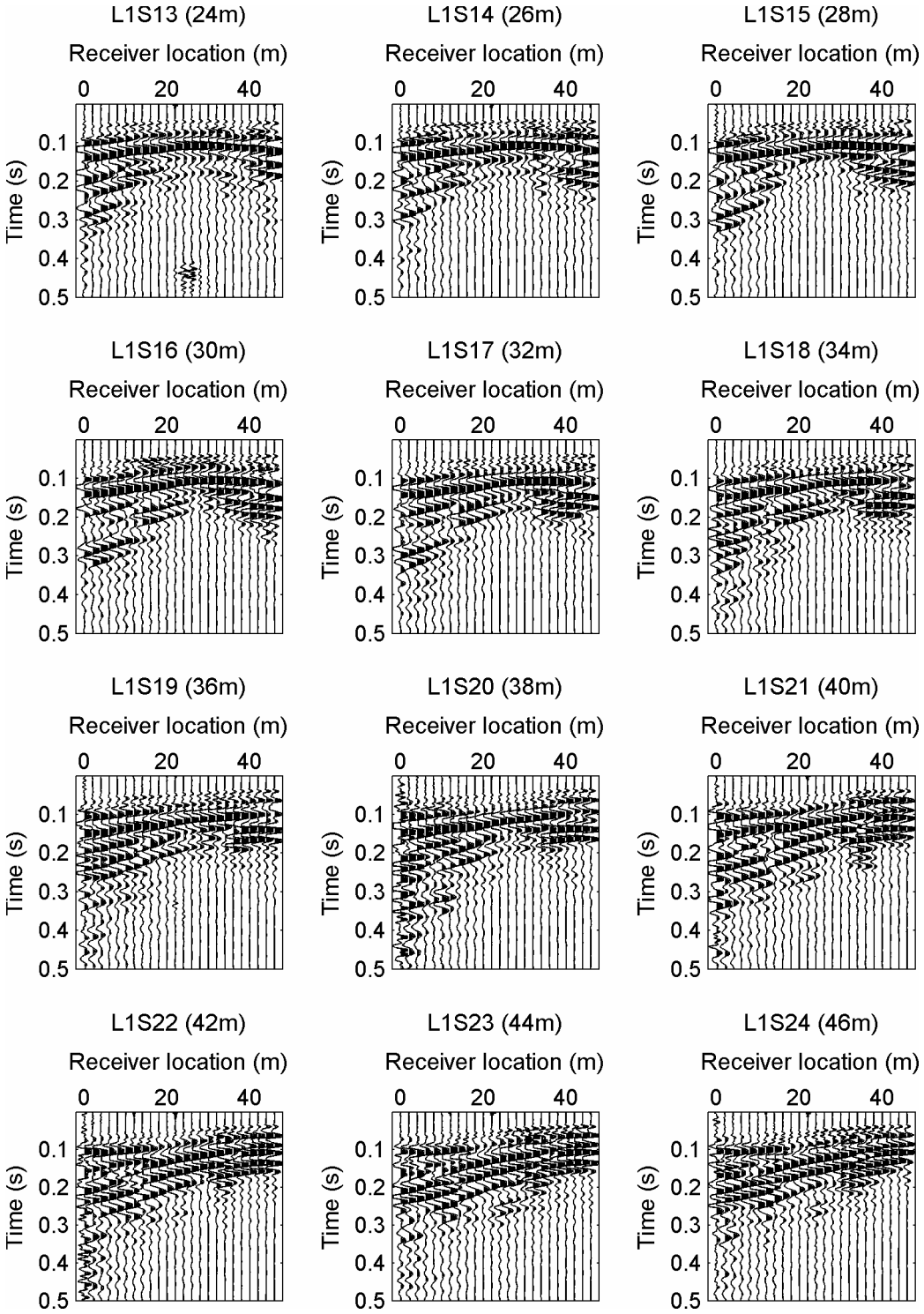

Figure G-2. Shot gather L1S13-S24, receiver located at L6

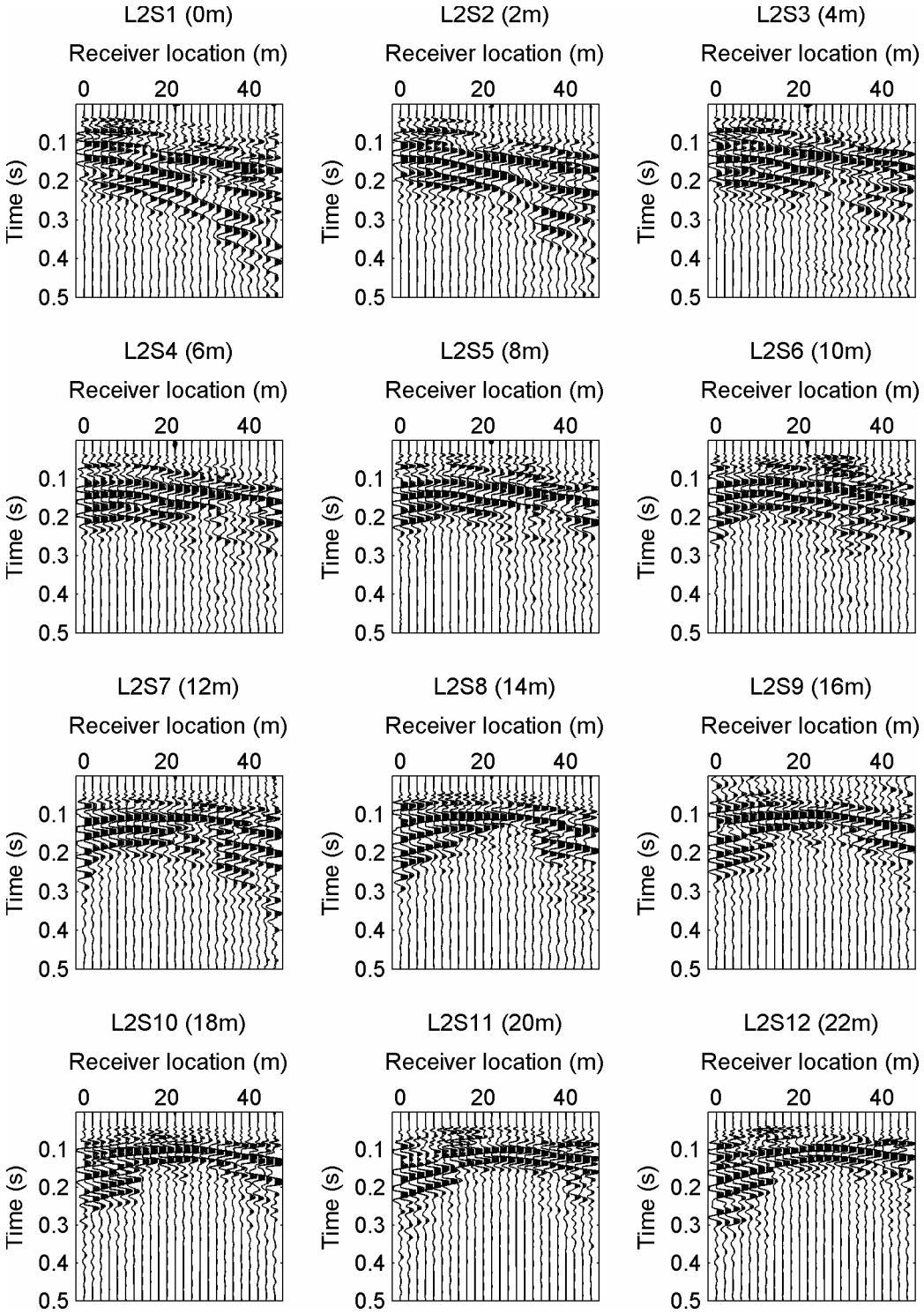

Figure G-3. Shot gather L2S1-S12, receiver located at L6

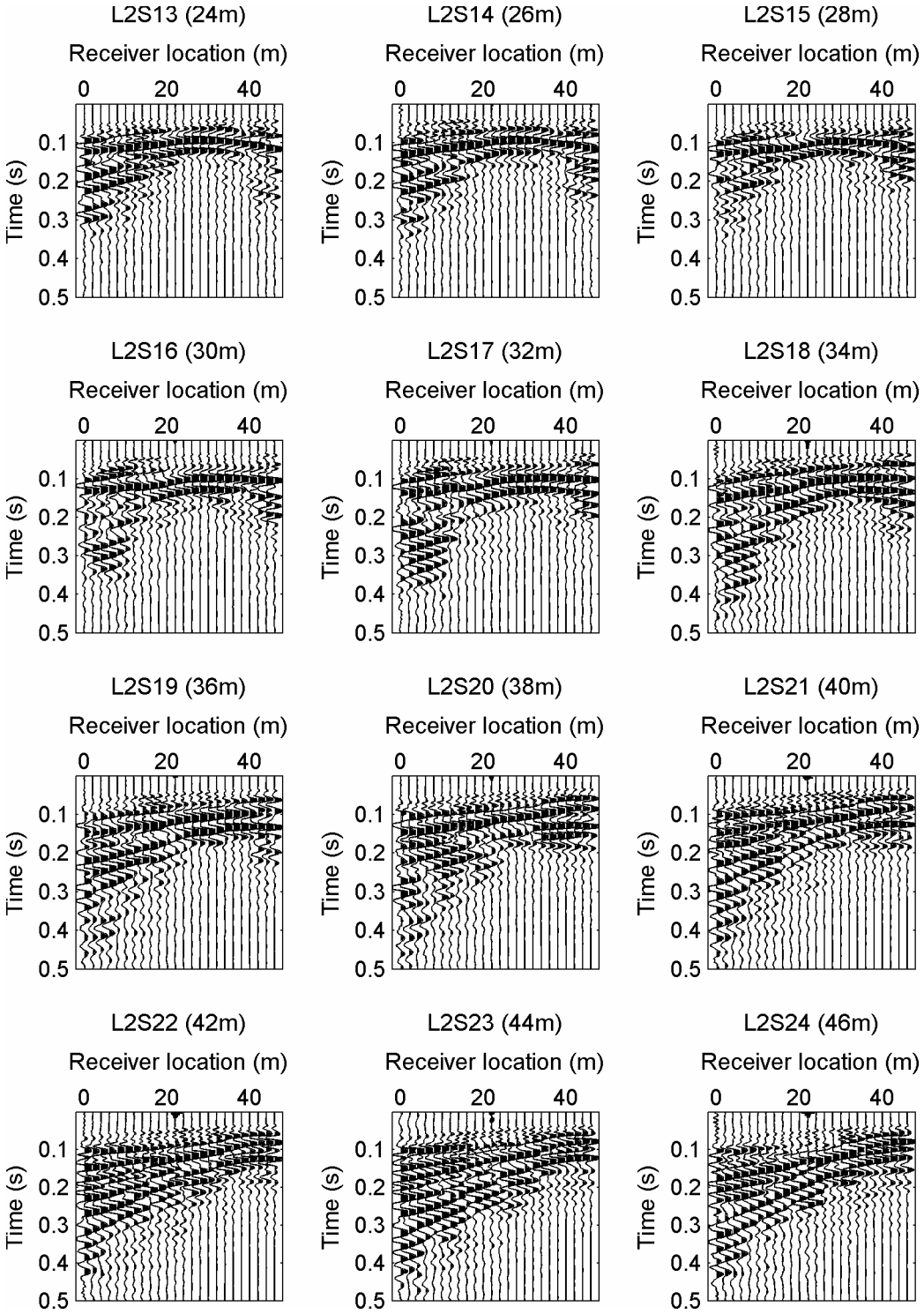

Figure G-4. Shot gather L1S12-S24 at mineshaft 1, receiver located at L6

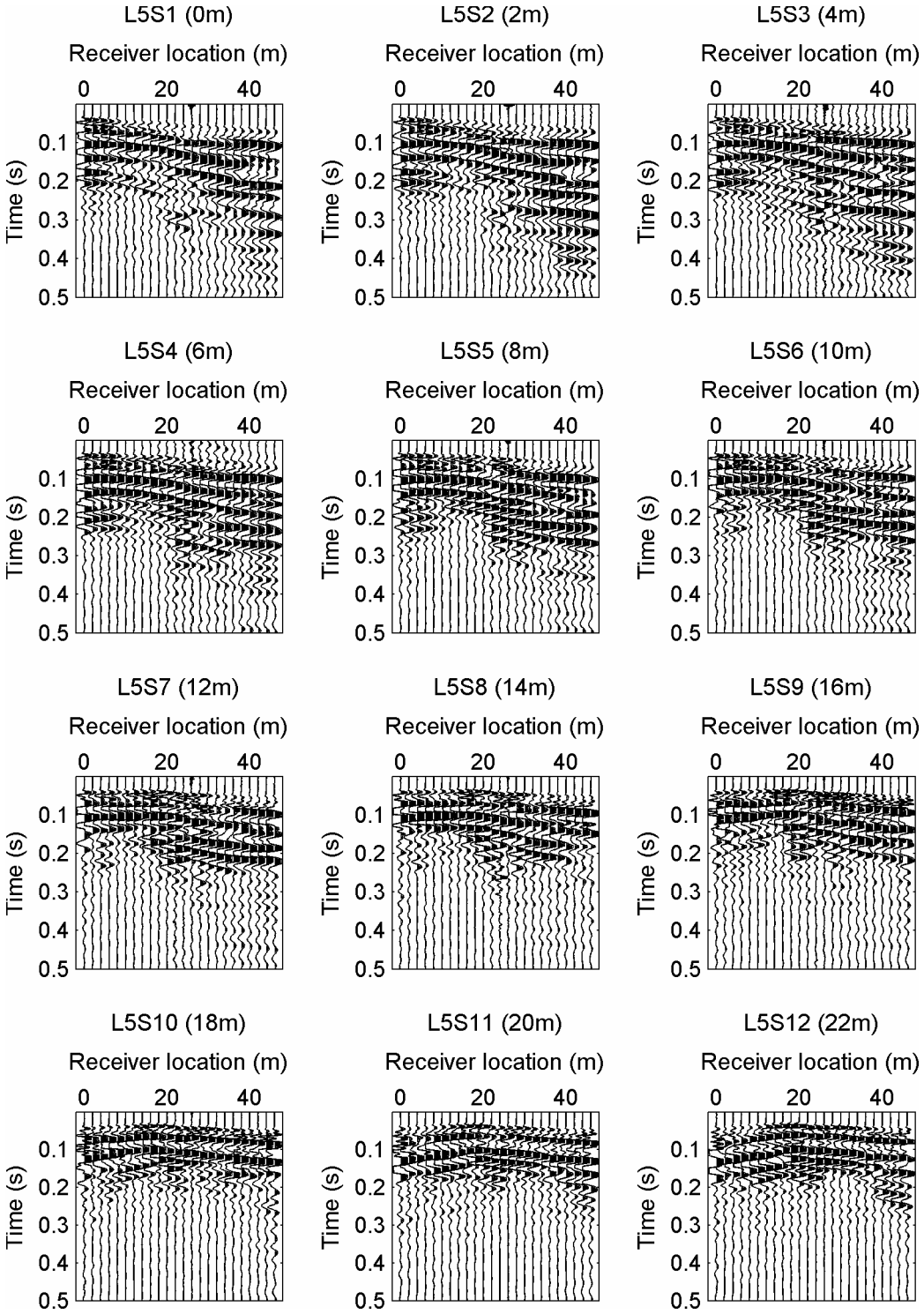

Figure G-5. Shot gather L5S1-S12 at mineshaft 1, receiver located at L1

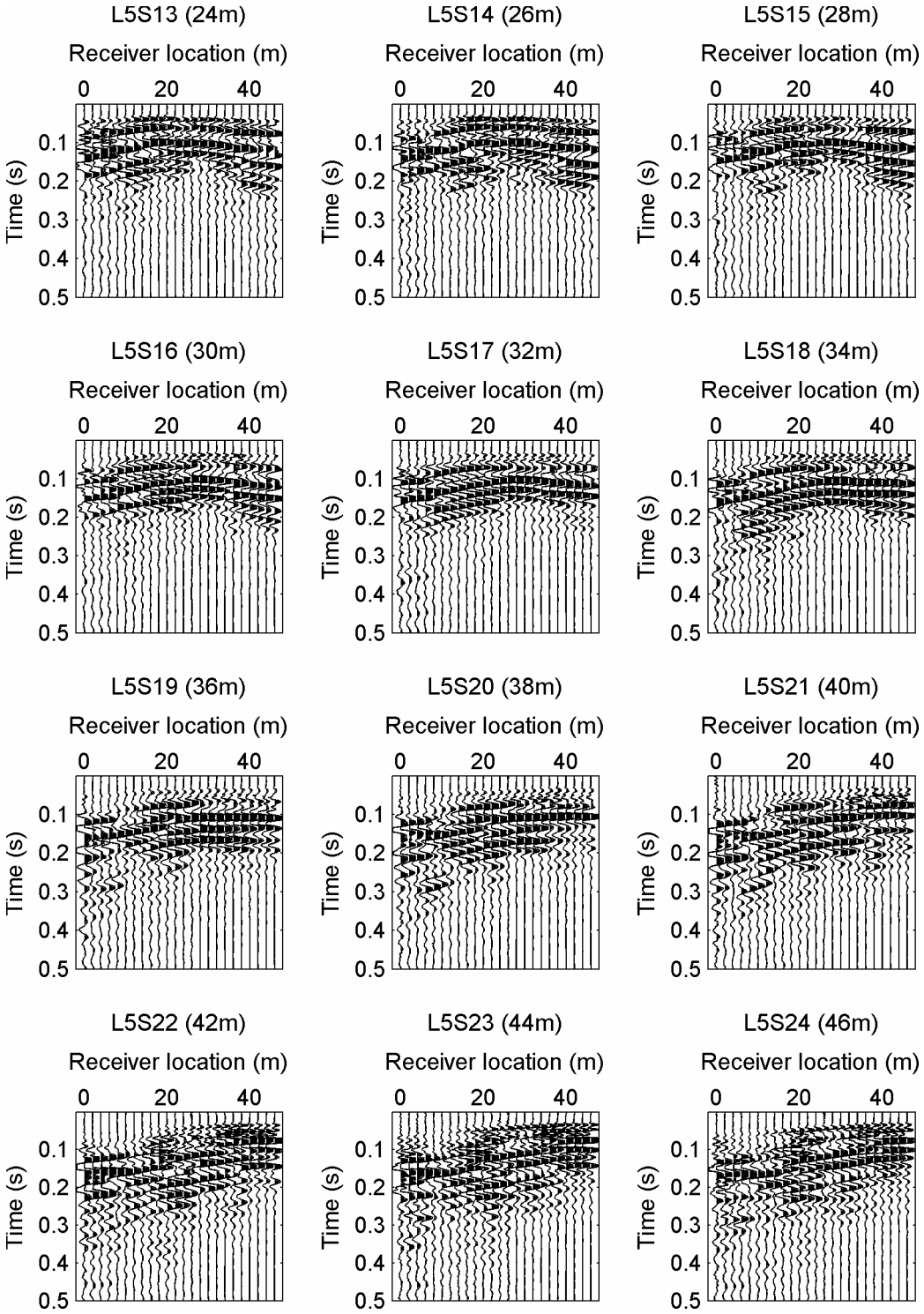

Figure G-6. Shot gather L5S12-S24 at mineshaft 1, receiver located at L1

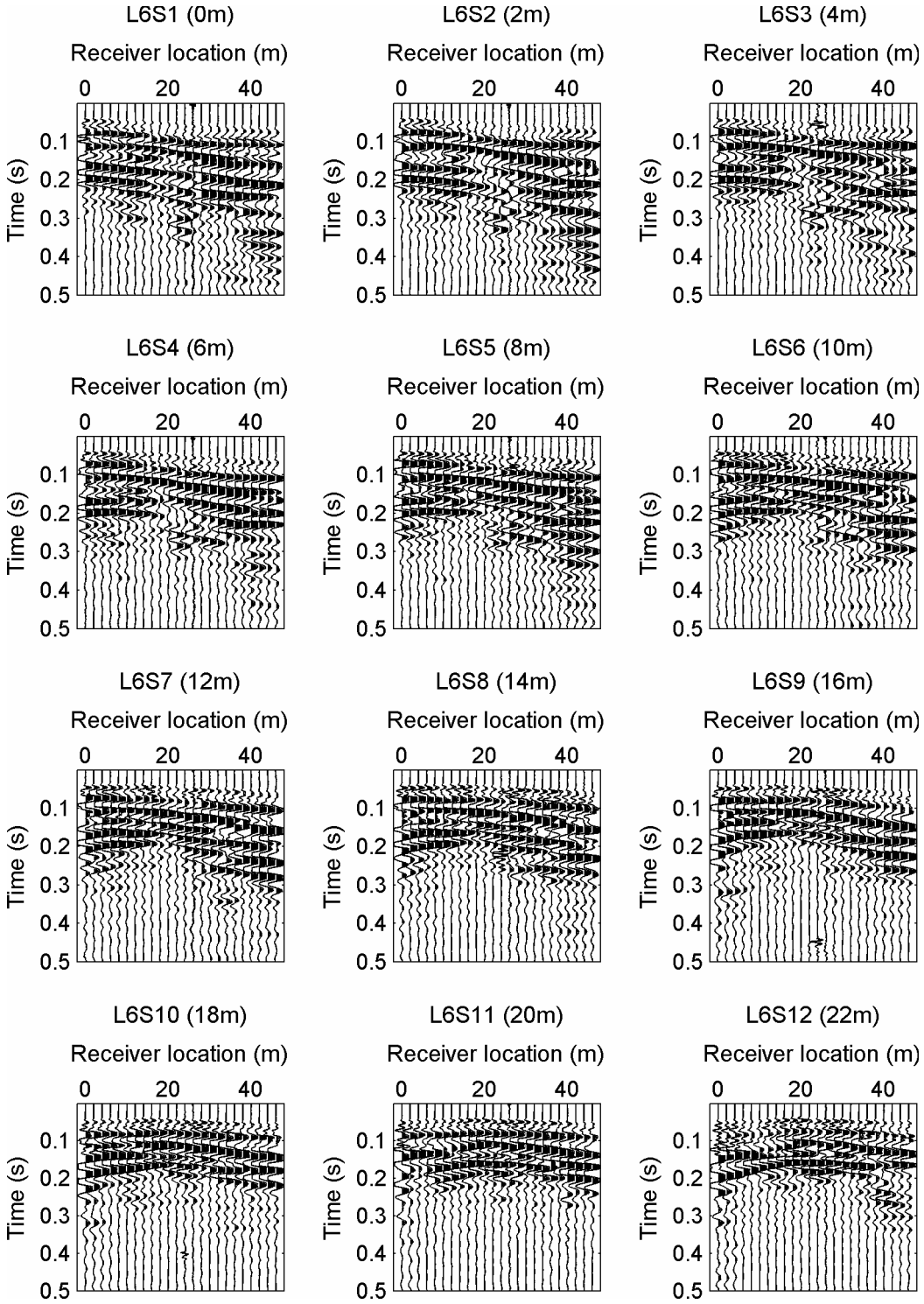

Figure G-7. Shot gather L6S1-S12 at mineshaft 1, receiver located at L1

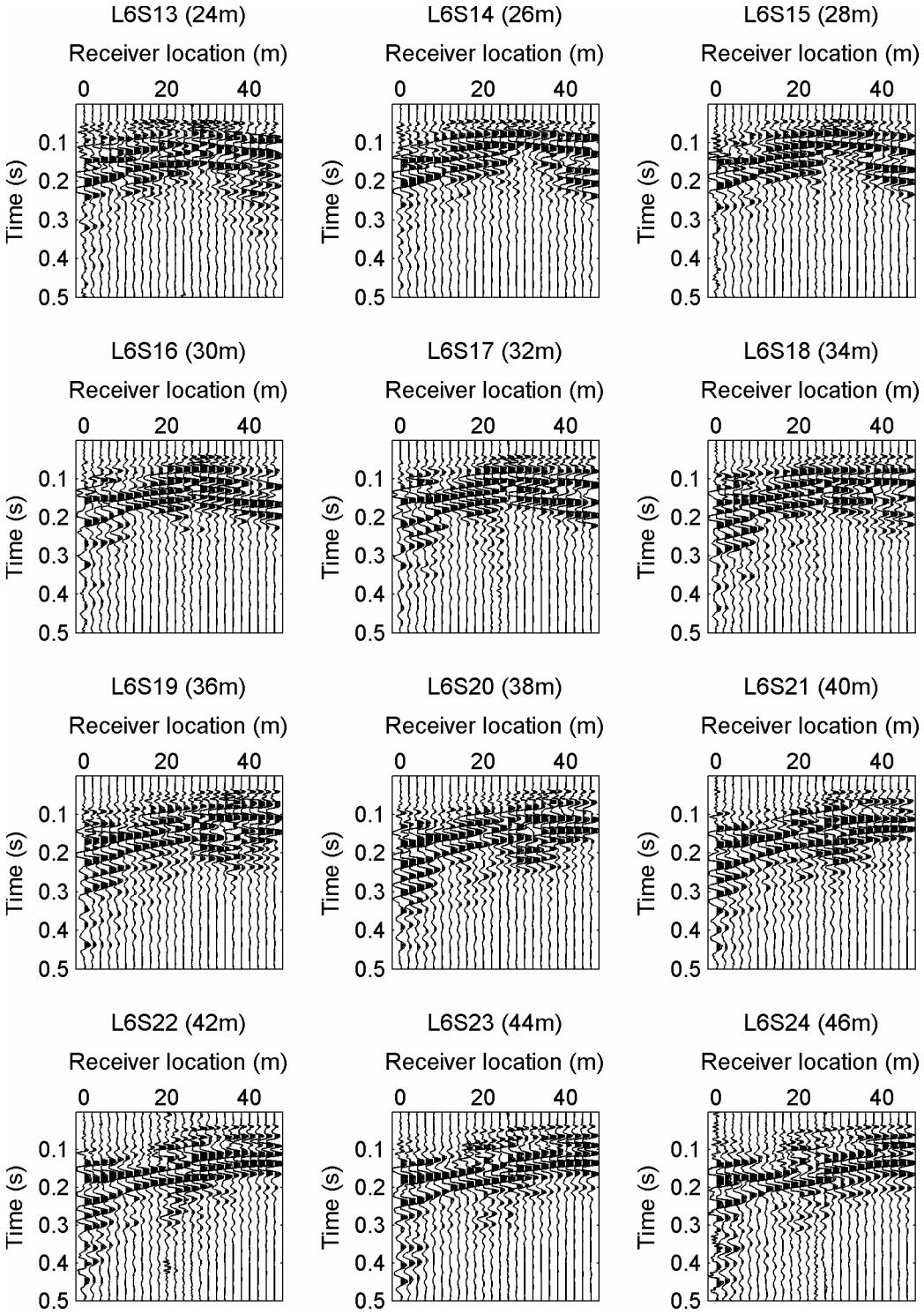

Figure G-8. Shot gather L6S12-S24 at mineshaft 1, receiver located at L1

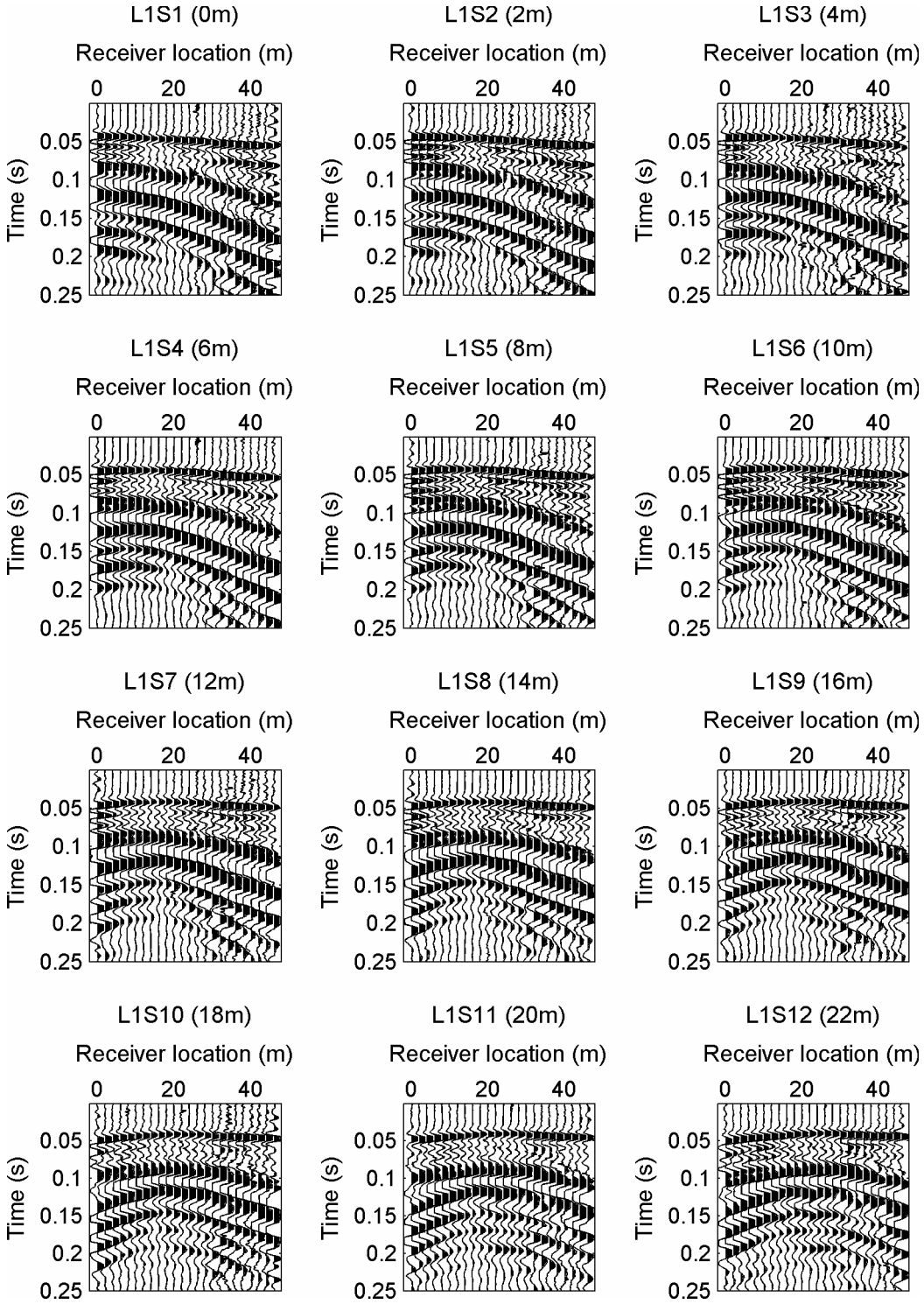

Figure G-9. Shot gather L1S1-S12 at mineshaft 2, receiver located at L6

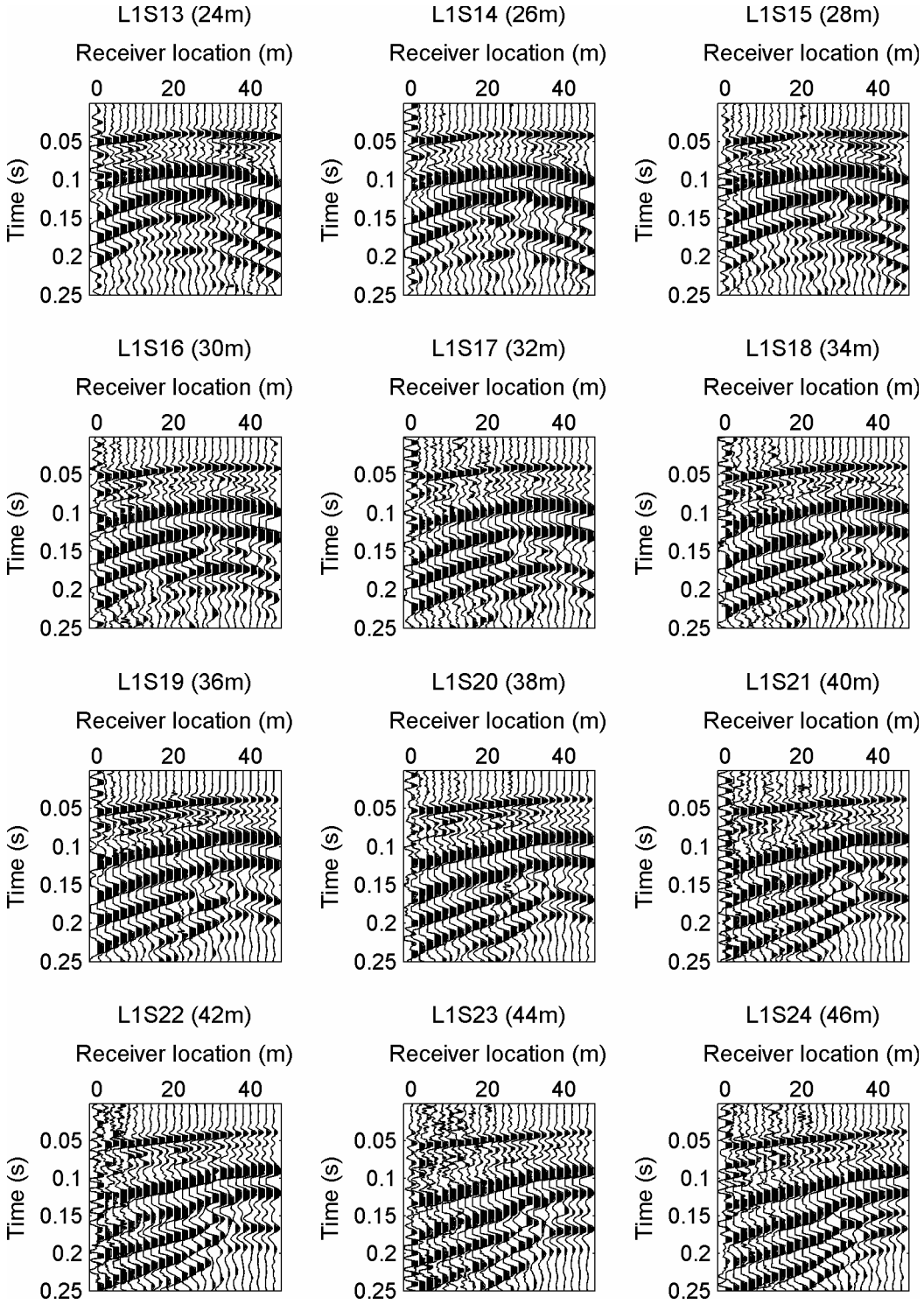

Figure G-10. Shot gather L1S12-S24 at mineshaft 2, receiver located at L6

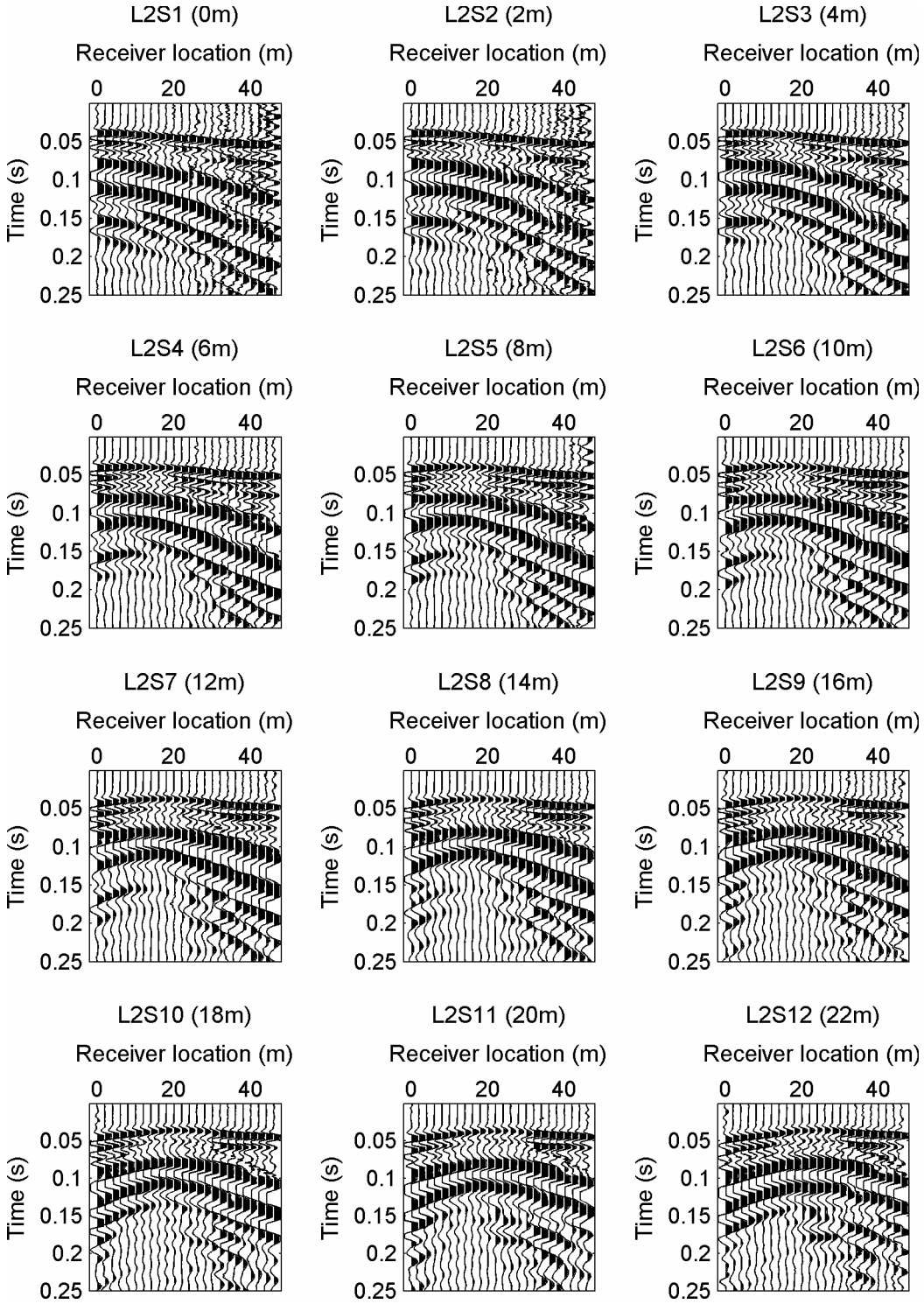

Figure G-11. Shot gather L1S1-S12 at mineshaft 2, receiver located at L6

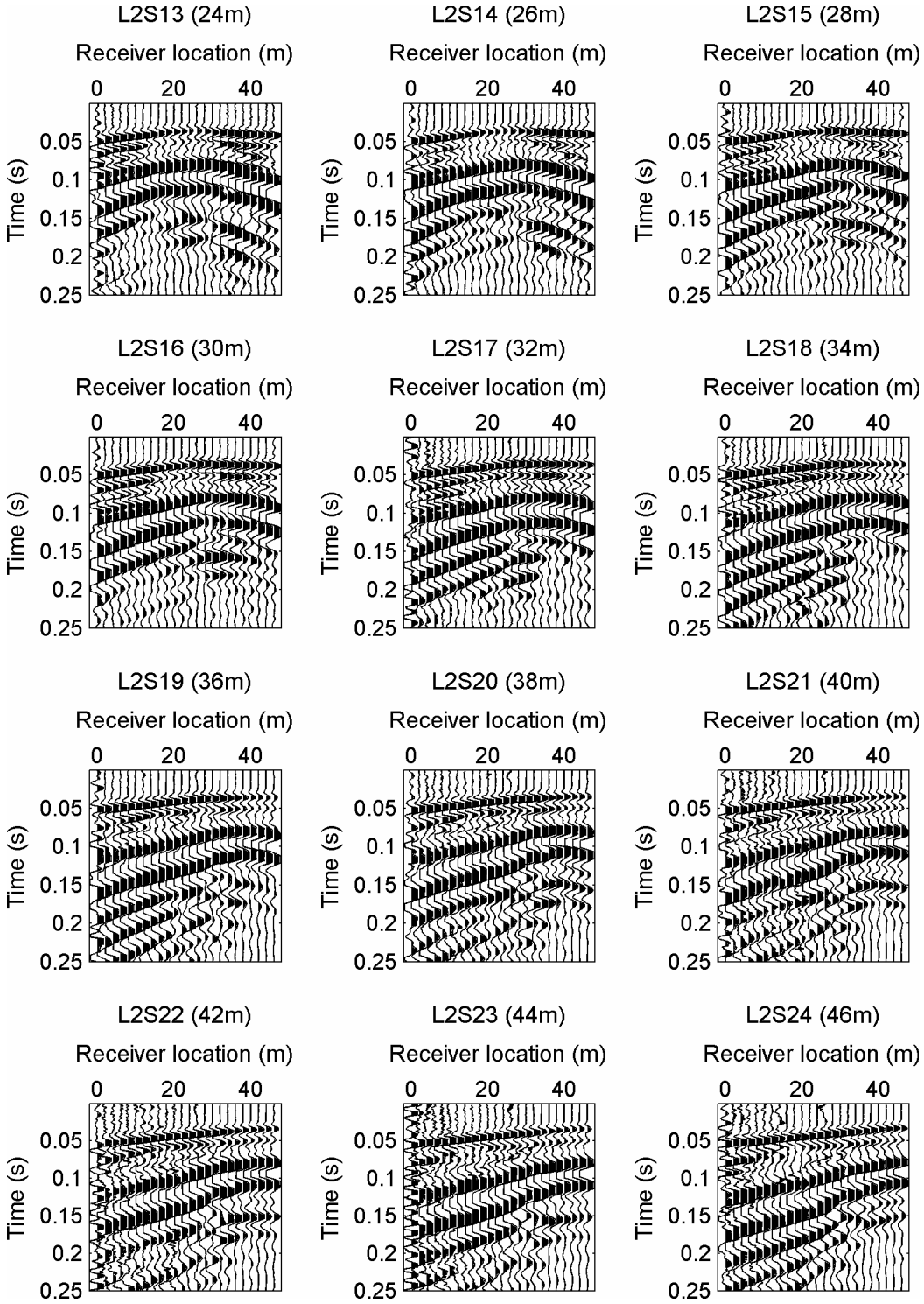

Figure G-12. Shot gather L2S13-S24 at mineshaft 2, receiver located at L6

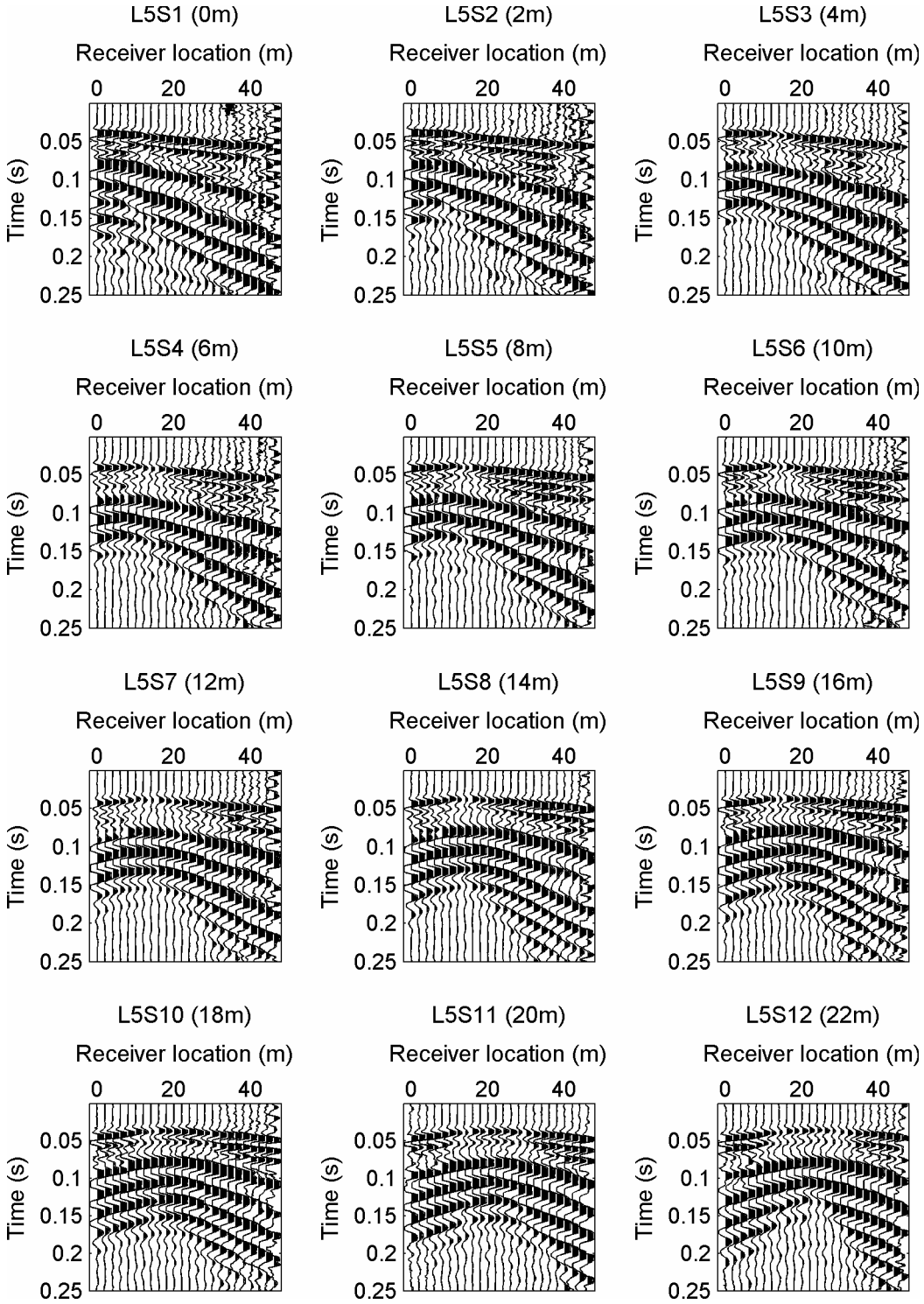

Figure G-13. Shot gather L5S1-S12 at mineshaft 2, receiver located at L1

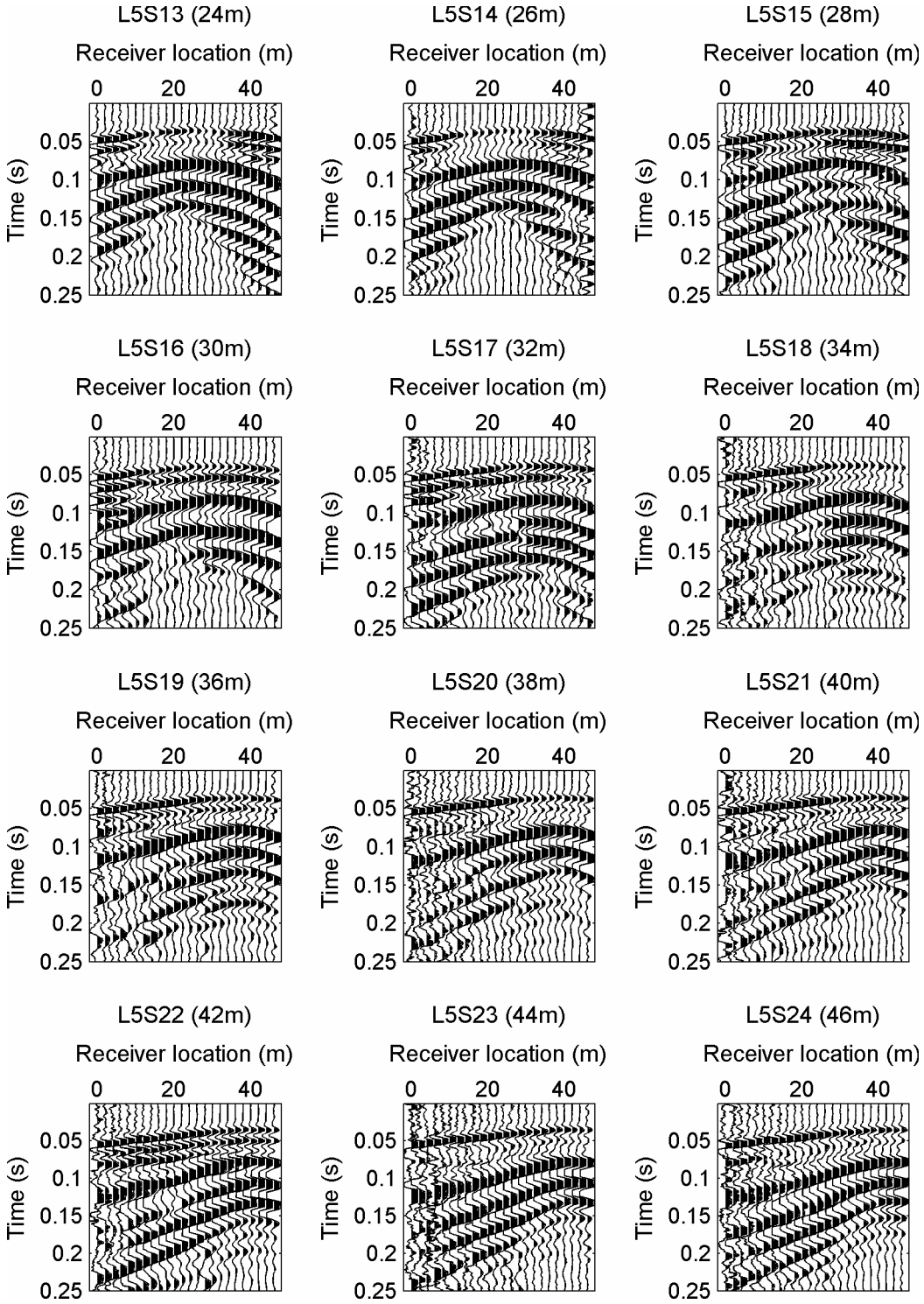

Figure G-14. Shot gather L5S13-S24 at mineshaft 2, receiver located at L1

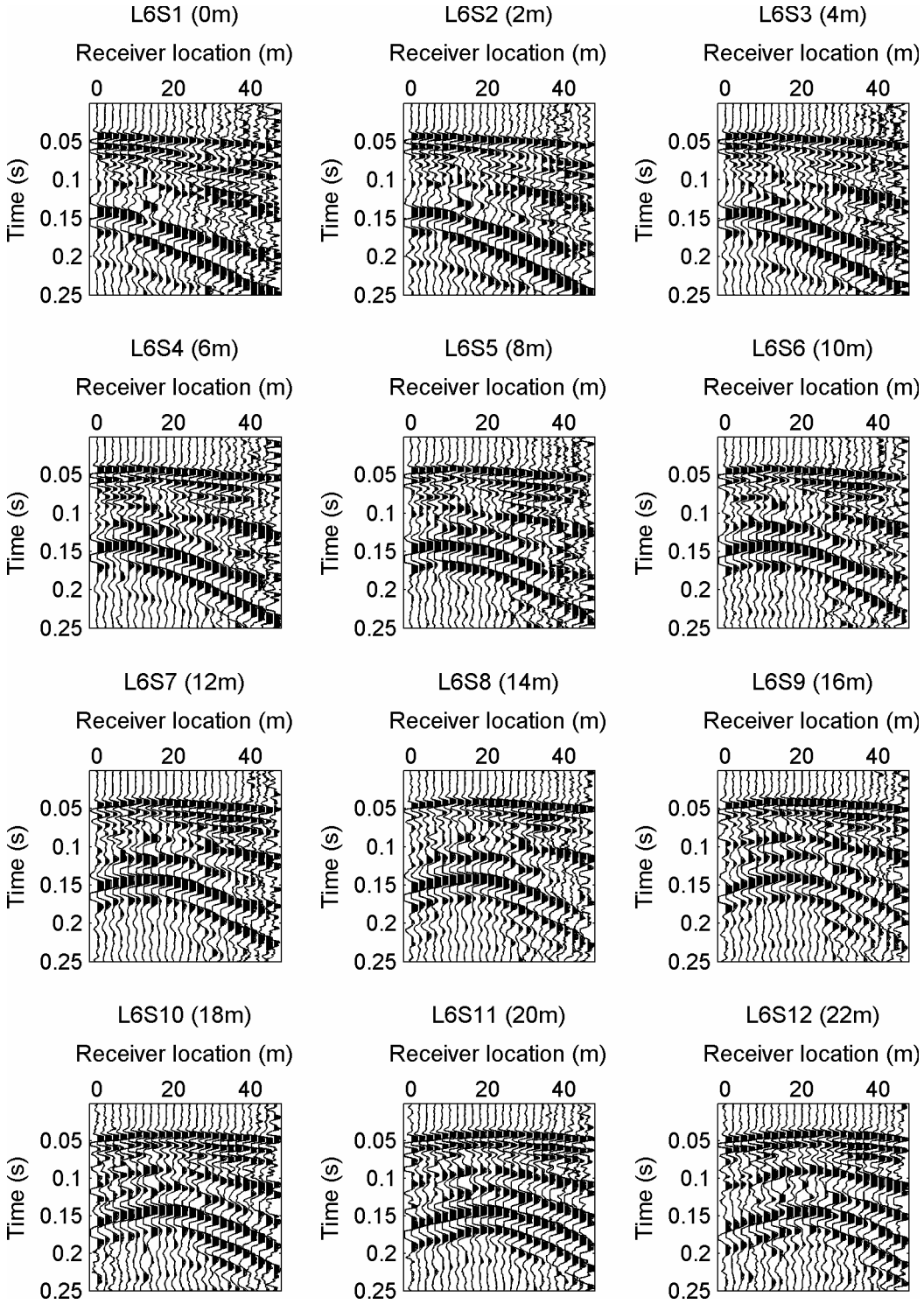

Figure G-15. Shot gather L6S1-S12 at mineshaft 2, receiver located at L1

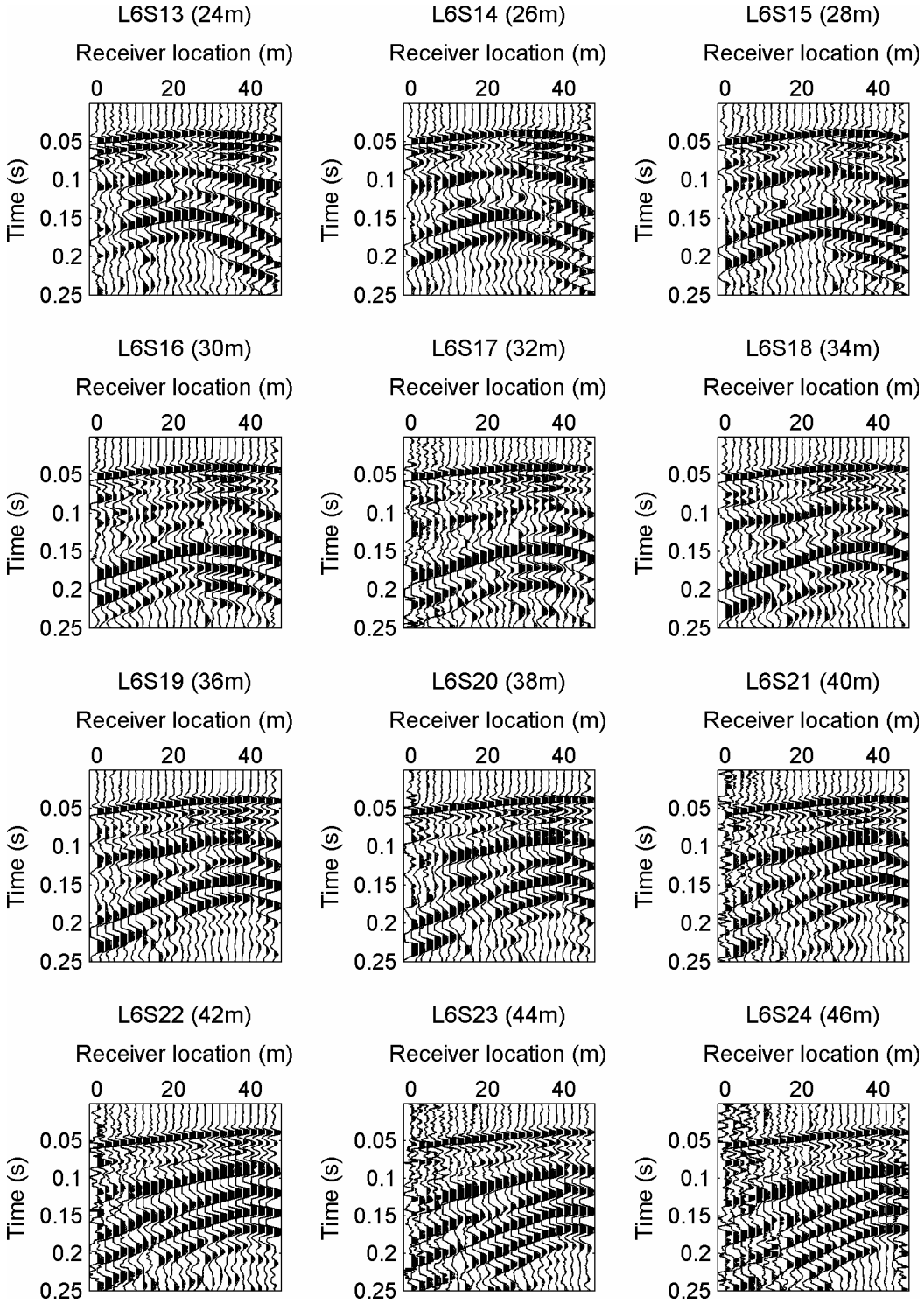

Figure G-16. Shot gather L6S13-S24 at mineshaft 2, receiver located at L1

Appendix H - Diffraction imaging

There exist various diffraction imaging techniques such as MDS – multipath diffraction summation (*Keydar, 2004; Shtivelman and Keydar, 2005*), NCC – normalised cross correlation (*Neidell and Taner, 1971; Müller, 2000*) and SBM – semblance-based migration (*Müller, 2000; Heincke et al., 2006*). These diffraction imaging techniques are based on the same principle that diffracted energies stack up when summed together along the diffraction curve whereas other energies are stacked destructively. This diffraction curve can be calculated as follows:

$$t\left(x_d, z_d\right) = \frac{\sqrt{\left(x_s - x_d\right)^2 + \left(y_s - y_d\right)^2 + \left(z_s - z_d\right)^2}}{v} + \frac{\sqrt{\left(x_r - x_d\right)^2 + \left(y_r - y_d\right)^2 + \left(z_r - z_d\right)^2}}{v} \tag{H.1}$$

where t is the travel time, x, y and z are source receiver and the presumed diffraction locations – diffraction point projection. The v denotes the velocity of the elastic wave.

Two dimensional models – not presented in this thesis – showed that the SBM techniques provide a more focussed image than the MDS and the calculations are much faster than the NCC with similar results. Therefore only the SBM method is considered. The SBM methods can be expressed by the following equation:

$$SBM\left(x_d, y_d, z_d\right) = \frac{\sum_{j=t}^{t+N}\left[\sum_{i=1}^{M} f_{ij}\right]^2}{M\sum_{j=t}^{t+N}\sum_{i=1}^{M} f_{ij}^2} \tag{H.2}$$

where M is the total number of traces and f is the trace and its subscript i is the trace number and j is the time sample, t corresponding to the diffraction curve given by equation (H.1). N is the length of a time window selected by the user. An optimized time window approximates the time frame of the diffracted wave. By using a time window more diffracted energies are stacked positively resulting in a better signal-to-noise ratio.

Figure H-2 shows the concept of the semblance based migration. The figure shows a synthetic seismogram of a simple 2D model without any bedrock and a 3m mineshaft without backfilling. Figure H-1 represents this model. The depth to the top of the mineshaft is 20m.

There are 24 receivers assigned which all measure the vertical velocity. The receiver spacing is 1m and the shot point is located at 1m before the first receiver. Additionally another five shot gathers are simulated with the shot point along the survey line with shot point spacing of 5m.

In Figure H-2, a diffracted P-wave event can easily be observed at distances from 1m to 13m around 0.12s.

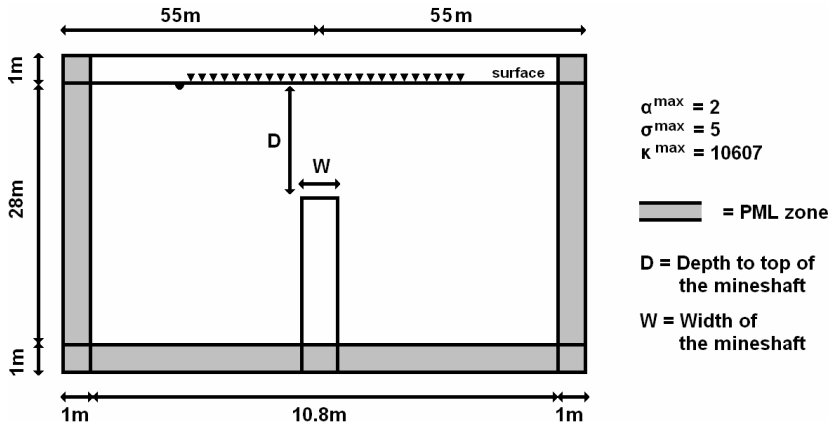

Figure H-1. Simple representation of 2D model of a mineshaft used for the simulations of seismograms Figure H-2 (figure is not to scale)

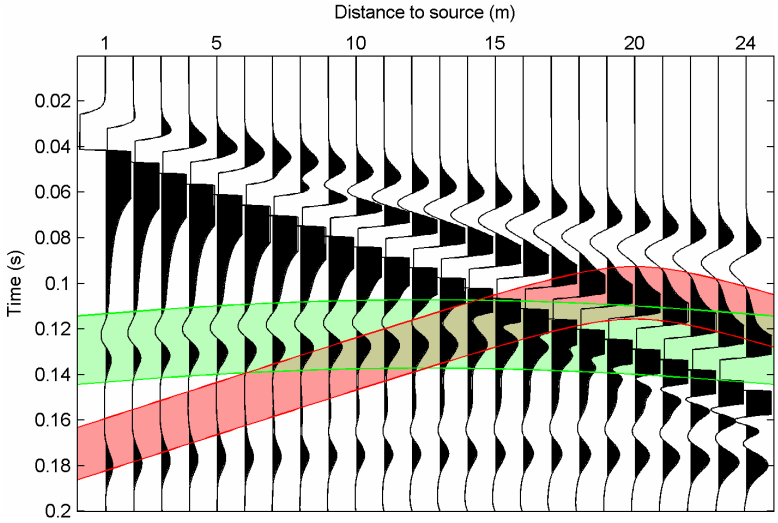

Figure H-2. The SBM is estimated along tubes which follow the migration curves; green tube follows the correct diffraction curve whereas the red tube follows does not

Assuming that the projected diffraction point is at the mineshaft top, summing the amplitude values of the traces along the diffraction curves confined to the green lines will add the energies of this event constructively. The surface waves on the right hand side between green lines are uncorrelated to the diffraction curve and will more or less add up destructively. The non-diffracted events can cause noise and lower the semblance values.

On the other hand summing the energies of a diffraction point projection away from the actual diffraction point will sum all the amplitudes destructively. For example the red curves resemble a diffraction point projection at 20m and 2.5m deep and moreover the diffraction velocity is selected too low. It is clear that none of the seismic events are correlated to these red curves and hence all the amplitudes are summed destructively, which results in very low semblance values.

Figure H-3 shows the result of the semblance calculations using the synthetic seismograms of 2D model presented in Figure H-1. The total data set consisted of the six shot gathers simulated with this model. Note that the semblance values in

figure are not normalised by the denominator in equation (H.2). The data contains no noise and for some diffraction point projections the denominator becomes zero or close to zero. This leads to uncorrelated high semblance values.

Figure H-3 shows high semblance values around 20m depth and along 12.5m along the survey line. The location of these high semblance values correlates perfectly with the location of the top of the mineshaft – the diffraction point in the model. Note that high values can be observed in the top 5m. These values are associated with strong surface waves which are not completely destructively summed together.

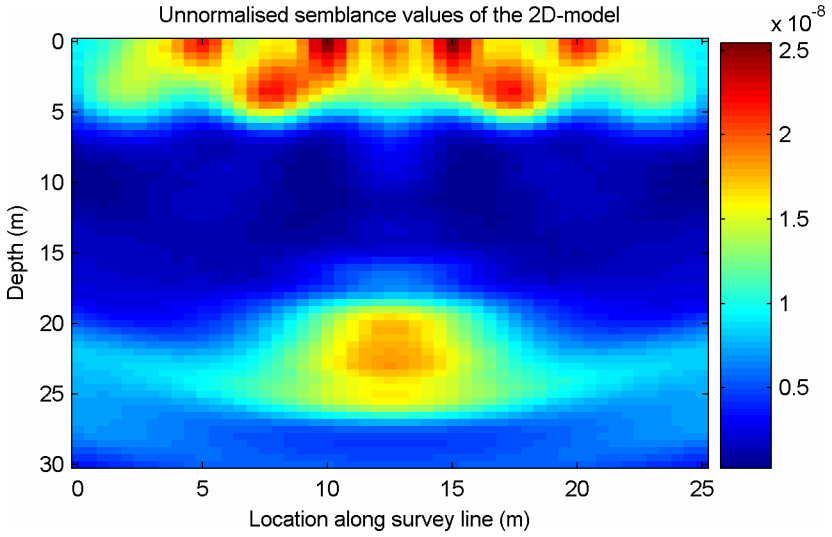

Figure H-3. The semblance values of the 2D model using six shot gathers; note that the semblance is not normalised

H.1. Results

The results of the diffraction imaging by the SBM method at the capped mineshaft are presented in Figure H-4. Semblance velocities between 300m/s to 800m/s with intervals of 100m/s are selected for the calculation of the SBM. In

this figure the iso-semblance values between the maximum and the 75% of the maximum are presented in red. The iso-semblance values between 75% and 50% of the maximum are presented in transparent blue.

The maximum semblance values for all the results are between 0.0145 and 0.0025. A semblance value of 1 means that the energies are constructively summed together along the diffraction without interference of other waves. In this light, it can be concluded that the semblance values in Figure H-4 are very low. It is very likely that these semblance values do not represent the amount of diffracted energies summed together, but actually represents the residual energies of strong surface waves that were not summed together destructively. Figure H-4 does not show any correlation between the higher iso-semblance values and the location of the mineshaft in the middle of the surveyed space.

The results of the diffraction imaging at the backfilled mineshaft are presented in Figure H-5. Similar to the capped mineshaft the maximum iso-semblance values are very low (0.0152-0.0032). The location of the mineshaft is unknown and hence the results cannot be correlated to the mineshaft presence.

H.2. Conclusions

Diffraction imaging works fine when the diffraction events arrive at the receivers un-interfered by other waves; for example voids at great depth (<15m). However, the top of void of the mineshafts is rarely located at great depth. In practice, diffracted events are often superimposed by stronger waves and hence the diffraction imaging cannot resolve the mineshaft location. Furthermore numerical 2D models showed that when the top of the void is located at the bedrock interface very little diffracted P-wave energies will come into existence.

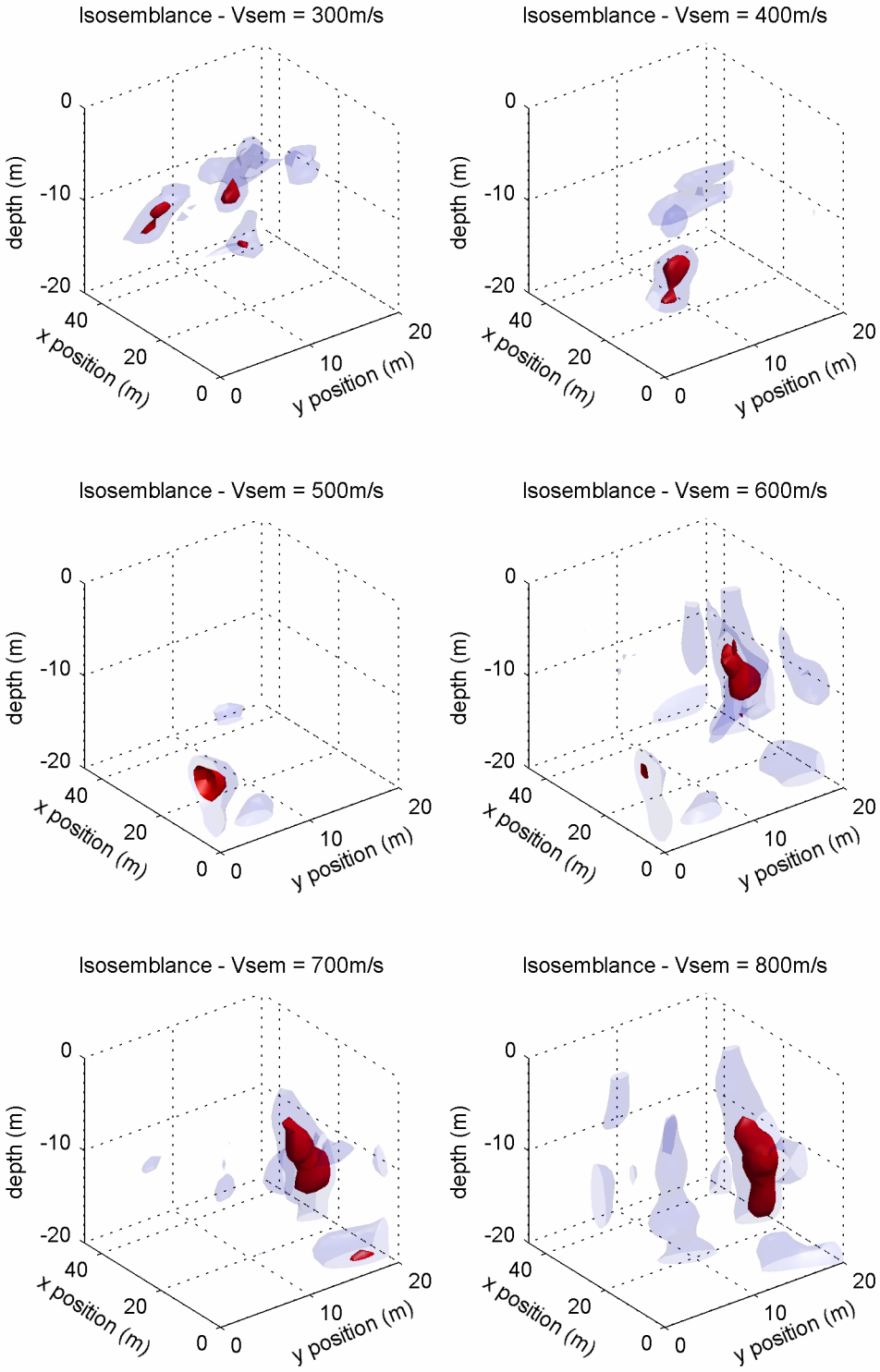

Figure H-4. Isosemblance plots of SBM results calculated for for various velocities at the capped mineshaft – in red high SBM values in blue medium SBM values

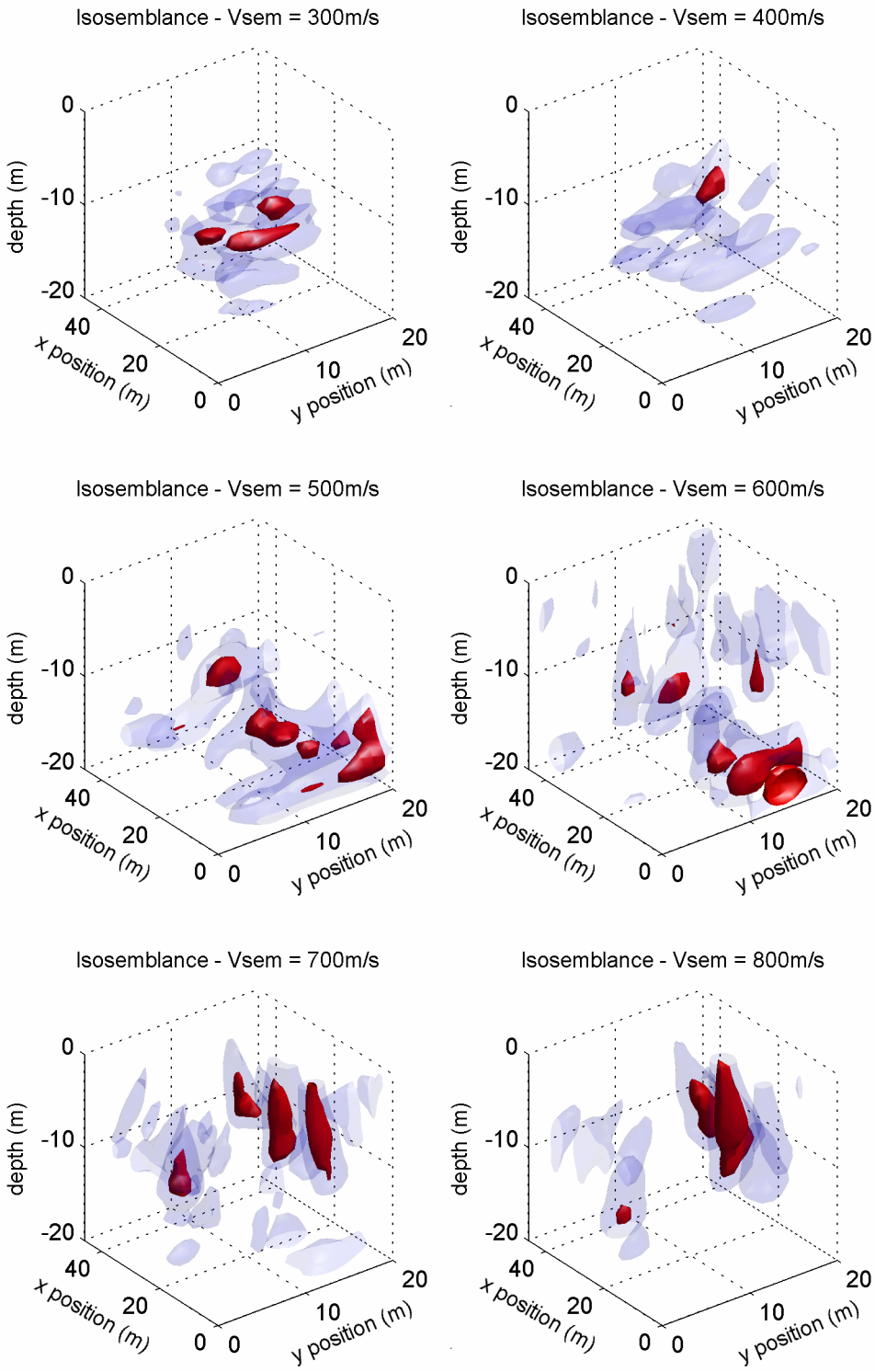

Figure H-5. Iso-semblance plots of SBM results calculated for various velocities at the backfilled mineshaft – in red high SBM values in blue medium SBM values

Appendix I - Awards and papers

This appendix lists the prize awarded and papers published. A copy of the awards and the journal papers are included.

Prizes and competitions:

- Miller prize awarded for the paper entitled 'Void detection beneath railway ballast using ground penetrating radar & resistivity' by the Institution of Civil Engineers, London (United Kingdom), 2006.
- Winner of South East Scotland qualification round of the Institution of Civil Engineers' Students and Young Graduates paper competition for the oral presentation on the paper entitled 'Void detection beneath railway ballast using ground penetrating radar & resistivity', Edinburgh (United Kingdom), 2006.
- Third place of East Scotland qualification round of the Institution of Civil Engineers' Students and Young Graduates paper competition for the oral presentation on the paper entitled 'Void detection beneath railway ballast using ground penetrating radar & resistivity', Dundee (United Kingdom), 2006.

Journal papers:

- Drossaert, F. H., and A. Giannopoulos (2007). Complex frequency shifted convolution PML for FDTD modelling of elastic waves. *Wave motion*, 44, pp 593-604.

- Drossaert, F. H., and A. Giannopoulos (2007). A Non-split Complex Frequency Shifted PML based on recursive integration for FDTD modeling of elastic waves. *Geophysics*, 72, pp T9-T17.

Conference papers:

- F. Drossaert, A. Giannopoulos, P.J. Fenning, K.A. Farah, R.D. Gray, M.C. Forde (2007). Field trials to detect abandoned mineshafts, *Railway Engineering 2007*, pp 13.
- F. Drossaert, A. Giannopoulos (2006). A novel non-split PML for elastic wave modelling, *Near Surface 2006*, Helsinki (Finland), pp 5.
- F. Drossaert, A. Giannopoulos, D. McCann, M.C. Forde, P.J. Fenning (2006); Mineshaft detection: Aspects of numerical model development, *Conference Structural Faults & Repair*, Edinburgh (United Kingdom), pp 12.
- F. Drossaert, D. Parker, E. Robertson, A. Giannopoulos, P.J. Fenning, M.C. Forde (2005). Void detection beneath the ballast using GPR & Resistivity, *Railway Engineering 2005*, London (United Kingdom), pp 12.
- F. Drossaert, M.C. Forde, A. Giannopoulos, P.J. Fenning, D.M. McCann (2004). Identifying Abandoned Mineshafts Near Railroads, *Abandoned Underground Mines Conference*, Tucson (Arizona), pp 12.
- F. Drossaert, M.C. Forde, A. Giannopoulos, D.M. McCann, P.J. Fenning (2004). Review of geophysical methods to detect concealed mineshafts, *Railway Engineering 2004*, London (United Kingdom), pp 17.
- F. Drossaert, M.C. Forde, A. Giannopoulos, D.M. McCann, P.J. Fenning (2004). Numerical experiments to develop guidelines for selecting geophysical methods for identifying abandoned mineshafts, *Railway Engineering 2004*, London (United Kingdom), pp 21.

Miller Prize 2006

awarded to

Francis Drossaert

for a paper entitled

' Void detection beneath railway ballast using ground penetrating radar & resistivity '

September 2006

ice

THE INSTITUTION OF CIVIL ENGINEERS · SCIENTIA ET INGENIO

Gordon Masterton

President
Institution of Civil Engineers

Director General and Secretary
Institution of Civil Engineers

VOID DETECTION BENEATH RAILWAY BALLAST USING GROUND PENETRATING RADAR & RESISTIVITY

Francis Drossaert
PhD Student
University of Edinburgh
Infrastructure and Environment Institute
School of Engineering & Electronics
Alexander Graham Bell Building
Kings Buildings
Edinburgh EH9 3JL
UK

F.Drossaert@ed.ac.uk

KEYWORDS: Void detection, geophysics, ground penetrating radar, GPR, resistivity

ABSTRACT
This paper discusses the issues related to voids beneath railway track ballast. An experiment at the University of Edinburgh is described where a 25 L plastic container is buried beneath a full scale railway track.

Data is presented using resistivity and ground penetrating radar. The results show that resistivity was effective, but radar was unable to detect the presence of the plastic container. The interpretation of the results is discussed in detail.

INTRODUCTION

The integrity of a railway track is pivotal for the safety of the railway traffic. The existence of cavities near railways can constitute a potential hazard. The origin of these cavities can be either natural, such as sinkholes in limestone and chalk or man-made such as mineshafts, addits, drifts and tunnels (Culshaw and Waltham, 1987). Other man-made cavities can be sewers and other utility pipes.

The collapse of a cavity, natural or man-made, beneath the railway embankment can cause serious damage to the stability of the railway and therefore these potential hazards have to be treated accordingly. Often cavities have been identified by drilling boreholes, but drilling proves to be slow and expensive. Moreover drilling is destructive and therefore not suitable for identification of cavities near railway tracks.

Geophysical methods have been widely used to identify voids in the subsurface. Most of these methods are non-destructive and furthermore depending on the chosen method, geophysical methods can be time-effective and cost-effective. Various geophysical surveys have been conducted at railway sites, but results were unsatisfactory. The effectiveness and limitations of geophysical methods at normal sites are well understood, but the effectiveness and limitations at railway sites are poorly understood. Previous studies showed that the performance of geophysical methods is severely limited due to the presence of the railway (Drossaert et al, 2004).

Experiments have been carried out in order to assess the performance of geophysical methods when surveying on the ballast. This paper briefly describes the results of experiments which were conducted at the University of Edinburgh's full-scale railway trackbed. Only the results of the ground penetrating radar and resistivity imaging are outlined in this paper.

GEOPHYSICAL METHODS

There exist numerous geophysical methods and even more variations on these methods. In general the methods can be divided into subgroups as listed in Table 1. In the same table the expected performance of the survey at the ballast and off track are also given. As can be seen in the table most of the methods have poor performance when surveying at the ballast.

Magnetic and electromagnetic methods are considered completely ineffective due to the presence of metal at the surface. Seismic methods experience bad coupling between the geophone and ballast and furthermore seismic methods have not sufficient resolution to resolve small voids. Practical surface wave methods have not evolved yet. Microgravity is probably the most successful method to identify cavities, but the method is slow, expensive and sensitive to vibration. Long duration of possession of the track is required, which is not desirable.

Technique	Difficulties	Expected performance	
		At ballast	Off track
Microgravity	Elevation Correction for the embankment	Good	Good
Magnetic	Metal in the tracks, posts and fences	Poor	Medium
Electro-magnetic	Metal elements EM waves from overhead wires	Poor	Medium
GPR	Lack of penetration depth	Good-poor	Good-poor
Electrical	High resistance	Poor	Medium
Seismic Refraction	Bad coupling Attenuation of high frequencies	Poor	Medium
Seismic Reflection	Bad coupling Attenuation of high frequencies	Poor	Medium
Surface waves	Practical method not evolved yet Interference ballast layer	Poor	Poor

Table 1: Expected performance and limitations of geophysical methods (after Drossaert et al, 2004)

Ground penetrating radar (GPR) has been used widely at railways in order to evaluate the condition of the ballast, but little is known about the feasibility of GPR to detect voids beneath the ballast.

Electrical resistance surveys to detect cavities have been conducted since the fifties. Resistivity methods have regularly been used to delineate voids and have been particularly successful in identifying sinkholes. Although it has never been established, it is perfectly reasonable to assume that resistivity methods will fail at the ballast since ballast consists largely of air which means that ballast has a very high resistance.

TEST SITE

The University of Edinburgh possesses a full scale trackbed, which was built at the end of the nineties in order to test the applicability of GPR to assess the condition of the ballast (Clark et al, 2000). The trackbed is about 10.5 metres long. The sleepers consist of two different brands of reinforced concrete sleepers and on the edges wooden sleepers.

The ballast consists of granite aggregate and is about 65cm thick. The right hand side of the ballast consists of clean ballast and the left hand side is made of spent ballast i.e. contaminated with dirt and oils. Between the clean ballast and spent ballast there is a zone that consists of mixed ballast (Figure 1).

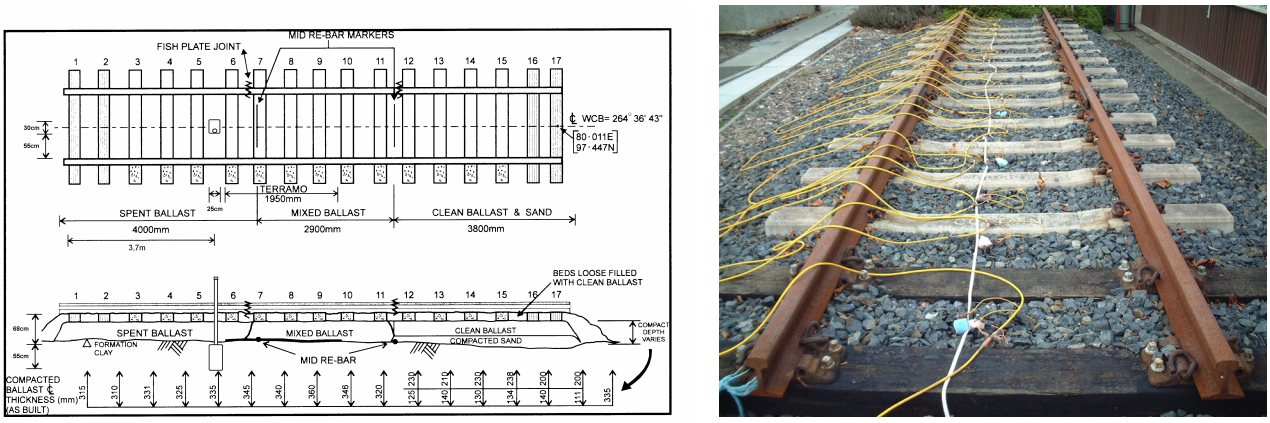

Figure 1: Description of the full scale trackbed and the resistivity setup

RESISTIVITY IMAGING

The resistivity survey was conducted at two different periods. The first survey was prior to the insertion of the void into the trackbed. The resistivity experiment equipment used was a Syscal Pro system to which 18 electrodes are connected. The electrodes were placed in the middle between successive sleepers with a separation of 65cm. Since the contact resistance was too high to get electrical current into the ground, the first measurement failed; contact improving measures were necessary. These measures consisted of adding extra electrodes and sponges which were saturated with an electrolyte solution (Figure 1).

A resistivity model has been calculated with the Res2Dinv software. The results of the inversion can be found in Figure 2. The error between the resistivity model and the actual measured resistivity values is only 7.7%, which is reasonably good. The resistivity profile of the trackbed can be divided into two separate zones: a high resistivity (100-300 Ωm) zone at

the top and a low resistivity (100 Ωm and less) zone beneath the high resistivity zone. The location of the high resistivity zone matches the location the ballast layer. The thickness of this zone is approximately 50 cm and corresponds to the actual thickness of the ballast when taking in account the dimensions of the electrodes. Between 7.5 and 8.5 metre there is an unexpected high resistivity anomaly. This anomaly can not directly be correlated to features in the trackbed. A possible explanation is that the anomaly is produced by errors in the measurements caused by the high contact resistance at the electrodes. The right hand side of the ballast consists of clean ballast which should be higher resistive, whereas the rest of the ballast consists of aggregate contaminated with soils which should lower the electrical resistance of the ballast. Despite the anomaly the resistivity image can be considered reasonable good and it can be concluded that resistivity imaging can be used at railways.

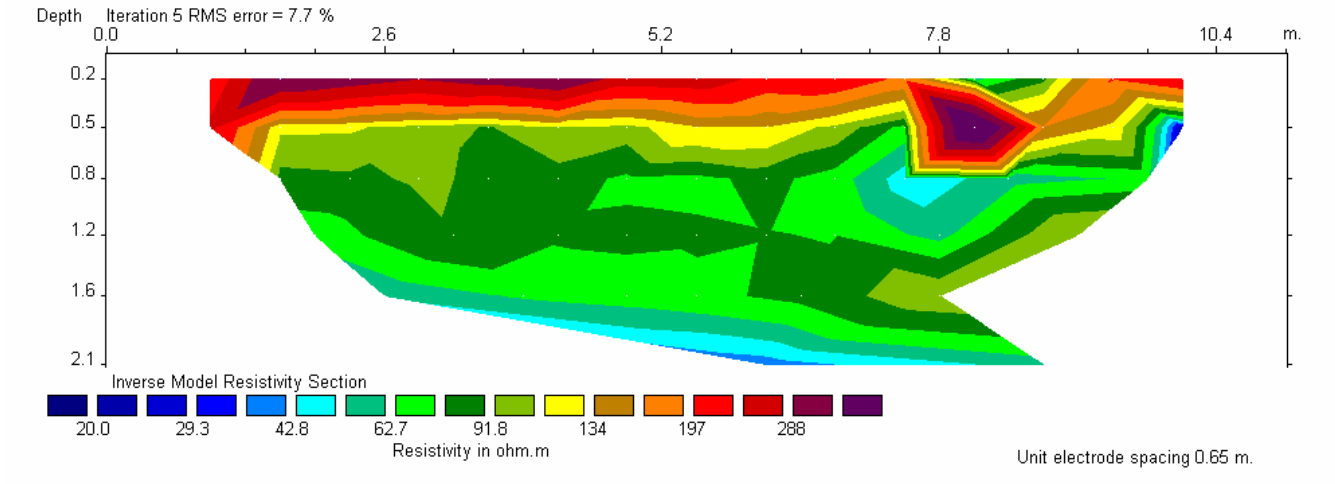

Figure 2: Resistivity profile, no canister present

The second survey was conducted after the plastic canister was placed beneath the ballast layer. The canister was filled with water. The equipment used is the Syscal Junior and the acquisition is similar to the first survey. Early indications showed that the contact resistance is not too high to conduct the experiment without contact improving measures; weather conditions were different. The interpretation of the data can be found in Figure 3. The error between the resistivity model and the actual measured resistivity values is more than 50%, which is very high. The boundary between the low and high resistivity zone does not match the ballast-clay interface at all. A possible explanation for the error is that the high contact resistance causes errors in the measurements, which where not striking at first sight. Despite the bad data, a low resistivity zone at 3.9 metre can easily be identified. This low resistivity zone matches the location of the water filled canister perfectly.

It is reasonable to assume when contact improving measures are used the resistivity model would be more reliable, but despite the unreliable model the water filled canister could clearly be identified. This indicates that electrical imaging methods can be useful to delineate voids beneath the ballast layer.

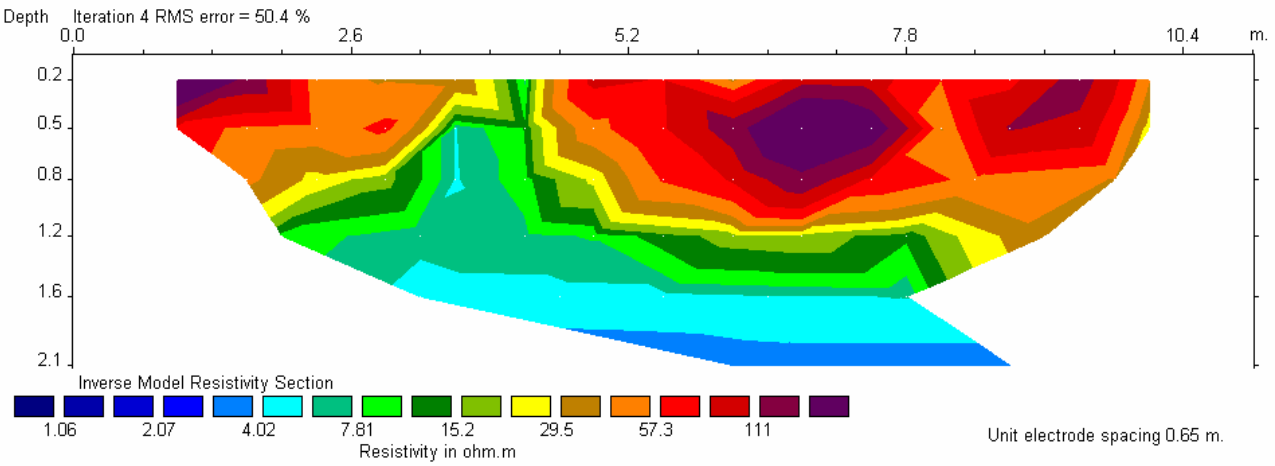

Figure 3: Resistivity profile with water filled canister (no contact improving measures taken)

GROUND PENETRATING RADAR (GPR)

Radar has been receiving growing attention from the railway engineering community in the last decade. Radar has been used to evaluate railway structures such as bridges and tunnels, but ground penetrating radar has also been used in ballast quality assessment (Gallagher et al 1999). GPR is a modern geophysical technique which can provide engineers with quick information about the thickness and condition of the ballast, but GPR has rarely been used in order to detect the ground conditions beneath the ballast layer.

GPR can provide rapid high resolution of the subsurface but as a trade off the depth penetration of the system can be limited. There are various factors that affect the maximum penetration depth, but the single most important factor is the conductivity of the subsurface. The aggregate consists of granite and air which are low conductive materials. Therefore the penetration depth of the GPR would be expected to be sufficient. Note that radar does not penetrate conductors such as clay.

In order to test the GPR system various surveys have been conducted with different antenna type and configurations. The PulsEKKO 1000 system and the GSSI Sir 10A system have been used. Bow-tie antennas were both ground-coupled and elevated from the ground (i.e. air coupled). The antennas were located in the centre of the railway track and some tests have been conducted beside the sleepers. In this paper only the results of ground coupled PulsEKKO data are used; the GSSI Sir 10A did not show any significant differences in the data. The air-coupled data are discarded since they did not contain any substantive information.

The data presented in this paper are:

- 900 MHz antenna beside the sleepers but on the ballast
- 900 MHz antenna in the centre of the railway
- 450 MHz antenna in the centre of the railway

The first data set discussed is the results of the survey with the PulsEKKO 900 MHz antennas located beside the sleepers (Figure 5). The ballast-clay interface can clearly be identified

between 10 and 14ns. The variation in thickness is most likely produced by velocity variations instead of variations in the thickness. As could expected there is no clear indication of the canister.

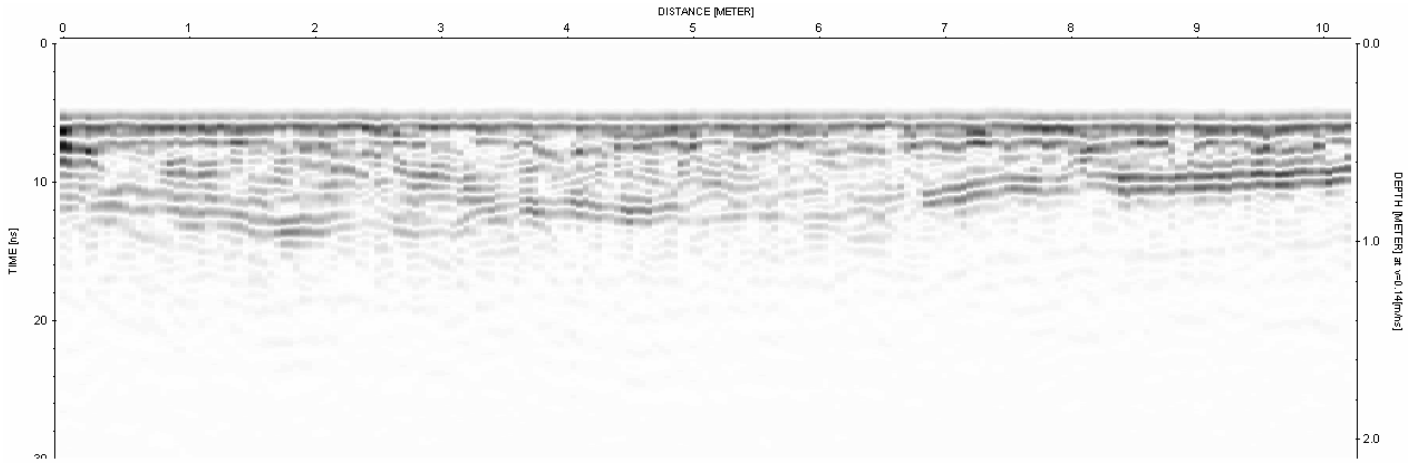

Figure 4: 900 MHz antenna, beside the track on ballast

The second data set consists of the same equipment and acquisition; but the antennas are located at the centre of the railway. The differences between the data sets Figure 4 and Figure 5 are striking. Clearly the presence of the reinforced concrete and the wooden sleepers have a significant effect on the radar signals. Reflections from the ballast-clay interface only happen when the antennas are located between the sleepers. The reflections are easily to identify at the right-hand-side of the data set, but on the left-hand-side the reflections are less well-defined. The logical explanation for this behaviour is that the right-hand-side and the middle part consist of contaminated, i.e. spent, aggregate which would affect the performance of the GPR.

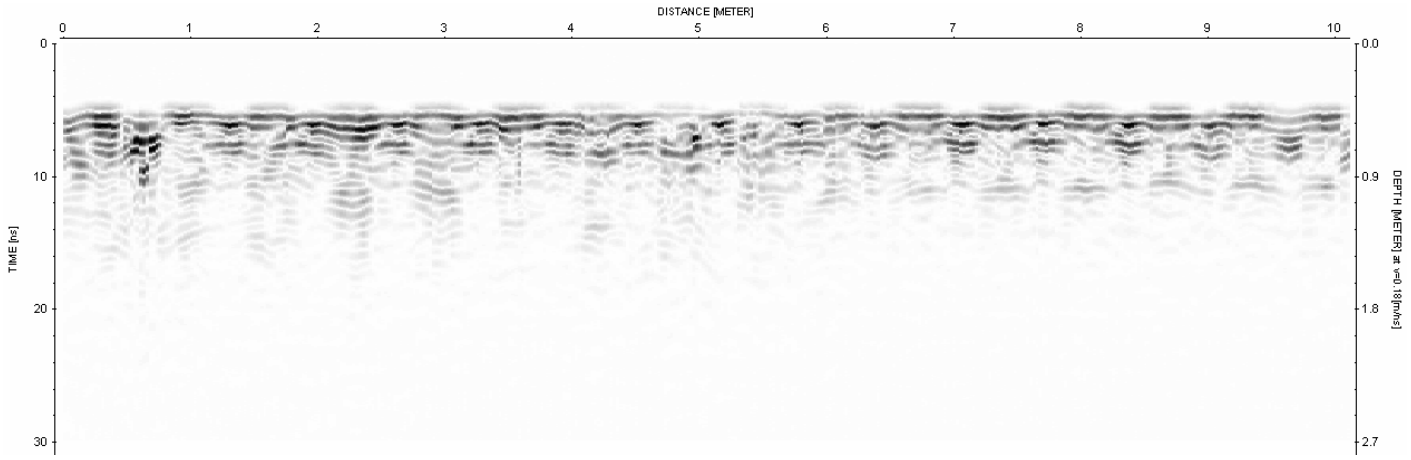

Figure 5: Raw GPR data with 900 MHz antenna

In Figure 6 the results of the 450 MHz antenna can be found. The sleepers have even more negative influence on the GPR data than for the 900 MHz antenna. The sleepers cause diffraction and/or refraction of the emitted electromagnetic (EM) pulse, which results in an odd constructive and destructive wave pattern in the ballast layer. The ballast-clay interface can

not easily be identified. At the hand right side of the track, where the clean ballast exists, the amplitude of the EM signal decreases significantly after ± 13ns. This decrease in amplitude could be related to the ballast-clay interface. There is no indication of the presence of the canister.

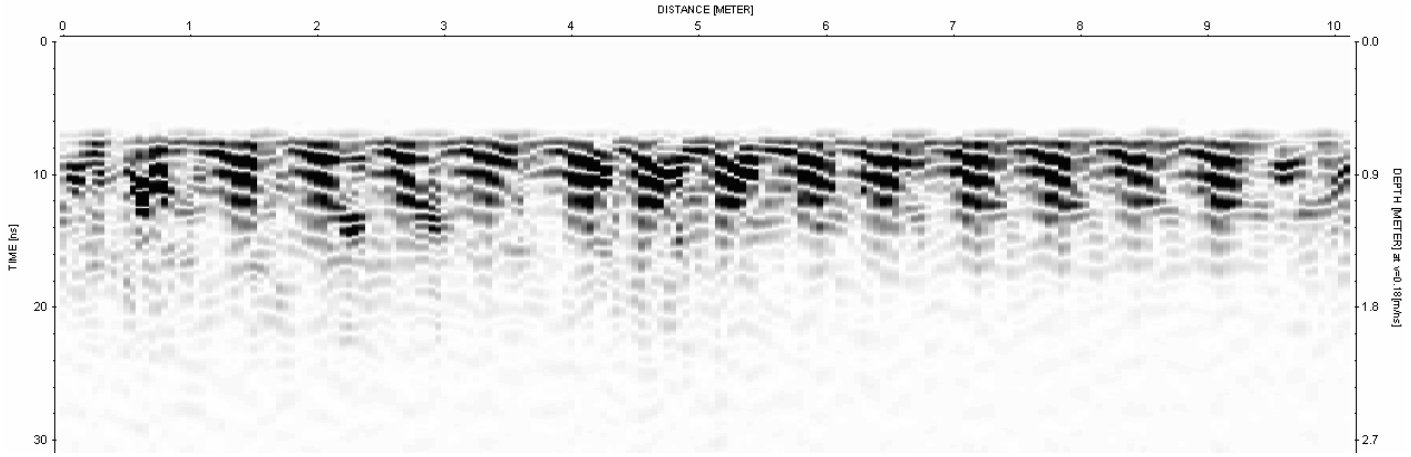

Figure 6: Raw GPR data with 450 MHz antenna

DISCUSSION

From the resistivity surveys it is clear that the contact resistance is very high and that contact resistance improving measures are required. Although these measures greatly improve the quality of the data, it is clear from Figure 2 that errors can arise due to the high resistance. An example of what happens when no countermeasures are taken can be found in Figure 3. The error between the model and the data is more than 50% which is very high and unacceptable for interpretation; however a low electrical resistance area roughly matches the location of the air filled canister. To date no surveys have been carried out with the canister inserted in the embankment and the correct contact resistance counter measures employed. (This is the next stage of experimental work.) It is very likely considering the results of surveys that the resistivity imaging method would provide a reliable image of the subsurface and that the canister can easily identified.

All the ground penetrating radar surveys failed to detect the canister and most ground penetrating radar failed to identify the ballast-clay interface. Comparison of the 900MHz PulsEKKO data measured beside sleepers and the data obtained in the centre of the railway indicates that the steel reinforced sleepers are severely hampering the performance of the GPR method. The steel reinforced sleepers cause diffraction/refraction of the emitted signal of 450 MHz which results in a peculiar pattern of constructive and destructive waves. The other reason for not detecting the canister is the fact that the canister is inserted in clay. It is common knowledge that the penetration depth of electromagnetic pulses is very small in high conductive material. Lower frequencies can penetrate deeper, but the resolution of the lower frequencies is such that the wavelength is too large to identify the ballast clay-interface.

CONCLUSIONS

(1) The detection of voids beneath the ballast layer is of crucial importance for the safety of railway traffic.

(2) From previous literature researches (Drossaert et al, 2004) it is clear that the performance of most geophysical methods is seriously limited by the presence of the railway.
(3) From the resistivity surveys conducted at the railway track bed at the University of Edinburgh, it can be concluded that resistivity methods are able to detect voids beneath the ballast layer, but contact improving measures are required.
(4) The results of the various ground penetrating radar surveys did not show any indication of the presence of the void. The reason for this is that the void was located in very high conductive clay and also the presence of sleepers has devastated influence on the radar signal.

ACKNOWLEDGEMENTS
The author would to thank Peggy Wong, Duncan Parker and Ewan Robertson for their contribution to the resistivity and ground penetrating radar tests. The financial support of Network Rail is gratefully acknowledged.

REFERENCES
- Clark, MR, Gillespie, R. Kemp, T., McCann, D.M. & Forde, M.C. (2001) Electromagnetic Properties of Railway Ballast, *NDT&E International*, Elsevier Science, 34, 305-311.
- Drossaert, F.H., M.C. Forde, A. Giannopoulos, D.M. McCann, P.J. Fenning; *"Review of geophysical methods to detect concealed mineshafts"*, Railway Engineering 2004 - 7th International Conference, 17pp, 6th-7th July, 2004, ISSN 0-947644-55-5.
- Gallagher, G, Leiper, Q, Williamson, R, Clark, MR & Forde, MC (1999) The application of time domain ground penetrating radar to evaluate railway track ballast, *NDT&E International*, Vol 32, No 8, 463-468.

GEOPHYSICS, VOL. 72, NO. 2 (MARCH-APRIL 2007); P. T9–T17, 7 FIGS., 1 TABLE.
10.1190/1.2424888

A nonsplit complex frequency-shifted PML based on recursive integration for FDTD modeling of elastic waves

Francis H. Drossaert[1] and Antonios Giannopoulos[1]

ABSTRACT

In finite-difference time-domain (FDTD) modeling of elastic waves, absorbing boundary conditions are used to mitigate undesired reflections that can arise at the model's truncation boundaries. The perfectly matched layer (PML) is generally considered to be the best available absorbing boundary condition. An important but rarely addressed limitation of current PML implementations is that their performance is severely reduced when waves are incident on the PML interface at near-grazing angles. In addition, very low frequency waves as well as evanescent waves could cause spurious reflections at the PML interface. In electromagnetic modeling, similar problems are circumvented by using a complex frequency-shifted stretching function in the PML formulas. However, in elastic-wave modeling using the conventional PML formulation — based on splitting the velocityand stress fields — it is difficult to adopt a complex frequency--shifted stretching function. We present an alternative implemen-tation of a PML that is based on recursive integration and does not require splitting of the velocity and stress fields. Modeling re-sults show that the performance of our implementation using a standard stretching function is identical to that of the convention-al split-field PML. Then we show that the new PML can be modified easily to include the complex frequency-shifted stretching function. Results of models with an elongated domain show that this modification can substantially improve the performance of the PML boundary condition. An efficient implementation of the new PML requires less memory than the conventional split-field PML, and, therefore, is a very attractive alternative to the conventional PML. By adopting the complex frequency-shifted stretching function, the PML can accommodate a wide variety of model problems, and hence it is more generic.

INTRODUCTION

Modeling of elastic wave propagation is useful for understanding wave phenomena in any complex media. Finite-difference modeling schemes are very popular because they provide complete wavefield responses and are relatively simple to implement. In finite-difference modeling, the energy of the waves needs to be absorbed at artificial boundaries in order to avoid spurious reflections caused by the truncation of the computer model. Therefore, absorbing boundary conditions have been developed in order to effectively simulate infinite space. The development of stable and effective absorbing boundary conditions has been an important issue in numerical modeling over the past three decades. Numerous techniques have been developed: for example, one-wave equations (Clayton and Engquist, 1977; Liao et al., 1984; Higdon, 1991), damping zones (Cerjan et al., 1985; Sochacki et al., 1987), and optimal boundary conditions (Peng and Töksoz, 1995). Unfortunately, most absorbing boundary conditions are not very effective for waves impinging on them at all angles of incidence, and they often exhibit instabilities.

Bérenger (1994) introduced a new and very effective absorb ing boundary layer for electromagnetic wave modeling. This absorbing layer appears to work very well for a wide range of incident angles and frequencies. In a continuous domain, Bérenger's boundary condition causes no reflection at the interface between the absorbing layer and the interior; hence the name *perfectly matched layer* (PML). Although small reflections can arise from the discretization of the equations, the PML is now generally considered to be the optimal available absorbing-boundary-condition method. Chew and Liu (1996) and Hastings et al. (1996) independently demonstrated

Manuscript received by the Editor May 26, 2006; revised manuscript received September 14, 2006; published online January 25, 2007.
[1]University of Edinburgh, Institute for Infrastructure and Environment, Edinburgh, United Kingdom. E-mail: F.Drossaert@ed.ac.uk; A.Giannopoulos@ed.ac.uk.

that the PML also can be used effectively for finite-difference modeling of elastic waves.

The most popular formulation of the PML for elastic wave modeling is based on the concept of coordinate stretching. The basic principle of the PML formulation is that space in the boundary layer is stretched by a complex function. Most current finite-difference, time-domain (FDTD) implementations of coordinate-stretching PMLs require an artificial splitting of the velocity and stress fields in the PMLs.

Implementations of the PML that do not require splitting of the fields were thought to be computationally ineffective because they must take into account a convolution term in their implementation. However, effective techniques that do not require splitting of the fields have been developed for electromagnetic wave modeling (Sacks et al., 1995) and elastic wave modeling (Wang and Tang, 2003). Most of these techniques make use of either the auxiliary differential-equation technique (Gedney, 1998) or the recursive convolution technique (Roden and Gedney, 2000). To deduce the PML formulation, we introduce a different approach that results in an alternative implementation of a nonsplit PML based on the calculation of an integral. In order to avoid confusion, we refer to this implementation as the *recursive integration PML*; hereafter called the RIPML.

Realistic 3D models are computationally demanding. We could use slender models to minimize the model size, depending on model requirements and acquisition geometry, but we found that waves impinging the PML interface at a near-grazing angle create spurious reflections that can mask true signals. This phenomenon also has been observed in electromagnetic wave modeling (Bérenger, 2002a). In electromagnetic wave modeling, the complex frequency-shifted stretching function (Roden and Gedney, 2000) has been used in the PML to mitigate these spurious waves. Furthermore, the complex frequency-shifted PML can also be used to model very low frequency waves that are reflected at the interface between the PML and the interior when using the conventional PML stretching function. The PML with the complex frequency-shifted stretching function can also be used to mitigate evanescent waves that are little absorbed by the conventional PML. This characteristic can be useful for earthquake-hazard modeling, for example. In the second part of this paper, we show that the complex frequency-shifted stretching function can be easily incorporated in our implementation of the PML.

RECURSIVE INTEGRATION PML

Here we present the derivation of the wave-propagation formulas in the RIPML zone for a first-order velocity-stress system (Virieux, 1986). For brevity, we derive the formulas for only a 2D isotropic medium. The RIPML can be easily formulated for elastic wave propagation in any elastic media.

To obtain absorbing properties in the PML, the velocity-stress equations are transformed into a stretched-coordinate domain using a complex stretching function (Chew and Liu, 1996). In the frequency domain, the 2D stretching functions ε for the x- and z-direction can be written as

$$\varepsilon_x = 1 + \frac{\sigma_x}{i\omega},$$

$$\varepsilon_z = 1 + \frac{\sigma_z}{i\omega}, \tag{1}$$

where the attenuation factor σ represents the loss in the PML. The spatial derivatives in the stretched-coordinate PML space can then be written as

$$\frac{\partial}{\partial \tilde{x}} \Rightarrow \frac{1}{\varepsilon_x}\frac{\partial}{\partial x},$$

$$\frac{\partial}{\partial \tilde{z}} \Rightarrow \frac{1}{\varepsilon_z}\frac{\partial}{\partial z}. \tag{2}$$

Using equations 2, the first-order velocity and stress equations in the stretched-coordinate space can now be written as the following set of coupled equations:

$$i\omega\rho\tilde{v}_x = \frac{1}{\varepsilon_x}\frac{\partial\tilde{\tau}_{xx}}{\partial x} + \frac{1}{\varepsilon_z}\frac{\partial\tilde{\tau}_{xz}}{\partial z},$$

$$i\omega\rho\tilde{v}_z = \frac{1}{\varepsilon_x}\frac{\partial\tilde{\tau}_{xz}}{\partial x} + \frac{1}{\varepsilon_z}\frac{\partial\tilde{\tau}_{zz}}{\partial z},$$

$$i\omega\tilde{\tau}_{xx} = (\lambda + 2\mu)\frac{1}{\varepsilon_x}\frac{\partial\tilde{v}_x}{\partial x} + \lambda\frac{1}{\varepsilon_z}\frac{\partial\tilde{v}_z}{\partial z},$$

$$i\omega\tilde{\tau}_{xz} = \mu\left(\frac{1}{\varepsilon_x}\frac{\partial\tilde{v}_z}{\partial x} + \frac{1}{\varepsilon_z}\frac{\partial\tilde{v}_x}{\partial z}\right),$$

$$i\omega\tilde{\tau}_{zz} = (\lambda + 2\mu)\frac{1}{\varepsilon_z}\frac{\partial\tilde{v}_z}{\partial z} + \lambda\frac{1}{\varepsilon_x}\frac{\partial\tilde{v}_x}{\partial x}, \tag{3}$$

where a time dependence of $e^{i\omega t}$ is assumed. The velocity and stress fields are denoted as v and τ. The tilde denotes their frequency-domain counterpart. The parameters describing the media are μ, the shear modulus; λ, the Lamé modulus; and ρ, the density.

The basic principle of the RIPML is to rewrite the velocity-stress equations by introducing two new auxiliary tensors, the stress-rate tensor **S** and the strain-rate tensor **E**. Their components are denoted as

$$\tilde{S}_{xx} = \frac{1}{\varepsilon_x}\frac{\partial\tilde{\tau}_{xx}}{\partial x},$$

$$\tilde{S}_{xz} = \frac{1}{\varepsilon_z}\frac{\partial\tilde{\tau}_{xz}}{\partial z},$$

$$\tilde{S}_{zx} = \frac{1}{\varepsilon_x}\frac{\partial\tilde{\tau}_{xz}}{\partial x},$$

$$\tilde{S}_{zz} = \frac{1}{\varepsilon_z}\frac{\partial\tilde{\tau}_{zz}}{\partial z}, \tag{4}$$

and

$$\tilde{E}_{xx} = \frac{1}{\epsilon_x}\frac{\partial\tilde{v}_x}{\partial x},$$

$$\tilde{E}_{xz} = \frac{1}{\epsilon_z}\frac{\partial\tilde{v}_x}{\partial z},$$

$$\tilde{E}_{zx} = \frac{1}{\epsilon_x}\frac{\partial\tilde{v}_z}{\partial x},$$

$$\tilde{E}_{zz} = \frac{1}{\epsilon_z}\frac{\partial \tilde{v}_z}{\partial z}, \tag{5}$$

By introducing the stress-rate and strain-rate tensors, it is no longer necessary to split the velocity and stress fields in separate components. After transforming the velocity-stress equations 3 back in the time domain and making use of equations 4 and 5, the velocity-stress equations then simply become as follows:

$$\begin{aligned}
\frac{\partial v_x}{\partial t} &= \frac{1}{\rho}(S_{xx} + S_{xz}),\\
\frac{\partial v_z}{\partial t} &= \frac{1}{\rho}(S_{zx} + S_{zz}),\\
\frac{\partial \tau_{xx}}{\partial t} &= (\lambda + 2\mu)E_{xx} + \lambda E_{zz},\\
\frac{\partial \tau_{xz}}{\partial t} &= \mu(E_{zx} + E_{xz}),\\
\frac{\partial \tau_{zz}}{\partial t} &= (\lambda + 2\mu)E_{zz} + \lambda E_{xx}.
\end{aligned} \tag{6}$$

Because introducing **S** and **E** does not alter the structure of equations 6, the RIPML can be implemented readily for any medium (anisotropic and heterogeneous) that can be described by the velocity-stress equations. The velocity-stress equations 6 are solved straightforwardly by first- or higher-order Taylor expansions when the stress-rate and strain-rate tensors are known.

There are various techniques available that can be used to solve the stress-rate and strain-rate tensors. An auxiliary differential-equation technique (Taflove and Hagness, 2000) could be used to solve for the tensors but requires the calculation of a time derivative of the spatial derivates. A different and more efficient method to solve for the tensors is by rearranging the equations, which will result in the calculation of an integral. This integral can be solved recursively to yield an efficient and stable scheme that does not require more memory space than the splitting formulation of PML (SPML), and less than a possible PML, on the basis of the auxiliary differential-equation technique.

Equations 4 are rewritten to solve the stress-rate tensors **S** by direct integration. Inserting the stretching functions given by equation 1 into equations 4, rearranging the components, and transforming them from the frequency domain into the time domain result in the following equations:

$$\begin{aligned}
\int_0^t \sigma_x S_{xx} dt &= \frac{\partial \tau_{xx}}{\partial x} - S_{xx},\\
\int_0^t \sigma_z S_{xz} dt &= \frac{\partial \tau_{xz}}{\partial z} - S_{xz},\\
\int_0^t \sigma_x S_{zx} dt &= \frac{\partial \tau_{xz}}{\partial x} - S_{zx},\\
\int_0^t \sigma_z S_{zz} dt &= \frac{\partial \tau_{zz}}{\partial z} - S_{zz}.
\end{aligned} \tag{7}$$

For an effective finite-difference scheme, the easiest method to approximate the time integral uses the trapezoidal integration rule. Other integration approximations could be more accurate, but tend to be more complex and to increase the required memory space. Therefore, by using a trapezoidal integration, the component S_{xx} at time step n can be approximated by

$$\int_0^{n\Delta t} \sigma_x S_{xx} dt \approx \tfrac{1}{2}\Delta t \sigma_x S^0_{xx} + \Delta t \sum_{t=1}^{n-1} \sigma_x S^t_{xx} + \tfrac{1}{2}\Delta t \sigma_x S^n_{xx}, \tag{8}$$

where Δt is the time-step size. Inserting this approximation into equation 7 and setting the tensor values at the initial time step to zero result in the following equation for component S_{xx}:

$$S^n_{xx}\left(1 + \tfrac{1}{2}\Delta t \sigma_x\right) + \Delta t \sum_{t=1}^{n-1} \sigma_x S^t_{xx} = \frac{\partial \tau^n_{xx}}{\partial x}. \tag{9}$$

After rearranging the terms in equation 9, the update of all the stress-rate tensor components now can be done effectively as follows:

$$\begin{aligned}
S^n_{xx} &= \xi_x\left(\frac{\partial \tau^n_{xx}}{\partial x} - \Delta t \Omega^{n-1}_{xx}\right),\\
S^n_{xz} &= \xi_z\left(\frac{\partial \tau^n_{xz}}{\partial z} - \Delta t \Omega^{n-1}_{xz}\right),\\
S^n_{zx} &= \xi_x\left(\frac{\partial \tau^n_{xz}}{\partial x} - \Delta t \Omega^{n-1}_{zx}\right),\\
S^n_{zz} &= \xi_z\left(\frac{\partial \tau^n_{zz}}{\partial z} - \Delta t \Omega^{n-1}_{zz}\right),
\end{aligned} \tag{10}$$

where the stress-rate sums $\boldsymbol{\Omega}$ represent the values of the sum as in equation 9 and the multiplication factors ξ are defined by

$$\begin{aligned}
\xi_x &= \frac{1}{\frac{1}{2}\Delta t \sigma_x + 1},\\
\xi_z &= \frac{1}{\frac{1}{2}\Delta t \sigma_z + 1}.
\end{aligned} \tag{11}$$

Formulating the equations as just described is beneficial because the stress-rate sums can be calculated recursively. After the update of the stress-rate tensor and the velocity field, the stress-rate sums $\boldsymbol{\Omega}$ are updated

$$\begin{aligned}
\Omega &= \Omega^{n-1}_{xx} + \sigma_x S^n_{xx},\\
\Omega &= \Omega^{n-1}_{xz} + \sigma_z S^n_{xz},\\
\Omega^n_{zx} &= \Omega^{n-1}_{zx} + \sigma_x S^n_{zx},\\
\Omega^n_{zz} &= \Omega^{n-1}_{zz} + \sigma_z S^n_{zz}.
\end{aligned} \tag{12}$$

A similar set of equations can be derived for the update of the strain-rate tensor **E**

$$\begin{aligned}
E^{n+\frac{1}{2}}_{xx} &= \xi_x\left(\frac{\partial v_x^{n+\frac{1}{2}}}{\partial x} - \Delta t \Psi^{n-\frac{1}{2}}_{xx}\right),\\
E^{n+\frac{1}{2}}_{xz} &= \xi_z\left(\frac{\partial v_x^{n+\frac{1}{2}}}{\partial z} - \Delta t \Psi^{n-\frac{1}{2}}_{xz}\right),
\end{aligned}$$

$$E_{zx}^{n+\frac{1}{2}} = \xi_x\left(\frac{\partial v_z^{n+\frac{1}{2}}}{\partial x} - \Delta t\,\Psi_{zx}^{n-\frac{1}{2}}\right),$$
$$E_{zz}^{n+\frac{1}{2}} = \xi_x\left(\frac{\partial v_z^{n+\frac{1}{2}}}{\partial x} - \Delta t\,\Psi_{zx}^{n-\frac{1}{2}}\right),$$

(13) where the formulas for the multiplication factors are the same as the ones used in equations 11. The update of the strain-rate sum $\boldsymbol{\Psi}$ is done as

$$\begin{aligned}
\Psi_{xx}^{n+\frac{1}{2}} &= \Psi_{xx}^{n-\frac{1}{2}} + \sigma_x E_{xx}^{n+\frac{1}{2}},\\
\Psi_{xz}^{n+\frac{1}{2}} &= \Psi_{xz}^{n-\frac{1}{2}} + \sigma_z E_{xz}^{n+\frac{1}{2}},\\
\Psi_{zx}^{n+\frac{1}{2}} &= \Psi_{zx}^{n-\frac{1}{2}} + \sigma_x E_{zx}^{n+\frac{1}{2}},\\
\Psi_{zz}^{n+\frac{1}{2}} &= \Psi_{zz}^{n-\frac{1}{2}} + \sigma_z E_{zz}^{n+\frac{1}{2}}.
\end{aligned} \tag{14}$$

Note that for updating the stress-rate tensor **S** and the strain-rate tensor **E**, their values at the previous time step are not required, and therefore there is no need to allocate extra computer memory for them. The only auxiliary values that need to be stored in the computer memory are the values of the recursive sums $\boldsymbol{\Psi}$ and $\boldsymbol{\Omega}$.

The total amount of memory needed to implement the RIPML or SPML depends on how efficiently the solutions are implemented. For a 2D model, we can divide the absorbing boundary zones in corners and edges in order to save memory space. For a 3D model, we need additional faces. Then we can make use of the fact that some attenuation coefficients are zero in certain PML zones; see Figure 1 for an example. Consequently, some of the stress-rate and strain-rate sums, as defined by the equations in 12 and 14, remain zero. Hence there is no need to take these sums into account.

In Table 1, we compare the minimum amount of variables required to be stored in the memory by the RIPML with the minimum required by the SPML. In this table, we take into account the fact that you only need to store the split field components for the SPML and not the field components themselves. Because the corner areas are small in most cases, compared to the size of the edges and faces, the implementation of the RIPML requires less memory than the SPML. For a large 3D model with RIPML, the amount of memory saved can be up to 12%. However, if for practical reasons the PML implementation is not subdivided in separate zones, and no account is taken of variables and equations that can be left out, the RIPML will require more memory than the SPML. Furthermore, another advantage of the RIPML over the SPML is that the velocity and stress fields are calculated inside the PML zone, greatly simplifying the interaction between the PML zone and the interior of the model.

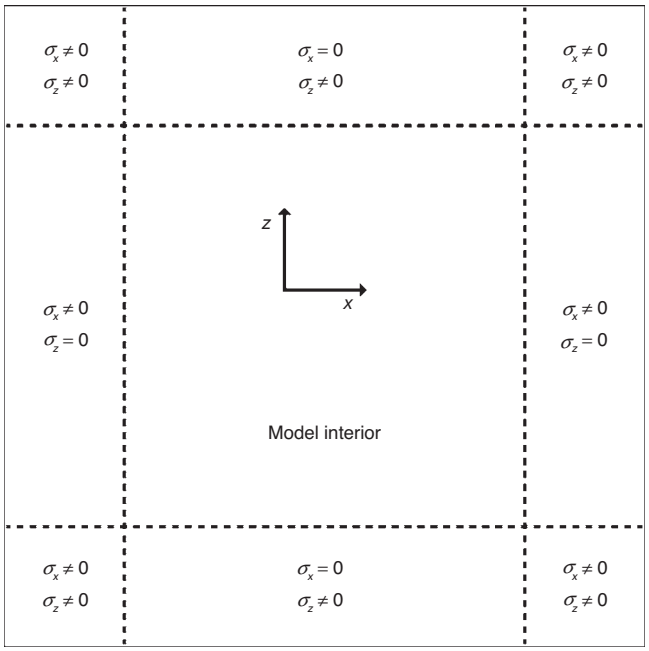

Figure 1. Allocation of the attenuation coefficients (σ) in the PML zones.

Table 1. Minimum number of variables required to store in memory per PML cell for different zones and for different models.

Model	2D SPML	2D RIPML	3D SPML	3D RIPML
Faces	-	-	17	15
Edges	10	9	24	21
Corners	10	13	24	27

ATTENUATION COEFFICIENT

To obtain PML absorbing properties in the RIPML formulation, the values of the attenuation coefficient σ have to be chosen such that only its orthogonal components are nonzero, whereas the parallel components are set to zero. Figure 1 illustrates a general 2D case.

In a continuous domain, the boundary between the PML and the interior is perfectly matched, i.e., no reflection will arise because of the presence of the interface, regardless of the physical properties at each side of the interface. However, in finite-difference modeling, spurious reflections can arise because of the discretization of the space domain. To avoid the numerical reflections from the interface between the PML and the computational domain, the attenuation coefficients have to increase gradually. A commonly used polynomial scaling function for the attenuation coefficient (Collino and Tsogka, 2001) is given by

$$\sigma_i(l) = \sigma_i^{\max}\left(\frac{l}{d}\right)^m, \tag{15}$$

when $0 \le l \le d$ and where the interface between the PML and the interior is assumed to be located at $l = 0$, d is the thickness of the PML, and m is the scaling order. The optimum value for $\sigma^{\max}$ can be calculated by the following empirical formula used by various authors (Collino and Tsogka, 2001),

$$\sigma_i^{\max} = \frac{3v_P}{2d}\log\left(\frac{1}{R}\right), \tag{16}$$

where R is the theoretical reflection coefficient after discretization and v_P is the P-wave velocity. For the models used here, we have adopted the value $R = 1 \times 10^{-5}$ and $m = 2$.

RIPML — NUMERICAL RESULTS

In this section, we present some results from models truncated by the RIPML and compare them with results from the same models using a SPML. Through the use of MATLAB, both PML formulations have been implemented in an FDTD scheme based on the rotated staggered grid (Saenger et al., 2000; Saenger and Bohlen, 2004). Note that the formulas for the update of stress-rate tensors and strain-rate tensors (equations 11 and 13) are derived independently from the grid definition; hence the RIPML formulation is valid for any velocity-stress finite-difference scheme (e.g., Virieux, 1986; Randall, 1989; Saenger and Bohlen, 2004).

Figure 2 illustrates the 77.5- $\times$ 77.5-m model used to demonstrate the performance of the RIPML. The cell size is 0.25 by 0.25 m, and the time step is 0.64 ms. We used a 20-Hz Ricker source, and the model is truncated by a five-cell-thick PML zone. The values of the attenuation coefficient σ are calculated by using equations 15 and 16 with a scaling order of $m = 2$. Synthetic seismograms are calculated at the receiver located as indicated in Figure 2 for the model with the RIPML and for the model with the SPML. A reference seismogram has been computed by using a sufficiently large model to have any boundary reflections arrive outside our time window.

The results of the modeling are presented in Figure 3. From the seismograms in Figure 3a, it is clear that both PML implementations absorb the outgoing wave energies very effectively such that any possible differences are hard to observe. Closer comparison of the results can be found in Figure 3b and c, where the differences between the seismograms of both PML models and the seismogram of the reference model are presented. It was found that the RIPML has the same performance as the SPML. Despite the fact that both implementations are different, the results match exactly throughout the model. The difference between them is down to numerical noise levels; hence it appears that the RIPML works with the same accuracy as the SPML.

COMPLEX FREQUENCY-SHIFTED RIPML

A rarely addressed but important limitation of current PML implementations is that their performance is severely reduced when waves are incident on them at near-grazing angles (Bérenger, 2002b). This phenomenon has been observed in electromagnetic modeling as well in some of our models. Grazing angles of incidence are important when a scatterer or a source is located close to the PML. Near-grazing angles are also common in elongated models. Elongated domains can be useful in earthquake hazard modeling, as well as in models including tunnels or mineshafts and many other modeling scenarios. In addition, Bérenger (2002a) reported that evanescent waves may be strongly reflected at the interface between the boundary layer and the model interior. Another limitation of current PML implementations is that modeling low-frequency waves could lead to spurious reflections at the PML interface. The main reason for this deterioration in performance is that the stretching function given by equation 1 becomes singular for very low frequencies or for waves with a long-time interaction with the PML interface (Kuzuoglu and Mittra, 1996; Roden and Gedney, 2000). To circumvent these problems, Kuzuoglu and Mittra (1996) proposed the complex frequency-shifted (CFS) stretching function for PMLs for electromagnetic wave modeling. Use of this function shifts the singularity in the stretching function off the real axis into the negative imaginary half of the complex plane and improves the performance of the PML. In this section, we demonstrate that the CFS stretching function can be easily incorporated into the RIPML formulation. For completeness, we have included the formulation of the CFS RIPML for a general 3D case in Appendix A.

The CFS stretching function as proposed by Kuzuoglu and Mittra (1996) can be written for a 2D case as

$$\varepsilon_x = \kappa_x + \frac{\sigma_x}{\alpha_x + i\omega},$$
$$\varepsilon_z = \kappa_z + \frac{\sigma_z}{\alpha_z + i\omega}, \tag{17}$$

where κ and α are auxiliary attenuation coefficients. The attenuation κ mainly affects waves that impinge the PML interface at near-grazing angles, whereas the attenuation coefficient α mainly affects low-frequency waves. However, numerical tests show that a combination

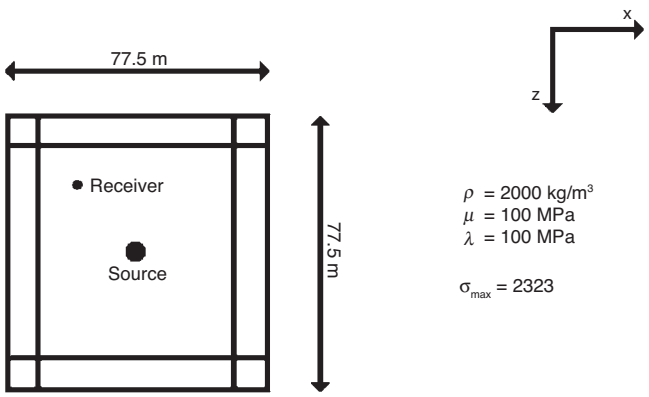

Figure 2. FDTD model used to compute the synthetic seismograms for the models with the RIPML and split PML.

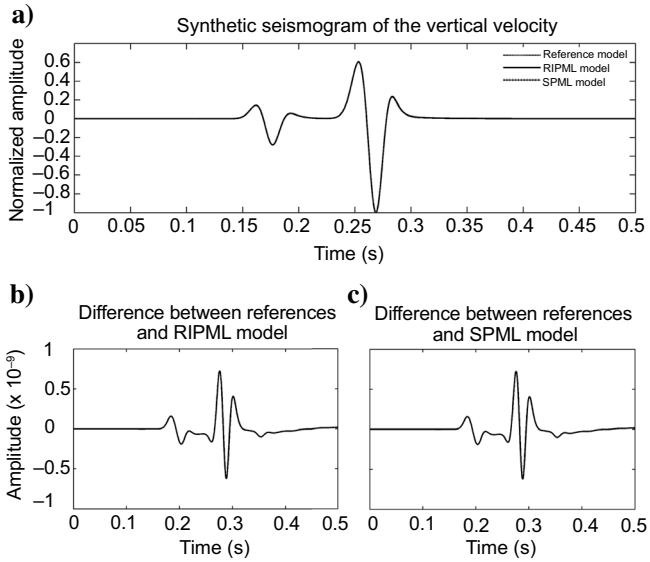

Figure 3. Comparison of the results of the modeling. (a) Synthetic seismograms of the vertical velocity computed for the RIPML, the split PML (SPML) model, and the reference model. Both PML models perform very well, and hence their seismograms are coincident with the seismogram of the reference model. (b) The difference between the reference model and the RIPML model. (c) The difference between the reference model and the SPML model.

of both attenuation coefficients can lead to optimum performance. Their optimal scaling and maximum values are problem dependent.

Similar to the simple stretching function 1, we introduce the strain-rate tensor **E** and the stress-rate tensor S in the velocity-stress equations. The derivation of the formulas for the wave propagation in the CFS RIPML is similar to the derivation of the standard RIPML without the CFS stretching function. The update of the stress-rate tensor **S** is now as follows:

$$S_{xx}^{n} = \xi_x \frac{\partial \tau_{xx}^{n}}{\partial x} - \varphi_x \Omega_{xx}^{n-1},$$

$$S_{xz}^{n} = \xi_z \frac{\partial \tau_{xz}^{n}}{\partial z} - \varphi_z \Omega_{xz}^{n-1},$$

$$S_{zx}^{n} = \xi_x \frac{\partial \tau_{xz}^{n}}{\partial x} - \varphi_x \Omega_{zx}^{n-1},$$

$$S_{zz}^{n} = \xi_z \frac{\partial \tau_{zz}^{n}}{\partial z} - \varphi_z \Omega_{zz}^{n-1}. \tag{18}$$

After calculation of the stress-rate tensor, the velocity field is updated by simply using equation 6. Then, the stress-rate sums $\mathbf{\Omega}$ have to be updated by using

$$\Omega_{xx}^{n} = \Omega + \Lambda_x S_{xx}^{n} - \alpha_x \frac{\partial \tau_{xx}^{n}}{\partial x},$$

$$\Omega_{xz}^{n} = \Omega_{xz}^{n-1} + \Lambda_z S_{xz}^{n} - \alpha_z \frac{\partial \tau_{xz}^{n}}{\partial z},$$

$$\Omega = \Omega_{zx}^{n-1} + \Lambda_x S_{zx}^{n} - \alpha_x \frac{\partial \tau_{xz}^{n}}{\partial x},$$

$$\Omega_{zz}^{n} = \Omega_{zz}^{n-1} + \Lambda_z S_{zz}^{n} - \alpha_z \frac{\partial \tau_{zz}^{n}}{\partial z}. \tag{19}$$

Similar to equation 18, the update of the strain-rate tensor **E** is given by

$$E_{xx}^{n+\frac{1}{2}} = \xi_x \frac{\partial v_x^{n+\frac{1}{2}}}{\partial x} - \varphi_x \Psi_{xx}^{n-\frac{1}{2}},$$

$$E_{xz}^{n+\frac{1}{2}} = \xi_z \frac{\partial v_x^{n+\frac{1}{2}}}{\partial z} - \varphi_z \Psi_{xz}^{n-\frac{1}{2}},$$

$$E_{zx}^{n+\frac{1}{2}} = \xi_x \frac{\partial v_z^{n+\frac{1}{2}}}{\partial x} - \varphi_x \Psi_{zx}^{n-\frac{1}{2}},$$

$$E_{zz}^{n+\frac{1}{2}} = \xi_z \frac{\partial v_z^{n+\frac{1}{2}}}{\partial z} - \varphi_z \Psi_{zz}^{n-\frac{1}{2}}. \tag{20}$$

and the strain-rate sums $\mathbf{\Psi}$ required for the next time step are updated by

$$\Psi_{xx}^{n+\frac{1}{2}} = \Psi_{xx}^{n-\frac{1}{2}} + \Lambda_x E_{xx}^{n+\frac{1}{2}} - \alpha_x \frac{\partial v_x^{n+\frac{1}{2}}}{\partial x},$$

$$\Psi_{xz}^{n+\frac{1}{2}} = \Psi_{xz}^{n-\frac{1}{2}} + \Lambda_z E_{xz}^{n+\frac{1}{2}} - \alpha_z \frac{\partial v_z^{n+\frac{1}{2}}}{\partial z},$$

$$\Psi_{zx}^{n+\frac{1}{2}} = \Psi_{zx}^{n-\frac{1}{2}} + \Lambda_x E_{zx}^{n+\frac{1}{2}} - \alpha_x \frac{\partial v_z^{n+\frac{1}{2}}}{\partial x},$$

$$\Psi_{zz}^{n+\frac{1}{2}} = \Psi_{zz}^{n-\frac{1}{2}} + \Lambda_z E_{zz}^{n+\frac{1}{2}} - \alpha_z \frac{\partial v_z^{n+\frac{1}{2}}}{\partial z}. \tag{21}$$

The multiplication factors Λ, ξ, and φ in equations 18–21 are defined as

$$\Lambda_x = \sigma_x + \alpha_x \kappa_x,$$

$$\Lambda_z = \sigma_z + \alpha_z \kappa_z,$$

$$\xi_x = \frac{1 + \frac{1}{2}\Delta t \alpha_x}{\frac{1}{2}\Delta t\left(\sigma_x + \alpha_x \kappa_x\right) + \kappa_x},$$

$$\xi_z = \frac{1 + \frac{1}{2}\Delta t \alpha_z}{\frac{1}{2}\Delta t\left(\sigma_z + \alpha_z \kappa_z\right) + \kappa_z},$$

$$\varphi_x = \frac{\Delta t}{\frac{1}{2}\Delta t\left(\sigma_x + \alpha_x \kappa_x\right) + \kappa_x},$$

$$\varphi_z = \frac{\Delta t}{\frac{1}{2}\Delta t\left(\sigma_z + \alpha_z \kappa_z\right) + \kappa_z}. \tag{22}$$

Note that by setting the attenuation coefficients α and κ to 0 and 1, respectively, the CFS RIPML formulas reduce to the standard RIPML formulation. Also note that because the multiplication factors in equation 22 are time independent, they can be precalculated and stored in vectors. Therefore, the more generic CFS RIPML does not require any more computer memory, nor does CFS RIPML significantly increase the computational time compared to the RIPML with the simple stretching function as given by equation 1.

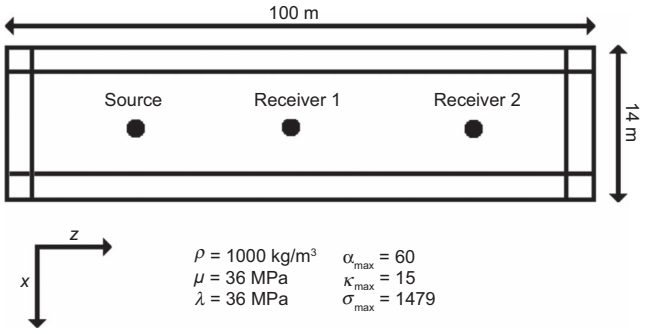

Figure 4. Model with an elongated domain and the model parameters.

CFS RIPML — NUMERICAL RESULTS

To demonstrate the potential of the complex frequency-shifted stretching function, we present the results of a model with an elongated domain where the boundary conditions are defined by the RIPML. Figure 4 illustrates the 100- × 14-m model used in the example. The model is discretized spatially with a uniform grid spacing of 0.2 m and temporally with a time step of 0.6 ms. The excitation point is indicated in Figure 4, and the time signature of the excitation

is a Ricker-shaped pulse in the z-direction with a center frequency of 25 Hz. The model is terminated by a 10-cell-thick PML. The optimal maximum value of the attenuation coefficients σ is determined by using the empirical formula given by equation 16. The scaling of the attenuation coefficient κ throughout the PML is similar to the scaling of the attenuation coefficient σ as in equation 15. A reversed second-order polynomial scaling has been used to scale the attenuation coefficient α as suggested by Roden and Gedney (2000). The values for $\alpha^{\max}$ and $\kappa^{\max}$ have been determined experimentally.

Synthetic seismograms are computed for the receiver line as indicated in Figure 4. The results of the computation are presented in Figure 5. From the seismograms, it is clear that the seismogram calculated with CFS RIPML contains much less noise than the seismogram calculated with the PML without the CFS stretching function. Figure 6 presents the computed traces for receiver 1 and receiver 2. It is clear from both traces that the model without the CFS stretching function fails to simulate the waves correctly — especially at greater distance from the source. Strong spurious reflections mask the shear waves completely, and the amplitude of the compressional waves is affected considerably by the boundary condition. Closer observations of snapshots show that seismic waves impinging on the PML zone at grazing angles not only cause reflections but also are converted into evanescent waves traveling along the interface. Because these waves travel parallel to the PML interface, their amplitudes are not attenuated, and seismic energy leaks back into the model interior. Although the CFS RIPML still causes small reflections, it is clear from the seismograms that the CFS RIPML mitigates the problems caused by the low-angle incident waves considerably more effectively than the PMLs without the CFS stretching function.

For a better insight into the effect of attenuation coefficients α and κ, contour plots of the normalized error between the seismic trace and reference trace have been calculated as a function of the $\alpha^{\max}$ and $\kappa^{\max}$. The value for $\sigma^{\max}$ is set to the optimum value of 1.232×10^3. Figure 7 shows the results of the calculations for receiver 1 and receiver 2. From these plots, it is clear that the performance of the CFS RIPML is strongly influenced by the value of $\kappa^{\max}$ and, to a lesser degree, by the value of $\alpha^{\max}$. The influence of $\alpha^{\max}$ on the absorbing performance becomes stronger when the receiver is farther away from the source and when grazing angles become more of a problem. By choosing optimum values for the $\kappa^{\max}$ and $\alpha^{\max}$, it is clear from the contour plot at receiver 2 that using the CFS RIPML can greatly enhance the performance of the boundary condition. Unfortunately, the optimum values are dependent on the location, i.e., when observing contour plots of receivers closer to the source, we will see that the minimum error shifts toward the left to lower $\kappa^{\max}$ values. For normal incidence waves, the CFS RIPML does not perform any better than the standard PML.

DISCUSSION

Results from computer modeling have shown that the performance of the RIPML is exactly the same as the SPML. However, the RIPML formulation does not require splitting of the velocity and stress fields and hence can be used easily to model anisotropic materials.

Effective implementation of the RIPML requires less memory space in the boundary zone than the required memory for the SPML. For large 3D models, the total memory required to solve the unknown variables in the PML can be reduced by 12%.

Three limitations of current PML implementations — namely, reduced absorption and spurious reflection of waves incident at grazing angles, low-frequency waves, and evanescent waves — can be circumvented by using a CFS stretching function. We have demonstrated that the CFS stretching function can be implemented easily in the RIPML formulation. The auxiliary attenuation coefficients α and

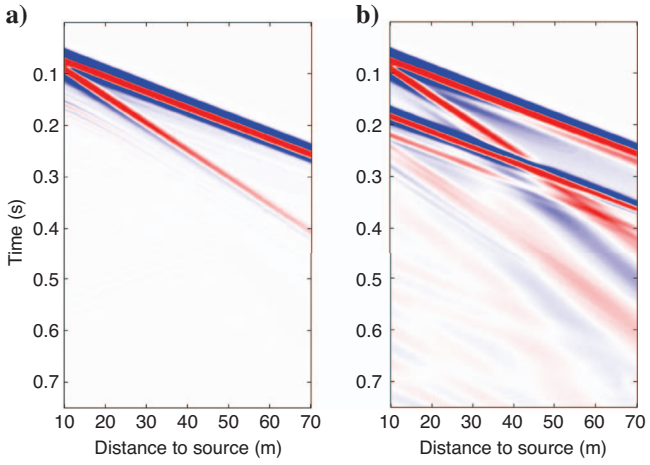

Figure 5. Seismograms of the vertical velocity as modeled by (a) CFS RIPML and (b) SPML. The amplitudes are scaled by a factor of 10.

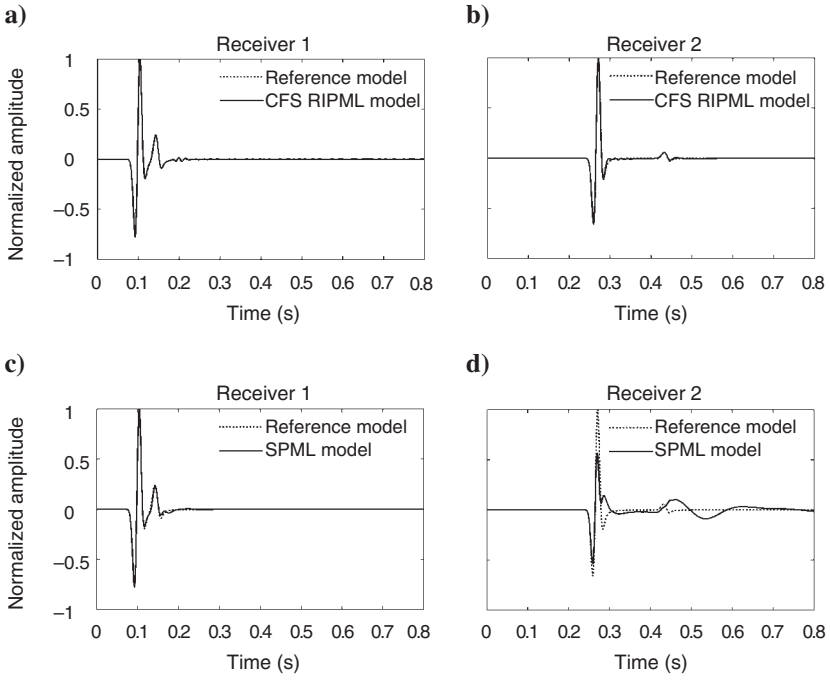

Figure 6. Computed synthetic seismograms for (a and c) receiver 1 and (b and d) receiver 2 for the models with (a and b) CFS RIPML and (c and d) SPML.

κ give the user more options to manipulate the performance of the PML. Selecting the optimum values for α^{max} and κ^{max} and the polynomial scaling of the attenuation coefficients can improve the performance of the boundary condition considerably.

Although in many modeling problems, the CFS RIPML does not enhance the absorbing performance of the boundary condition, it is clear from our model using an elongated domain that the CFS RIPML can dramatically enhance the quality of the data when grazing angles are important. Although not tested, the CFS RIPML should improve the performance of the PML when modeling very low frequency waves and when modeling evanescent waves in shallow models. Furthermore, the nonsplit CFS RIPML should be able to be applied in finite-element modeling, because it does not require the artificial splitting of the fields.

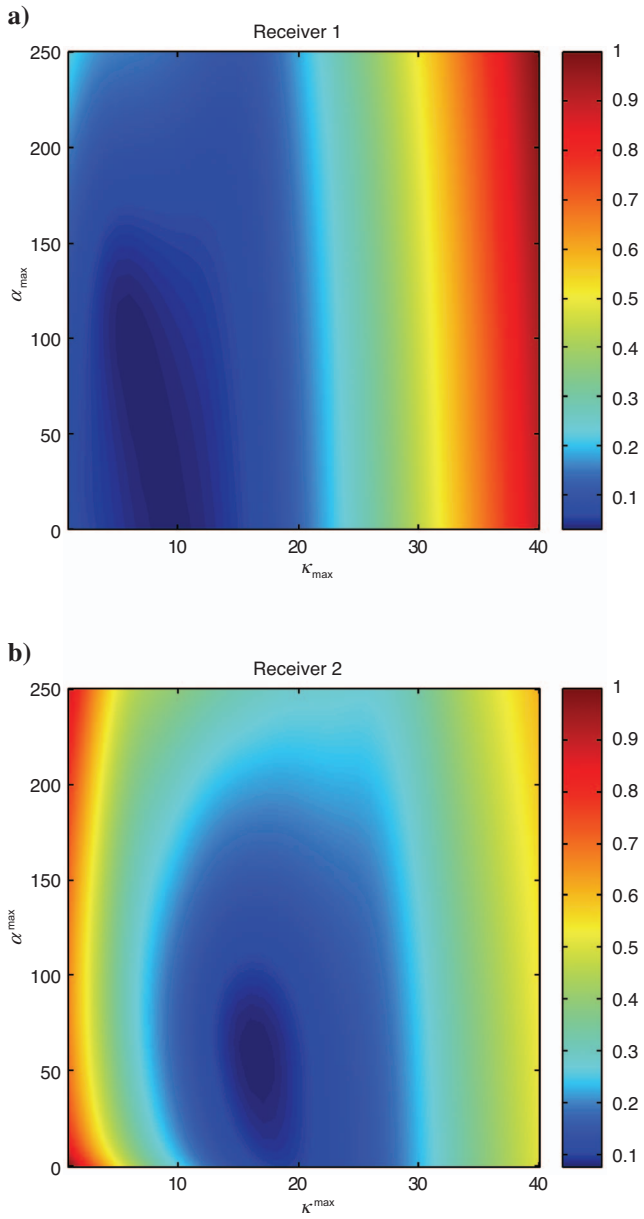

Figure 7. Contour plots of the error as function of the α^{max} and κ^{max} for (a) receiver 1 and (b) receiver 2.

CONCLUSIONS

We have developed an alternative implementation of the PML for FDTD modeling of elastic waves, based on the calculation of an integral. Our implementation does not require splitting of the velocity and stress fields. The formulation is derived independently from the grid definition, and therefore the RIPML can be applied for any staggered grid. Problems in current PML implementations, including reduced absorption and spurious reflection of waves incident at grazing angles, can be circumvented by using a CFS stretching function. The CFS stretching function can be introduced easily into FDTD modeling by using our RIPML formulation. The CFS RIPML does not require more memory space and does not increase the computation time significantly when compared to the SPML. Thus, employing the CFS RIPML provides the user with a nonsplit PML, which is more generic and can be adapted easily to conform to the characteristics of the modeling problem.

ACKNOWLEDGMENTS

We thank Network Rail for their financial support and, in particular, Brian Bell and John Stothard. We thank Mike Forde, Dave McCann, and Peter Fenning for their scientific contributions to the project. Finally, we are grateful to Ian Main, Erik Saenger, and to two anonymous reviewers for their very helpful comments that helped us to improve the paper.

APPENDIX A

CFS RIPML FOR A GENERAL 3D CASE

For completeness, we show the formulation of the CFS RIPML for a general 3D case. The velocity field and the stress fields are updated one-half time step from each other in a staggered grid model. We update the velocity field first. In indicial notation, we can describe the update of the velocity field in discretized time and space. The first step is to calculate the stress-rate tensor $\mathbf{S}$ at time step n

$$S_{ij}^{n} = \xi_j \partial_j \tau_{ij}^{n} - \varphi_j \Omega_{ij}^{n-1}, \tag{A-1}$$

where $\mathbf{\Omega}$ is the stress-rate sum and $\partial_j \tau_{ij}$ is the spatial derivate of stress field τ_{ij} in the j-direction. The subscripts i, j are x, y, or z. Then the velocity field v can be calculated as

$$v_i^{n+(1/2)} = v_i^{n-(1/2)} + \beta \Delta t S_{ij}^{n}, \tag{A-2}$$

where Δt is the time-step size and β is the inverse of the density. For an efficient implementation, we need to update the stress-rate sum Ω that is needed to calculate the stress-rate tensor $\mathbf{S}$ at the next time step:

$$\Omega_{ij}^{n} = \Omega_{ij}^{n-1} + \Lambda_j S_{ij}^{n} - \alpha_j \partial_j \tau_{ij}^{n}, \tag{A-3}$$

where α is the attenuation coefficient of the complex frequency-shifted stretching function.

After the upate of the velocity field and the stress-rate sum, the next step is to update the stress field τ and the strain-rate sum $\mathbf{\Psi}$. Similar to the update of the velocity field, the first step is to calculate the strain-rate tensor $\mathbf{E}$

$$E_{kl}^{n+\frac{1}{2}} = \xi_l \partial_l v_k^{n+\frac{1}{2}} - \varphi_l \Psi_{ij}^{n-\frac{1}{2}}, \tag{A-4}$$

where the subscripts k, l are x, y, or z and $\partial_l v_k$ is the spatial derivate of the k-component of the velocity field in the l-direction. After the calculation of the strain-rate tensor, the stress field can be updated as follows:

$$\tau_{ij}^{n+1} = \tau_{ij}^{n} + \Delta t C_{ijkl} E_{kl}^{n+\frac{1}{2}}, \tag{A-5}$$

where $\mathbf{C}$ is the elasticity tensor and τ is the stress field. The update of the strain-rate sums, required for the calculation of the strain-rate tensor at the next time step, is given by

$$\Psi_{kl}^{n+\frac{1}{2}} = \Psi_{kl}^{n-\frac{1}{2}} + \Lambda_l E_{kl}^{n+\frac{1}{2}} - \alpha_l \partial_l v_k^{n+\frac{1}{2}}. \tag{A-6}$$

After the update of the strain-rate sum, the process starts again with the calculation of the stress-rate tensor (equation A-1) for the next time step, and the whole process is repeated until the end time has been reached. The multiplication factors used in the formulas in this appendix are defined as follows:

$$\begin{aligned} \Lambda_i &= \sigma_i + \alpha_i \kappa_i, \\ \xi_i &= \frac{1 + \frac{1}{2}\Delta t \alpha_i}{\frac{1}{2}\Delta t\left(\sigma_i + \alpha_i \kappa_i\right) + \kappa_i}, \\ \varphi_i &= \frac{\Delta t}{\frac{1}{2}\Delta t\left(\sigma_i + \alpha_i \kappa_i\right) + \kappa_i}, \end{aligned} \tag{A-7}$$

where α, κ, and σ are the attenuation coefficients of the complex frequency-shifted stretching function. It should be pointed out that the values of the multiplication factors depend on their location in the grid.

It is important to note that the location in the FDTD grid of the parameters in the appendix formulas — as well as the way the spatial derivatives are calculated — depend on the grid definition. Auxiliary parameters are collocated with the fields that are being updated, e.g., the stress-rate tensor and the stress-rate sums are collocated with the velocity field, whereas the strain-rate tensor and the strain-rate sum are collocated with the stress field.

REFERENCES

Bérenger, J. P., 1994, A perfectly matched layer for absorption of electromagnetic waves: Journal of Computational Physics, **114**, 185–200.

———, 2002a, Application of the CFS PML to the absorption of evanescent waves in waveguides: IEEE Microwave and Wireless Components Letters, **12**, 218–220.

———, 2002b, Numerical reflection from FDTD-PMLs: A comparison of the split PML with the unsplit and CFS PMLs: IEEE Transactions on Antennas and Propagation, **50**, 258–265.

Cerjan, C., D. Kosloff, R. Kosloff, and M. Reshef, 1985, A non-reflecting boundary condition for discrete acoustic and elastic wave equation: Geophysics, **50**, 705–708.

Chew, W. C., and Q. H. Liu, 1996, Perfectly matched layers for elastodynamics: A new absorbing boundary condition: Journal of Computational Acoustics, **4**, 341–359.

Clayton, R., and B. Engquist, 1977, Absorbing boundary conditions for acoustic and elastic wave equations: Bulletin of the Seismological Society of America, **67**, 1529–1540.

Collino, F., and C. Tsogka, 2001, Application of the perfectly matched absorbing layer model to the linear elastodynamic problem in anisotropic heterogeneous media: Geophysics, **68**, 294–307.

Gedney, S. D., 1998, The perfectly matched layer absorbing medium, *in* A. Taflove, ed., Advances in computational electrodynamics: The finite-difference time-domain method: Artech House.

Hastings, F. D., J. B. Schneider, and S. L. Broschat, 1996, Application of the perfectly matched layer (PML) absorbing boundary condition to elastic wave propagation: Journal of the Acoustical Society of America, **100**, 3061–3069.

Higdon, R. L., 1991, Absorbing boundary condition for elastic waves: Geophysics, **56**, 231–241.

Kuzuoglu, M., and R. Mittra, 1996, Frequency dependence of the constitutive parameters of causal perfectly matched anisotropic absorbers: IEEE Microwave and Guided Wave Letters, **6**, 447–449.

Liao, Z. P., H. L. Wong, B. P. Yang, and Y. F. Yuan, 1984, A transmitting boundary for transient wave analysis: Scientia Sinica, **27**, 1063–1076.

Peng, C. B., and M. N. Töksoz, 1995, An optimal absorbing boundary condition for elastic wave modeling: Geophysics, **60**, 296–301.

Randall, C. J., 1989, Absorbing boundary condition for the elastic wave equation: Velocity-stress formulation: Geophysics, **54**, 1141–1152.

Roden, J. A., and S. D. Gedney, 2000, Convolutional PML (CPML): An efficient FDTD implementation of the CFS-PML for arbitrary media: Microwave and Optical Technology Letters, **27**, 334–339.

Sacks, Z. S., D. M. Kingsland, R. Lee, and J. F. Lee, 1995, A perfectly matched anisotropic absorber for use as an absorbing boundary condition: IEEE Transactions on Antennas and Propagation, **43**, 1460–1463.

Saenger, E. H., and T. Bohlen, 2004, Finite-difference modeling of viscoelastic and anisotropic wave propagation using the rotated staggered grid: Geophysics, **69**, 583–591.

Saenger, E. H., N. Gold, and S. A. Shapiro, 2000, Modeling the propagation of elastic waves using a modified finite-difference grid: Wave Motion, **31**, 77–92.

Sochacki, J., R. Kubichek, J. George, W. R. Fletcher, and S. Smithson, 1987, Absorbing boundary conditions and surface waves: Geophysics, **52**, 60–71.

Taflove, A., and S. C. Hagness, 2000, Computational electrodynamics: The finite-difference time-domain method: Artech House.

Virieux, J., 1986, P-SV wave propagation in heterogeneous media: Velocity-stress finite-difference method: Geophysics, **51**, 889–901.

Wang, T., and X. Tang, 2003, Finite-difference modeling of elastic wave propagation: A nonsplitting perfectly matched layer approach: Geophysics, **68**, 1749–1755.

Available online at www.sciencedirect.com
ScienceDirect
Wave Motion 44 (2007) 593–604
WAVE MOTION
www.elsevier.com/locate/wavemoti

Complex frequency shifted convolution PML for FDTD modelling of elastic waves

Francis H. Drossaert *, Antonios Giannopoulos

Institute for Infrastructure and Environment, University of Edinburgh, King's Building, Edinburgh EH9 3JL, United Kingdom

Received 14 September 2006; received in revised form 24 January 2007; accepted 13 March 2007
Available online 25 March 2007

Abstract

The perfectly matched layer (PML) is nowadays considered as the best optimum absorbing boundary condition available. However, the PML with the classical stretching tensor has certain limitations. Strangely, these limitations have rarely been addressed in elastic wave modelling. For example, substantial reflections occur when strong evanescent waves are propagating parallel to the interface. To circumvent problems like this, the complex frequency shifted stretching tensor has been introduced in electromagnetic modelling. In this paper we show that the convolution PML with this stretching tensor as used in electromagnetic modelling can be adapted for elastic wave modelling. Numerical results of a model where the presence of evanescent waves is predominant show that the PML based on the complex frequency shifted stretching tensor can improve the performance of the absorbing boundary layer considerably.

Keywords: Perfectly matched layer (PML); Boundary condition; Numerical modelling

1. Introduction

In the numerical modelling of elastic waves, absorbing boundary conditions are used to mitigate spurious reflections caused by the truncation of the model. Numerous techniques have been developed to circumvent this problem. Unfortunately, most absorbing boundary condition techniques are not very effective at all angles of incidence and often exhibit instabilities. In 1996 Bérenger [1] introduced a stable absorbing boundary condition for electromagnetic wave modelling, which has the remarkable property that it effectively absorbs wave energies impinging on it at a wide range of incident angles and frequencies. In a continuous domain Bérenger's boundary condition causes no reflection at the interface between the absorbing layer and the interior; hence the name perfectly matched layer (PML). Although small reflections can occur due to the discretization of the equations, the PML is nowadays generally considered to be the optimal available absorbing boundary condition. Chew and Liu [2] and Hastings [3] independently demonstrated that it can also effectively be used to absorb elastic waves.

* Corresponding author.
E-mail addresses: F.Drossaert@ed.ac.uk (F.H. Drossaert), A.Giannopoulos@ed.ac.uk (A. Giannopoulos).

0165-2125/$ - see front matter © 2007 Elsevier B.V. All rights reserved.
doi:10.1016/j.wavemoti.2007.03.003

One of the formulations of the PML is based on the concept of coordinate stretching. The basic principle of this formulation is that space in the boundary layer is stretched by a complex tensor in such a way that the damping affects only the orthogonal wave field components. In the finite-difference time-domain (FDTD) modelling of elastic waves the conventional method to solve for the stretched wave propagation equations requires splitting the wave field components. The equations in the boundary layer are different from the ones in the interior and hence two different sets of equations have to be solved for.

Wang and Tang [4] introduced a non-split PML (NPML) for elastic wave modelling and showed that non-split formulations can be used such that the PML acts as a perturbation to the original wave propagation equations. In their formulation the stretched wave propagation equations are transformed directly into the time domain resulting into equations containing convolution terms. A different non-split approach (RIPML) has been proposed by Drossaert and Giannopoulos [5] where the coupled stress–velocity wave propagation equations are rewritten as a four coupled system of equations by introducing two auxiliary tensors. In the time domain these tensors are simply solved by approximating their integrals by the Trapezoidal integration rule. Although, in the latter paper, the PML is not formulated as a perturbation it can easily be modified to do so. Also, in the same paper it has been shown that PMLs using the classical stretching function have a degradation in performance in certain cases such as when modelling elongated domains. This phenomenon has also been observed in electromagnetic wave modelling [6]. To circumvent a problem like this, Kuzuoglu and Mittra [7] introduced the complex frequency shifted (CFS) stretching tensor, which can improve the performance of the PML. Drossaert and Giannopoulos [5] showed that this stretching tensor can be adopted in their FDTD formulation and that it can dramatically enhance the performance of the PML when modelling an elongated domain. In finite element modelling of elastic waves similar non-classical stretching functions have been used to absorb evanescent waves [8,9].

In this paper we derive the formulation for the PML using a similar approach as Wang and Tang's and replace the classical stretching tensor by the CFS tensor. However, in this paper we solve for the convolution terms by adopting the recursive convolution technique (CPML) as proposed by Roden and Gedney [10] resulting in an efficient algorithm. In order to avoid confusion we refer our approach as the complex frequency shifted convolution perfectly matched layer (CFS CPML). The chosen approach, whether the NPML, RIPML, CPML or a possible ADEPML [11] should not affect the performance of the PML as long as the operators have the same order of accuracy. In order to demonstrate the performance of the CFS CPML we show an example of modelling strongly evanescent waves.

2. Formulation of the CFS CPML

For brevity we deduce the formulas for the complex frequency shifted convolution perfectly matched layer (CFS CPML) in a general 3D first-order velocity–stress system [12] using the indicial notation. Using this notation, the stretched velocity–stress equations in the boundary layer can simply be written in the frequency domain as

$$\begin{aligned} \mathrm{i}\omega\rho\tilde{v}_j &= \frac{1}{\varepsilon_k}\frac{\partial\tilde{\tau}_{jk}}{\partial x_k} \\ \mathrm{i}\omega\tilde{\tau}_{jk} &= C_{jklm}\frac{1}{\varepsilon_m}\frac{\partial\tilde{v}_l}{\partial x_m}, \quad \text{where } j,k,l,m = x,y,z \end{aligned} \tag{1}$$

where v and τ are the velocity and stress fields and where the tilde denotes their frequency domain counterpart; ρ, C are the density and the elasticity tensor. ε denotes the complex stretching tensor. The classical stretching tensor which is commonly used in elastic wave modelling [2,3] can lead to large reflections for waves with long time interaction with the PML zone such low incident, low frequency and evanescent waves. One reason for the large reflections is that the classical tensor becomes singular for low frequencies. In electromagnetic wave modelling, it was found that the CFS stretching tensor can overcome these limitations by shifting the singularity in the tensor off the real-axis into the negative imaginary half of the complex plane. This improves the performance of the PML [7]. This tensor can be written as

$$\varepsilon_k = \kappa_k + \frac{\sigma_k}{\alpha_k + \mathrm{i}\omega} \tag{2}$$

Note that by setting the attenuation coefficients α and κ to 0 and 1, respectively, we obtain the classical stretching tensor. It has been shown that the CFS tensor is both causal and stable assuming that $\alpha \geqslant 0$, $\kappa \geqslant 1$ and $\sigma \geqslant 0$ and that their values are real [13].

The PML formulation states that only the orthogonal field components are absorbed in the boundary layer and that the parallel field components are unaffected. Therefore the attenuation coefficients inside the PML and parallel to the PML interface α, κ and σ have to be set to 0, 1 and 0, respectively, to obtain normal wave propagation in the parallel direction e.g., $\alpha_x = 0$, $\kappa_x = 1$, $\sigma_x = 0$, $\alpha_z > 0$, $\kappa_z > 1$ and $\sigma_z > 0$ for PML boundary layer with z-normal interface boundaries. Furthermore, in order to avoid spurious reflections due to discretization of the space domain, the attenuation coefficients α, κ and σ need to be polynomialy scaled [10].

In order to solve for the velocity–stress equations (1) we adopt the Roden and Gedney [10] approach for electromagnetic wave modelling and convert it to elastic wave equations. Their adopted approach is based a recursive-convolution technique [14,15] which leads to a computational efficient set of equations. The first step in the deduction is to transform the equations back into the time domain making use of the following relation

$$F^{-1}\left(\frac{1}{\varepsilon_k}\frac{\partial}{\partial x_k}\right) = F^{-1}\left(\frac{1}{\left(\kappa_k + \frac{\sigma_k}{\alpha_k + i\omega}\right)}\frac{\partial}{\partial x_k}\right) = \left(\frac{\delta(t)}{\kappa_k} - \frac{\sigma_k}{\kappa_k^2}e^{-\left(\frac{\sigma_k}{\kappa_k}+\alpha_k\right)t}\right) * \frac{\partial}{\partial x_k} \tag{3}$$

where F^{-1} is inverse Fourier transform and $*$ denotes a convolution operator. Since the convolution of a function with a Dirac delta function is the function itself the velocity–stress equations can simply be written as

$$\begin{aligned} \rho\frac{\partial v_j}{\partial t} &= \frac{1}{\kappa_k}\frac{\partial \tau_{jk}}{\partial x_k} + \zeta_k * \frac{\partial \tau_{jk}}{\partial x_k} \\ \frac{\partial \tau_{jklm}}{\partial t} &= C_{jklm}\left(\frac{1}{\kappa_m}\frac{\partial v_l}{\partial x_m} + \zeta_m * \frac{\partial v_l}{\partial x_m}\right) \end{aligned} \tag{4}$$

where,

$$\zeta_k = -\frac{\sigma_k}{\kappa_k^2}e^{-\left(\frac{\sigma_k}{\kappa_k}+\alpha_k\right)t} \tag{5}$$

Implementing the discrete convolutions straightforwardly would be computationally too expensive in terms of memory and number of floating point operators. To solve the equations, Wang and Tang [4] rewrites the convolution terms as integrals and approximate these integrals by the Trapezoidal rule. Although their formulation does not include the CFS stretching function it can easily be modified to do so. In this paper, however, the convolution terms are approximated by a recursive-convolution technique. Roden and Gedney [10] showed that the form of $\zeta_k(t)$ allows the convolution of it with a spatial derivative to be approximated by the recursive-convolution technique [14,15]. Using this technique the convolution operators in the equations can be approximated in the discretized time domain at time step n as

$$\begin{aligned} \Psi_{ij}^n &= \zeta_j(n\Delta t) * \frac{\partial \tau_{ij}(n\Delta t)}{\partial x_j} \approx b_j \Psi_{ij}^{n-1} + c_j \frac{\partial \tau_{ij}^n}{\partial x_j} \\ \Omega_{ij}^n &= \zeta_j(n\Delta t) * \frac{\partial v_i(n\Delta t)}{\partial x_j} \approx b_j \Omega_{ij}^{n-1} + c_j \frac{\partial v_i^n}{\partial x_j} \end{aligned} \tag{6}$$

where the multiplication factors are given by

$$\begin{aligned} b_j &= e^{-\left(\frac{\sigma_j}{\kappa_j}+\alpha_j\right)} \\ c_j &= \frac{\sigma_j}{\sigma_j\kappa_j + \kappa_j^2\alpha_j}\left(e^{-\left(\frac{\sigma_j}{\kappa_j}+\alpha_j\right)} - 1\right) \end{aligned} \tag{7}$$

The recursive convolution tensors Ψ and Ω are discrete variables and need to be calculated before the update of the velocity and stress fields. These tensors are collocated with their associated field in the time domain e.g. Ψ_{xx} is collocated with v_x and Ω_{xz} is collocated with τ_{xz}. Unlike the stress field tensor these auxiliary tensors are

not symmetrical. To solve the auxiliary tensors by equations, their values at the previous time step and the spatial derivatives at the present time step are required. In the NPML formulation by Wang and Tang [4] the calculation of their auxiliary tensors requires in addition the spatial derivatives at the previous time step. This can potentially lead to a more complicated or less effective implementation of the PML.

The wave propagation equations (4) can now be simply written as

$$\begin{aligned}\rho\frac{\partial v_j}{\partial t} &= \frac{1}{\kappa_k}\frac{\partial \tau_{jk}}{\partial x_k} + [\Psi_{jk}]\\ \frac{\partial \tau_{jk}}{\partial t} &= C_{jklm}\frac{1}{\kappa_m}\frac{\partial v_l}{\partial x_m} + \left[C_{jklm}\Omega_{lm}\right]\end{aligned} \tag{8}$$

In an efficient implementation of a PML it is beneficial to formulate it as a perturbation to the original wave propagation equation in order to take into account the effect of the boundary layer. This can easily be achieved by rewriting the inverse of κ such that the wave propagation equations become

$$\begin{aligned}\rho\frac{\partial v_j}{\partial t} &= \frac{\partial \tau_{jk}}{\partial x_k} + \left[\frac{1-\kappa_k}{\kappa_k}\frac{\partial \tau_{jk}}{\partial x_k} + \Psi_{jk}\right]\\ \frac{\partial \tau_{jk}}{\partial t} &= C_{jklm}\frac{\partial v_l}{\partial x_m} + \left[\frac{1-\kappa_m}{\kappa_m}\frac{\partial v_l}{\partial x_m} + \Omega_{lm}\right]\end{aligned} \tag{9}$$

The terms between the square brackets act as perturbations to the original wave propagation equations. Unlike the CPML formulation by Roden and Gedney [10], this formulation does not involve the attenuations coefficient κ in the original equations. Therefore its implementation in a computer code becomes more refined and easier. Furthermore for large models where the interior domain is substantially larger than the boundary layers this can lead to a reduction in total number floating point operators and thus computation time.

The calculation of the convolution tensors requires their value at the previous time step, hence it is necessary that Ψ and Ω tensors are stored in the memory. Note for example that b_z and c_z are 1 and 0, respectively, in the PML zone with the x-normal interface and hence the tensor components Ψ_{xz} and Ψ_{zz} in this PML are never updated. Therefore it is not necessary to calculate and store all the components of the Ψ field in every PML zone, which can lead to a considerable reduction in the total memory space and number of floating point operators. Drossaert and Giannopoulos [5] demonstrated that an efficient implementation of a RIPML requires less memory than the conventional split field PML. Since the CFS CPML requires the same number of variables to be stored in the memory as the RIPML it is just as efficient in terms of memory. For large 3D models, the memory required for the CFS CPML boundary layers can be 12% less than the memory required for the conventional split-field PML.

3. FDTD implementation of the CFS CPML for elastic wave modelling

In this section the discretized implementation of the CFS CPML for a 2D isotropic media is presented. This implementation is based on the rotated staggered grid [16] where the derivatives are approximated with central differences, resulting in second order FDTD scheme. The rotated staggered grid can be useful for modelling strong heterogeneous media, such as voids in the earth. The formulation can easily be modified to be based on other grid definitions such as the more common Virieux grid [12]. This scheme can easily be extended to higher orders schemes.

In our implementation the stresses are updated a half time step after the update of the velocity. The first step in our formulation is to update the velocity field in the whole computational domain, including the boundary layer, using the following equations

$$\begin{aligned}v_{xi,j}^{n+\frac{1}{2}} &= v_{xi,j}^{n-\frac{1}{2}} + \frac{\Delta t}{\rho_{i,j}}\left(\left.\frac{\partial \tau_{xx}^{n}}{\partial x}\right|_{i,j} + \left.\frac{\partial \tau_{xz}^{n}}{\partial z}\right|_{i,j}\right)\\ v_{zi,j}^{n+\frac{1}{2}} &= v_{zi,j}^{n-\frac{1}{2}} + \frac{\Delta t}{\rho_{i,j}}\left(\left.\frac{\partial \tau_{xz}^{n}}{\partial x}\right|_{i,j} + \left.\frac{\partial \tau_{zz}^{n}}{\partial z}\right|_{i,j}\right)\end{aligned} \tag{10}$$

Note that the subscripts i and j now denote the location of the variable in the grid. The Δt is the time step complying to the Neumann stability condition.

After the update of the velocity in the whole domain, the velocity field in the boundary layers needs to be perturbed in order to take into account the CFS CPML. The first step is to calculate the required convolution tensors in boundary layer

$$\begin{aligned}
\Psi^{n}_{xxi,j} &= b_{xi,j}\Psi^{n-1}_{xxi,j} + c_{xi,j}\left.\frac{\partial \tau^{n}_{xx}}{\partial x}\right|_{i,j} \\
\Psi^{n}_{xzi,j} &= b_{zi,j}\Psi^{n-1}_{xzi,j} + c_{zi,j}\left.\frac{\partial \tau^{n}_{xz}}{\partial z}\right|_{i,j} \\
\Psi^{n}_{zxi,j} &= b_{xi,j}\Psi^{n-1}_{zxi,j} + c_{xi,j}\left.\frac{\partial \tau^{n}_{xz}}{\partial x}\right|_{i,j} \\
\Psi^{n}_{zzi,j} &= b_{zi,j}\Psi^{n-1}_{zzi,j} + c_{zi,j}\left.\frac{\partial \tau^{n}_{zz}}{\partial z}\right|_{i,j}
\end{aligned} \tag{11}$$

In our formulation we make use of the fact that the stress tensor is symmetrical. Note that the convolution tensors are not symmetrical. In the same computational loop of the update the above convolution tensor the velocity field is now be perturbed by

$$\begin{aligned}
v^{n+\frac{1}{2}}_{xi,j} &= v^{n+\frac{1}{2}}_{xi,j} + \frac{\Delta t}{\rho_{i,j}}\left(d_{xi,j}\left.\frac{\partial \tau^{n}_{xx}}{\partial x}\right|_{i,j} + \Psi^{n}_{xxi,j} + d_{zi,j}\left.\frac{\partial \tau^{n}_{xz}}{\partial z}\right|_{i,j} + \Psi^{n}_{xzi,j}\right) \\
v^{n+\frac{1}{2}}_{zi,j} &= v^{n+\frac{1}{2}}_{zi,j} + \frac{\Delta t}{\rho_{i,j}}\left(d_{xi,j}\left.\frac{\partial \tau^{n}_{xz}}{\partial x}\right|_{i,j} + \Psi^{n}_{zxi,j} + d_{zi,j}\left.\frac{\partial \tau^{n}_{zz}}{\partial z}\right|_{i,j} + \Psi^{n}_{zzi,j}\right)
\end{aligned} \tag{12}$$

It should be pointed out that these perturbation formulas are not a time update, since the velocity field on the right hand is the same as the velocity field on the left hand side of the equation.

In the rotated staggered grid definition the stresses are located in the middle of the grid cell and are updated half time step after the velocity update. The stress field in whole computational domain can be updated as

$$\begin{aligned}
\tau^{n+1}_{xxi+\frac{1}{2},j+\frac{1}{2}} &= \tau^{n}_{xxi+\frac{1}{2},j+\frac{1}{2}} + \Delta t\left(\left(\lambda_{i+\frac{1}{2},j+\frac{1}{2}} + 2\mu_{i+\frac{1}{2},j+\frac{1}{2}}\right)\left(\left.\frac{\partial v_x^{n+\frac{1}{2}}}{\partial x}\right|_{i+\frac{1}{2},j+\frac{1}{2}}\right) + \lambda_{i+\frac{1}{2},j+\frac{1}{2}}\left(\left.\frac{\partial v_z^{n+\frac{1}{2}}}{\partial z}\right|_{i+\frac{1}{2},j+\frac{1}{2}}\right)\right) \\
\tau^{n+1}_{xzi+\frac{1}{2},j+\frac{1}{2}} &= \tau^{n}_{xzi+\frac{1}{2},j+\frac{1}{2}} + \Delta t\left(\mu_{i+\frac{1}{2},j+\frac{1}{2}}\left(\left.\frac{\partial v_z^{n+\frac{1}{2}}}{\partial x}\right|_{i+\frac{1}{2},j+\frac{1}{2}} + \left.\frac{\partial v_x^{n+\frac{1}{2}}}{\partial z}\right|_{i+\frac{1}{2},j+\frac{1}{2}}\right)\right) \\
\tau^{n+1}_{zzi+\frac{1}{2},j+\frac{1}{2}} &= \tau^{n}_{zzi+\frac{1}{2},j+\frac{1}{2}} + \Delta t\left(\left(\lambda_{i+\frac{1}{2},j+\frac{1}{2}} + 2\mu_{i+\frac{1}{2},j+\frac{1}{2}}\right)\left(\left.\frac{\partial v_z^{n+\frac{1}{2}}}{\partial z}\right|_{i+\frac{1}{2},j+\frac{1}{2}}\right) + \lambda_{i+\frac{1}{2},j+\frac{1}{2}}\left(\left.\frac{\partial v_x^{n+\frac{1}{2}}}{\partial x}\right|_{i+\frac{1}{2},j+\frac{1}{2}}\right)\right)
\end{aligned} \tag{13}$$

Similar to the calculation of the velocity field in the boundary zone, the convolution tensors need to be updated before the stress field can be perturbed.

$$
\begin{aligned}
\Omega^{n+\frac{1}{2}}_{xxi+\frac{1}{2},j+\frac{1}{2}} &= b_x \Omega^{n-\frac{1}{2}}_{xxi+\frac{1}{2},j+\frac{1}{2}} + c_x \left.\frac{\partial v_x^{n+\frac{1}{2}}}{\partial x}\right|_{i+\frac{1}{2},j+\frac{1}{2}} \\
\Omega^{n+\frac{1}{2}}_{xzi+\frac{1}{2},j+\frac{1}{2}} &= b_z \Omega^{n-\frac{1}{2}}_{xzi+\frac{1}{2},j+\frac{1}{2}} + c_z \left.\frac{\partial v_x^{n+\frac{1}{2}}}{\partial z}\right|_{i+\frac{1}{2},j+\frac{1}{2}} \\
\Omega^{n+\frac{1}{2}}_{zxi+\frac{1}{2},j+\frac{1}{2}} &= b_x \Omega^{n-\frac{1}{2}}_{zxi+\frac{1}{2},j+\frac{1}{2}} + c_x \left.\frac{\partial v_z^{n+\frac{1}{2}}}{\partial x}\right|_{i+\frac{1}{2},j+\frac{1}{2}} \\
\Omega^{n+\frac{1}{2}}_{zzi+\frac{1}{2},j+\frac{1}{2}} &= b_z \Omega^{-\frac{1}{2}}_{zzi+\frac{1}{2},j+\frac{1}{2}} + c_z \left.\frac{\partial v_z^{n+\frac{1}{2}}}{\partial z}\right|_{i+\frac{1}{2},j+\frac{1}{2}}
\end{aligned}
\tag{14}
$$

and the stress field in the CFS CPML is perturbed using the following equations

$$
\begin{aligned}
\tau^{n+1}_{xxi+\frac{1}{2},j+\frac{1}{2}} &= \tau^{n+1}_{xxi+\frac{1}{2},j+\frac{1}{2}} + \Delta t \left(\left(\lambda_{i+\frac{1}{2},j+\frac{1}{2}} + 2\mu_{i+\frac{1}{2},j+\frac{1}{2}}\right) \left(c_{xi+\frac{1}{2},j+\frac{1}{2}} \left.\frac{\partial v_x^{n+\frac{1}{2}}}{\partial x}\right|_{i+\frac{1}{2},j+\frac{1}{2}} + \Omega^{n+\frac{1}{2}}_{xxi+\frac{1}{2},j+\frac{1}{2}} \right) \right. \\
&\quad \left. + \lambda \left(c_{zi+\frac{1}{2},j+\frac{1}{2}} \left.\frac{\partial v_z^{n+\frac{1}{2}}}{\partial z}\right|_{i+\frac{1}{2},j+\frac{1}{2}} + \Omega^{n+\frac{1}{2}}_{zzi+\frac{1}{2},j+\frac{1}{2}} \right) \right) \\
\tau^{n+1}_{xzi+\frac{1}{2},j+\frac{1}{2}} &= \tau^{n+1}_{xzi+\frac{1}{2},j+\frac{1}{2}} + \Delta t \mu_{i+\frac{1}{2},j+\frac{1}{2}} \left(c_{xi+\frac{1}{2},j+\frac{1}{2}} \left.\frac{\partial v_z^{n+\frac{1}{2}}}{\partial x}\right|_{i+\frac{1}{2},j+\frac{1}{2}} + \Omega^{n+\frac{1}{2}}_{zxi+\frac{1}{2},j+\frac{1}{2}} + c_{zi+\frac{1}{2},j+\frac{1}{2}} \left.\frac{\partial v_x^{n+\frac{1}{2}}}{\partial z}\right|_{i+\frac{1}{2},j+\frac{1}{2}} + \Omega^{n+\frac{1}{2}}_{xzi+\frac{1}{2},j+\frac{1}{2}} \right) \\
\tau^{n+1}_{zzi+\frac{1}{2},j+\frac{1}{2}} &= \tau^{n+1}_{zzi+\frac{1}{2},j+\frac{1}{2}} + \Delta t \left(\left(\lambda_{i+\frac{1}{2},j+\frac{1}{2}} + 2\mu_{i+\frac{1}{2},j+\frac{1}{2}}\right) \left(c_{xi+\frac{1}{2},j+\frac{1}{2}} \left.\frac{\partial v_z^{n+\frac{1}{2}}}{\partial z}\right|_{i+\frac{1}{2},j+\frac{1}{2}} + \Omega^{n+\frac{1}{2}}_{zzi+\frac{1}{2},j+\frac{1}{2}} \right) \right. \\
&\quad \left. + \lambda \left(c_{zi+\frac{1}{2},j+\frac{1}{2}} \left.\frac{\partial v_x^{n+\frac{1}{2}}}{\partial x}\right|_{i+\frac{1}{2},j+\frac{1}{2}} + \Omega^{n+\frac{1}{2}}_{xxi+\frac{1}{2},j+\frac{1}{2}} \right) \right)
\end{aligned}
\tag{15}
$$

The spatial derivatives of the velocity in a rotated staggered grid as used in equations (13)–(15) are obtained by

$$
\begin{aligned}
\left.\frac{\partial v_x^{n+\frac{1}{2}}}{\partial x}\right|_{i+\frac{1}{2},j+\frac{1}{2}} &= \frac{v^{n+\frac{1}{2}}_{xi+1,j+1} - v^{n+\frac{1}{2}}_{xi,j} + v^{n+\frac{1}{2}}_{xi+1,j} - v^{n+\frac{1}{2}}_{xi,j+1}}{2\Delta x} \\
\left.\frac{\partial v_x^{n+\frac{1}{2}}}{\partial z}\right|_{i+\frac{1}{2},j+\frac{1}{2}} &= \frac{v^{n+\frac{1}{2}}_{xi+1,j+1} - v^{n+\frac{1}{2}}_{xi,j} + v^{n+\frac{1}{2}}_{xi,j+1} - v^{n+\frac{1}{2}}_{xi+1,j}}{2\Delta z} \\
\left.\frac{\partial v_z^{n+\frac{1}{2}}}{\partial x}\right|_{i+\frac{1}{2},j+\frac{1}{2}} &= \frac{v^{n+\frac{1}{2}}_{zi+1,j+1} - v^{n+\frac{1}{2}}_{zi,j} + v^{n+\frac{1}{2}}_{zi+1,j} - v^{n+\frac{1}{2}}_{zi,j+1}}{2\Delta x} \\
\left.\frac{\partial v_z^{n+\frac{1}{2}}}{\partial z}\right|_{i+\frac{1}{2},j+\frac{1}{2}} &= \frac{v^{n+\frac{1}{2}}_{zi+1,j+1} - v^{n+\frac{1}{2}}_{zi,j} + v^{n+\frac{1}{2}}_{zi,j+1} - v^{n+\frac{1}{2}}_{zi+1,j}}{2\Delta z}
\end{aligned}
\tag{16}
$$

and the spatial derivatives of stresses used in equations (10)–(12) are defined as

$$
\begin{aligned}
\left.\frac{\partial \tau_{xx}^{n+1}}{\partial x}\right|_{i,j} &= \frac{\tau_{xxi+\frac{1}{2},j+\frac{1}{2}}^{n+1} - \tau_{xxi-\frac{1}{2},j-\frac{1}{2}}^{n+1} + \tau_{xxi+\frac{1}{2},j-\frac{1}{2}}^{n+1} - \tau_{xxi-\frac{1}{2},j+\frac{1}{2}}^{n+1}}{2\Delta x} \\
\left.\frac{\partial \tau_{xz}^{n+1}}{\partial z}\right|_{i,j} &= \frac{\tau_{xzi+\frac{1}{2},j+\frac{1}{2}}^{n+1} - \tau_{xzi-\frac{1}{2},j-\frac{1}{2}}^{n+1} + \tau_{xzi-\frac{1}{2},j+\frac{1}{2}}^{n+1} - \tau_{xzi+\frac{1}{2},j-\frac{1}{2}}^{n+1}}{2\Delta z} \\
\left.\frac{\partial \tau_{xz}^{n+1}}{\partial x}\right|_{i,j} &= \frac{\tau_{xzi+\frac{1}{2},j+\frac{1}{2}}^{n+1} - \tau_{xzi-\frac{1}{2},j-\frac{1}{2}}^{n+1} + \tau_{xzi+\frac{1}{2},j-\frac{1}{2}}^{n+1} - \tau_{xzi-\frac{1}{2},j+\frac{1}{2}}^{n+1}}{2\Delta x} \\
\left.\frac{\partial \tau_{zz}^{n+1}}{\partial z}\right|_{i,j} &= \frac{\tau_{zzi+\frac{1}{2},j+\frac{1}{2}}^{n+1} - \tau_{zzi-\frac{1}{2},j-\frac{1}{2}}^{n+1} + \tau_{zzi-\frac{1}{2},j+\frac{1}{2}}^{n+1} - \tau_{zzi+\frac{1}{2},j-\frac{1}{2}}^{n+1}}{2\Delta z}
\end{aligned}
\tag{17}
$$

The multiplication factors used in the above formulas in this section, for example the multiplication factors used in formula and are defined by

$$
\begin{aligned}
b_{xi,j} &= \mathrm{e}^{-\left(\frac{\sigma_{xi,j}}{\kappa_{xi,j}}+\alpha_{xi,j}\right)} \\
c_{xi,j} &= \frac{\sigma_{xi,j}}{\sigma_{xi,j}\kappa_{xi,j} + \kappa_{xi,j}^2\alpha_{xi,j}}\left(\mathrm{e}^{-\left(\frac{\sigma_{xi,j}}{\kappa_{xi,j}}+\alpha_{xi,j}\right)} - 1\right) \\
d_{xi,j} &= \frac{1-\kappa_{xi,j}}{\kappa_{xi,j}}
\end{aligned}
\tag{18}
$$

Similar multiplication factors can be derived for the z-direction by replacing x by z and for other grid locations by replacing i, j by $i + 1/2$, $j + 1/2$ and etcetera.

4. Modelling evanescent waves

In this section we present an elastic modelling case where PMLs without the CFS stretching tensor could lead to strong spurious reflections. The model we used comprises of a long elongated domain with a surface and three PML zones. Models like this can be used for earthquake hazard modelling, where large regions have to be modelled in order to assess the potential risks of earthquakes. It should be pointed out that the purpose of this example is merely to demonstrate the performance the CFS CPML. To decrease the size of the model and hence required memory space and calculation time we can opt for a thin slab model. However, similar to electromagnetic wave modelling, in elastic wave modelling strong evanescent waves with the wave propagation direction parallel to the boundary layer interface can result in very large reflections.

In order to demonstrate the performance of the CFS CPML we only model homogeneous material such that waves measured at the geophones are purely direct and surface waves and are not contaminated with refracted, reflected and diffracted waves. In Fig. 1 a schematic overview of the model is represented along with

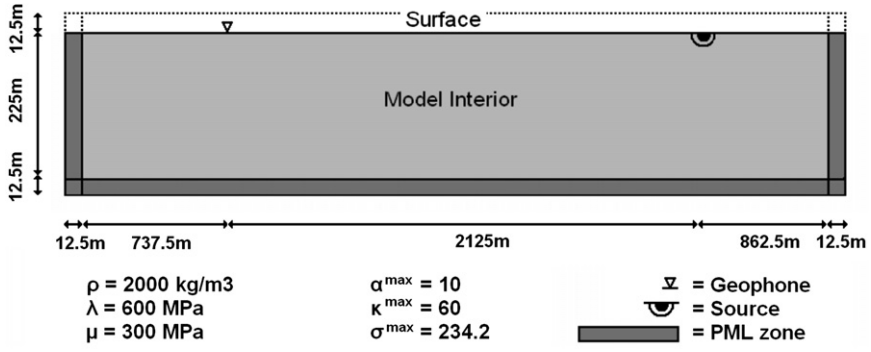

Fig. 1. Diagram of the model used in the example (not to scale).

the model parameters. The source used is a Gaussian shaped impulse force in the vertical direction with a centre frequency of 1.5 Hz. The space cell size is 2.5 m and the time step size is 3.2 ms.

In Fig. 2a and b, the synthetic seismograms computed at the geophone location as indicated in Fig. 1 can be found for the model with a CPML using the classical stretching tensor and the model with the CFS PML, respectively. In order to model the PML with the classical stretching function, we simply set $\alpha^{\max} = 0$ and $\kappa^{\max} = 1$ which reduces the CFS stretching tensor to the classical stretching tensor. For the CFS CPML model, we scaled the attenuation coefficients σ and κ by an increasing 2nd order polynomial function, whereas the attenuation coefficient α is scaled by a decreasing 2nd order polynomial function [10]. The maximum values for attenuation coefficients were chosen to be $\alpha^{\max} = 10$, $\kappa^{\max} = 25$ and $\sigma^{\max} = 232.4$.

In order to compare the results we calculated a reference seismogram using a sufficient large model such that boundary reflections do not interfere with the data. It is clear from Fig. 2a that the model without the CFS stretching function fails to model the surface waves correctly. The amplitudes of surface waves at about 6 s are modelled too high. Furthermore strong low frequency reflections can be found after the arrival of the surface waves. The synthetic seismogram of the model truncated by the PML based on the CFS stretching tensor (Fig. 2b) shows that the CFS CPML absorbs the evanescent waves considerably better. Although the amplitudes of the surface waves are slightly attenuated, the low frequency reflections do not appear in the seismogram.

Snapshots at 2.2 s of the same models with and without the CFS stretching tensor can be found in Fig. 3a and b, respectively. It is clear form Fig. 3a that PMLs with the classical stretching tensor is inadequate to absorb strongly evanescent waves. Evanescent waves are reflected at the PML interface and strong spurious low frequency waves come into existence. The snapshot of the model with the CFS CPML (Fig. 3b) does not show any strong reflections coming from the PML interface. Overall the performance of the CFS CPML is considerably better than the performance of CPML using the classical stretching function.

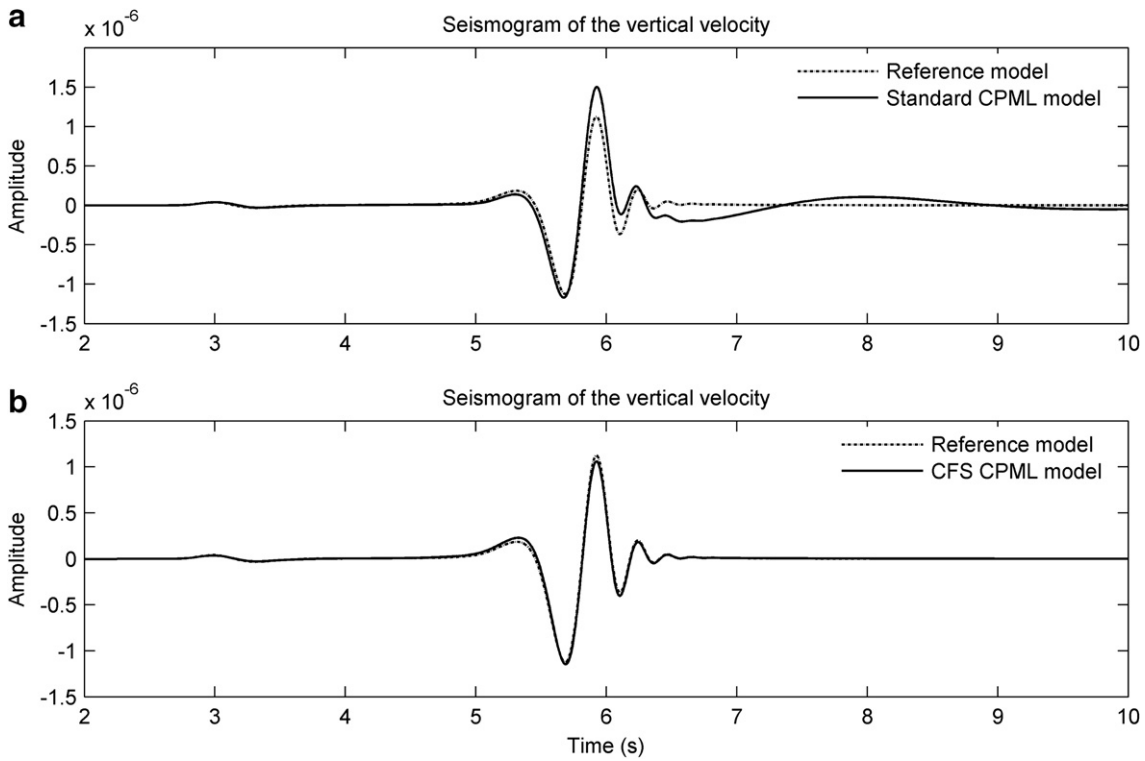

Fig. 2. Synthetic seismograms calculated at the geophone location for CPML model without the CFS stretching tensor (a) and the CFS CPML model (b).

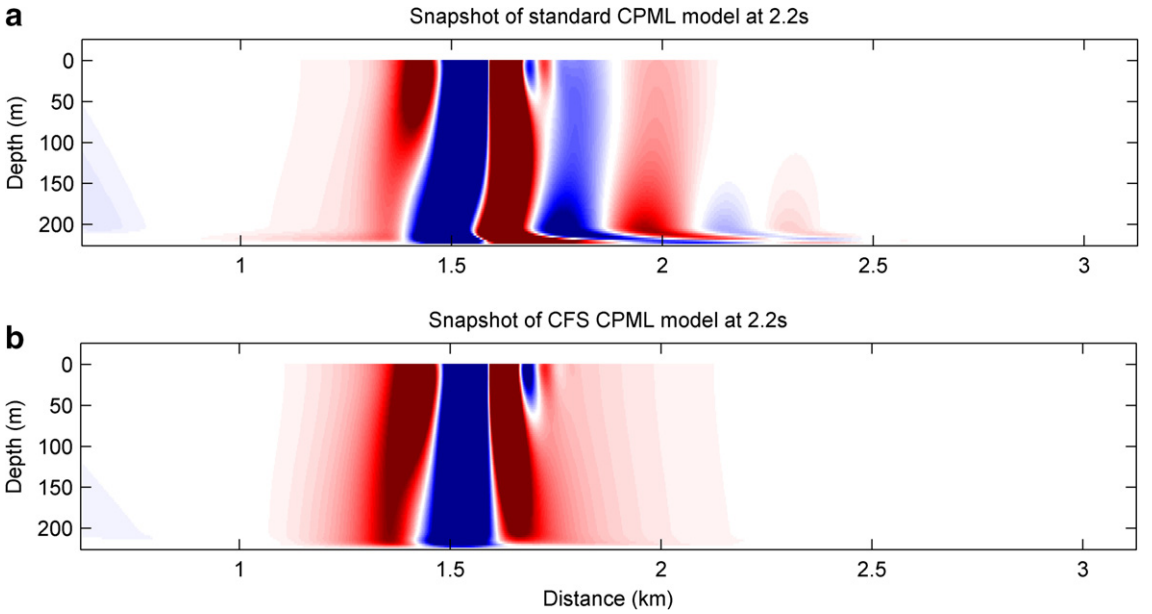

Fig. 3. Snapshots of both models with the CPML and the CFS CPML (not to scale). The amplitudes are scaled by a factor of 10.

5. Parametric analysis of the attenuation coefficients

In this section the behaviour of the attenuation coefficients α and κ are examined using the same model in the above example. For comparison a reference solution has been obtained using a sufficient large model with large absorbing boundaries layers such that evanescent waves cause no problem. An identical source is used and the field-observation points are located at the same position relative to the source as the model with the CFS CPML. A global error is then defined as a function of the maximum value of the attenuation coefficients, $\alpha^{\max}$ and $\kappa^{\max}$, as

$$\text{Global error}(\kappa^{\max}, \alpha^{\max}) = 20\log_{10}\left(\sum_t \sum_i \sum_j \left| v^t_{zi,j} - v^t_{zi,jref} \right| \right) \tag{19}$$

For the calculation of the global error, a set of grid points is selected which is representative for the whole model. Furthermore we define a local error along the horizontal line $(i,j = 85)$ as

$$\text{Local error}(i, \kappa^{\max}, \alpha^{\max}) = 20\log_{10}\left(\sum_t \left| v^t_{zi,85} - v^t_{zi,85ref} \right| \right) \tag{20}$$

The model used to calculate the errors is truncated by a 5-cell thick CFS CPML. The attenuation coefficients κ and σ are polynomial scaled with an order of 2. The optimum value for $\sigma^{\max}$ is calculated using the empirical formulas as used by Collino and Tsogka [17]. The attenuation coefficient α is reversely scaled with the same scaling order. The errors are calculated for a simulation time window of 12 s simulation. Fig. 4 represents the results of the calculations of the error. From Fig. 4a it can be found that the minimum global error is around -34 dB for this case and can be found for attenuation coefficients values of $\alpha^{\max} = 7$ and $\kappa^{\max} = 65$. The global error of a CPML without the CFS stretching function can simply be found by selecting $\alpha^{\max} = 0$ and $\kappa^{\max} = 1$. This global error of -20 dB is considerably larger than the minimum global error of around -34 dB.

From Fig. 4a, it can be observed that the global error depends strongly on the $\kappa^{\max}$ and in a lesser degree on the $\alpha^{\max}$. Although $\alpha^{\max}$ affects the global error less than the $\kappa^{\max}$, it is clear from the contour plot that using both attenuation coefficients can enhance the performance of the boundary condition.

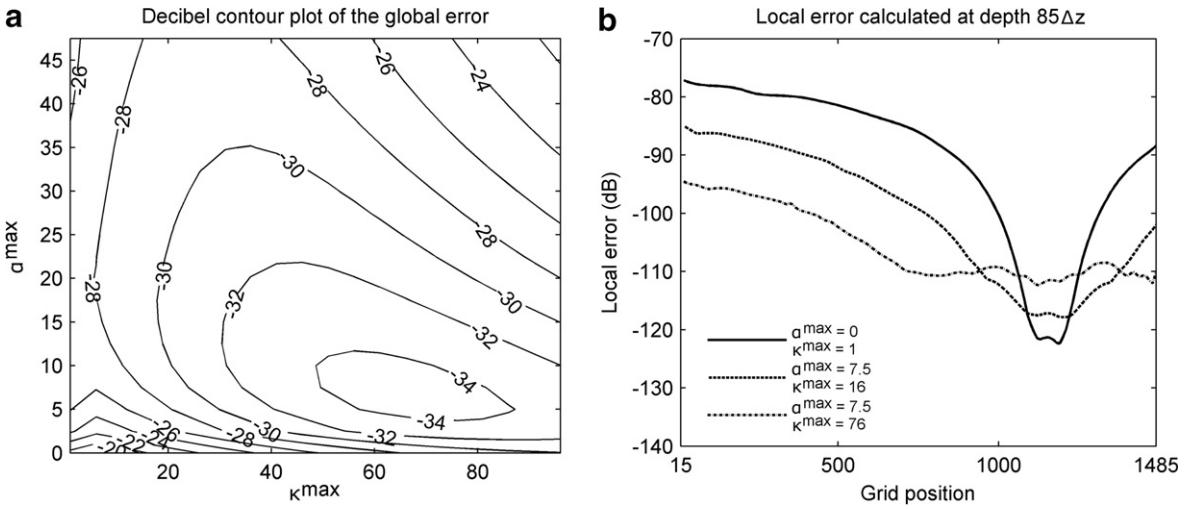

Fig. 4. Results of calculation of the error (a) decibel contour plot of the global error as function of the $\alpha^{\max}$ and $\kappa^{\max}$ where $\sigma^{\max}$ is kept constant; (b) plot of the local error for the grid points at $85\Delta z$.

In Fig. 4b the results of the calculation of the local error for various attenuation coefficients can be found. From this plot it can be concluded that the CPML without the CFS stretching function fails to model the evanescent wave correctly. Although it outperforms the CFS CPML near the source location, the local error increases rapidly further away from the source where evanescent waves are becoming more dominant and the local error reaches unacceptable levels. The CFS CPML absorbs the evanescent waves considerably better. By choosing suitable values for the attenuation coefficients the local errors can be kept as low as -95 dB. The price to pay for this enhancement of the performance is that the error close to the source increases. However, these error levels are still very acceptable.

In order to assess the effect of the thickness of the boundary layer, the local error has been calculated for boundary layer thickness of 3, 5, 7 and 10 cells. The size of the interior model remains constant. The results are calculated for the CPML without the CFS stretching function and for the CFS CPML. The attenuation coefficient $\sigma^{\max}$ is set to the optimum value and is the same for both PMLs and for CFS CPML we set $\alpha^{\max} = 8$ and $\kappa^{\max} = 60$.

Increasing the thickness of the boundary layer would normally lead to better absorption. From Fig. 5a it can be seen that the local error close to the location of the source decreases with increasing boundary layer

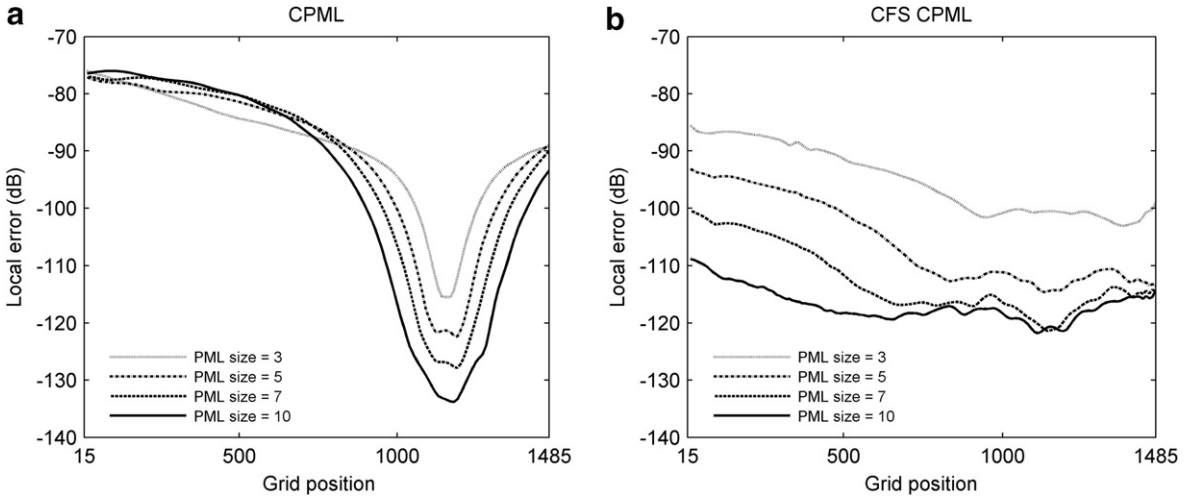

Fig. 5. Results of the calculation of the local error at the grid points at $85\Delta z$ for various thicknesses of the (a) CPML without the CFS stretching function and the (b) CFS CPML.

thickness. However, further away from the source evanescent waves become more dominant and the CPML fails to absorb these waves correctly. Remarkably, a thicker boundary layer does not lead to better performance for these evanescent waves. The 3-cell thick boundary layer actually absorbs the evanescent slightly better than the 10-cell thick layer. In Fig. 5b the local error of the CFS CPML can be observed. Although near the source the absorption is less compared to the CPML with the classical stretching function, the local error does not increase significantly when evanescent waves come into existence. Furthermore from Fig. 5b it can be observed that increasing the thickness of the CFS CPML does increase the performance. The 10-cell thick CFS CPML boundary layer performs excellent for all the existing waves and even absorbs the direct waves near source location adequately.

It should be mentioned that increasing the boundary layer thickness to 15 and 20 cells, the solutions suffered from depletion in accuracy and hence the performance of the absorbing boundary condition decreased slightly.

6. Discussion

In this paper, we showed that the CFS stretching tensor can be incorporated in the PML formulation for FDTD modelling of elastic waves. The approach taken here follows mostly the convolution PML method by Roden and Gedney [10] for electromagnetic wave modelling. This method makes use of the recursive convolution technique, resulting in an effective implementation of a PML with a CFS stretching tensor. It has been demonstrated in this paper that the CFS CPML can formulated such that it acts as a perturbation to the original wave propagation equations without needing to rewrite these equations.

The numerical results in this paper show that the CFS CPML can effectively absorb strong evanescent waves where the standard PML will create spurious reflections. This can lead to considerable reduction in the required size of the model and hence a reduction to the computational resources. Furthermore, although not demonstrated in this paper, the CFS CPML can be used to mitigate waves with long time interaction with the PML interface for example waves impinging the PML interface at very low angle and very low frequency waves. From the numerical analysis of the attenuation coefficients it can be concluded that including the CFS stretching tensor decreases the absorption of non-evanescent waves close to the source. However, this error is still acceptable. When evanescent waves become dominant and traversing through the boundary layer, the PML without the CFS stretching tensor fail to absorb these waves correctly and the global error becomes unacceptable large. Remarkably, increasing the thickness of a PML which is based on the classical stretching tensor does not increase the absorption performance for evanescent waves, whereas the CFS CPML performs better with increasing boundary layer thickness. In the model presented in this paper, a 10-cell thick CFS CPML has an excellent absorption of body waves as well as evanescent waves.

7. Conclusion

In this paper it has been shown that the CFS CPML as used in the electromagnetic wave modelling can be used in elastic wave modelling and that it can considerably enhance the performance of the boundary condition when strong evanescent waves are present. Since the CFS CPML does not require more memory nor does it require more calculations compared to the CPML without CFS stretching tensor, it is an attractive absorbing boundary condition which provides the user more options to improve the performance when compared to PMLs with the classical stretching tensor.

Acknowledgements

The authors thank Mike Forde, Peter Fenning and Dave McCann for their scientific contribution to the project. Furthermore we thank Network Rail for their funding and especially John Stothard and Brian Bell.

References

[1] J.P. Bérenger, A perfectly matched layer for absorption of electromagnetic waves, J. Comput. Phys. 114 (1994) 185–200.

[2] W.C. Chew, Q.H. Liu, Perfectly matched layers for elastodynamics: a new absorbing boundary condition, J. Comput. Acoustics 4 (1996) 341–359.
[3] F.D. Hastings, J.B. Schneider, S.L. Broschat, Application of the perfectly matched layer (PML) absorbing boundary condition to elastic wave propagation, J. Acoust. Soc. Am. 100 (1996) 3061–3069.
[4] T. Wang, X. Tang, Finite-difference modelling of elastic wave propagation: a nonsplitting perfectly matched layer approach, Geophysics 68 (2003) 1749–1755.
[5] F.H. Drossaert, A. Giannopoulos, A Non-split Complex Frequency Shifted PML based on recursive integration for FDTD modeling of elastic waves, Geophysics 72 (2007) 9.
[6] J.P. Bérenger, Application of the CFS PML to the absorption of evanescent waves in waveguides, IEEE Microw. Wireless Components Lett. 12 (2002) 218–220.
[7] M. Kuzuoglu, R. Mittra, Frequency dependence of the constitutive parameters of causal perfectly matched anisotropic absorbers, IEEE Microw. Guided Wave Lett. 6 (1996) 447–449.
[8] U. Basu, A.K. Chopra, Perfectly matched layers for transient elastodynamics of unbounded domains, Int. J. Numerical Methods Eng. 59 (2004) 1039–1074.
[9] U. Basu, A.K. Chopra, Perfectly matched layers for time-harmonic elastodynamics of unbounded domains: Theory and finite-element implementation, Comput. Methods Appl. Mech. Eng. 192 (2003) 1337–1375.
[10] J.A. Roden, S.D. Gedney, Convolutional PML (CPML): an efficient FDTD implementation of the CFS-PML for arbitrary media, Microw. Opt. Technol. Lett. 27 (2000) 334–339.
[11] O. Ramadan, Auxiliary differential equation formulation: an efficient implementation of the perfectly matched layer, IEEE Microw. Wireless Components Lett. 13 (2003) 69–71.
[12] J. Virieux, P-SV wave propagation in heterogeneous media: velocity–stress finite-difference method, Geophysics 51 (1986) 889–901.
[13] E. Bécache, P.G. Petropoulos, S.D. Gedney, On the long-time behavior of unsplit perfectly matched layers, IEEE Trans. Antennas Propagation 52 (2004) 1335–1342.
[14] L.R. Herrman, E.F. Peterson, A numerical procedure for visco-elastic stress analysis: 7th meeting of ICRPG mechanical behavior working group, (1968).
[15] R.J. Luebbers, F. Hunsberger, FDTD for *N*th-order dispersive media, IEEE Trans. Antennas Propagation 40 (1992) 1297–1301.
[16] E.H. Saenger, T. Bohlen, Finite-difference modeling of viscoelastic and anisotropic wave propagation using the rotated staggered grid, Geophysics 69 (2004) 583–591.
[17] F. Collino, C. Tsogka, Application of the perfectly matched absorbing layer model to the linear elastodynamic problem in anisotropic heterogeneous media, Geophysics 68 (2001) 294–307.